VAAL UNIVERSITY OF TECHNOLOGY

NOVEL NANOSTRUCTURED TERNARY METAL OXIDE COMPOSITE FOR SEQUESTRATION OF TRACE METALS FROM SIMULATED AQUEOUS SOLUTIONS.

ALBERT JERRY KAFUSHE KUPETA

Student number: 209134550

B.Sc, B.Tech, M.Tech (Chemistry)

Thesis submitted in fulfillment of the requirement for the degree of

DOCTOR OF TECHNOLOGY: CHEMISTRY

FACULTY OF APPLIED AND COMPUTER SCIENCES

DEPARTMENT OF CHEMISTRY

PROMOTER: Prof A.E. OFOMAJA (B.Sc Hons, M.Sc, D.Tech)

CO-PROMOTER: Prof E.B. NAIDOO (B.Sc Hons, M.Sc, Ph.D)

June 2020

DECLARATION

I declare that unless indicated, this thesis is my own, unaided work. It is being submitted for the degree Doctor of Technology to the Department of Chemistry, Vaal University of Technology, Vanderbijlpark, South Africa and has not been submitted before for any degree or examination to any other University.

Albert J.K. Kupeta on this *29th* day of *June* 2020

CANDIDATE

Eliazer B. Naidoo on this *29th* day of *June* 2020

CO-PROMOTER

DEDICATION

In memory of my late loving father, Maxwell.

ACKNOWLEDGEMENTS

I sincerely wish to express my profound appreciation and gratitude to the following for their various contributions:

- My doctorate promoters, the late Prof. A.E Ofomaja (may his soul rest in eternal peace) and Prof. E.B Naidoo for their educative and constructive comments, guidance, inputs, and support throughout this research.
- SASOL and Vaal University of Technology, through the Research & Higher Degrees Directorate for providing the research funding. The Department of Chemistry for providing the structures necessary for the research.
- Postgraduate students and postdoctoral fellows in the Biosorption & Wastewater Treatment Research Laboratory for creating an academic, supportive and friendly working environment.
- My dear mother, Enisia and siblings, Abigail, Ethel and Gerald, for their undying support and encouragement. Thank you for being my pillar of strength.
- My late father, Maxwell, for giving me a good education. Thank you daddy. I am because of you.
- God, the Almighty for giving me the strength and opportunity to tackle this herculean task.

PRESENTATIONS AND PUBLICATIONS

The work highlighted in this thesis has been presented at academic conferences and published in an international conference proceedings paper of the International Conference on Pure and Applied Chemistry (ICPAC).

CONFERENCE PRESENTATIONS

- KUPETA, A.J.K., NAIDOO, E.B. and OFOMAJA, A.E. International Conference on Pure and Applied Chemistry (ICPAC), Flic en Flac, Mauritius, July 2018, Oral presentation, *Preparation and application of Mn-Fe bimetal oxide for chromium removal*.

- KUPETA, A.J.K., NAIDOO, E.B. and OFOMAJA, A.E. 3rd VUT Interdisciplinary Research and Postgraduate Conference, Vanderbijlpark, South Africa, October 2018, Oral presentation, *Kinetic and equilibrium study on remediation of chromate ion infested industrial wastewater*.

PUBLICATION

- KUPETA, A.J.K., NAIDOO, E.B. and OFOMAJA, A.E. (2019) Chromate ion adsorption onto nanostructured Mn-Fe oxide: Kinetics and equilibrium study. In: *Chemistry for a Clean and Healthy Planet*. Springer, Cham. pp. 269-282.

ABSTRACT

A novel low-cost ternary Mn-Fe-Cu (MFC) metal oxide nanocomposite adsorbent was fabricated using facile co-precipitation method and successfully applied for the sequestration of Cr(VI) and As(III) from simulated aqueous efflent. The central composite design (CCD) of the response surface methodology (RSM) optimization technique determined the optimal working parameters for the preparation of the ternary MFC metal oxide nanocomposite. The spectroscopic microstructural analysis of the ternary MFC metal oxide nanocomposite was performed using fourier transform infrared (FTIR) spectroscopy, transmission electron microscopy (TEM), scanning electron microscopy (SEM), X-ray photoelectron spectroscopy (XPS) and X-ray diffraction (XRD) spectroscopy. The spectroscopic analyses revealed a rough surface with hydroxyl groups and the presence of mixed metal oxides in different valence states. The BET surface area, pore volume and pore size of the nanostructured MFC ternary metal oxide composite were found to be 77.2427 m^2/g, 0.2409 cm^3/g and 14.7560 nm, respectively. The pH drift method determined that the pH_{pzc} of the adsorbent was 6.75. The batch technique was employed to investigate the adsorption dynamics (effects of ionic strength, co-existing anions, adsorbent regeneration and reuse) and optimum parameters (solution pH, adsorbent dosage concentration, desorption) of Cr(VI) and As(III) adsorption onto the MFC nanocomposite. The fitting of non-linear kinetic (pseudo-first-order, pseudo-second-order and Elovich), diffusion (intraparticle and Boyd) and isotherm (Langmuir, Freundlich and Dubinin-Radushkevich) models to the Cr(VI) and As(III) experimental adsorption data gave an insight into the adsorption mechanisms. The Langmuir adsorption capacities, q_m (mg/g), were 168.71 at solution pH 3 and 35.07 at solution pH 9 for Cr(VI) and As(III) adsorption, respectively. The adsorption of Cr(VI) onto the ternary MFC metal oxide nanocomposite was physical and formed outer-sphere surface complexes through electrostatic interactions, while the removal of As(III) was specific due to inner-sphere surface complexation and ligand/ion exchange reactions. The results from XPS and FTIR analysis after the adsorption of Cr(VI) and As(III) showed that the surface hydroxyl groups on the MFC nanocomposite interacted with the Cr(VI) and As(III) species during the formation of the surface complexes. To facilitate ease of adsorbent removal from the treated simulated aqueous effluent, the ternary MFC metal oxide system was co-precipitated onto biochar support.

TABLE OF CONTENTS

LISTS OF ABBREVIATIONS AND SYMBOLS

Nomenclature

ε	Polanyi adsorption potential
α	Elovich initial adsorption rate constant at zero coverage
β	Elovich adsorption constant related to the degree of surface coverage and activation energy for chemisorption.
a	radius of sphere
C	thickness of the boundary layer or surface adsorption in intraparticle diffusion
C_d	adsorbate concentration in eluted solution after desorption
C_e	equilibrium concentration of adsorbate
C_o	initial adsorbate concentration
D_1	film diffusion coefficient
D_2	pore diffusion coefficient
E	D-R mean free energy
E_a	activation energy
h	the pseudo-second-order initial adsorption rate
k_1	pseudo-first-order rate constant
k_2	pseudo-second-order rate constant
k_{id}	intraparticle diffusion rate constant
K_{DR}	D–R constant related to the adsorption energy
K_F	Freundlich constant
k_s	external mass transfer diffusion rate constant
n	Freundlich intensity parameter
K_L	Langmuir adsorbate-adsorbent affinity constant
m	mass of the adsorbent
q_{DR}	D-R maximum adsorption capacity
q_e	adsorption capacity at equilibrium
q_e (exp)	experimental adsorption capacities at equilibrium
q_m	Langmuir maximum saturation monolayer adsorption capacity at equilibrium

q_t	adsorption capacity at time t
R^2	coefficient of determination
R	universal gas constant
R_L	dimensionless separation factor
$t^{0.5}$	the time in minutes raised to the power of 0.5
V	solution volume
$\% R$	percent removal
$\% var$	percent variance
ΔG^o	free Gibbs energy change
ΔH^o	enthalpy change
ΔS^o	change in entropy

Abbreviations

AAS	atomic absorption spectroscopy
BET	Brunauer-Emmett-Teller
BJH	Barrett-Joyna-Halenda
CCD	central composite design
DPC	1.5-diphenylcarbazide
EDS	electron dispersive X-ray spectroscopy
FTIR	fourier-transform infrared
ICP-OES	inductively coupled plasma-optical emission spectroscopy
ISE	ion selective electrode
K	Kelvin
MC	manganese-copper
MF	manganese-iron
MFC	manganese-iron-copper
MFCb	manganese-iron-copper-biochar
MCL	maximum contaminant level
pH_{pzc}	pH at point of zero charge
PFO	pseudo-first-order
PSO	pseudo-second-order
rpm	revolutions per minute
RSM	response surface methodology
SEM	scanning electron microscopy

SRB	sulphate-reducing bacteria
T	Kelvin temperature
TEM	transmission electron microscopy
USEPA	United States Environmental Protection Agency
UV-vis	UV-visible
WHO	World Health Organisation
XRD	X-ray diffraction
XPS	X-ray photoelectron spectroscopy

LISTS OF FIGURES

LISTS OF TABLES

CHAPTER 1

1 INTRODUCTION

1.1 BACKGROUND

The earth appears blue when viewed from space, a clear sign that a large proportion of it is water (Grey et al., 2013). Water constitutes approximately two-thirds of the earth, but less than one percent can sustain terrestrial life, inclusive of that locked in ice at the poles (Adeleye et al., 2016). Urbanisation and technological advancement have resulted in the effluent from industries, municipalities and agricultural activities laden with harmful inorganic and organic compounds being continually disposed of into fragile freshwater reservoirs (Ebrahiem et al., 2017; Marcos et al., 2020). Water scientists and engineers have forecasted that by 2025, half of the world's population might not have access to potable water since currently, only about a fifth of wastewater globally is undergoing proper decontamination (Zhang et al., 2016). This makes it critical to develop efficient wastewater treatment technologies which require low capital investment to save the small amounts of water fit for human use (Anjum et al., 2019). Water pollutants of particular concern are trace metals since they are not easily removed from solution using conventional methods (Carolin et al., 2017). Nanotechnology, through manipulation of mixed metal oxide nanoparticles, is showing great potential in providing alternative trace metal clean-up techniques. The nanoscale metal oxide composites have unique physicochemical characteristics due to quantum-size effects, large surface areas and have been utilised in the fields of catalysis, medicine, cosmetics, electronics, sensing, energy storage and thermal insulation among others (Yufanyi et al., 2015).

1.2 TRACE METALS

Trace metals exist in very small concentrations in the hydrosphere ($\leq$ 100 mg/dm^3 or ppm). Some of these trace metal elements are essential to life as they are needed in minute quantities (mg/kg) by flora and fauna as they form part of nutritional and physiological requirements (El-Ramady et al., 2016; Rose, 2016; Andresen et al., 2018). The list of trace metals includes among others: magnesium, zinc, selenium, arsenic, chromium, iron, vanadium, copper and cobalt (Burakov et al., 2018). Levels of trace metals above and below certain thresholds can be deleterious to humans causing pathological conditions. These metals are not biodegradable and

bioaccumulate in the ecological food chain (Akpor et al., 2014). The presence of high concentrations of trace metals, especially in the hydrosphere presents many environmental and human health challenges. The metals are highly toxic in their most stable oxidation states, eg. Cd(II), Cr(VI) and As(III) and can react with biomolecules forming very stable biotoxic compounds (Mishra et al., 2019). This promulgates the need for extensive research to develop efficient but affordable technologies for their sequestration to acceptable levels in water bodies especially in rural and underdeveloped communities (Chowdhury et al., 2016). The decontamination of As(III) and Cr(VI) laden wastewaters using a ternary metal oxide nanocomposite is recommended since the two trace metal ions are not easily removed from the hydrosphere using current conventional wet chemistry methods. Currently, the *modus operandi* of trace metal removal from an aqueous solution using metal oxides is poorly understood. To date, mostly mono and binary metal oxides have been utilised in the removal of trace metals from aqueous solution (Luo et al., 2013; Sani et al., 2017; Singh et al., 2018; Penke et al., 2019; Wei et al., 2019; Yu et al., 2019).

1.3 As(III) AND Cr(VI) ADSORPTION ONTO METAL OXIDES

Several researchers have utilised mono metal oxides like β-MnO_2 (Wei et al., 2019), TiO_2 (Yu et al., 2019), Fe_2O_3 and CeO_2 (Hua et al., 2012) for As(III) and Cr(VI) sequestration. The different forms of β-MnO_2 were fabricated using precipitation technique and showed As(III) adsorption capacities between 0.952 and 1.483 mg/g. The TiO_2 was prepared by precipitation and exhibited As(III) adsorption capacity of 36.6 mg/g. The Fe_2O_3 and CeO_2 were prepared with the sol-gel and precipitation methods, respectively and had Cr(VI) adsorption capacities of 17.0 and 15.4 mg/g, respectively.

Numerous researchers have also applied binary metal oxides including Fe-Mn (Li et al., 2012), Ti-Zr (Yu et al., 2019) and Fe-Zr (Wang et al., 2015) for the adsorption of As(III) and Cr(VI) ions from solution. The binary metal oxides show better adsorption activity than mono metal oxides. The mixed metal oxides are synergistic in their sequestration of metal ion pollutants. They do not just adsorb the metal species but are also able to oxidise or reduce them to less harmful or easily adsorbed forms, accounting for their superior adsorption capacities. The Fe-Mn and Ti-Zr binary metal oxides were prepared by precipitation method and had As(III) removal capacity of 44.91 and 61.0 mg/g, respectively. The Fe-Zr binary metal oxide composite was synthesized by templating on cetyltrimethylammoniumbromide (CTAB)

followed by coprecipitation and exhibited a Cr(VI) adsorption capacity of 44.91 mg/g. To emphasize the effectiveness of binary composites over mono metal oxide systems, manganese doped goethite prepared by co-precipitation showed a two- to three-fold increase in adsorption capacity of trace metals [Pb(II), Cd(II), Cu(II) and Zn(II)] in comparison to pure goethite (Rout et al., 2014).

Limited publications are available on the use of ternary metal oxide systems to adsorb As(III) [A*l*-Ti-Mn (Thanh et al., 2016), Fe-Ni-Mn (Nasir et al., 2018), Ce-A*l*-Fe (Sun et al., 2016), Fe-Ti-Mn (Zhang et al., 2018), Fe-Ni-Mn (Nasir et al., 2019)] and Cr(VI) [Ni-Mg-A*l* (Lei et al., 2017)] from aqueous solution. To the best of my knowledge, no research work has to date been published on the use of nanoscale Mn-Fe-Cu ternary metal oxide system as an adsorbent for As(III) and Cr(VI) from solution. The available literature on ternary metal oxide adsorbents is on their applications to remove fluorides and phosphates from aqueous media (Lü et al., 2013; Zhou et al., 2016; Li et al., 2017; Chen et al., 2018; Kondalkar et al., 2018; Raghav et al., 2018).

1.4 PROBLEM STATEMENT

The strict legislation on the discharge of arsenic and chromium coupled with their adverse effects on human health and the environment makes it paramount for environmental scientist and engineers to develop efficient technologies for their removal. The European Union, World Health Organisation and the United States Environmental Protection Agency have set maximum contaminant levels (MCL) or tolerance limits for arsenic (10 μg/dm^3) and chromium (50 μg/dm^3) in industrial and civil effluent before its discharge into potable waters due to their toxicity (Di Natale et al., 2015; Nigra et al., 2017). Several studies have shown the ability of mono- and bimetal oxides of iron, manganese and copper to sequester trace metals from aqueous media (Li et al., 2014; Lu et al., 2014; Wang et al., 2015). These metal oxide adsorbents are environmentally benign (Zheng et al., 2020) and though effective their applicability in wastewater decontamination is limited due to (1) cost of some pure metal oxides is relatively high, (2) reduced adsorption capacity of metal anions at high pH due to low pH at point of zero charge (pH_{pzc}) of the metal oxide adsorbents, (3) the binary metal oxides despite inheriting excellent adsorptive capabilities of the parent oxides cannot be applied in flow-through or fixed-bed systems because of their nanosized particles which result in poor hydraulic properties and excessive pressure drop (Li et al., 2012; Zhang et al., 2013; Ballav et al., 2014), (4) the nanosize adsorbents are also difficult to remove from the treated water

(except for magnetic iron-based nanoparticles) making adsorbent regeneration and metal pollutant recovery or recycling difficult, (5) nanosize metal oxides are prone to agglomeration reducing capacity and selectivity and (6) expensive nanoparticle synthetic routes requiring expensive and toxic chemical reagents (Dubey & Sharma, 2017). The As(III) and Cr(VI) ions have different chemical properties making it difficult to apply a single adsorbent with high adsorption capacities for both species. To circumvent the aforementioned problems and further improve the trace metal removal capacity of the composites, this research seeks to prepare a novel nanoscale ternary metal oxide system from manganese, iron and copper (MFC) for application in the remediation of As(III) and Cr(VI) from simulated aqueous effluent.

1.5 HYPOTHESIS

A novel Mn-Fe-Cu (MFC) ternary metal oxide nanocomposite is capable of As(III) and Cr(VI) sequestration from simulated aqueous effluent.

1.6 OBJECTIVES

The research aim was fabrication of a novel Mn-Fe-Cu (MFC) ternary metal oxide nanocomposite using facile co-precipitation capable of As(III) and Cr(VI) sequestration from simulated aqueous effluent by achieving the following objectives:

1. Optimization of the preparation method of the ternary metal oxide nanocomposite system using central composite design of research surface methodology.
2. Characterization of the nanostructured ternary metal oxide composite using FTIR, SEM-EDS, TEM, XRD, XPS, BET analysis and pH drift method.
3. Application of the novel nanostructured adsorbent in the removal of Cr(VI) and As(III) from a simulated aqueous effluent.
4. Investigation of the adsorption dynamics (competing anions, ionic strength, desorption, regeneration and reuse of exhausted adsorbents) and the mechanistic pathway for As(III) and Cr(VI) sequestration from aqueous medium.
5. To co-precipitate the ternary MFC metal oxide system on biochar support for ease of adsorbent separation from the treated simulated aqueous effluent.

1.7 RESEARCH OUTLINE

The thesis comprises of seven chapters:

Chapter 1

It covers the introduction, problem statement, hypothesis and objectives giving an insight into the research project.

Chapter 2

The literature review on trace metal pollutants, available wastewater treatment techniques, types of adsorbents, biochar support, response surface methodology optimization technique and mathematical modelling of experimental adsorption data is presented in this chapter. The calculation of and use of statistical error functions are described.

Chapter 3

The optimization of working parameters for the synthesis of the ternary MFC nanometal oxide composite and characterization of the adsorbent are presented. The batch adsorption experimental procedures for the decontamination of As(III) and Cr(VI) simulated wastewater are described. To facilitate ease of removal of the nanocomposite adsorbent from the treated effluent, the MFC metal oxide system was co-precipitated on biochar support. The preparation of the biochar support from pine cone, the fabrication of the MFCb composite and its application as an adsorbent for As(III) and Cr(VI) are presented.

Chapter 4

The chapter highlights the determination of optimal parameters for fabrication of the novel MFC ternary metal oxide composite from response surface methodology technique. The characterization of the ternary metal oxide nanocomposite using spectroscopic techniques is discussed.

Chapter 5

The fitting of the batch adsorption experimental data onto kinetic and diffusion models is described.

Chapter 6

The determination of isotherm and thermodynamic parameters of the experimental adsorption data is presented. The proposed mechanistic pathway for the adsorption of As(III) and Cr(VI) onto the ternary MFC metal oxide nanocomposite is discussed. The characterization and adsorption experiments using the MFCb composite are presented.

Chapter 7

A general conclusion of the thesis and recommendations for future research work are highlighted.

1.8 REFERENCES

1. ADELEYE, A.S., CONWAY, J.R., GARNER, K., HUANG, Y., SU, Y. and KELLER, A.A. (2016) Engineered nanomaterials for water treatment and remediation: Costs, benefits and applicability, *Chemical Engineering Journal*. 286, pp. 640-662.

2. AKPOR, O.B., OHIOBOR, G.O. and OLAOLU, T.D. (2014) Heavy metal pollutants in wastewater effluents: Sources, effects and remediation, *Advances in Bioscience and Bioengineering*. 2, pp. 37-43.

3. ANDRESEN, E., PEITER, E. and KÜPPER, H. (2018) Trace metal metabolism in plants, *Journal of Experimental Botany*. 69, pp. 909-954.

4. ANJUM, M., MIANDAD, R., WAQAS, M., GEHANY, F. and BARAKAT, M.A., (2019) Remediation of wastewater using various nano-materials, *Arabian Journal of Chemistry*. 12, pp. 4897-4919.

5. BALLAV, N., CHOI, H.J., MISHRA, S.B. and MAITY, A. (2014) Synthesis, characterization of Fe_3O_4@glycine doped polypyrrole magnetic nanocomposites and their potential performance to remove toxic Cr(VI), *Journal of Industrial and Engineering Chemistry*. 20, pp. 4085–4093.

6. BURAKOV, A.E., GALUNIN, E.V., BURAKOVA, I.V., KUCHEROVA, A.E., AGARWAL, S., TKACHOV, A.G. and GUPTA, V.K. (2018) Adsorption of heavy metal on conventional and nanostructured materials for wastewater treatment purposes: A review, *Ecotoxicology and Environmental Safety*. 148, pp. 702-712.

7. CAROLIN, C.F., KUMAR, P.S., SARAVANAN, A., JOSHIBA, G.J. and NAUSHAD, M. (2017) Efficient techniques for the removal of toxic heavy metals from aquatic environment: A review, *Journal of Environmental Chemical Engineering*. 5, pp. 2782-2799.

8. CHEN, P., WANG, T., XIAO, Y., TIAN, E., WANG, W., ZHAO, Y., TIAN, L., JIANG, H. and LUO, X. (2018) Efficient fluoride removal from aqueous solution by synthetic Fe-Mg-La tri-metal nanocomposite and the analysis of its adsorption mechanism, *Journal of Alloys and Compounds*. 738, pp. 118-129.

9. CHOWDHURY, S., MAZUMDER, M.J., AL-ATTAS, O. and HUSAIN, T. (2016) Heavy metals in drinking water: occurrences, implications, and future needs in developing countries, *Science of the Total Environment*. 569, pp. 476-488.

10. DI NATALE, F. ERTO, A. and MUSMARRA, D. (2015) Equilibrium and dynamic study on hexavalent chromium adsorption onto activated carbon, *Journal of Hazardous Materials*. 218, pp. 47-55.

11. DUBEY, S and SHARMA, Y.C. (2017) *Calotropis procera* mediated one pot green synthesis of Cupric oxide nanoparticles (CuO-NPs) for adsorptive removal of Cr(VI) from aqueous solutions, *Applied Organometallic Chemistry*. 31, pp. 1-15.

12. EBRAHIEM, E.E., AL-MAGHRABI, M.N. and MOBARKI, A.R. (2017) Removal of organic pollutants from industrial wastewater by applying photo-Fenton oxidation technology, *Arabian Journal of Chemistry*. 10, pp. S1674-S1679.

13. EL-RAMADY, H., ABDALLA, N., TAHA, H.S., ALSHAAL, T., EL-HENAWY, A., SALAH, E.D.F., SHAMS, M.S., YOUSSEF, S.M., SHALABY, T., BAYOUMI, Y. and ELHAWAT, N. (2016) Selenium and nano-selenium in plant nutrition, *Environmental Chemistry Letters*, 14, pp. 123-147.

14. GREY, D., GARRICK, D., BLACKMORE, D., KELMAN, J., MULLER, M. and SADOFF, C. (2013) *Philosophical Transactions of the Royal Society A: Mathematical, Physical and Engineering Sciences*. http.//dx.doi.org/10.1098/rsta.2012.0406.

15. HUA, M., ZHANG, S., PAN, B., ZHANG, W., LV, L. and ZHANG, Q. (2012) Heavy metal removal from water/wastewater by nanosized metal oxides: A review, *Journal of Hazardous Materials*. 211-212, pp. 317-331.

16. KONDALKAR, M., FEGADE, U., ATTARDE, S. and INGLE, S. (2018) Experimental investigation on phosphate adsorption, mechanism and desorption properties of Mn-Zn-Ti oxide trimetal alloy nanocomposite, *Journal of Dispersion Science and Technology*. 39, pp. 1635-1643.

17. LI, G., GAO, S., ZHANG, G. and ZHANG, X. (2014) Enhanced adsorption of phosphate from aqueous solution by nanostructured iron (III)-copper (II) binary oxides, *Chemical Engineering Journal*. 235, pp. 124-131.

18. LI, X., HE, K., PAN, B., ZHANG, S., LU, L. and ZHANG, W. (2012) Efficient As (III) removal by macroporous anion exchanger-supported Fe-Mn binary oxide: Behavior and mechanism, *Chemical Engineering Journal*. 193-194, pp. 131-138.
19. LI, L., ZHU, Q., MAN, K. and XING, Z. (2017) Fluoride removal from liquid phase by Fe-Al-La trimetal hydroxides adsorbent prepared by iron and aluminum leaching from red mud, *Journal of Molecular Liquids*, 237, pp. 164-172.
20. LU, J., LIU, H., ZHAO, X., JEFFERSON, W., CHENG, F. and QU, J. (2014) Phosphate removal from water using freshly formed Fe-Mn binary oxide: Adsorption behaviors and mechanisms, *Colloids and Surfaces A: Physicochemical and Engineering Aspects*. 455, pp. 11-18.
21. LǓ, J., LIU, H., LIU, R., ZHAO, X., SUN, L. and QU, J. (2013) Adsorptive removal of phosphate by a nanostructured Fe–Al–Mn trimetal oxide adsorbent, *Powder Technology*. 233, pp. 146-154.
22. LUO, C., TIAN, Z., YANG, B., ZHANG, L. and YAN, S. (2013) Manganese dioxide/iron oxide/acid oxidized multi-walled carbon nanotube magnetic nanocomposite for enhanced hexavalent chromium removal, *Chemical Engineering Journal*. 234, pp. 256-265.
23. MARCOS, C.,MEDORO, V. and ADAWY, A. (2020) Modified vermiculite as adsorbent of hexavalent chromium in aqueous solution, *Minerals*. 10, pp. 749.
24. MISHRA, S., BHARAGAVA, R.N., MORE, N., YADAV, A., ZAINITH, S., MANI, S. and CHOWDHARY, P. (2019) Heavy metal contamination: An alarming threat to environment and human health. In *Environmental biotechnology: For sustainable future*. Springer, Singapore, pp. 103-125.
25. NASIR, A.M., GOH, P.S. and ISMAIL, A.F. (2018) Novel synergistic hydrous iron-nickel-manganese (HINM) trimetal oxide for hazardous arsenite removal, *Chemosphere*. 200, pp. 504-512.
26. NASIR, A.M., GOH, P.S. and ISMAIL, A.F. (2019) Highly adsorptive polysulfone/hydrous iron-nickel-manganese (PSF/HINM) nanocomposite hollow fiber membrane for synergistic arsenic removal, *Separation and Purification Technology*. 213, pp. 162-175.
27. NIGRA, A.E., SANCHEZ, T.R., NACHMAN, K.E., HARVEY, D.E., CHILLRUD, S.N., GRAZIANO, J.H. and NAVAS-ACIEN, A. (2017) The effect of the Environmental Protection Agency maximum contaminant level on arsenic exposure in

the USA from 2003 to 2014: an analysis of the National Health and Nutrition Examination Survey (NHANES). *The Lancet Public Health*, 2, pp. 513-521.

28. PENKE, Y.K., ANANTHARAMAN, G., RAMKUMAR, J. and KAR, K.K. (2019) Redox synergistic Mn-Al-Fe and Cu-Al-Fe ternary metal oxide nano adsorbents for arsenic remediation with environmentally stable As (0) formation, *Journal of hazardous materials*. 364, pp. 519-530.
29. RAGHAV, S., NAIR, M. and KUMAR, D. (2018) Trimetallic oxide entrapped in alginate polymeric matrix employed for adsorption studies of fluoride, *Surfaces and Interfaces*. 13, pp. 112-132.
30. ROSE, J. ed., (2016) *Trace elements in health: a review of current issues*. Butterworth-Heinemann.
31. ROUT, K., DASH, A., MOHAPATRA, M. and ANAND, S. (2014) Manganese doped goethite: Structural, optical and adsorption properties, *Journal of Environmental Chemical Engineering*. 2, pp. 434-443.
32. SANI, H.A., AHMAD, M.B., HUSSEIN, M.Z., IBRAHIM, N.A., MUSA, A. and SALEH, T.A. (2017) Nanocomposite of ZnO with montmorillonite for removal of lead and copper ions from aqueous solutions, *Process Safety and Environmental Protection*. 109, pp.97-105.
33. SINGH, N.H., KEZO, K., DEBNATH, A. and SAHA, B. (2018) Enhanced adsorption performance of a novel Fe-Mn-Zr metal oxide nanocomposite adsorbent for anionic dyes from binary dye mix: Response surface optimization and neural network modeling, *Applied Organometallic Chemistry*. 32, pp. 4165.
34. SUN, C., QIU, J., ZHANG, Z., MARHABA, T.F. and ZHANG, Y. (2016) Removal of arsenite from Water by Ce-Al-Fe trimetal oxide adsorbent: kinetics, isotherms, and thermodynamics, *Journal of Chemistry*. 2016.
35. THANH, D.N., BASTL, Z., ČERNÁ, K., ULBRICH, P. and LEDERER, J. (2016) Amorphous nanosized Al–Ti–Mn trimetal hydrous oxides: synthesis, characterization and enhanced performance in arsenic removal, *RSC Advances*. 6, pp. 100732-100742.
36. WANG, Y., LIU, D., LU, J. and HUANG, J. (2015) Enhanced adsorption of hexavalent chromium from aqueous solutions on facilely synthesized mesoporous iron-zirconium bimetal oxide, *Colloids and Surfaces A: Physicochemical and Engineering Aspects*. 481, pp. 133-142.

37. WANG, A., ZHOU, K., LIU, X., LIU, F., ZHANG, C. and CHEN, Q. (2017) Granular tri-metal oxide adsorbent for fluoride uptake: adsorption kinetic and equilibrium studies, *Journal of Colloid and Interface Science*. 505, pp. 947-955.

38. WEI, Z., WANG, Z., YAN, J., LIU, Y., WU, Y., FANG, Y., YU, L., CHENG, G., PAN, Z. and HU, G. (2019) Adsorption and oxidation of arsenic by two kinds of β-MnO_2. *Journal of Hazardous Materials*. 373, pp. 232-242.

39. YU, Y., ZHOU, Z., DING, Z., ZUO, M., CHENG, J. and JING, C. (2019) Simultaneous arsenic and fluoride removal using {201} TiO_2–ZrO_2: Fabrication, characterization, and mechanism, *Journal of Hazardous Materials*. 377, pp. 267-273.

40. YUFANYI, D.M., ONDOH, A.M., FOBA-TENDO, J. and MBADCAM, K.J. (2015) Effect of decomposition temperature on the crystallinity of α-Fe_2O_3 (hematite) obtained from an iron (III)-hexamethylenetetramine precursor, *American Journal of Chemistry*. 5, pp. 1-9.

41. ZHANG, Y., WU, B., XU, H., LIU, H., WANG, M., HE, Y. and PAN, B. (2016) Nanomaterials-enabled water and wastewater treatment, *NanoImpact*. 3-4, pp. 22-39.

42. ZHANG, W., ZHANG, G., LIU, C., LI, J., ZHENG, T., MA, J., WANG, L., JIANG, J. and ZHAI, X. (2018) Enhanced removal of arsenite and arsenate by a multifunctional Fe-Ti-Mn composite oxide: photooxidation, oxidation and adsorption, *Water Research*. 147, pp. 264-275.

43. ZHENG, Q., HOU, J., HARTLEY, W., REN, L., WANG, M., TU, S. and TAN, W. (2020) As (III) adsorption on Fe-Mn binary oxides: Are Fe and Mn oxides synergistic or antagonistic for arsenic removal?, *Chemical Engineering Journal*. 389, pp. 124470.

44. ZHOU, C.Y., GUAN, D.X., WILLIAMS, P.N., LUO, J. and MA, L.Q. (2016) Novel DGT method with tri-metal oxide adsorbent for in situ spatiotemporal flux measurement of fluoride in waters and sediments, *Water Research*. 99, pp. 200-208.

CHAPTER 2

2 LITERATURE REVIEW

2.1 INTRODUCTION

Current literature on the types of metal pollutants in wastewater, existing technologies for wastewater remediation, adsorption, types of adsorbents, optimization using response surface methodology and mathematical models applied to adsorption experimental data is reviewed.

2.2 TRACE METAL POLLUTANTS IN AQUEOUS EFFLUENT

Municipal and industrial effluents are major pollutants of potable waters as they contain dyes, aromatics and trace metals. These pollutants cause disease, allergies, organ failure, chromosomal defects, tumours, death and reduce the aesthetics of quality of water by colouring it (Akpor et al., 2014; Du et al., 2014; Lakshmipathy et al., 2015). Trace metal pollutants are of major interest to environmental engineers and scientists as they occur naturally in the environment and are not biodegradable. The flow chart presented in Fig 2.1 shows the geogenic and anthropogenic sources of trace metal elements and their mobility in the ecosystem. Geological processes like weathering of rocks, spreading of mid-ocean ridges and volcanic eruptions release trace metals into the environment (McCann et al., 2018). Anthropogenic activities such as mining, agriculture, electronic engineering and metallurgical industries introduce trace metal elements into the environment increasing metal geoaccumulation indices in water, soil and sediments (Carolin et al., 2017; Vareda et al. 2019). The mining of metals and their processing in Europe contributes about 48 % of the total metal pollutants in the ecosystem (Panagos et al., 2013). Above certain prescribed threshold concentrations, trace metals become toxic as they bioaccumulate in organisms (Wen et al., 2019). They cause a myriad of clinical, neurological, gastrointestinal, physiological and immunological conditions in humans (Zhang et al., 2019). The WHO (2017) has set maximum contaminant levels for the trace metals in municipal and industrial wastewater. This makes it critical to develop low-cost and effective wastewater decontamination technologies for the following trace metals.

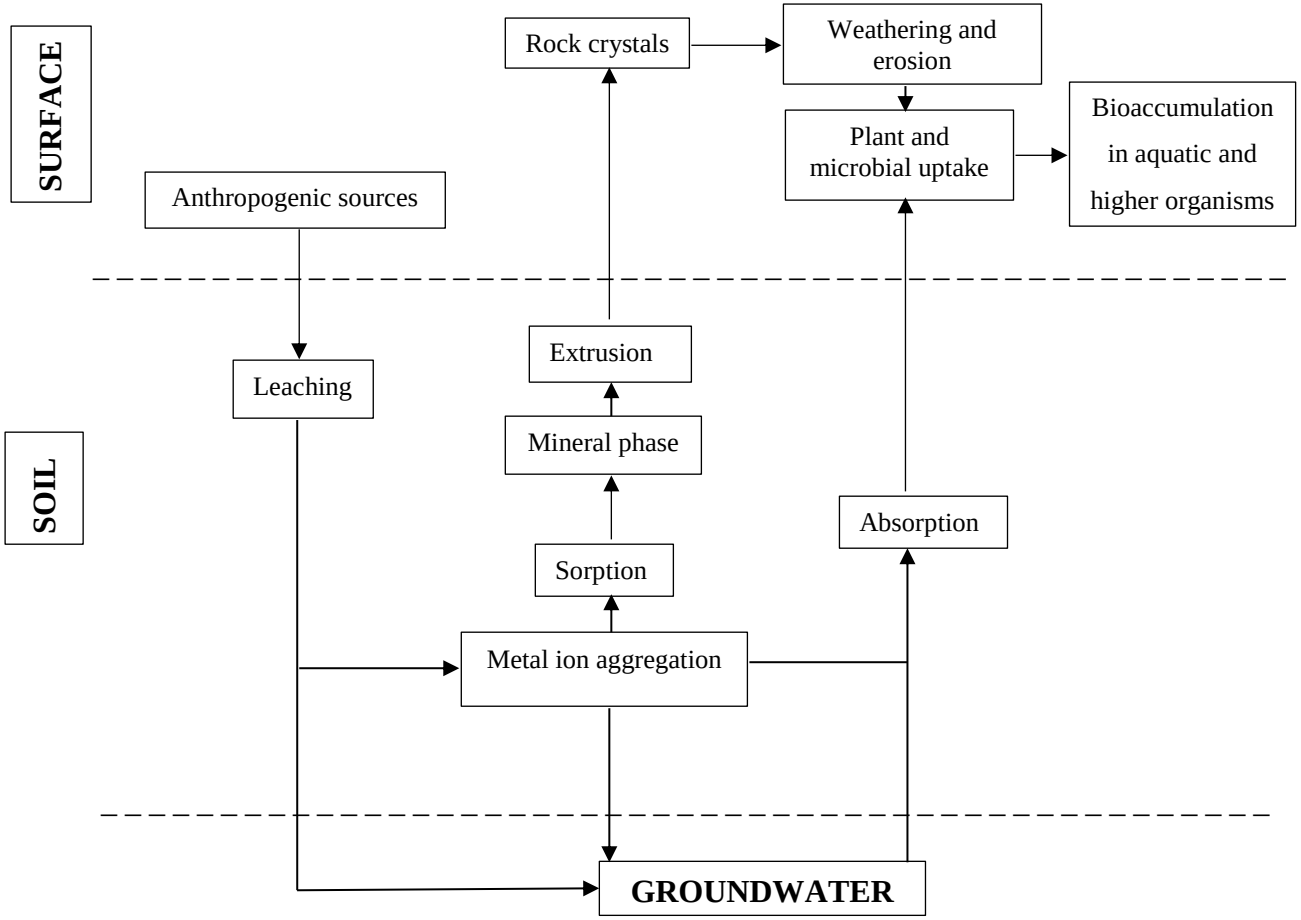

Fig 2.1 Sources and mobility of trace metal elements in the environment (Vareda et al. 2019).

2.2.1 Arsenic

The trace metal is present in the ecosystem in organic or inorganic form. The inorganic arsenic species especially oxyanions of As(III) and As(V) are toxic while some organic arsenicals such as arsenobetaine and arsenocholine found in food are non-toxic (Palaneeswari et al., 2013). Inorganic arsenic is mobilised through anthropogenic or natural processes like weathering, geochemical, biological and volcanic activities (Zhang et al., 2014). Anthropogenic activities include the use of arsenical agriproducts (herbicides, pesticides, poultry feed, wood preservatives, etc), fossil fuel combustion (especially coal), mining (since arsenic is usually found attached to transition metals like silver, cadmium, gold, tungsten, etc), metallurgy (alloying usually with copper and lead), medicine (for treatment of trypanosomiasis, chronic myeloid leukaemia, syphilis, etc) and in electronics as an n-type dopant in semiconductors (Yun et al., 2016; Kobielska et al., 2018; Zhang et al., 2018). Arsenic is highly toxic with little nutritional or physiological benefits to life. It is reported in the literature to be of benefit in trace amounts to human metabolic pathways such as catalysis in the synthesis of glutathione, the biochemistry of the phospholipids' bilayer in cell membranes and stimulation of bile secretion (Mertz, 2012). Effects of its deficiency in humans are not well documented in literature as with other trace metals like iron. Long-term ingestion of this trace metal by humans may be carcinogenic to internal organs (liver, kidney, lungs, bladder, prostate, brain and gastrointestinal tract) and skin (hyperkeratosis). Since arsenic is toxic and is a potential carcinogen, its maximum contaminant level (MCL) in drinking water has been set at 10 $\mu g/dm^3$ by the World Health Organization (WHO, 2017) since 2006 (Li et al., 2017). Arsenic is also classified as a Class A carcinogen by the International Agency for Research on Cancer (Ociński et al., 2016). It may also cause non-cancerous ailments such as diabetes mellitus, reproductive abnormalities, cerebrovascular and cardiovascular diseases. Arsenic related illnesses are generally referred to as arsenicosis (Lou et al., 2017; Ryu et al., 2017; Singh et al., 2017).

Arsenic has four known oxidation states, that is, arsine (-3), arsenic (0), arsenite (+3) and arsenate (+5), with the +III and +V forms being predominant in the hydrosphere. In aqueous media, arsenite [As(III)] exists as non-ionic arsenious acid (H_3AsO_3; pK_{a1}=9.22) and arsenate [As(V)] as inorganic oxyanions ($H_2AsO_4^-$ and $HAsO_4^{2-}$; pK_{a1}=2.19 and pk_{a2}=6.94, respectively) under anoxic and oxic conditions respectively (Zheng et al., 2020). This makes arsenic a problematic pollutant in water as both As(III) and As(V) are mobile over a wider pH

range and redox conditions (Sarkar & Paul, 2016). It is only in the presence of highly reduced sulphur in water, that arsenic can be precipitated as sulphides such as As_2S_3, As_4S_3, etc. The speciation of As(III) and As(V) as a function of pH is plotted on Fig 2.2. Arsenite is more toxic than arsenate to fauna due to its long retention time in the body as it has a very high affinity for the –SH (sulfhydryl) functional group of cysteine protein residue (Kotyzova et al., 2013; Zhang et al., 2019).

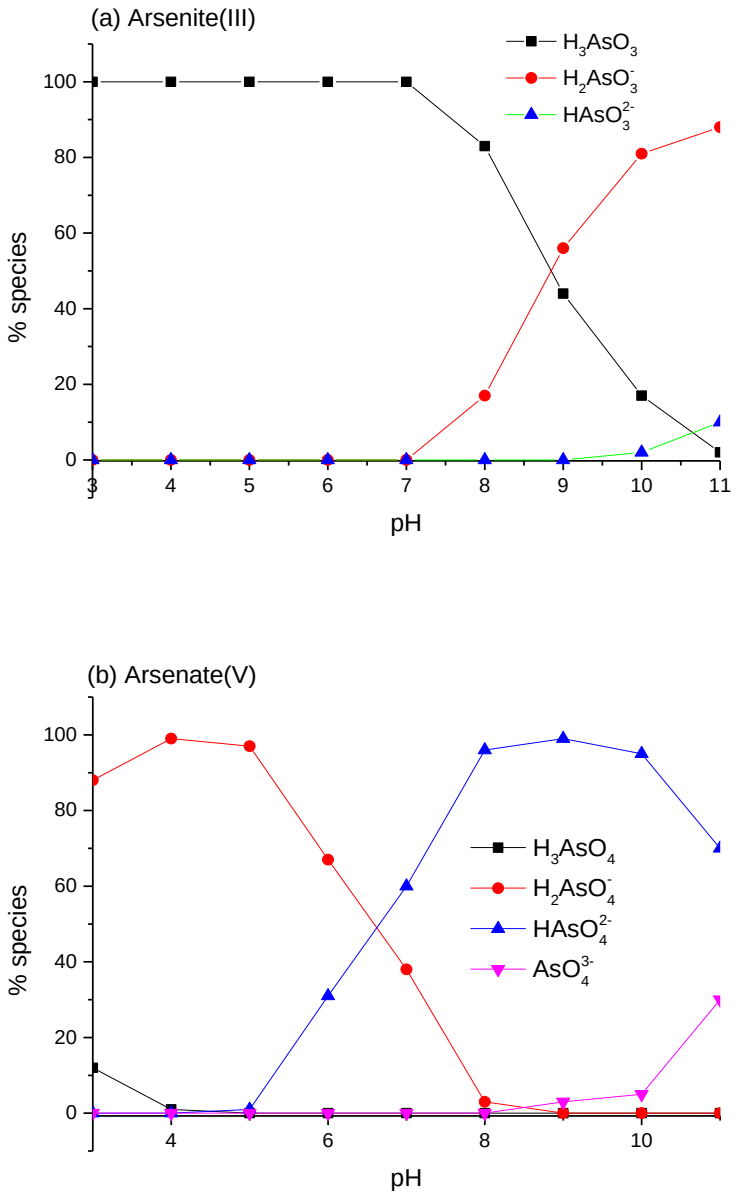

Fig 2.2 Speciation of (a) arsenite(III) and (b) arsenate(V) as a function of solution pH (Zheng et al., 2020).

At low to neutral pH in aqueous media, As(III) exists as non-ionic H_3AsO_3 and is difficult to adsorb from solution due to its low affinity for adsorbents, unlike As(V) which exists as oxyanions which are easily adsorbed at low pH on protonated adsorbent surfaces (Zhang et al., 2018). Due to the weak adsorption properties of As(III) coupled with its high toxicity in comparison to As(V), it is necessary to oxidise As(III) to As(V) in the sequestration of total As from solution. This oxidation reaction which is oxygen-depended can take place naturally in underground water but is so slow with reaction kinetic half-times of up to a year (Gorny et al., 2015). Therefore, to improve the removal of total arsenic from solution, oxidants with faster kinetics need to be explored. Several researchers have explored ozone, chlorine and hydrogen peroxide as potential oxidants for the crucial arsenite to arsenate oxidation with little success due to the formation of toxic by-products (Hou et al., 2017). It is known that Mn and Fe oxides exist naturally in the soil and their adsorption reactions control the mobility of arsenic in the environment (McCann et al., 2018). The oxides of Mn have high oxidation potentials (E^o=1.22 V for birnessite, MnO_2) and can oxidise As(III) to As(V) and are also able to adsorb the arsenic ions from solution. The oxides of Fe(III) have a high affinity for As(V) and easily adsorb it. Several environmental scientists/engineers have applied Mn and Fe oxides either as single or binary metal systems for removal of arsenic from water (Shan & Tong, 2013; Cui et al., 2014; Bai et al., 2016; Phanthasria et al., 2018; Wen et al., 2019). The binary oxides show higher As(III) adsorption capacity since they combine the removal capabilities of two different metal oxide systems. The removal of As(III) by Mn-Fe binary oxides is synergistic involving: (1) oxidation of As(III) to As(V) by Mn oxides (Ryu et al., 2017) and (2) the adsorption of As(V) by Fe(III) oxides. The pre-oxidation step complicates the sequestration of As(III) as it forms Mn(II) ions which leach into the treated water (Molinari & Argurio, 2017). The ions of Mn(II) are toxic as it is a known neurotoxin causing hallucinations and intellectual impairment (Ryu et al., 2017). The pre-oxidation step creates a secondary problem but is also depended on the type of Mn oxide. The equations showing the oxidation of trivalent arsenite to pentavalent arsenate on MnO_2 are presented as Eq's 2.1-2.3 (Zhang et al., 2018):

$$MnO_2 + H_3AsO_3 + 2H^+ \rightleftharpoons Mn^{2+} + H_3AsO_4 + H_2O \quad (2.1)$$

$$2MnO_2 + H_3AsO_3 + H_2O \rightleftharpoons 2MnOOH^* + H_3AsO_4 \quad (2.2)$$

$$2MnOOH^* + H_3AsO_3 + 4H^+ \rightleftharpoons 2Mn^{2+} + H_3AsO_4 + 3H_2O \quad (2.3)$$

The oxidation of trivalent arsenic to its pentavalent form (Eq's 2.1-2.3) can be inhibited by competitive ions such as PO_4^{3-}, Fe^{2+}, Pb^{2+}, Ni^{2+} and Zn^{2+} through surface passivation of active sites on the Mn oxide surface. The oxidation rate is also negatively influenced by the presence of As(V) ions (Villalobos et al., 2014; Wu et al., 2015; Hou et al., 2018).

2.2.2 Chromium

Chromium shows uniqueness from other toxic heavy metals by existing in a myriad of oxidation states, from -2 to +6, with Cr(III) and Cr(VI) being the most stable in the hydrosphere (Dhal et al., 2013; Headlam & Lay, 2016). Cr(III) is cationic, less toxic (only harmful at high concentrations) and exists naturally in the environment from weathering of rocks and volcanic activity, with trace quantities having physiological benefits to mankind (Aigbe et al., 2018; Hamilton et al., 2018). It is known to ameliorate obesity, diabetes and other ailments associated with metabolic syndrome as it regulates insulin and metabolism of glucose (Vincent, 2014; Bai et al., 2015). It affects the metabolic activity of heterotrophs above 10 mg/L (Chang et al., 2012). On the other hand, Cr(VI) results from anthropogenic activities, though the trivalent chromite can be oxidized to the hexavalent state in the presence of manganese oxides in the environment (Kaprara et al., 2015). Hexavalent chromate is about 500 times more toxic than the trivalent form even at ppb levels and has no physiological benefits to humans (Kan et al., 2017; Pradhan et al., 2017). It exists mainly as anions of $Cr_2O_7^{2-}$, CrO_4^{2-}, $HCrO_4^-$ or H_2CrO_4 species in aqueous media depending on pH (Barrera-Díaz et al., 2012, Hamilton et al., 2018). The speciation of Cr(VI) in aqueous solution as a function of pH is shown in Fig 2.3 and determines chemical and biological characteristics. The following equations represent some of the equilibrium reactions governing Cr(VI) ion speciation in aqueous media:

$$H_2CrO_4 \rightleftharpoons H^+ + HCrO_4^- \qquad pk_{a1} = 0.74 \qquad (2.4)$$

$$HCrO_4^- \rightleftharpoons H^+ + CrO_4^{2-} \qquad pk_{a2} = 6.50 \qquad (2.5)$$

$$2HCrO_4^- \rightleftharpoons Cr_2O_7^{2-} + H_2O \qquad (2.6)$$

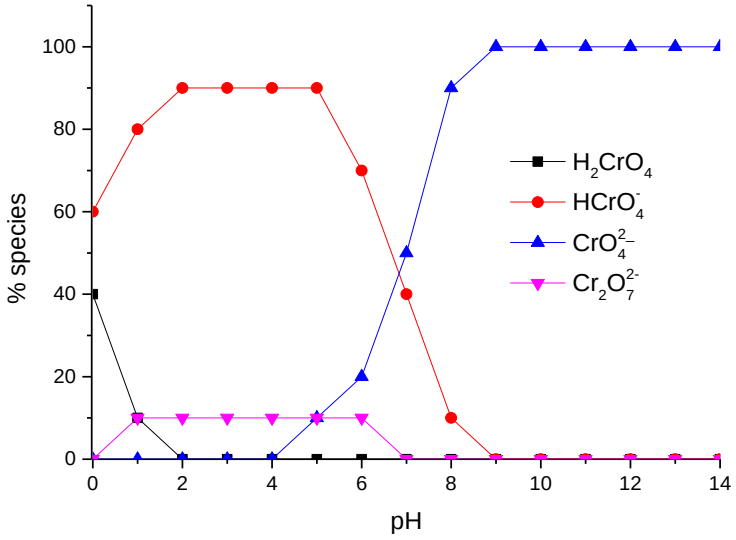

Fig 2.3 Speciation of Cr(VI) species in aqueous solution at different pH values (Barrera-Díaz et al., 2012).

Cr(VI) is mostly found in industrial effluent from metallurgy, electroplating, alloying factories, nuclear power stations, photography, cement manufacture, leather tanning processes, wood preservation, paint and pigment production, etc (Butera et al., 2015; Chen et al., 2016). The hexavalent species are very mobile, strongly oxidising, toxic agents that are carcinogenic, mutagenic and teratogenic in the biosphere (Medda & Mondal, 2017). Human exposure or ingestion of Cr(VI) causes dermatitis, pneumonitis, gastrointestinal discomfort, bronchogenic carcinoma and haemorrhage amongst a myriad of other health problems due to its strong oxidising ability and solubility into the cell matrix (Yadav et al., 2013). All forms of chromium have no metabolic or physiological benefit to plant life but merely inhibit plant development by interfering with important physiological processes such as nutrient uptake and chlorophyll synthesis (Shahid et al., 2017).

The hexavalent form of chromium is difficult to remove from aqueous solution by chemical precipitation since it does not form insoluble compounds. Hexavalent chromium can be reduced to less mobile, less harmful and easily precipitable trivalent chromium using various techniques and reagents. Cr(III) is precipitated as $Cr(OH)_3$ from aqueous media. The reduction of Cr(VI) to Cr(III) is usually performed using ferrous salts. The reduction is very slow, taking months or even years but the rate increases significantly at pH values less than 3 (Jardine et al., 1999):

$$6Fe^{2+} + Cr_2O_7^{2-} + 14H^+ \rightleftharpoons 6Fe^{3+} + 2Cr^{3+} + 7H_2O \quad (2.7)$$

$$3Fe^{2+} + HCrO_4^- + 7H^+ \rightleftharpoons 3Fe^{3+} + Cr^{3+} + 4H_2O \quad (2.8)$$

$$Cr^{3+} + 3OH^- \rightleftharpoons Cr(OH)_3 \downarrow \quad (2.9)$$

Increase in reduction rate at low pH can be due to charge distribution and configurational changes caused by the formation of hydro-complexes. The process yields a solid sludge of ferric hydroxide causing disposal problems. It is also not appropriate for remediation of dilute Cr(VI) solutions as large volumes of chemical precipitants are required. Other techniques such as electrochemical methods, photocatalysis and use of microbes have been reported in the literature for the reduction of Cr(VI) to Cr(III). The biological method is inexpensive since it only requires a carbon source but at high Cr(VI) concentrations, the cellular matrix is destroyed. Studies show that Cr(III) can be oxidised by MnO_2 to Cr(VI), hence its imperative to measure total chromium when determining water quality standards for chromium in the environment, rather than just base it on the measurement of Cr(VI). This is due to the possibility of interconversions between the +3 and +6 chromium species due to presence of iron and manganese oxides in the lithosphere (Schroeder & Lee, 1975; Izbicki et al., 2015).

2.3 TOXIC METALS DECONTAMINATION TECHNIQUES

Water can rid itself of dirt through natural sedimentation and dilution processes. The presence of pollutants at high concentrations in municipal and industrial wastewater renders these processes useless. Environmental scientists and engineers have applied biological, chemical and physical methods for remediation of metal ions from wastewater. The methods utilised include microbial, solvent extraction, membrane technologies, photochemical, electrochemical, precipitation, aerobic and anaerobic digestion, adsorption, etc (Fu et al., 2012; Vander Hoogerstraete et al., 2013; Lakherwal, 2014; Gunatilake, 2015; Edebali & Pehlivan, 2016; Al-Saydeh et al., 2017; Priyadharsan et al., 2017; Smily & Sumithra, 2017; Abdi et al., 2018; Mei & Tang, 2018). The conventional removal methods show drawbacks such as: (1) the need for high technical expertise, (2) expensive chemical reagents and operating conditions, (3) high energy demand, (4) production of toxic waste products creating a secondary disposal problem and (5) poor removal efficiency at trace pollutant concentrations (Semerjian, 2018). The adsorption process is the best option amongst the various conventional pollutant sequestration methods due to its simple design, the possibility of metal recovery through the

regeneration of adsorbent and ability to decontaminate wastewater at very low pollutant concentrations (µg/dm^3 or ppb levels) (Renu et al., 2017; Al-Senani et al., 2018; Fang et al., 2018).

2.3.1 Chemical precipitation

Metal ions react with hydroxides, sulphides, carbonates and other chemicals to form insoluble metal precipitates (Chen et al., 2018). The technique produces large quantities of sludge which may be toxic or difficult to dispose of and is not metal selective (Gunarathne et al., 2019). Two of the main chemical precipitation methods used are hydroxide and sulphide precipitation, but commercial chelating agents such as dithiocarbamate, dithiocarbamic acid dipotassium salt, amino dithiocarbamate and thiourea can also be used to precipitate metal ions (Ma et al., 2019).

2.3.1.1 *Hydroxide precipitation*

It involves the use of metal hydroxides to raise the solution pH to between 9 and 11 forming insoluble hydroxides (Wang & Chen, 2019). The formation of the insoluble precipitate is shown in Eq 2.10:

$$M^{n+} + n(OH)^{-} \rightarrow M(OH)_n \downarrow \quad (2.10)$$

where M^{n+} denotes the soluble pollutant metal ions, OH^- is the hydroxide precipitant and $M(OH)_n$ represents the pollutant metal hydroxide precipitate. Mirbagheri & Hosseini (2005), using $Ca(OH)_2$ and NaOH removed Cr(VI) and Cu(II) from aqueous solution at pHs 8.7 and 12, respectively. They reported a reduction of Cr(VI) concentration from 30 mg/dm^3 to 0.01 mg/dm^3 and that of Cu(II) from 48.51 mg/dm^3 to 0.694 mg/dm^3. Addition of coagulants such as iron salts and alum has been reported to reduce residual trace metal concentration during hydroxide precipitation (Azimi et al., 2017). Major limitations to the removal process include (1) accumulation of large volumes of toxic, low-density sludge causing disposal and dewatering problems, and (2) since some metal hydroxides are amphoteric, in an effluent with mixed metals, the optimum pH for precipitation of one metal might end up putting the other back into the mother liquor (Lewis, 2017).

2.3.1.2 *Sulphide precipitation*

Metal sulphides are not amphoteric and are less soluble than metal hydroxides resulting in a reduced residual concentration of trace metals over a wider pH range. The sulphide sludges also show better thickening and dewatering properties than their corresponding hydroxide sludges. The process involving the use of iron pyrites at low pH (< 3) was used by Li and co-researchers (2019) in the removal of T*l*(I) to less than 1 μg/dm^3. The main drawback is that the process can result in the evolution of toxic H_2S fumes as shown in the following equations:

$$FeS + 2H^+ \rightarrow H_2S \uparrow + Fe^{2+} \quad (2.11)$$

$$M^+ + H_2S \rightarrow M_2S \downarrow + 2H^+ \quad (2.12)$$

where M^+ represents a monovalent metal ion, and M_2S is the insoluble metal sulphide. Another disadvantage is that the sulphide precipitates are colloidal causing separation problems, especially during settling or filtration. Metal ions can also be precipitated using sulphate-reducing bacteria (SRB) (Zhu et al., 2019), under anoxic conditions as represented in the following equation:

$$3SO_4^{2-} + 2CH_3CH(OH)COOH \rightarrow 3H_2S + 6HCO_3^- \quad (2.13)$$

where $CH_3CH(OH)COOH$ is an organic compound. The H_2S reacts with the divalent metal ion as in Eq 2.12 forming an insoluble metal sulphide. Studies utilising the SRB in the treatment of acid mine drainage have been reported in the literature (Sato et al., 2018).

2.3.2 Ion exchangers

Natural (clay, zeolites, soil humus, montmorillonite) or man-made ion exchange resins can decontaminate toxic metal ions from large solution volumes. They exchange their ions for the metal ions in solution. The synthetic resins can be anionic, cationic or amphoteric depending on the type of active ion groups (Na^+, K^+, Cl^-, H^+, OH^-, COO^-, NH_3^+, SO_4^{2-}, PO_4^{3-}, et cetera) that they possess. This accounts for their fast kinetics and good metal ion selectivity (Nemati et al., 2017; Calmon, 2018):

$$n(R - SO_3H) + M^{n+} \rightarrow (R - SO_3^-)_n M^{n+} + nH^+ \quad (2.14)$$

$$n(R - COOH) + M^{n+} \rightarrow (R - COO^-)_n M^{n+} + nH^+ \quad (2.15)$$

where M^{n+} is the pollutant metal cation. The major limitations of ion exchangers include (1) waste disposal after regeneration of the active sites, (2) sensitive to wastewater pH, (3) high level of technical expertise, (4) expensive plant operation and maintenance costs, (5) matrix fouling due to the presence of organics and particulate matter in the effluent and (6) the presence of competing ions (Kononova et al., 2015; Zewail & Yousef, 2015; Figueiredo et al., 2018).

2.3.3 Membrane technology

It involves physical separation of components utilizing a permeable membrane and encampuses several separation and purification techniques such as (1) pressure-driven (microfiltration, nanofiltration, reverse osmosis, ultrafiltration), (2) concentration driven (dialysis, pervaporation, forward osmosis), (3) electric potential driven (electrodialysis, membrane electrolysis, electrofiltration, electrodeionization) and (4) temperature-driven (membrane distillation) (Qiu & Mao, 2013; Pal et al., 2014; Víctor-Ortega & Ratnaweera, 2017). The membrane techniques use fewer chemicals and generate low amounts of waste but have high operating costs and require a high level of technical expertise (Abejón et al., 2015).

2.3.4 Electrochemical treatment

It involves passing a current through the metal infested effluent across electric plates. The electric discharge of the metal cations takes place at the cathode. This technology is presumed to be 'clean' as it does not use chemical reagents. It includes techniques such as electrodeposition, electrofloatation and electrocoagulation (Adjeroud et al., 2015; Thakur & Mondal, 2017). The main disadvantage of electrochemical treatment is that the techniques are expensive due to periodic replacement of electrodes, high technical expertise and high energy demand (Hashim et al., 2017; Rosales et al., 2018). A 100 % removal efficiency of both Ni(II) and Zn(II) was reported by Kabdaşli and co-workers (2009) using electrocoagulation technique. Khelifa et al. (2005) achieved removal efficiency of 98 % during reclaiming of Ni(II) and Cu(II) infested wastewater using electrofloatation. Using electrodeposition together with ultrasound, Chang and colleagues (2009) treated EDTA-copper effluent, simultaneously recovering elemental copper and decomposing EDTA.

2.3.5 Photocatalysis

This wastewater reclamation technique simultaneously degrades organics and recovers metals at very low concentrations in one-pot systems (Shayegan et al., 2018). This gives the process an edge over classical metal recovery techniques like hydrometallurgy which are inhibited if the effluent contains organics. The photocatalysts transmit electrons from organic molecules to metal ions. Photocatalysis involves irradiation of semiconductor-electrolyte interface using ultraviolet-near visible region photons with energy greater than the semiconductor band gap. The irradiation creates electron-hole pairs (e^-/h^+) in the conduction band (CB) and valence band (VB) of the semiconductor. The e^-/h^+ pairs need to be trapped using chemical species to avoid their recombination. Hydroxide ions are used to trap the holes generating highly oxidising hydroxyl radicals ($OH^{\cdot}$). Adsorbed oxygen species trap the electrons forming strong reducing superoxide species (O_2^-) (Litter, 2017). A variety of semiconductor catalysts which include CeO_2, CdS, TiO_2 and ZnO, among others have been used with the best degradation performance being reported with TiO_2. The proposed mechanism for photocatalysis over TiO_2 involves:

$$TiO_2 + hv \rightarrow TiO_2 + e_{CB}^- + h_{VB}^+ \quad (2.16)$$

$$TiO_2 + OH^- + h^+ \rightarrow TiO_2 - OH^- \quad (2.17)$$

$$O_2 + e^- \rightarrow O_2^- \quad (2.18)$$

The photocatalysts can also be doped enhancing their remediation activity. Rengaraj et al. (2007) doped TiO_2 with neodymium (Nd) using sol-gel method and applied the composite for photocatalytic reduction of Cr(VI) with ultraviolet radiation.

2.3.6 Adsorption

Adsorption is a 'green' surface separation technique in which gas or liquid particles (adsorbate) form a thin layer on the internal and external surfaces of solid particles (adsorbent or substrate) (Yang et al., 2019). It is a multi-step process on porous materials as shown in Fig 2.4, involving (1) the bulk transport of adsorbent into the adsorbate solution, (2) film diffusion of adsorbate to the external surface of adsorbent across the hydrodynamic film or boundary layer, (3) intraparticle diffusion of adsorbate onto the internal surface of the adsorbent, and (4) attachment of adsorbate to an adsorbent surface (Tran et al., 2017).

The adsorption process is simple, selective, inexpensive, sludge-free and leads to metal recovery after regeneration of adsorption active sites (Hu & Zhang, 2019). Adsorption is the most effective micropollutant remediation technique and forms no toxic intermediates or by-products unlike most degradation techniques (Gao et al., 2017; Gan et al., 2018). There are four types of adsorption: (1) physical, (2) chemical, (3) ion exchange and (4) microprecipitation (Robalds et al., 2016).

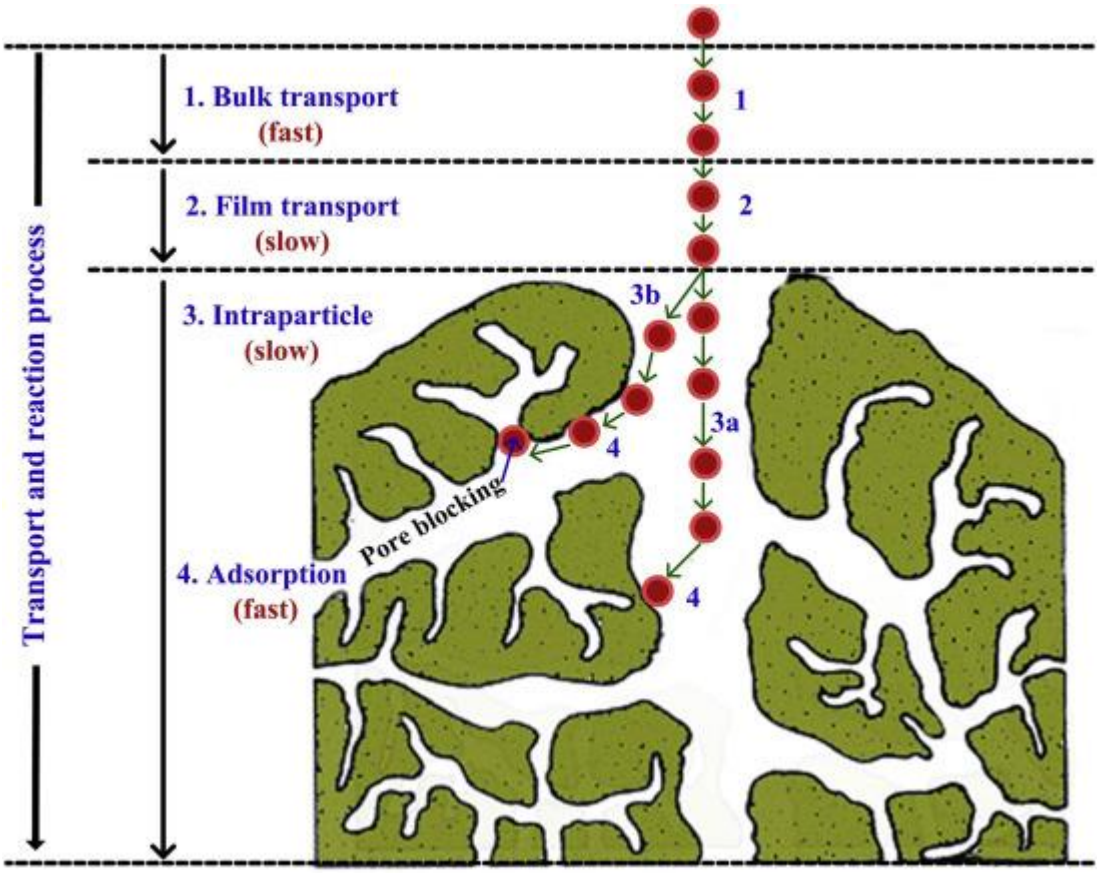

Fig 2.4 Schematic diagram showing adsorption on a porous adsorbent (Tran et al., 2017).

2.3.6.1 *Physical adsorption*

Physical adsorption or physisorption is non-specific and is due to electrostatic and van der Waals' forces (Keesom, Debye and London interactions). The process is reversible (activation energy is low) and is depended on the surface area. It is exothermic with low free Gibbs energy ranging between -20 and 0 kJ/mol and a decrease in entropy (Anatsopoulos & Kyzas, 2016; Sarkar & Paul, 2016). This type of adsorption can result in mono- or multilayers of the adsorbate.

2.3.6.2 *Chemical adsorption*

Chemical adsorption or chemisorption is specific and due to valence forces between the adsorbent and adsorbate forming a chemical bond. The process is irreversible with free Gibbs energy in the range -400 to -80 kJ/mol (Anastopoulos & Kyzas, 2016). It only results in monolayer adsorption.

2.3.6.3 *Ion exchange adsorption*

It is a physicochemical process entailing the exchange of ions between the surface functions on the adsorbent and the adsorbate ions.

2.3.6.4 *Microprecipitation or surface precipitation*

This is localised precipitation of adsorbate on the adsorbent surface or inside adsorbent pores (Robalds et al., 2016).

2.3.6.5 *Factors affecting the adsorption of metal ions*

The type and intensity of interaction between adsorbent surface functions and adsorbate metal ions depend on several experimental variables such as adsorbent particle size, size of metal ions, solution pH, initial concentration of metal ions, presence of competing ions, adsorbent dose, agitation speed, contact time, etc (Peng et al., 2017). The following are some of the factors that affect the immobilization of metal ions from the liquid onto the solid phase:

2.3.6.5.1 Adsorbent particle size

A decrease in particle size of adsorbent might result in an increase in adsorption capacity of metal ions due to an increase in the number of exposed adsorption active sites. Ben-Ali and co-researchers (2017), showed an increase in uptake of Cu(II) ions on raw pomegranate peel adsorbent with a decrease in adsorbent particle size. Other researchers showed that a decrease in adsorbent particle size does not necessarily translate into a concomitant increase in adsorption capacity of metal ions especially with adsorption on porous materials (Rouquerol et al., 2014). The authors deduced that adsorption capacity should be depended on an increase in the internal surface area since on porous adsorbents the contribution of the external surface area to the total surface area is negligible.

2.3.6.5.2 Size of metal ions

Adsorption of metal ions depends on adsorbate ionic radius. A large ionic radius will result in a quick saturation of adsorption sites, largely due to steric overcrowding (Wang et al., 2017; Fakhre & Ibrahim, 2018)

2.3.6.5.3 pH of solution

The most important variable affecting metal ion adsorption is the pH of the medium as it influences the type of adsorbate-adsorbent interaction. Wei and co-workers (2019) reported different As(III) adsorption capacities onto β-MnO_2 at pH's 4, 7 and 9. The pH of the solution influences the amount of electric charge on the surface of the adsorbent. If solution pH > pH_{pzc} (pH_{pzc} is the pH at point of zero charge and denotes the solution pH at which the adsorbent surface charge is zero) the adsorbent surface has a negative charge, and if pH < pH_{pzc} the adsorbent surface is positively charged. Solution pH also determines the adsorbate speciation and adsorbate availability for adsorption (Kupeta et al., 2018). At low solution pH, H_3O^+ ions compete with metal ions for adsorption sites, while at high solution pH, some metal ions besides competing with OH^- ions for adsorption sites precipitate as insoluble hydroxides giving false adsorption capacities. A change in pH can be used to achieve the desorption of metal ions and the regeneration of adsorption sites (Park et al., 2017).

2.3.6.5.4 The initial concentration of metal ions

The initial metal ion concentration determines the concentration gradient required to overcome the resistance to mass transfer at the liquid-solid interface (Gupta et al., 2017). Ibisi and Asoluka (2018), showed an increase in uptake of Pb(II) and Cd(II) ions on *Musa paradisiaca* peels (agro-waste) adsorbent with an increase in initial metal ion concentration up to a certain level, showing saturation of adsorption sites.

2.3.6.5.5 Temperature

Temperature is the average kinetic energy of the particles during the adsorption process and influences the ionization of functional groups since the dissociation constants, *pK* values are temperature-dependent. It also affects the stability of metal ions and the adsorption complexes at the adsorption binding sites (Fakhre & Ibrahim, 2018; Ibisi & Asoluka, 2018). The experimental data on the effects of temperature is used to calculate the adsorption thermodynamic parameters.

2.3.6.5.6 Adsorbent dosage concentration

The increase in the mass amount of adsorbent increases the number of adsorption binding sites and the adsorption capacity. Some researchers have observed a decrease in adsorption capacity with an increase in adsorbent dose. This was attributed to a shortage of pollutant in solution causing some adsorption sites to remain vacant or interference between adsorption binding sites (Gupta et al., 2017; Foroutan et al., 2018; Huang et al., 2018).

2.3.6.6 *Limitations of adsorption*

Adsorption has not attained much prominence on commercial-scale applications, regardless of its inherent merits over other wastewater treatment technologies. This might be attributed to: (1) failure of adsorbents to reclaim effluents with a myriad of pollutants, (2) inability of the adsorbents to perform optimally on commercial-scale columns, and (3) lack of adsorbents exhibiting superior adsorption capacities towards the target pollutants (Santhosh et al., 2016). Despite the drawbacks, adsorption is still a promising technology in wastewater treatment for the future. Current scholarly interest is focused on nanosize adsorbents as they show unique properties towards contaminants in wastewater due to their small size, high porosity and active surfaces towards different chemical species.

2.4 DESORPTION

The desorption process involves the reversal of the adsorbate-adsorbent interaction at the adsorption binding site. The desorption experimental data is useful in the determination of the adsorption mechanism, metal recycling and regeneration of the adsorption binding sites (Dubey & Sharma, 2017). The use of chemical reagents such as HC*l*, NaOH, CH_3COOH and H_2O to desorb the metal ions gives an insight into the type of adsorbate-adsorbent interaction. A small volume of the desorbing agent is utilised and it should not alter the adsorption binding sites to enable the use of adsorbent in the next adsorption cycles.

2.5 TYPES OF ADSORBENTS

The traditional adsorbents are clays, zeolites, carbons, activated alumina, silica gel, polymers and resins (Rao & Kashifuddin, 2016; Tzvetkov et al., 2016; Sui et al., 2017; Wang et al., 2017; Zhu et al., 2017; Jiang et al., 2018; Kumari et al., 2019). The majority of these adsorbents are synthetic, expensive and non-biodegradable. Micro-organisms and agricultural waste products have been investigated as potential low-cost and effective adsorbents (Rwiza et al., 2018; Elahi

et al., 2020). With the advent of nanotechnology, nanoscale metal oxides have been widely applied as adsorbents for several pollutants in wastewater (Zhang et al., 2013; Wang et al., 2015). A number of these metal oxides such as those of Mn, Fe and Cu are already present in the environment and show no toxicity to life.

2.5.1 Nanosize metal oxides (NMOs)

Naturally occurring metal oxides are known to immobilise trace metal species from the hydrosphere (Zhang et al., 2012). Current scholarly research has shown that nanosize oxides of polyvalent metals like Cu(II), A*l*(III), Fe(III), Mn(IV), Ti(IV) and Zr(IV) have excellent adsorption capacities, high surface area and selectivity towards trace metal ions from aqueous solution (Wang et al., 2015; Nasir et al., 2019). These nanosize metal oxides (NMOs) show very different characteristics from their bulk counterparts due to the size-quantization effect (Namratha & Byrappa, 2012). The NMOs do not just adsorb the trace metal ions but are also able to oxidise or reduce them to less toxic and easily removable species from aqueous solutions (Zhang et al., 2012). Interactions between trace metals and NMOs are not fully understood and this hinders the development of appropriate trace metal remediation technologies. Since the retention mechanism of heavy metal ions on NMOs is not completely known, the term 'sorption' should describe the process correctly. Sorption implies the removal of metal ion species from the liquid onto the solid phase and encompasses adsorption, surface precipitation and fixation (diffusion of adsorbed metal ions into metal oxide lattice). A variety of methods such as co-precipitation (Sharma & Ghose, 2014), simultaneous redox and co-precipitation (Lü et al., 2013), sol-gel (Tabesh et al., 2018), microwave-assisted (Cheng et al., 2016) and biological (Gunalan et al., 2012) procedures have currently been used to synthesize NMOs.

2.5.1.1 *Importance of impregnating NMOs on a porous support*

The NMOs have high affinity and fast kinetics towards inorganic and organic contaminants in wastewater. A major drawback of NMOs is agglomeration into large particles in aqueous media due to van der Waals forces and/or other interactions resulting in a reduction of adsorption capacity (Santhosh et al., 2016). This hampers their use in flow-through or fixed-bed systems. The NMOs are usually synthesized as fine and ultrafine particles lacking mechanical strength causing pressure drops when applied in a column. To overcome such technical bottlenecks, it is necessary to impregnate the NMOs onto large porous support such as activated carbon, clays,

graphene, silica, synthetic polymers, etc (Hua et al., 2012). Adsorption capacity of 413.22 mg/g on congo red removal was achieved by Satheesh et al. (2016) using α-Fe_2O_3 (haematite) nanoparticles.

2.5.1.2 *Magnetic nanosize metal oxides*

Magnetic nanosize metal oxide and/or magnetic nanoparticle (MNP) adsorbents which are easy to recycle and regenerate in a magnetic field have been synthesized and applied for environmental cleanup in aqueous systems. This greatly reduces process cost and improves operational efficiency. A magnetic $MnFe_2O_4$-graphene composite achieved adsorption capacities of 100 mg/g and 76.90 mg/g for sequestration of Pb(II) and Cd(II) at pHs 5 and 7 respectively from wastewater (Chella et al., 2015). Muthukumaran et al. (2016), using Fe_3O_4 (magnetite) MNPs reported an adsorption capacity of 166.17 mg/g for remediation of crystal violet from wastewater.

2.5.1.3 *Adverse effects of metal oxides nanoparticles*

The cytotoxicity and/or genotoxicity of metal oxide nanoparticles to human tissue is not fully understood and requires further investigation (Dasari et al., 2013; Goix et al., 2014; Ko & Kong, 2014). Some authors have published on potential effects of NMOs to plants and microbes due to their involvement in biological and geochemical cycling in the environment. Nanotoxicity of the metal oxides is predicted to be largely due to the release of ions from the nanoparticle adsorbents (Seabra & Durán, 2015). This is particularly important during reclamation of wastewaters at low pH since it is known that metallic ions can leach in very acidic media.

2.5.1.4 *Biogenic (green) synthesis of nanosize metal oxides*

Classical synthetic routes of NMOs require toxic reagents, sophisticated instrumentation and high temperatures. This has led some researchers to develop eco-friendly biological synthetic pathways for the metal oxide nanoparticles using different microflora (bacteria, fungi, algae, etc). The biological/biogenic synthetic pathways are simple and cost-effective since there is no intensive use of hazardous chemicals and electrical energy. The main technical challenges to biogenic synthetic routes include (1) problems with scaling up production, (2) difficulty with the design of reproducible procedures, (3) lack of control of nanoparticle sizes and distribution, and (4) failure to elucidate the biochemical reaction mechanisms for the formation of the

nanoparticles (Gunalan et al., 2012; Adner et al. 2013; Arthi et al. 2015; Bai et al. 2015; Hajizadeh-Oghaz et al. 2015; Seabra & Durán, 2015).

2.5.2 Low-costs adsorbents

An adsorbent can be considered low-cost if it requires little processing, is abundant in nature or is a by-product or waste material from another industry. These include micro-organisms, industrial by-products and agricultural wastes.

2.5.2.1 *Micro-organisms*

Micro-organisms (fungi, algae and bacteria) are eco-friendly, low-cost and effective adsorbents in wastewater decontamination. Substantial research has been conducted on the use of live and dead microbial cells as adsorbents for pollutant removal from wastewater. Use of dead microbes is advantageous because (1) they do not need a constant supply of nutrients hence a decrease in the levels of chemical oxygen demand and biological oxygen demand, (2) the adsorbents can be easily regenerated and reused for several cycles, and (3) dead microbes are not affected by toxic waste (Jobby et al. 2018). Many yeast, algae and bacteria have shown the capability to remove metal ions from dilute aqueous solutions. Dead cells can remove heavy metal ions to the same or greater extent than living cells. The reason for this is the inhibition of microbial growth when the concentration of metal ions becomes high or when significant amounts of metal ions have been adsorbed by the micro-organisms. Cell walls of eubacteria are made up of a polysaccharide called peptidoglycan and that of archaebacteria consists of the polysaccharide pseudomurein. The fungal cell walls are made from the polysaccharides chitin and chitosan. Algae cell walls are mainly cellulose. These polysaccharides have functional groups (amino, amido, carboxyl, hydroxyl, phosphate and sulphate) which can act as adsorption active sites for metal immobilization. Metal uptake by different parts of inactive microbial cells is a complex phenomenon. It can occur via different passive processes including complexation, chelation, co-ordination, ion-exchange, precipitation and reduction. The metal adsorption kinetics has been proposed to take place in two stages. The first rapid stage, thought to be physical adsorption or ion-exchange occurs at the cell surface. The subsequent stage is slower and due to chemisorption. Chemicals isolated from the microbial biomass (e.g. chitin, chitosan and alginate) are also used as adsorbents (Bishnoi, 2016; Hussain et al., 2016; Esmaeili & Beni, 2018; Shen & Chirwa, 2020).

2.5.2.2 *Industrial by-products*

Industrial activities in power generation, metallurgy, fertiliser, paper, and leather industries produce huge amounts of solid waste. Use of these industrial by-products as low-cost adsorbents reduces the volume of waste materials and pollution of industrial wastewaters. Some of the industrial wastes products that have been investigated as adsorbents for sequestration of heavy metal ions include fly ash, metallurgical slag, red mud, activated sludge, etc (Crini et al., 2019; Kumar et al., 2019; Sellner et al., 2019).

2.5.2.3 *Agricultural wastes*

Agricultural by-products are high volume, low value and underutilized biopolymers which can pose a serious environmental disposal problem. Their use in adsorption will contribute significantly to environmental protection and additional income to farmers. Use of agricultural by-products as adsorbents is a cost-effective alternative for wastewater treatment. Usually, the biomass that one would not suspect to have adsorptive properties can show the ability to effectively remove metal ions from solution, for example, crushed eggshells, bones, etc (Sulyman, 2016; Tabatabaee et al., 2016; Anastopoulos et al., 2017; Sulyman et al., 2017; Afroze & Sen, 2018; Sharma et al., 2018).

Agricultural waste products (biosorbents) are used in the treatment of industrial wastewater in their natural form or after modification. Biosorbent modification involves physical (usually thermal) or chemical manipulation of biomaterial surface properties such as type and amount of functional groups, surface area and porosity by extraction of chemical components. The use of untreated agricultural waste as adsorbents results in high chemical and biological oxygen demand caused by leaching of soluble organics, reducing the content of oxygen in water thus threatening aquatic organisms. Hence, modification of biomass is essential to preventing colouration of treated wastewater and disintegration of biosorbent during prolonged contact with water, thereby (1) increasing the adsorption capacity of the biosorbent by swelling of the material to increase the internal and external surfaces, and (2) modifying biosorbent surface to increase cation exchange capacity and allow for penetration of polyfunctional organic moieties into the biosorbent matrix to increase biosorption sites (Afroze et al., 2016, Ali et al., 2016; Gupta et al., 2016; Wang et al., 2016; Zhou et al., 2016).

Agricultural waste materials show good reactivity since most are lignocellulosic (mainly contain lignin, hemicelluloses and cellulose). They possess acetamido, hydroxyl, carboxyl, carbonyl, phenolic, imine, amine, imidazole, thioether, phosphate, phosphodiester and sulphydryl functional groups. These functional groups can undergo chemical derivatization via esterification, etherification, hydrolysis, enzymatic degradation, oxidation or grafting reactions (Ghani et al., 2017; Guo et al., 2017; Noor et al., 2017; Yang et al., 2019). Several biomass modification techniques which include the use of mineral or organic acids (sulphuric acid, nitric acid, phosphoric acid, hydrochloric acid, citric acid, tartaric acid), strong bases (calcium hydroxide, sodium hydroxide, sodium carbonate), oxidising agents (Fenton's reagent, potassium permanganate), organic compounds (ethylenediaminetetraacetic acid, formaldehyde, epichlorohydrin), grafting and solvent extraction have been reported in the literature by several authors (Ofomaja et al., 2012; Reddy et al., 2012; Pholosi et al., 2013, Qiu et al., 2017; Kupeta et al., 2018; Owu-Owolabi et al., 2018; Wen et al., 2018; Pyrzynska, 2019).

2.6 BIOCHAR

Biochar consists of 30-70 percent carbon and is fabricated by thermal combustion of biomass in limited or zero amount of oxygen (Ahmad et al., 2014, Guo et al., 2019). For ages, farmers have been utilising biochar for soil amendment and in recent times, environmental scientists and engineers have applied it for remediation of heavy metal-laden wastewaters. The carbon skeleton in the biochar can act as a nucleophile or Lewis base facilitating reduction and/or immobilization of heavy metals (Pradhan et al., 2017). In comparison to activated carbon, biochar is a low-cost adsorbent since it is carbonized below 800 °C. The physicochemical properties of biochar depend on the biomass feed and preparation conditions (Li et al., 2018). The biochar has high porosity giving it a large surface area and making it a good candidate to act as a host/support for nanometal oxides which tend to agglomerate or aggregate during adsorption (Lee et al., 2017; Yang et al., 2019). The engineered biochar-nanometal oxide composites have exhibited excellent heavy metal adsorptive capabilities (Zhou et al., 2018).

2.7 OPTIMIZATION OF WORKING PARAMETERS

The optimization of experimental procedures entails the determination of levels of independent variables that produce the maximum desired result (response). This can be accomplished using the one-variable-at-a-time technique, which has two main disadvantages: (1) the interaction between independent variables is ignored and (2) many experiments need to be performed

increasing operational expenses (Bezerra et al., 2008). As an alternative, researchers exploit multivariate techniques such as response surface methodology (RSM).

2.7.1 Response surface methodology (RSM)

Response surface methodology uses mathematical modelling to establish the relationship between several independent variables and the response(s) (Sadhukan et al., 2016). The multivariate technique comprises experimental design, statistical analysis and optimization techniques. It was first developed by Box and Wilson (1951) and is applicable in situations were (1) several independent variables determine the response(s) and (2) the relationship or underlying mechanism between the independent variables and the response(s) is/are unknown. The technique simultaneously optimizes the levels of the independent variables to attain the maximum response and generates a response function which describes the process (Baş & Boyacı, 2007). The term response surface methodology emanates from a graphical presentation of the independent variables and the response. The response values are viewed as a surface lying above the plane of the independent variables as in Fig 2.5(a), which shows the graphical relationship between the response (yield %) and the two independent variables (time and temperature). When all points with the same response in the plane of the independent variables are joined as in Fig 2.5(b), a contour plot results (Myers et al., 2008).

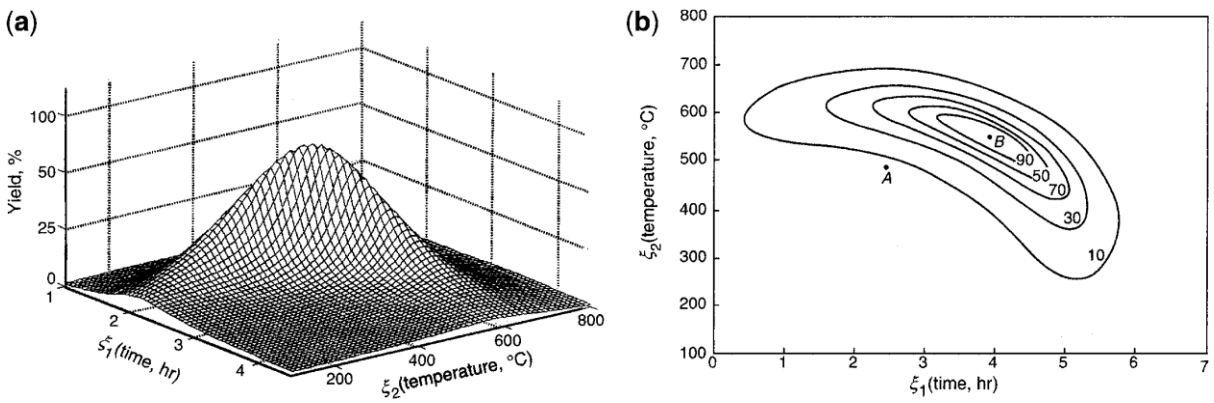

Fig 2.5 (a) Response surface between yield % (response) and the independent variables (time and temperature) and (b) Contour plot of the response surface (Myers et al., 2008).

2.7.2 Phases in response surface methodology

The optimization of independent variables using response surface methodology is undertaken in phases: (1) screening experiment to eliminate independent variables with little effect on the response and identification of the experimental region, (2) coding of independent variables, (3)

experimental design to estimate the applicable response function using linear or quadratic response modelling, (4) statistical evaluation of the response function, and (5) determination of optimum levels of the independent variables (Bezerra et al., 2008).

2.8 MODELLING OF ADSORPTION DATA

The mathematical fitting of adsorption experimental data to kinetic and equilibrium isotherm equations serves to measure the potential of the adsorbent, influence engineering design of the adsorption system and contributes towards the elucidation of the remediation mechanism. In addition to kinetic and equilibrium isotherm parameters, the adsorption mechanistic pathway is correctly postulated by also considering (1) speciation of the adsorbate, (2) surface properties of adsorbent, (3) data from analytical instrumentation, (4) desorption studies and (5) thermodynamic parameters (Albadarin et al., 2012; Tran et al., 2017).

2.8.1 Kinetics of adsorption

Adsorption experimental data is analysed using kinetic and diffusion parameters to establish the rate of adsorbate transportation to the adsorbent external and internal surfaces (Tran et al., 2017). The kinetic and diffusion parameters are studied using different mathematical models including pseudo-first-order (Lagergren, 1898), pseudo-second-order (Blachard et al., 1984), intraparticle diffusion models (Weber & Morris, 1963) etc. and are useful in the determination of the adsorption mechanism. To determine the adsorption mechanism, the adsorption kinetics and diffusion parameters should be used in conjunction with (1) analytical and spectroscopic methods, (2) knowledge of the physicochemical properties of an adsorbent surface, (3) data on the chemical speciation of the adsorbent in solution, and (4) adsorption thermodynamics parameters (Lima et al., 2015; Lima et al., 2016; Tran et al., 2016).

2.8.2 Equilibrium studies

The equilibrium isotherms are invaluable curves showing the relations at a constant temperature between equilibrium concentrations of the adsorbate on the solid phase and in the liquid phase. The isotherm equation parameters can describe the adsorption mechanism, surface properties, adsorption capacities and compare adsorption performance. Since the isotherms express the adsorptive capability of the adsorbent this enables the evaluation of parameters which are important in optimising the adsorption process. The equilibrium isotherm models have been proposed in terms of three fundamental approaches: (1) kinetic

considerations, (2) thermodynamics, and (3) potential theory (Foo & Hameed, 2010; Ayawei et al., 2017). They can be classified according to the number of model equation parameters (Saadi et al., 2015). The Freundlich (Freundlich, 1906) and Langmuir (Langmuir, 1918) models (two-parameter) are the most commonly preferred isotherms. The other two-parameter models include Temkin (Temkin & Pyzhev, 1940), Dubinin-Radushkevich (Dubinin & Radushkevich, 1947), Halsey (Halsey, 1948) and Flory-Huggins (Flory, 1953). The two-parameter models are usually used due to their simplicity which makes them easy to linearize. Linearization of the equations allows for the fitting of experimental data and determination of the isotherm parameters. The three-parameter isotherm models include Redlich-Petersen (Redlich & Petersen, 1959), Hill (Hill, 1946), Sips (Sips, 1948), Tóth (Tóth, 1971), Radke-Prausnitz (Radke & Prausnitz, 1972), Khan (Khan et al., 1996) and Koble-Corrigan (Koble & Corrigan, 1952). The four-parameter models include Weber-Van Vliet (Weber & Van Vliet, 1979), Fritz-Schundler (Fritz & Schundler, 1974) and Baudu (Baudu, 1990). The five-parameter models include Fritz-Schundler (Fritz & Schundler, 1974) and BET (Brunauer et al., 1938). In essence, isotherm model accuracy is a function of the number of independent parameters. A summary of equilibrium adsorption isotherms is presented in Fig 2.6.

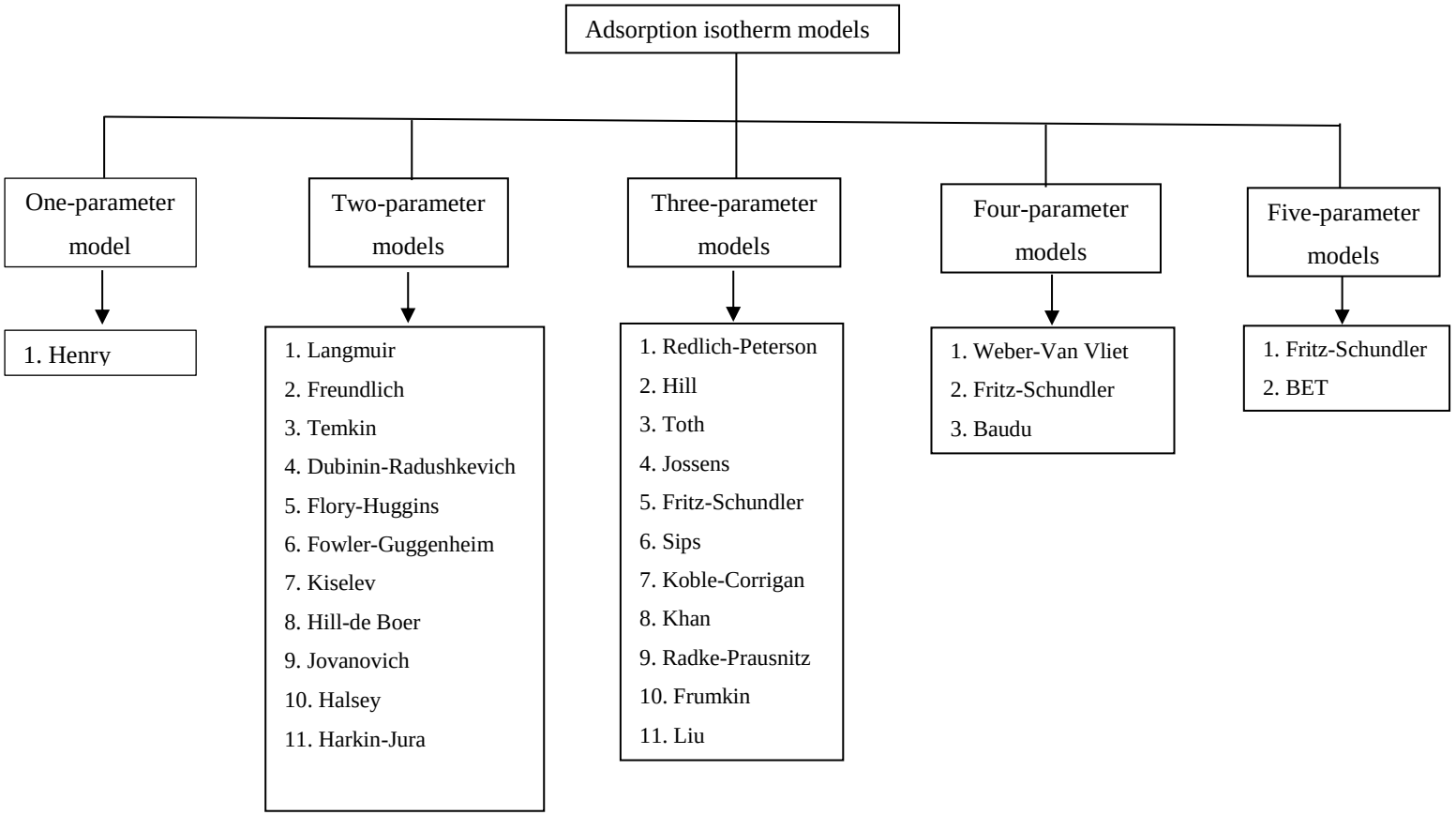

Fig 2.6 Adsorption isotherm models (Rangabhashiyam et al., 2014).

2.8.3 Effect of linearization of kinetic and isotherm models

The linear regression of kinetic and isotherm models makes it easy to determine the model parameters in liquid-phase adsorption systems. A drawback is that it can lead to biased estimates of non-linear model parameters. It is recommended that non-linear optimization of kinetic and equilibrium isotherm data be applied to eliminate bias between adsorption capacity values obtained from experiment and those estimated from mathematical models (Trans et al., 2017).

2.8.4 Error functions

Statistical error functions are used as a guideline to measure the accuracy of linear and non-linear mathematical models. They substantiate the quality of fit between experimental and modelled data (Tan & Hameed, 2017).

2.8.4.1 *Linear error functions*

1. The coefficient of determination, R^2

It represents the proportion of variance in the dependent variable that can be explained by the linear regression line $0 \leq R^2 \leq 1$, with zero indicating that zero percent of the variation of the dependent variable (q_e) has been explained by the regression equation. The coefficient of determination, R^2 can be calculated using the following equation:

$$R^2 = \frac{(q_e - q_{e,m})^2}{\Sigma(q_e - q_{e,m})^2 + (q_e - q_{e,m})^2} \tag{2.19}$$

where $q_{e,m}$ (mg/g) is the calculated adsorption capacity and q_e (mg/g) is the experimental adsorption capacity also known as the base value.

2. Percentage variance, % var

Percentage variance or percentage variable error shows the ratio of the absolute variation to the base value. An absolute variation is a difference between $q_{e,m}$ (mg/g) and q_e (mg/g). The following equation can be used to elucidate the percentage variance:

$$\%\ var = \frac{100}{n} \sum_{i=1}^{n} \left(\frac{q_{e,m} - q_e}{q_e} \right) \tag{2.20}$$

The larger the % variance, the greater the variation between the calculated and experimental adsorption capacities.

2.8.4.2 *Non-linear error functions*

The following are non-linear error functions for non-linear mathematical modelling:

1. Sum of absolute errors (SAE):

$$SAE = \sum_{i=1}^{n} \left| q_{e,m} - q_e \right|_i \tag{2.21}$$

2. Sum square errors (SSE):

$$SSE = \sum_{i=1}^{n} \left(q_{e,m} - q_e \right)_i^2 \tag{2.22}$$

3. Average relative error (ARE):

$$ARE = \frac{100}{n} \sum_{i=1}^{n} \left| \frac{q_e - q_{e,m}}{q_e} \right|_i \tag{2.23}$$

4. Hybrid fractional error function (HYBRID):

$$HYBRID = \frac{100}{n-p} \sum_{i=1}^{n} \left[\frac{\left(q_e - q_{e,m} \right)^2}{q_e} \right]_i \tag{2.24}$$

5. Marquardt's percent standard deviation (MPSD):

$$MPSD = 100 \sqrt{\frac{1}{n-p} \sum_{i=1}^{n} \left(\frac{q_e - q_{e,m}}{q_e} \right)_i^2} \tag{2.25}$$

6. Spearman's correlation coefficient:

$$r_s = 1 - \frac{6 \sum_{i=1}^{n} \left(q_e - q_{e,m} \right)_i^2}{n(n-1)^2} \tag{2.26}$$

7. Standard deviation of relative errors (SRE):

$$SRE = \sqrt{\frac{\sum_{i=1}^{n} \left[\left(q_e - q_{e,m} \right) - ARE \right]_i^2}{n-1}} \tag{2.27}$$

8. Non-linear chi-square test:

$$\chi^2 = \sum_{i=1}^{n} \frac{\left(q_{e,m} - q_e \right)^2}{q_e} \tag{2.28}$$

2.9 CONCLUSION

Literature review on the types of trace metal pollutants in aqueous effluent, water decontamination techniques, types of adsorbents, response surface methodology and the mathematical modelling of experimental adsorption data is presented in this chapter.

2.10 REFERENCES

1. ABDI, G., ALIZADEH, A., ZINADINI, S. and MORADI, G. (2018) Removal of dye and heavy metal ion using a novel synthetic polyethersulfone nanofiltration membrane modified by magnetic graphene oxide/metformin hybrid, *Journal of Membrane Science*. 552, pp. 326-335.
2. ABEJÓN, A., GAREA, A. and IRABIEN, A. (2015) Arsenic removal from drinking water by reverse osmosis: Minimization of costs and energy consumption, *Separation and Purification Technology*. 144, pp. 46-53.
3. ADJEROUD, N., DAHMOUNE, F., MERZOUK, B., LECLERC, J.P. and MADANI, K. (2015) Improvement of electrocoagulation–electroflotation treatment of effluent by addition of *Opuntia ficus indica* pad juice, *Separation and Purification Technology*. 144, pp. 168-176.
4. ADNER, D., KORB, M., SCHULZE, S., HIETSCHOL, M. and LANG, H. (2013) A straight forward approach to oxide-free copper nanoparticles by thermal decomposition of a copper(I) precursor, *Chemical Communications*. 49, pp. 6855-6857.
5. AFROZE, S. and SEN, T.K. (2018) A review on heavy metal ions and dye adsorption from water by agricultural solid waste adsorbents, *Water, Air, & Soil Pollution*, 229, p. 225.
6. AFROZE, S., SEN, T.K. and ANG, H.M. (2016) Adsorption removal of zinc (II) from aqueous phase by raw and base modified Eucalyptus sheathiana bark: Kinetics, mechanism and equilibrium study, *Process Safety and Environmental Protection*. 102, pp. 336-352.
7. AHMAD, M., RAJAPAKSHA, A.U., LIM, J.E., ZHANG, M., BOLAN, N. and MOHAN, D. (2014) Biochar as a sorbent for contaminant management in soil and water: a review, *Chemosphere*. 99, pp. 19–33.
8. AIGBE, U.O., DAS, R., HO, W.H., SRINIVASU, V. and MAITY, A. (2018) A novel method for removal of Cr (VI) using polypyrrole magnetic nanocomposite in the presence of unsteady magnetic fields, *Separation and Purification Technology*. 194, pp. 377-387.

9. AKPOR, O.B., OHIOBOR, G.O. and OLAOLU, T.D. (2014) Heavy metal pollutants in wastewater effluents: Sources, effects and remediation, *Advances in Bioscience and Bioengineering*. 2, pp. 37-43.

10. ALBADARIN, A.B., MANGWANDI, C., AL-MUHTASEB, A.H., WALKER, G.M., ALLEN, S.J. and AHMAD, N.M. (2012) Kinetic and thermodynamics of chromium ions adsorption onto low-cost dolomite adsorbent, *Chemical Engineering Journal*. 179, pp. 193-202.

11. ALI, A., SAEED, K. and MABOOD, F. (2016) Removal of chromium (VI) from aqueous medium using chemically modified banana peels as efficient low-cost adsorbent, *Alexandria Engineering Journal*. 55, pp. 2933-2942.

12. AL-SAYDEH, S.A., EL-NAAS, M.H. and ZAIDI, S.J. (2017) Copper removal from industrial wastewater: A comprehensive review, *Journal of Industrial and Engineering Chemistry*. 56, pp. 35-44.

13. AL-SENANI, G.M and AL-FAWZAN, F.F. (2018) Adsorption study of heavy metal ions from aqueous solution by nanoparticle of wild herbs, *Egyptian Journal of Aquatic Research*. 44, 187–194.

14. ANASTOPOULOS, I., KARAMESOUTI, M., MITROPOULOS, A.C. and KYZAS, G.Z. (2017) A review for coffee adsorbents, *Journal of Molecular Liquids*. 229, pp. 555-565.

15. ANASTOPOULOS, I and KYZAS, G.Z. (2016) Are the thermodynamic parameters correctly estimated in liquid-phase adsorption phenomena, *Journal of Molecular Liquids*. 218, pp. 174-185.

16. ARTHI, G., ARCHANA, J., NAVANEETHAN, M., PONNUSAMY, S., HAYAKAWA, Y. and MUTHAMIZHCHELVAN, C. (2015) Solvothermal growth of diethylamine capped TiO_2 nanoparticles and functional properties, *Journal of Materials Science: Materials in Electronics*. 26, pp. 2380-2383.

17. AYAWEI, N., EBELEGI, A.N. and WANKASI, D. (2017) Modelling and interpretation of adsorption isotherms, *Journal of Chemistry*. 2017.

18. AZIMI, A., AZARI, A., REZAKAZEMI, M. and ANSARPOUR, M. (2017) Removal of heavy metals from industrial wastewaters: a review, *ChemBioEng Reviews*. 4, pp. 37-59.

19. BAI, X., LI, J., LIU, H., TAN, L., LIU, T. and MENG, X. (2015) Solvothermal synthesis of ZnO nanoparticles and anti-infection application *in vivo*, *ACS Applied Materials & Interfaces*. 7, pp. 1308-1317.

20. BAI, Y., YANG, T., LIANG, J. and QU, J. (2016) The role of biogenic Fe-Mn oxides formed in situ for arsenic oxidation and adsorption in aquatic ecosystems, *Water Research*. 98, pp. 119-127.

21. BARRERA-DÍAZ, C.E., LUGO-LUGO, V. and BILYEU, B. (2012) A review of chemical, electrochemical and biological methods for aqueous Cr(VI) reduction, *Journal of Hazardous Materials*. 223-224, pp.1-12.

22. BAŞ, D. and BOYACI, I.H. (2007) Modeling and optimization I: Usability of response surface methodology. *Journal of Food Engineering*. 78, pp.836-845.

23. BAUDU, M. (1990) Étude des interactions solute-fibres de charbon actif. Application et regeneration, Ph.D. Thesis, Université de Renners.

24. BEN-ALI, S., JAOUALI, I., SOUISSI-NAJAR, S. and OUEDERNI, A. (2017) Characterization and adsorption capacity of raw pomegranate peel biosorbent for copper removal, *Journal of Cleaner Production*. 142, pp. 3809-3821.

25. BEZERRA, M.A., SANTELLI, R.E., OLIVEIRA, E.P., VILLAR, L.S. and ESCALEIRA, L.A. (2008) Response surface methodology (RSM) as a tool for optimization in analytical chemistry, *Talanta*. 76, pp. 965-977.

26. BISHNOI, N.R. (2016) A Review on Biosorption of Potentially Toxic Metallic Pollutants from Wastewaters by Bacterial Adsorbents, *Journal of Applied Life Sciences International*, pp. 1-11.

27. BLANCHARD, G., MAUNAYE, M. and MARTIN, G. (1984) Removal of heavy metals from waters by means of natural zeolites, *Water research*. 18, pp. 1501-1507.

28. BOX, G.E.P. and WILSON, K.B. (1951) On the experimental attainment of optimum conditions, *Journal of Royal Statistics Society: Series B (Methodological)*. 13, pp. 1-45.

29. BRUNAUER, S., EMMETT, P.H. and TELLER, E. (1938) Adsorption of gases in multimolecular layers, *Journal of American Chemical Society*. 60, pp. 309-319.

30. BUTERA, S., TRAPP, S., ASTRUP, T.F. and CHRISTENSEN, T.H. (2015) Soil retention of hexavalent chromium released from construction and demolition waste in a road-based-application scenario, *Journal of Hazardous Materials*. 298, 361-367.

31. CALMON, C. (2018) Specific ion exchangers, In *Ion Exchange Pollution Control*. CRC Press, pp. 150-154.

32. CAROLIN, C.F., KUMAR, P.S., SARAVANAN, A., JOSHIBA, G.J. and NAUSHAD, M. (2017) Efficient techniques for the removal of toxic heavy metals from aquatic environment: A review, *Journal of Environmental Chemical Engineering*. 5, pp. 2782-2799.

33. CHARUMATHI, D. and DAS, N. (2012) Packed bed column studies for the removal of synthetic dyes from textile wastewater using immobilised dead *C. tropicalis*, *Desalination*. *285*, pp. 22-30.

34. CHEN, Q., YAO, Y., LI, X., LU, J., ZHOU, J. and HUANG, Z. (2018) Comparison of heavy metal removals from aqueous solutions by chemical precipitation and characteristics of precipitates, *Journal of Water Process Engineering*. 26, pp. 289-300.

35. CHIEN, S.H. and CLAYTON, W.R. (1980) Application of Elovich equation to the kinetics of phosphates release and sorption in soils, *Soil Science Society of America Journal*. 44, pp. 265-268.

36. CHIN, L.S., CHEUNG, W.H., ALLEN, S.J. and McKAY, G. (2012) Error analysis of adsorption isotherm models for acid dyes onto bamboo derived activated carbon, *Chinese Journal of Chemical Engineering*. 20, pp. 535-542.

37. CHANG, Y-Y., LIM, J-W. and YANG, J-K. (2012) Removal of As(V) and Cr(VI) in aqueous solution by sand media simultaneously coated with Fe and Mn oxides, *Journal of Industrial and Engineering Chemistry*. 18, pp. 188–192.

38. CHELLA, S., KOLLU, P., KOMARALA, E.V.P.R., DOSHI, S., SARANYA, M., FELIX, S., RAMACHANDRAN, R., SARAVANAN, P., KONERU, V.I., VENUGOPAL, V., JEONG, S.K., NIRMALA, A. and GRACE, A.N. (2015)

Solvothermal synthesis of $MnFe_2O_4$-graphene composite-Investigation of its adsorption and antimicrobial properties, *Applied Surface Science*. 327, pp. 27-36.

39. CHEN, T., CHANG, Q., LIU, J., CLEVERS, J. and KOOISTRA, L. (2016) Identification of soil heavy metal sources and improvement in spatial based mapping on soil spectral information: A case study in northwest China, *Science of the Total Environment*. 565, pp. 155-164.

40. CHEN, Q., YAO, Y., LI, X., LU, J., ZHOU, J. and HUANG, Z. (2018) Comparison of heavy metal removals from aqueous solutions by chemical precipitation and characteristics of precipitates, *Journal of Water Process Engineering*. 26, pp. 289-300.

41. CHIEN, S.H. and CLAYTON, W.R. (1980) Application of Elovich equation to the kinetics of phosphates release and sorption in soils, *Soil Science Society of America Journal*. 44, pp. 265-268.

42. CRINI, G., LICHTFOUSE, E., WILSON, L.D. and MORIN-CRINI, N. (2019) Conventional and non-conventional adsorbents for wastewater treatment, *Environmental Chemistry Letters*. 17, pp. 195-213.

43. CUI, H-J., CAI, J-K., ZHAO, H., YUAN, B., AI, C-L. and FU, M-L. (2014) Fabrication of magnetic porous Fe–Mn binary oxide nanowires with superior capability for removal of As(III) from water, *Journal of Hazardous Materials*. 279, pp. 26–31.

44. DASARI, T.P., PATHAKOTI, K. and HWANG, H (2013) Determination of the mechanism of photoinduced toxicity of selected metal oxide nanoparticles (ZnO, CuO, Co_3O_4 and TiO_2) to E.coli bacteria, *Journal of Environmental Sciences*. 25, pp. 882-888.

45. DHAL, B., THATOI, H.N., DAS, N.N. and PANDEY, B.D. (2013) Chemical and microbial remediation of hexavalent chromium from contaminated soil and mining/metallurgical solid waste: A review, *Journal of Hazardous Materials*. 250-251, pp. 272-291.

46. DU, Y., ZHENG, G., WANG, J., WANG, L., WU, J. and DAI, H. (2014) MnO_2 nanowires in situ grown on diatomite: Highly efficient absorbents for the removal of Cr(VI) and As(V), Microporous and Mesoporous Materials. 200, pp. 27–34.

47. DUBEY, S and SHARMA, Y.C. (2017) *Calotropis procera* mediated one pot green synthesis of Cupric oxide nanoparticles (CuO-NPs) for adsorptive removal of Cr(VI) from aqueous solutions, *Applied Organometallic Chemistry*. 31, pp. 1-15.

48. DUBININ, M.M. and RADUSHKEVICH, L.V. (1947) Equation of the characteristic curve of activated charcoal, *Proceedings of the Academy of Sciences (USSR)*. 55, pp. 331-333.

49. EDEBALI, S. and PEHLIVAN, E. (2016) Evaluation of chelate and cation exchange resins to remove copper ions, *Powder Technology*. 301, pp. 520-525.

50. ELAHI, A., AROOJ, I., BUKHARI, D.A. and REHMAN, A. (2020) Successive use of microorganisms to remove chromium from wastewater, *Applied Microbiology and Biotechnology*. pp. 1-15.

51. ESMAEILI, A. and BENI, A.A. (2018) Optimization and design of a continuous biosorption process using brown algae and chitosan/PVA nano-fiber membrane for removal of nickel by a new biosorbent, *International Journal of Environmental Science and Technology*. 15, pp. 765-778.

52. FAKHRE, N.A. and IBRAHIM, B.M. (2018) The use of new chemically modified cellulose for heavy metal ion adsorption, *Journal of Hazardous Materials*. 343, pp. 324-331.

53. FANG, L., LI, L., QU, Z., XU, H., XU, J, YAN, N. (2018) A novel method for the sequential removal and separation of multiple heavy metals from wastewater, *Journal of Hazardous Materials*. 342, pp. 617–624.

54. FIGUEIREDO, B.R., CARDOSO, S.P., PORTUGAL, I., ROCHA, J. and SILVA, C.M. (2018) Inorganic ion exchangers for cesium removal from radioactive wastewater, S*eparation & Purification Reviews*, 47, pp. 306-336.

55. FLORY, P.J. (1953) *Principles of polymer chemistry*. Cornell University Press.

56. FOO, K.Y. and HAMEED, B.H. (2010) Insights into the modelling of adsorption isotherm systems, *Chemical Engineering Journal.* 156, pp. 2-10.

57. FOROUTAN, R., ESMAEILI, H., ABBASI, M., REZAKAZEMI, M. and MESBAH, M. (2018) Adsorption behavior of Cu (II) and Co (II) using chemically modified marine algae, *Environmental Technology*. 39, pp. 2792-2800.

58. FREUNDLICH, H. (1906) Uber die adsorption in losungen, *Zeitschrift fur Physikalische Chemie (Leipzig)*. 57A, pp. 385-470.

59. FRITZ, W. and SCHUNDLER, E.U. (1974) Simultaneous adsorption equilibria of organic solutes in dilute aqueous solutions on activated carbon, *Chemical Engineering Science*. 29, pp. 1279-1282.

60. FU, F., XIE, L., TANG, B., WANG, Q. and JIANG, S. (2012) Application of a novel strategy—Advanced Fenton-chemical precipitation to the treatment of strong stability chelated heavy metal containing wastewater, *Chemical Engineering Journal*. 189, pp. 283-287.

61. GAN, Y., WEI, Y., XIONG, J. and CHENG, G. (2018) Impact of post-processing modes of precursor on adsorption and photocatalytic capability of mesoporous TiO_2 nanocrystallite aggregates towards ciprofloxacin removal, *Chemical Engineering Journal*. 349, pp. 1-16.

62. GAO, Z., XIE, S., ZHANG, B., QIU, X. and CHEN, F. (2017) Ultrathin Mg-Al layered double hydroxide prepared by ionothermal synthesis in a deep eutectic solvent for highly effective boron removal, *Chemical Engineering Journal*. 319, pp. 108-118.

63. GHANI, N.I.A., YUSUF, N.Y.M., ISAHAK, W.N.R.W. and MASDAR, M.S. (2017) Modification of Activated Carbon from Biomass Nypa and Amine Functional Groups as Carbon Dioxide Adsorbent, *Journal of Physical Science*. 28, pp. 227-240.

64. GOIX, S., LÉVÊQUE, T., XIONG, T., SCHREK, E., BAEZA-SQUIBAN, A., GERET, F. UZU, G., AUSTRUY, A. and DUMAT. C. (2014) Environmental and health impacts of fine and ultrafine metallic particles: Assessment of threat scores, *Environmental Research*. 133, pp. 185-194.

65. GORNY, J., BILLON, G., LESVEN, L., DUMOULIN, D., MADÈ, B. and NOIRIEL, C. (2015) Arsenic behavior in river sediments under redox gradient: a review, *Science of the Total Environment*. 505, pp. 423-434.

66. GUNALAN, S., RAJESHWARI, S. and RAJENDRAN, V. (2012) *Aloe barbadensis Miller* mediated green synthesis of mono-disperse copper oxide nanoparticles: Optical properties, *Spectrochimica Acta Part A: Molecular and Biomolecular Spectroscopy*. 97, pp. 1140-1144.

67. GUNARATHNE, V., RAJAPAKSHA, A.U., VITHANAGE, M., ADASSOORIYA, N., COORAY, A., LIYANAGE, S., ATHAPATTU, B., RAJAKARUNA, N., IGALAVITHANA, A.D., HOU, D. and ALESSI, D.S. (2019) Heavy metal dissolution mechanisms from electrical industrial sludge, *Science of The Total Environment*. pp. 1-11.

68. GUNATILAKE, S.K. (2015) Methods of removing heavy metals from industrial wastewater, *Journal of Multidisciplinary Engineering Science Studies*. 1, pp. 12-18.

69. GUO, J., YAN, C., LUO, Z., FANG, H., HU, S. and CAO, Y. (2019) Synthesis of a novel ternary HA/Fe-Mn oxides-loaded biochar composite and its application in cadmium(II) and arsenic(V) adsorption, *Journal of Environmental Sciences*. 85, pp. 168–176.

70. GUO, Z., ZHANG, J., LIU, H. and KANG, Y. (2017) Development of a nitrogen-functionalized carbon adsorbent derived from biomass waste by diammonium hydrogen phosphate activation for Cr (VI) removal, *Powder Technology*. 318, pp. 459-464.

71. GUPTA, V.K., AGARWAL, S., BHARTI, A.K. and SADEGH, H. (2017) Adsorption mechanism of functionalized multi-walled carbon nanotubes for advanced Cu (II) removal, *Journal of Molecular Liquids*. 230, pp. 667-673.

72. GUPTA, V.K., CARROTT, P.J.M., SINGH, R., CHAUDHARY, M. and KUSHWAHA, S. (2016) Cellulose: a review as natural, modified and activated carbon adsorbent, *Bioresource Technology*. 216, pp. 1066-1076.

73. HAJIZADEH-OGHAZ, M., RAZAVI, R.S. and KHAJELAKZAY, M. (2015) Optimizing sol-gel synthesis of magnesia-stabilized zirconia (MSZ) nanoparticles using Taguchi robust design for thermal barrier coatings (TBCs) applications. *Journal of Sol-Gel Science and Technology*. 73, pp. 227-241.

74. HALSEY, G. (1948) Physical adsorption on non-uniform surfaces, *Journal of Chemical Physics*. 16, pp. 931-937.

75. HAMILTON, E.M., YOUNG, S.D., BAILEY, E.H. and WATTS, M.J. (2018) Chromium speciation in foodstuffs: A review, *Food Chemistry*. 250, pp. 106-112.

76. HASHIM, K.S., SHAW, A., AL KHADDAR, R., PEDROLA, M.O. and PHIPPS, D. (2017) Iron removal, energy consumption and operating cost of electrocoagulation of drinking water using a new flow column reactor, *Journal of Environmental Management*. 189, pp. 98-108.

77. HEADLAM, H.A. and LAY, P.A. (2016) Spectroscopic characterization of genotoxic chromium (V) peptide complexes: Oxidation of chromium (III) triglicine, tetraglycine and pentaglycine complexes, *Journal of Inorganic Biochemistry*. 162, pp 227.

78. HILL, T.L. (1946) Statistical mechanics of multimolecular adsorption II. Localized and mobile adsorption and absorption, *The Journal of Chemical Physics*. 14, pp. 441–453.

79. HO, Y.S., WASE, D.J. and FORSTER, C.F. (1996) Kinetic studies of competitive heavy metal adsorption by sphagnum moss peat, *Environmental Technology*. 17, pp. 71-77.

80. HOU, J., SHA, Z., HARTLEY, W., TAN, W., WANG, M., XIONG, J., LI, Y., KE, Y., LONG, Y. and XUE, S. (2018) Enhanced oxidation of arsenite to arsenate using tunable K^+ concentration in the OMS-2 tunnel, *Environmental Pollution*. 238, pp. 524-531.

81. HU, Q. and ZHANG, Z. (2019) Application of Dubinin–Radushkevich isotherm model at the solid/solution interface: A theoretical analysis, *Journal of Molecular Liquids*. 277, pp. 646-648.

82. HUA, M., ZHANG, S., PAN, B., ZHANG, W., LV, L. and ZHANG, Q. (2012) Heavy metal removal from water/wastewater by nanosized metal oxides: A review, *Journal of Hazardous Materials*. 211-212, pp. 317-331.

83. HUANG, Y., ZENG, X., GUO, L., LAN, J., ZHANG, L. and CAO, D. (2018) Heavy metal ion removal of wastewater by zeolite-imidazolate frameworks, *Separation and Purification Technology*. 194, pp. 462-469.

84. HUSSAIN, S.N., TRZCINSKI, A.P., ASGHAR, H.M.A., SATTAR, H., BROWN, N.W. and ROBERTS, E.P.L. (2016) Disinfection performance of adsorption using graphite adsorbent coupled with electrochemical regeneration for various microorganisms present in water, *Journal of Industrial and Engineering Chemistry*. 44, pp. 216-225.

85. IBISI, N.E. and ASOLUKA, C.A. (2018) Use of agro-waste (*Musa paradisiaca* peels) as a sustainable biosorbent for toxic metal ions removal from contaminated water, *Chemistry International*. 4, pp. 52-59.

86. IZBICKI, J.A., WRIGHT, M.T., SEYMOUR, W.A., McCLESKEY, R.B., FRAM, M.S., BELITZ, K. and ESSER, B.K. (2015) Cr(VI) occurance and geochemistry in water from public-supply wells in California, *Applied Geochemistry*. 63, pp. 203-217.

87. JARDINE, P.M., FENDORF, S.E., MAYES, M.A., LARSEN, I.L., BROOKS, S.C. and BAILEY, W.B. (1999) Fate and transport of hexavalent chromium in undisturbed heterogeneous soil, *Environmental Science & Technology*. 33, pp. 2939-2944.

88. JIANG, N., SHANG, R., HEIJMAN, S.G. and RIETVELD, L.C. (2018) High-silica zeolites for adsorption of organic micro-pollutants in water treatment: A review, *Water Research*. 144, pp. 145-161.

89. JOBBY, R., JHA, P., YADAV, A.K. and DESAI, N. (2018) Biosorption and biotransformation of hexavalent chromium [Cr (VI)]: a comprehensive review, *Chemosphere*. 207, pp. 255-266.

90. KAN, C-C., IBE, A.H., RIVERA, K.K.P., ARAZO, R.O. and de LUNA, M.D.G. (2017) Hexavalent chromium removal from aqueous solution by adsorbents synthesized from groundwater treatment residuals, *Sustainable Environment Research*. 27, pp. 163-171.

91. KAPRARA, E., KAZAKIS, N., SIMEONIDIS, K., COLES, S., ZOUBOULIS, A.I., SAMARAS, P. and MITRAKAS, M. (2015) Occurrence of Cr (VI) in drinking water of Greece and relation to the geological background, *Journal of Hazardous Materials*. 281, pp. 2-11.

92. KHAN, A.R., AL-WAHEAB, I.R. and AL-HADDAD, A. (1996) A generalized equation for adsorption isotherms for multi-component organic pollutants in dilute aqueous solution, *Environmental Technology*. 17, pp.13-23.

93. KO, K. and KONG, I.C. (2014) Toxic effects of nanoparticles on bioluminescence activity, seed germination and gene mutation, *Applied Microbiology and Biotechnology*. 98, pp. 3295-3303.

94. KOBLE, R.A. and CORRIGAN, T.E. (1952) Adsorption isotherms for pure hydrocarbons, *Industrial and Engineering Chemistry*. 44, pp. 383-387.

95. KONONOVA, O.N., BRYUZGINA, G.L., APCHITAEVA, O.V. and KONONOV, Y.S. (2015) Ion exchange recovery of chromium (VI) and manganese (II) from aqueous solutions, *Arabian Journal of Chemistry*. https://doi.org/10.1016/j.arabjc.2015.05.021

96. KOTYZOVÁ, D., BLUDOVSKÁ, M. and EYBL, V. (2013) Differential influences of various arsenic compounds on antioxidant defense system in liver and kidney of rats, *Environmental toxicology and pharmacology*, 36, pp.1015-1021.

97. KUMAR, R., LASKAR, M.A., HEWAIDY, I.F. and BARAKAT, M.A.(2019) Modified adsorbents for removal of heavy metals from aqueous environment: a review, *Earth Systems and Environment*. 3, pp. 83-93.

98. KUMARI, U., BEHERA, S.K. and MEIKAP, B.C. (2019) A novel acid modified alumina adsorbent with enhanced defluoridation property: kinetics, isotherm study and applicability on industrial wastewater, *Journal of Hazardous Materials*. 365, pp. 868-882.

99. KUPETA, A.J.K., NAIDOO, E.B. and OFOMAJA, A.E. (2018) Kinetics and equilibrium study of 2-nitrophenol adsorption onto polyurethane cross-linked pine cone biomass, *Journal of Cleaner Production*. 179, pp. 191-209.

100. LAGERGREN, S. (1898) Zur theorie der sogenannten adsorption gelöster stoffe, *Kungliga Svenska Vetenskapsakademiens Handlingar*. 24, pp. 1-39.

101. LAKHERWAL, D. (2014) Adsorption of Heavy Metals: A Review, *International Journal of Environmental Research and Development*. 4, pp. 41-48.

102. LAKSHMIPATHY, R., SARADA, N.C. and JAYAPRAKASH, N. (2015) Agricultural wastes as low cost adsorbents for sequestration of heavy metal ions and synthetic dyes from aqueous solution: A mini review, *International Journal of ChemTech Research*. 8, pp. 25-31.

103. LANGMUIR, I. (1918) The adsorption of gases on plane surfaces of glass, mica and platinum, *Journal of American Chemical Society*. 40, pp. 1361-1403.

104. LEE, J., YANG, X., CHO, S.H., KIM, J.K., LEE, S.S., TSANG, D.C.W., OK, Y.S. and KWON, E.E. (2017) Pyrolysis process of agricultural waste using CO_2 for waste management, energy recovery, and biochar fabrication, *Appl. Energ*. 185, pp. 214–222.

105. LEWIS, A. (2017) Precipitation of Heavy Metals. In *Sustainable Heavy Metal Remediation*. Springer, Cham, pp. 101-120.

106. LI, J., GYOTEN, H., SONODA, A., FENG, Q. and XUE, M. (2017) Removal of trace arsenic to below drinking water standards using a Mn–Fe binary oxide, *RSC Advances*. 7, pp. 1490-1497.

107. LI, X., HE, K., PAN, B., ZHANG, S., LU, L. and ZHANG, W. (2012) Efficient As (III) removal by macroporous anion exchanger-supported Fe-Mn binary oxide: Behavior and mechanism, *Chemical Engineering Journal*. 193-194, pp. 131-138.

108. LI, R., WANG, J.J., GASTON, L.A., ZHOU, B., LI, M., XIAO, R., WANG, Q., ZHANG, Z., HUANG, H., LIANG, W., HUANG, H. and ZHANG, X. (2018) An overview of carbothermal synthesis of metal-biochar composites for the removal of oxyanion contaminants from aqueous solution, *Carbon*. 229, pp. 674-687.

109. LI, H., ZHANG, H., LONG, J., ZHANG, P. and CHEN, Y. (2019) Combined Fenton process and sulfide precipitation for removal of heavy metals from industrial wastewater: bench and pilot scale studies focusing on in-depth thallium removal, *Frontiers of Environmental Science & Engineering*. 13, p. 49.

110. LIMA, E.C., ADEBAYO, M.A. and MACHADO, F.M. (2015) Kinetic and equilibrium models of adsorption. In: *Carbon nanomaterials as adsorbents for environmental and biological applications*, pp. 33-69. Springer, Cham.

111. LIMA, E.C., CESTARI, A.R. and ADEBAYO, M.A. (2016) Comments on the paper: a critical review of the applicability of Avrami fractional kinetic equation in adsorption-based water treatment studies. *Desalination and Water Treatment*, 57, pp.19566-19571.

112. LITTER, M.I. (2017) Last advances on TiO_2-photocatalytic removal of chromium, uranium and arsenic, *Current Opinion in Green and Sustainable Chemistry*. 6, pp. 150-158.

113. LOU, Z., CAO, Z., XU, J., ZHOU, X., ZHU, J., LIU, X., BAIG, S.A., ZHOU, J. and XU, X., (2017) Enhanced removal of As (III)/(V) from water by simultaneously supported and stabilized Fe-Mn binary oxide nanohybrids. *Chemical Engineering Journal*, 322, pp.710-721.

114. LÜ, J., LIU, H., LIU, R., ZHAO, X., SUN, L. and QU, J. (2013) Adsorptive removal of phosphate by a nanostructured Fe-Al-Mn trimetal oxide adsorbent, *Powder Technology*. 233, pp. 146-154.

115. MA, W., CHEN, D., PAN, M., GU, T., ZHONG, L., CHEN, G., YAN, B. and CHENG, Z. (2019) Performance of chemical chelating agent stabilization and cement solidification on heavy metals in MSWI fly ash: A comparative study, *Journal of Environmental Management*. 247, pp. 169-177.

116. McCANN, C.M., PEACOCK, C.L., HUDSON-EDWARDS, K.A., SHRIMPTONA, T., GRAY, N.D. and JOHNSON, K.L. (2018) In situ arsenic oxidation and sorption by a Fe-Mn binary oxide waste in soil, *Journal of Hazardous Materials*. 342, pp. 724–731.

117. MEDDA, S. and MONDAL, N.K. (2017) Chromium toxicity and ultrastructural deformation of *Cicer arietinum* with special reference of root elongation and coleoptile growth, *Annals of Agrarian Science*. 15, pp.396-401.

118. MEI, Y. and TANG, C.Y. (2018) Recent developments and future perspectives of reverse electrodialysis technology: A review, *Desalination*. 425, pp. 156-174.

119. MERTZ, W (ed). (2012) *Trace elements in human and animal nutrition*, 5th ed. New York: Academic Press.

120. MIRBAGHERI, S.A. and HOSSEINI, S.N. (2005) Pilot plant investigation on petrochemical wastewater treatment for the removal of copper and chromium with the objective to reuse, *Desalination*. 171, pp. 85-93.

121. MOLINARI, R. and ARGURIO, P. (2017) Arsenic removal from water by coupling photocatalysis and complexation-ultrafiltration processes: a preliminary study, *Water Research*. 109, pp. 327-336.

122. MOURABET, M., RHILASSI, A. BOUJAADY, H., BENNANI-ZIATNI, M., TAITAI, A. (2017) Use of response surface methodology for optimization of fluoride adsorption in an aqueous solution by Brushite, *Arabian Journal of Chemistry*. 10, pp. S3292-S3302.

123. MUTHUKURAMAN, C., SIVAKUMAR, V.M. and THIRUMARIMURUGAN, M. (2016) Adsorption isotherms and kinetic studies of crystal violet dye removal from aqueous solution using surfactant modified magnetic nanoadsorbent, *Journal of the Taiwan Institute of Chemical Engineers*. 63, pp. 354-362.

124. NAMRATHA, K. and BYRAPPA, K. (2012) Novel solution routes for synthesis of metal oxide and hybrid metal oxide nanocrystals, *Progress in Crystal Growth and Characterization of Materials*. 58, pp. 14-42.

125. NASIR, A.M., GOH, P.S. and ISMAIL, A.F. (2019) Highly adsorptive polysulfone/hydrous iron-nickel-manganese (PSF/HINM) nanocomposite hollow fiber membrane for synergistic arsenic removal, *Separation and Purification Technology*. 213, pp. 162-175.

126. NEMATI, M., HOSSEINI, S.M. and SHABANIAN, M. (2017) Novel electrodialysis cation exchange membrane prepared by 2-acrylamido-2-methylpropane sulfonic acid; heavy metal ions removal, *Journal of Hazardous Materials*. 337, pp. 90-104.

127. NOOR, N.M., OTHMAN, R., MUBARAK, N.M. and ABDULLAH, E.C. (2017) Agricultural biomass-derived magnetic adsorbents: Preparation and application for heavy metals removal, *Journal of the Taiwan Institute of Chemical Engineers*. 78, pp. 168-177.

128. OCIŃSKI, D., JACUKOWICZ-SOBALA, I., MAZUR, P., RACZYK, J. and KOCIOŁEK-BALAWEJDER, E. (2016) Water treatment residuals containing iron and manganese oxides for arsenic removal from water–Characterization of physicochemical properties and adsorption studies, *Chemical Engineering Journal*. 294, pp. 210-221.

129. OFOMAJA, A.E., NGEMA, S.L. and NAIDOO, E.B. (2012) The grafting of acrylic acid onto biosorbents: Effect of plant components and initiator concentration, *Carbohydrate Polymers*. 90, pp. 201-209.

130. OLU-OWOLABI, B.I., DIAGBOYA, P.N., UNUABONAH, E.I., ALABI, A.H., DÜRING, R.A. and ADEBOWALE, K.O. (2018) Fractal-like concepts for evaluation of toxic metals adsorption efficiency of feldspar-biomass composites, *Journal of Cleaner Production*. 171, pp. 884-891.

131. PAL, P., CHAKRABORTTY, S. and LINNANEN, L. (2014) A nanofiltration–coagulation integrated system for separation and stabilization of arsenic from groundwater, *Science of the Total Environment*. 476, pp. 601-610.

132. PALANEESWARI, S.M., RAJAN, P.A.S. and SILAMBANAN, S. J. (2013) Blood arsenic and cadmium concentrations in end-stage renal disease patients who were on maintenance haemodialysis, *Journal of Clinical and Diagnostic Research*. 7, pp.809-813.

133. PANAGOS, P., VAN LIEDEKERKE, M., YIGINI, Y. and MONTANARELLA, L. (2013) Contaminated sites in Europe: Review of the current situation based on data collected through a European network, *Journal of Environmental and Public Health*. 11, https://doi.org/10.1155/2013/158764.

134. PARK, C.M., HAN, J., CHU, K.H., AL-HAMADANI, Y.A., HER, N., HEO, J. and YOON, Y. (2017) Influence of solution pH, ionic strength, and humic acid on cadmium adsorption onto activated biochar: experiment and modeling, *Journal of Industrial and Engineering Chemistry*. 48, pp. 186-193.

135. PENG, W., LI, H., LIU, Y. and SONG, S. (2017) A review on heavy metal ions adsorption from water by graphene oxide and its composites, *Journal of Molecular Liquids*. 230, pp. 496-504.

136. PHANTHASRIA, J., KHAMDAHSAG, P., JUTAPORN, P., SORACHOTI, K., WANTALA, K. and TANBOONCHUY, V. (2018) Enhancement of arsenite removal using manganese oxide coupled with iron (III) trimesic, *Applied Surface Science*. 427, pp. 545–552.

137. PHOLOSI, A., OFOMAJA, A.E. and NAIDOO, E.B. (2013) Effect of chemical extractants on the biosorptive properties of pine cone powder: Influence on Pb (II) removal mechanism, *Journal of Saudi Chemical Society*. 17, pp. 77-86.

138. PRADHAN, D., SUKLA, L.B., SAWYER, M. and RAHMAN, K.S.M. (2017) Recent bioreduction of hexavalent chromium in wastewater treatment: A review, *Journal of Industrial and Engineering Chemistry*. 55, pp. 1-20.

139. PRIYADHARSAN, A., VASANTHAKUMAR, V., KARTHIKEYAN, S., RAJ, V., SHANAVAS, S. and ANBARASAN, P.M. (2017) Multi-functional properties of ternary CeO_2/SnO_2/rGO nanocomposites: visible light driven photocatalyst and heavy metal removal, *Journal of Photochemistry and Photobiology A: Chemistry*. 346, pp. 32-45.

140. PYRZYNSKA, K. (2019) Removal of cadmium from wastewaters with low-cost adsorbents, *Journal of Environmental Chemical Engineering*. 7, pp. 102795.

141. QIU, H., LIANG, C., YU, J., ZHANG, Q., SONG, M. and CHEN, F. (2017) Preferable phosphate sequestration by nano-La (III)(hydr) oxides modified wheat straw with excellent properties in regeneration, *Chemical Engineering Journal*. 315, pp. 345-354.

142. QIU, Y.R. and MAO, L.J. (2013) Removal of heavy metal ions from aqueous solution by ultrafiltration assisted with copolymer of maleic acid and acrylic acid, *Desalination*. 329, pp. 78-85.

143. RADKE, C.J. and PRAUSNITZ, J.M. (1972) Adsorption of organic solutes from dilute aqueous solution of activated carbon, *Industrial and Engineering Chemistry Fundamentals*. 11, pp. 445-451.

144. RANGABHASHIYAM, S., ANU, N., NANDAGOPAL, M.S.G. and SELVARAJU, N. (2014) Relevance of isotherm models in biosorption of pollutants by agricultural byproducts, *Journal of Environmental Chemical Engineering*. 2, pp. 398-414.

145. RAO, R.A.K. and KASHIFUDDIN, M. (2016) Adsorption studies of Cd (II) on ball clay: Comparison with other natural clays, *Arabian Journal of Chemistry*. 9, pp. S1233-S1241.

146. REDDY, D.H.K., SESHAIAH, K., REDDY, A.V.R. and LEE. S.M. (2012) Optimization of Cd (II), Cu (II) and Ni (II) biosorption by chemically modified *Moringa oleifera* leaves powder, *Carbohydrate Polymers*. 88, pp. 1077-1086.

147. REDLICH, O. and PETERSON, D.L. (1959) A useful adsorption isotherm, *Journal of Physical Chemistry*. 63, pp. 1024.

148. RENGARAJ, S., VENKATARAJ, S., YEON, J.W., KIM, Y., LI, X.Z., PANG, G.K.W. (2007) Preparation, characterization and application of Nd-TiO_2 photcatalyst for the reduction of Cr(VI) under UV light illumination, *Applied Catalysis B: Environment*. 77, pp. 157-165.

149. RENU, M.A., SINGH, K., UPADHYAYA, S. and DOHARE, R.K. (2017) Removal of heavy metals from wastewater using modified agricultural adsorbents, *Materials Today: Proceedings*. 4, pp. 10534–10538.

150. ROBALDS, A, NAJA, G.M. and KLAVINS, M. (2016) Highlighting inconsistencies regarding metal biosorption, *Journal of Hazardous Materials*. 304, pp. 553-556.

151. ROSALES, M., COREÑO, O. and NAVA, J.L. (2018) Removal of hydrated silica, fluoride and arsenic from groundwater by electrocoagulation using a continuous reactor with a twelve-cell stack, *Chemosphere*. 211, pp. 149-155.

152. ROUQUEROL, F., ROUQUEROL, J., SING, K.S., LLEWELLYN, P. and MAURIN, G. (2014) Adsorption by powders and porous solids: Principles, methodology & applications. 2nd edition. Cambridge: Academic Press. pp. 1-24.

153. RWIZA, M.J., OH, S.Y., KIM, K.W. and KIM, S.D. (2018) Comparative sorption isotherms and removal studies for Pb (II) by physical and thermochemical modification of low-cost agro-wastes from Tanzania, *Chemosphere*. 195, pp. 135-145.

154. RYU, S-R., JEON, E-K., YANG, J-S. and BAEK, K. (2017) Adsorption of As(III) and As(V) in groundwater by Fe–Mn binary oxide-impregnated granular activated carbon (IMIGAC), *Journal of the Taiwan Institute of Chemical Engineers*. 72, pp. 62–69.

155. SADHUKAN, B., MONDAL, N.K. and CHATTORAJ, S. (2016) Optimization using central composite design (CCD) and the desirability function for sorption of methylene blue from aqueous solution onto *Lemna major*, *Karbala International Journal of Modern Science*. 2, pp. 145-155.

156. SANTHOSH, C., VELMURUGAN, V., JACOB, G., JEONG, S.K., GRACE, A.N. and BHATNAGAR, A. (2016) Role of nanomaterials in water treatment applications: A review, *Chemical Engineering Journal*. 306, pp. 1116-1137.

157. SARKAR, A. and PAUL, B. (2016) The global menace of arsenic and its conventional remediation - A critical review, *Chemosphere*. 158, pp. 37-49.

158. SATHEESH, R., VIGNESH, K., RAJARAJAN, M., SUGANTHI, A.SREEKATHAN, S., KANG, M. and KWAK, B.S. (2016) Removal of congo red from water using quercetin modified α-Fe_2O_3 nanoparticles as effective nanoadsorbent, *Materials Chemistry and Physics*. 180, pp. 53-65.

159. SATO, Y., HAMAI, T., HORI, T., HABE, H., KOBAYASHI, M. and SAKATA, T. (2018) Year-round performance of a passive sulfate-reducing bioreactor that uses rice bran as an organic carbon source to treat acid mine drainage, *Mine Water and The Environment*. 37, pp. 586-594.

160. SCHROEDER, D.C. and LEE, G.F. (1975) Potential transformations of Cr in natural water, *Water, Air and Soil Pollution*. 4, pp. 355-365.

161. SEABRA, A.B. and DURÁN, N. (2015) Nanotoxicology of metal oxide nanoparticles, *Metals*. 5, pp. 934-975.

162. SELLNER, B.M., HUA, G., AHIABLAME, L.M., TROOIEN, T.P., HAY, C.H. and KJAERSGAARD, J. (2019) Evaluation of industrial by-products and natural minerals for phosphate adsorption from subsurface drainage, *Environmental Technology*. 40, pp. 756-767.

163. SEMERJIAN, L. (2018) Removal of heavy metals (Cu, Pb) from aqueous solutions using pine (*Pinus halepensis*) sawdust: Equilibrium, kinetic, and thermodynamic studies, *Environmental Technology & Innovation*. 12, pp. 91-103.

164. SHAHID, M., SHAMSHAD, S., RAFIQ, M., KHALID, S., BIBI, I., NIAZI, N.K., DUMAT, C. and RASHID, M.I. (2017) Chromium speciation, bioavailability, uptake, toxicity and detoxification in soil-plant system: A review, *Chemosphere*. 178, pp. 513-533.

165. SHAN, C. & TONG, M. (2013) Efficient removal of trace arsenite through oxidation and adsorption by magnetic nanoparticles modified with Fe-Mn binary oxide, *Water Research*. 47, pp. 3411-3421.

166. SHARMA, R., DHILLON, A. and KUMAR, D. (2018) Biosorbents from Agricultural By-products: Updates After 2000s, In *Bio-and Nanosorbents from Natural Resources*. Springer, Cham, pp. 1-20.

167. SHARMA, R.K. and GHOSE, R. (2014) Synthesis of nanocrystalline CuO-ZnO mixed metal oxide powder by a homogeneous precipitation method, *Ceramics International*. 40, pp.10919-10926.

168. SHAYEGAN, Z., LEE, C.S. and HAGHIGHAT, F. (2018) TiO2 photocatalyst for removal of volatile organic compounds in gas phase–a review, *Chemical Engineering Journal*. 334, pp. 2408-2439.

169. SHEN, N. and CHIRWA, E.M. (2020) Live and lyophilized fungi-algae pellets as novel biosorbents for gold recovery: Critical parameters, isotherm, kinetics and regeneration studies, *Bioresource Technology*. p. 123041.

170. SINGH, P., DUTTA, S.R., PASSI, D. and BHARTI, J. (2017) Benefits of alcohol on arsenic toxicity in rats, *Journal of clinical and diagnostic research*. 11, pp. 1-6.

171. SIPS, R. (1948) Combined form of Langmuir and Freundlich equations, *Journal of Chemical Physics.* 16, pp. 490-495.

172. SMILY, J.R.M.B. and SUMITHRA, P.A. (2017) Optimization of chromium biosorption by fungal adsorbent, *Trichoderma sp*. BSCR02 and its desorption studies, *HAYATI Journal of Biosciences*. 24, pp. 65-71.

173. SUI, H., LIU, H., AN, P., HE, L., LI, X. and CONG, S. (2017) Application of silica gel in removing high concentrations toluene vapor by adsorption and desorption process, *Journal of the Taiwan Institute of Chemical Engineers*. 74, pp. 218-224.

174. SULYMAN, M. (2016) Agricultural by-products/waste as dye and metal ions adsorbents: a review. *Research Inventy: International Journal of Engineering And Science*. 6, pp. 1-20.

175. SULYMAN, M., NAMIESNIK, J. and GIERAK, A. (2017) Low-cost Adsorbents Derived from Agricultural By-products/Wastes for Enhancing Contaminant Uptakes from Wastewater: A Review, *Polish Journal of Environmental Studies*. 26, pp. 479-510.

176. TABATABAEE, A., DASTGOSHADEH, F. and TABATABAEE, A. (2016) Biosorption of heavy metals by low cost adsorbents, *World Academy of Science, Engineering and Technology International Journal of Environmental and Ecological Engineering*. 8, pp. 699-704.

177. TABESH, S., DAVAR, F. and LOGHMAN-ESTARKI, M.R. (2018) Preparation of γ-Al2O3 nanoparticles using modified sol-gel method and its use for the adsorption of lead and cadmium ions, *Journal of Alloys and Compounds*. 730, pp. 441-449.

178. TAN, K.L. and HAMEED, B.H. (2017) Insight into the adsorption kinetics models for the removal of contaminants from aqueous solutions, *Journal of the Taiwan Institute of Chemical Engineers*. 74, pp. 25-48.

179. THAKUR, L.S. and MONDAL, P. (2017) Simultaneous arsenic and fluoride removal from synthetic and real groundwater by electrocoagulation process: parametric and cost evaluation, *Journal of Environmental Management*. 190, pp. 102-112.

180. TÓTH, J. (1971) State equations of the solid gas interface layer, *Acta Chimica Academiae Scientiarum Hungaricae*. 69, pp. 311-317.

181. TRAN, H.N., YOU, S.J. and CHAO, H.P. (2016) Thermodynamic parameters of cadmium adsorption onto orange peel calculated from various methods: a comparison study, *Journal of Environmental Chemical Engineering*. 4, pp. 2671-2682.

182. TRAN, H.N. YOU, S-J., HOSSEINI-BANDEGHARAEI, A. and CHAO, H-P. (2017) Mistakes and inconsistencies regarding adsorption of contaminants from aqueous solutions: A critical review, *Water Research*. 120, pp. 88-116.

183. TZVETKOV, G., MIHAYLOVA, S., STOITCHKOVA, K., TZVETKOV, P. and SPASSOV, T. (2016) Mechanochemical and chemical activation of lignocellulosic material to prepare powdered activated carbons for adsorption applications, *Powder Technology*. 299, pp. 41-50.

184. VANDER HOOGERSTRAETE, T., ONGHENA, B. and BINNEMANS, K. (2013) Homogeneous Liquid−Liquid Extraction of Metal Ions with a Functionalized Ionic Liquid, *The Journal of Physical Chemistry Letters*. 4, pp. 1659−1663.

185. VAREDA, J.P., VALENTE, A.J.M. and DURÃES, L. (2019) Assessment of heavy metal pollution from anthropogenic activities and remediation strategies: A review, *Journal of Environmental Management*. 246, pp. 101–118.

186. VÍCTOR-ORTEGA, M.D. and RATNAWEERA, H.C. (2017) Double filtration as an effective system for removal of arsenate and arsenite from drinking water through reverse osmosis, *Process Safety and Environmental Protection*. 111, pp. 399-408.

187. VILLALOBOS, M., ESCOBAR-QUIROZ, I.N. and SALAZAR-CAMACHO, C. (2014) The influence of particle size and structure on the sorption and oxidation behavior of birnessite: I. Adsorption of As(V) and oxidation of As(III), *Geochimica et Cosmochimica Acta*. 125, 564–581.

188. VINCENT, J.B. (2014) Is chromium pharmacologically relevant, *Journal of Trace Elements in Medicine and Biology*. 28, pp. 397-405.

189. WANG, L.P. and CHEN, Y.J. (2019) Sequential precipitation of iron, copper, and zinc from wastewater for metal recovery, *Journal of Environmental Engineering*. 145, p. 04018130.

190. WANG, X., LI, H. and HUANG, J. (2017) Adsorption of p-chlorophenol on three amino-modified hyper-cross-linked resins, *Journal of* Colloid *and Interface Science*. 505, pp. 585-592.

191. WANG, P., MA, Q., HU, D. and WANG, L. (2016) Adsorption of methylene blue by a low-cost biosorbent: citric acid modified peanut shell, *Desalination and Water Treatment*. 57, pp. 10261-10269.

192. WANG, F., PAN, Y., CAI, P., GUO, T. and XIAO, H. (2017) Single and binary adsorption of heavy metal ions from aqueous solutions using sugarcane cellulose-based adsorbent, *Bioresource Technology*. 241, pp. 482-490.

193. WANG, J., ZHANG, B., WANG, L., WANG, M. and GAO, F. (2015) One-pot synthesis of water-soluble superparamagnetic iron oxide nanoparticles and their MRI contrast effects in the mouse brains, *Materials Science and Engineering: C*. 48, pp. 416-423.

194. WANG, Y., LIU, D., LU, J. and HUANG, J. (2015) Enhanced adsorption of hexavalent chromium from aqueous solutions on facilely synthesized mesoporous iron-zirconium

bimetal oxide, *Colloids and Surfaces A: Physicochemical and Engineering Aspects*. 481, pp. 131-142.

195. WEBER, W.J. and MORRIS, J.C. (1963) Kinetics of adsorption on carbon from solution, *Journal of the Sanitary Engineering Division (ASCE)*, 89, pp. 31-59.

196. WEBER, W.J. and VAN VLIET, B.M. (1979) A general isotherm explicit in terms of solution concentration. *Rep. No. EWRE*, 10379.

197. WEI, Z., WANG, Z., YAN, J., LIU, Y., WU, Y., FANG, Y., YU, L., CHENG, G., PAN, Z. and HU, G. (2019) Adsorption and oxidation of arsenic by two kinds of β-MnO_2. *Journal of Hazardous Materials*. 373, pp. 232-242.

198. WEN, X., YAN, C., SUN, N., LUO, T., ZHOU, S. and LUO, W. (2018) A Biomass Cationic Adsorbent Prepared From Corn Stalk: Low-Cost Material and High Adsorption Capacity, *Journal of Polymers and the Environment*. 26, pp. 1642-1651.

199. WEN, Z., ZHANG, Y., CHENG, G., WANG, Y. and CHEN, R. (2019) Simultaneous removal of As(V)/Cr(VI) and acid orange 7 (AO7) by nanosized ordered magnetic mesoporous Fe-Ce bimetal oxides: Behavior and mechanism, *Chemosphere*. 218, pp. 1002-1013.

200. WORLD HEALTH ORGANIZATION (2017) Guidelines for Drinking Water Quality: First Addendum to the Fourth edition.

201. WU, Y., LI, W. and SPARKS, D.L. (2015) The effects of iron(II) on the kinetics of arsenic oxidation and sorption on manganese oxides, *Journal of Colloid Interface Science*. 457, 319–328.

202. YADAV, S., SRIVASTAVA, V., BANERJEE, S., WENG, C.H. and SHARMA, Y.C. (2013) Adsorption characteristics of modified sand for the removal of hexavalent chromium ions from aqueous solutions: kinetic, thermodynamic and equilibrium studies, *Catena*. 100, pp. 120-127.

203. YANG, X., WAN, Y., ZHENG, Y., HE, F., YU, Z., HUANG, J., WANG, H., OK, Y.S., JIANG, Y. and GAO, B. (2019) Surface functional groups of carbon-based adsorbents and their roles in the removal of heavy metals from aqueous solutions: a critical review, *Chemical Engineering Journal*. 366, pp. 608-621.

204. YANG, F., ZHANG, S, CHO, D-W., DU, Q., SONG, J. and TSANG, D.C.W. (2019) Porous biochar composite assembled with ternary needle-like iron-manganese-sulphur hybrids for high-efficiency lead removal, *Bioresource Technology*. 272, pp. 415–420.

205. YUN, S.M., WOO, S.H., OH, S.T., HONG, S.E., CHOE, T.B., YE, S.K., KIM, E.K., SEONG, M.K., KIM, H.A., NOH, W.C. and LEE, J.K. (2016) Melatonin enhances arsenic trioxide-induced cell death via sustained upregulation of Redd1 expression in breast cancer cells, *Molecular and cellular endocrinology*. *422*, pp. 64-73.

206. ZEWAIL, T.M. and YOUSEF, N.S. (2015) Kinetic study of heavy metal ions removal by ion exchange in batch conical air spouted bed, *Alexandria Engineering Journal*. 54, pp. 83-90.

207. ZHANG, G., LIU, H., QU, J. and JEFFERSON, W. (2012) Arsenate uptake and arsenite simultaneous sorption and oxidation by Fe-Mn binary oxides: Influence of Mn/Fe ratio, pH, Ca^{2+} and humic acid, *Journal of Colloid and Interface Science*. 366, pp. 141-146.

208. ZHANG, G., REN, Z., ZHANG, X. and CHEN, J. (2013) Nanostructured iron (III)-copper (II) binary oxide: A novel adsorbent for enhanced arsenic removal from aqueous solutions, *Water Research*. 47, pp. 4022-4031.

209. ZHANG, W., LIU, C., WANG, L., ZHENG, T., REN, G., LI, J. and MA, J. (2019) A novel nanostructured Fe-Ti-Mn composite oxide for highly efficient arsenic removal: Preparation and performance evaluation, *Colloids and Surfaces A*. 561, pp. 364–372.

210. ZHANG, W., FU, J., ZHANG, G. and ZHANG, X. (2014) Enhanced arsenate removal by novel Fe–La composite (hydr)oxides synthesized via coprecipitation, *Chemical Engineering Journal*. 251, pp. 69–79.

211. ZHANG, W., LIU, C., ZHENG, T., MA, J., ZHANG, G., REN, G., WANG, L. and LIU, Y., (2018) Efficient oxidation and sorption of arsenite using a novel titanium (IV)-manganese (IV) binary oxide sorbent, *Journal of Hazardous Materials*. 353, pp.410-420.

212. ZHANG, W., ZHANG, G., LIU, C., LI, J., ZHENG, T., MA, J., WANG, L., JIANG, J. and ZHAI, X. (2018) Enhanced removal of arsenite and arsenate by a multifunctional Fe-Ti-Mn composite oxide: Photooxidation, oxidation and adsorption, *Water Research*. 147, pp. 264-275.

213. ZHANG, Y., WU, B., XU, H., LIU, H., WANG, M., HE, Y. and PAN, B. (2016) Nanomaterials-enabled water and wastewater treatment, *NanoImpact*. 3-4, pp. 22-39.

214. ZHENG, Q., HOU, J., HARTLEY, W., REN, L., WANG, M., TU, S. and TAN, W. (2020) As (III) adsorption on Fe-Mn binary oxides: Are Fe and Mn oxides synergistic or antagonistic for arsenic removal?,*Chemical Engineering Journal*. 389, pp. 124470.

215. ZHOU, Q.W., LIAO, B.H., LIN, L.N., QIU, W.W. and SONG, Z.G. (2018) Adsorption of Cu(II) and Cd(II) from aqueous solutions by ferromanganese binary oxide-biochar composites, *Science for the Total Environment*. 615, pp. 115–122.

216. ZHOU, R., ZHOU, R., ZHANG, X., TU, S., YIN, Y., YANG, S. and YE, L. (2016) An efficient bio-adsorbent for the removal of dye: Adsorption studies and cold atmospheric plasma regeneration, *Journal of the Taiwan Institute of Chemical Engineers*. 68, pp. 372-378.

217. ZHU, Y., FAN, W., ZHOU, T. and LI, X. (2019) Removal of chelated heavy metals from aqueous solution: A review of current methods and mechanisms, *Science of the Total Environment*. 678, pp. 253-266.

218. ZHU, F., LI, L. and XING, J. (2017) Selective adsorption behavior of Cd (II) ion imprinted polymers synthesized by microwave-assisted inverse emulsion polymerization: Adsorption performance and mechanism, *Journal of Hazardous Materials*, 321, pp. 103-110.

CHAPTER 3

3 EXPERIMENTAL PROCEDURES

3.1 INTRODUCTION

This chapter is divided into five main sections. The first part deals with the fabrication of the nanostructured ternary MFC metal oxide composite. It describes how the synthesis is optimized using the central composite design of response surface methodology technique. The second section involves characterization of the metal oxide nanocomposite using Fourier transform infrared spectroscopy, scanning electron microscopy, transmission electron microscopy, X-ray photoelectron spectroscopy, BET analysis and X-ray diffraction. Experiments to determine the surface charge of the adsorbent are also presented. The third and fourth segments describe experiments to determine the adsorption dynamics of Cr(VI) and As(III) anions onto the nanostructured MFC ternary metal oxide composite from simulated aqueous effluent. The fifth section covers the co-precipitation of the MFC metal oxide system onto biochar support and its application in the adsorption of As(III) and Cr(VI).

3.2 CHEMICAL REAGENTS

The chemical reagents were of analytical grade requiring no further purification and were supplied by Sigma-Aldrich (South Africa). The borosilicate glassware used in the investigations were soaked in and cleaned with 1 % HNO_3 and rinsed several times with ultrapure water (18 mΩ.cm) from a MERCK Millipore Direct-Q® 8 UV (Germany) instrument before use. The use of ultrapure water is important since the oxides have a very high affinity for metal cations. The Cr(VI) and As(III) stock solutions and standards were prepared from potassium dichromate ($K_2Cr_2O_7.7H_2O$) and sodium arsenite ($NaAsO_2$), respectively using ultrapure water. The different solution concentrations of Cr(VI) and As(III) at different pH values were prepared by serial dilution of the respective stock solutions and the pH values adjusted accordingly with 0.1 mol/dm^3 of either HC*l* or NaOH. All the experiments were performed in a closed system.

3.3 PREPARATION OF NANOMETAL OXIDE COMPOSITES

3.3.1 Multivariate optimization of the preparation of the ternary MFC metal oxide composite using Response Surface Methodology (RSM)

A three-level-four-factor central composite design (CCD) method was applied from the Design-Expert software version 11.1.2.0 from Stat-Ease (USA) in the investigation of the effect of variables and the corresponding variable interactions on the responses to optimize the co-precipitation of the nanostructured MFC ternary metal oxide. The independent test variables for the synthesis displayed in Table 3.1 were coded using the equation:

$$X = \frac{x-[x_{max}+x_{min}]/2}{[x_{max}-x_{min}]/2} \quad (3.1)$$

where X is the coded variable (dimensionless), x is the independent variable, x_{min} and x_{max} are the maximum and minimum values of the independent variable. The required responses were: (1) Cr(VI) adsorption capacity, (2) concentration of Cr(III) in solution after the adsorption of Cr(VI), (3) As(III) adsorption capacity, and (4) concentration of As(V) in solution after the adsorption of As(III).

Table 3.1 Coded levels of the independent test variables.

Parameters	Units	Coded levels		
		-1	0	+1
A: Time	mins	30	75	120
B: $MnCl_2$	mol	0.015	0.022	0.030
C: $FeCl_3.6H_2O$	mol	0.015	0.022	0.030
D: $CuSO_4.5H_2O$	mol	0.015	0.022	0.030

The experimental design matrix consisted of 30 runs comprising of 16 factorial runs, 8 axial runs and 6 replicate runs at the centre point obtained from the equation:

$$N = 2^n + 2n + n_c = 2^4 + (2 \times 4) + 6 = 30 \quad (3.2)$$

with *n* and *N* being the number of the coded independent variables and total experimental runs, respectively. The analysis of experimental results was performed by the Design-Expert software version 11.1.2.0 with the second-degree polynomial (quadratic) equation being utilized in analysing the interaction between independent and dependent variables as shown:

$$Y = b_0 + \sum_{i=1}^{3} b_i x_i + \sum_{i=1}^{3} b_{ii} x_i^2 + \sum_{i=1}^{3} \sum_{i=j}^{3} b_{ij} x_i x_j \quad (3.3)$$

where the response variable is represented by Y, the coded variables x_i and x_j determine Y, the constant coefficient is given as b_0, the linear coefficient is b_i, interaction coefficient is b_{ij} while the quadratic coefficient is b_{ii}. The single x-terms in the second-order polynomial equation are referred to as the main effects, the squared terms are the quadratic or curvature effects (model curvature in the response surface) and the interaction (two-factor) terms model interactions between the variables (Martinez & Martinez, 2015).

3.3.2 Fabrication of nanostructured metal oxide composites

The nanostructured ternary metal oxide nanocomposite was fabricated using optimal working parameters determined using CCD in section 4.2.1.5. To evaluate the superior adsorption efficacy of the ternary MFC metal oxide system, two binary (MC and MF) metal oxide nanocomposites were synthesized alongside the ternary MFC metal oxide composite for comparison.

Three mixed metal oxide composites were prepared by facile co-precipitation method using Mn:Fe:Cu mole ratios of 2:1:2 (MFC), 1:0:1 (MC) and 2:1:0 (MF) at room temperature. Accurately weighed amounts of $MnCl_2$, $FeCl_3.6H_2O$ and $CuSO_4.5H_2O$ were separately dispersed in 500 cm^3 ultrapure water in volumetric flasks. Equal volumes (150 cm^3) of the metal solutions were mixed according to the aforementioned predetermined mole ratios of the three metal oxides in separate Erlenmeyer flasks. The mixtures were magnetically stirred at 400 rpm and 3 mol/dm^3 NaOH solution added dropwise until pH was in the range 8-9. The formed suspensions were continuously stirred for 1 h at room temperature and then aged for 4 h. The suspensions were not subjected to a heating programme to prevent the formation of large crystals due to Ostwald ripening. The aged suspensions were centrifuged at 6000 rpm for 2 mins, washed several times with ultrapure water and then dried at 333 K in a thermostatic vacuum oven for 24 h. The resultant solids were pulverised and calcined under normal

atmospheric conditions at 773 K for 6 h. The nanometal oxide samples were stored in separate airtight desiccators for further analysis.

3.4 CHARACTERIZATION OF METAL OXIDE NANOCOMPOSITES

3.4.1 Fourier transform infrared (FTIR) analysis

The analysis of surface functions was done using a Perkin-Elmer (USA) FTIR Spectra 400 spectrophotometer in the mid-infrared region (4000-400 cm^{-1}).

3.4.2 Scanning electron microscopy (SEM)

To investigate the surface morphology and physicochemical properties (elemental distribution) of the nanomaterials, a ZEISSUltra/Plus FEG-SEM (Germany) scanning electron microscope coupled to an energy dispersive X-ray analyzer was used at different magnifications. The samples were gold-coated before analysis.

3.4.3 Transmission electron microscopy (TEM)

Detailed physical observation of nanometal oxides structure and particle size distributions were observed on a Tecnai F20 (USA) transmission electron microscope.

3.4.4 X-ray photoelectron spectroscopy (XPS)

XPS was used to determine the surface valence states of the nanocomposites. The analysis was carried out on a PHI 5000 scanning ESCA microprobe (Japan) with a 100 μm diameter monochromatic Al Kα X-ray beam (hυ=1486.6 eV) generated by a 25 W, 15 kV electron beam to analyze different binding energy peaks. Origin 9 (Graphing & Analysis) software using Gaussian–Lorentz fits was utilized to analyse the spectra.

3.4.5 Brunauer-Emmett-Teller (BET) analysis

The nanometal oxides BET specific surface area, pore volumes and pore sizes distributions were determined by computer-controlled N_2 adsorption at 77 K using a Tristar 3000 analyzer coupled to a VacPrep 061 degassing unit. Degassing was carried out for 1 h at 363 K and increased to 393 K for 2 h. Both instruments were supplied by Micromeritics Instrument Corporation (Australia).

3.4.6 X-ray diffraction (XRD) spectroscopy

An X-ray diffractometer, D8 ADVANCE from BRUKER (Germany) with a LynxEye position-sensitive detector was used to determine the crystalline phases of the nanostructured metal oxides (CuKα anode; λ = 0.154 nm). The samples were scanned at 40 kV and 40 mA from 10-80 2-theta degrees at a scan rate of 1°C/min. The metal oxides crystalline phases were determined by referring to the JCPDS database.

3.4.7 Surface charge

The pH drift method was used to determine the pH at point of zero charge (pH_{pzc}) of the MF, MC and MFC nanostructured oxides. To a series of 100 cm^3 glass bottles, 45 cm^3 of 0.01 mol/dm^3 KNO_3 solution were transferred. The initial pH (pH_i) values of the solutions were adjusted to between pH 2 and 12 by addition of either 0.1 mol/dm^3 HCl or NaOH on a pH meter with constant stirring. The total volume of the solution in each bottle was made up to 50 cm^3 by addition of KNO_3 solution of the same strength. The pH_i of the solutions was accurately noted, and 0.1 g of either MF, MC or MFC oxides were added to each glass bottle, which was then immediately closed. The suspensions were allowed to equilibrate for 48 h on a shaker operating at 200 rpm. The final pH (pH_f) values of the supernatant were accurately noted and the difference between the initial and final pH values ($\Delta pH = pH_i - pH_f$) was plotted against the pH_f. The point of intersection of the resulting curve at which $\Delta pH = 0$ gave the pHpzc.

3.5 ADSORBENT STABILITY/LEACHING TEST

The concentration amounts of Mn, Fe and Cu adsorbent metal components of each of MF, MC and MFC oxide composites, leaching into treated water at different pH values (2-7) were measured at 299 K, by separately agitating 0.05 g of MF, MC and MFC adsorbents at 200 rpm in 100 cm^3 ultrapure water for 2 h. The suspensions were centrifuged and the supernatant solutions were spectroscopically analyzed to determine the concentrations of Mn, Fe and Cu using AAS.

3.6 ADSORPTION OF TRACE METALS

The batch adsorption technique was utilized to determine the process parameters and the dominant mechanistic pathways during the sequestration of Cr(VI) and As(III) ions from

simulated aqueous effluents onto the nanosized MF, MC and MFC metal oxide composites by investigating the:

- influence of solution pH,
- effect of adsorbent dose,
- adsorption isotherms,
- adsorption kinetics,
- effect of co-existing anions,
- influence of electrolytes,
- desorption, and
- regeneration and reuse of the metal oxide nanocomposites.

3.6.1 Data modelling

The adsorption performance was quantified by calculating the mass of adsorbate removed per unit mass of adsorbent at equilibrium. The adsorption capacities at equilibrium, q_e (mg/g) were determined using Eq 3.4:

$$q_e = \frac{(C_o - C_e)V}{m} \tag{3.4}$$

where C_o and C_e are the initial and equilibrium adsorbate ions concentrations (mg/dm^3), V is the adsorbate volume (dm^3) and m is the mass of adsorbent (g). The time-dependent adsorption capacity, q_t (mg/g) was computed from Eq 3.5:

$$q_t = \frac{(C_o - C_t)V}{m} \tag{3.5}$$

where C_t (mg/dm^3) is the concentration of adsorbate ions at time t (mins). The reusability of the metal oxide composite adsorbents was determined by desorption and regeneration investigations. The amount of desorbed adsorbate was calculated as:

$$\%\, desorption = \frac{C_d}{C_0 - C_e} \times 100 \tag{3.6}$$

where C_d is the Cr (VI) concentration in eluted solution (mg/dm^3).

3.6.2 Quantitative analytical instrumentation

The adsorption samples were stored in acid-washed glass bottles. All the analyses were performed within 24 h of collection.

3.6.2.1 *UV-visible (UV-vis) spectroscopy*

The concentration amount of Cr(VI) ions present in aqueous solution were determined on a Perkin-Elmer (USA) Lambda 25 UV-vis spectrophotometer. A derivatization agent, 1.5-diphenylcarbazide (DPC), was initially added to the analyte solution to form a red-violet complex which was analysed at 540 nm.

3.6.2.2 *Atomic absorption spectroscopy (AAS)*

Atomic absorption using a SHIMADZU AA-7000 (Japan) spectrometer was used to determine the total chromium concentration in standard and treated aqueous solutions. The concentration amount of Cr(III) left in solution after the adsorption of Cr(VI), $[Cr(III)]$ (mg/dm^3), was determined using Eq 3.7:

$$[Cr(III)] = [total\ Cr]_{from\ AAS} - [Cr(VI)]_{from\ UV-vis} \tag{3.7}$$

where $[total\ Cr]_{from\ AAS}$ and $[Cr(VI)]_{from\ UV-vis}$ denote the concentration amounts (mg/dm^3) of total Cr from AAS and Cr(VI) from UV-vis, respectively.

3.6.2.3 *Inductively coupled plasma-optical emission spectroscopy (ICP-OES)*

A ThermoSCIENTIFIC iCAP 7000 (China) inductively coupled plasma-optical emission spectrometer was used to determine the total arsenic concentration in the standard and treated solutions. Arsenic speciation cartridges were used to separate the As(III) and As(V) species from the treated wastewater. The cartridges retain the As(V) and allow the As(III) to elute around pH 4-9. The concentration amount of the eluted As(III) was then determined using ICP-OES.

3.6.3 Batch adsorption studies of Cr(VI) and As(III)

The batch adsorption experiments were performed in acid washed 250 cm^3 glass stoppered bottles on a thermostatic shaker at 200 rpm for 2 h. The adsorption processes were stopped by

centrifugation at 6000 rpm for 2 mins before the quantitative determination of residual chromium and arsenic using AAS and ICP-OES, respectively.

3.6.3.1 *Effect of solution pH*

Chromium(VI): An accurately weighed amount (0.01 g) of each of the three different nanometal oxide samples (MFC, MF and MC) was placed in separate glass bottles. To each bottle, 100 cm^3 of 100 mg/dm^3 Cr(VI) solution whose pH had each been adjusted to 2, 3, 4, 5, 6 and 7 using 0.1 mol/dm^3 of either HC*l* or NaOH was then separately added. The glass bottles were agitated on a shaker at 299 K before analysis to determine the residual pollutant concentration.

Arsenic(III): The experiment was performed in the same manner as for Cr(VI) adsorption but using As(III) solutions whose pH had separately been adjusted to 2, 4, 6, 7, 8, 9, 10 and 12.

3.6.3.2 *Adsorbent dose*

Chromium(VI): The experiments were performed by agitating on a thermostatic shaker known masses (0.01, 0.05, 0.10, 0.15 and 0.2 g) of the three nanometal oxide samples (MFC, MF and MC) in glass bottles containing 100 cm^3 of 100 mg/dm^3 Cr(VI) solution at pH 3 and 299 K. The supernatant was analysed to determine the amount of residual pollutant after the adsorption process.

Arsenic(III): The investigations were performed in the same way as for the adsorption of Cr(VI) but using 100 cm^3 of 50 mg/dm^3 As(III) solution at pH 8 (MF) and pH 9 (MC and MFC).

3.6.3.3 *Isotherm studies*

Chromium(VI): The experiments were done at 299, 304, 309, 314 and 319 K. Accurately weighed amounts (0.05 g) of each of the three different nanometal oxide samples (MFC, MF and MC) were separately placed in glass bottles, each containing 100 cm^3 of either 50, 100, 200, 300 or 400 mg/dm^3 Cr(VI) solution at pH 3. The glass bottles were agitated on a shaker and the residual pollutant concentration determined after the adsorption process.

Arsenic(III): The experimental was the same as for Cr(VI) adsorption but using 100 cm^3 of either 50, 100, 200, 300 or 400 mg/dm^3 As(III) solution at pH 8 (MF) and pH 9 (MC and MFC).

3.6.3.4 *Adsorption kinetics*

Chromium(VI): The effect of concentration on adsorption kinetics experiments were conducted using different concentrations of Cr(VI) (10, 20, 25, 50 and 75 mg/dm^3) at pH 3. The effect of temperature on adsorption kinetics experiments were performed at pH 3 using 100 cm^3 of 10 mg/dm^3 Cr(VI) solution at different temperatures (299, 304, 309, 314 and 319 K). In both investigations, aliquot samples (0.5 cm^3) were pipetted from the mother liquor at different time intervals (0.5, 1, 2, 3, 5, 30, 45, 60, 75, 90 and 120 mins) and the remaining chromium concentration was spectroscopically determined.

Arsenic(III): The experiments were performed as for Cr(VI) adsorption but using As(III) solutions at pH 8 (MF) and pH 9 (MC and MFC).

3.6.3.5 *Effect of co-existing anions*

Chromium(VI): To determine the effect of co-existing ions, 0.05 g of nanometal adsorbent (MFC, MF and MC) were separately contacted with 100 cm^3 of 100 mg/dm^3 Cr(VI) solution containing 0.1 mg/dm^3 of either Na_2SO_4, Na_2CO_3, NaCl, or NaH_2PO_4 at pH 3 in glass bottles at 299 K and agitated on a shaker. The adsorption was stopped and the remaining chromium concentration determined in the supernatant.

Arsenic(III): The experimental was the same as for Cr(VI) adsorption but using 100 cm^3 of 50 mg/dm^3 As(III) solution containing 0.1 mg/dm^3 of either Na_2SO_4, Na_2CO_3, NaCl, or NaH_2PO_4 at pH 8 (MF) and pH 9 (MC and MFC).

3.6.3.6 *Effect of ionic strength*

Chromium(VI): The studies on effect of electrolyte on Cr(VI) adsorption were conducted by separately contacting 0.05 g adsorbent (MFC, MF and MC) with 100 cm^3 of 100 mg/dm^3 Cr(VI) solution containing 0.00, 0.01, 0.05, 0.1, 0.15 and 0.2 mg/dm^3 of $NaNO_3$ agitated at 299 K at pH 3. The adsorption process was halted and total residual chromium concentration determined.

Arsenic(III): The studies were done as for Cr(VI) adsorption but using 100 cm^3 of 50 mg/dm^3 As(III) solution containing 0.00, 0.01, 0.05, 0.1, 0.15 and 0.2 mg/dm^3 of $NaNO_3$ at pH 8 for the MF metal oxide composite and pH 9 for the MC and MFC metal oxides. The adsorption process was stopped and total residual arsenic concentration determined in the supernatant.

3.6.3.7 *As(III)/NO_3^- exchange coefficients*

Arsenic(III): Accurately weighed amounts (2 g) of each of the nanostructured MC, MF and MFC metal oxide composites were dispersed in 100 cm^3 of 50 mg/dm^3 $NaNO_3$ solution set at pH 5 at 299 K. The suspensions were shaken for 5 h and centrifuged. The residues were washed with ultrapure water and dried at 333 K for 12 h. The dried NO_3^--loaded nanostructured metal oxide composites (0.5 g) were weighed and individually dispersed in 100 cm^3 of each of 0, 5, 10, 25 and 50 mg/dm^3 of As(III) solution set pH 8 for the MF oxide and pH 9 for the MC and MFC metal oxide composite adsorbents at 299 K. The suspensions were agitated at 200 rpm for 2 h and centrifuged. The concentration amounts of residual arsenic and the released NO_3^- ions in the supernatant were determined using ICP-OES and an ion-selective electrode (ISE) from HANNA instruments (USA).

3.6.3.8 *Desorption experiments*

Chromium(VI): An accurately weighed amount (0.1 g) of each of the MC, MF and MFC metal oxides was separately contacted with 100 cm^3 of 50 mg/dm^3 of Cr(VI) solution (pH 3) at 299 K and thermostatically shaken. The adsorption was stopped and the residual total chromium concentration in the supernatant determined. The residue was washed with ultrapure water, dried at 333 K for 8 h and used in the subsequent desorption experiment. The desorption experiments were performed by contacting 0.05 g residue of each of the MC, MF and MFC metal oxides and 100 cm^3 of 0.1 mol/dm^3 of either NaOH, CH_3COOH or H_2O at 299 K and agitated on a shaker. After the desorption process, the concentration amount of total chromium in the supernatant was quantified.

Arsenic(III): The experiments were the same as for Cr(VI) desorption but with 100 cm^3 of 50 mg/dm^3 of As(III) solution (pH 8 for MF metal oxide, pH 9 for MC and MFC metal oxide).

3.6.3.9 *Regeneration and reuse studies*

Chromium(VI): The nanometal oxides (MFC, MF and MC) were subjected to five adsorption/desorption cycles to investigate on desorption of Cr(VI) and reuse of the spent metal oxide adsorbents. The metal composite oxides (0.2 g) were separately placed in four glass bottles containing 50 cm^3 of 50 mg/dm^3 Cr(VI) solution at 299 K (pH 3) and agitated. The adsorption was stopped and the remaining total chromium concentration quantified. The residual solids were repeatedly washed with ultrapure water and dried in a thermostatic vacuum oven at 333 K for 8 h. The spent adsorbents from each glass bottle were separately placed in 50 cm^3 of 0.1 mol/dm^3 of NaOH and agitated on a shaker at 299 K. The desorption process was stopped by centrifuging and the total chromium concentration in the supernatant determined. The samples were rinsed with ultrapure water and dried at 333 K in an oven for 8 h. The adsorption/desorption cycle was repeated a further four times.

Arsenic(III): The experimental was the same as for Cr(VI) but using 100 cm^3 of 50 mg/dm^3 As(III) solution at 299 K (pH 8 for MF oxide, pH 9 for MC and MFC oxides).

3.7 BIOCHAR SUPPORT

A drawback on the use of nanostructured metal oxides as adsorbents in aqueous solution is their tendency to (1) aggregate or agglomerate reducing adsorption capacity and selectivity for the target pollutant (Guo et al., 2019), (2) cause column fouling in continuous flow-through systems and (3) are difficult to remove from the treated effluent and reuse in subsequent adsorption cycles (Ballav et al., 2014; Manyangadze et al., 2020). This investigation seeks to overcome the drawbacks by co-precipitating the ternary metal oxide system onto biochar support. The biochar was prepared from pine cone powder which is an agro-waste product. The biochar was chosen as the support for the ternary metal oxide nanocomposite since adsorption studies have shown that the adsorption capabilities of raw or modified biochars towards Cr(VI) and As(III) were very limited (Dong et al. 2017), hence the support is anticipated not to interfere with the Cr(VI) and As(III) adsorption mechanistic pathways onto the MFC metal oxide. Numerous studies have shown that biochar-based metal oxides are effective for decontamination of heavy metal-laden wastewater (Zhou et al., 2018). It is important to highlight that this research focuses on the efficacy of the ternary metal oxide to sequestrate Cr(VI) and As(III) from aqueous solution. The role of the biochar is merely to act as a support for the ternary metal oxide system. The adsorption is anticipated to occur on the metal oxide

surface with the biochar support eliminating the tendency of the adsorbent nanoparticles to agglomerate or aggregate and facilitating easy separation of the nanoadsorbent particles from the treated aqueous solution.

3.7.1 Preparation of pine cone powder

The pine cones were collected from pine trees at a plantation in Sasolburg, Free State province in South Africa. The cones were washed with ultrapure water and oven-dried at 80 °C for 48 h to remove impurities and some volatile organics like resin acids. The pine cone scales were peeled, pulverised and sieved. The pine cone particles between 45 and 90 µm were stored in a desiccator to be used for the synthesis of the biochar.

3.7.2 Preparation of biochar

The pulverized pine cone powder (10 g) was dispersed in 75 cm^3 of 2 mol/dm^3 diammonium hydrogen phosphate, $(NH_4)_2HPO_4$. The slurry mixture was stirred at 400 rpm for 24 h at 299 K, oven-dried at 110 ℃ for 8 h and then crushed to a powder. The pine cone powder was covered with A*l* foil, placed in a quartz reactor and then loaded into a tubular furnace from CARBOLITE GERO (UK). The sample was heated at a heating rate of 10 °C/min and carbonized at 600 °C for 2 h under an inert atmosphere of N_2 gas flow (50 cm^3/min) to obtain the biochar.

3.7.3 Co-precipitation of metal oxide composite within biochar support

The Mn-Fe-Cu-biochar (MFCb) nanocomposite was prepared as described in section 3.3.2 using 1 g of biochar.

3.7.4 Characterization of MFCb composite

The characterization of the raw biochar and the MFCb composite was done using FTIR (3.4.1), SEM (3.4.2), TEM (3.4.3) and BET (3.4.5). The pH_{pzc} was determined using the pH drift method (3.4.7).

3.7.5 Cr(VI) and As(III) adsorption experiments

3.7.5.1 *The influence of solution pH*

The investigation was performed as described in section 3.6.3.1 with 0.05 g of MFCb composite adsorbent.

3.7.5.2 *Regeneration and reuse of spent MFCb*

The experimental desribed in section 3.6.3.9 was utilized using MFCb composite adsorbent.

3.8 REFERENCES

1. BALLAV, N., CHOI, H.J., MISHRA, S.B. and MAITY, A. (2014) Synthesis, characterization of Fe_3O_4@glycine doped polypyrrole magnetic nanocomposites and their potential performance to remove toxic Cr(VI), *Journal of Industrial and Engineering Chemistry*. 20, pp. 4085–4093.

2. BURKS, T., AVILA, M., AKHTAR, F., GÖTHELID, M., LANSÅKER, P.C., TOPRAK, M.S., MUHAMMED, M. and UHEIDA, A. (2014) Studies on the adsorption of chromium (VI) onto 3-mercaptopropionic acid coated superparamagnetic iron oxide nanoparticles, *Journal of Colloid and Interface Science*. 425, pp. 36-43.

3. DONG, H., DENG, J., XIE, Y., ZHANG, C., JIANG, Z., CHENG, Y., HOU, K. and ZENG, G. (2017) Stabilization of nanoscale zero-valent iron (nZVI) with modified biochar for Cr (VI) removal from aqueous solution, *Journal of Hazardous Materials*. 332, pp. 79-86.

4. GE, X., LIU, J., SONG, X., WANG, G., ZHANG, H., ZHANG, Y. and ZHAO, H. (2016) Hierarchical iron containing γ-MnO_2 hollow microspheres: a facile one-step synthesis and effective removal of As (III) via oxidation and adsorption, *Chemical Engineering Journal*. 301, pp. 139-148.

5. GUO, J., YAN, C., LUO, Z., FANG, H., HU, S. and CAO, Y. (2019) Synthesis of a novel ternary HA/Fe-Mn oxides-loaded biochar composite and its application in cadmium (II) and arsenic (V) adsorption, *Journal of Environmental Sciences*. 85, pp. 168-176.

6. ISLAM, M.A., ANGOVE, M.J., MORTON, D.W., PRAMANIK, B.K. and AWUAL, M.R. (2019) A mechanistic approach of chromium (VI) adsorption onto manganese oxides and boehmite, *Journal of Environmental Chemical Engineering*. pp. 103515.

7. LI, N., FU, F., LU, J., DING, Z., TANG, B. and PANG, J. (2017) Facile preparation of magnetic mesoporous MnFe2O4@ SiO2− CTAB composites for Cr (VI) adsorption and reduction, *Environmental Pollution*. 220, pp. 1376-1385.

8. MANYANGADZE, M., CHIKURUWO, N.H.M., NARSAIAH, T.B., CHAKRA, C.S., RADHAKUMARI, M. and DANHA, G. (2020) Enhancing adsorption capacity of

nano-adsorbents via surface modification: A review, *South African Journal of Chemical Engineering*. 31, pp. 25-32.

9. MARTINEZ, W.L. and MARTINEZ, A.R. (2015) *Computational Statistics Handbook with MATLAB*. Chapman and Hall/CRC.

10. PARSONS, J.G., HERNANDEZ, J., GONZALEZ, C.M. and GARDEA-TORRESDEY, J.L. (2014) Sorption of Cr (III) and Cr (VI) to high and low pressure synthetic nano-magnetite (Fe_3O_4) particles, *Chemical Engineering Journal*. 254, pp. 171-180.

11. YANG, K., ZHOU, J., LOU, Z., ZHOU, X., LIU, Y., LI, Y., BAIG, S.A. and XU, X. (2018) Removal of Sb (V) from aqueous solutions using Fe-Mn binary oxides: The influence of iron oxides forms and the role of manganese oxides, *Chemical Engineering Journal*. 354, pp. 577-588.

12. ZELMANOV, G. and SEMIAT, R. (2011) Iron (Fe^{3+}) oxide/hydroxide nanoparticles-based agglomerates suspension as adsorbent for chromium (Cr^{6+}) removal from water and recovery, *Separation and Purification Technology*. 80, pp. 330-337.
13. ZHOU, Q.W., LIAO, B.H., LIN, L.N., QIU, W.W., SONG, Z.G. (2018) Adsorption of Cu(II) and Cd(II) from aqueous solutions by ferromanganese binary oxide-biochar composites, *Science for the Total Environment*. 615, pp. 115–122.

CHAPTER 4

4 RESULTS AND DISCUSSION

4.1 INTRODUCTION

The chapter highlights the determination of optimal working parameters for the synthesis of the nanostructured ternary MFC metal oxide composite using central composite design of the response surface methodology technique. The chapter also presents and describes the spectroscopic characterization of the nanostructured metal oxides using fourier transform infrared spectroscopy, X-ray diffraction spectroscopy, scanning electron microscopy, transmission electron microscopy, X-ray photoelectron spectroscopy and Brunauer-Emmett-Teller analysis. The pH at point of zero charge (pH_{pzc}) of the nanocomposite adsorbents were determined. The characterization is divided into three sections (1) MF, (2) MC and (3) MFC nanocomposites.

4.2 OPTIMIZATION OF ADSORBENT SYNTHESIS PARAMETERS

4.2.1 Determination of optimal working parameters

The design matrix of the optimization investigations is presented in Table 4.1. The tabulated results show the coded independent variables and the generated response variables per each experimental run.

Table 4.1 Response surface methodology design of experiments and responses using Design-Expert 11 software.

Run	Coded independent variables				Responses			
	A:time (mins)	B:$MnCl_2$ (mol)	C:$FeCl_3$ (mol)	D:$CuSO_4$ (mol)	Cr(VI) adsorption capacity[a] (mg/g)	[Cr(III)] (mg/dm^3)	As(III) adsorption capacity[b] (mg/g)	[As(V)] (mg/dm^3)
1	0	-1	-1	-1	17,815	6,137	8,756	4,387
2	-1			1	11,005	8,579	1,097	5,476
3	0	-1	-1	-1	22,005	1,399	7,321	3,591
4	1		1		21,275	4,745	1,374	5,782
5	0	-1	-1	-1	31,475	5,705	9,543	5,179
6	1	1			27,5	0,54	2,754	6,073
7	0	-1	1	-1	18,947	1,279	11,759	2,104
8	1	1	1	1	13,44	2,112	13,573	1,378
9	1				0	2,29	0	1,483
10	0		-1	-1	34,57	4,786	4,386	2,759
11	-1	-1	-1	-1	36,03	0,994	10,873	3,981
12	-1		1	1	35	0,752	7,548	1,094
13	0	-1	-1		26,01	3,798	9,573	0,576
14	1			1	15,749	4,831	6,359	2,932
15	0	-1	-1	-1	31,475	5,705	15,402	1,737
16	0	-1	-1	1	28,38	8,724	12,763	2,864
17	-1	1			3,605	5,279	4,925	4,985

18	1	-1	-1	-1	28,195	3,061	16,083	2,867
19	-1	1		1	12,376	2,971	11,789	2,765
20	1		1	1	13,625	2,075	5,893	4,892
21	-1		1		22,185	5,063	4,679	3,861
22	-1	1	1		1,785	4,443	3,742	5,893
23	0	-1	-1	-1	20,545	4,091	11,764	2,651
24	0	1	-1	-1	25,83	9,534	16,529	2,435
25	0	-1		-1	24,19	0,962	12,649	3,219
26	0	-1	-1	-1	1,055	2,789	9,726	1,792
27	1	1	1		24,92	3,716	10,794	0,641
28	-1	1	1	1	12,165	1,567	8,573	2,379
29	-1				0	2,29	0	1,483
30	1	1		1	14,762	1,851	13,117	2,874

[a] pH = 2 and [b] pH = 8.

To optimize the synthesis variables of the MFC ternary metal oxide adsorbent to yield high Cr(VI) and As(III) adsorption capacities, with low solution concentrations of Cr(III) and As(V) after the Cr(VI) and As(III) adsorption processes, respectively, the CCD experimental data response functions were analysed using multiple regression techniques. The quadratic model was chosen by the Design-Expert version 11.1.2.0 software as the most suitable model for the four responses. The generated second-order polynomial equations were evaluated using the analysis of variance (ANOVA) at 95 % confidence level ($p < 0.05$). The ANOVA parameters of the quadratic model of the four responses are presented in Table 4.2. The statistically significant model terms have p-values < 0.05, while those with p-values > 0.1 are statistically insignificant. The fitted models for Cr(VI) adsorption capacity, Cr(III) left in solution, As(III) adsorption capacity and As(V) left in solution after the insignificant terms were discarded are Eq's (4.1-4.4):

$$Y_{Cr(VI)ads\ cap} = +25.85 + 1.77A - 0.9471B + 3.17C + 1.91D + 4.33AB - 1.61AC - 4.13AD - 4.36BC - 2.16BD - 0.8902CD + 1.63A^2 - 8.91C^2 - 3.29D^2 \quad (4.1)$$

$$Y_{[Cr(III)]} = +4.60 + 0.3502A - 1.08B + 0.8988C + 1.13D - 1.33AB + 1.78AC + 1.05AD - 0.9667BC - 1.58BD - 2.03A^2 + 2.60B^2 - 2.44C^2 + 2.20D^2 \quad (4.2)$$

$$Y_{As(III)\ ads\ cap} = +11.79 + 0.8123A + 2.70B + 0.4525C + 2.57D + 0.7379AB + 0.3608AC - 0.9116CD - 2.93B^2 - 0.6832C^2 - 1.92D^2 \quad (4.3)$$

$$Y_{[As(V)]} = +2.82 - 0.3553A - 0.2092C - 0.2791D - 0.5207AB + 0.1196AC + 0.2566AD - 0.7601BC - 0.7426BD - 0.4723CD + 0.8906A^2 + 0.2781C^2 - 0.6634D^2 \quad (4.4)$$

where the responses $Y_{Cr(VI)ads\ cap}$, $Y_{[Cr(III)]}$, $Y_{As(III)\ ads\ cap}$ and $Y_{[As(V)]}$ refer to Cr(VI) adsorption capacity (mg/g), concentration of Cr(III) in solution (mol/dm^3), As(III) adsorption capacity (mg/g) and concentration of As(V) in solution (mol/dm^3),respectively. A is co-precipitation time (mins), B, C and D represent mole amounts of $MnCl_2$, $FeCl_3.6H_2O$ and $CuSO_4.5H_2O$, respectively. The influence of a variable on the response is denoted by the sign and magnitude of the coefficient in the second-order polynomial equation (Sarkar & Majumdar, 2011). The size and sign of the coefficient refer to the intensity and type of influence,

respectively. A positive sign implies that the influence of the variable on the response is synergistic, while a negative sign shows an antagonistic relationship between the variable and the response (Owolabi et al., 2018; Zargazi & Entezari, 2020). ANOVA showed that the quadratic model F-values of Cr(VI) adsorption capacity, Cr(III) left in solution, As(III) adsorption capacity and As(V) left in solution were 104.88, 128.28, 131.35 and 62.16, respectively with $p < 0.0001$ implying that the estimated models are significant and that there is 0.01 % probability of the predicted model F-values occurring due to noise. The results predicted that the coefficients of A, B, C, D, AB, AC, AD, BC, BD, CD, A^2, C^2 and D^2 were the significant variables for Cr(VI) adsorption capacity, A, B, C, D, AB, AC, AD, BC, BD, A^2, B^2, C^2 and D^2 were significant for Cr(III) in solution, A, B, C, D, AB, AC, CD, B^2, C^2 and D^2 were significant for As(III) adsorption while A, C, D, AB, AC, AD, BC, BD, CD, A^2, C^2 and D^2 were significant for As(V) left in solution. Among the significant variables for Cr(VI) adsorption capacity and concentration of As(V) left in solution, the interaction effect of $MnCl_2$ moles and $FeCl_3$ moles (BC) was the most significant variable influencing the Cr(VI) adsorption capacity and concentration of As(V) left in solution. The interaction effect of co-precipitation time and $FeCl_3$ moles (AC) was predicted to be the most significant variable influencing the concentration of Cr(III) left in solution. The first-order effect of $MnCl_2$ moles (B) on the other hand was predicted to be the most significant variable influencing the As(III) adsorption capacity. The lack of fit (LOF) gives conclusive evidence whether a model is significant or insignificant since it refers to the variation of the data around the model (Shahri & Niazi, 2015). The LOF F-values were 1.05 for Cr(VI) adsorption capacity, 1.18 for Cr(III) left in solution, 6.69 for As(III) adsorption capacity and 0.6079 for As(V) left in solution. The LOF F-values for the four responses suggests that their LOFs were not significant relative to the pure error. Furthermore, non-significant marks appeared for the LOF on each response showing the suitability of the quadratic model to fit each of the four response functions.

Table 4.2 ANOVA parameters for the optimization of synthesis of nanostructured MFC ternary metal oxide.

	Cr(VI) adsorption capacity		[Cr(III)] in solution		As(III) adsorption capacity		[As(V)] in solution	
	F-value[a]	p-value[b]	F-value[a]	p-value[b]	F-value[a]	p-value[b]	F-value[a]	p-value[b]
Model	104.88	< 0.0001	128.28	< 0.0001	131.35	< 0.0001	62.16	< 0.0001
A-time (min)	39.86	< 0.0001	15.46	< 0.0013	46.54	< 0.0001	55.69	< 0.0001
B-MnCl_2 (mol)	11.46	0.0041	146.69	< 0.0001	513.37	< 0.0001	0.5950	0.4525
C-FeCl_3 (mol)	128.71	< 0.0001	101.83	< 0.0001	14.44	0.0017	19.31	0.0005
D-$CuSO_4$ (mol)	46.43	< 0.0001	160.60	< 0.0001	464.10	< 0.0001	34.36	< 0.0001
AB	213.19	< 0.0001	198.90	< 0.0001	34.14	< 0.0001	106.32	< 0.0001
AC	29.55	< 0.0001	354.25	< 0.0001	8.16	0.0120	5.61	0.0318
AD	193.90	< 0.0001	123.59	< 0.0001	0.5214	0.4814	25.81	0.0001
BC	216.20	< 0.0001	104.72	< 0.0001	0.2654	0.6139	226.55	< 0.0001
BD	52.82	< 0.0001	281.17	< 0.0001	2.05	0.1727	216.24	< 0.0001
CD	9.00	0.0090	0.7104	0.4126	52.10	< 0.0001	87.48	< 0.0001
A^2	4.89	0.0429	74.69	< 0.0001	0.0837	0.7763	50.37	< 0.0001
B^2	0.0881	0.7707	122.98	< 0.0001	87.15	< 0.0001	0.0842	0.7757
C^2	146.08	< 0.0001	107.66	< 0.0001	4.74	0.0459	4.91	0.0426
D^2	19.86	0.0005	88.18	< 0.0001	37.40	< 0.0001	27.95	< 0.0001
Lack of fit	1.05	0.5124	1.18	0.4531	6.69	0.0244	0.6079	0.7650

[a] Test for comparing model variance with residual (error) variance.

[b] Probability of seeing the observed F value if the null hypothesis is true (prob > F)

The fit error statistical parameters for Cr(VI) adsorption capacity, Cr(III) left in solution, As(III) adsorption capacity and As(V) left in the solution presented on Table 4.3 verified the fit of the quadratic model for each response. Analysis of variance (ANOVA) depicting close to unity coefficient of determination, R^2 values coupled with low p-values implies that the predicted quadratic model is valid for the response. The R^2 values were 0.9899 for Cr(VI) adsorption capacity, 0.9917 for Cr(III) left in solution, 0.9919 for As(III) adsorption capacity and 0.9831 for As(V) left in solution. This implies that approximately all the variations of each response could be explained by the model signifying the ability of the model in predicting the results. The significance of the model was shown by the lower values of the adjusted coefficients of determination, *Adj*-R^2 to the R^2 values for the four responses. The *Adj*-R^2 values were noted as 0.9804 for Cr(VI) adsorption capacity, 0.9840 for Cr(III) left in solution, 0.9844 for As(III) adsorption capacity and 0.9672 for As(V) left in solution, respectively. The predicted coefficients of determination, *Pred*-R^2 were 0.9535 for Cr(VI) adsorption capacity, 0.9600 for Cr(III) left in solution, 0.9398 for As(III) adsorption capacity and 0.9344 for As(V) left in solution, respectively. The results showed reasonable agreement between the *Pred*-R^2 and the *Adj*-R^2 since there is a difference of less than 0.2 between the two values implying a good correlation between the predicted and experimental values. The coefficient of variation (*C.V.*), also known as relative standard deviation is expressed as a percentage and indicates whether a model is reproducible and precise (*C.V.* < 10 %). The obtained C.V. % results of 6.04 for Cr(VI) adsorption capacity, 7.87 for Cr(III) left in solution, 5.93 for As(III) adsorption capacity and 6.51 for As(V) left in solution showed a small deviation between predicted and experimental values since they were all less than 10 %. The ANOVA results also showed the adequate precision, *AP* which is a numerical measure of the signal to noise ratio, with desirable values being above 4. The obtained *AP* values (Cr(VI) adsorption capacity = 41.3325, Cr(III) left in solution = 55.4386, As(III) adsorption capacity = 39.5778 and As(V) left in solution = 40.1447) suggest an adequate model discrimination.

Table 4.3 Fit statistics of CCD experimental design results.

	C.V. %	R^2	Adjusted R^2	Predicted R^2	Adequate precision
Cr(VI) adsorption capacity	6.04	0.9899	0.9804	0.9535	41.3325
[Cr(III)] in solution	7.87	0.9917	0.9840	0.9600	55.4386
As(III) adsorption capacity	5.93	0.9919	0.9844	0.9398	39.5778
[As(V)] in solution	6.51	0.9831	0.9672	0.9344	40.1447

The normal probability plots of studentized residuals presented in Figs 4.1a, 4.2a, 4.3a and 4.4a for Cr(VI) adsorption capacity, the concentration of Cr(III) left in solution, As(III) adsorption capacity and concentration of As(V) left in solution, respectively, show that the errors are normally distributed and independent. A good correlation between predicted responses and experimental responses is shown in Figs 4.1b, 4.2b, 4.3b and 4.4b for Cr(VI) adsorption capacity, Cr(III) left in solution, As(III) adsorption capacity and As(V) left in solution, respectively. The results reveal that the distribution of data points of actual responses obtained from the experiments are very close to the straight line suggesting that predicted responses from the quadratic model were in good agreement with the experimental data.

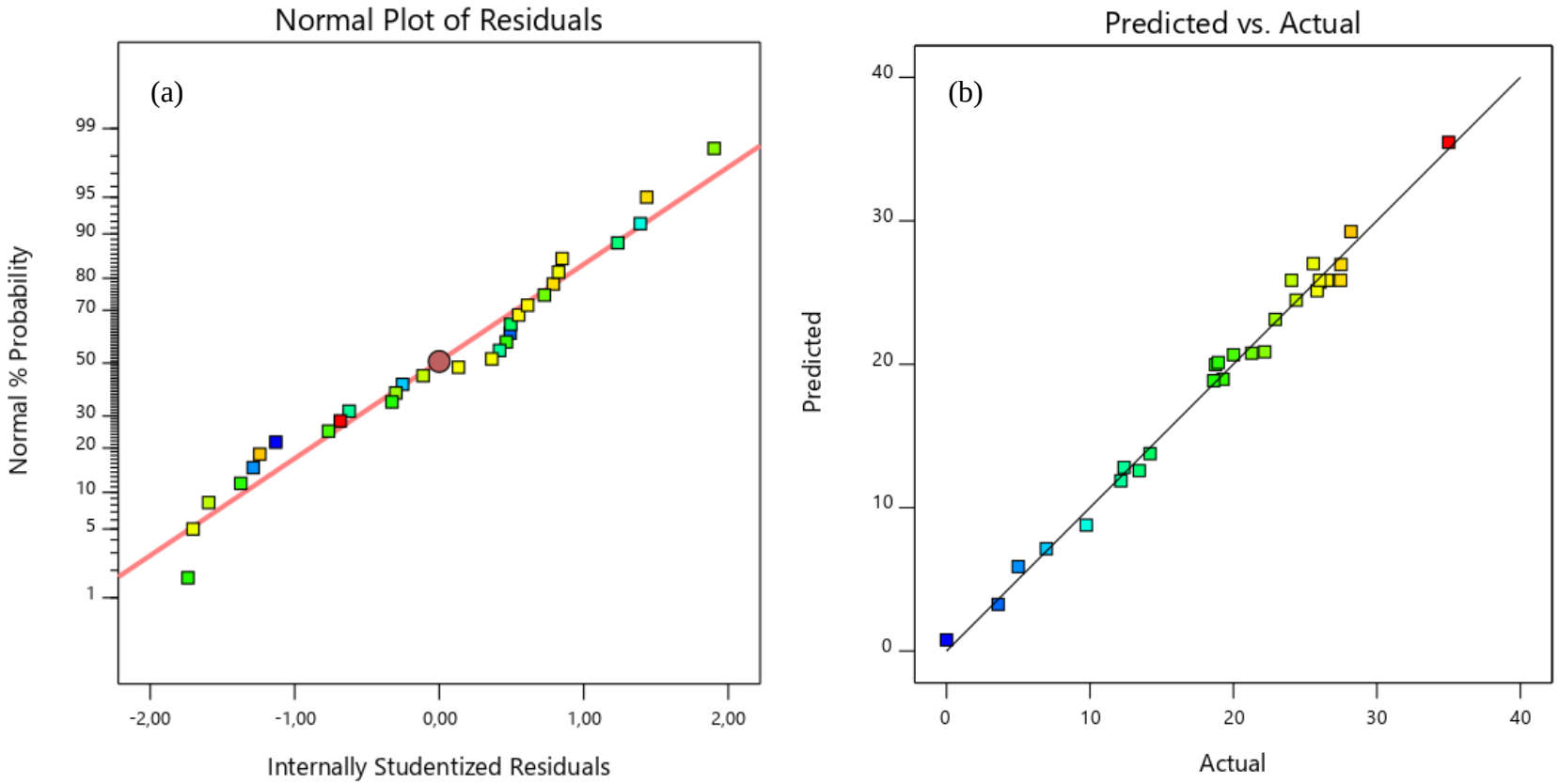

Fig 4.1 (a) Normal probability plot of residuals and (b) predicted responses vs actual responses plot for Cr(VI) adsorption capacity.

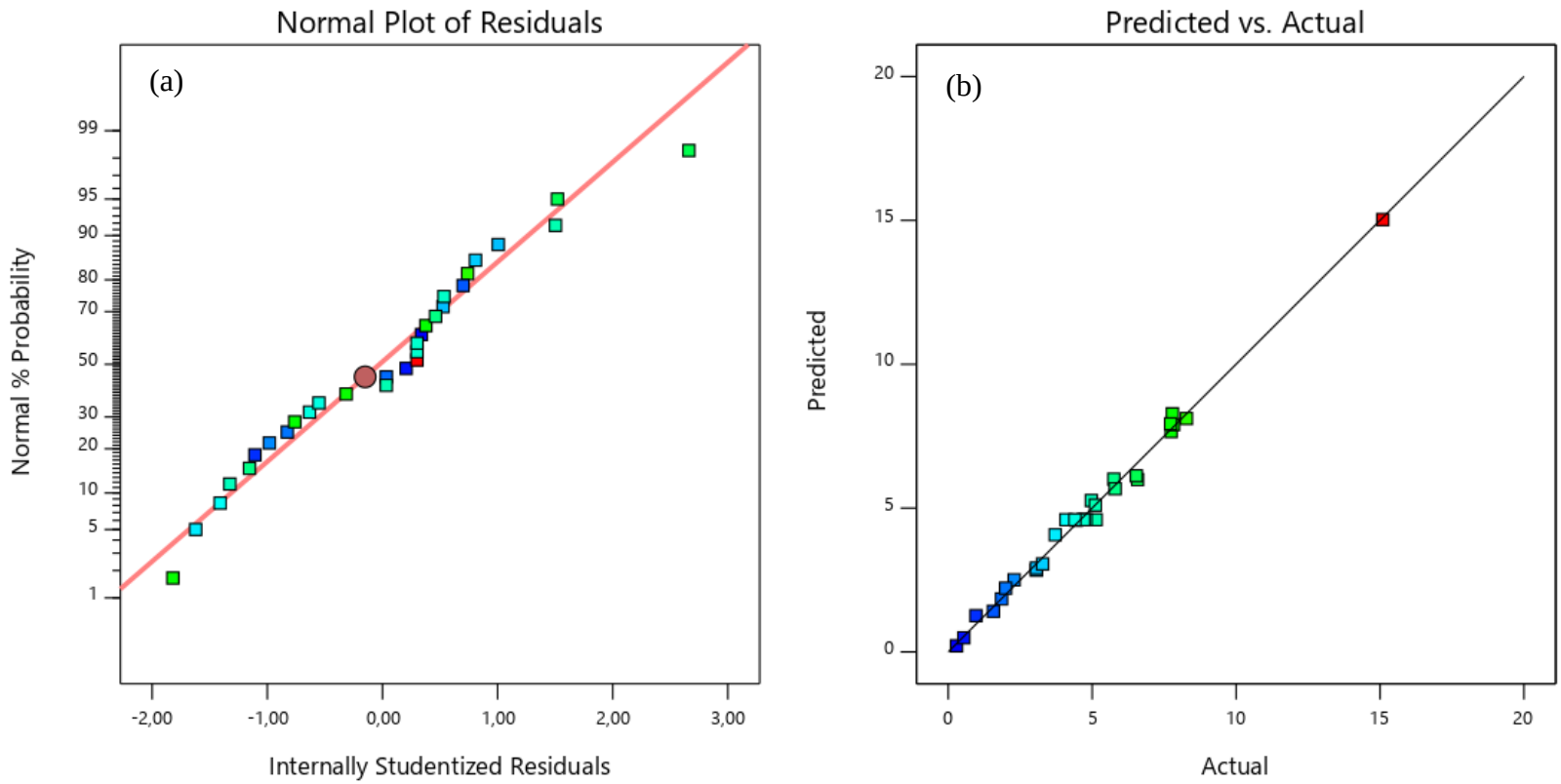

Fig 4.2 (a) Normal % probability plot of residuals and (b) predicted responses vs actual responses plot for Cr(III) concentration in solution after adsorption.

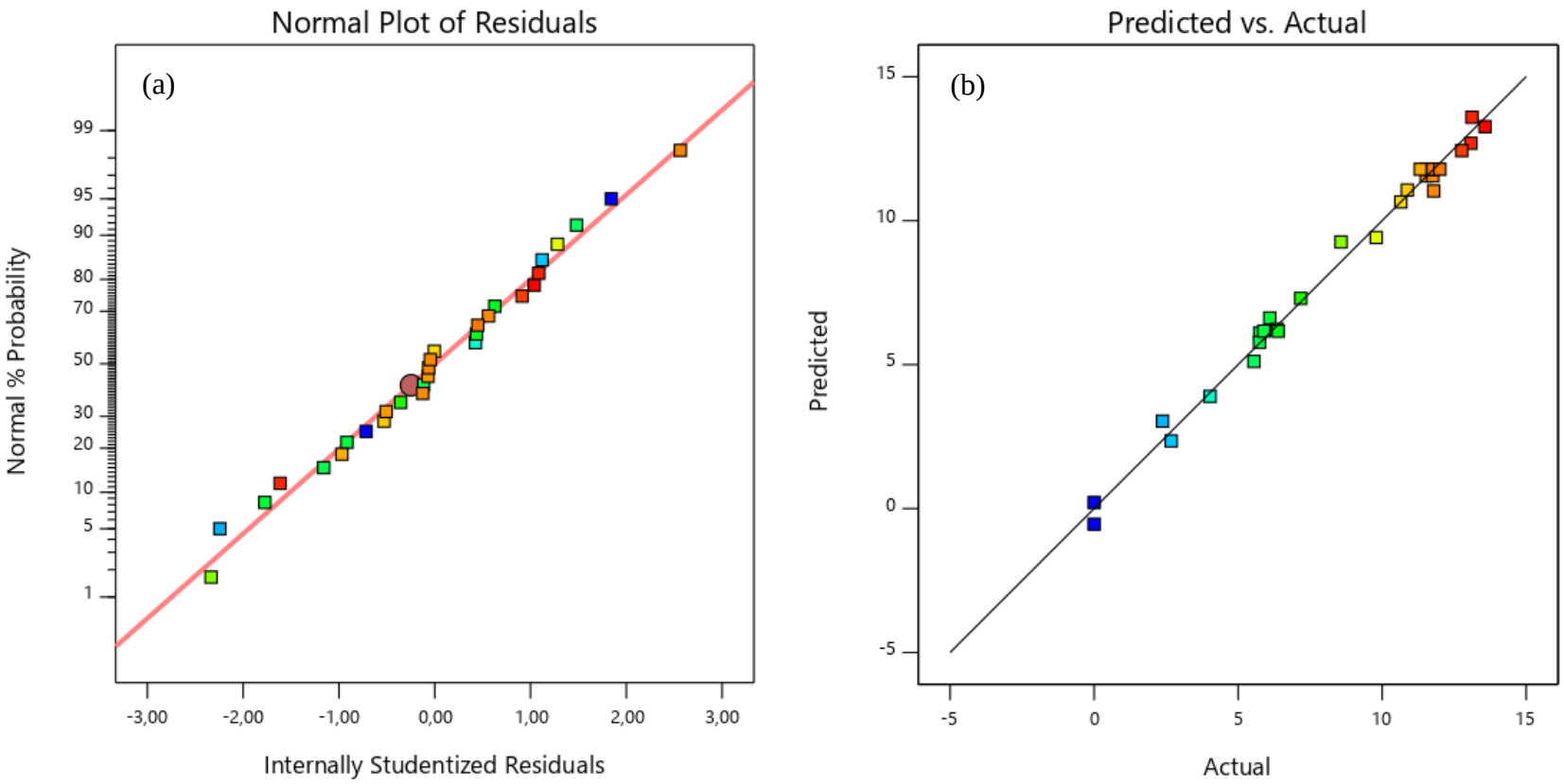

Fig 4.3 (a) Normal % probability plot of residuals and (b) predicted responses vs actual responses plot for As(III) adsorption capacity.

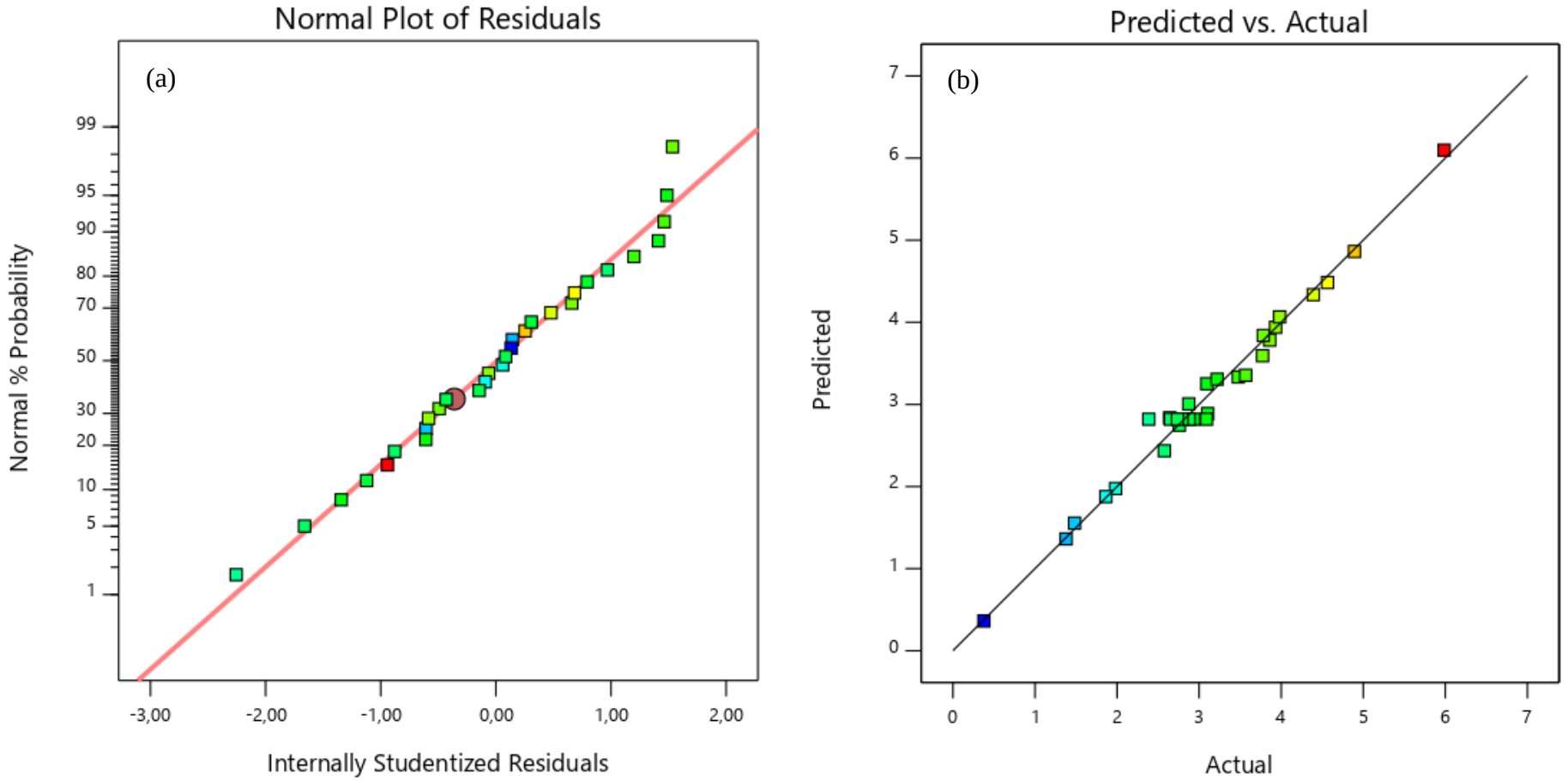

Fig 4.4 (a) Normal % probability plot of residuals and (b) predicted responses vs actual responses plot for [As(V)] in solution after As(III) adsorption.

4.2.2 Response surface analysis

The interactive effects between two independent variables on the response are presented on the 3D response surface graphs and contour plots in Figs 4.5a-f, 4.6a-e, 4.7a-c and 4.8a-f. The 3D graphs emanate from the response forming a surface above the two interacting independent variables while the other two variables are held constant around a central level. The contour plots are in 2D and their shapes show the intensity of the interaction between the two independent variables on the response (Zargazi & Entezari, 2020). A circular contour plot signifies minimal or zero interaction between the two independent variables, while a strong interaction forms elliptical contours and a direct relationship between the two independent variables results in a linear contour plot (Makareviciene et al., 2014).

4.2.2.1 *Effect of moles of $MnCl_2$, $FeCl_3$, $CuSO_4$ and co-precipitation time on Cr(VI) adsorption capacity*

ANOVA results show that the interaction between co-precipitation time-moles of $MnCl_2$ (AB), co-precipitation time- moles of $FeCl_3$ (AC), co-precipitation time-moles of $CuSO_4$ (AD), moles of $MnCl_2$–moles of $FeCl_3$ (BC), moles of $MnCl_2$-moles of $CuSO_4$ (BD) and moles of $FeCl_3$-moles of $CuSO_4$ (CD) showed the most significant influence on Cr(VI) adsorption capacity. The 3D response surface and contour plot on Fig 4.5a show the effect between the interaction of moles of $MnCl_2$ and co-precipitation time on Cr(VI) adsorption capacity when moles of $FeCl_3$ and moles of $CuSO_4$ were held constant. Fig 4.5b shows the 3D response surface and contour plot of the influence of the interaction between moles of $FeCl_3$ and co-precipitation time on Cr(VI) adsorption capacity when moles of $MnCl_2$ and moles of $CuSO_4$ were held constant. Fig 4.5c shows the 3D response surface and contour plot of the influence between the interaction of moles of $CuSO_4$ and co-precipitation time on Cr(VI) adsorption capacity when moles of $MnCl_2$ and moles of $FeCl_3$ were held constant. Fig 4.5d shows the 3D response surface and contour plot of the influence between the interaction of moles of $MnCl_2$ and moles of $FeCl_3$ on Cr(VI) adsorption capacity when moles of $MnCl_2$ and co-precipitation time were held constant. Fig 4.5e shows the 3D response surface and contour plot of the influence between the interaction of moles of $MnCl_2$ and moles of $CuSO_4$ on Cr(VI) adsorption capacity when moles of $FeCl_3$ and co-precipitation time were held constant. Fig 4.5f shows the 3D response surface and contour plot of the influence of the interaction between moles of $FeCl_3$ and moles of $CuSO_4$

on Cr(VI) adsorption capacity when moles of $MnCl_2$ and co-precipitation time were held constant.

The 3D response surface and contour plots on Fig 4.5a reveal that an increase in co-precipitation time and decrease in moles of $MnCl_2$ during synthesis favoured an increase in Cr(VI) adsorption capacity. The plots on Fig 4.5b show that an increase in co-precipitation time and increase in mole amounts of $FeCl_3$ increased the removal of Cr(VI). Fig 4.5c shows that a decrease in co-precipitation time and decrease in mole amounts of $CuSO_4$ caused an increase in adsorption, while Fig 4.5d exhibited that an increase in mole amount of $MnCl_2$ and a decrease in moles of $FeCl_3$ favoured Cr(VI) adsorption. An increase in Cr(VI) adsorption is noted in Fig 4.5e due to a decrease in moles of $MnCl_2$ and an increase in mole amount of $CuSO_4$. In Fig 4.5f, an increase in mole amounts of both $FeCl_3$ and $CuSO_4$ was observed to favour Cr(VI) removal.

The most significant term for Cr(VI) adsorption capacity was the antagonistic effect between moles of $MnCl_2$ and moles of $FeCl_3$. The oxides of Fe(III) can adsorb Cr(VI) forming Fe(II) in the process, but the oxides of Fe(II) reduce Cr(VI) to Cr(III). The role of manganese oxides is to keep the Fe in the +III valence state since the ions of Mn are strong oxidising agents (Yang et al., 2018). The manganese oxides also have a strong affinity for the formed Cr(III). Hence, increasing the moles of $MnCl_2$ and reducing moles of $FeCl_3$ increased the Cr(VI) adsorption capacity. The role of the copper oxide is to increase the pH at point of zero charge (pH_{pzc}).

(i) (ii)

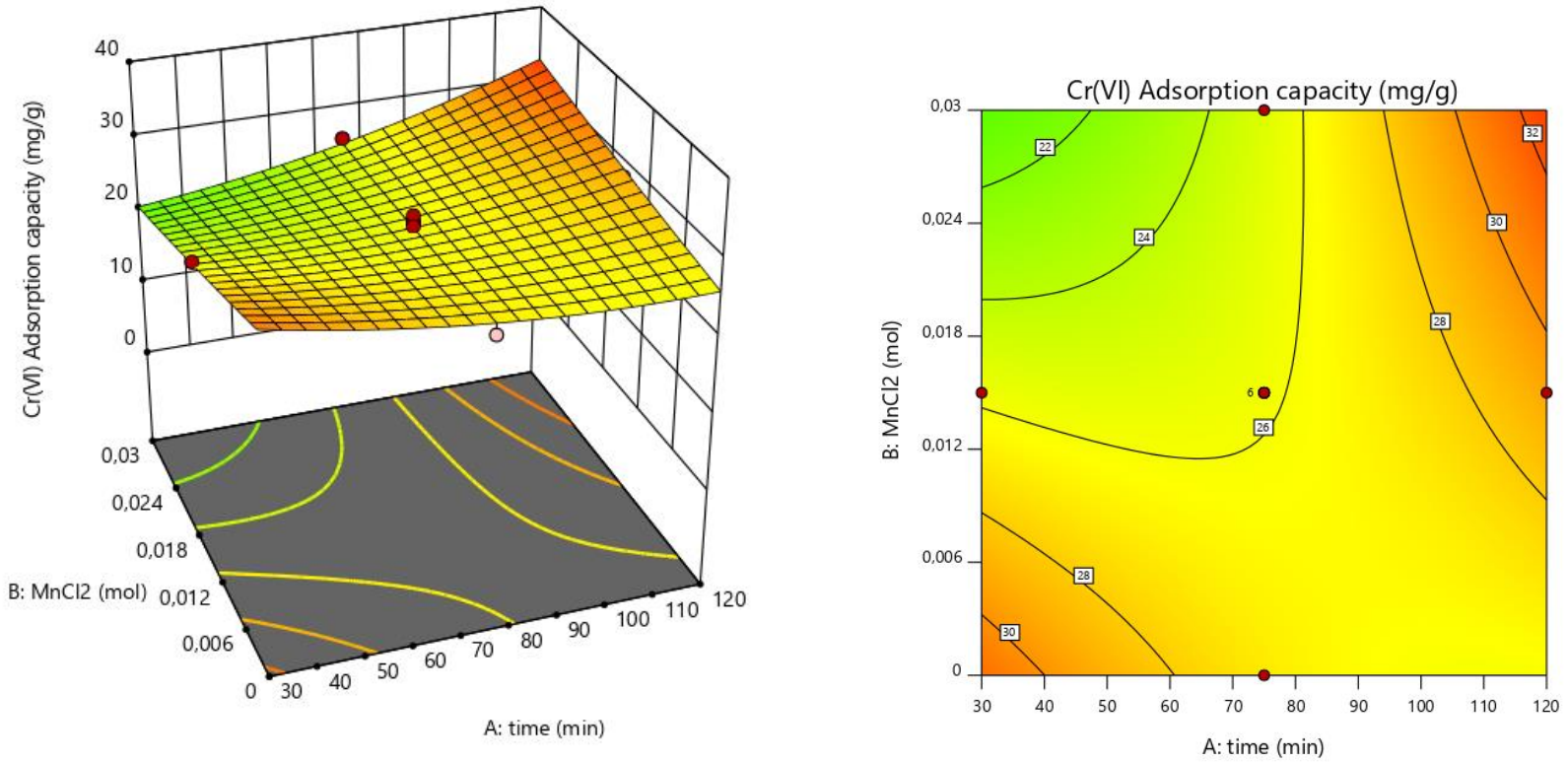

Fig 4.5a (i) 3D response surface and (ii) contour plot of effect of interaction between moles of $MnCl_2$ and co-precipitation time on Cr(VI) adsorption capacity.

(i) (ii)

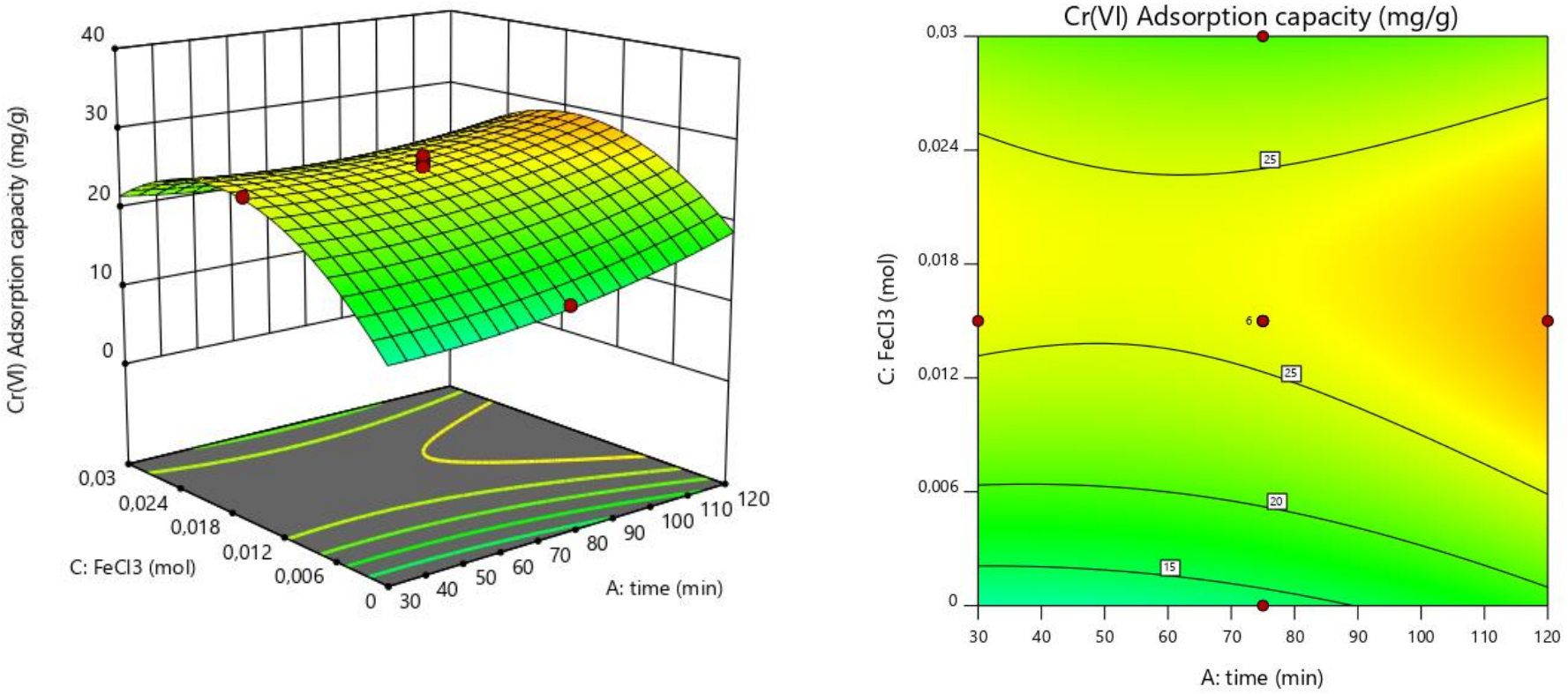

Fig 4.5b (i) 3D response surface and (ii) contour plot of effect of interaction between moles of $FeCl_3$ and co-precipitation time on Cr(VI) adsorption capacity.

(i) (ii)

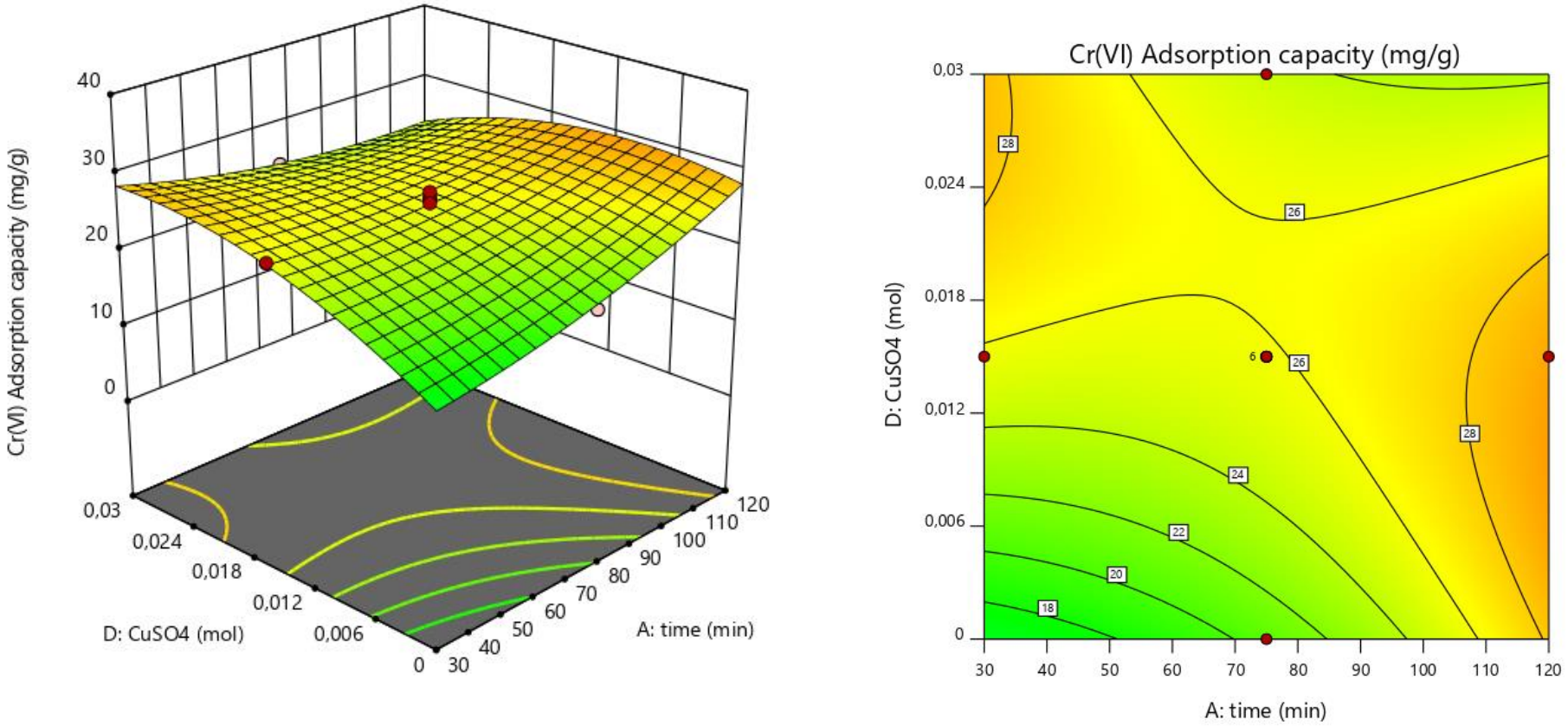

Fig 4.5c (i) 3D response surface and (ii) contour plot of effect of interaction between moles of $CuSO_4$ and co-precipitation time on Cr(VI) adsorption capacity.

(i)

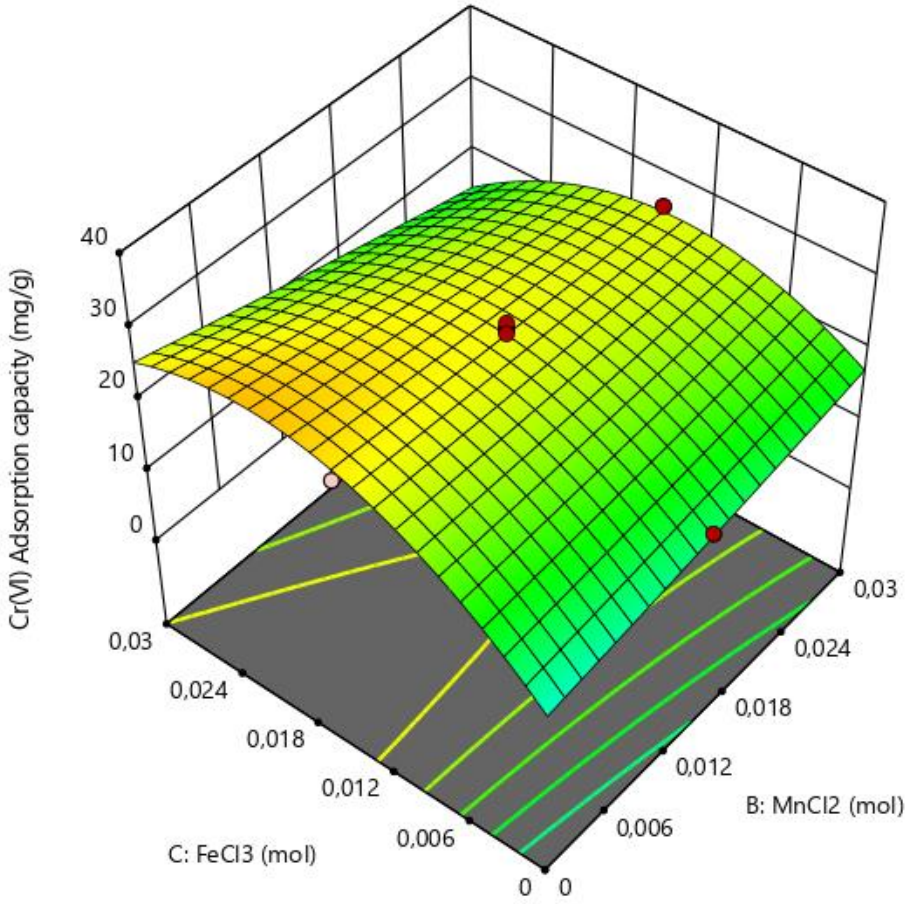

(ii)

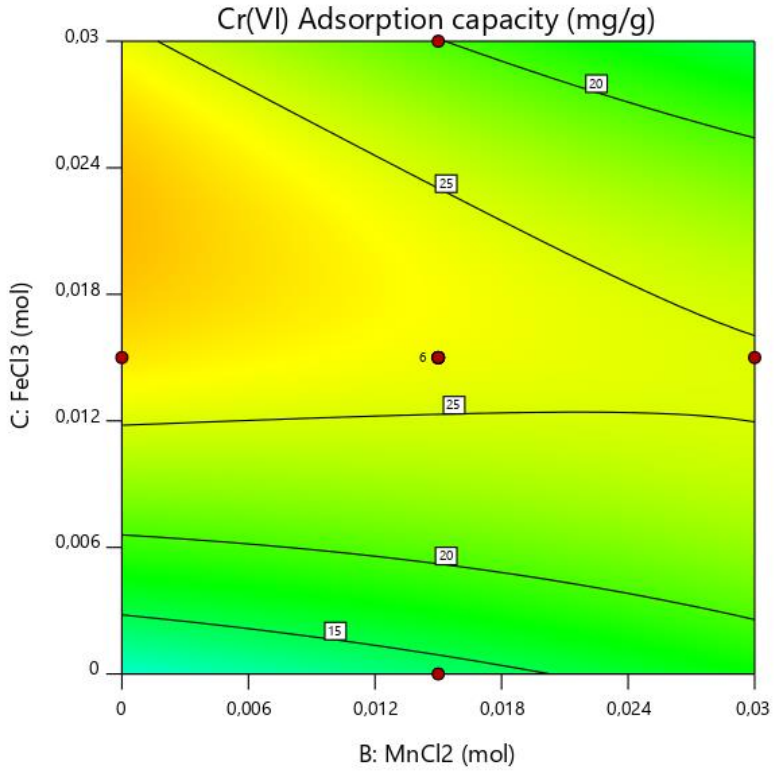

Fig 4.5d (i) 3D response surface and (ii) contour plot of effect of interaction between moles of $FeCl_3$ and moles of $MnCl_2$ on Cr(VI) adsorption capacity.

(i)

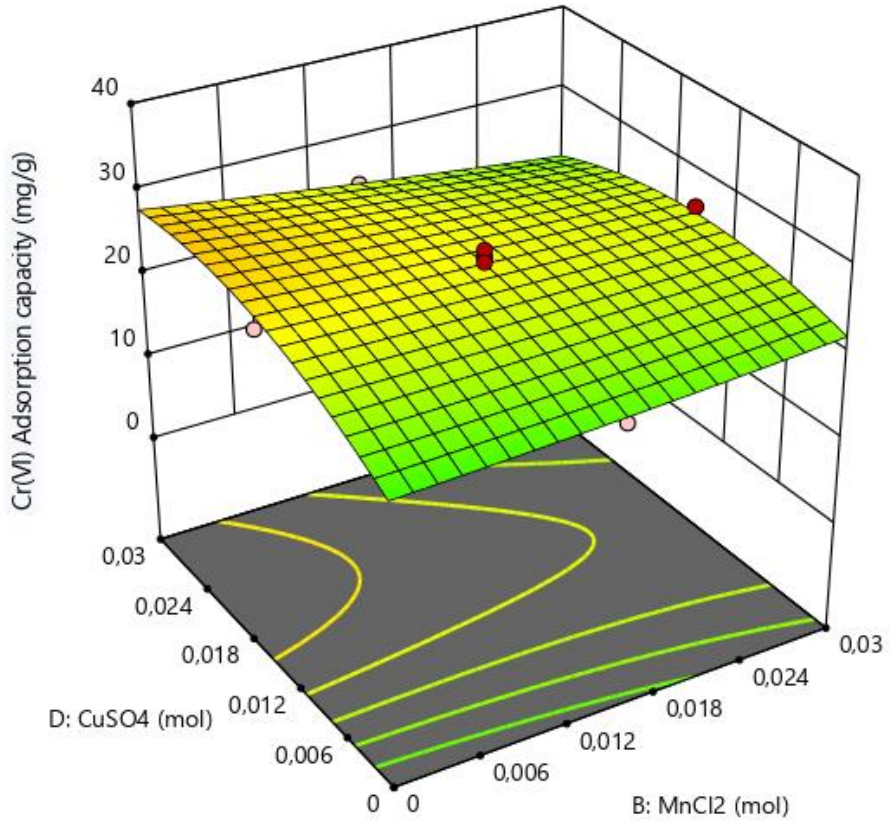

(ii)

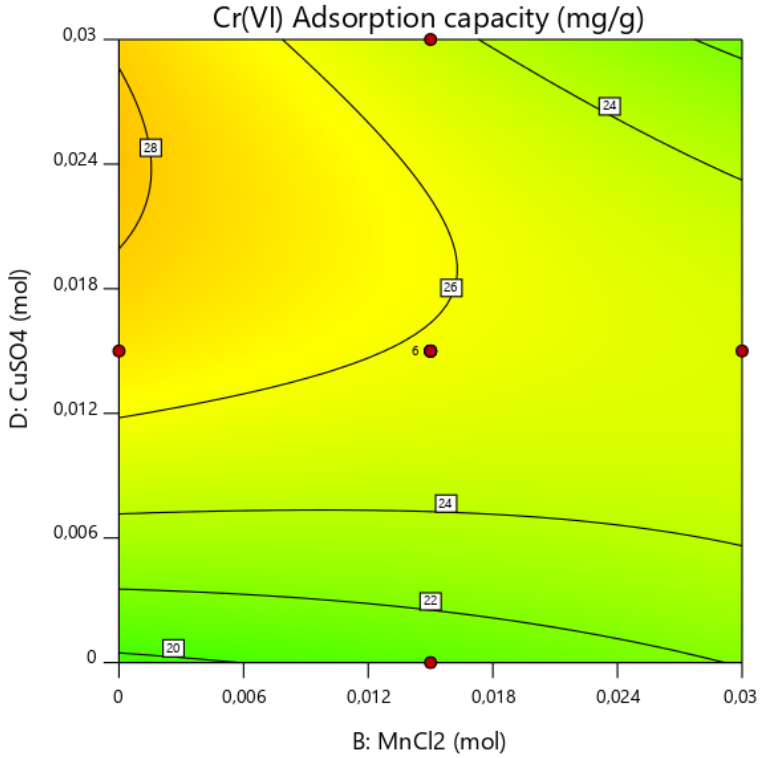

Fig 4.5e (i) 3D response surface and (ii) contour plot of effect of interaction between moles of $MnCl_2$ and moles of $CuSO_4$ on Cr(VI) adsorption capacity.

(i) (ii)

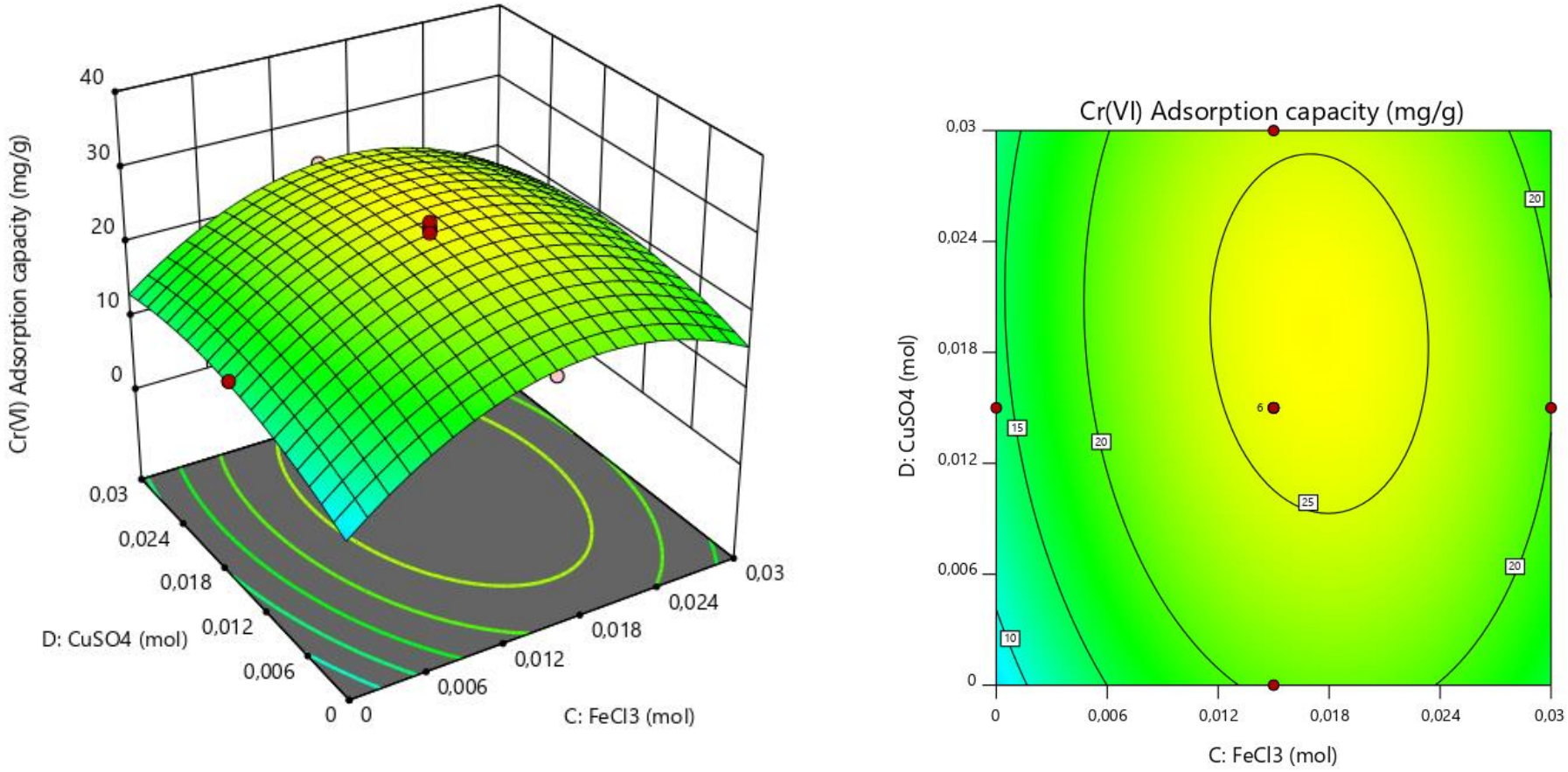

Fig 4.5f (i) 3D response surface and (ii) contour plot of effect of interaction between moles of $FeCl_3$ and moles of $CuSO_4$ on Cr(VI) adsorption capacity.

4.2.2.2 *Effect of moles of $MnCl_2$, $FeCl_3$, $CuSO_4$ and co-precipitation time on concentration of Cr(III) left in solution after adsorption of Cr(VI)*

The interaction between co-precipitation time-moles of $MnCl_2$ (AB), coprecipitation time-moles of $FeCl_3$ (AC), co-precipitation time-moles of $CuSO_4$ (AD) and moles of $MnCl_2$–moles of $FeCl_3$ (BC) showed the most significant influence on the concentration of Cr(III) left in solution after Cr(VI) adsorption. The 3D response surface and contour plot on Fig 4.6a show the effect of the interaction between moles of $MnCl_2$ and co-precipitation time on Cr(III) left in solution when moles of $FeCl_3$ and moles of $CuSO_4$ were held constant. Fig 4.6b shows the 3D response surface and contour plot of the influence between the interaction of moles of $FeCl_3$ and co-precipitation time on Cr(III) left in solution when moles of $MnCl_2$ and moles of $CuSO_4$ were held constant. Fig 4.6c shows the 3D response surface and contour plot of the influence of the interaction between moles of $CuSO_4$ and co-precipitation time on Cr(III) left in solution when moles of $MnCl_2$ and moles of $FeCl_3$ were held constant. Fig 4.6d shows the 3D response surface and contour plot of the influence of the interaction between moles of $MnCl_2$ and moles of $FeCl_3$ on Cr(III) left in solution when moles of $MnCl_2$ and co-precipitation time were fixed.

An analysis of the plots on Fig 4.6a revealed that the concentration amount of Cr(III) left in solution after adsorption was reduced as the mole amount of $MnCl_2$ increased at shorter co-precipitation time. Fig 4.6b showed that prolonged co-precipitation time and more mole amount of $FeCl_3$ decreased the concentration amount of Cr(III) left in solution, whereas in Fig 4.6c, a reduction in both co-precipitation time and mole amounts of $CuSO_4$ reduced the quantity of Cr(III) left in solution. The plots on Fig 4.6d exhibit that reduction of mole amounts of $FeCl_3$ and increase in mole quantity of $MnCl_2$ result in a reduction of Cr(III) left in solution.

The most significant term for reduced concentration amounts of Cr(III) left in solution after the adsorption process was the synergistic effect between co-precipitation time and the moles of $FeCl_3$. Longer co-precipitation times and increased mole amounts of $FeCl_3$ decreased the concentration amount of Cr(III) ions left in solution after the adsorption process.

(i) (ii)

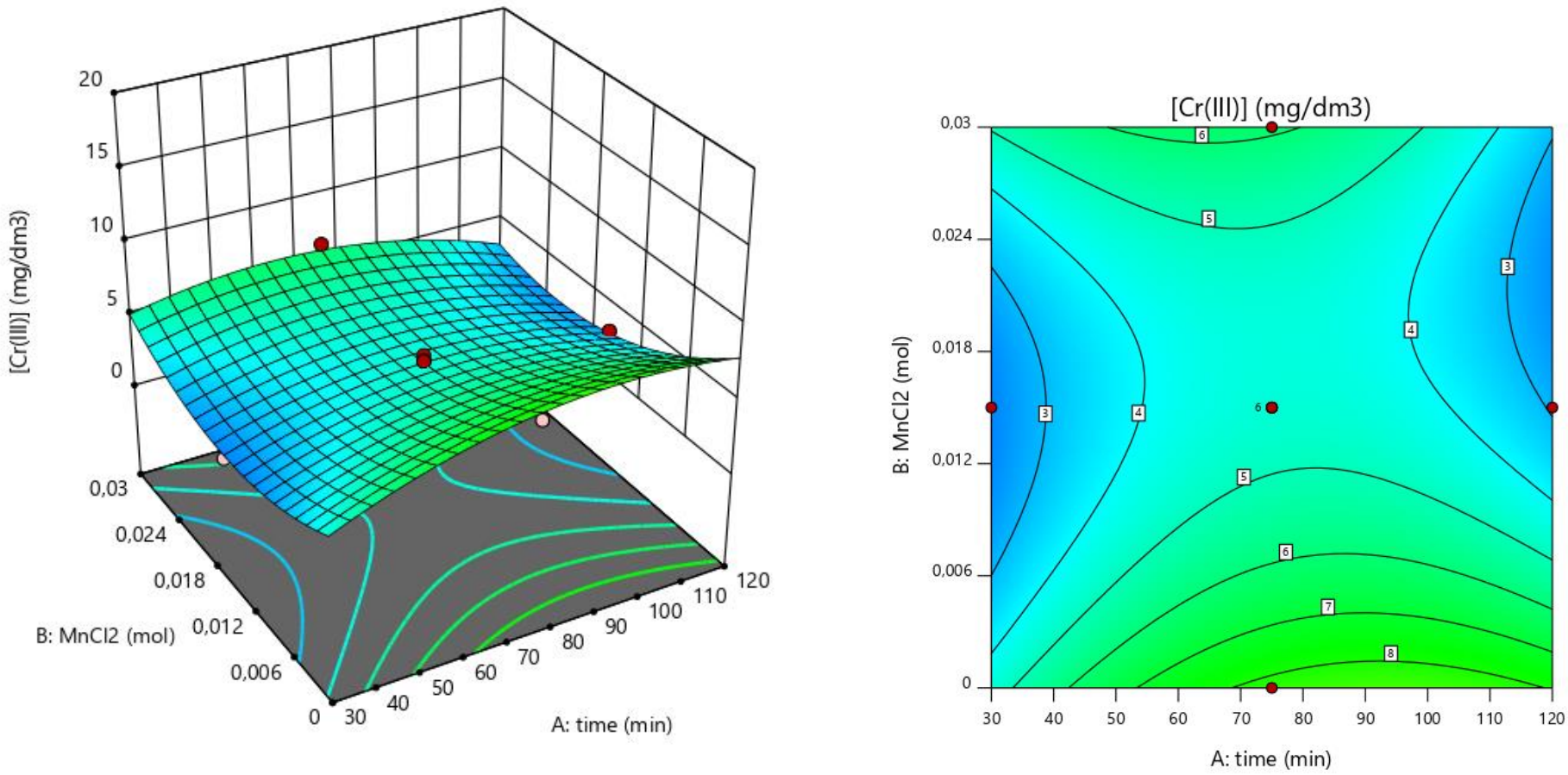

Fig 4.6a (i) 3D response surface and (ii) contour plot of effect of interaction between moles of $MnCl_2$ and co-precipitation time on [Cr(III)] in solution after Cr(VI) adsorption.

(i)

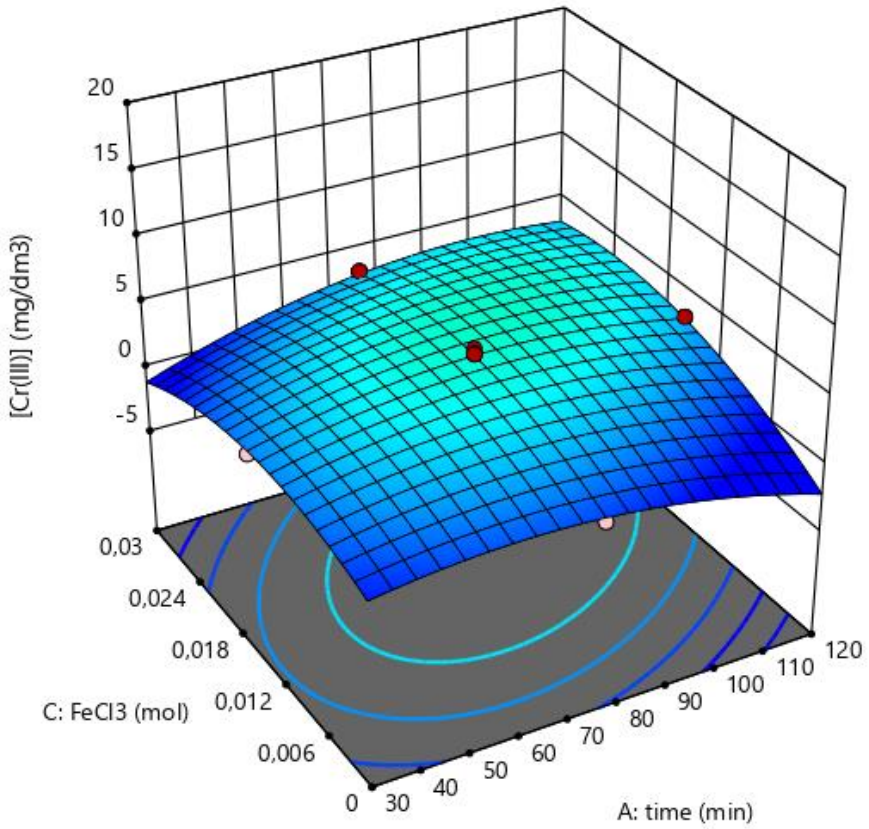

(ii)

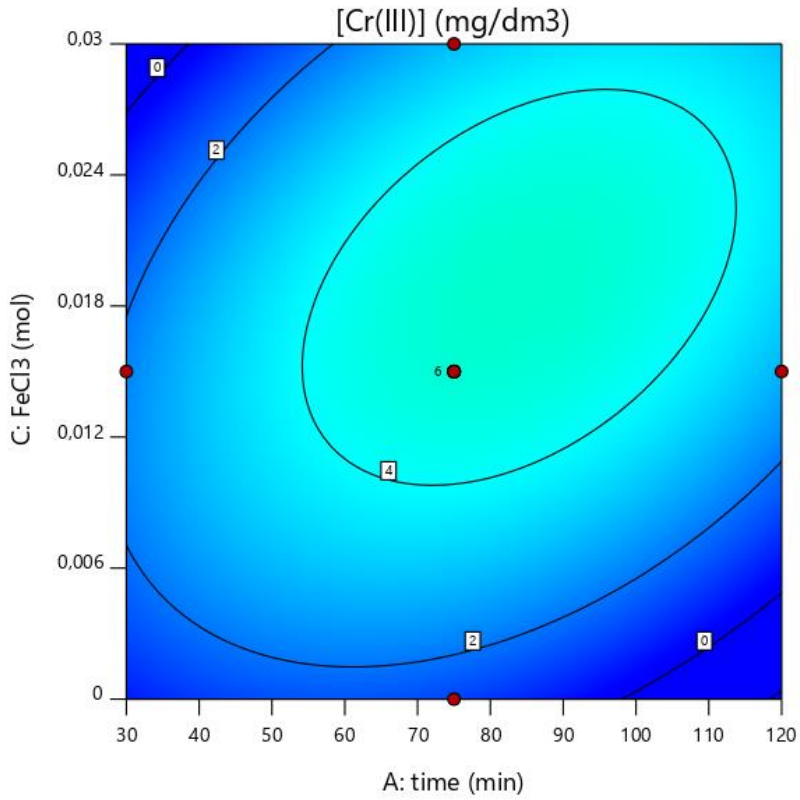

Fig 4.6b (i) 3D response surface and (ii) contour plot of effect of interaction between moles of $FeCl_3$ and co-precipitation time on [Cr(III)] in solution after Cr(VI) adsorption.

(i)

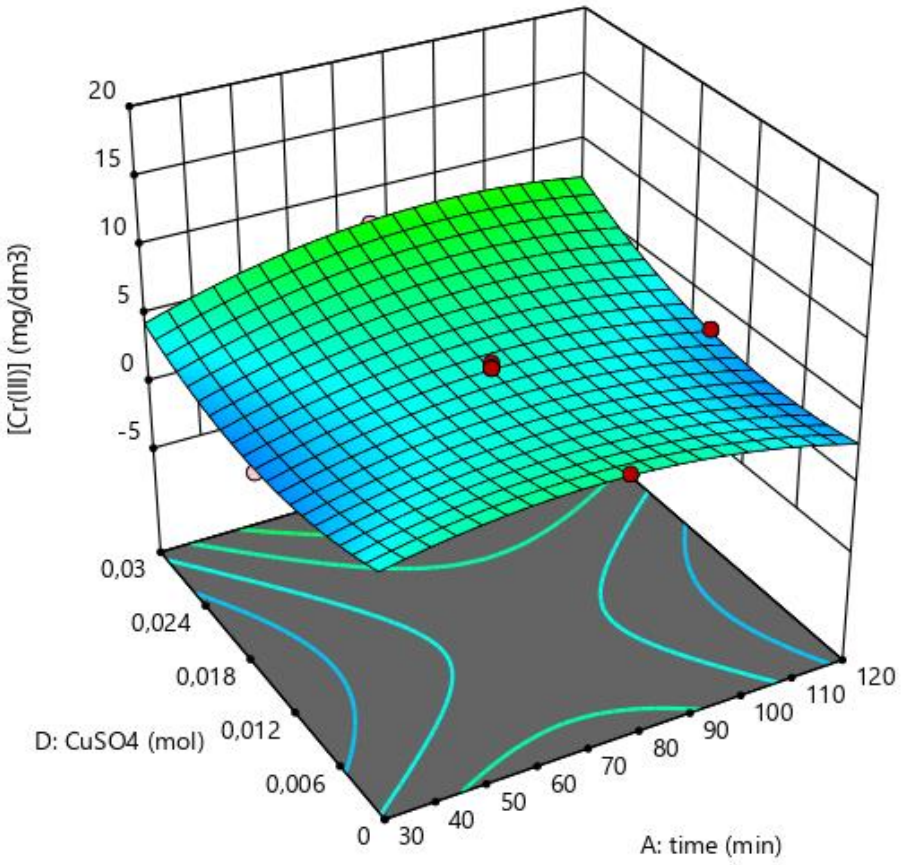

(ii)

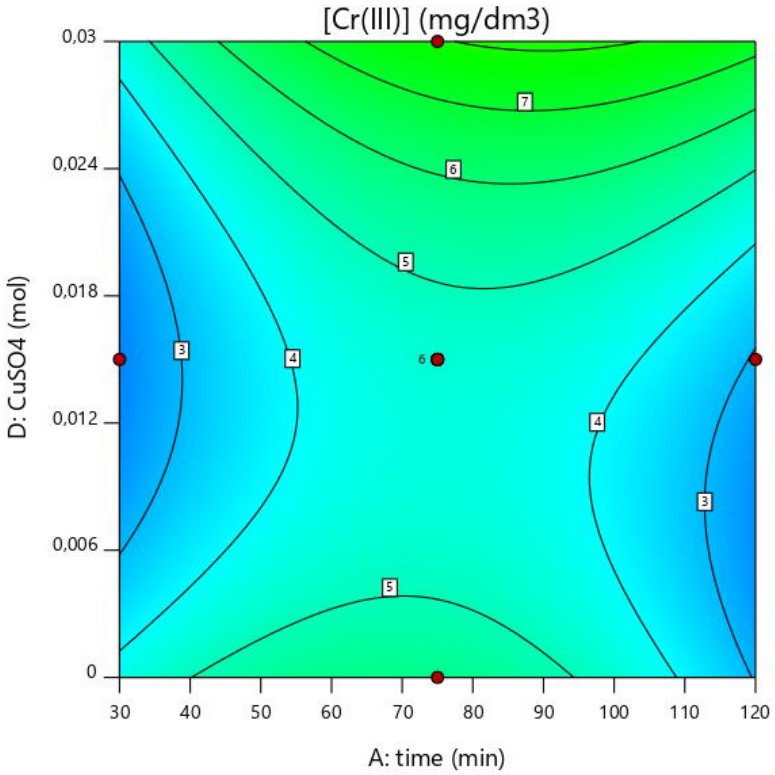

Fig 4.6c (i) 3D response surface and (ii) contour plot of effect of interaction between moles of $CuSO_4$ and co-precipitation time on [Cr(III)] in solution after Cr(VI) adsorption.

(i) (ii)

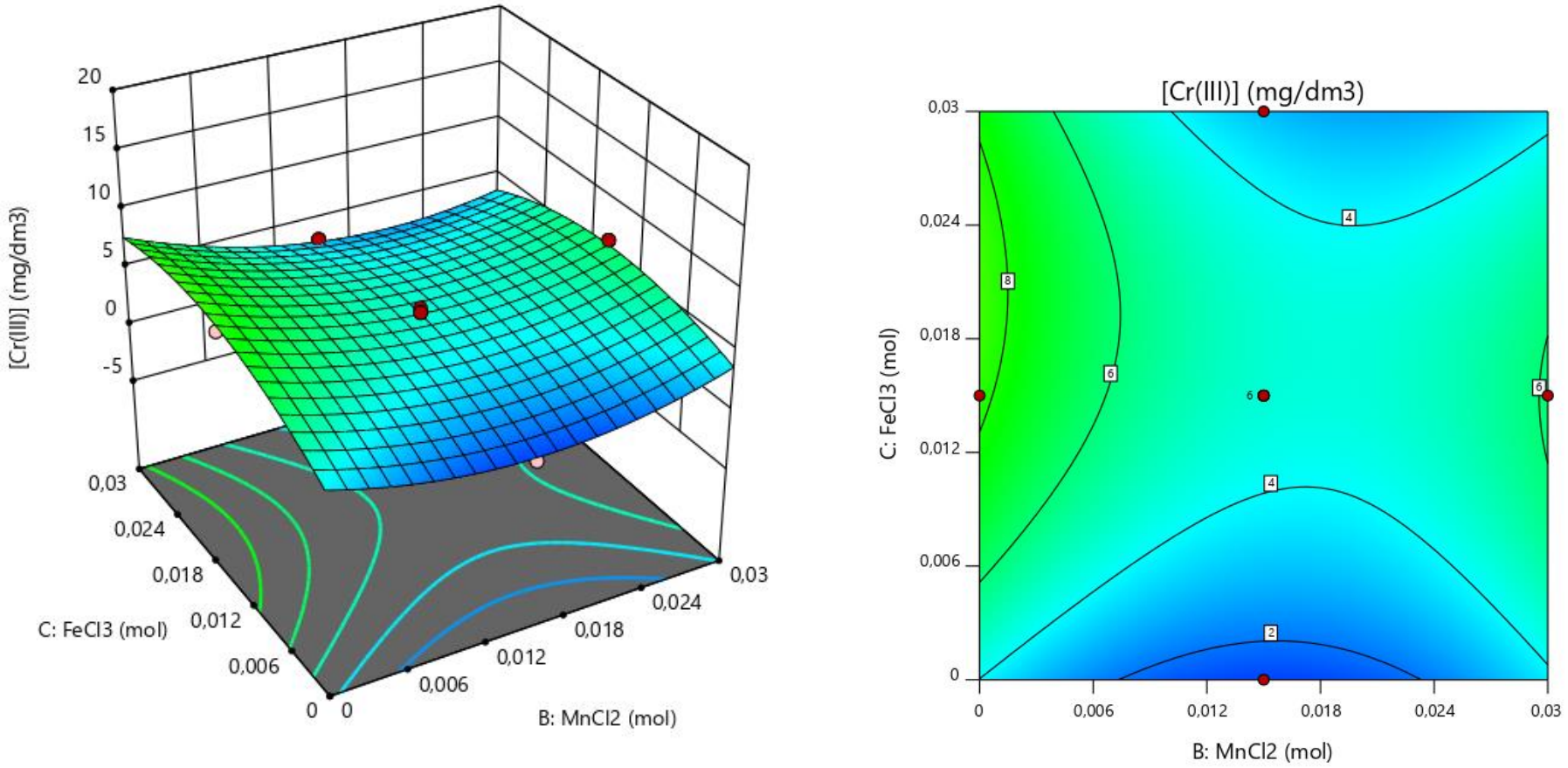

Fig 4.6d (i) 3D response surface and (ii) contour plot of effect of interaction between moles of $FeCl_3$ and moles of $MnCl_2$ on [Cr(III)] in solution after Cr(VI) adsorption.

(i) (ii)

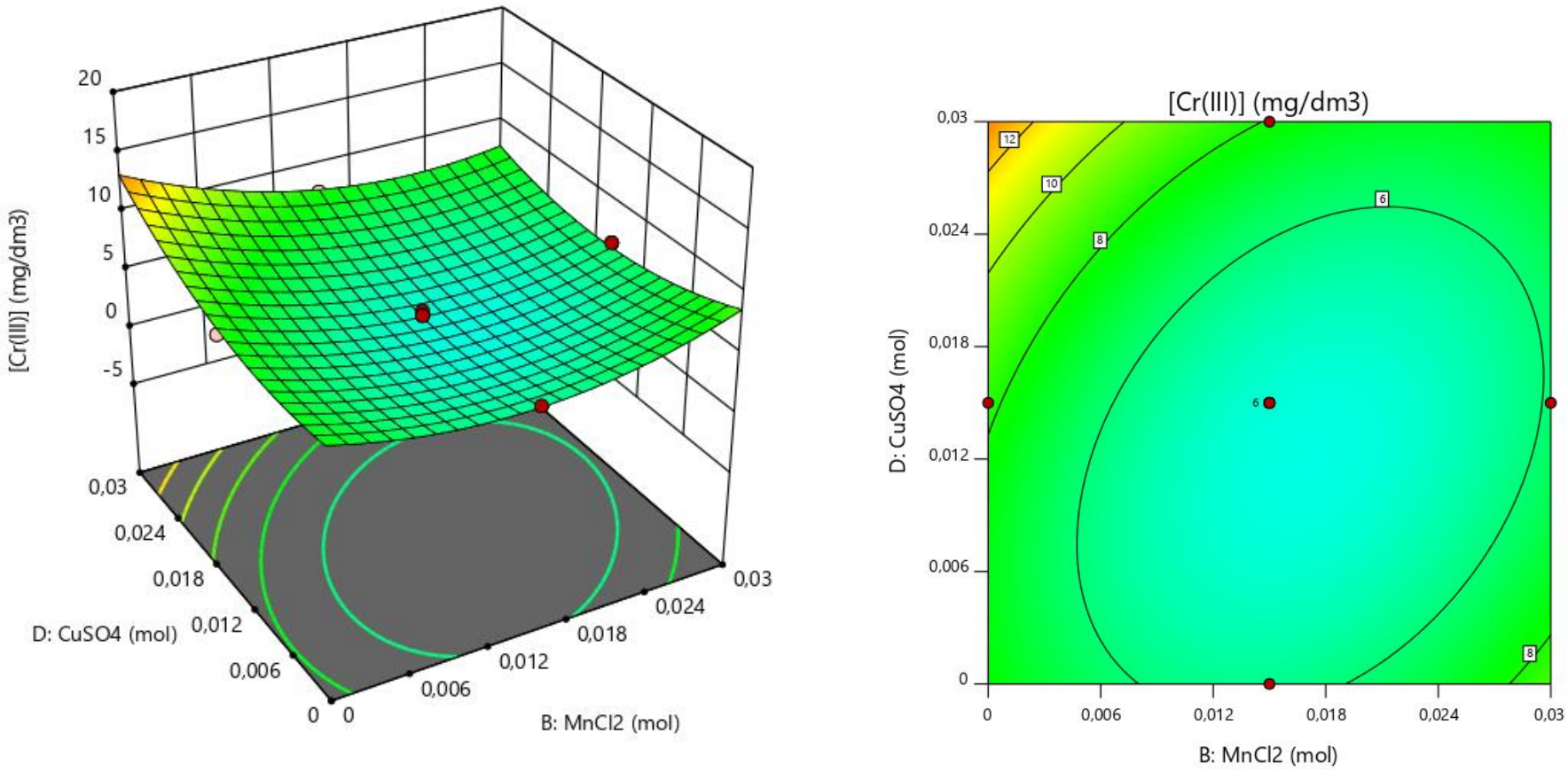

Fig 4.6e (i) 3D response surface and (ii) contour plot of effect of interaction between moles of $MnCl_2$ and moles of $CuSO_4$ on [Cr(III)] in solution after Cr(VI) adsorption.

4.2.2.3 *Effect of moles of $MnCl_2$, $FeCl_3$, $CuSO_4$ and co-precipitation time on As(III) adsorption capacity*

The interaction between co-precipitation time-moles of $MnCl_2$ (AB), coprecipitation time-moles of $FeCl_3$ (AC) and moles of $FeCl_3$-moles of $CuSO_4$ (CD) showed the most significant influence on adsorption capacity of As(III). The 3D response surface and contour plot on Fig 4.7a show the effect of the interaction between moles of $MnCl_2$ and co-precipitation time on As(III) adsorption when moles of $FeCl_3$ and moles of $CuSO_4$ were fixed. Fig 4.7b shows the 3D response surface and contour plot of the influence of the interaction between moles of $FeCl_3$ and co-precipitation time on As(III) adsorption when moles of $MnCl_2$ and moles of $CuSO_4$ were held constant. Fig 4.7c shows the 3D response surface and contour plot of the influence of the interaction between moles of $FeCl_3$ and moles of $CuSO_4$ on As(III) adsorption when moles of $MnCl_2$ and co-precipitation time were held constant.

The response surface and contour plots on Fig 4.7a reveal an increase in adsorption of As(III) as the mole amount of $MnCl_2$ and co-precipitation time are increased. Fig 4.7b shows that an increase in $FeCl_3$ moles and longer co-precipitation time both increased As(III) adsorption capacity. Fig 4.7c also showed that the adsorption capacity of As(III) increased with greater mole amounts of both $FeCl_3$ and $CuSO_4$.

The most significant term for As(III) adsorption capacity was the synergistic effect of the mole amount of $MnCl_2$. The main role of manganese oxides was to oxidise As(III) to As(V) which has a stronger affinity for iron oxides. Zheng and co-workers (2020) showed that increasing the mole amount of Mn in a binary Mn-Fe composite oxide increased the uptake capacity of the As(III) onto the adsorbent. The main role of the copper oxides was to raise the pH_{pzc} of the ternary metal oxide system since the manganese oxides have very low pH_{pzc} (2-3) so that the adsorbent can be applicable over a wider pH range.

(i) (ii)

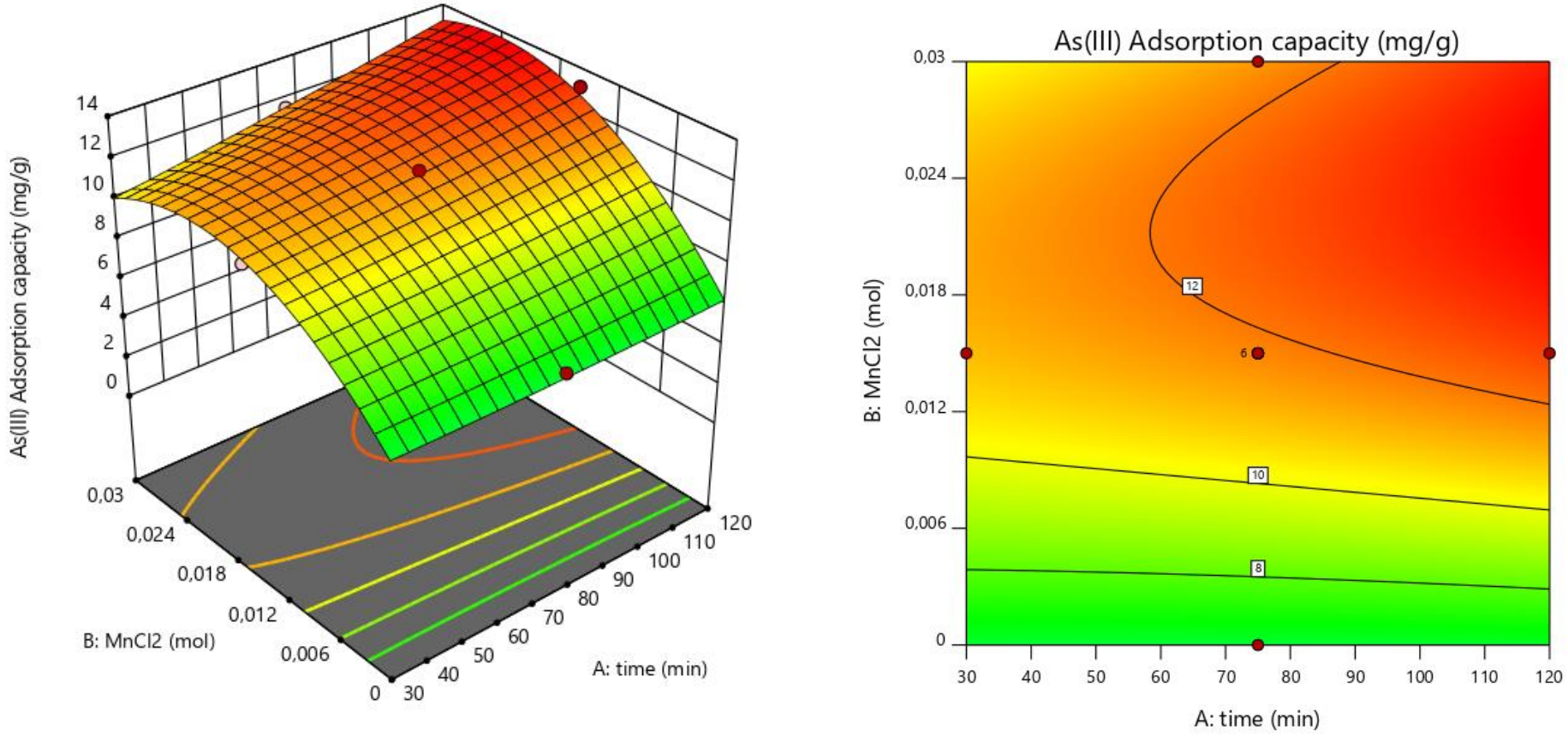

Fig 4.7a (i) 3D response surface and (ii) contour plot of effect of interaction between moles of $MnCl_2$ and co-precipitation time on As(III) adsorption capacity.

(i)

(ii)

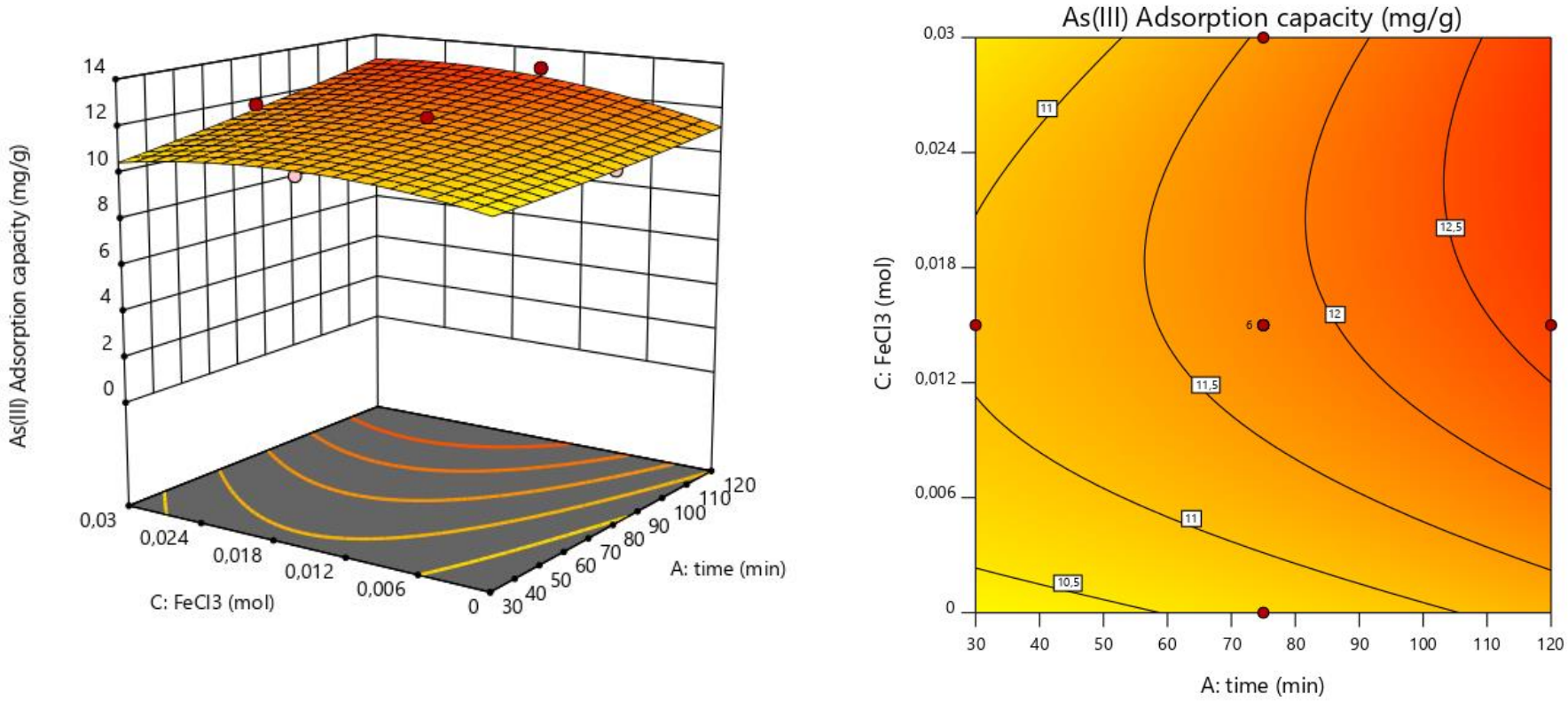

Fig 4.7b (i) 3D response surface and (ii) contour plot of effect of interaction between moles of $FeCl_3$ and co-precipitation time on As(III) adsorption capacity.

(i) (ii)

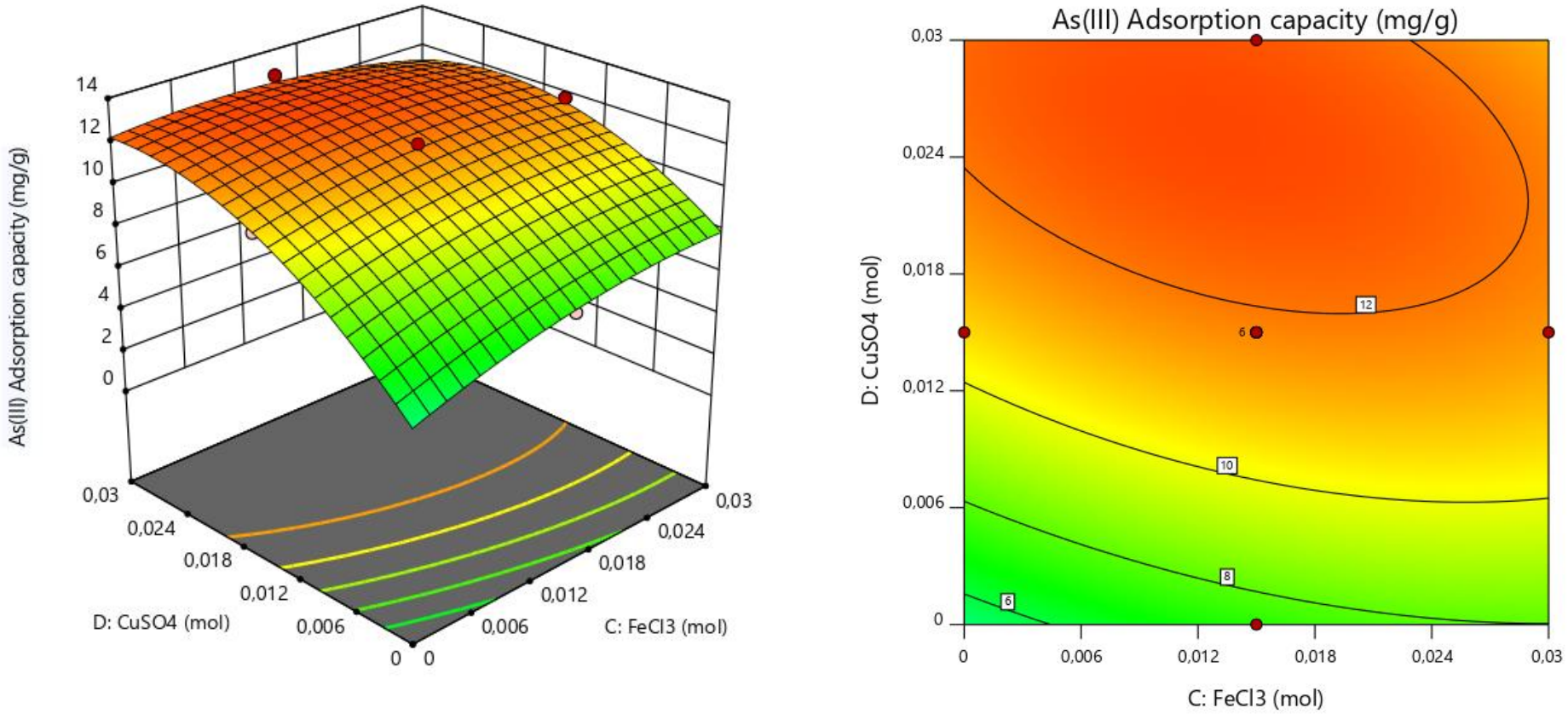

Fig 4.7c (i) 3D response surface and (ii) contour plot of effect of interaction between moles of $FeCl_3$ and moles of $CuSO_4$ on As(III) adsorption capacity.

4.2.2.4 *Effect of moles of $MnCl_2$, $FeCl_3$, $CuSO_4$ and co-precipitation time on concentration of As(V) left in solution after adsorption of As(III)*

The interaction between co-precipitation time-moles of $MnCl_2$ (AB), coprecipitation time-moles of $FeCl_3$ (AC), co-precipitation time-moles of $CuSO_4$ (AD), moles of $MnCl_2$–moles of $FeCl_3$ (BC), moles of $MnCl_2$-moles of $CuSO_4$ (BD) and moles of $FeCl_3$-moles of $CuSO_4$ (CD) showed the most significant influence on the concentration of As(V) left in solution after As(III) adsorption. The 3D response surface and contour plot on Fig 4.8a show the effect of the interaction between moles of $MnCl_2$ and co-precipitation time on As(V) left in solution when moles of $FeCl_3$ and moles of $CuSO_4$ were held constant. Fig 4.8b shows the 3D response surface and contour plot of the influence of the interaction between moles of $FeCl_3$ and co-precipitation time on As(V) left in solution when moles of $MnCl_2$ and moles of $CuSO_4$ were fixed. Fig 4.8c shows the 3D response surface and contour plot of the influence of the interaction between moles of $CuSO_4$ and co-precipitation time on As(V) left in solution when moles of $MnCl_2$ and moles of $FeCl_3$ were held constant. Fig 4.8d shows the 3D response surface and contour plot of the influence of the interaction between moles of $MnCl_2$ and moles of $FeCl_3$ on As(V) left in solution when moles of $MnCl_2$ and co-precipitation time were held constant. Fig 4.8e shows the 3D response surface and contour plot of the influence of the interaction between moles of $MnCl_2$ and moles of $CuSO_4$ on As(V) left in solution when moles of $FeCl_3$ and co-precipitation time were held constant. Fig 4.8f shows the 3D response surface and contour plot of the influence of the interaction between moles of $FeCl_3$ and moles of $CuSO_4$ on As(V) left in solution when moles of $MnCl_2$ and co-precipitation time were held constant.

The 3D response surface and contour plots on Fig 4.8a show that shorter co-precipitation time and reduction in moles of $MnCl_2$ favoured reduced amounts of concentration of As(V) left in solution after adsorption of As(III). The plots on Fig 4.8b show that an increase in co-precipitation time and increase in mole amounts of $FeCl_3$ decreased the concentration amount of As(V) left in solution. Fig 4.8c shows that longer co-precipitation time and increase in mole amounts of $CuSO_4$ reduced As(V) left in solution, while Fig 4.8d exhibited that an increase in mole amount of $FeCl_3$ and decrease in moles of $MnCl_2$ resulted in a decrease in concentration amount of As(V) left in solution. A reduction in As(V) left in solution is observed on Fig 4.8e due to a decrease in mole amounts of both $MnCl_2$ and $CuSO_4$. In Fig 4.8f, an increase in mole

amounts of $FeCl_3$ and decrease in mole amounts of $CuSO_4$ were noted to reduce As(III) left in solution.

The most significant term for the concentration amount of As(V) left in solution after the adsorption of As(III) was the antagonistic effect of moles of $MnCl_2$ and moles of $FeCl_3$. An increase in the mole amounts of $FeCl_3$ and the decrease in the mole amounts of $MnCl_2$ resulted in low concentration amounts of As(V) left in solution after the adsorption process.

(i) (ii)

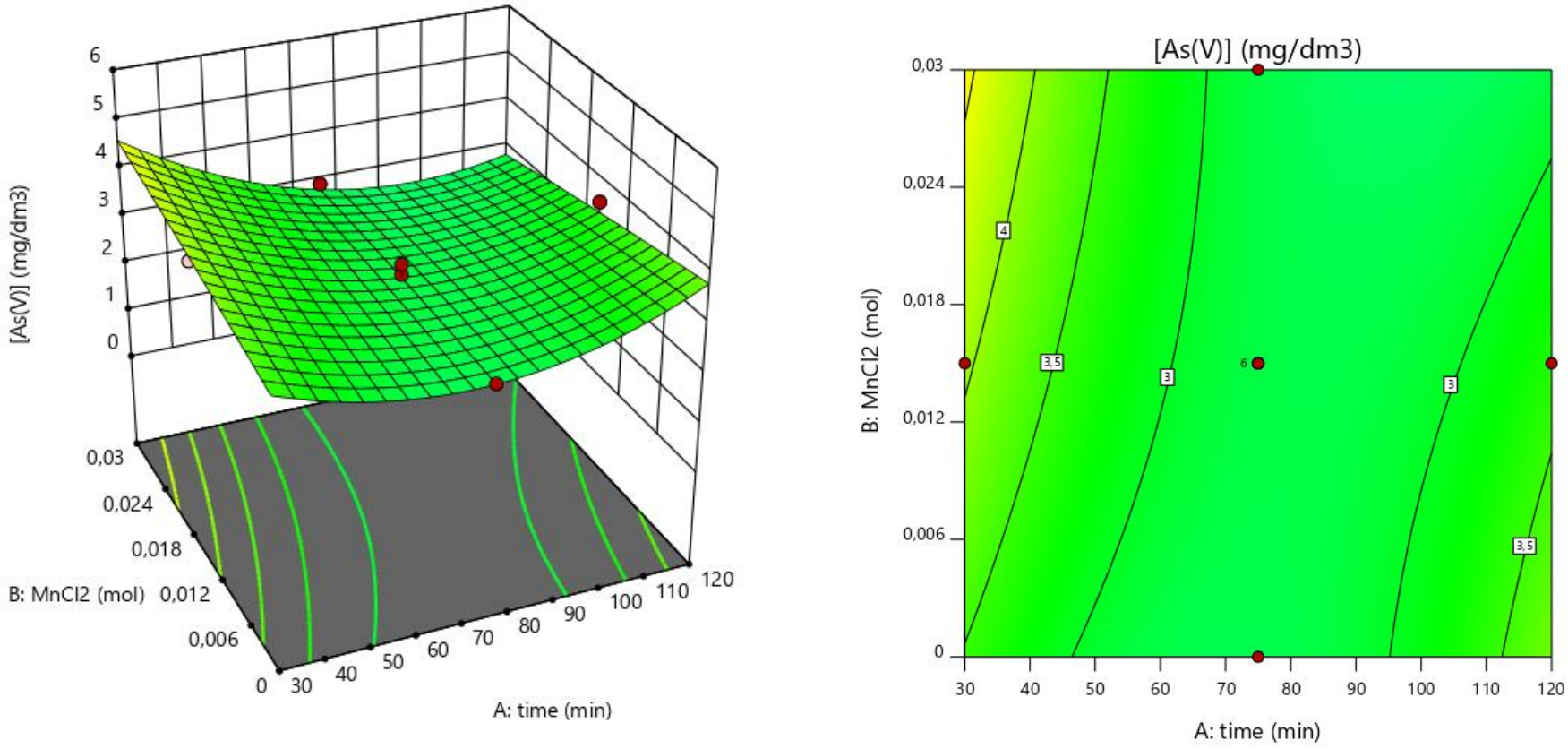

Fig 4.8a (i) 3D response surface and (ii) contour plot of effect of interaction between moles of $MnCl_2$ and co-precipitation time on [As(V)] in solution after As(III) adsorption.

(i) (ii)

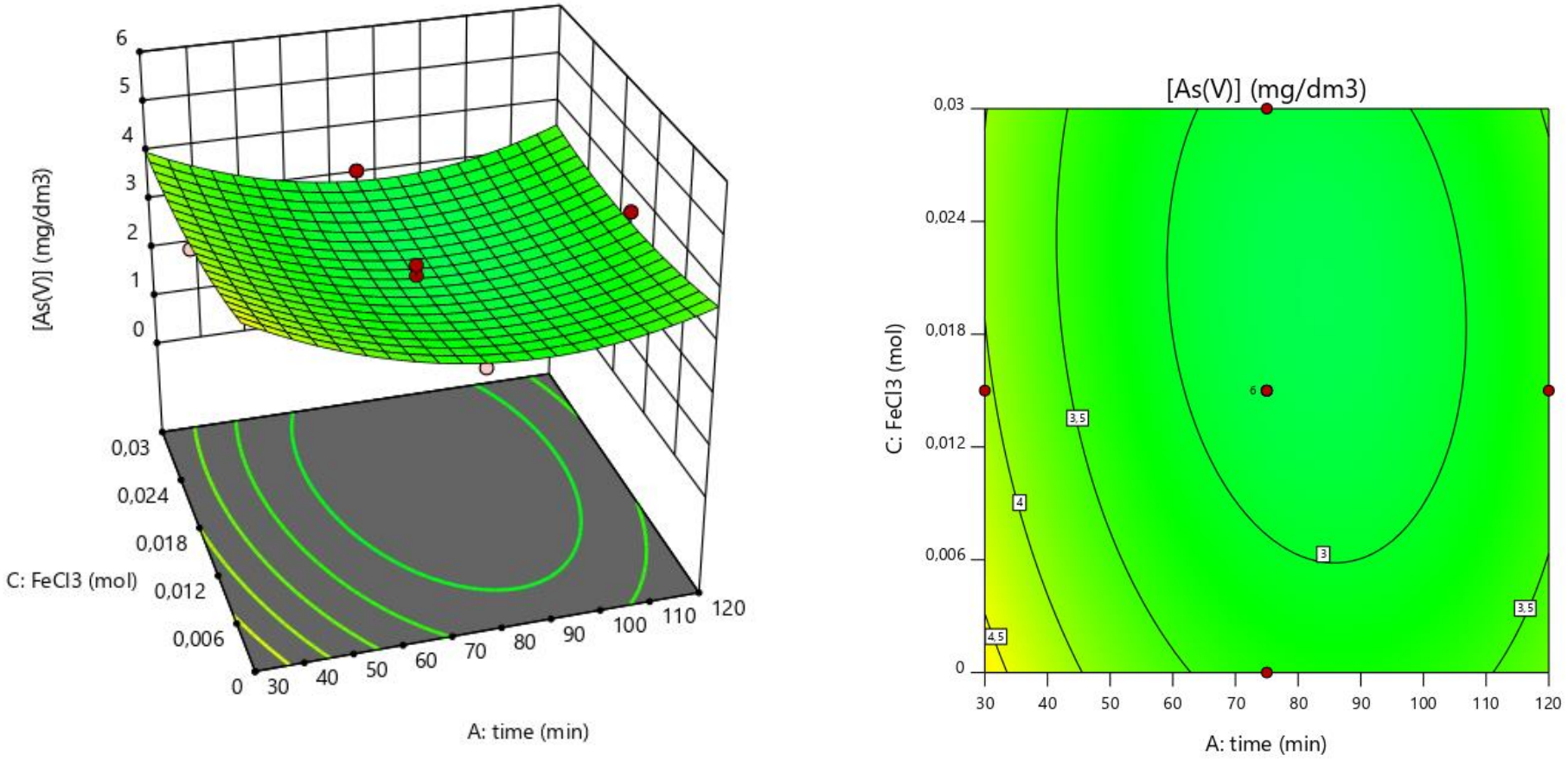

Fig 4.8b (i) 3D response surface and (ii) contour plot of effect of interaction between moles of $FeCl_3$ and co-precipitation time on [As(V)] in solution after As(III) adsorption.

(i)

(ii)

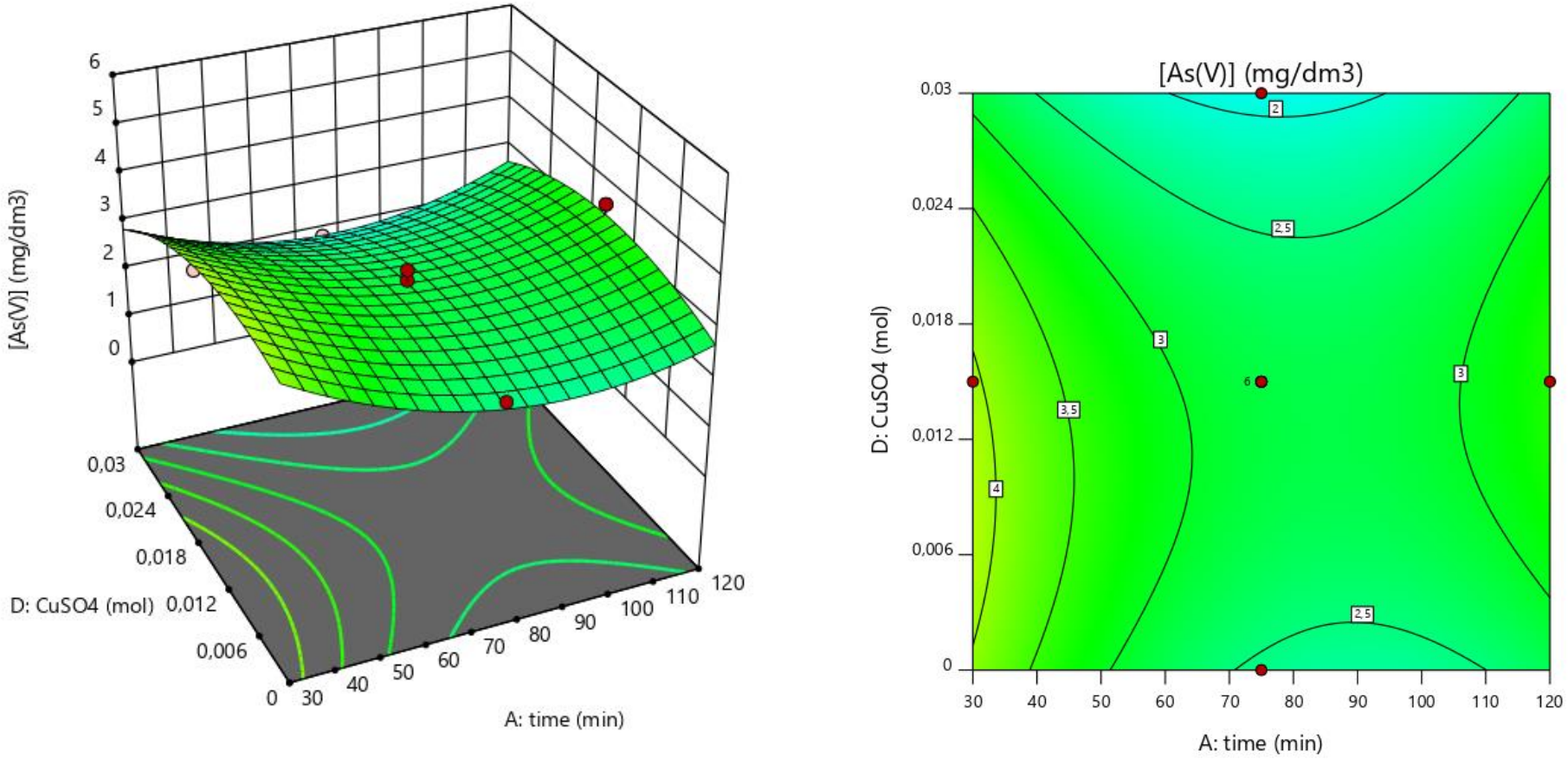

Fig 4.8c (i) 3D response surface and (ii) contour plot of effect of interaction between moles of $CuSO_4$ and co-precipitation time on [As(V)] in solution after As(III) adsorption.

(i) (ii)

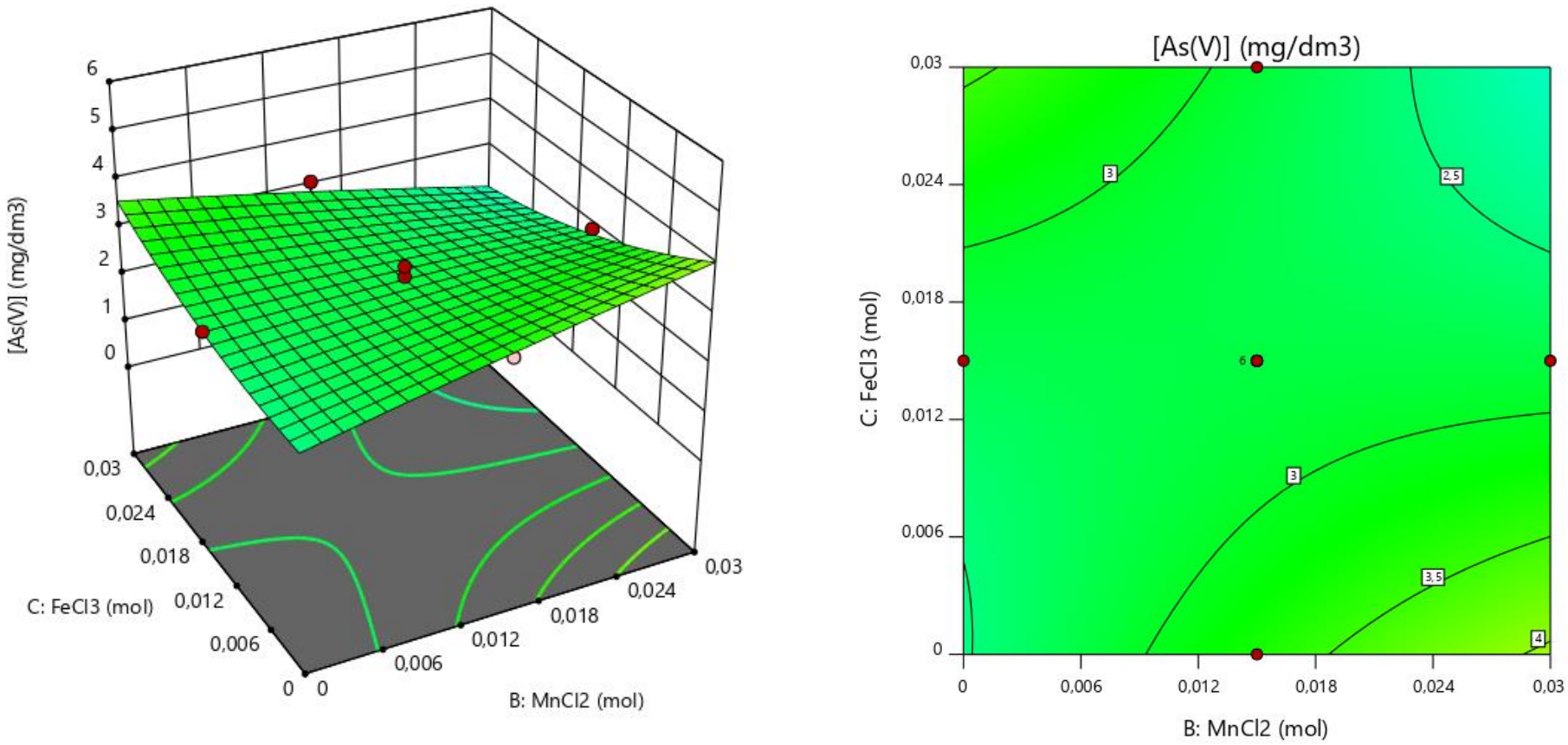

Fig 4.8d (i) 3D response surface and (ii) contour plot of effect of interaction between moles of $FeCl_3$ and moles of $MnCl_2$ on [As(V)] in solution after As(III) adsorption.

(i) (ii)

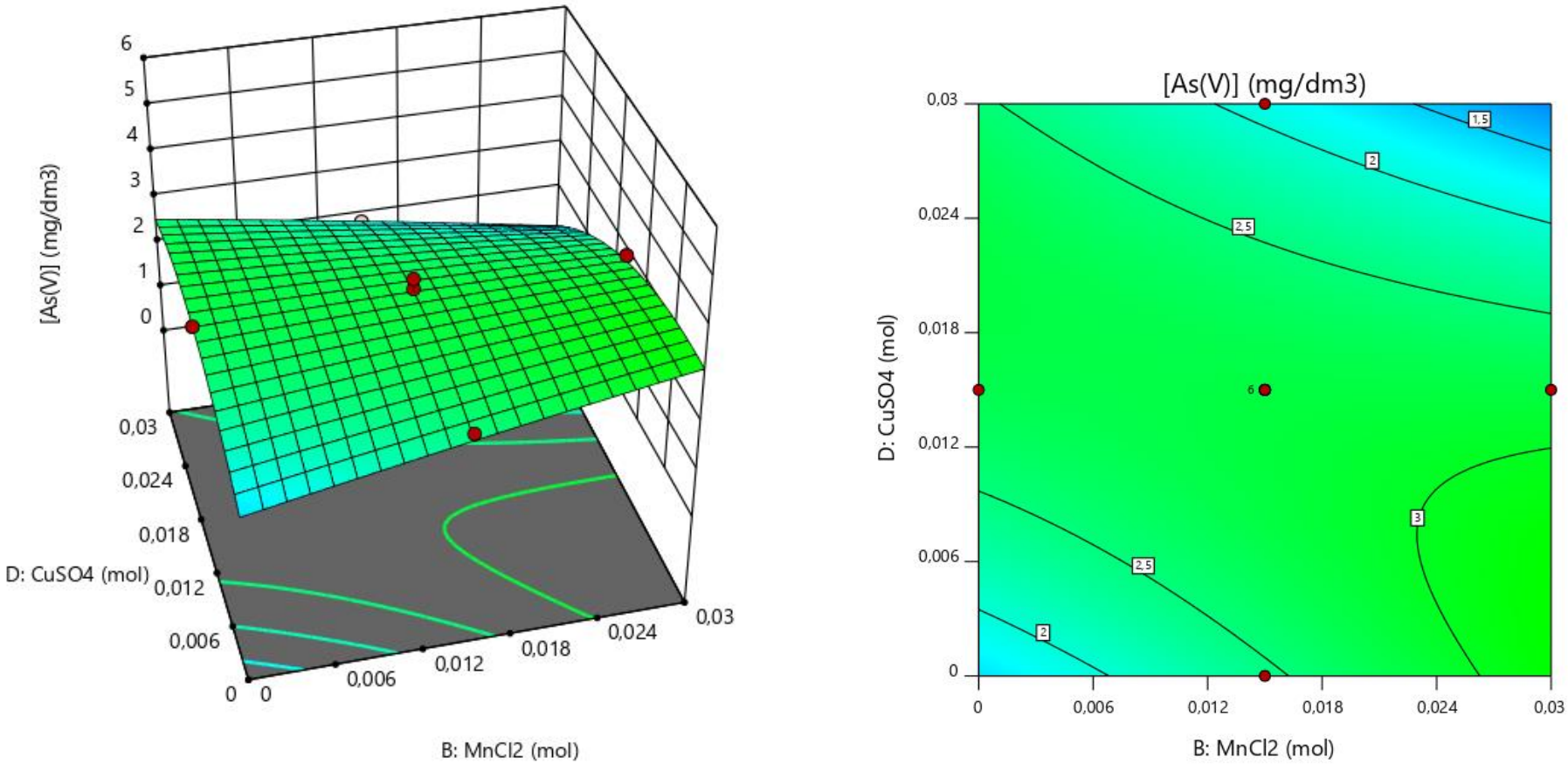

Fig 4.8e (i) 3D response surface and (ii) contour plot of effect of interaction between moles of $MnCl_2$ and moles of $CuSO_4$ on [As(V)] in solution after As(III) adsorption.

(i)

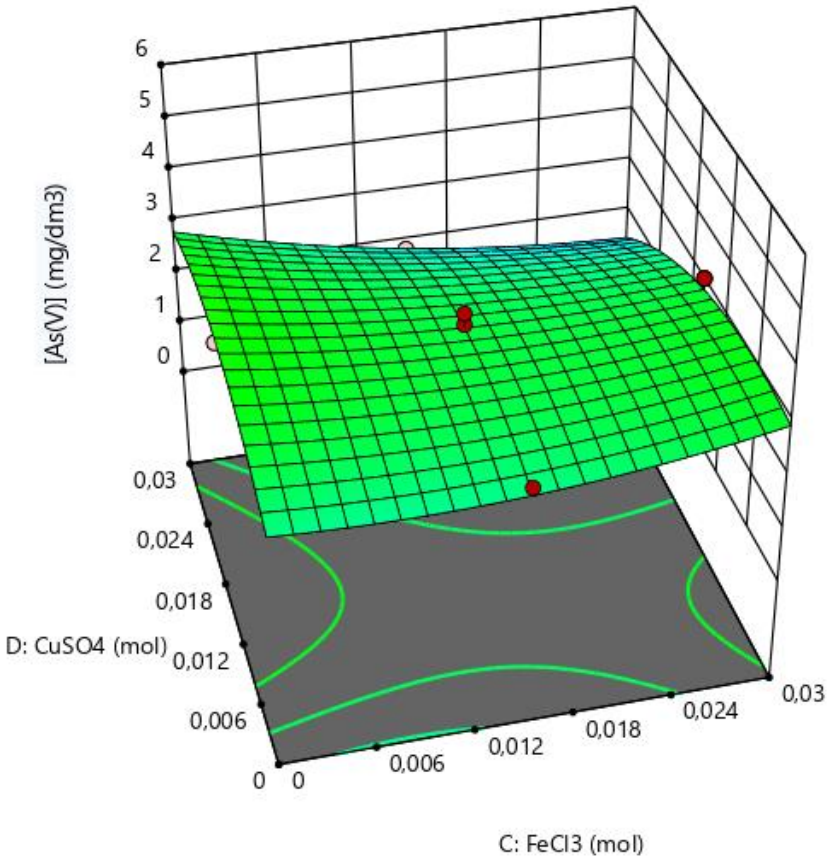

(ii)

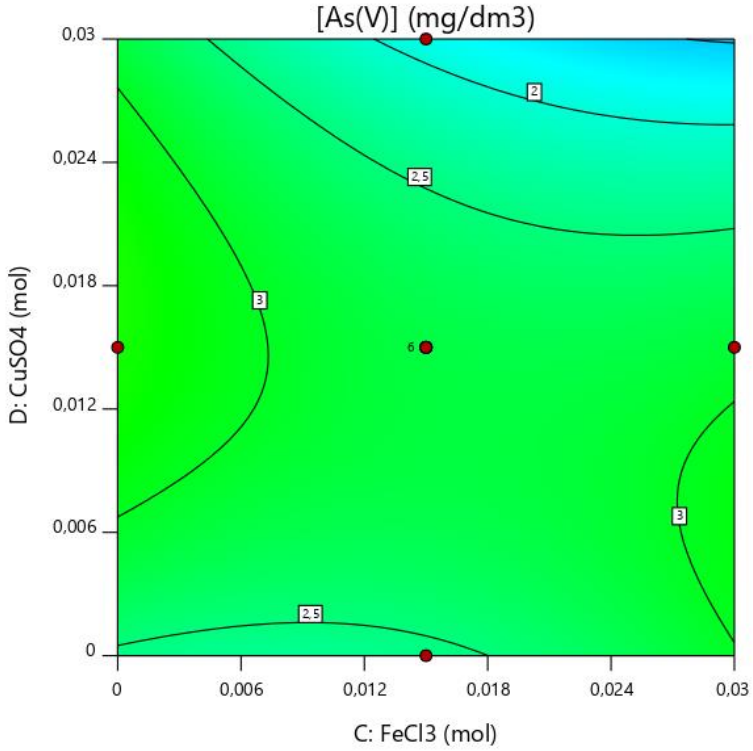

Fig 4.8f (i) 3D response surface and (ii) contour plot of effect of interaction between moles of $FeCl_3$ and moles of $CuSO_4$ on [As(V)] in solution after As(III) adsorption.

4.2.3 Optimum working conditions for the synthesis of the ternary MFC metal oxide composite

The optimum mole amounts of the $MnCl_2$, $FeCl_3.6H_2O$ and $CuSO_4.5H_2O$ salts and the co-precipitation time for the fabrication of the ternary MFC metal oxide nanocomposite adsorbent with high pollutant [As(III) and Cr(VI)] adsorption capacities and low solution concentrations of As(V) and Cr(III) after As(III) and Cr(VI) adsorption, respectively were determined from the response optimization plot and are presented on Table 4.4. The optimal working parameters were found to be a co-precipitation time of 58 mins, 0.028 moles of $MnCl_2$, 0.013 moles of $FeCl_3.6H_2O$ and 0.025 moles of $CuSO_4.5H_2O$. The derived responses were 41.472 mg/g Cr(VI) adsorption capacity, 2.037 mg/dm^3 of Cr(III) remaining in solution after Cr(VI) adsorption, 23.976 mg/g As(III) adsorption capacity and 3.579 mg/dm^3 As(V) left in solution after adsorption of As(III). The results gave a desirability score of 1.

Table 4.4 Optimum synthesis variables for the ternary MFC metal oxide composite.

Independent variables				Responses				
A:time (mins)	B:$MnCl_2$ (mol)	C:$FeCl_3.6H_2O$ (mol)	D:$CuSO_4.5H_2O$ (mol)	Cr(VI) adsorption capacity (mg/g)	[Cr(III)] (mg/dm^3)	As(III) adsorption capacity (mg/g)	[As(V)] (mg/dm^3)	Desirability score
58	0.028	0.013	0.025	41.472	2.037	23.976	3.579	1

4.3 SPECTROSCOPIC CHARACTERIZATION

4.3.1 MF binary metal oxide

4.3.1.1 *Fourier transform infrared (FTIR) spectroscopy*

The FTIR spectrum of nanostructured MF binary metal oxide is presented in Fig 4.9. The broad absorption band at 3342 cm^{-1} is characteristic of the stretching vibration of surface hydroxyl groups (Boujelben et al., 2009; Du et al., 2017). The absorption peak at 1619 cm^{-1} is due to the deformation of adsorbed H_2O molecules (Zhang et al., 2009). The peak at 1099 cm^{-1} is ascribed to bending vibration of the hydroxyl group of Mn-OH (Zhang et al., 2009; Du et al., 2017). The peak at 916 cm^{-1} represents δ- and γ-OH (in-plane and out-of-plane) bending modes of Fe-OH (Lakshmipathiraj et al., 2006). The peak at 508 cm^{-1} is responsible for Mn-O stretching modes of octahedral and tetrahedral sites (Du et al., 2014; Jiang et al., 2015; Islam et al., 2018). The peak at 427 cm^{-1} is characteristic of Fe-O stretching vibration (Liu et al., 2018) and bending modes of Fe-O (Trpkov et al., 2018). The low-frequency absorptions (400–1000 cm^{-1}) are generally due to metal-hydroxyl and metal-oxygen vibrations (Liu et al., 2012).

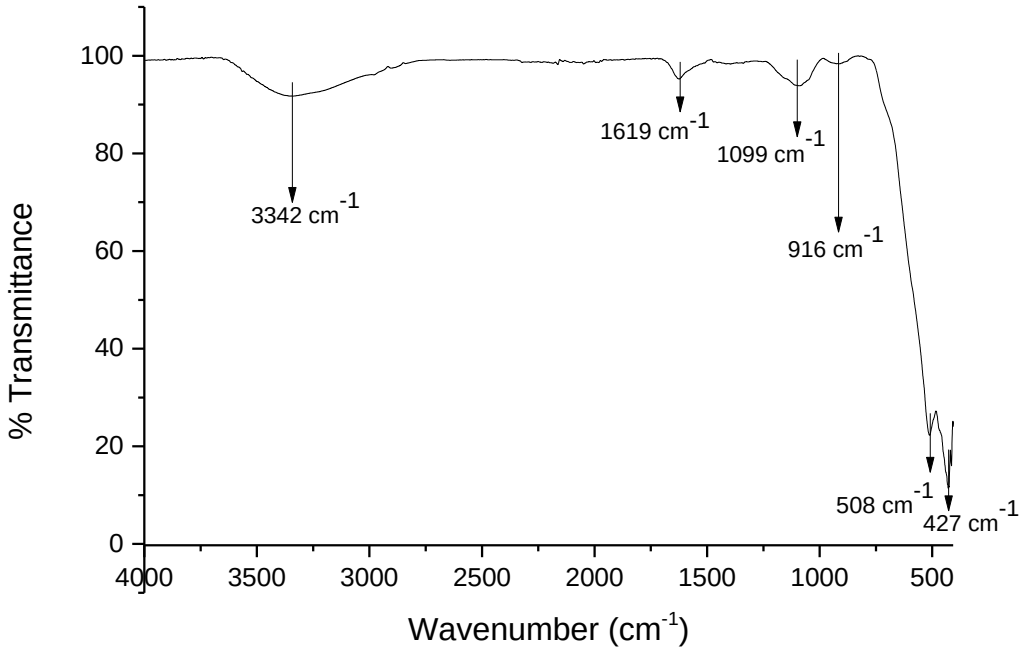

Fig 4.9 Fourier transform infrared spectrum of nanostructured binary MF metal oxide.

4.3.1.2 *Scanning electron microscopy (SEM)*

The SEM image in Fig 4.10a shows the surface morphology of MF binary metal oxide. The micrograph shows nanograins of different shapes and sizes. The oxide surface appears rough and has pores. The surface roughness indicates the availability of a large surface area (Roy et al., 2017). The porous nature can be attributed to the evolution of gases during drying in the vacuum oven (Yufanyi et al., 2015). The image is consistent with previous research (Zhang et al., 2007). Surface distribution of manganese, iron, and oxygen on the nanomaterial obtained from energy-dispersive X-ray spectroscopy (EDS) is presented in Fig 4.10b. It shows the elemental weight percent composition of the nanometal oxide to be: manganese 8.90, iron 50.58 and oxygen 40.42. The EDS analysis data is qualitative since it is representative of a minuscule portion of the nanomaterial. More information on the MF composite surface elemental distribution is shown by the elemental map in Fig 4.10c. The elemental map shows that the metal oxide particles are sparsely distributed and that the manganese and iron oxides are in different phases.

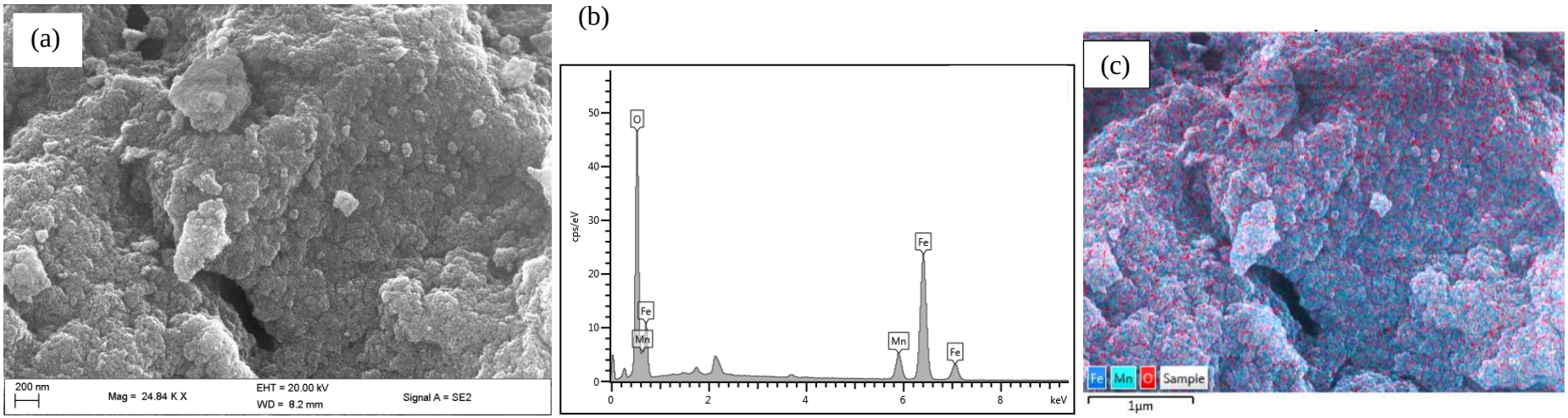

Fig 4.10 Surface analysis of nanostructured binary MF oxide: (a) scanning electron micrograph, (b) EDS data and (c) elemental map.

4.3.1.3 *Transmission electron microscopy (TEM)*

The TEM micrograph of MF oxide is shown in Fig 4.11a. It shows that the metal oxides are spherical, aggregated and homogenous in the composite. The micrograph is similar to that of calcined Mn-Fe surface (Shu et al., 2013). Image J software was used to determine the nanoparticle size distribution and the result is presented in Fig 4.11b. The nanoparticle sizes range from 0.2 to 1.2 nm with an average nanoparticle size of 0.62 ± 0.05 nm.

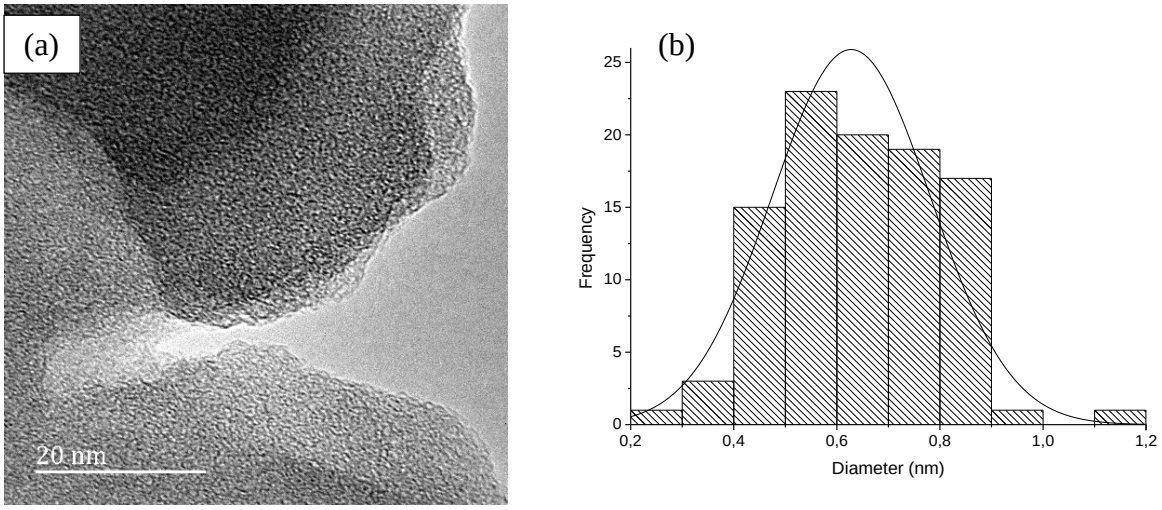

Fig 4.11 (a) TEM image and (b) particle size distribution of MF nanostructured metal oxide.

4.3.1.4 *X-ray photoelectron spectroscopy (XPS)*

The surface electronic states on the MF nanocomposite were determined using X-ray photoelectron spectroscopy. The XPS survey spectra of the MF metal oxide is presented in Fig 4.12a. It shows major peaks at 712, 642 and 529 eV characteristic of Fe 2p, Mn 2p and O 1s, respectively. The detailed X-ray photoelectron spectra of Fe 2p, Mn 2p and O 1s are shown on Figs 4.12b-d. The Fe 2p spectrum in Fig 4.12b showed major peaks characteristic of γ-Fe_2O_3 at 724.3 and 710.7 eV corresponding to Fe $2p_{1/2}$ and Fe $2p_{3/2}$, respectively (Yu et al., 2013; Ouma et al., 2018). The satellite peaks at 732.7 and 718.6 eV confirmed the presence of Fe(III) in the nanocomposite (Weilong & Xiaobo, 2013). Deconvolution of the Fe $2p_{3/2}$ photoelectron peak at 710.7eV gave two peaks characteristic of Fe(II) and Fe(III) with atomic concentrations of 37.51 and 62.49 %, respectively. The Mn 2p spectrum in Fig 4.12c showed major photoelectron peaks at 653.5 and 641.8 eV due to Mn $2p_{1/2}$ and Mn $2p_{3/2}$, respectively. The deconvolution of the Mn $2p_{3/2}$ peak resulted in two peaks at 642.1 and 641.6 eV characteristic

of the presence of Mn(III) and Mn(IV) at atomic concentrations of 60.11 and 39.89 %, respectively (Wang et al., 2012). The Mn $2p_{3/2}$ peak position for Mn(II) is noted around 639.75 eV, Mn(III) 641.38-641.69 eV and Mn(IV) at 642.00-642.23 eV (Nesbitt & Banerjee, 1998). The O 1s spectrum in Fig 4.12d showed a major peak at 529.7 eV. The Gaussian-Lorentz fit of the O 1s peak resulted in three peaks corresponding to the three different types of surface oxygen groups found in metal oxides. The oxygen species comprised of lattice oxygen (O^{2-}), hydroxide oxygen (OH^-) and oxygen in molecular H_2O (adsorbed or structural) with atomic concentrations of 60.02, 34.27 and 5.71 %, respectively. The binding energies of lattice O^{2-} are in the range 529.29-529.47 eV, hydroxide oxygen 530.91-530.99 eV and oxygen in molecular H_2O from 532.07-532.50 eV (Wang et al., 2012). The XPS results showed that the MF nanocomposite comprised of mixed metal hydr(oxides) of Fe(II), Fe(III), Mn(III) and Mn(IV). This corroborates with the analysis of infrared data which revealed the presence of surface hydroxyl groups on the nanocomposite.

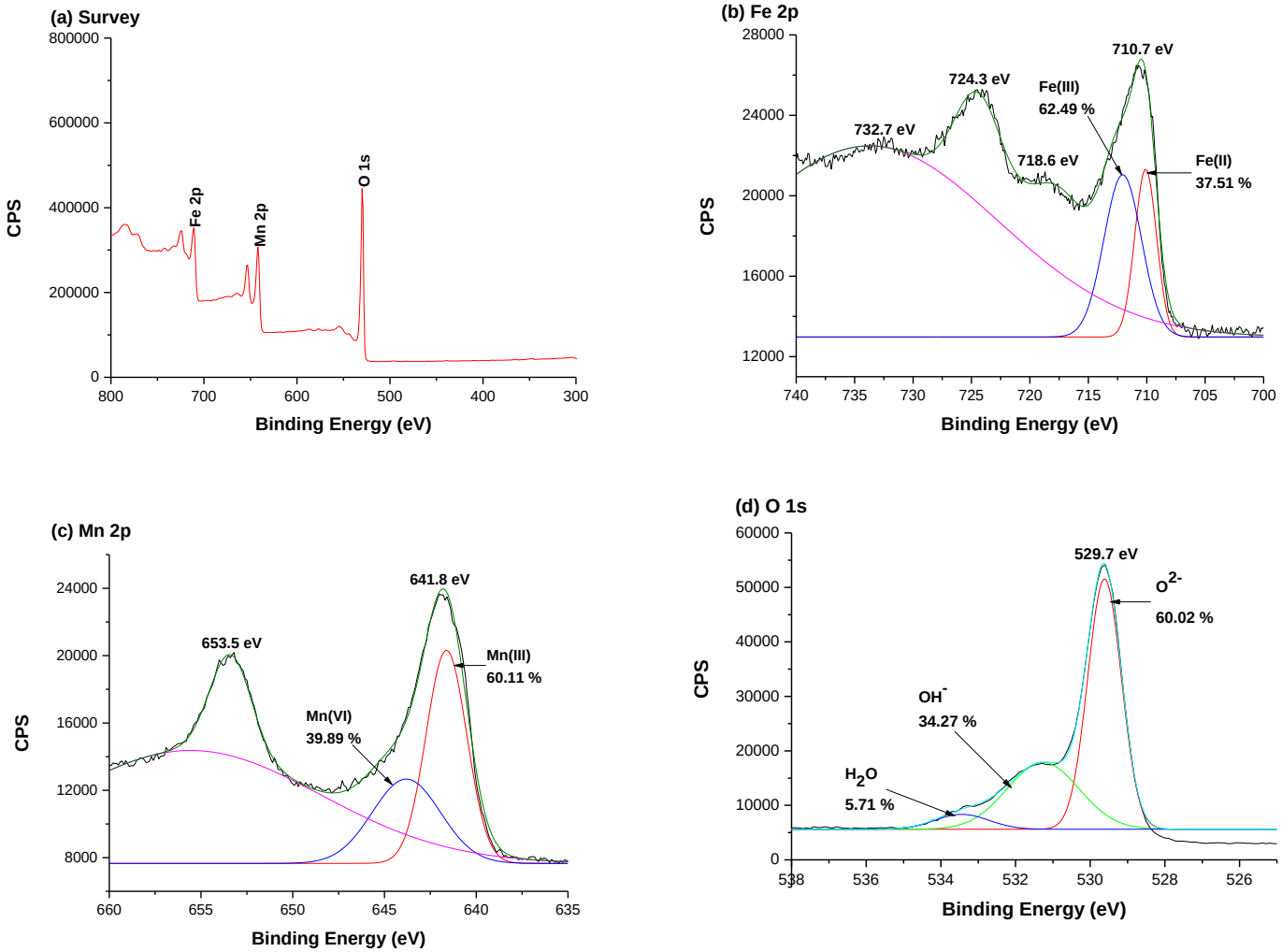

Fig 4.12 X-ray photoelectron spectra (a) MF low-resolution survey scan, and high-resolution detailed scans for (b) Fe 2p, (c) Mn 2p and (d) O 1s.

4.3.1.5 *X-ray diffraction (XRD) spectroscopy*

The X-ray diffraction micrograph of MF binary composite is shown in Fig 4.13. It shows that the composite is made up of a mixture of different species of Mn and Fe oxides. The binary oxide is composed of two Fe oxide and two Mn oxide phases. The iron oxide phases include wuestite (FeO) identified with JCPDS Card No. 01-074-1886 having peaks at 34, 43, and 60 º and haematite (α-Fe_2O_3) identified with JCPDS Card No. 33-0664 having peaks at 24, 33, 35, 42, 57, 62 and 72 º. The two identified Mn oxide phases were hausmannite (Mn_3O_4) identified with JCPDS Card No. 24-0734 having peaks at 37, 45 and 54 º and bixbyite-C (Mn_2O_3) identified with JCPDS Card No. 41-1442 having peaks at 18, 38, 48, 49, 64, 66, 71 and 76 º.

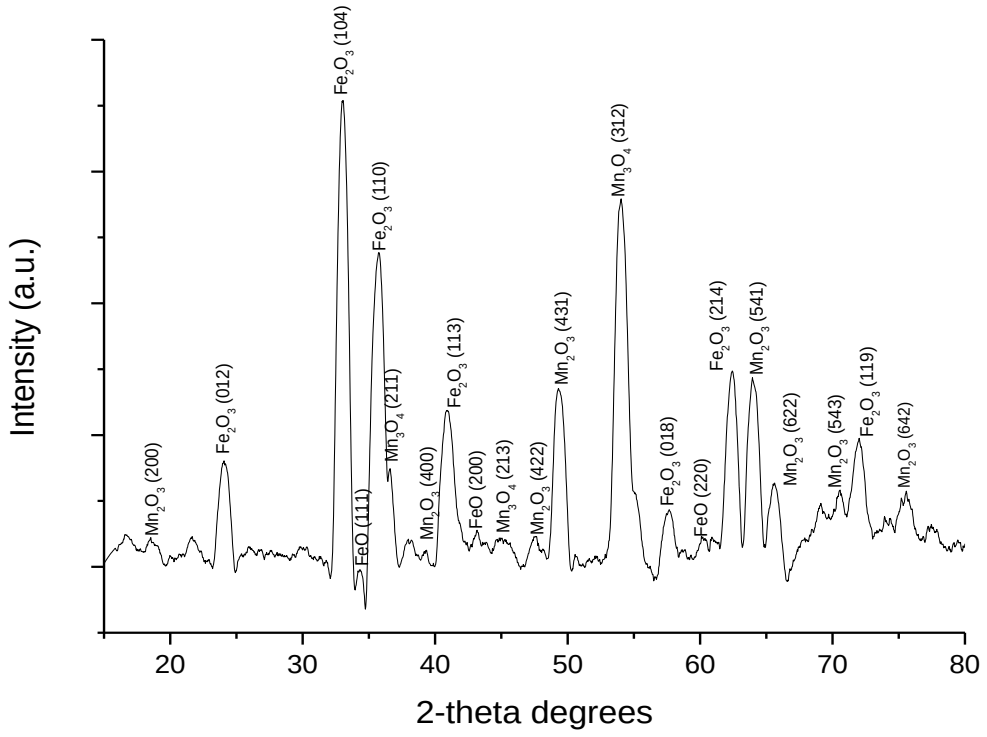

Fig 4.13 X-ray diffraction pattern of MF binary composite.

4.3.1.6 *Textural properties*

To elucidate the pore structure of the nanometal oxide, N_2 gas physisorption measurements were undertaken to determine BET surface area, pore volume and pore size. The BET surface area, pore volume and pore size of the MF nanometal oxide were determined to be 217.5228 m^2/g, 0.2832 cm^3/g and 4.3657 nm, respectively.

The N_2 adsorption/desorption isotherm for MF metal oxide is shown in Fig 4.14a. It shows a type IV isotherm (IUPAC classification) with an H2 type hysteresis loop at P/P_0 = 0.40 to 0.85 due to capillary condensation characteristic of mesoporous materials with narrow pore size distributions (Sing et al., 1985; Luo et al., 2003; Lou et al., 2017). The shapes of adsorption hysteresis loops are associated with pore structure. Mesopores are classified as pores exhibiting width diameters between 2 and 50 nm, with macropores being above 50 nm and micropores below 2 nm (Sing et al., 1985, Rouquerol et al., 1994). The pore size distribution for MF oxide is presented in Fig 4.14b and was determined using the Barrett-Joyna-Halenda (BJH) adsorption model (Barrett et al.,1951). The result shows the presence of pores in the mesoporous region, mainly in the range 2-8 nm.

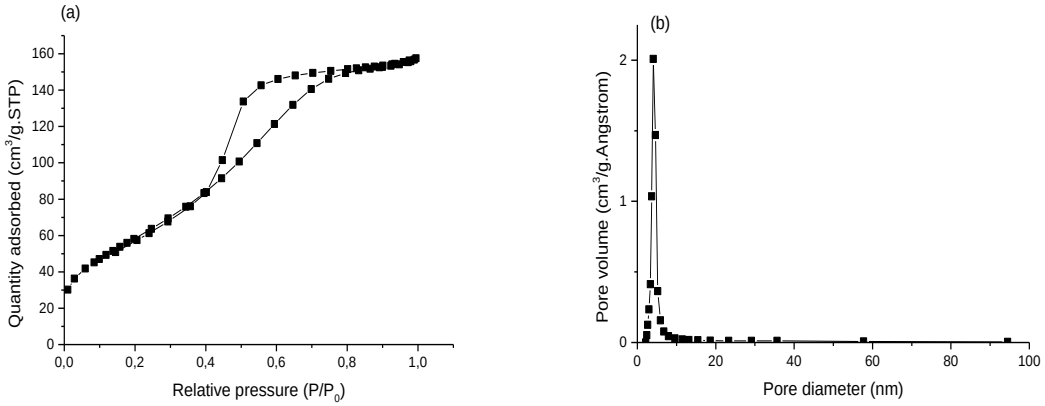

Fig 4.14 (a) N_2 adsorption/desorption isotherm and (b) pore size distribution for binary MF nanometal oxide.

4.3.1.7 *pH at point of zero charge (pH_{pzc})*

The pH at point of zero charge (pH_{pzc}) is the solution pH at which the adsorbent surface is neutral. The pH_{pzc} of the MF nanometal oxide determined using the pH drift method is presented in Fig 4.15. The result shows that MF oxide had a pH_{pzc} of 6.69. The presence of high manganese content in the composite oxide reduces the pH_{pzc}, whilst iron oxide increases the pH_{pzc}. This is attributed to the low pH_{pzc} of manganese oxides (pH_{pzc}=2-3) and the high pH_{pzc} of iron oxides (pH_{pzc}=7-9) (Zhang et al., 2012; Sousa & Teixeira, 2013; Lan et al., 2017). The adsorbent surface is negative when solution pH > pH_{pzc} and it is positive when solution pH < pH_{pzc}. The knowledge on an adsorbent surface charge is important as it informs of the type of interaction with the adsorbate during the adsorption process.

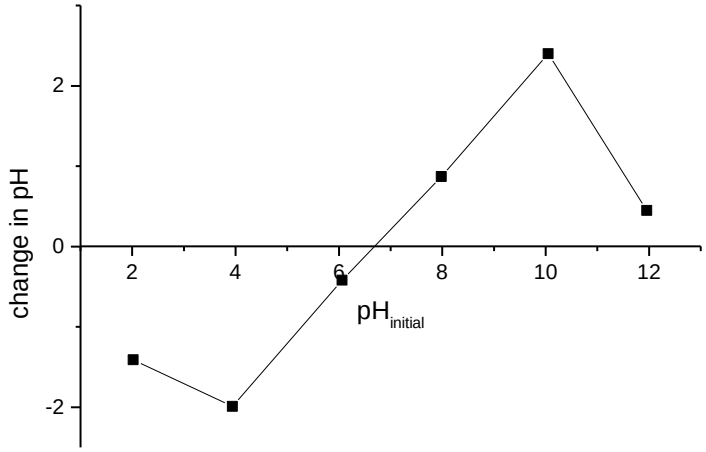

Fig 4.15 pH_{pzc} of nanometal composite oxide of MF.

4.3.2 MC binary metal oxide

4.3.2.1 *Fourier transform infrared (FTIR) spectroscopy*

The FTIR spectrum of nanostructured MC binary metal oxide is presented in Fig 4.16. The wide absorption band at 3179 cm^{-1} is ascribed to hydroxyl group vibrations. The absorption peak at 1660 cm^{-1} represents adsorbed H_2O vibrations (Lakshmipathiraj et al., 2006; Zhang et al., 2009; Du et al, 2017). The peaks at 1488 and 1090 cm^{-1} are ascribed to Mn-OH structural vibrations (Gupta et al., 2010; Du et al., 2015). The infrared absorption peaks at 825 cm^{-1} may be due to Mn-O-Mn stretching vibration (Wei et al., 2019). The absorption peak at 653 cm^{-1} can be due to Mn_2O_3 phase vibrations of the Mn-O bond (Morales et al., 2009). The band at 631 cm^{-1} is due to the stretching vibration of Cu-O (Ethiraj & King, 2012). The absorption band at 591 cm^{-1} is attributed to an overlap of Cu-O and Mn-O vibrations (Morales et al., 2009; Wang et al., 2013; Bozkurt et al., 2014, Mohan et al., 2015). The absorption peak at 448 cm^{-1} is due to Cu-O stretching vibration (Dar et al., 2008; Nogueira et al., 2016).

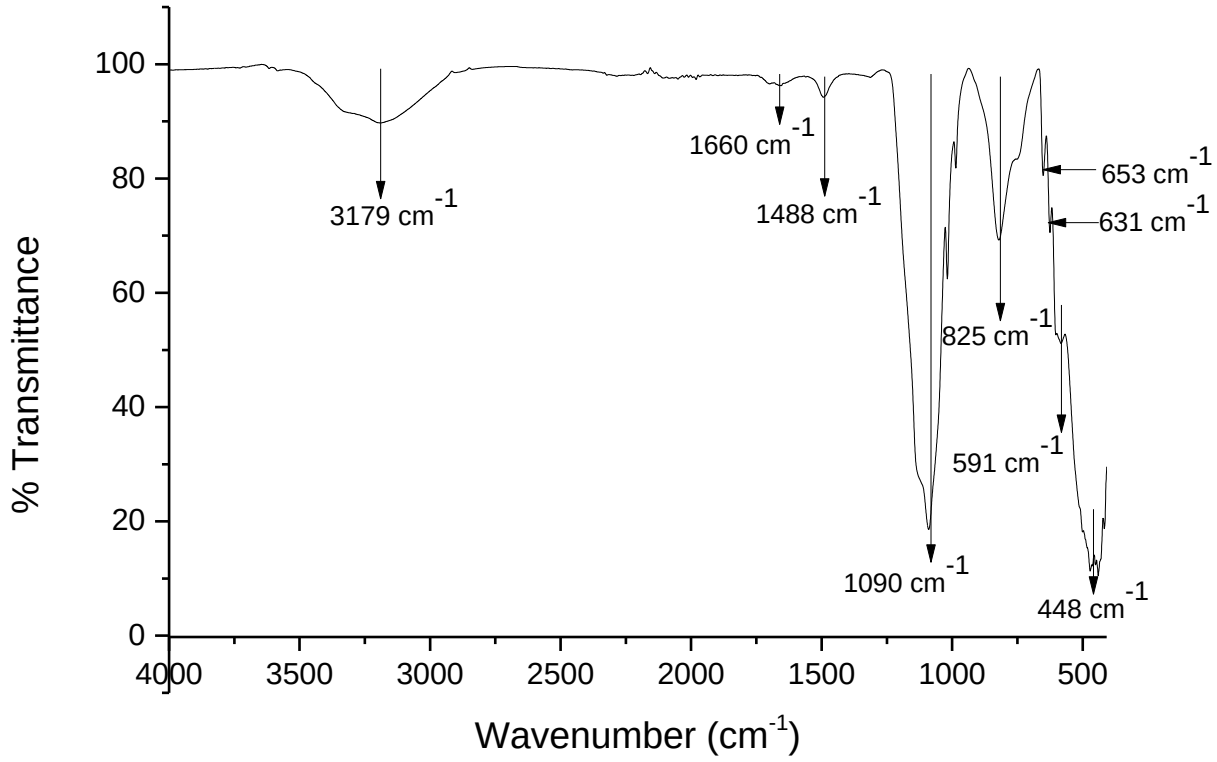

Fig 4.16 Fourier transform infrared spectrum of nanostructured binary MC metal oxide.

4.3.2.2 *Scanning electron microscopy (SEM)*

The scanning electron micrograph in Fig 4.17a shows the surface morphology of nanostructured MC oxide. It shows a rough surface with non-uniform shaped rod-like structures which appear clustered with pores in between them. The elemental surface distribution of MC metal oxide from EDS analysis is presented in Fig 4.17b. It shows the elemental weight percent composition of the nanometal oxide to be: manganese 4.31, copper 90.74 and oxygen 4.95. The elemental map of the MC metal oxide is shown in Fig 4.17c. The elemental map shows that the manganese, copper and oxygen particles are evenly distributed and that the manganese and copper oxides are in different phases.

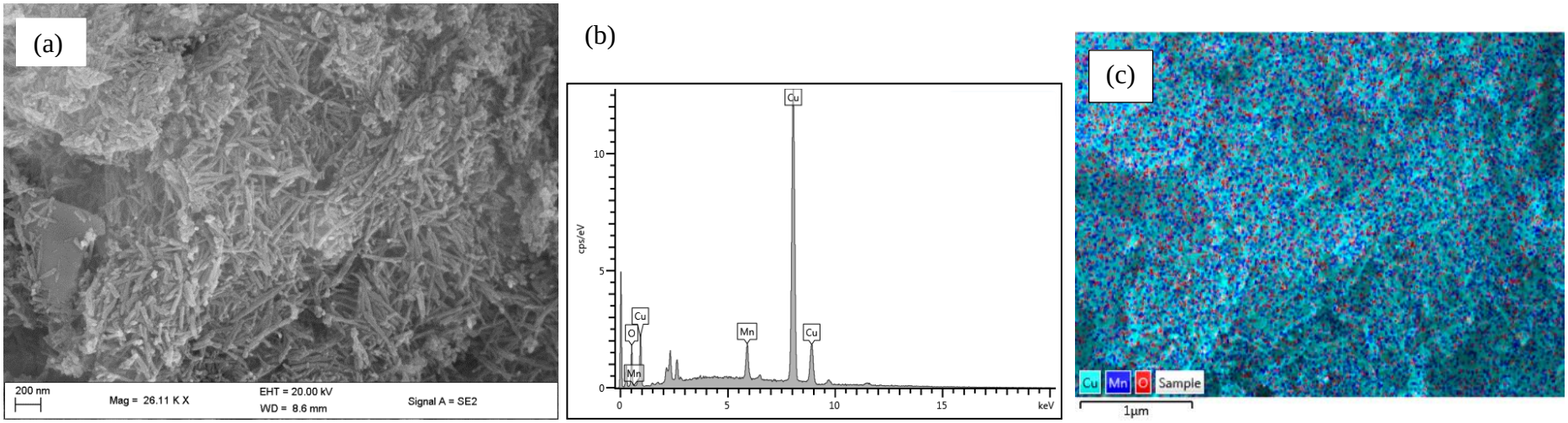

Fig 4.17 Surface analysis of nanostructured binary MC oxide: (a) scanning electron micrograph, (b) EDS data and (c) elemental map.

4.3.2.3 *X-ray diffraction (XRD) spectroscopy*

The X-ray diffraction pattern of MC binary oxide composite is presented in Fig 4.18. The XRD plot shows that the binary composite consists of separate Mn and Cu oxides crystallite phases. The binary oxide is composed of a single Cu oxide and two Mn oxide phases. The copper oxide phase is tenorite (CuO) identified with JCPDS Card No. 48-1548 having peaks at 32, 34, 37, 49, 53, 58, 61 and 68 º. The two identified Mn oxide phases were hausmannite (Mn_3O_4) identified with JCPDS Card No. 24-0734 having peaks at 17, 25, 36, 45, 52 and 73 º and bixbyite-C (Mn_2O_3) identified with JCPDS Card No. 41-1442 having peaks at 18, 22, 39, 40, 43, 47, 66 and 75 º.

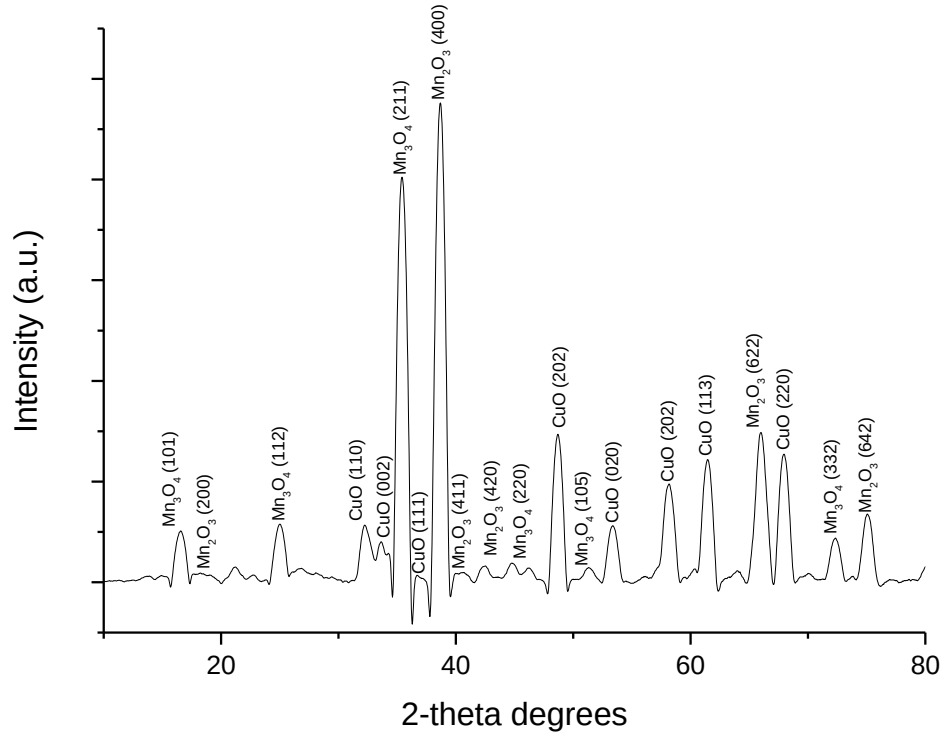

Fig 4.18 X-ray diffraction pattern of MC binary metal oxide composite.

4.3.2.4 *Transmission electron microscopy (TEM)*

The TEM image of MC oxide is shown in Fig 4.19a. It shows that the metal oxides are irregularly shaped, aggregated and in different phases in the composite. Image J software was used to determine the particle size distribution and the result is presented in Fig 4.19b. The particle sizes range from 0.2-0.9 nm with an average particle size of 0.60 ± 0.05 nm.

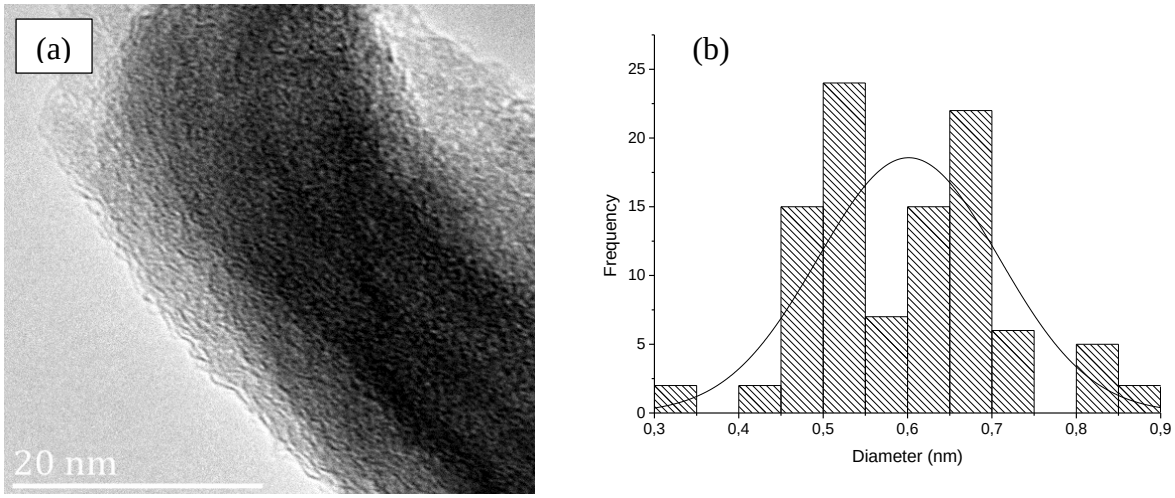

Fig 4.19 (a) TEM image and (b) particle size distribution of MC nanostructured metal oxide.

4.3.2.5 *X-ray photoelectron spectroscopy (XPS)*

The XPS survey spectra of the MC nanocomposite is presented in Fig 4.20a and it shows the major peaks at 935, 643 and 531 eV characteristic of Cu 2p, Mn 2p and O 1s, respectively. The detailed X-ray photoelectron spectra of Mn 2p, Cu 2p and O 1s are shown on Figs 4.20b-d. The Mn 2p spectrum in Fig 4.20b showed major peaks at 653.7 and 641.9 eV characteristic of Mn $2p_{1/2}$ and Mn $2p_{3/2}$, respectively. The spectra revealed a shake-up satellite signal at 649.3 eV which was ascribed to the presence of Mn(III) in the nanocomposite (Dong et al., 2014). The deconvolution of the Mn $2p_{3/2}$ photoelectron peak gave two peaks at 641.2 and 642.4 eV due to Mn(III) and Mn(IV) with atomic concentrations of 16.24 and 83.76 %, respectively (Nesbitt & Banarjee, 1998; Weilong & Xiaobo, 2013). The Cu 2p spectrum in Fig 4.20c showed Cu $2p_{3/2}$ and Cu $2p_{1/2}$ signals at 934.8 and 954.9 eV. The photoelectron peaks at 943.2 and 962.9 eV represent satellite peaks due to Cu $2p_{3/2}$ and Cu $2p_{1/2}$. The satellite signals are characteristic of the presence of Cu(II). The Cu $2p_{3/2}$ peak at 934.8 eV was deconvoluted using the Gaussian-Lorentz fit to give two peaks at 931.2 and 934.7 eV corresponding to the presence of Cu(I) and Cu(II) with atomic concentrations of 5.09 and 94.91 %, respectively (Dong et al., 2014). The O 1s spectrum in Fig 4.20d showed a major peak at 530.0 eV. The O 1s photoelectron peak was split into three peaks at 530.1, 531.7 and 533.5 eV representing O^{2-} (metal oxide-47.95 %), OH^- (surface oxygen-47.23 %) and O in adsorbed H_2O (4.82 %) (Wang et al., 2012). The XPS results showed that the MC nanocomposite metal oxide consisted of mixed metal hydr(oxides) of Cu(I), Cu(II), Mn(III) and Mn(IV).

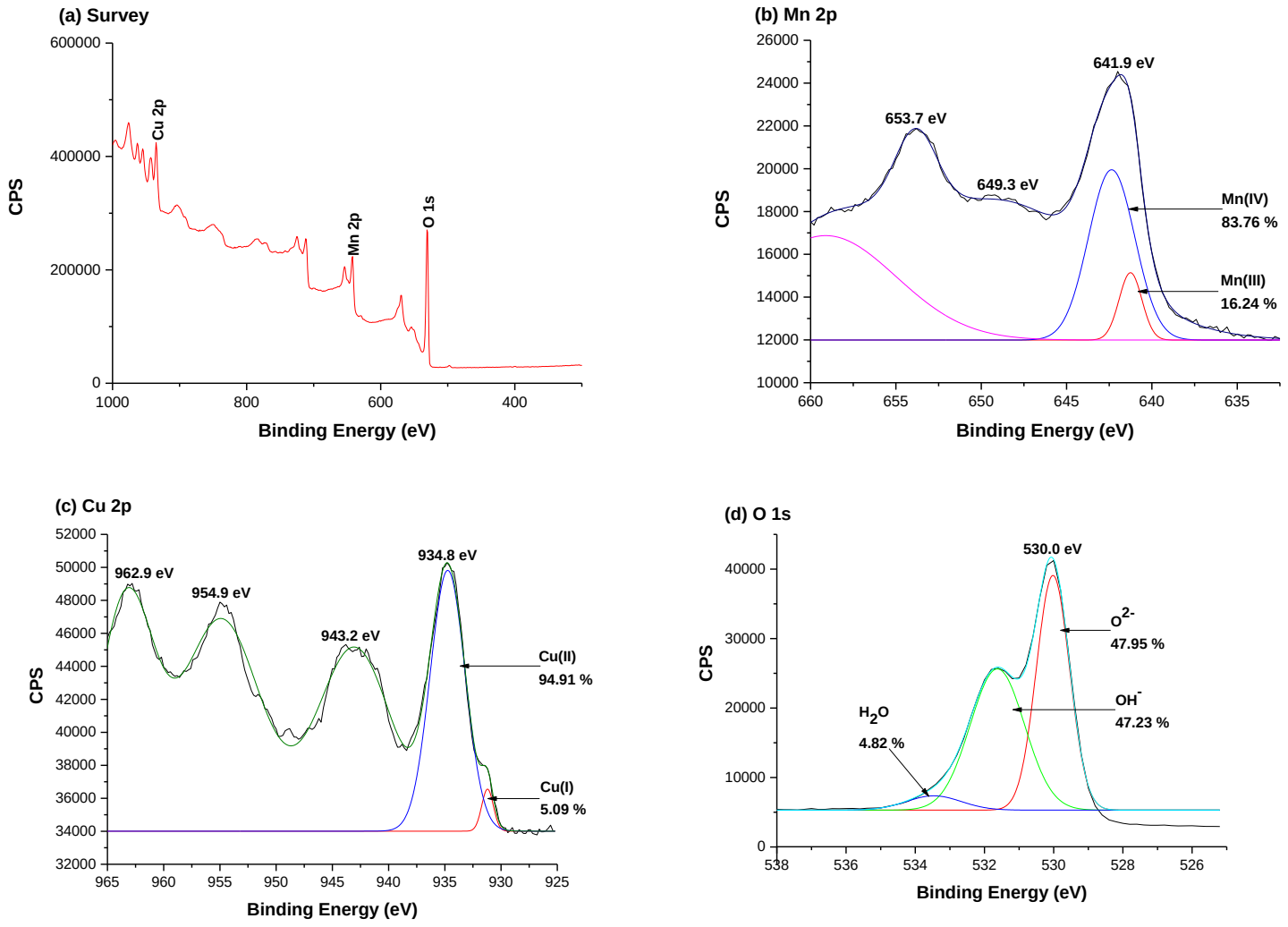

Fig 4.20 X-ray photoelectron spectra of binary MC metal oxide (a) low-resolution survey scan and high-resolution detailed scans (b) Mn 2p, (c) Cu 2p and (d) O 1s.

4.3.2.6 *Textural properties*

The BET surface area, pore volume and pore size of MC oxide were found to be 21.5550 m^2/g, 0.1267 cm^3/g and 27.3204 nm, respectively. According to IUPAC classification, the N_2 adsorption/desorption isotherm presented in Fig 4.21a shows a type II isotherm with an H3 type hysteresis loop at P/P_0 = 0.14 to 0.98 suggesting aggregation of the nanoparticles resulting in slit-shaped pores. The type II isotherm is characteristic of non-porous or macroporous adsorbents (Sing et al., 1985). The pore size distribution for MC oxide is presented in Fig 4.21b. The result shows the presence of pores in the mesoporous and macroporous region, in the range 5-120 nm.

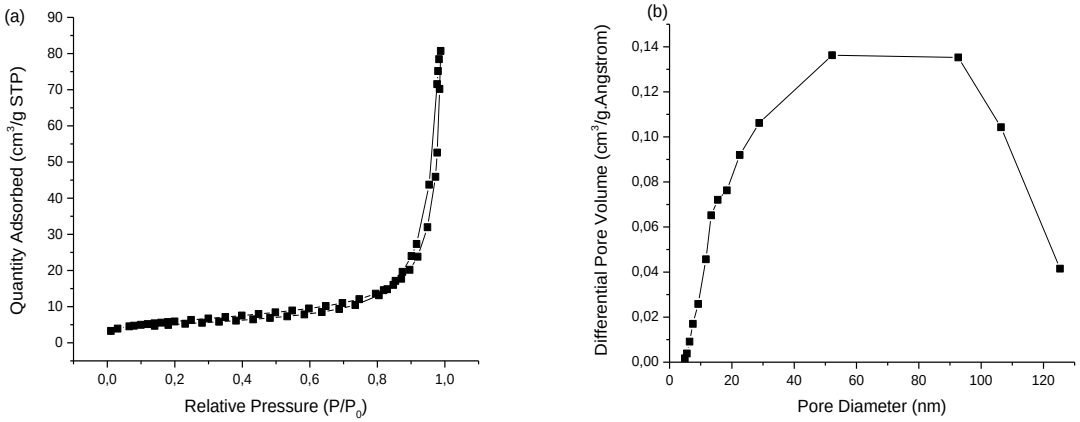

Fig 4.21 (a) N_2 adsorption-desorption isotherm and (b) pore size distribution of binary MC nanometal oxide.

4.3.2.7 *pH at point of zero charge (pHpzc)*

The pH_{pzc} of the MC nanometal oxide composite was determined from Fig 4.22 and found to be 6.82. The presence of manganese oxide in the composite oxide reduces the pH_{pzc}, whilst copper oxide increases the pH_{pzc}. This is attributed to the low pH_{pzc} of manganese oxides (pH_{pzc}=2-3) and the high pH_{pzc} of copper oxides (pH_{pzc}=9-10) (Zhang et al., 2012; Sousa & Teixeira, 2013; Lan et al., 2017).

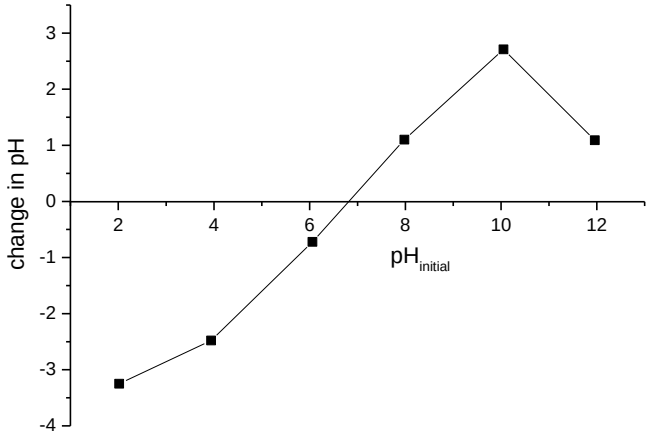

Fig 4.22 pH_{pzc} of nanometal composite oxide of MC.

4.3.3 MFC ternary metal oxide

4.3.3.1 *Fourier transform infrared (FTIR) spectroscopy*

The FTIR spectrum of the nanostructured MFC ternary metal oxide composite is presented in Fig 4.23. The broad absorption band at 3211 cm^{-1} is attributed to vibration of surface hydroxyl groups (Lakshmipathiraj et al., 2006; Zhang et al., 2009; Du et al, 2017). The absorption peak at 1665 cm^{-1} is ascribed to vibrations of adsorbed H_2O molecules (Zhang et al., 2009). The peak at 1086 cm^{-1} is due to Mn-OH vibration (Gupta et al., 2010; Du et al., 2017). The peaks at 986 and 811 cm^{-1} are attributed to Mn-O-Mn vibrations (Wei et al., 2019). The absorption peak at 733 cm^{-1} is assigned to Fe-O and Mn-O-Mn vibrations (Chen et al., 2011; Wei et al., 2019). The absorption at 526 cm^{-1} is assigned to an overlap of Mn-O and Cu-O stretching vibrations and the peak at 467 cm^{-1} is ascribed to the overlap of Fe-O and Cu-O stretching vibrations and bending modes (Morales et al., 2009; Wang et al., 2013; Bozkurt et al., 2014; Nogueira et al., 2016; Liu et al., 2018; Trpkov et al., 2018).

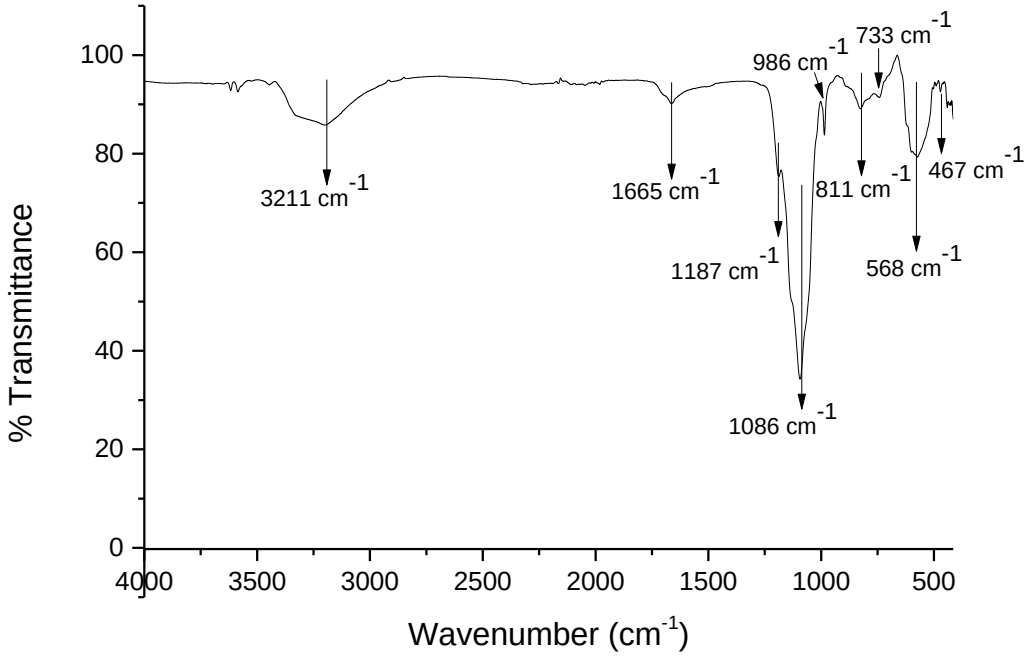

Fig 4.23 Fourier transform infrared spectrum of nanostructured ternary MFC metal oxide.

4.3.3.2 *Scanning electron microscopy (SEM)*

The SEM image in Fig 4.24a shows the surface morphology of MFC ternary metal oxide composite. The micrograph shows an aggregation of rod-like and spherical MFC nanograins of different sizes making the oxide surface appear rough and porous. The elemental surface distribution and elemental mapping of manganese, iron, copper and oxygen on the nanomaterial obtained from energy-dispersive X-ray spectroscopy (EDS) is presented on Figs 4.24b and c. The elemental weight percent composition of the nanometal oxide was found to be: manganese 2.36, iron 24.89, copper 58.45 and oxygen 14.30. The elemental map shows the uneven distribution of manganese, iron and copper on the metal oxide surface. The information from the elemental map suggests that the oxides of manganese, iron and copper are in different phases in the composite.

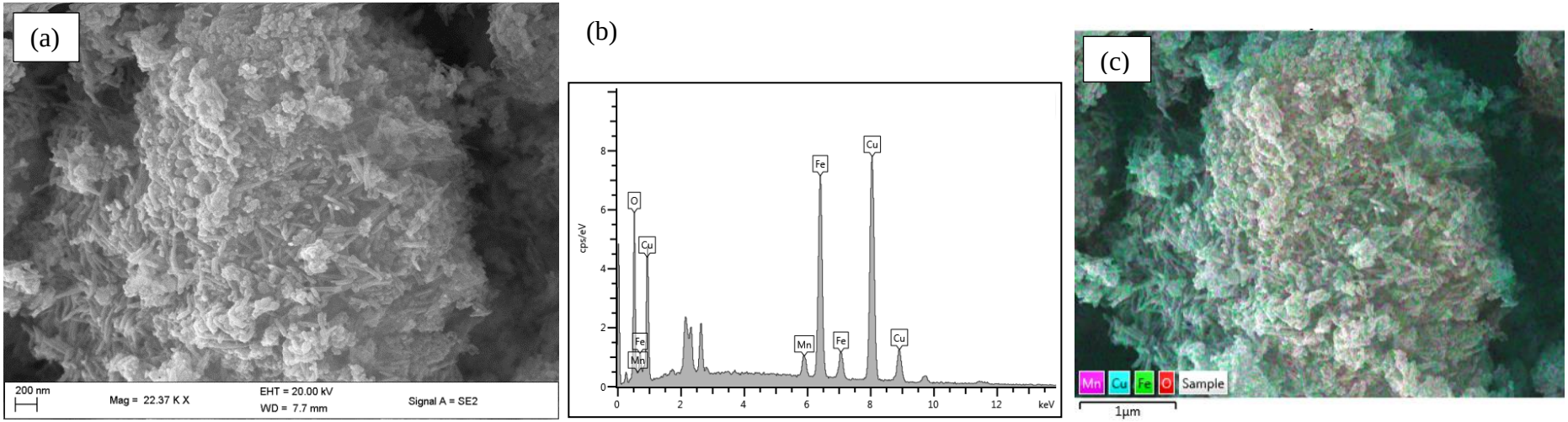

Fig 4.24 Surface analysis of nanostructured ternary MFC oxide: (a) SEM image, (b) EDS data and (c) elemental map.

4.3.3.3 *Transmission electron microscopy (TEM)*

The TEM image of MFC oxide is shown in Fig 4.25a. It shows that the metal oxides are aggregated and in different phases in the composite. Image J software was used to determine the particle size distribution and the result is presented in Fig 4.25b. The particle sizes range from 0.5 to 1.8 nm with an average particle size of 0.90 ± 0.05 nm.

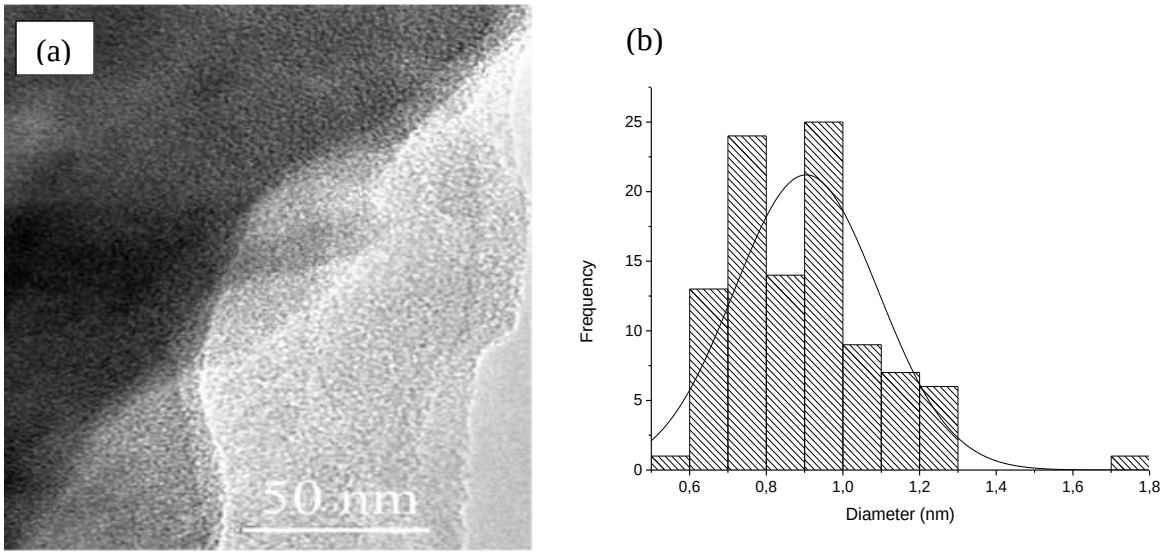

Figure 4.25 (a) TEM image and (b) particle size distribution of ternary MFC nanostructured metal oxide.

4.3.3.4 *X-ray photoelectron spectroscopy (XPS)*

The X-ray photoelectron survey spectra of the MFC nanocomposite is presented in Fig 4.26a and it shows the major peaks at 954, 712, 642 and 531 eV characteristic of Cu 2p, Fe 2p, Mn 2p and O 1s, respectively. The detailed X-ray photoelectron spectra of Mn 2p, Fe 2p, Cu 2p and O 1s are shown on Figs 4.26b-e. The Mn 2p spectrum in Fig 4.26b showed major peaks at 653.7 and 641.9 eV characteristic of Mn $2p_{1/2}$ and Mn $2p_{3/2}$, respectively. The spectra revealed a shake-up satellite signal at 648.8 eV due to Mn(III) present in the nanocomposite. The shake-up signals emanate from the interaction between an ejected photoelectron and a valence electron. The ejected photoelectron excites or shakes-up the valence electron to a higher energy level reducing the kinetic energy of the core electron but increasing its binding energy resulting in a satellite peak (Watts & Wolstenholme, 2003). Multiplet splitting of the Mn $2p_{3/2}$ photoelectron peak gave two peaks at 641.1 and 642.3 eV due to Mn(III) and Mn(IV) with atomic concentrations of 17.56 and 82.44 %, respectively (Weilong & Xiaobo, 2013). The Fe

2p spectrum in Fig 4.26c showed major peaks characteristic of γ-Fe_2O_3 at 724.7 and 711.0 eV corresponding to Fe $2p_{1/2}$ and Fe $2p_{3/2}$, respectively (Ouma et al., 2018). The satellite peaks at 734.5 and 719.3 eV further confirmed the presence of Fe(III) in the nanocomposite (Weilong & Xiaobo, 2013). Use of the Gauss-Lorentz distribution to fit the multiplet Fe $2p_{3/2}$ peak at 711.0 eV gave two peaks at 710.5 and 712.9 eV characteristic of Fe(II) and Fe(III) with atomic concentrations of 36.43 and 63.57 %, respectively. The Cu 2p spectrum in Fig 4.26d showed Cu $2p_{3/2}$ and Cu $2p_{1/2}$ signals at 934.8 and 954.9 eV with satellite peaks at 943.3 and 962.9 eV, respectively. The photoelectron satellite signals due to Cu $2p_{3/2}$ and Cu $2p_{1/2}$ revealed the presence of Cu(II) in the nanocomposite metal oxide with a d^9 configuration in the ground state (Biesinger et al., 2010; de Godoi et al., 2013). The Cu $2p_{3/2}$ peak at 934.8 eV was deconvoluted using the Gaussian-Lorentzian distribution and yielded two peaks at 930.9 and 934.7 eV corresponding to the presence of Cu(I) and Cu(II) with atomic concentrations of 3.49 and 96.51 %, respectively (Dong et al., 2014). The O 1s spectrum in Fig 4.26e showed a major peak at 530.1 eV. The O 1s photoelectron peak was split into three peaks at 529.9, 531.5 and 533.5 eV representing O^{2-} (46.96 %), OH^- (47.58 %) and O in adsorbed H_2O (5.46 %) (Wang et al., 2012). The XPS results showed that the MFC nanocomposite metal oxide consisted of mixed metal hydr(oxides) of Mn(III), Mn(IV), Fe(II), Fe(III), Cu(I) and Cu(II).

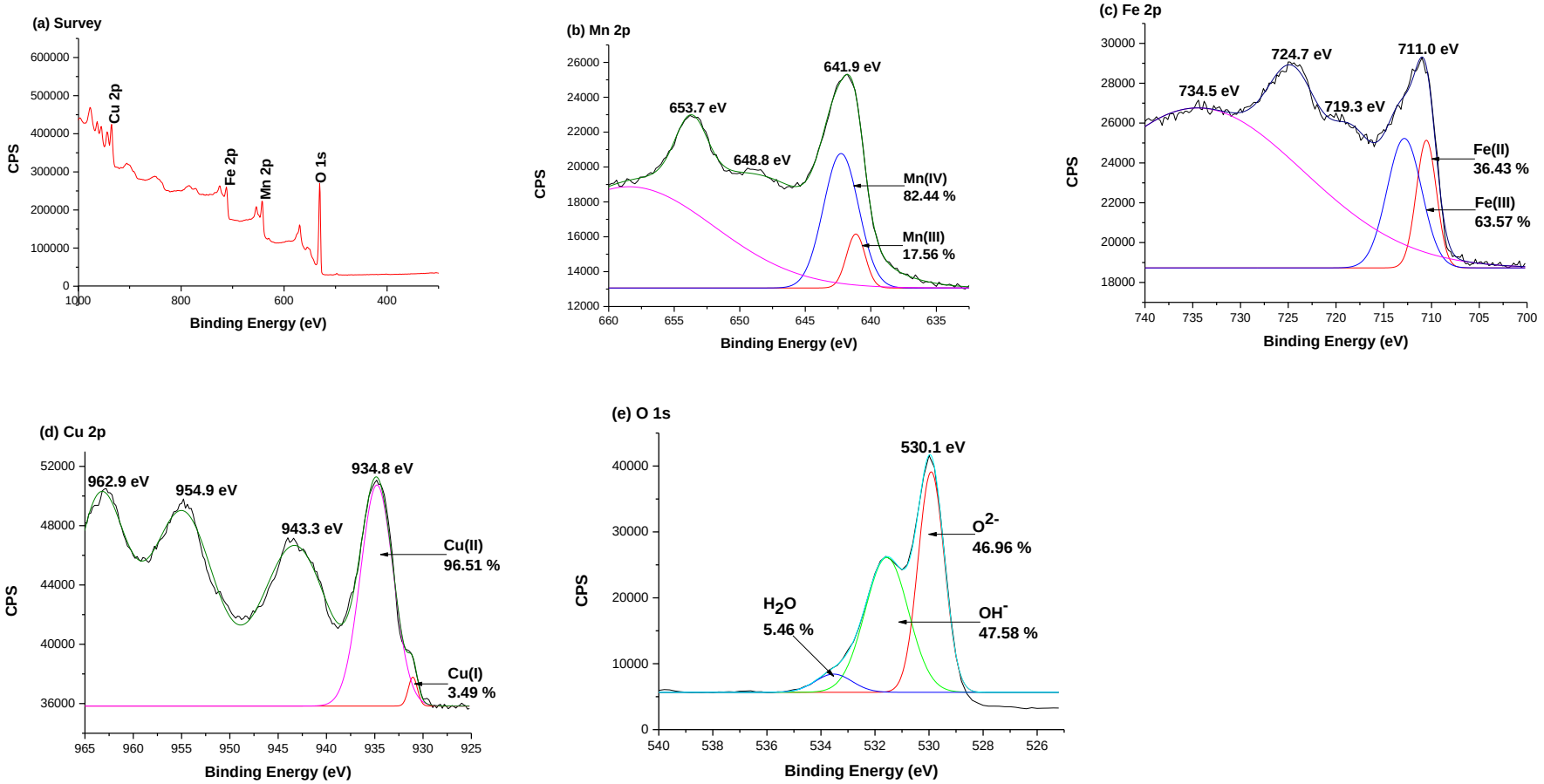

Fig 4.26 X-ray photoelectron spectra of MFC nanocomposite (a) low-resolution survey scan and high-resolution detailed scans for (b) Mn 2p, (c) Fe 2p, (d) Cu 2p and (e) O 1s.

4.3.3.5 *Textural properties*

The BET surface area, pore volume and pore size of MFC oxide composite were found to be 77.2427 m^2/g, 0.2409 cm^3/g and 14.7560 nm, respectively. The N_2 adsorption/desorption isotherm of the oxide is presented on Fig 4.27a and shows a type II isotherm with an H3 type hysteresis loop at P/P_0 = 0.15 to 0.98. The H3 hysteresis loop signifies the presence of slit-shaped pores (Sing et al., 1985). The type II isotherm is characteristic of non-porous or macroporous adsorbents. The pore size distribution of MFC nanometal oxide is shown on Fig 4.27b. The figure shows a very broad distribution of pore sizes in the mesoporous and macroporous regions, in the range 1.5-125 nm.

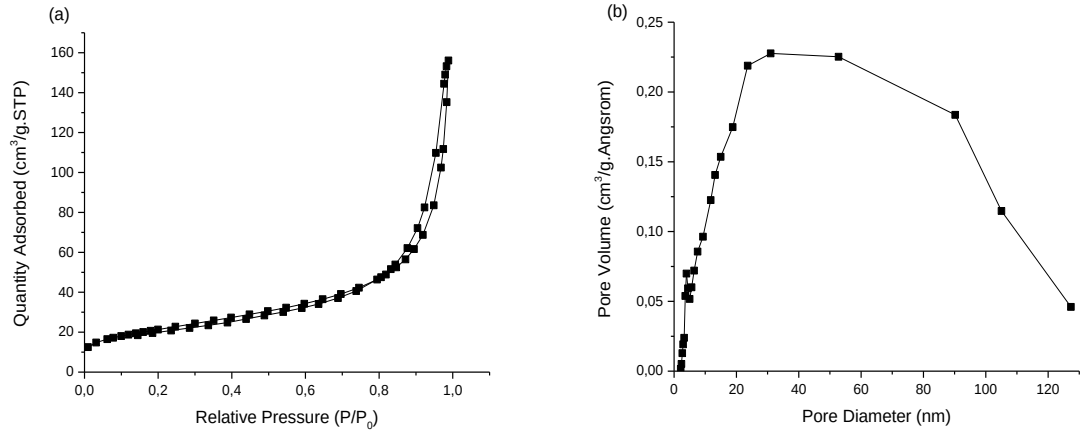

Fig 4.27 (a) N_2 adsorption-desorption isotherm and (b) pore size distribution of nanostructured ternary MFC metal oxide.

4.3.3.6 *X-ray diffraction (XRD) spectroscopy*

The X-ray diffraction pattern of MFC ternary composite is shown in Fig 4.28. It shows that the composite is made up of a mixture of different species of Mn, Fe and Cu oxides. The ternary oxide is composed of a single Fe oxide, a single Cu oxide and two Mn oxide phases. The iron oxide phase is haematite (α-Fe_2O_3) identified with JCPDS Card No. 33-0664 having peaks at 25, 36, 49, 63, 64 and 72 º. The copper oxide phase present is tenorite identified with JCPDS Card No. 48-1548 having peaks at 33, 37, 54, 58, and 68 º. The two identified Mn oxide phases were hausmannite (Mn_3O_4) identified with JCPDS Card No. 24-0734 having peaks at 17 and 30 º and bixbyite-C (Mn_2O_3) identified with JCPDS Card No. 41-1442 having peaks at 18, 39, 41, 43, 66 and 75 º.

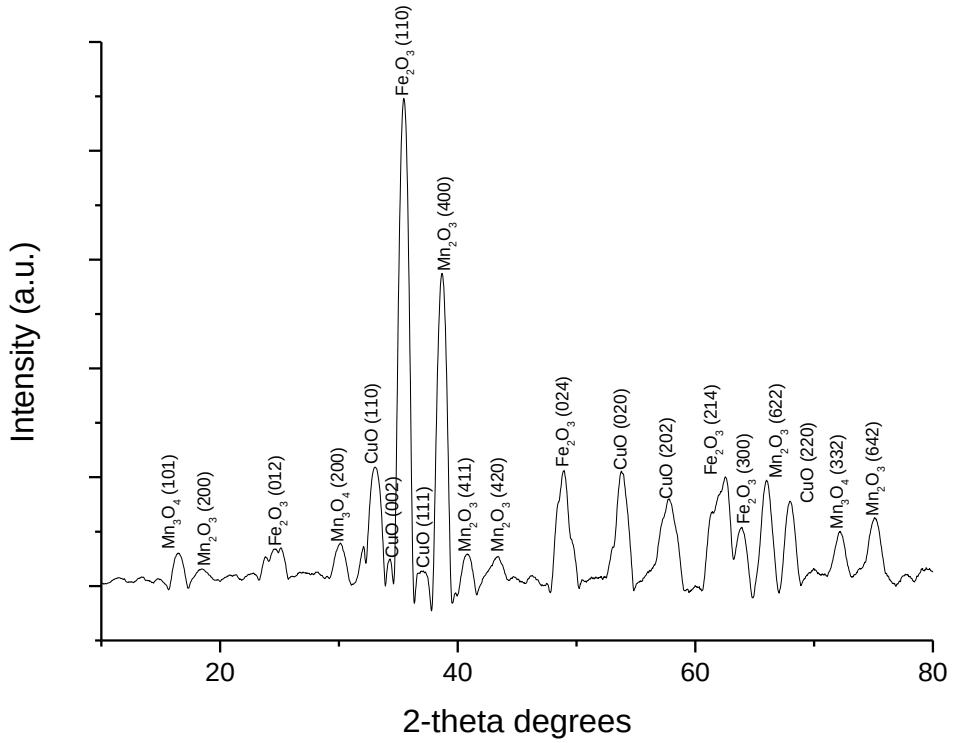

Fig 4.28 X-ray diffraction pattern of nanostructured ternary MFC metal oxide.

4.3.3.7 *pH at point of zero charge (pH_{pzc})*

The pH_{pzc} of the MFC nanometal oxide composite was determined from Fig 4.29 and found to be 6.75 using the pH drift method. The MFC composite oxide adsorbent surface is neutral at solution pH = 6.75, negative at solution pH > 6.75 and it is positive when solution pH < 6.75.

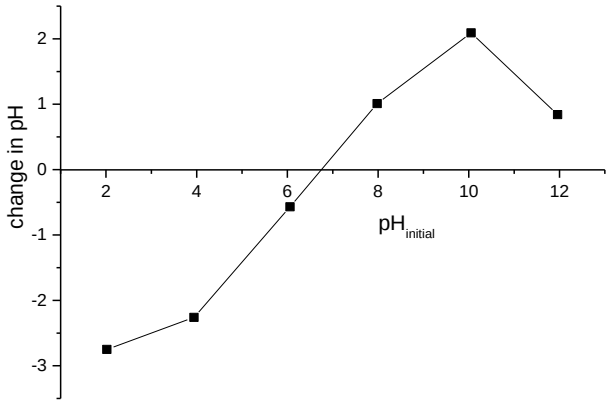

Fig 4.29 pH_{pzc} of nanometal MFC composite oxide.

4.4 CONCLUSION

The optimal working parameters for fabrication of the ternary MFC metal oxide nanocomposite as determined from CCD were a co-precipitation of 58 mins and Mn:Fe:Cu mole ratio of 0.028:0.013:0.025 with a desirability score of 1. Spectroscopic characterization facilitated the microstructural investigation of the synthesized MC, MF and MFC metal oxide nanocomposites. The SEM images showed the rough and homogeneous nature of the nanocomposite surfaces which is characteristic of mixed metal oxides. This corroborated with results from XRD analysis which showed the presence of Mn, Fe and Cu oxides in different valence states. The analysis of infrared data revealed the presence of surface hydroxyl groups on the metal oxide surfaces. The analysis of XPS results revealed that redox processes took place during the co-precipitation of the metal oxide nanoparticles. The BET textural studies showed the presence of mesopores and macropores on the adsorbent surfaces. It also showed that the nanocomposites had large surface areas (217.52 m^2/g for MF) which is characteristic of the rough surfaces observed on the nanoparticles by SEM. The analysis of transmission electron micrographs exhibited that the ternary MFC metal oxide nanocomposite had the largest average particle size (0.90±0.05). The magnitudes of the surface charges (pH_{pzc}) of the MC, MF and MFC metal oxide composites were determined using the pH drift method.

4.5 REFERENCES

1. BARRETT, E.P., JOYNER, L.G. and HALENDA, P.P. (1951) The determination of pore volume and area distributions in porous substances. I. Computations from nitrogen isotherms, *Journal of the American Chemical society*. 73, pp. 373-380.
2. BIESINGER, M.C., LAU, L.W.M., GERSON, A.R. and SMART, R., St.C. (2010) Resolving surface chemical states in XPS analysis of first row transition metals, oxides and hydroxides: Sc, Ti, V, Cu and Zn, *Applied Surface Science*. 257, pp. 887-898.
3. BOUJELBEN, N., BOUZID, J. and ELOVEAR, Z. (2009) Adsorption of nickel and copper onto natural iron oxide-coated sand from aqueous solutions: Study in single and binary systems, *Journal of Hazardous Materials*. 163, pp. 376-382.
4. BOZKURT, G., BAYRAKÇEKEN, A. and ÖZER, A.K. (2014) Synthesis and characterization of CuO at nanoscale, *Applied Surface Science*. 318, pp. 244-250.
5. CHEN, H., CHU, P.K., HE, J., HU, T. and YANG, M. (2011) Porous magnetic manganese oxide nanostructures: Synthesis and their applications in water treatment, *Journal of Colloid and Interface Science*. 359, pp. 68-74.
6. DAR, M.A., KIM, Y.S., KIM, W.B., SOHN, J.M. and SHIN, H.S. (2008) Structural and magnetic properties of CuO nanoneedles synthesized by hydrothermal method, *Applied Surface Science*. 254, pp. 7477-7481.
7. DE GODOI, F.C., RODRIGUEZ-CASTELLON, E., GUIBAL, E. and BEPPU, M.M. (2013) An XPS study of chromate and vanadate sorption mechanism by chitosan membrane containing copper nanoparticles, *Chemical Engineering Journal*. 234, pp. 423-429.
8. DONG, G., TAN, G., LUO, Y., LIU, W., XIA, A. and REN, H. (2014) Charge defects and highly enhanced multiferroic properties in Mn and Cu co-doped $BiFeO_3$ thin films, *Applied Surface Science*. 305, pp. 55-61.
9. DU, Y., WANG, L., WANG, J., ZHENG, G., WU, J. and DAI, H. (2015) Flower-, wire-, and sheet-like MnO_2-deposited diatomites: Highly efficient absorbents for the removal of Cr (VI), *Journal of Environmental Sciences*. 29, pp. 71-81.
10. DU, X., HAN, Q., LI, J. and LI, H. (2017) The behaviour of phosphate adsorption and its reactions on the surfaces of Fe–Mn oxide adsorbent, *Journal of the Taiwan Institute of Chemical Engineers*. 76 pp. 167–175.

11. DU, Y., ZHENG, G., WANG, J., WANG, L., WU, J. and DAI, H. (2014) MnO_2 nanowires in situ grown on diatomite: Highly efficient absorbents for the removal of Cr(VI) and As(V), *Microporous and Mesoporous Materials*. 200, pp. 27–34.
12. ETHIRAJ, A.S. and KANG, D.J. (2012) Synthesis and characterization of CuO nanowires by a simple wet chemical method, *Nanoscale Research Letters*. 7, pp. 1-5.
13. GUPTA, K., MAITY, A. and GHOSH, U.C. (2010) Manganese associated nanoparticles agglomerate of iron (III) oxide: Synthesis, characterization and arsenic (III) sorption behavior with mechanism, *Journal of Hazardous Materials*. 184, pp. 832-842.
14. ISLAM, M.A., MORTON, D.W., JOHNSON, B.B., MAINALI, B. and ANGOVE, M.J. (2018). Manganese oxides and their application to metal ion and contaminant. Journal of Water removal from wastewater, *Process Engineering*. 26, pp. 264–280.
15. JIANG, L., XIAO, S. and CHEN, J. (2015) Removal behavior and mechanism of Co(II) on the surface of Fe–Mn binary oxide adsorbent, *Colloids and Surfaces A: Physicochemical Engineering Aspects*. 479, pp. 1–10.
16. LAKSHMIPATHIRAJ, P., NARASIMHAN, B.R.V., PRABHAKAR, S. and RAJU, J.B. (2006) Adsorption studies of arsenic on Mn-substituted iron oxyhydroxide, *Journal of Colloid and Interface Science*. 304, pp. 317-322.
17. LAN, S., WANG, X., XIANG, Q.A., YIN, H., TAN, W., QIU, G., LIU, F., ZHANG J. and FENG, X. (2017) Mechanisms of Mn(II) catalytic oxidation on ferrihydrite surfaces and the formation of manganese (oxyhydr)oxides, *Geochimica et Cosmochimica Acta*. 211, pp. 79–96.
18. LI, G., GAO, S., ZHANG, G. and ZHANG, X. (2014) Enhanced adsorption of phosphate from aqueous solution by nanostructured iron (III)-copper (II) binary oxides, *Chemical Engineering Journal*. 235, pp. 124-131.
19. LIU, J., YANG, H. and XUE, X. (2018) A new and simple route to prepare c-Fe_2O_3 with iron oxide scale, *Materials Letters*. 229, pp. 156–159.
20. LIU, W., ZHANG, J., ZHANG, C. and REN, L. (2012) Preparation and evaluation of activated carbon-based iron-containing adsorbents for enhanced Cr (VI) removal: mechanism study, *Chemical Engineering Journal*. 189, pp. 295-302.
21. LOU, Z., CAO, Z., XU, J., ZHOU, X., ZHU, J., LIU, X., BAIG, S.A., ZHOU, J. and XU, X. (2017) Enhanced removal of As(III)/(V) from water by simultaneously

supported and stabilized Fe-Mn binary oxide nanohybrids, *Chemical Engineering Journal*. 322, pp. 710–721.

22. LUO, H., WANG, C. and YAN, Y. (2003) Synthesis of mesostructured titania with controlled crystalline framework, *Chemistry of Materials*. 15, pp. 3841-3846.
23. MAKAREVICIENE, V., SKORUPSKAITE, V., LEVISAUSKAS, D., ANDRULEVICIUTE, V. and KAZANCEV, K. (2014) The optimization of biodiesel fuel production from microalgae oil using response surface methodology, *International journal of green energy*. 11, pp. 527-541.
24. MOHAN, S., SINGH, Y., VERMA, D.K. and HASAN, S.H. (2015) Synthesis of CuO nanoparticles through green route using Citrus limon juice and its application as nanosorbent for Cr(VI) remediation: Process optimization with RSM and ANN-GA based model, *Process Safety and Environmental Protection*. 96, pp. 156–166.
25. MORALES, M.R., BARBERO, B.P., LOPEZ, T., MORENO, A. and CADÚS, L.E. (2009) Evaluation and characterization of Mn–Cu mixed oxide catalysts supported on TiO_2 and ZrO_2 for ethanol total oxidation, *Fuel*. 88, pp. 2122-2129.
26. NESBITT, H.W. and BANERJEE, D. (1998) Interpretation of XPS Mn (2p) spectra of Mn oxyhydroxides and constraints on the mechanism of MnO_2 precipitation, *American Mineralogist*. 83, pp. 305-315.
27. NOGUEIRA, A.E., GIROTO, A.S., NETO, A.B.S. and RIBEIRO, C. (2016) CuO synthesized by solvothermal method as a high capacity adsorbent for hexavalent chromium, *Colloids and Surfaces A: Physicochemical. Engineering. Aspects*. 498, pp. 161–167.
28. OUMA, I.L., NAIDOO, E.B. and OFOMAJA, A.E. (2018) Thermodynamic, kinetic and spectroscopic investigation of arsenite adsorption mechanism on pine cone-magnetite composite, *Journal of Environmental Chemical Engineering*. 6, pp. 5409-5419.
29. OWOLABI, R.U., USMAN, M.A. and KEHINDE, A.J. (2018) Modelling and optimization of process variables for the solution polymerization of styrene using response surface methodology, *Journal of King Saud University-Engineering Sciences*. 30, pp. 22-30.
30. ROUQUEROL, J., AVNIR, D., FAIRBRIDGE, C.W., EVERETT, D.H., HAYNES, J.H., PERNICONE, N., RAMSAY, J.D.F., SING, K.S.W. and UNGER, K.K. (1994)

Recommendations for the characterization of porous solids, *Pure & Applied Chemistry*. 66, pp. 1739-1758.

31. ROY, P., DEY, U., CHATTORAJ, S., MUKHOPADHYAY, D. and MONDAL, N.K. (2017) Modeling of the adsorptive removal of arsenic (III) using plant biomass: a bioremedial approach, *Applied Water Science*. 7, pp. 1307-1321.
32. SARKAR, M. and MAJUMDAR, P. (2011) Application of response surface methodology for optimization of heavy metal biosorption using surfactant modified chitosan bead, *Chemical Engineering Journal*. 175, pp. 376-387.
33. SHAHRI, F.B. and NIAZI, A. (2015) Synthesis of modified maghemite nanoparticles and its application for removal of Acridine Orange from aqueous solutions by using Box-Behnken design, *Journal of Magnetism and Magnetic Materials*. 396, pp. 318-326.
34. SHU, Z., CHEN, Y.,HUANG, W.,CUI, X.,ZHANG, L.,CHEN, H., ZHANG, J., FAN, X., WANG, Y., TAO, G., HE, D. and SHI, J. (2013) Room-temperature catalytic removal of low-concentration NO over mesoporous Fe–Mn binary oxide synthesized using a template-free approach, *Applied Catalysis B: Environmental*. 140–141, pp. 42–50.
35. SING, K.S.W., EVERETT, D.H., HAUL, R.A.W., MOSCOU, L., PIEROTTI, R.A., ROUQUEROL, J., SIEMIENIEWSKA, T. (1985) Reporting physisorption data for gas/solid systems with special reference to the determination of surface area and porosity, *Pure & Applied Chemistry*. 57, pp. 603-619.
36. SOUSA, V.S. and TEIXEIRA, M.R. (2013) Aggregation kinetics and surface charge of CuO nanoparticles: The influence of pH, ionic strength and humic acids, *Environmental Chemistry*. 10, pp. 313-322.
37. TRPKOV, D., PANJANB, M., KOPANJA, L. and TADIĆ, M. (2018) Hydrothermal synthesis, morphology, magnetic properties and self-assembly of hierarchical α-Fe_2O_3 (hematite) mushroom-, cube- and sphere-like superstructures, *Applied Surface Science*. 457, pp. 427–438
38. WANG, X., LAN, S., ZHU, M., GINDER-VOGEL, M., YIN, H., LIU, F., TAN, W. and FENG X. (2015) The presence of ferrihydrite promotes abiotic Mn(II) oxidation and formation of birnessite. *Soil Science Society of America Journal*. 79, pp. 1297–1305.

39. WANG, Y., FENG, X., VILLALOBOS, M., TAN, W. and LIU, F. (2012) Sorption behaviour of heavy metals on birnessite: Relationship with its Mn average oxidation state and implications for types of sorption sites, *Chemical Geology*. 292-293, pp. 25-34.
40. WANG, Y., LIU, L., CAI, Y., CHEN, J. and YAO, J. (2013) Preparation and photocatalytic activity of cuprous oxide/carbon nanofibres composite films, *Applied Surface Science*. 270, pp. 245-251.
41. WATTS, J.F. and WOLSTENHOLME, J. (2003) *An introduction to surface analysis by XPS and AES*. John-Wiley & Sons Ltd: West Sussex. pp. 71.
42. WEI, Z., WANG, Z., YAN, J., LIU, Y., WU, Y., FANG, Y., YU, L., CHENG, G., PAN, Z. and HU, G. (2019) Adsorption and oxidation of arsenic by two kinds of β-MnO_2. *Journal of Hazardous Materials*. 373, pp. 232-242.
43. WEILONG, W. and XIAOBO, F. (2013) Efficient removal of Cr(VI) with Fe/Mn mixed metal oxide nanocomposites synthesized by a grinding method, *Journal of Nanomaterials*. 2013, pp. 1-8.
44. YU, X., TONG, S., GE, M., ZUO, J., CAO, C. and SONG, W. (2013) One-step synthesis of magnetic composites of cellulose@ iron oxide nanoparticles for arsenic removal, *Journal of Materials Chemistry A*. 1, pp. 959-965.
45. YUFANYI, D.M., ONDOH, A.M., FOBA-TENDO, J. and MBADCAM, K.J. (2015) Effect of decomposition temperature on the crystallinity of α-Fe_2O_3 (hematite) obtained from an iron (III) hexamethylenetetramine precursor, *American Journal of Chemistry*. 5, pp. 1-9.
46. ZARGAZI, M. and ENTEZARI, M.H. (2020) Sono-electrodeposition of novel bismuth sulphide films on the stainless steel mesh: Photocatalytic reduction of Cr(VI), *Journal of Hazardous Materials*. 384, pp. 121300.
47. ZHANG, G., LIU, H., LIU, R. and QU, J. (2009) Adsorption behaviour and mechanism of arsenate at Fe-Mn binary oxide/water interface, *Journal of Hazardous Materials*. 168, pp. 820-825.
48. ZHANG, G., LIU, H., QU, J. and JEFFERSON, W. (2012) Arsenate uptake and arsenite simultaneous sorption and oxidation by Fe-Mn binary oxides: Influence of Mn/Fe ratio, pH, Ca^{2+} and humic acid, *Journal of Colloid and Interface Science*. 366, pp. 141-146.

49. ZHANG, G., QU, J., LIU, H., LIU, R. and WU, R. (2007) Preparation and evaluation of a novel Fe-Mn binary oxide adsorbent for effective arsenite removal, *Water Research*. 41, pp. 1921-1928.
50. ZHENG, Q., HOU, J., HARTLEY, W., REN, L., WANG, M., TU, S. and TAN, W. (2020) As (III) adsorption on Fe-Mn binary oxides: Are Fe and Mn oxides synergistic or antagonistic for arsenic removal?. *Chemical Engineering Journal*. 389, pp. 124470.

CHAPTER 5

5 RESULTS AND DISCUSSION

5.1 INTRODUCTION

This chapter describes the adsorption kinetics of Cr(VI) and As(III) onto the MF, MC and MFC metal oxide nanocomposites. The effect of solution pH and determination of the optimum adsorbent dosage concentration for the adsorption process are discussed.

5.2 ADSORPTION DYNAMICS

5.2.1 Influence of solution pH

The adsorbent surface charge, degree of ionisation and adsorbate speciation are highly dependent on the solution pH (Akram et al., 2017). The adsorbent surface is electrically neutral at pH at point of zero charge (pH_{pzc}). It is positively charged at pH < pH_{pzc}, and is negatively charged at pH > pH_{pzc}. The pH_{pzc} of the MF, MC and MFC metal oxides were found to be 6.69, 6.82 and 6.75, respectively.

Chromium(VI): The effect of pH on Cr(VI) adsorption on the MF, MC and MFC metal oxides is shown in Fig 5.1.

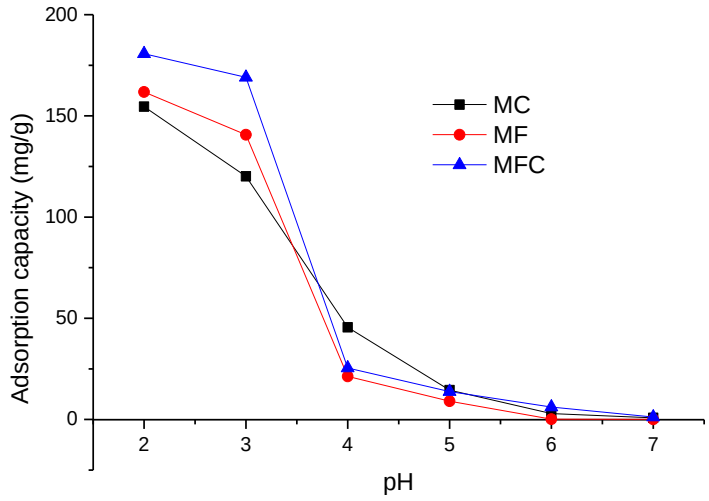

Fig 5.1 Effect of pH on adsorption of Cr(VI) onto MC, MF and MFC metal oxides.

The plot shows that the adsorption of the Cr(VI) is influenced by solution pH, with maximum adsorption capacity for the MF (q_e = 162.21 mg/g), MC (q_e = 154.04 mg/g) and MFC (q_e = 180.58 mg/g) metal oxides taking place at pH 2. The adsorption capacities are high at low pH values and decrease with an increase in solution pH, suggesting that electrostatic interactions or ion exchange might be part of the adsorption mechanism (Panda et al., 2017). The same result was reported by Belachew and Hinsene (2020) on adsorption of Cr(VI) anions onto cationic surfactant-modified Ethiopian kaolin at different pH values. The pK_{a1} and pK_{a2} values of chromic acid (H_2CrO_4) are 0.74 and 6.50, respectively (Jiang et al., 2013). At low to slightly neutral pH, the Cr(VI) mainly exists as bichromate, $HCrO_4^-$ anions in aqueous solution, (Barrera-Diaz et al., 2012; Zhang et al., 2018) while the metal oxide adsorbent surfaces are highly protonated resulting in strong electrostatic attractions between the adsorbate and the adsorbent increasing the adsorption capacity. It has been shown that metal ions can leach into solution at low pH values (Guo et al., 2019). A study of the stability of the MF, MC and MFC metal oxides at pH's 2-7 was done and the results are presented in Figs 5.2a-c, respectively. To determine the optimum pH for the adsorption of Cr(VI) on each of the metal oxides in this investigation, the USEPA and WHO prescribed maximum contaminant levels (MCL) of Mn, Fe and Cu, which are 0.05, 0.3 and 1.3 mg/dm^3, respectively were taken into consideration (Praharaj et al., 2002; Lemley et al., 2005; Orisakwe et al., 2006). At pH 2, where the maximum adsorption of the pollutant anions is taking place, leaching of the adsorbent metal ion components into solution is also very high at that acidic pH. Hence, a pH of 3 was taken as the optimum for the adsorption of the Cr(VI) on the MF (q_e = 141.07 mg/g), MC (q_e = 120.52 mg/g) and MFC (q_e = 168.13 mg/g) metal oxides, since at pH 3, the amounts of Mn, Fe and Cu ions leaching into the treated water were all below the permissible maximum contaminant levels. The same conclusion was also reached at by Inyang and co-workers (2016), who reported that the amount of adsorbent metal ions leached at pH 2 is far much greater than that leached at pH 3 in aqueous media. The pH investigations showed that an increase in solution pH increased stability of the metal oxide adsorbents, but greatly reduced the Cr(VI) adsorption capacities. The reduction in the adsorption capacities at higher pH values might be due to: (i) electrostatic repulsion between the negatively charged adsorbent surface (pH > pH_{pzc}) and the predominant Cr(VI) anions (CrO_4^{2-}), (ii) competition for active sites between the CrO_4^{2-} anions and OH^-, and (iii) the predominant CrO_4^{2-} oxyanion has lower free energy (-2.1 to -0.3 kcal/mol) than $HCrO_4^-$ (-2.5 to -0.6 kcal/mol) and shows low affinity for the adsorbent (Liu et al., 2018; Wu et al., 2018), since it binds to two positive centres resulting in rapid depletion of

adsorption active sites (Nogueira et al., 2016). An analogous interpretation was made by Gheju et al. (2016), on studying the effects of solution pH on Cr(VI) anions removal using MnO_2. The MFC ternary metal oxide showed better adsorptive capabilities than either the MF or MC binary metal oxides as it had higher adsorption capacities at pH's 2 and 3. Further investigations on adsorption of Cr(VI) were done at pH 3 mainly due to the increase in stability of the metal oxide systems at this pH. This study seeks to remove Cr(VI) from solution with minimal or negligible conversion to Cr(III). The reduction of Cr(VI) can occur as:

$$3Fe^{2+} + HCrO_4^- + 7H^+ \rightleftharpoons 3Fe^{3+} + Cr^{3+} + 4H_2O \quad (5.1)$$

or

$$HCrO_4^- + 7H^+ + 3e^- \rightleftharpoons Cr^{3+} + 4H_2O \quad (5.2)$$

The reduction process is very slow in the environment, taking months or even years but the rate increases significantly at pH values less than 3 (Jardine et al., 1999). Duranoğlu and co-workers (2012) also reported a similar finding in their investigation on the adsorption of Cr(VI) onto activated carbon derived from acrylonitrile-divinylbenzene co-polymer. The researchers observed that Cr(III) ions were only observed at pH 2 during the adsorption process and proposed that this might be due to (1) a deficiency of H^+ protons required to facilitate the reduction of Cr(VI) at pH values above 2, and (2) possibly the Cr(VI) reduction took place but the formed Cr(III) ions were rapidly adsorbed onto the surface of the adsorbent due to a deficiency of H^+ protons which can compete with the Cr(III) cations for adsorption active sites above a solution pH of 2. Hence, application of pH 3 as the optimum is anticipated to alleviate the formation of Cr(III) from the reduction of Cr(VI) during the adsorption process.

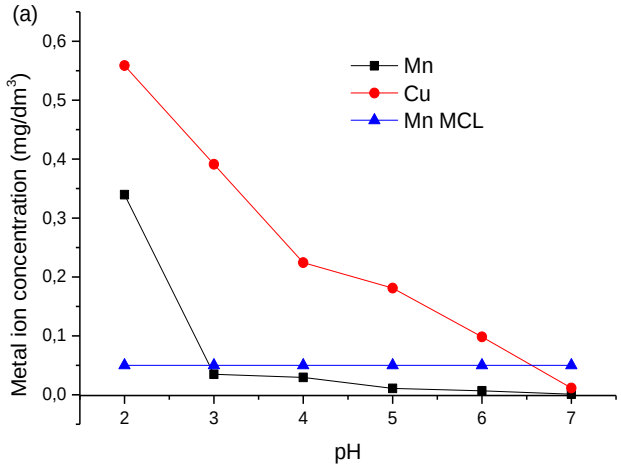

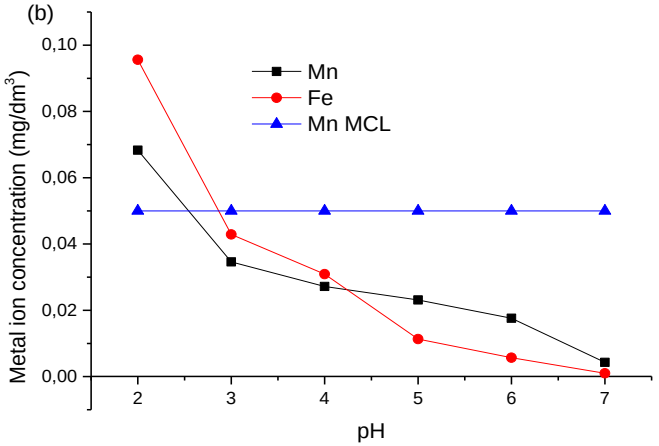

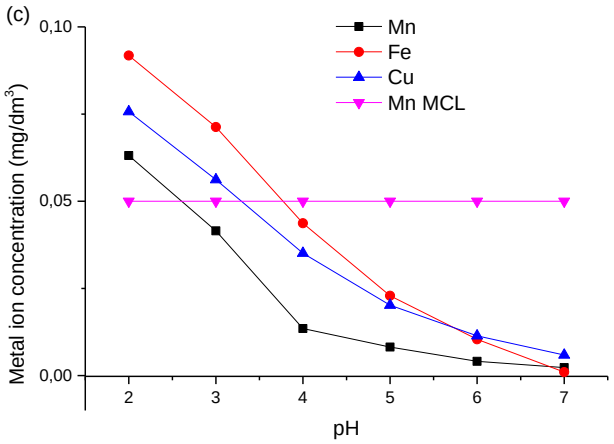

Fig 5.2 Effect of pH on stability of the (a) MC, (b) MF and (c) MFC metal oxide adsorbents (the MCL of ions of Fe and Cu are not shown since they are much higher than the concentration amounts of Fe and Cu ions leaching from the metal oxide systems into the treated water – MCL: Fe = 0.3 mg/dm^3 and Cu = 1.3 mg/dm^3).

Arsenic(III): The plot of effect of pH on As(III) adsorption onto MC, MF and MFC metal oxide composites is presented in Fig 5.3. The adsorption capacities are low in acidic and very alkaline solution conditions, with maximum adsorption taking place at pH 8 for the MF (q_e = 32.42 mg/g), and at pH 9 for the MC (q_e = 34.51 mg/g) and MFC (q_e = 42.34 mg/g) metal oxides. The MFC ternary metal oxide exhibited the highest adsorption capacity suggesting that its surface has a higher affinity for the As(III) species. The predominant form of As(III) is H_3AsO_3 at pH < 9 (Xiu et al., 2018).

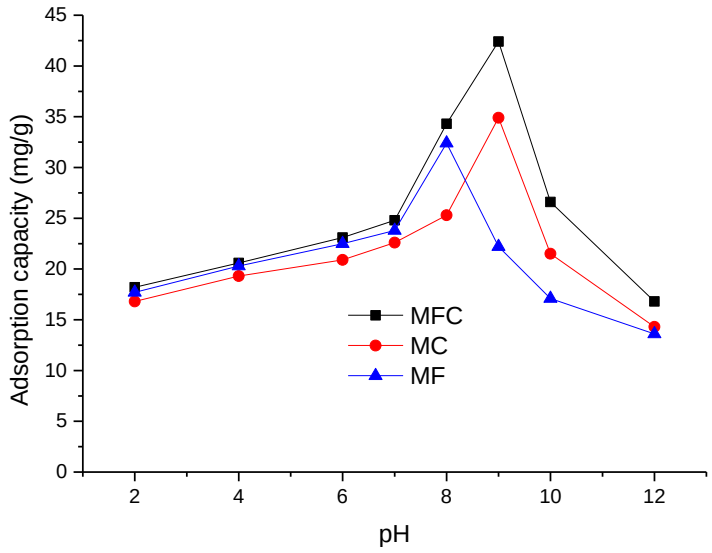

Fig 5.3 Effect of solution pH on adsorption of As(III) on MC, MF and MFC metal oxide composite adsorbents.

The low adsorption capacities at low solution pH (ie., pH < pH_{pzc}) are due to reduced affinity between the protonated adsorbent surface and the neutral H_3AsO_3 [Äs(OH)$_3$]. At circumneutral solution pH, the metal oxide surface and the neutral H_3AsO_3 form Lewis acid-base interactions creating inner-sphere surface complexes increasing adsorption (Cumbal & Sengupta, 2005; Zhang et al., 2018). Other researchers have reported the same result and concluded that the maximum uptake of weak acids such as arsenious acid (H_3AsO_3; pK_{a1} = 9.22) by metal oxides usually takes place at solution pH values close to pK_{a1} values of the weak acids (Zhang et al., 2012; Zhang et al., 2013). The decrease in adsorption at high pH is probably due to (1) increase in electrostatic repulsion between the dominant $H_2AsO_3^-$ and $HAsO_3^{2-}$ anionic forms of As(III) and the negatively charged adsorbent surface (since the solution pH > pH_{pzc}), and (2) the

increase in competition for active sites between the OH^- ions and the arsenite anions (Shan & Tong, 2013; Zhang et al., 2013; Wen et al., 2019). As maximum adsorption of As(III) is at a pH > pH_{pzc} of the MC (pH_{pzc} = 6.82), MF (pH_{pzc} = 6.69) and MFC (pH_{pzc} = 6.75) metal oxide adsorbents, surface complexation via chemisorption and not electrostatic interactions controls the uptake of adsorbate from solution (Chandra et al., 2010; Cheng et al., 2016). The same conclusion about As(III) adsorption process was also reported by Roy et al. (2017) using *Azadirachta indica* (neem) bark powder.

5.2.2 Adsorbent dosage concentration

Chromium(VI): The plots in Figs 5.4a-c show the effect of the MF, MC and MFC metal oxides adsorbent masses on Cr(VI) adsorption capacity and the Cr(VI) removal percentage from solution during the adsorption process. For the MF oxide adsorbent, an increase in mass decreased the adsorption capacity but caused an increase in the percentage removal of the adsorbate as shown in Fig 5.4a. The Cr(VI) adsorption capacity showed a marked decrease from 85.93 mg/g to 65.29 mg/g as the MF oxide adsorbent mass increased from 0.01 g to 0.05 g, but only decreases from 65.29 mg/g to 58.85 mg/g as the adsorbent mass increased from 0.05 g to 0.1 g. As more mass of adsorbent was added from 0.05 g to 0.2 g, a pattern could be observed, that is, for each stage increase in adsorbate mass, the resulting decrease in adsorption capacity became smaller. The percentage removal of Cr(VI) from solution showed a marked increase from 14.07 % to 34.71 % as the mass of adsorbent increased from 0.01 g to 0.05 g, but showed a small increase from 34.71 % to 41.16 % as adsorbent mass increased from 0.05 g to 0.1 g. As the adsorbent mass increased from 0.05 g to 0.2 g, it was noted that the increase in % removal of adsorbate became smaller at each mass incremental stage.

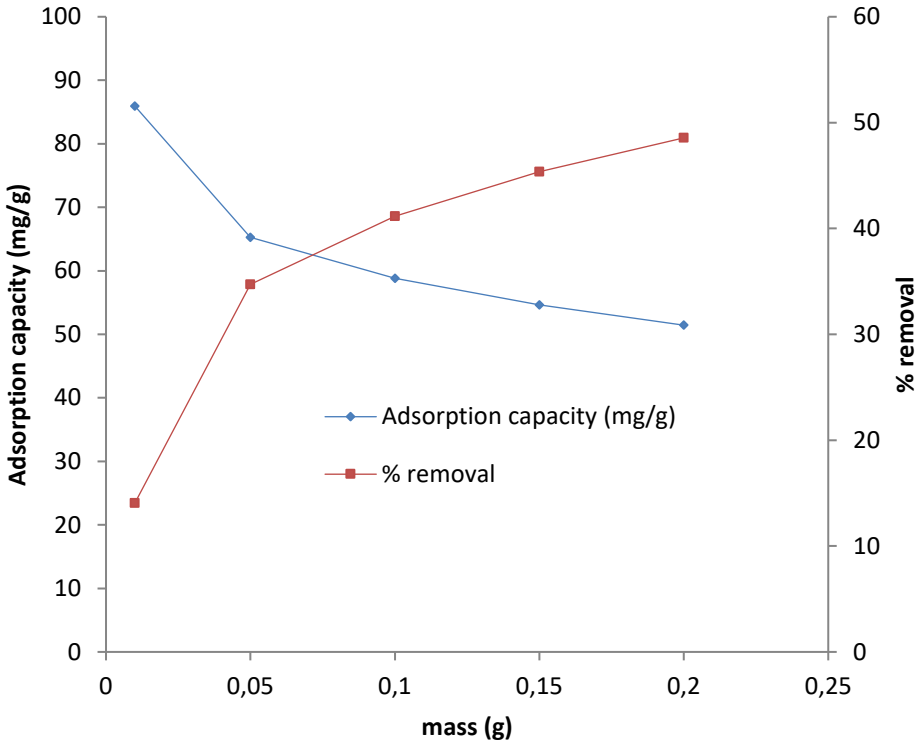

Fig 5.4a The effect of MF metal oxide dose on the adsorption of Cr(VI).

For the MC metal oxide adsorbent, as the mass increased, the adsorption capacity decreased but the percentage removal of adsorbate increased. The Cr(VI) adsorption capacity showed a decrease from 120.15 mg/g to 67.56 mg/g as the MC oxide adsorbent mass increased from 0.01 g to 0.05 g and decreases from 67.56 mg/g to 36.70 mg/g as the adsorbent mass increased from 0.05 g to 0.1 g. The percentage removal of Cr(VI) from solution increased from 12.02 % to 33.78 % as the mass of adsorbent increased from 0.01 g to 0.05 g, but showed a small increase from 33.78 % to 36.70 % as adsorbent mass increased from 0.05 g to 0.1 g. The plot in Fig 5.4b shows that as the mass of MC oxide adsorbent increases from 0.01 g to 0.05 g, there is a marked decrease in adsorption capacity of Cr(VI) from solution, but a smaller decrease in the adsorption capacity is observed when the mass of adsorbent increases from 0.05 g to 0.1 g. The same pattern was noted for subsequent increases in MC adsorbent dose after 0.05 g.

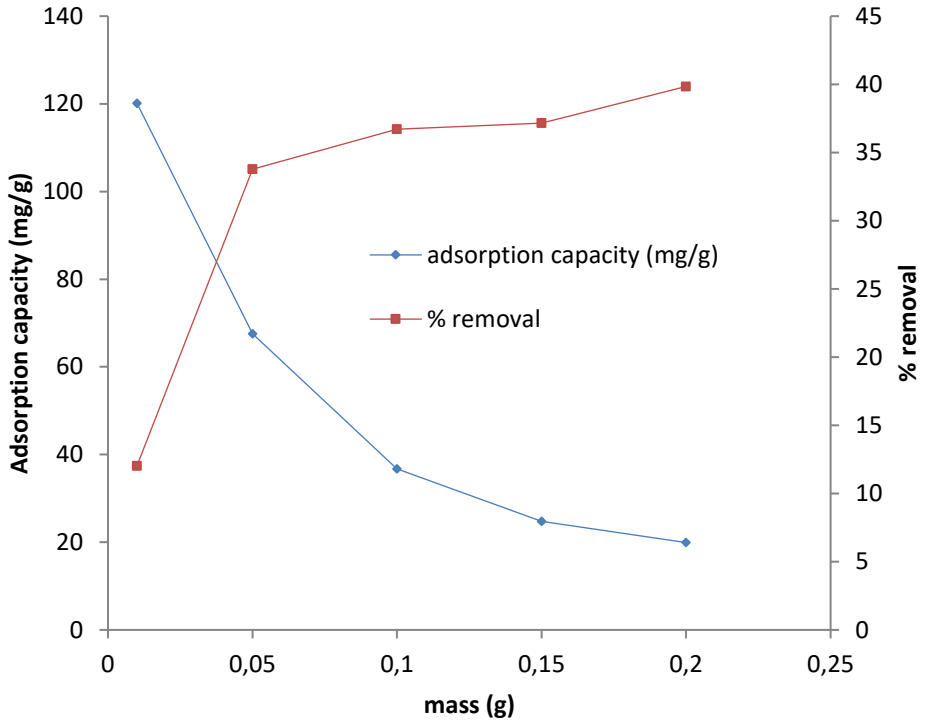

Fig 5.4b The effect of MC metal oxide dose on the adsorption of Cr(VI).

The plot in Fig 5.4c shows the effect of MFC metal oxide adsorbent mass on Cr(VI) adsorption capacity and the removal percentage of Cr(VI) from solution during the adsorption process. The plot shows that as the mass of MFC oxide adsorbent increased, the adsorption capacity decreased, but the % removal of the adsorbate increased. The Cr(VI) adsorption capacity showed a marked decrease from 169.03 mg/g to 85.72 mg/g as the MFC oxide adsorbent mass increased from 0.01 g to 0.05 g, but only decreases from 85.72 mg/g to 53.72 mg/g as the adsorbent mass increased from 0.05 g to 0.1 g. As more mass of adsorbent was added from 0.05 g to 0.2 g, a pattern could be observed, that is, for each stage increase in adsorbate mass, the resulting decrease in adsorption capacity became smaller. The percentage removal of Cr(VI) from solution increased from 16.90 % to 42.86 % as the mass of adsorbent increased from 0.01 g to 0.05 g, but showed a small increase from 42.86 % to 53.72 % as adsorbent mass increased from 0.05 g to 0.1 g. A trend was noted, that as adsorbent mass was increased from 0.05 g to 0.2 g, the increase in % removal of adsorbate became smaller after each mass increase.

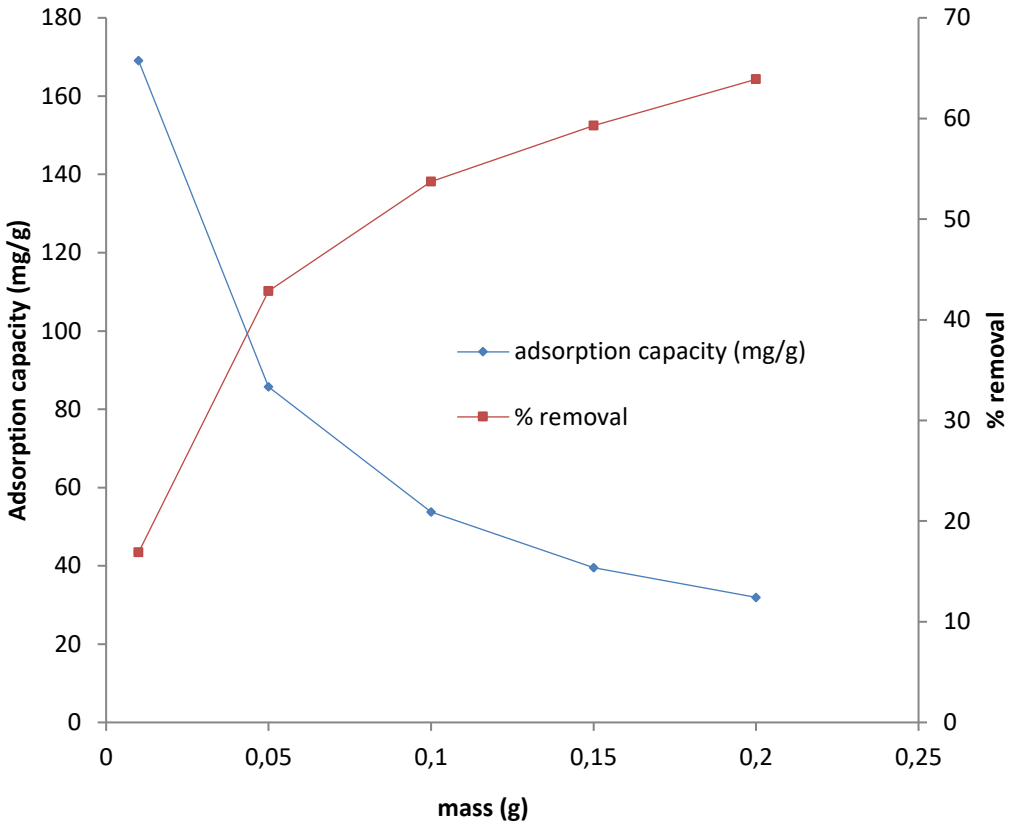

Fig 5.4c The effect of MFC metal oxide dose on the adsorption of Cr(VI).

The decrease in Cr(VI) adsorption capacity due to an increase in the MF, MC and MFC metal oxide adsorbent doses with a fixed concentration and fixed volume of Cr(VI) is attributed to an increase in the number of adsorbent particles and adsorption active sites. During the adsorption process, some adsorbent active sites remain unoccupied due to: (1) a shortage of adsorbate resulting in lower adsorption capacities (Algothmi et al., 2013), (2) a decrease in total surface area due to aggregation and/or overlapping of adsorption active sites, and (3) an increase in diffusion path length (Franca et al., 2009). The observed large initial increase in the percentage removal of Cr(VI) with an increase in the mass of the metal oxide adsorbents up to 0.05 g with a fixed concentration and fixed volume of adsorbate is due to an increase in the number of adsorption active sites resulting in more adsorbate being removed from solution (Ofomaja, 2010; Huang et al., 2015). As more mass of adsorbent is added, the increase in % removal of adsorbate becomes smaller after 0.05 g. This is attributed to a shortage of adsorbate due to the large availability of the adsorption active sites (Goswami et al., 2012). Therefore, 0.05 g was chosen as the optimum metal oxide adsorbent mass and used in subsequent investigations for the MF, MC and MFC metal oxide adsorbents.

Arsenic(III): The effect of the mass of the MF, MC and MFC metal oxide adsorbents on As(III) ions adsorption capacities and the % removal of As(III) from solution is presented in Figs 5.5a-c. The plot in Fig 5.5a shows that as the mass of the MF oxide was increased from 0.01 g to 0.2 g, the As(III) adsorption capacity decreased, but the removal percentage of As(III) increased. The MF oxide adsorbent mass was increased in stages, that is, from 0.01 g to 0.05 g, 0.05 g to 0.1 g, 0.1 g to 0.15 g, and 0.15 g to 0.2 g. The adsorption capacities associated with each mass increase stage were noted as 38.10 mg/g, 34.30 mg/g, 20.02 mg/g, 14.29 mg/g and 11.29 mg/g, respectively. The removal percentages of As(III) for each of the above-stated mass increase intervals were observed to be 7.62, 34.30, 40.04, 42.86 and 45.16, respectively.

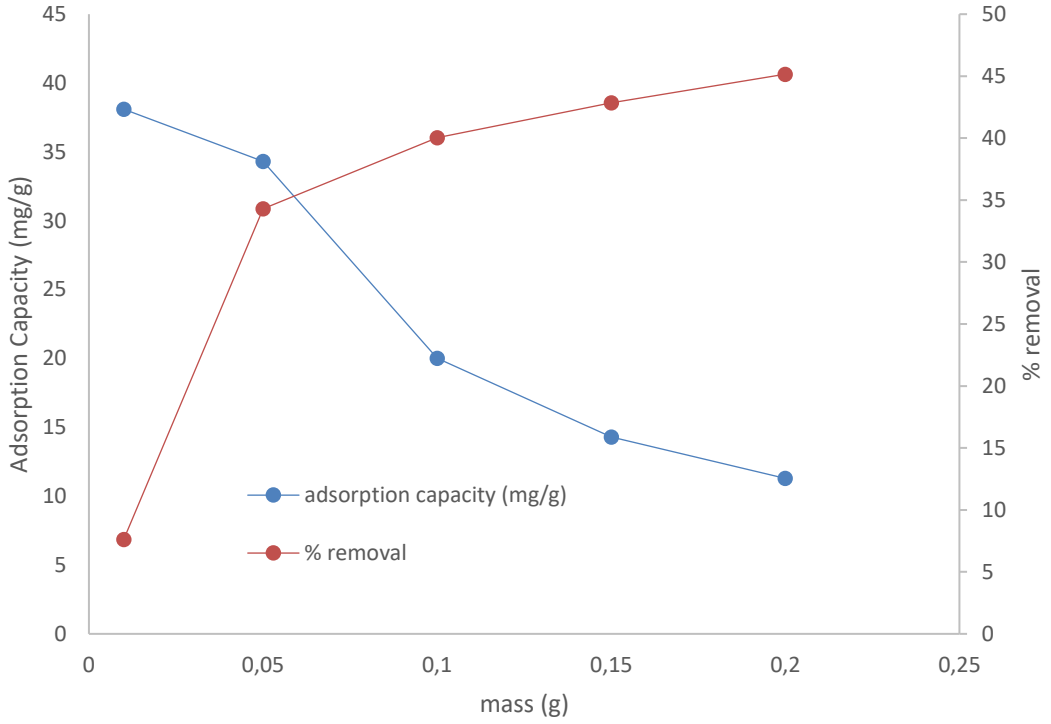

Fig 5.5a The effect of MF binary metal oxide dose on adsorption of As(III).

The plot in Fig 5.5b shows the effect of the MC oxide adsorbent dose on As(III) adsorption capacity and the % removal of As(III) from solution. From the plot, it is observed that as the mass of MC oxide was increased from 0.01 g to 0.2 g, the As(III) adsorption capacity decreased, but the removal percentage of As(III) increased. The MC oxide adsorbent mass was increased from 0.01 g to 0.05 g, 0.05 g to 0.1 g, 0.1 g to 0.15 g, and 0.15 g to 0.2 g. The adsorption capacities associated with each mass increase stage were noted as 39.40 mg/g, 36.04 mg/g, 21.94 mg/g, 15.08 mg/g and 11.50 mg/g, respectively. The removal percentages of

As(III) for each of the above-stated mass increase intervals were observed to be 7.88, 36.04, 43.88, 45.24 and 45.98, respectively.

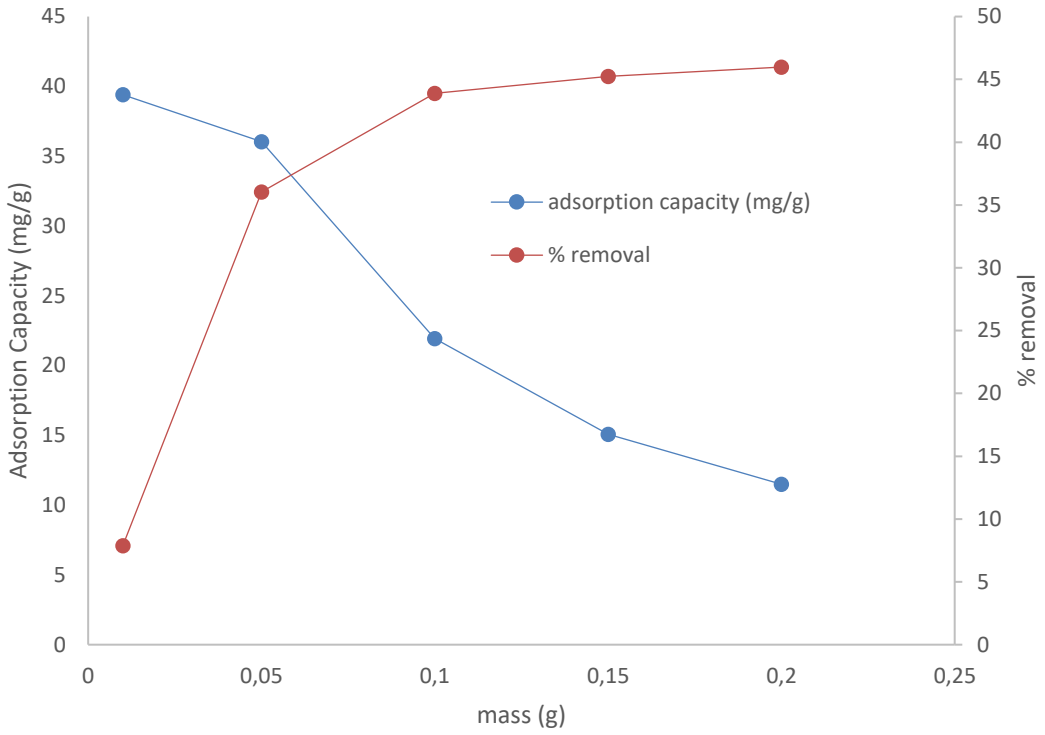

Fig 5.5b The effect of the MC binary metal oxide dose on adsorption of As(III).

The effect of the mass of the MFC metal oxide adsorbent on As(III) adsorption capacity and the % removal of As(III) from solution is presented in Fig 5.5c. The plot shows that as the mass of MFC oxide was increased from 0.01 g to 0.2 g, the As(III) adsorption capacity decreased, but the removal percentage of As(III) increased. The MFC oxide adsorbent mass was increased from 0.01 g to 0.05 g, 0.05 g to 0.1 g, 0.1 g to 0.15 g, and 0.15 g to 0.2 g. The adsorption capacities associated with each mass increase were noted as 70.30 mg/g, 40.92 mg/g, 21.99 mg/g, 15.39 mg/g and 11.72 mg/g, respectively. The removal percentages of As(III) for each of the above-stated mass increase intervals were observed to be 14.06, 40.92, 43.98, 46.18 and 46.86, respectively.

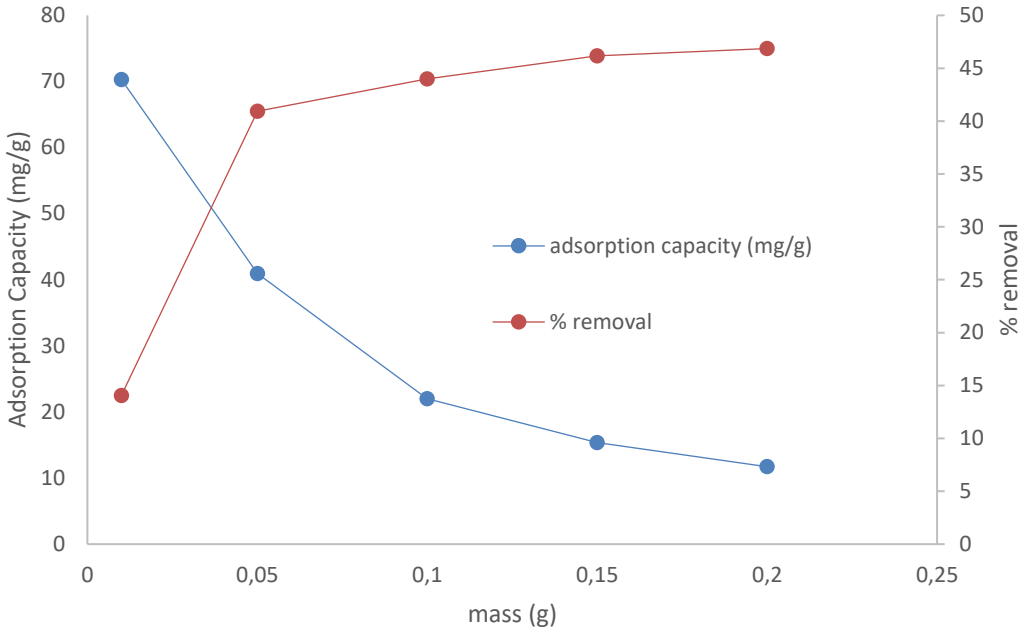

Fig 5.5c The effect of the MFC ternary metal oxide dose on adsorption of As(III).

The decrease in As(III) adsorption capacity due to an increase in the mass of each of the MF, MC and MFC metal oxide adsorbents with a fixed concentration and fixed volume of As(III) is attributed to an increase in the number of adsorbent particles and adsorption active sites. This causes some adsorption active sites to remain unoccupied due to the limited amount of adsorbate, resulting in a decrease in adsorption capacities (Ofomaja, 2010b; Algothmi et al., 2013).

The observed large initial increase in the percentage removal of As(III) with an increase in the mass of each of the MF, MC and MFC metal oxide adsorbents with fixed concentration and a fixed volume of adsorbate is attributed to an increase in the number of adsorption active sites resulting in more adsorbate being removed from solution (Ofomaja, 2010b; Huang et al., 2015). As more mass of adsorbent is added, the increase in % removal of adsorbate becomes smaller after 0.05 g. This is attributed to a shortage of adsorbate due to the large availability of the adsorption active sites (Goswami et al., 2012). Therefore, 0.05 g was chosen as the optimum adsorbent mass for each of the MF, MC and MFC metal oxides and used in subsequent investigations.

5.2.3 Kinetic studies

The study of adsorption kinetics is of paramount importance in the design and scale-up of an efficient adsorption system. The fitting of kinetic and diffusion models gives an insight of the rate-controlling step in the adsorption process since the adsorption of liquids on porous solid adsorbents involves a series of steps: (1) the bulk transport of adsorbate to the hydrodynamic film surrounding the external surface of the adsorbent, (2) adsorbate migration from the bulk to the surface of the adsorbent across the hydrodynamic film, (3) intraparticle (pore) diffusion, and (4) attachment of adsorbate onto the adsorbent surface (Tran et al., 2017). Step 1 is assumed to be negligible due to vigorous stirring of the adsorption system, while step 4 is known to be fast hence, cannot be rate-controlling during the adsorption process. Therefore, the slower process between film or pore diffusion (steps 3 and 4 respectively) maybe rate-controlling during the adsorption (Singh & Pant, 2006).

5.2.3.1 *Effect of concentration on adsorption kinetics*

The batch kinetic investigations were performed at varying initial concentrations (10, 20, 25, 50 and 75 mg/dm^3) of either Cr(VI) or As(III) as described in section 3.6.3.4.

5.2.3.1.1 Kinetic models: Pseudo-first-order, pseudo-second-order and the Elovich rate equations

The Cr(VI) and As(III) batch adsorption kinetic experimental data were fitted onto the non-linear forms of the pseudo-first-order, pseudo-second-order and Elovich rate equations using KyPlot version 5.0 software (Yoshioka, 2002). The software utilized a quasi-Newton non-linear regression algorithm to determine the adsorption parameters. The non-linear equations give more accurate model parameters than those calculated using linear techniques (Lima et al., 2015; Tran et al., 2017). The pseudo-first-order rate equation describes adsorption kinetics for diffusion across a boundary layer (Lagergren, 1898) and is presented as:

$$q_t = q_e(1 - e^{-k_1 t}) \tag{5.3}$$

where q_t (mg/g) and q_e (mg/g) are the adsorption capacities at time t (min) and equilibrium respectively; and k_1 (1/min) is the pseudo-first-order rate constant, which is calculated from a

non-linear plot of q_t against t. The pseudo-second-order rate equation describes adsorption kinetics taking place by surface chemisorption (Blanchard et al., 1984) and is presented as:

$$q_t = \frac{q_e^2 k_2 t}{1+k_2 q_e t} \tag{5.4}$$

where k_2 (g/mg.min) is the pseudo-second-order rate constant and is obtained from a non-linear plot of q_t against t. The initial adsorption rate, h (mg/g.min) is derived from a rearrangement of Eq 5.4 as t approaches zero (Ho et al., 1996), giving:

$$h = k_2 q_e^2 \tag{5.5}$$

The Elovich equation describes the kinetics of heterogenous chemisorption on solid adsorbents (Zeldowitsch, 1934) and is presented as:

$$q_t = \frac{1}{\beta}\ln(1 + \alpha\beta t) \tag{5.6}$$

where α (mg/g.min) is the initial adsorption rate constant at zero coverage and β (mg/g) is the adsorption constant related to the degree of surface coverage and activation energy for chemisorption. A non-linear plot of q_t against t gives the Elovich kinetic constants, α and β.

Chromium(VI): The kinetic parameters and error functions for pseudo-first-order, pseudo-second-order and Elovich rate equations for Cr(VI) adsorption on MC, MF and MFC nanostructured metal oxides are presented in Tables 5.1a-c.

Table 5.1a Kinetic modelling of different concentrations of Cr(VI) adsorption on MC binary metal oxide at 299 K.

Kinetic model	Parameters	Cr(VI) concentration (mg/dm^3)				
		10	20	25	50	75
	q_e (mg/g) (*exp*)	12.38	13.91	16.38	18.54	20.87
pseudo-first-order	q_e (mg/g)	11.51	12.74	15.08	17.11	19.17
	k_1 (1/min)	0.4266	0.3866	0.3273	0.2662	0.1758
	R^2	0.9498	0.9347	0.9199	0.9236	0.9076
	% variance	0.9089	1.3787	2.3244	2.7189	4.0629
pseudo-second-order	q_e (mg/g)	11.96	13.19	15.62	17.84	20.04
	k_2 (g.mg.min)	0.0559	0.0551	0.0546	0.0525	0.0501
	h (mg/g.min)	7.99	9.59	13.32	16.71	20.12
	R^2	0.9874	0.9807	0.9762	0.9841	0.9774
	% variance	0.2281	0.4071	0.6905	0.5644	0.9942
Elovich equation	β (mg/g)	0.52	0.55	0.59	0.63	0.65
	α (mg/g.min)	51.42	96.72	155.11	620.62	1206.45
	R^2	0.9891	0.9893	0.9907	0.9878	0.9903
	% variance	0.1971	0.2251	0.2693	0.4325	0.4265

Table 5.1b Kinetic modelling of different concentrations of Cr(VI) adsorption on MF binary metal oxide at 299 K.

Kinetic model	Parameters	Cr(VI) concentration (mg/dm^3)				
		10	20	25	50	75
	q_e (mg/g) (*exp*)	15.94	16.75	19.60	22.05	23.66
pseudo-first-order	q_e (mg/g)	14.58	15.60	18.18	21.05	22.06
	k_1 (1/min)	0.4014	0.3965	0.3807	0.3573	0.2749
	R^2	0.9561	0.9580	0.9496	0.9362	0.9277
	% variance	1.3042	1.3505	2.2199	3.6597	4.4331
pseudo-second-order	q_e (mg/g)	15.16	16.21	18.85	21.77	22.95
	k_2 (g.mg.min)	0.0409	0.0401	0.0391	0.0365	0.0348
	h (mg/g.min)	9.40	10.54	13.89	17.30	18.33
	R^2	0.9866	0.9917	0.9862	0.9827	0.9843
	% variance	0.3974	0.2665	0.6057	0.9922	0.9599
Elovich equation	β (mg/g)	0.49	0.51	0.53	0.58	0.70
	α (mg/g.min)	53.14	125.44	148.16	166.09	367.81
	R^2	0.9865	0.9768	0.9852	0.9843	0.9838
	% variance	0.3996	0.7476	0.6532	0.8982	0.9963

Table 5.1c Kinetic modelling of different concentrations of Cr(VI) adsorption on MFC ternary metal oxide at 299 K.

Kinetic model	Parameters	Cr(VI) concentration (mg/dm^3)				
		10	20	25	50	75
	q_e (mg/g) (*exp*)	16.95	18.84	22.09	25.53	27.71
pseudo-first-order	q_e (mg/g)	16.08	17.72	21.32	24.24	26.30
	k_1 (1/min)	0.4005	0.3096	0.2377	0.1869	0.1589
	R^2	0.9416	0.9455	0.9789	0.9846	0.9672
	% variance	2.0306	2.2132	1.2710	1.2033	2.9266
pseudo-second-order	q_e (mg/g)	16.65	18.34	22.14	25.20	27.31
	k_2 (g.mg.min)	0.0386	0.0382	0.0379	0.0369	0.0351
	h (mg/g.min)	10.71	12.88	18.57	23.44	26.19
	R^2	0.9814	0.9881	0.9977	0.9965	0.9968
	% variance	0.6455	0.4849	0.1401	0.2761	0.2832
Elovich equation	β (mg/g)	0.47	0.48	0.59	0.65	0.73
	α (mg/g.min)	71.22	157.26	198.64	283.94	350.74
	R^2	0.9900	0.9836	0.9555	0.9419	0.9639
	% variance	0.3467	0.6655	2.6889	4.5483	3.2202

The experimental and the pseudo-first-order and the pseudo-second-order adsorption capacities for MC, MF and MFC metal oxide adsorbents, showed an increase as the initial Cr(VI) concentration increased with a constant adsorbent dose. The experimental adsorption capacities, q_e (mg/g) for the metal oxides increased in the ranges: MC, 12.38-20.87; MF, 15.94-23.66; and MFC, 16.95-27.71, as the initial bulk concentration increased from 10-75 mg/dm^3. The pseudo-first-order and the pseudo-second-order adsorption capacities, q_e (mg/g) increased in the ranges: MC, 11.51-19.17; MF, 14.58-22.06; MFC, 16.08-26.30 and MC, 11.96-20.04; MF, 15.16-22.95; MFC, 16.65-27.31, respectively as the initial Cr(VI) concentration increased from 10-75 mg/dm^3. The increases in the adsorption capacities were attributed to an increase in the number of adsorbent particles resulting in many adsorption active sites being occupied. The magnitudes of the adsorption capacities for the mixed metal oxides were in the order MFC > MF > MC. This suggests that the MFC ternary metal oxide had the highest affinity for the Cr(VI) oxyanions with the MC binary metal oxide exhibiting the least affinity for the adsorbate particles.

The pseudo-first-order rate constants, k_1 (1/min), for the MC, MF and MFC oxides decreased with an increase in the initial bulk concentration at a fixed adsorbent mass. The noted decreases in the k_1 (1/min) values for each metal oxide adsorbent were: MC, 0.4266-0.1758; MF, 0.4014-0.2749; and MFC, 0.4005-0.1589 as the initial Cr(VI) concentration increased from 10-75 mg/dm^3. An interpretation of the units of the rate constants showed that the time needed for the adsorption process to attain equilibrium is given by $1/k_1$. Therefore, the smaller the values of k_1, the longer the time needed to reach adsorption equilibrium at higher initial Cr(VI) concentration (Tan & Hameed, 2017). At high initial adsorbate concentration, the following can increase the time needed to attain equilibrium: (1) an increase in boundary layer resistance which can be a result of an increase in solution viscosity (El Haddad et al., 2013) as the amount of solute per unit volume increases, (2) reduction in concentration driving force due to rapid uptake of Cr(VI), and (3) repulsion and/or steric effects between the adsorbate particles due to crowding around the adsorption active sites or surface saturation. The magnitudes of the k_1 (1/min) values of the metal oxide adsorbents are in the order: MC > MF > MFC. For example, at an initial Cr(VI) concentration of 10 mg/dm^3 the k_1 (1/min) values for each of MC, MF and MFC metal oxides were 0.4266, 0.4014 and 0.4005, respectively. The observed difference in the rate constant values might be due to the varying sizes of the adsorbent particles. The results from transmission electron microscopy showed that the average particle diameters of the metal oxides were: MC, 0.60 nm; MF, 0.62 nm and MFC, 0.90 nm. Therefore, the smaller the

adsorbent particles, the larger the k_1 (1/min) values. The same result was reported by Vincent and co-workers (2014) on adsorption of thallium(I) onto Prussian Blue-alginate composite adsorbent. Smaller particles have larger exposed surface areas and this reduces the distance that the adsorbate needs to travel to access the adsorption active sites (pore length), shortening the time needed for the adsorption process to attain equilibrium (Sutherland & Venkobachar, 2010).

The pseudo-second-order rate constants, k_2 (g/mg.min), for the MC, MF and MFC metal oxide adsorbents showed a decrease as the initial pollutant concentration was increased. The k_2 (g/mg.min) values for the metal oxides decreased as follows: MC, 0.0559-0.0501; MF 0.0409-0.0348; and MFC, 0.0386-0.0351, as the initial pollutant concentration increased from 10-75 mg/dm^3. The larger the k_2 value, the shorter the time needed to reach equilibrium ($1/k_2$), at high initial concentrations of the adsorbate. A comparison of the k_2 (g/mg.min) values for the MC, MF and MFC metal oxides at an initial Cr(VI) concentration of 10 mg/dm^3, showed that they were in the order: MC (0.0559) > MF (0.0409) > MFC (0.0386). The adsorbent particle sizes followed an opposite order, with MC oxide particles being the smallest and MFC oxide particles being the largest. The noted variations in the magnitudes of the pseudo-second-order rate constants were attributed to variations in the size of adsorbent particles, that is, the smaller the adsorbent particle size, the larger the exposed number of adsorption active sites, resulting in shorter equilibrium attainment periods, hence larger k_2 values. The pseudo-second-order initial adsorption rate constants, h (mg/g.min) for the MC, MF and MFC metal oxides increased as the initial bulk concentration increased. The h (mg/g.min) values increased as follows: MC, 7.99-20.12; MF, 9.40-18.33; and MFC, 10.70-26.19 as the initial concentration of Cr(VI) increased from 10-75 mg/dm^3. The increase in the pseudo-second-order initial rate constant as the initial bulk concentration is increased is attributed to an increase in collision frequency between the adsorbent and absorbate increasing the initial rate of adsorption. At an initial Cr(VI) concentration of 10 mg/dm^3, the magnitude of the h (mg/g.min) values for the metal oxides were in the order: MFC (10.70) > MF (9.40) > MC (7.99). A higher initial adsorption rate constant suggests greater affinity by the adsorbent's surface for the pollutant.

The modelling of the experimental kinetic data using the Elovich equation showed that the model parameters, that is, the initial adsorption rate constant, α (mg/g.min) and the adsorption constant, β (mg/g) increased as the initial concentration of Cr(VI) was increased. The magnitudes of the initial adsorption rate constants, α (mg/g.min) for the metal oxides increased in the following ranges: MC, 51.42-1206.45; MF, 53.14-367.83; and MFC, 71.22-350.74, as

the initial bulk concentration was increased from 10-75 mg/dm^3. The observed increases in the adsorption constants, β (mg/g) for the metal oxides as the initial adsorbate concentration increased from 10-75 mg/dm^3 were: MC, 0.52-0.65; MF, 0.49-0.70; and MFC, 0.47-0.73. The noted increases of the Elovich kinetic parameters were attributed to an increase in the number of adsorbate particles due to an increase in the initial bulk concentration, increasing the number of occupied adsorption active sites. The increases of the initial adsorption rate, α (mg/g.min) and the adsorption constant, β (mg/g) were both in the order: MFC > MF > MC and can be correlated with the adsorbent's surface affinity for the adsorbate.

The suitability of the kinetic models in describing the adsorption kinetics of Cr(VI) removal using the MC, MF and MFC metal oxides was determined by use of the coefficient of determination, R^2 and the percentage variable error, *% variance* error functions together with the kinetic isotherm plots in Figs 5.6a-c. The kinetic isotherms compare the agreement between the experimental adsorption capacities, q_e (mg/g)(*exp*), and the modelled adsorption capacities, q_e (mg/g) for the adsorption process. For the adsorption kinetics on the MC oxide, the pseudo-first-order model R^2 values were lower (0.9076-0.9498), while the *% variance* values were higher (0.9089-4.0629), the pseudo-second-order model R^2 values were lower (0.9762-0.9874) and the *% variances* were slightly higher (0.2281-9.9942), the Elovich model R^2 values were higher (0.9891-0.9903) and the *% variances* were lower (0.1971-0.4325). The error functions and kinetic isotherm plots comparing the experimental q_e (mg/g) and the modelled q_e (mg/g) in Fig 5.6a show that the Elovich equation is more suited to describe the adsorption kinetics of Cr(VI) on the MC oxide than either the pseudo-first- or pseudo-second-order models. This implies that the adsorption removal might be chemisorption and that the MC adsorbent surface is heterogeneous.

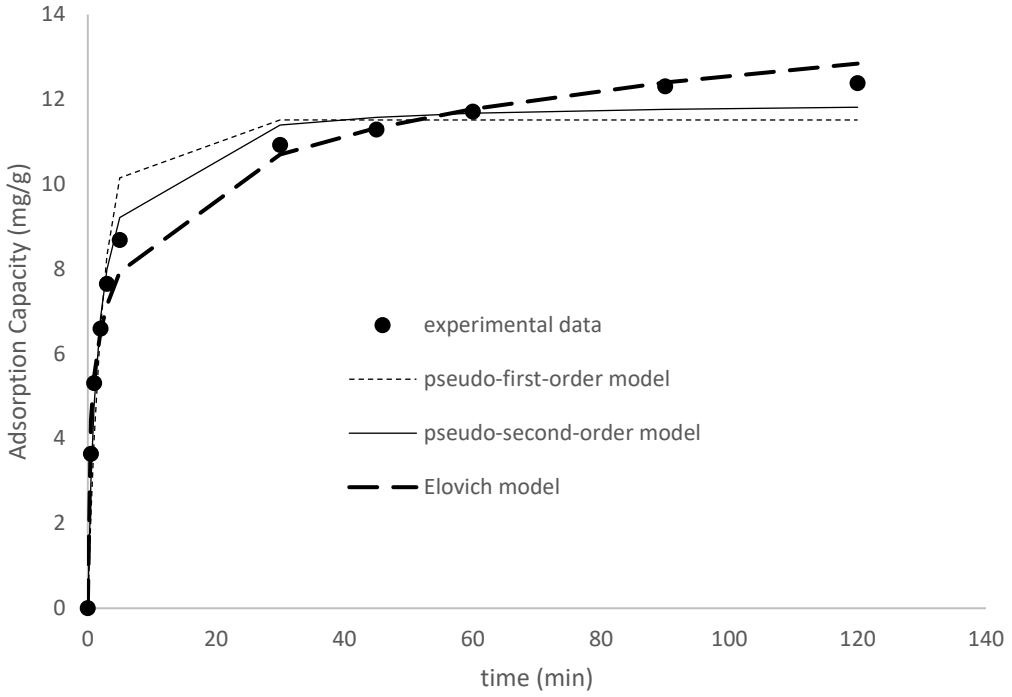

Fig 5.6a A comparison of predicted adsorption capacities of kinetic models with experimental data for Cr(VI) adsorption on MC binary metal oxide.

For the adsorption kinetics on the MF oxide, the pseudo-first-order model had lower R^2 values (0.9277-0.9580) and higher *% variances* (1.3042-4.4331), the pseudo-second-order model had high R^2 values (0.9827-0.9917) and lower *% variances* (0.2665-0.9922), with Elovich R^2 values between 0.9768-0.9865 and *% variance* values between 0.3996-0.9963. The error functions and the plot of the kinetic isotherms comparing the experimental q_e (mg/g) and the modelled q_e (mg/g) in Fig 5.6b show that the pseudo-second-order model was more suited to describing the adsorption kinetics of the Cr(VI) onto the MF oxide. The adsorption of the pollutant might be taking place following a chemisorption mechanism.

For the adsorption kinetics on MFC oxide, the pseudo-first-order model R^2 values were lower (0.9416-0.9846) and the *% variance* values were higher (1.2033-2.9266), the pseudo-second-order model R^2 values were higher (0.9814-0.9977) and the *% variance* values were lower (0.1401-0.6455), the Elovich model R^2 values were lower (0.9419-0.9900) and the *% variances* were higher (0.3467-4.5484). The error functions and the kinetic isotherm plots which compare the experimental q_e (mg/g) and the modelled q_e (mg/g) in Fig 5.6c, showed that the pseudo-second-order model was better suited in the description of the Cr(VI) adsorption kinetics on MFC adsorbent. The adsorption might be following a chemisorption mechanistic model.

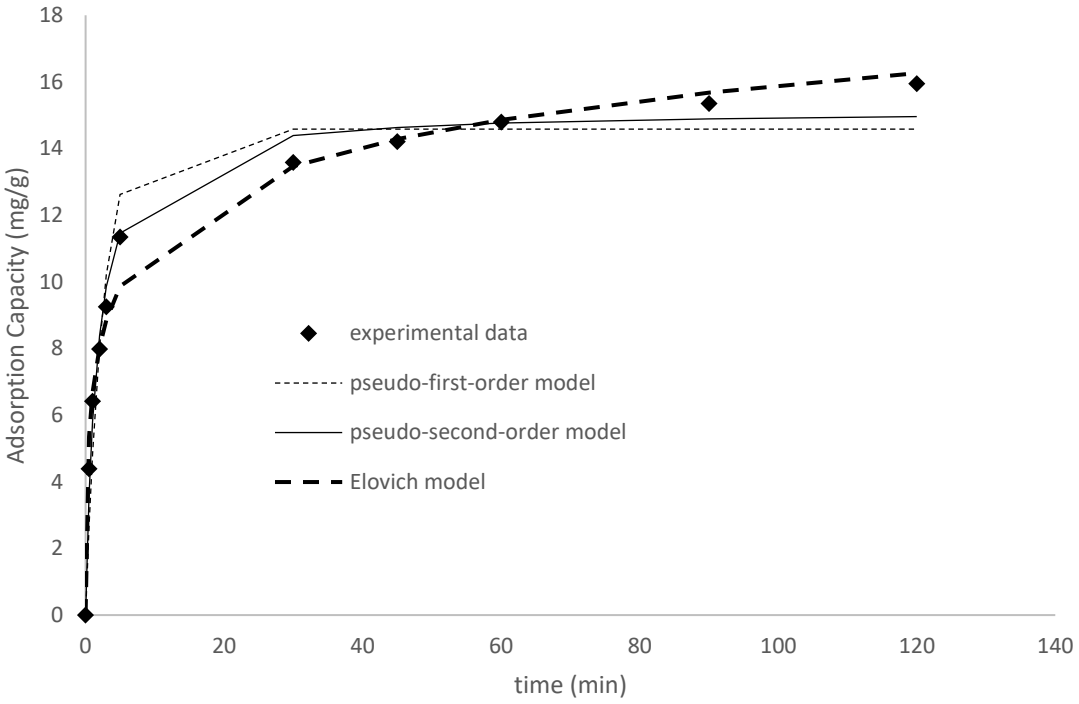

Fig 5.6b A comparison of predicted adsorption capacities of kinetic models with experimental data for Cr(VI) adsorption on MF binary metal oxide.

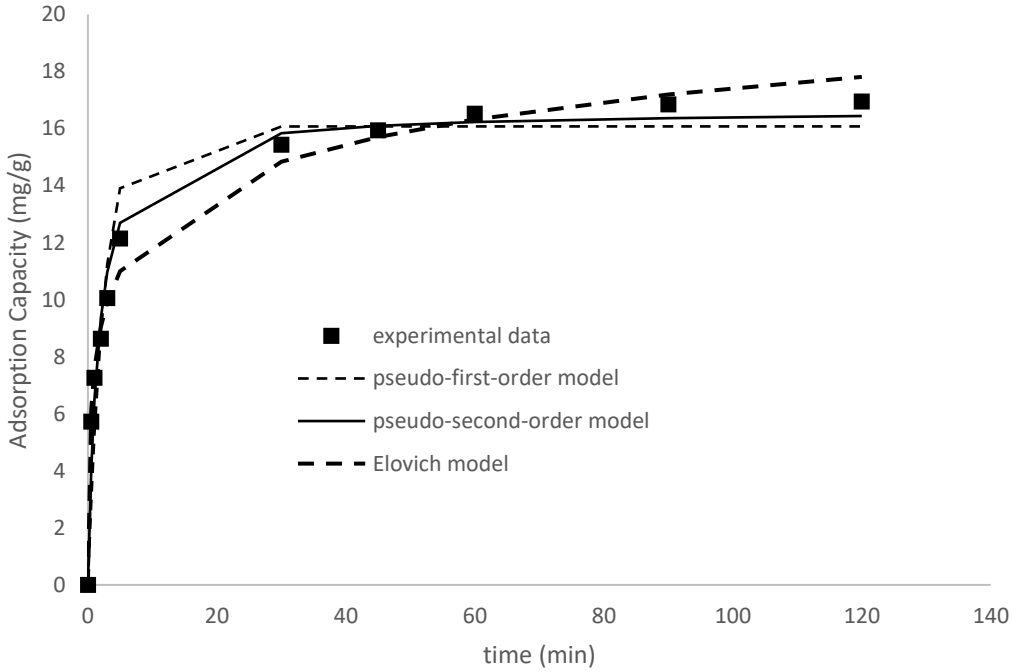

Fig 5.6c A comparison of predicted adsorption capacities of kinetic models with experimental data for Cr(VI) adsorption on MFC ternary metal oxide.

The kinetic isotherm plots in Figs 5.6a-c show that the pseudo-first-order model was in agreement with the experimental data only in the initial 5 minutes and not for the entire adsorption process for the MC, MF and MFC metal oxide adsorbents. The deviation of the pseudo-first-order model from the experimental data after the initial 5 minutes was attributed to a change in the mechanism, probably from film diffusion to pore diffusion (Hokkanen et al., 2015). This might be due to a decrease in the concentration gradient of the adsorbate between the bulk solution and the surface of the adsorbent caused by the rapid uptake of the adsorbent as there are many vacant adsorption sites during this initial stage of the adsorption process (Ofomaja, 2010a). This phenomenon can affect the transport of adsorbate species across the boundary layer to the adsorbent surface (Ofomaja, 2011).

Arsenic(III): The obtained kinetic parameters are presented in Tables 5.2a-c. The results show an increase in the values of the experimental, pseudo-first-order and pseudo-second-order adsorption capacities, q_e (mg/g) with an increase in the initial concentration of As(III) from 10-75 mg/dm^3, at a fixed dose of each of the MC, MF and MFC metal oxide adsorbents. The experimental adsorption capacities, q_e (mg/g) increased in the ranges: MC, 11.01-24.71; MF, 8.94-21.91; and MFC, 15.89-29.87; the pseudo-first-order adsorption capacities, q_e (mg/g) increased in the ranges: MC, 10.29-23.30; MF, 8.32-20.45; and MFC, 14.89-27.55; and the pseudo-second-order adsorption capacities, q_e (mg/g) increased in the ranges: MC, 10.72-23.30; MF, 8.68-21.35; and MFC, 15.55-28.84 as the initial As(III) concentration increased from 10-75 mg/dm^3.

Table 5.2a Kinetic modelling of different concentrations of As(III) adsorption on MC binary metal oxide at 299 K.

Kinetic model	Parameters	As(III) concentration (mg/dm^3)				
		10	20	25	50	75
	q_e (mg/g) (*exp*)	11.01	14.95	17.68	21.67	24.71
pseudo-first-order	q_e (mg/g)	10.29	14.06	16.51	20.40	23.30
	k_1 (1/min)	0.7091	0.8359	1.2906	1.1646	1.5504
	R^2	0.9516	0.9647	0.9723	0.9608	0.9709
	% variance	0.6337	0.8456	0.8559	1.8596	1.7154
pseudo-second-order	q_e (mg/g)	10.72	14.64	17.21	21.26	24.20
	k_2 (g.mg.min)	0.1258	0.1132	0.1089	0.0944	0.0922
	h (mg/g.min)	14.56	24.26	32.25	42.67	53.99
	R^2	0.9937	0.9955	0.9967	0.9964	0.9979
	% variance	0.0824	0.1088	0.1018	0.1689	0.1249
Elovich equation	α (mg/g.min)	287.74	468.93	616.31	981.07	1174.27
	β (mg/g)	0.90	0.78	0.71	0.64	0.59
	R^2	0.9736	0.9563	0.9587	0.9654	0.9696
	% variance	0.3458	1.0481	1.2728	1.6394	1.7919

Table 5.2b Kinetic modelling of different concentrations of As(III) adsorption on MF binary metal oxide at 299 K.

Kinetic model	Parameters	As(III) concentration (mg/dm^3)				
		10	20	25	50	75
	q_e (mg/g) (*exp*)	8.94	11.98	15.35	18.54	21.91
pseudo-first-order	q_e (mg/g)	8.32	11.14	13.87	17.07	20.45
	k_1 (1/min)	0.8832	1.1948	1.1195	1.3640	1.4360
	R^2	0.9722	0.9435	0.9080	0.9318	0.9545
	% variance	0.2344	0.8037	2.0727	2.2396	2.1176
pseudo-second-order	q_e (mg/g)	8.68	11.66	14.57	17.87	21.35
	k_2 (g.mg.min)	0.1661	0.1649	0.1214	0.1237	0.1121
	h (mg/g.min)	12.51	22.42	25.77	39.50	51.09
	R^2	0.9971	0.9926	0.9967	0.9969	0.9944
	% variance	0.0247	0.1053	0.0525	0.4311	0.2596
Elovich equation	α (mg/g.min)	398.31	540.47	723.05	929.16	1298.77
	β (mg/g)	1.23	1.06	0.79	0.73	0.69
	R^2	0.9515	0.9797	0.9739	0.9885	0.9515
	% variance	0.4084	0.2877	0.1374	0.3785	0.4084

Table 5.2c Kinetic modelling of different concentrations of As(III) adsorption on MFC ternary metal oxide at 299 K.

Kinetic model	Parameters	As(III) concentration (mg/dm^3)				
		10	20	25	50	75
	q_e (mg/g) (*exp*)	15.89	18.13	20.78	23.98	29.87
pseudo-first-order	q_e (mg/g)	14.89	17.08	19.49	22.23	27.55
	k_1 (1/min)	0.8212	1.0311	1.1317	1.3052	1.3639
	R^2	0.9615	0.9561	0.9498	0.9419	0.9283
	% variance	1.0487	1.4752	2.2209	3.2214	6.1648
pseudo-second-order	q_e (mg/g)	15.55	17.85	20.36	23.25	28.84
	k_2 (g.mg.min)	0.1037	0.0962	0.0854	0.0834	0.0735
	h (mg/g.min)	25.07	30.65	35.40	45.08	61.13
	R^2	0.9965	0.9967	0.9953	0.9913	0.9962
	% variance	0.0957	0.1118	0.2066	0.4816	0.8168
Elovich equation	α (mg/g.min)	521.47	722.49	935.66	1407.52	1610.63
	β (mg/g)	0.68	0.66	0.57	0.57	0.44
	R^2	0.9617	0.9708	0.9734	0.9838	0.9879
	% variance	1.0429	0.9818	1.1762	0.8996	1.0385

The increases in the adsorption capacities with an increase in the initial concentration of the As(III) was ascribed to an increase in occupancy of adsorption active sites due to an increase in the number of adsorbate particles and concentration gradient between the adsorbent surface and the bulk solution (Vieira et al., 2017). The adsorption capacities of the As(III) increased rapidly for the MC, MF and MFC metal oxide adsorbents in the initial 30 minutes of the adsorption process and thereafter became almost constant probably due to (1) saturation of adsorption active sites, (2) decrease in concentration gradient due to the initial rapid uptake of the As(III), and (3) repulsion and/or steric effects between adsorbed As(III) species and those in the bulk solution reducing access of adsorbate particles to the adsorption active sites (Nashine & Tembhurkar, 2016; Zhang et al., 2016). The magnitudes of the As(III) adsorption capacities for the mixed metal oxides were in the order MFC > MF > MC at all initial concentrations of the As(III). This suggests that the MFC ternary metal oxide had the highest affinity for the As(III) with the MF binary metal oxide exhibiting the least affinity for the adsorbate particles. The kinetic isotherm plots on Figs 5.7a-c, compare the agreement between the experimental adsorption capacities, q_e (mg/g)(*exp*), and the modelled adsorption capacities, q_e (mg/g) for the adsorption process.

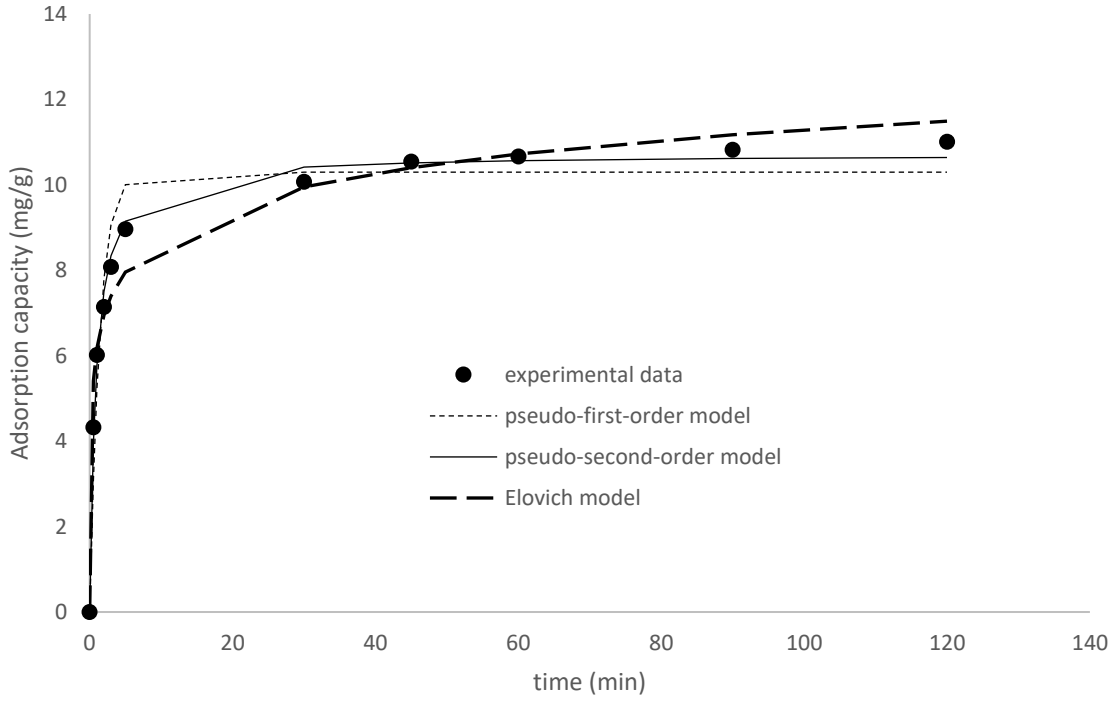

Fig 5.7a A comparison of predicted adsorption capacities of kinetic models with experimental data for As(III) ions adsorption on MC binary metal oxide.

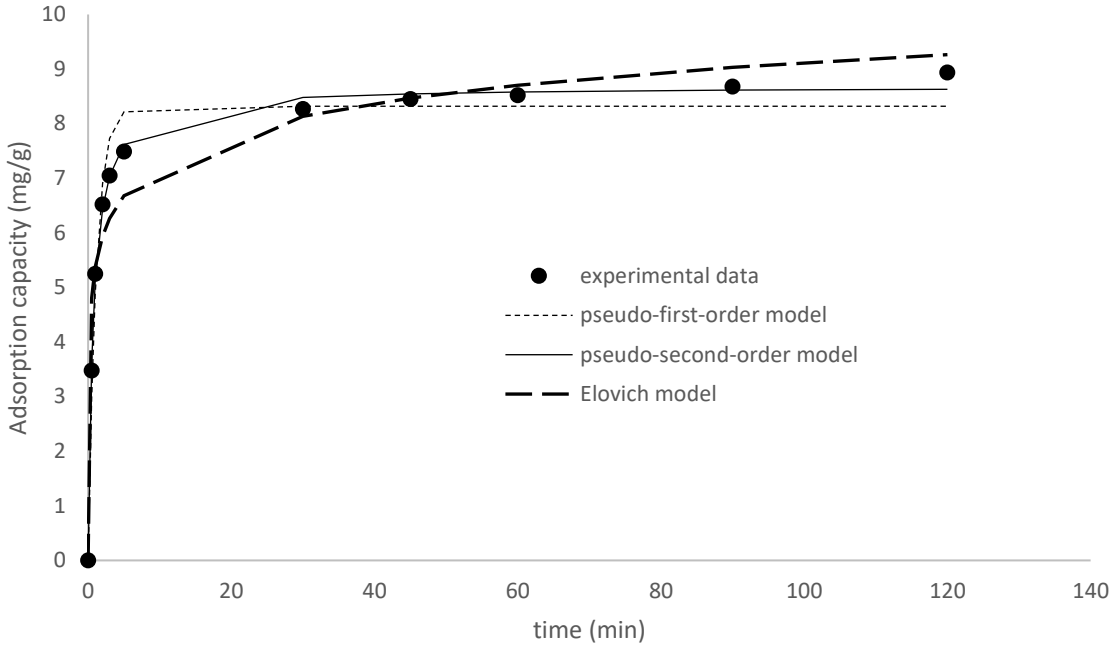

Fig 5.7b A comparison of predicted adsorption capacities of kinetic models with experimental data for As(III) ions adsorption on MF binary metal oxide.

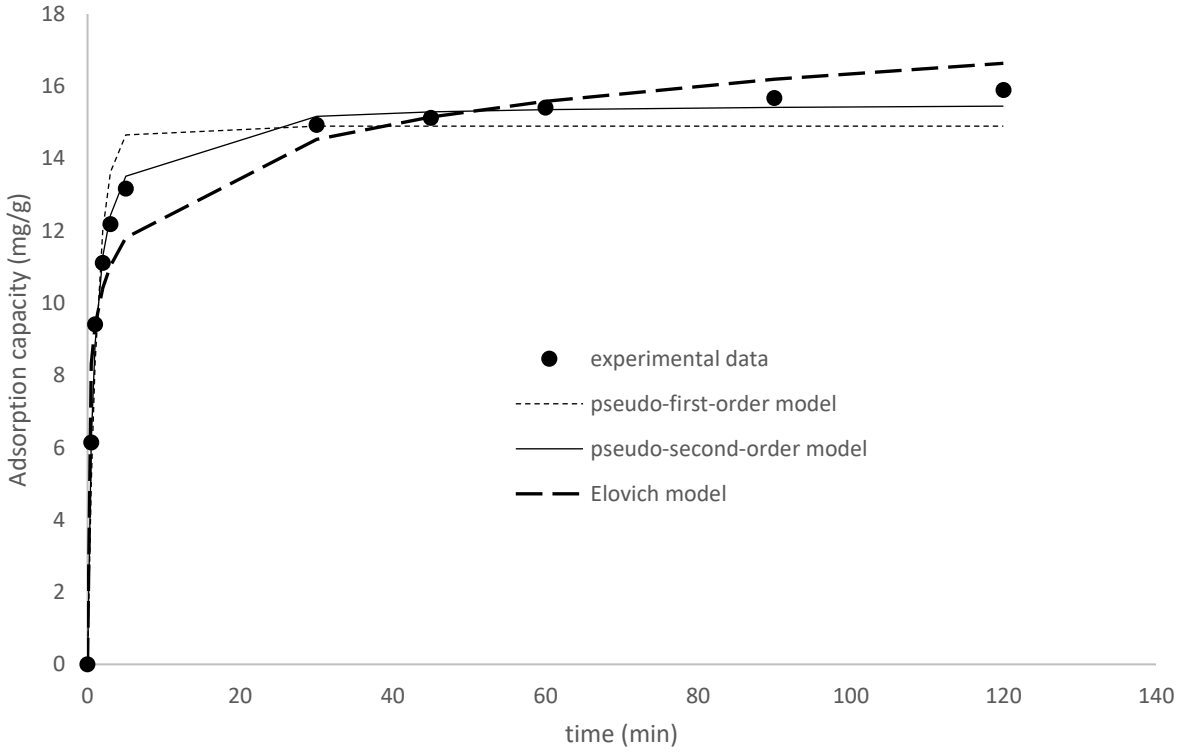

Fig 5.7c A comparison of predicted adsorption capacities of kinetic models with experimental data for As(III) ions adsorption on MFC ternary metal oxide.

The kinetic isotherm plots show good agreement between the pseudo-second-order model and the experimental adsorption capacities at the different initial concentrations of the As(III) for the whole adsorption process. The pseudo-first-order model only shows a good fit with the experimental data in the first 5 minutes of the adsorption process. The same result was reported by Ouma et al. (2018) during the investigation of arsenite adsorption mechanism on pine cone-magnetite composite.

The pseudo-first-order rate constants, k_1 (1/min), for the MC, MF and MFC oxides increased with an increase in the initial As(III) concentration at a fixed adsorbent mass. The increases in the k_1 (1/min) values for each metal oxide adsorbent were: MC, 0.7091-1.5504; MF, 0.8832-1.4360; and MFC, 0.8212-1.3639. The larger the values of k_1, the shorter the time needed to reach adsorption equilibrium at a higher initial concentration of As(III), probably due to a decrease in boundary layer resistance. The magnitudes of the k_1 (1/min) values of the metal oxide adsorbents are in the order: MC > MF > MFC. For example, at an initial As(III) concentration of 75 mg/dm^3, the k_1 (1/min) values for each of MC, MF and MFC metal oxides were 1.5504, 1,4360 and 1.3052, respectively. The difference in the pseudo-first-order rate constants can be attributed to the varying sizes of the adsorbent particles. The smaller the adsorbent particles, the larger the k_1 (1/min) values since smaller adsorbent particles have larger exposed surface areas. This reduces the distance that the adsorbate needs to travel to access the adsorption active sites, shortening equilibration time for the adsorption process (Sutherland & Venkobachar, 2010).

The pseudo-second-order rate constants, k_2 (g/mg.min) for the MC, MF and MFC metal oxide adsorbents showed a decrease as the initial As(III) concentration increased. The k_2 (g/mg.min) values for the metal oxides decreased as follows: MC, 0.1258-0.0922; MF 0.1661-0.1121; and MFC, 0.1037-0.0735, as the initial As(III) concentration increased from 10-75 mg/dm^3. The larger the k_2 value, the shorter the time needed to reach equilibrium ($1/k_2$), at high initial concentrations of the adsorbate. The pseudo-second-order initial adsorption rate constants, h (mg/g.min) for the MC, MF and MFC metal oxides increased as the initial As(III) concentration increased from 10-75 mg/dm^3. The h (mg/g.min) values increased as follows: MC, 14.56-53.99; MF, 12.51-51.09; and MFC, 25.07-51.09. The increase in the pseudo-second-order initial rate constant as the initial bulk concentration is increased is attributed to an increase in collision frequency between the adsorbent and absorbate. The MFC metal oxide adsorbent had higher h (mg/g.min) values at all initial concentrations of As(III) and the MF metal oxide

adsorbent had the least. A higher initial adsorption rate constant suggests greater affinity by the adsorbent's surface for the pollutant.

The modelling of the experimental kinetic data using the Elovich equation showed that the initial adsorption rate constant, α (mg/g.min), increased and the adsorption constant, β (mg/g), decreased as the initial concentration of As(III) was increased from 10-75 mg/dm^3. The magnitudes of the initial adsorption rate constants, α (mg/g.min) for the metal oxides increased in the following ranges: MC,287.74-1174.27; MF, 398.31-1298.77; and MFC, 521.47-1610.63. The observed decreases in the adsorption constants, β (mg/g) for the metal oxides were: MC,0.90-0.59; MF, 1.23-0.69; and MFC, 0.68-0.44. The increases of the initial adsorption rate constant, α (mg/g.min) with an increase in the initial concentration of As(III) is attributed to an increase in the number of adsorbate particles increasing the number of occupied adsorption active sites. The decrease of the surface coverage adsorption constant, β (mg/g) can be due to desorption of the adsorbate at higher concentrations.

The coefficient of determination, R^2 and the percentage variable error, *% variance* statistical error functions were applied to the modelled experimental kinetic data in order to determine the model best suited to describe the adsorption kinetics of the As(III) onto the MC, MF and MFC metal oxides. The results for the error functions are presented in Tables 5.5a-c. For the pseudo first-order model: $0.9516 < R^2 < 0.9723$ and $0.6337 <$ *% variance* < 1.8596 for the MC oxide; $0.9080 < R^2 < 0.9722$ and $0.2344 <$ *% variance* < 2.2396 for the MF oxide; and $0.9283 < R^2 < 0.9615$ and $1.0487 <$ *% variance* < 6.1648 for the MFC oxide. For the pseudo second-order model: $0.9937 < R^2 < 0.9979$ and $0.0824 <$ *% variance* < 0.1689 for the MC oxide; $0.9767 < R^2 < 0.9971$ and $0.0247 <$ *% variance* < 0.5257 for the MF oxide; and $0.9862 < R^2 < 0.9967$ and $0.0957 <$ *% variance* < 1.1868 for the MFC oxide. For the Elovich model: $0.9563 < R^2 < 0.9736$ and $0.3458 <$ *% variance* < 1.7919 for the MC oxide; $0.9515 < R^2 < 0.9885$ and $0.1374 <$ *% variance* < 0.4084 for the MF oxide; and $0.9617 < R^2 < 0.9879$ and $0.8996 <$ *% variance* < 1.1762 for the MFC oxide. The error functions show that the pseudo-second-order model showed a good fit to the adsorption kinetics at all initial concentrations of As(III) onto the MC, MF and MFC metal oxide adsorbents, with R^2 close to 1 and *% variance* close to zero. The error functions results and the kinetic isotherm plots show that the adsorption kinetics of As(III) uptake at different initial concentrations onto the MC, MF and MFC metal oxides is best described by the pseudo-second-order model. This suggests that the adsorption process onto the metal oxides might be chemisorption in nature and is controlled by the availability of vacant adsorption active sites

rather than by arsenic concentration as assumed by the pseudo-first-order model (Yoon et al., 2017).

5.2.3.1.2 Diffusion models: External mass transfer, intraparticle diffusion and the Boyd diffusion models

Chromium(VI): The adsorption process involves the mass transportation of adsorbate particles from the bulk solution to the adsorbent's external surface followed by diffusion into the pores of the adsorbent. In aqueous solution, a hydrodynamic film or boundary layer forms around the external surface of the solid adsorbent. The initial step during the adsorption process involves the mass transfer of adsorbate across the hydrodynamic film. The external mass transfer diffusion rate constant, k_s (1/min) was determined by plotting C_t/C_o at different initial concentrations of Cr(VI) against time at 299 K, and the results are presented in Figs 5.8a-c. The variables C_o and C_t represent the initial concentration of Cr(VI) (mg/dm^3) and at time t (mins), respectively. The initial slope of the graph represents the external mass transfer diffusion rate constant and is based on the premise that the C_t/C_o relationship is linear for the first 5 minutes, due to the rapid adsorption of Cr(VI) onto the MF, MC MFC metal oxides during this initial adsorption period. If the C_t/C_o against t plot is a straight line, it implies that film diffusion solely controls the adsorption process.

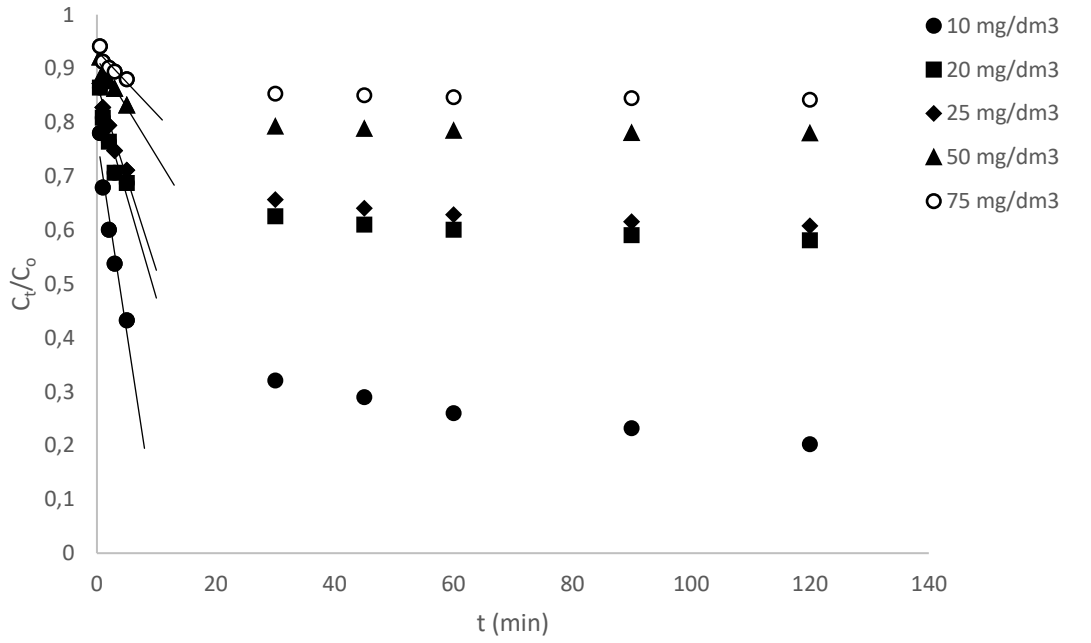

Fig 5.8a External mass transfer diffusion plot for Cr(VI) adsorption onto MF binary metal oxide.

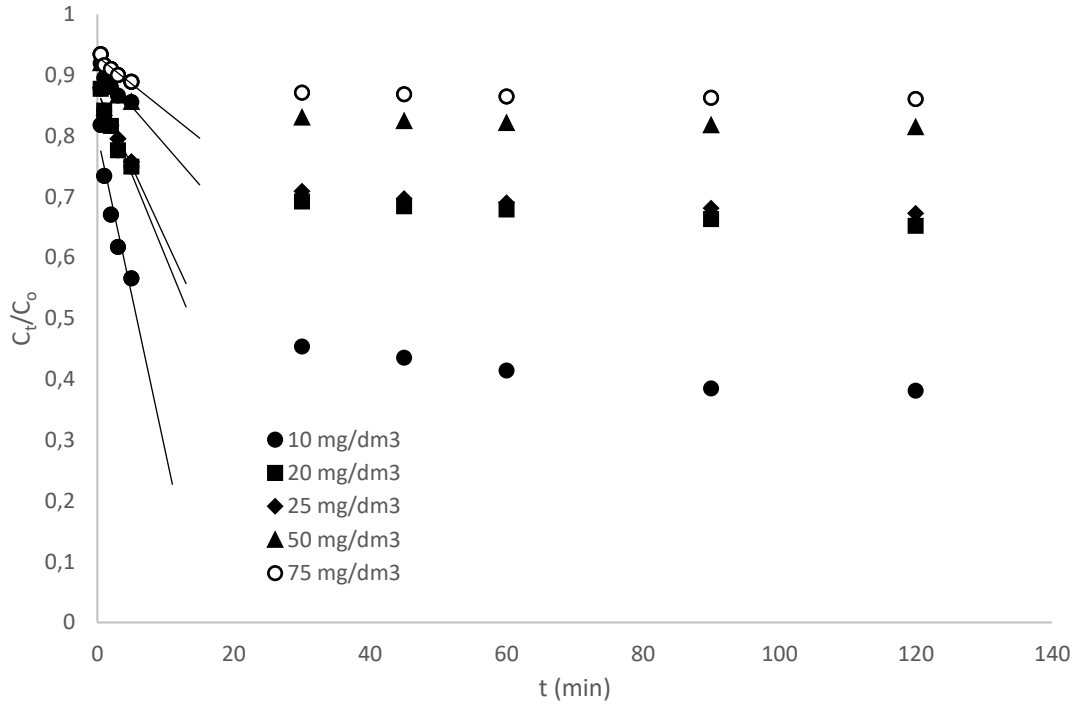

Fig 5.8b External mass transfer diffusion plot for Cr(VI) adsorption onto MC binary metal oxide.

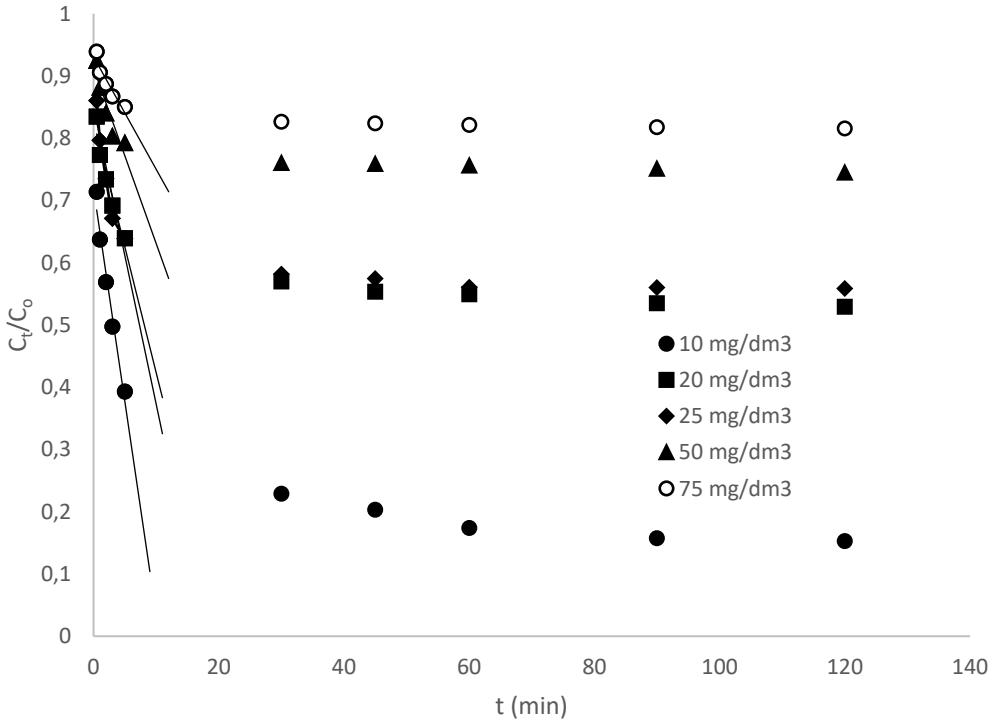

Fig 5.8c External mass transfer diffusion plot for Cr(VI) adsorption onto MFC ternary metal oxide.

Only the initial first section of the external mass transfer diffusion plot is linear, suggesting that film diffusion is not the only rate-controlling step of the adsorption process. The external mass transfer diffusion rate constants for the adsorption processes are presented in Tables 5.3a-c. The k_s (1/min) values for MC, MF and MFC oxides decreased in the ranges 0.0522-0.0090, 0.0682-0.0117 and 0.0774-0.0181, respectively, as the initial concentration of the bulk increased from 10-75 mg/dm^3. The decrease in the magnitudes of the external mass transfer diffusion rate constants due to an increase in initial pollutant concentration is attributed to an increase in resistance across the hydrodynamic film. This might be due to: (1) the increase in the initial adsorbate concentration with a fixed number of adsorbent particles reducing the available surface area for adsorption, increasing boundary effects (Ofomaja, 2011), (2) the wide adsorbent particle size and the tendency of the nanostructured metal oxide particles to agglomerate might increase boundary effects (Ociński et al., 2016), and (3) the increase in solution viscosity as the amount of solute per unit volume increases might also increase resistance across the boundary layer. At initial Cr(VI) concentration of 10 mg/dm^3, the k_s (1/min) values for the oxides were: MC, 0.0522; MF, 0.0682; and MFC, 0.0774. This suggests that external mass transfer during the initial rapid uptake of the pollutant during the adsorption process is more controlling for the MC metal oxide.

The intraparticle diffusion model was applied onto the kinetic experimental data to determine if the rate-determining step in the adsorption process is pore diffusion controlled. The simplified model equation is given as (Weber & Morris, 1963):

$$q_t = k_{id} t^{0.5} + C \tag{5.7}$$

where k_{id} is the rate constant for intraparticle diffusion (mg/g.min$^{0.5}$) and C (mg/g) is a constant which determines the thickness of the boundary layer or surface adsorption. A linear plot of q_t against $t^{0.5}$ gives k_{id} from the slope and C from extrapolation of the linear section to the ordinate intercept. If intraparticle diffusion is the rate-limiting step during the adsorption process, the plot of q_t against $t^{0.5}$, should be linear and pass through the origin.

Table 5.3a Diffusion coefficients for the adsorption of varying concentrations of Cr(VI) onto MC binary metal oxide.

Diffusion parameters	Concentration of Cr(VI) (mg/dm^3)				
	10	20	25	50	75
External mass transfer					
k_s (1/min)	0.0522	0.0274	0.0242	0.0129	0.0090
R^2	0.9347	0.9767	0.9542	0.9459	0.9237
Intraparticle diffusion					
k_{id} ($mg/g.min^{0.5}$)	0.283	0.298	0.321	0.271	0.331
C (mg/g)	9.438	10.622	12.911	15.665	17.874
R^2	0.9549	0.9919	0.9794	0.9686	0.9563
Boyd diffusion model					
($D_1 \times 10^{-17}$) (cm^2/s)	2.135	1.816	1.596	1.482	1.231
R^2	0.9678	0.9807	0.9639	0.9440	0.9546
($D_2 \times 10^{-17}$) (cm^2/s)	6.077	6.303	6.434	7.536	7.736
R^2	0.9500	0.9646	0.9351	0.9735	0.9619

Table 5.3b Diffusion coefficients for the adsorption of varying concentrations of Cr(VI) onto MF binary metal oxide.

Diffusion parameters	Concentration of Cr(VI) (mg/dm^3)				
	10	20	25	50	75
External mass transfer					
k_s (1/min)	0.0682	0.0380	0.0345	0.0181	0.0117
R^2	0.9321	0.9489	0.9874	0.9249	0.9657
Intraparticle diffusion					
k_{id} ($mg/g.min^{0.5}$)	0.423	0.321	0.437	0.441	0.453
C (mg/g)	11.361	13.412	14.972	19.575	20.475
R^2	0.9892	0.9697	0.9708	0.9364	0.9601
Boyd diffusion model					
($D_1 \times 10^{-17}$) (cm^2/s)	2.666	2.546	2.409	2.058	1.798
R^2	0.9829	0.9496	0.9848	0.9787	0.9098
($D_2 \times 10^{-17}$) (cm^2/s)	6.671	7.342	7.661	7.564	8.008
R^2	0.9336	0.9345	0.9591	0.9754	0.9442

Table 5.3c Diffusion coefficients for the adsorption of varying concentrations of Cr(VI) onto MFC ternary metal oxide.

Diffusion parameters	Concentration of Cr(VI) (mg/dm^3)				
	10	20	25	50	75
External mass transfer					
k_s (1/min)	0.0774	0.0477	0.0404	0.0282	0.0181
R^2	0.9127	0.9548	0.9374	0.9766	0.9811
Intraparticle diffusion					
k_{id} ($mg/g.min^{0.5}$)	0.281	0.291	0.214	0.282	0.311
C (mg/g)	14.071	15.776	19.926	22.341	24.367
R^2	0.9026	0.9594	0.9957	0.9753	0.9947
Boyd diffusion model					
($D_1 \times 10^{-17}$) (cm^2/s)	8.467	7.891	6.515	4.837	4.171
R^2	0.9970	0.9834	0.9308	0.9637	0.9546
($D_2 \times 10^{-17}$) (cm^2/s)	1.368	1.679	2.263	2.318	2.122
R^2	0.9673	0.9789	0.9541	0.9192	0.9687

The plots of q_t against $t^{0.5}$ are presented in Figs 5.9a-c and show that the rate-controlling step in the adsorption of Cr(VI) onto the metal oxides is not solely intraparticle diffusion since no linear segment of the graph passes through the origin. The plots are divided into two linear steps suggesting the presence of multiple mechanisms during the adsorption process (Tan & Hameed, 2017). The first, rapid stage is attributed to external surface adsorption controlled by adsorbate migration across the boundary layer to the external surface of the adsorbent. The second, slower stage shows the gradual adsorption of adsorbate particles and is controlled by intraparticle diffusion (Knocke & Hemphill, 1981). The two stages in the intraparticle diffusion plots suggest that the adsorption process is controlled by boundary layer diffusion of adsorbate during the initial stages, which then switches to intraparticle diffusion-controlled adsorption (Sarkar et al., 2014). The switch in the mechanism can be attributed to a decrease in the concentration gradient which increases the boundary effect as the adsorption process proceeds. The results of the calculated intraparticle diffusion parameters are presented in Tables 5.3a-c and reveal that the magnitudes of the k_{id} (mg/g.min$^{0.5}$) and C (mg/g) values increase with an increase in the initial bulk concentration. The same result was reported by Raji and Pakizeh (2014) during the adsorption of Hg(II) on ZnCl_2-MCM-41 adsorbent. The large values of k_{id} (mg/g.min$^{0.5}$) and C (mg/g) signify greater film diffusion resistance, which corresponds with the observed decrease in external mass transfer diffusion rate constants with an increase in the initial concentration of Cr(VI) in solution. A large C (mg/g) value also implies an enhanced influence of surface adsorption to the rate-limiting step. The magnitudes of the intraparticle rate constants at different pollutant concentrations were large for the MF oxide suggesting that intraparticle diffusion was more controlling on this metal oxide during the adsorption.

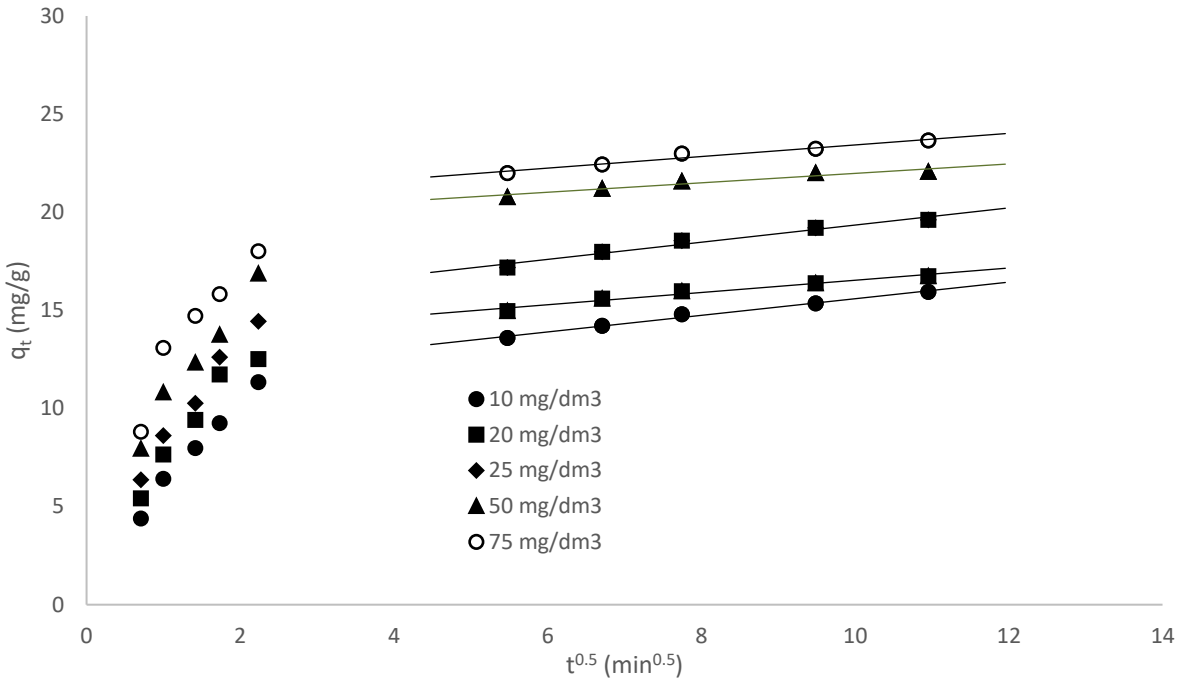

Fig. 5.9a Intraparticle diffusion treatment of Cr(VI) adsorption onto MF binary metal oxide at different initial Cr(VI) concentrations.

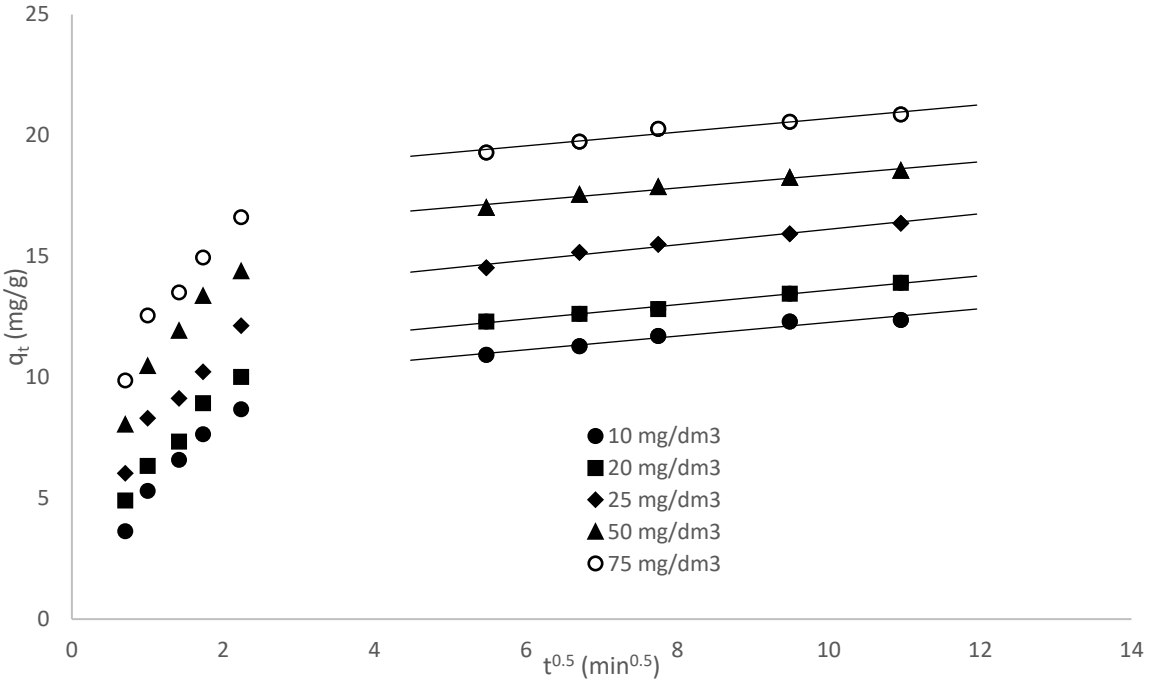

Fig. 5.9b Intraparticle diffusion treatment of Cr(VI) adsorption onto MC binary metal oxide at different initial Cr(VI) concentrations.

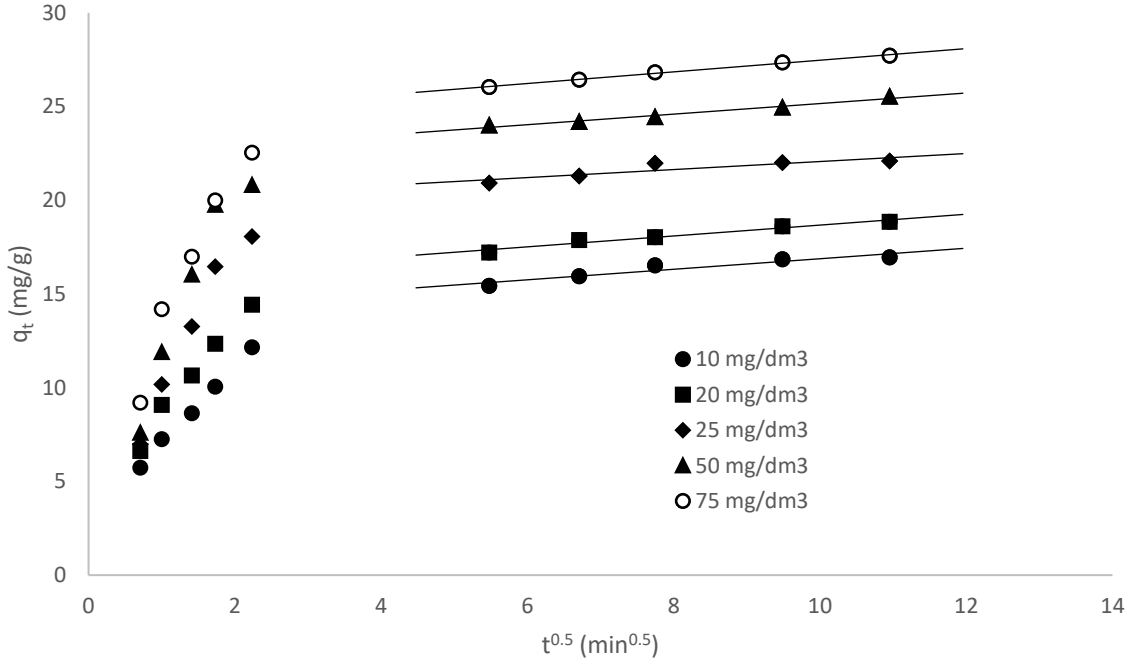

Fig. 5.9c Intraparticle diffusion treatment of Cr(VI) adsorption onto MFC ternary metal oxide at different initial Cr(VI) concentrations.

The effects of film and pore diffusion on the adsorption of Cr(VI) onto the metal oxides were investigated by fitting the kinetic experimental data onto the Boyd model (Boyd et al., 1947), to distinguish between film and intraparticle diffusion-controlled adsorption (Ociński et al., 2016). The model assumes that the adsorbent particles are spherical and that the diffusion follows Fick's second law giving the mathematical relation (Crank, 1975):

$$\frac{q_t}{q_e} = 6\left(\frac{D_t}{a^2}\right)^{0.5}\left\{\pi^{-0.5} + 2\sum_{n=1}^{\infty} ierfc\,\frac{\pi a}{D_t^{0.5}}\right\} - 3\frac{D_t}{a^2} \tag{5.8}$$

where a (cm) is the radius of the adsorbent. When t is small, D is replaced by D_1, and Eq 5.8 reduces to:

$$\frac{q_t}{q_e} = 6\left(\frac{D_1}{\pi a^2}\right)^{0.5} t^{0.5} \tag{5.9}$$

The graphs of fractional uptake, q_t/q_e against the square root of time, $t^{0.5}$ (min$^{0.5}$) are presented in Figs 5.10a-c. The plots are divided into two linear segments. The first initial stage is fast and precedes a much slower uptake stage. The magnitudes of the film diffusion coefficient, D_1

(cm^2/s) for the metal oxides at varying initial concentrations of Cr(VI) were computed from a gradient of the plots of q_t/q_e against $t^{0.5}$, and the results are presented in Tables 5.3a-c.

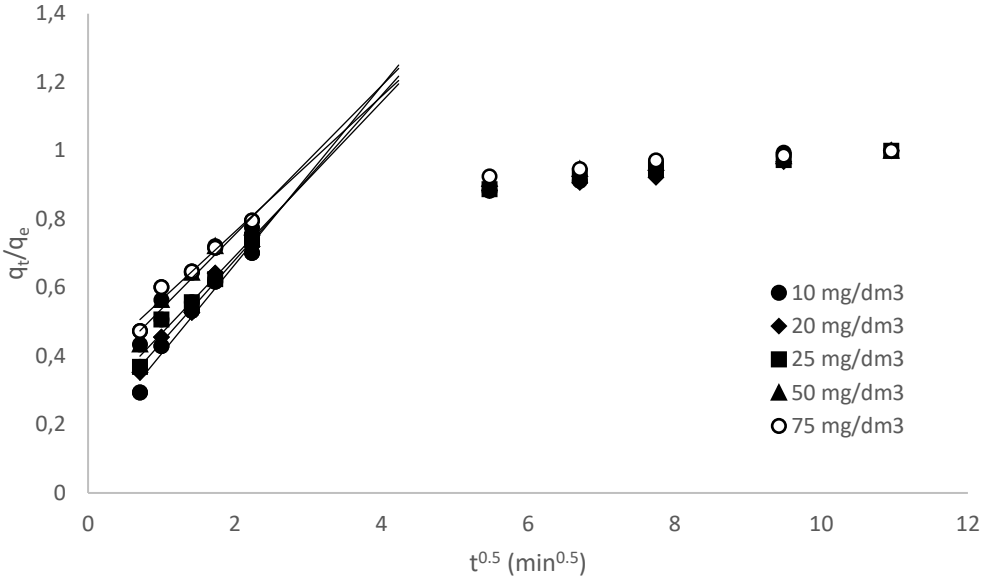

Fig 5.10a Fractional uptake of different concentrations of Cr(VI) on MC binary metal oxide against the square root of time.

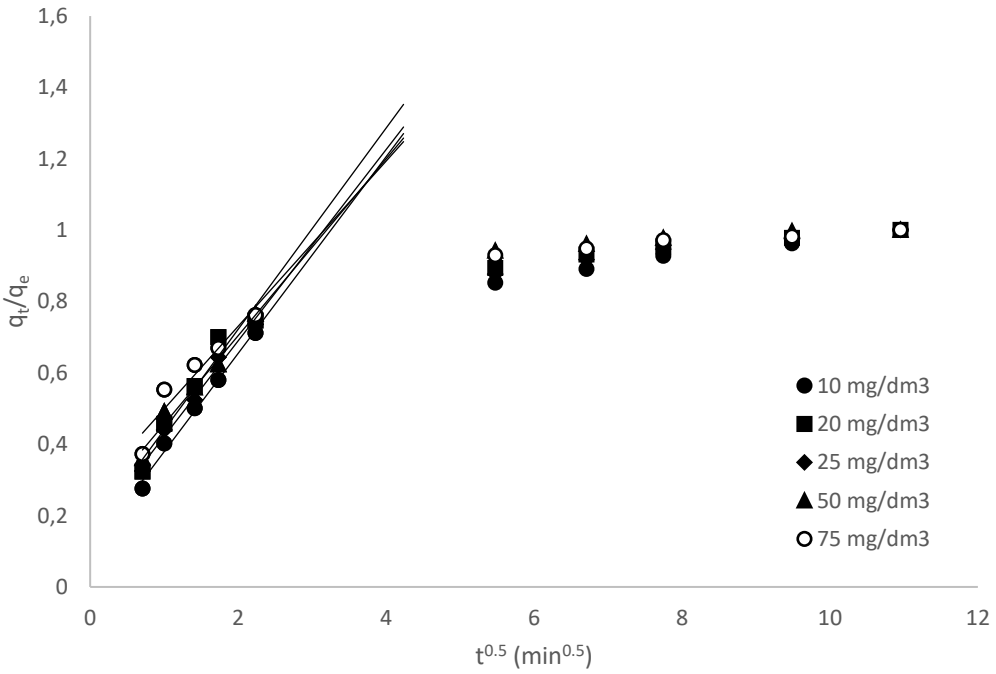

Fig 5.10b Fractional uptake of different concentrations of Cr(VI) on MF binary metal oxide against the square root of time.

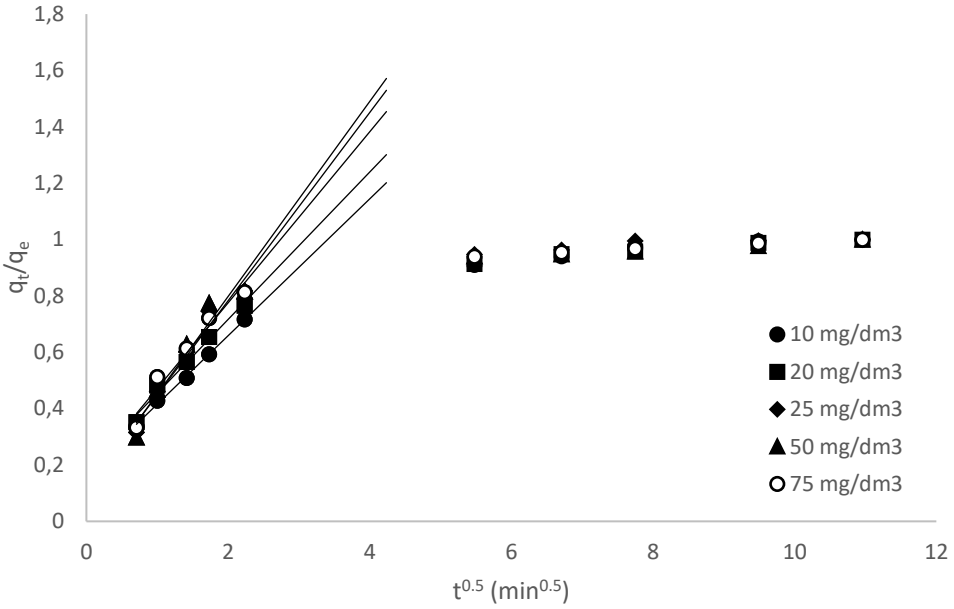

Fig 5.10c Fractional uptake of different concentrations of Cr(VI) on MFC ternary metal oxide against the square root of time.

As *t* becomes large, Eq 5.8 becomes (Boyd's equation):

$$\left(1 - \frac{q_t}{q_e}\right) = \frac{6}{\pi^2} exp\left(\frac{-D_2\pi^2}{a^2} t\right) \tag{5.10}$$

when $B = \pi^2 \frac{D_2}{a^2}$, Eq 5.10 solves to:

$$Bt = -0.4997 - \ln\left(1 - \frac{q_t}{q_e}\right) \tag{5.11}$$

The magnitude of *B* is computed from the gradient of a plot of *Bt* against *t* at different initial Cr(VI) concentrations. The value of *B* is then used to determine the pore diffusion coefficient, D_2 (cm^2/s), from $B = D_2\pi^2/a^2$, and the results are presented in Tables 5.3a-c. The Boyd plots of *Bt* against *t* are used to show whether external mass transport (film) or intraparticle (pore) diffusion controls the adsorption process. If the Boyd plot is linear and cuts through the origin, rate of adsorbate migration is intraparticle or pore diffusion controlled. A non-linear or linear Boyd plot which does not cut through the origin shows that the adsorption process is controlled by a chemical reaction or external mass transport (Cáceres-Jensen et al., 2013). The Boyd plots presented in Figs 5.11a-c, for the MC, MF and MFC metal oxides exhibit linear relationships

which do not pass through the origin during the beginning of the adsorption process. This reveals that external mass transport controls the adsorption process during the initial phase. The y-intercepts for the metal oxides as the initial bulk concentration increased from 10-75 mg/dm^3, were in the ranges: MC, -0.15-0.14; MF, -0.18-(-0.03); and MFC, -0.08-(-0.09). The y-intercept values of the binary MC and MF metal oxides shifted towards positive digits as the initial pollutant concentration increased. This was attributed to an increase in external mass transfer processes. The y-intercept values for the ternary MFC metal oxide shifted towards negative digits suggesting a decrease in external mass transfer processes. The noted differences between the binary and the ternary metal oxides might be due to differences in adsorbent particle sizes and their surface conformations which in turn might affect the boundary effects as the initial Cr(VI) concentration increased. The binary MC metal oxide showed the largest shift of y-intercept values to positive values, implying that as the initial concentration of the Cr(VI) increased, external mass transfer processes on this binary metal oxide were enhanced.

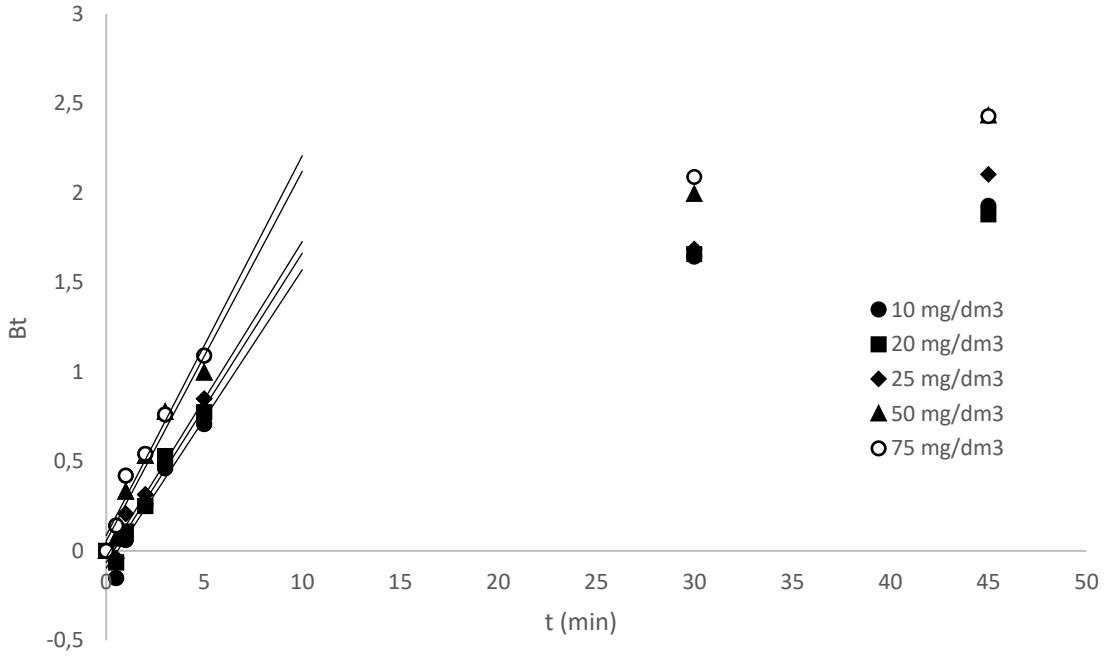

Fig 5.11a Boyd plots for adsorption of different concentrations of Cr(VI) on MC binary metal oxide.

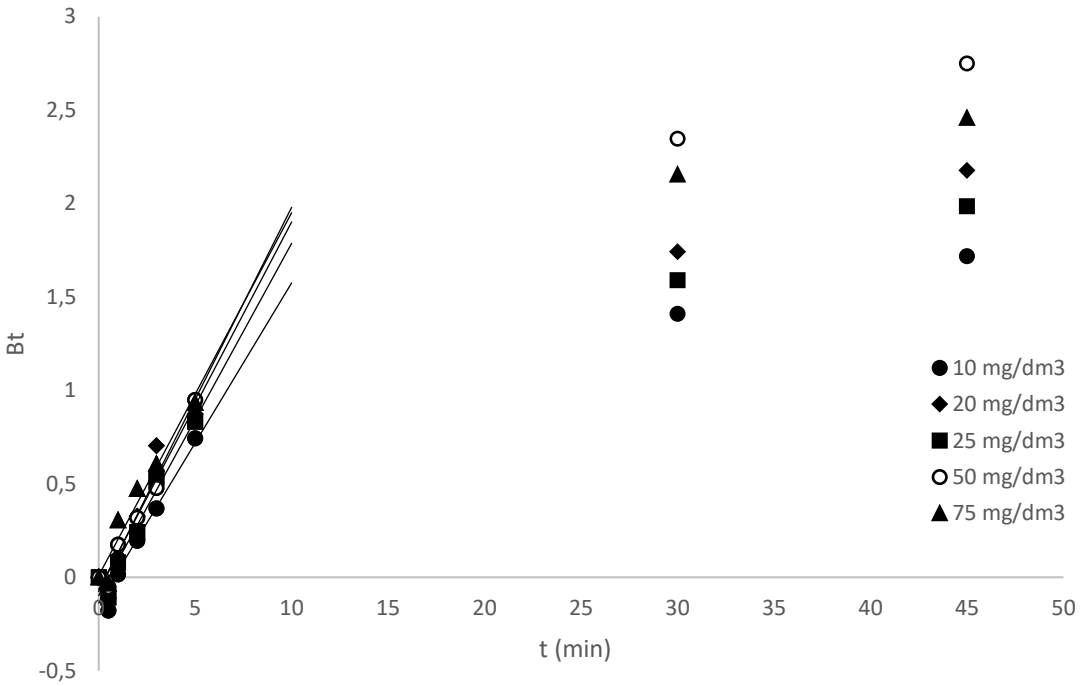

Fig 5.11b Boyd plots for adsorption of different concentrations of Cr(VI) on MF binary metal oxide.

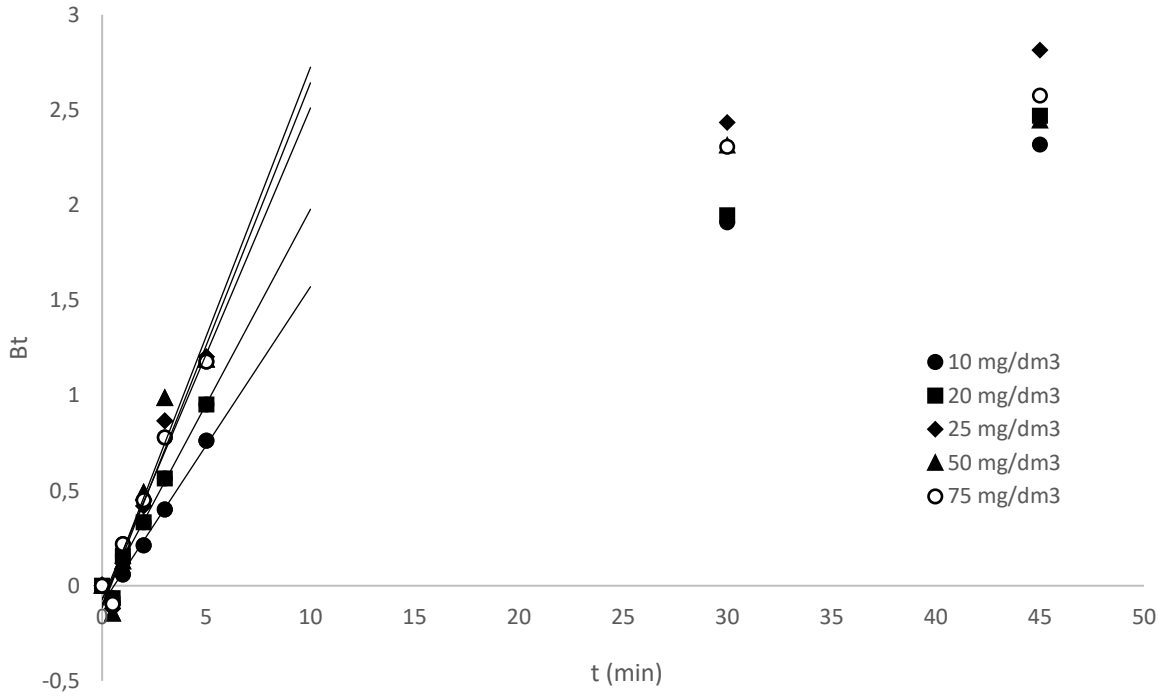

Fig 5.11c Boyd plots for adsorption of different concentrations of Cr(VI) on MFC binary metal oxide.

The film diffusion coefficients, D_1 (cm^2/s), decreased as the initial Cr(VI) concentration increased. The decrease in D_1 (cm^2/s) with increasing initial Cr(VI) concentration can be due to the increase in boundary layer resistance caused by an increase in viscosity as the number of solute particles increase per unit volume. The magnitudes of D_1 (cm^2/s) for the MFC metal oxide were higher than for the MC and MF metal oxides. The larger values of D_1 (cm^2/s) for the MFC metal oxide can be attributed to the larger MFC particle sizes which reduced the external surface area reducing the boundary layer effect. The pore diffusion coefficients, D_2 (cm^2/s), increased with an increase in the initial bulk concentration. The increase of D_2 (cm^2/s) with an increase in initial Cr(VI) concentration was attributed to an increase in the concentration gradient between the bulk solution and the external surface of the metal oxides as the initial pollutant concentration increased facilitating rapid diffusion of adsorbate particles into the pores on the adsorbent surface (Kupeta et al., 2018). The ternary MFC metal oxide exhibited larger D_2 (cm^2/s) values than for the binary MC and MF metal oxides. This suggests that the MFC surface was more porous or had pores of the right sizes to accommodate entry of the Cr(VI) oxyanions, enabling faster diffusion of the adsorbate particles into the pores. The diffusion coefficients of the metal oxides presented in Table 5.3a-c show that D_2 (cm^2/s) > D_1 (cm^2/s). This implies that the adsorbate particles encountered greater resistance to diffuse through the hydrodynamic film than to diffuse into the pores, suggesting that film diffusion controls the adsorption process at this stage.

Arsenic(III): The external mass transfer diffusion plots and rate constants, k_s (1/min) for the adsorption at different initial concentrations of As(III) onto MC, MF and MFC metal oxides are presented in Figs 5.12a-c and Tables 5.4a-c, respectively. The k_s (1/min) values for MC, MF and MFC oxides decreased in the ranges 0.0095-0.0021, 0.0079-0.0018 and 0.0136-0.0024, respectively, as the initial concentration of the As(III) increased from 10-75 mg/dm^3. The k_s (1/min) decreased due to an increase in boundary layer resistance. The increase in boundary layer resistance is attributed to: (1) an increase in solution viscosity caused by an increase in As(III) concentration, and (2) as the initial adsorbate concentration increases, with a fixed number of adsorbent particles, the available surface area for adsorption becomes smaller, increasing resistance across the hydrodynamic film (Ofomaja, 2011). The low k_s (1/min) values for the MF oxide showed that external mass transfer of As(III) at the different initial adsorbate concentrations was more controlling for this metal oxide and least for the MFC metal oxide. This might be due to the differences in adsorbent particle sizes, surface conformation and extend of agglomeration of the nanometal oxides particles.

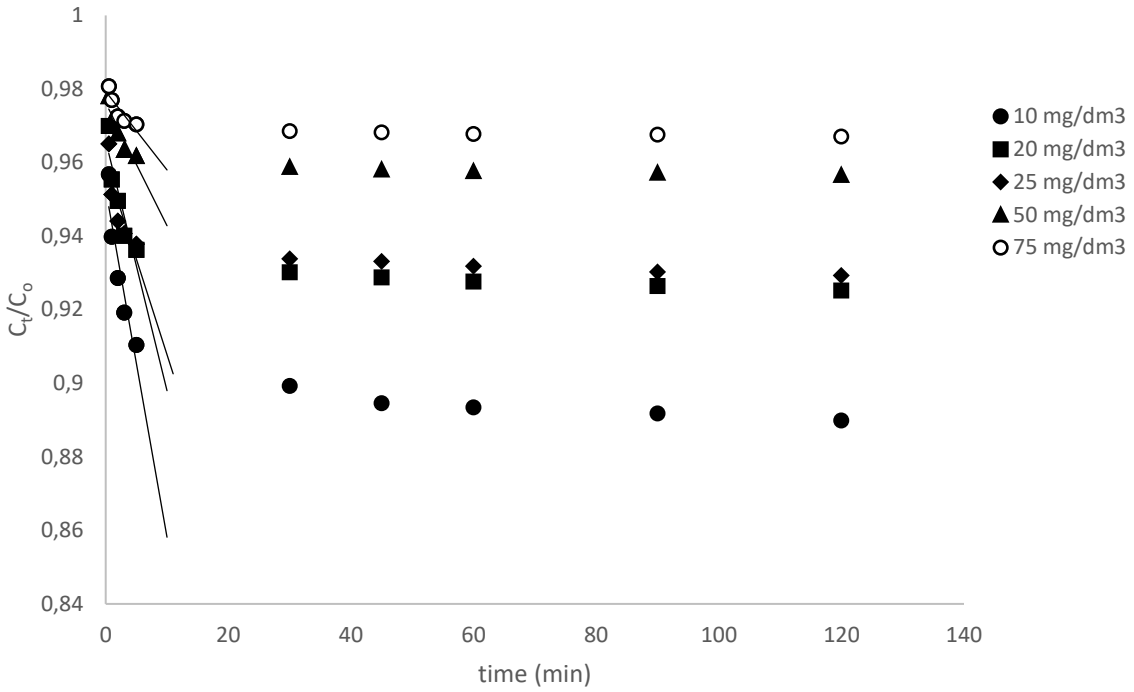

Fig 5.12a External mass transfer diffusion plot for adsorption of different initial concentrations of As(III) adsorption onto MC binary metal oxide at 299 K.

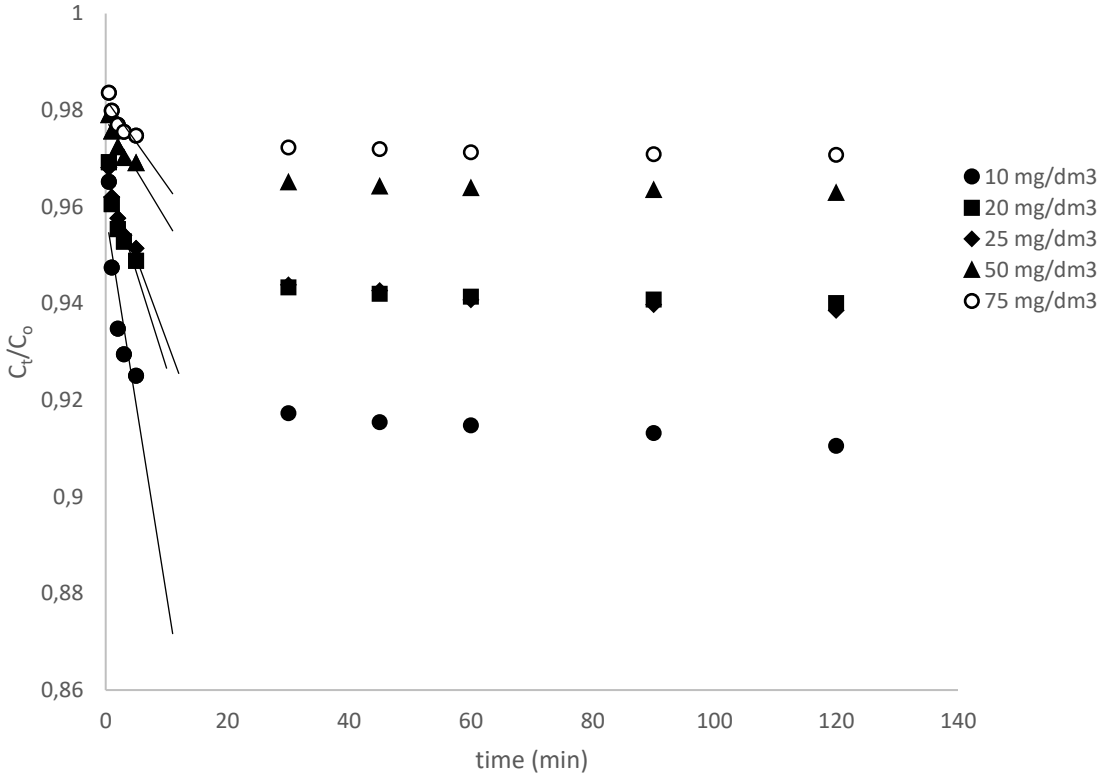

Fig 5.12b External mass transfer diffusion plot for adsorption of different initial concentrations of As(III) onto MF binary metal oxide at 299 K.

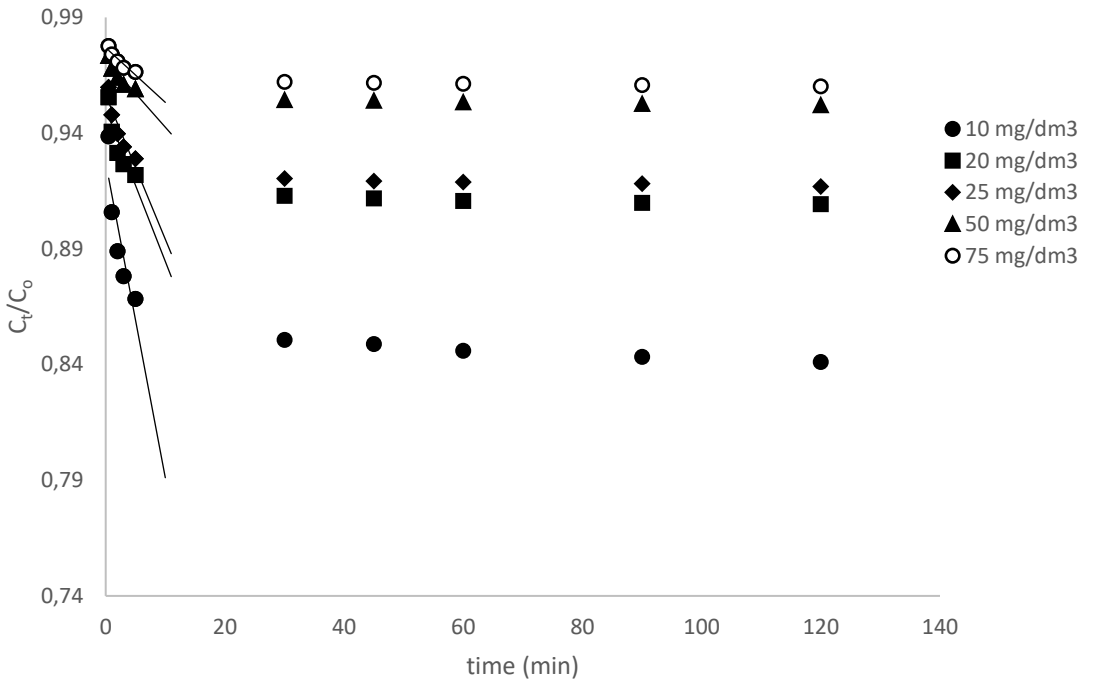

Fig 5.12c External mass transfer diffusion plot for adsorption of different initial concentrations of As(III) onto MFC ternary metal oxide at 299 K.

The intraparticle diffusion model equation (Eq 5.7) (Weber & Morris, 1963) was applied onto the kinetic experimental data to determine if the rate-determining step in the adsorption of varying concentrations of As(III) is pore diffusion controlled. The intraparticle diffusion plots of q_t against $t^{0.5}$ are presented in Figs 5.13a-c and show that intraparticle diffusion is not the only rate-controlling step in the adsorption of As(III) onto the MC, MF and MFC metal oxides. The plots are split into two linear sections, and none of them passes through the origin, showing that several mechanisms control the adsorption process. The initial rapid stage is attributed to external surface adsorption controlled by external mass transport since diffusion across the boundary layer to the adsorbent surface is only important at the beginning of the adsorption process (Cáceres-Jensen et al., 2013). The second stage signifies the slow adsorption of the adsorbate particles and is intraparticle diffusion-controlled. The switch in the adsorption mechanism can be ascribed to a decrease in the concentration driving force which increases the boundary effect as the adsorption process proceeds. The results of the calculated intraparticle diffusion parameters and the R^2 error functions are presented in Tables 5.4a-c.

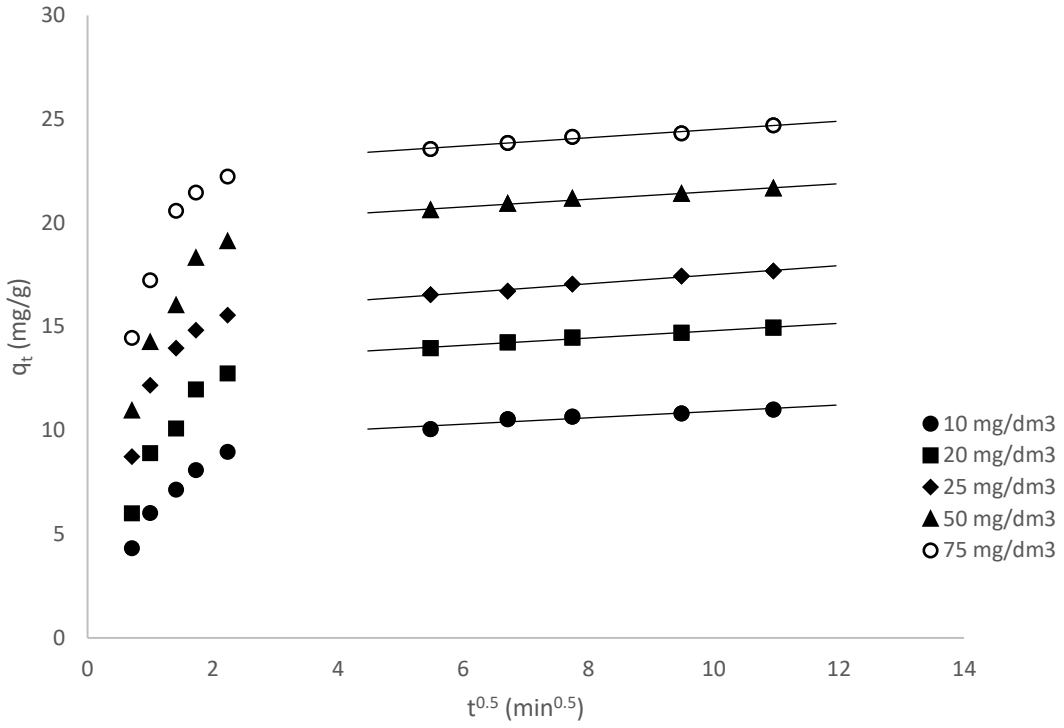

Fig. 5.13a Intraparticle diffusion treatment of As(III) adsorption onto MC binary metal oxide at different initial As(III) concentrations.

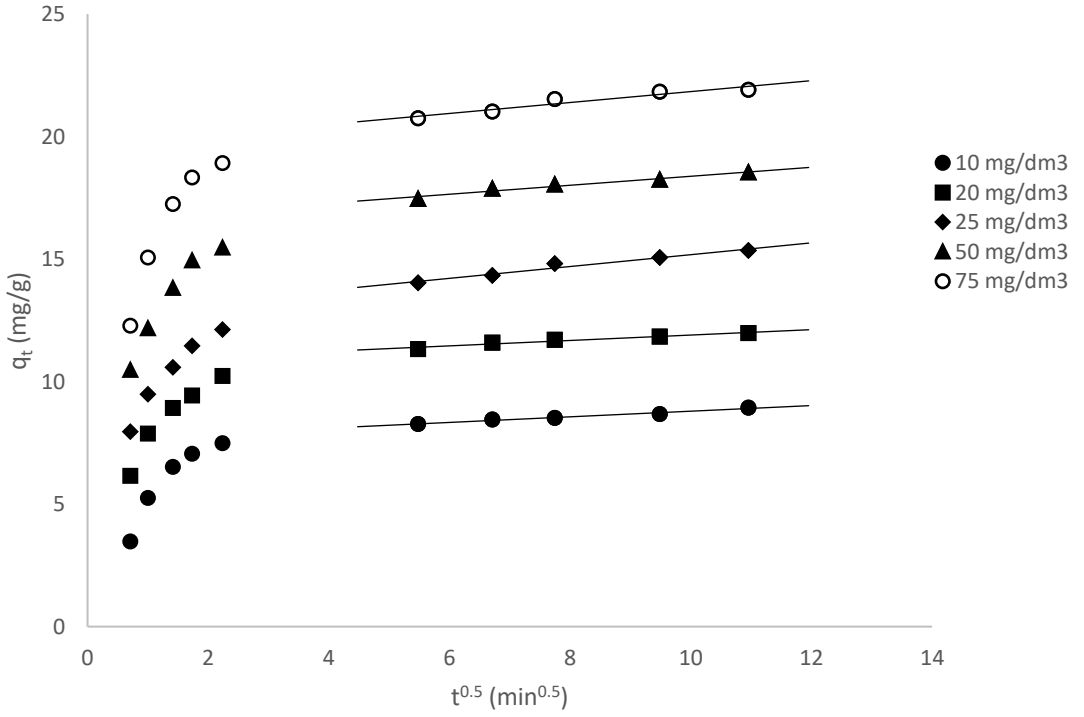

Fig. 5.13b Intraparticle diffusion treatment of As(III) adsorption onto MF binary metal oxide at different initial As(III) concentrations.

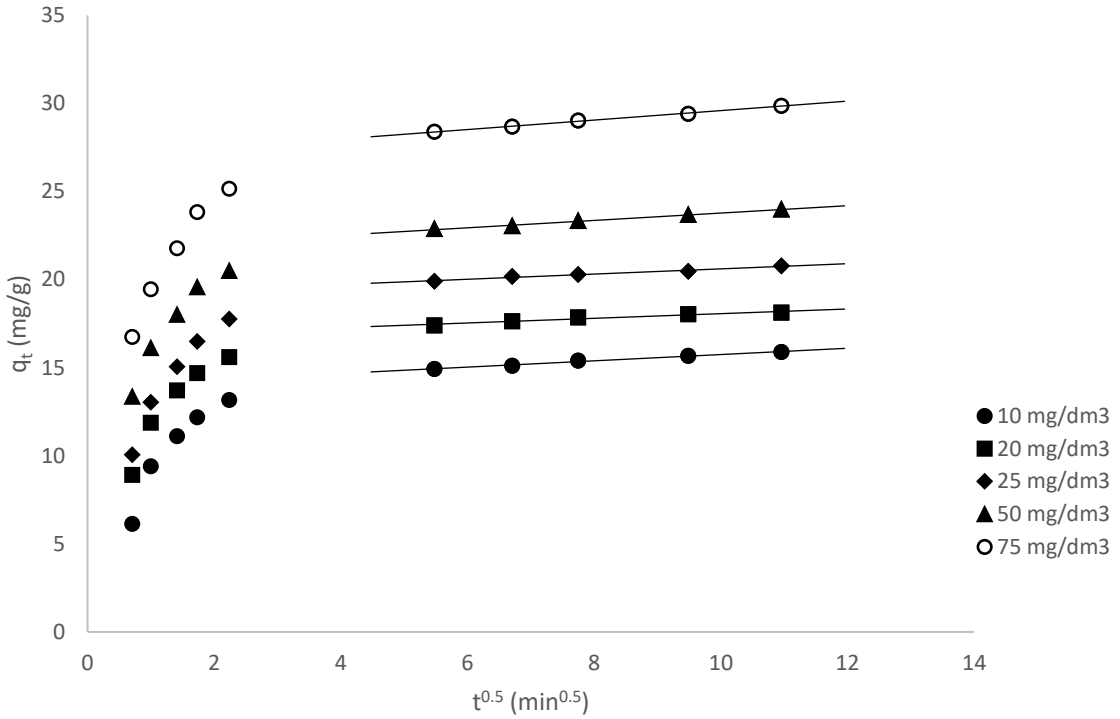

Fig. 5.13c Intraparticle diffusion treatment of As(III) adsorption onto MFC ternary metal oxide at different initial As(III) concentrations.

The results show that the magnitudes of the k_{id} (mg/g.$min^{0.5}$) and C (mg/g) increase as the initial concentration of the As(III) increases, signifying an increase in boundary effects which corresponds with the observed decrease in external mass transfer diffusion rate constants. The increase in the magnitudes of the intraparticle diffusion model constants can also be due to enhanced surface adsorption. The magnitudes of the intraparticle diffusion rate constants at different initial As(III) concentrations were large for the ternary MFC metal oxide than for the binary MC and MF metal oxides suggesting that intraparticle diffusion was more controlling on the ternary MFC metal oxide during the adsorption (Yoon et al., 2017). The smaller binary MC and MF metal oxide adsorbent particles experience less intraparticle diffusion resistance (Tan & Hameed, 2017). The failure of the experimental kinetic data to precisely conform to either the external mass transfer diffusion or the intraparticle diffusion models suggests that the adsorption process might be controlled by a chemical reaction (Ociński et al., 2016).

Table 5.4a Diffusion coefficients for the adsorption of different initial concentrations of As(III) onto MC binary metal oxide at 299 K.

Diffusion parameters	Initial concentration of As(III) (mg/dm^3)				
	10	20	25	50	75
External mass transfer					
k_s (1/min)	0.0095	0.0068	0.0052	0.0033	0.0021
R^2	0.9721	0.9557	0.9485	0.9431	0.9657
Intraparticle diffusion					
k_{id} ($mg/g.min^{0.5}$)	0.1542	0.1768	0.2185	0.1866	0.1989
C (mg/g)	9.375	13.039	15.319	19.649	22.514
R^2	0.9987	0.9884	0.9880	0.9834	0.9767
Boyd diffusion model					
($D_1 \times 10^{-17}$) (cm^2/s)	2.240	2.146	1.837	1.748	1.338
R^2	0.9535	0.9177	0.9482	0.9214	0.9836
($D_2 \times 10^{-17}$) (cm^2/s)	9.192	10.779	11.012	11.297	11.442
R^2	0.9135	0.9155	0.9522	0.9264	0.9515

Table 5.4b Diffusion coefficients for the adsorption of different initial concentrations of As(III) onto MF binary metal oxide at 299 K.

Diffusion parameters	Initial concentration of As(III) (mg/dm^3)				
	10	20	25	50	75
External mass transfer					
k_s (1/min)	0.0079	0.0040	0.0034	0.0021	0.0018
R^2	0.9576	0.9841	0.9773	0.9689	0.9509
Intraparticle diffusion					
k_{id} ($mg/g.min^{0.5}$)	0.1104	0.1147	0.1834	0.2231	0.2415
C (mg/g)	7.646	10.797	12.766	16.547	19.607
R^2	0.9775	0.9502	0.9648	0.9601	0.9199
Boyd diffusion model					
($D_1 \times 10^{-17}$) (cm^2/s)	2.670	1.474	1.263	1.056	1.016
R^2	0.9773	0.9184	0.9456	0.9294	0.9851
($D_2 \times 10^{-17}$) (cm^2/s)	10.859	11.667	11.882	12.222	14.710
R^2	0.9361	0.9401	0.9287	0.9050	0.9752

Table 5.4c Diffusion coefficients for the adsorption of different initial concentrations of As(III) onto MFC ternary metal oxide at 299 K.

Diffusion parameters	Initial concentration of As(III) (mg/dm^3)				
	10	20	25	50	75
External mass transfer					
k_s (1/min)	0.0136	0.0066	0.0062	0.0029	0.0024
R^2	0.9681	0.9574	0.9876	0.9775	0.9646
Intraparticle diffusion					
k_{id} ($mg/g.min^{0.5}$)	0.1785	0.1323	0.1474	0.2091	0.2688
C (mg/g)	13.963	16.746	19.136	21.688	26.907
R^2	0.9888	0.9502	0.9780	0.9937	0.9968
Boyd diffusion model					
($D_1 \times 10^{-17}$) (cm^2/s)	5.226	3.739	3.887	2.571	2.396
R^2	0.9887	0.9843	0.9362	0.9284	0.9590
($D_2 \times 10^{-17}$) (cm^2/s)	21.601	22.225	22.126	19.607	18.392
R^2	0.9135	0.9155	0.9522	0.9264	0.9515

The effects of film and pore diffusion on the adsorption of different initial concentrations of As(III) onto the MC, MF and MFC metal oxides were investigated by fitting the kinetic experimental data onto the Boyd model (Eq's 5.9 and 5.11) (Boyd et al., 1947). The graphs of fractional uptake, q_t/q_e against the square root of time, $t^{0.5}$ ($min^{0.5}$) are presented in Figs 5.14a-c. The plots are divided into two linear segments. The initial stage is fast and is followed by a much slower uptake stage. The film diffusion coefficients, D_1 (cm^2/s) and the pore diffusion coefficient, D_2 (cm^2/s) for the MC, MF and MFC metal oxides at varying initial concentrations of As(III) were computed from the plots of q_t/q_e against $t^{0.5}$ and Bt against t (min), respectively and the results are presented in Tables 5.4a-c.

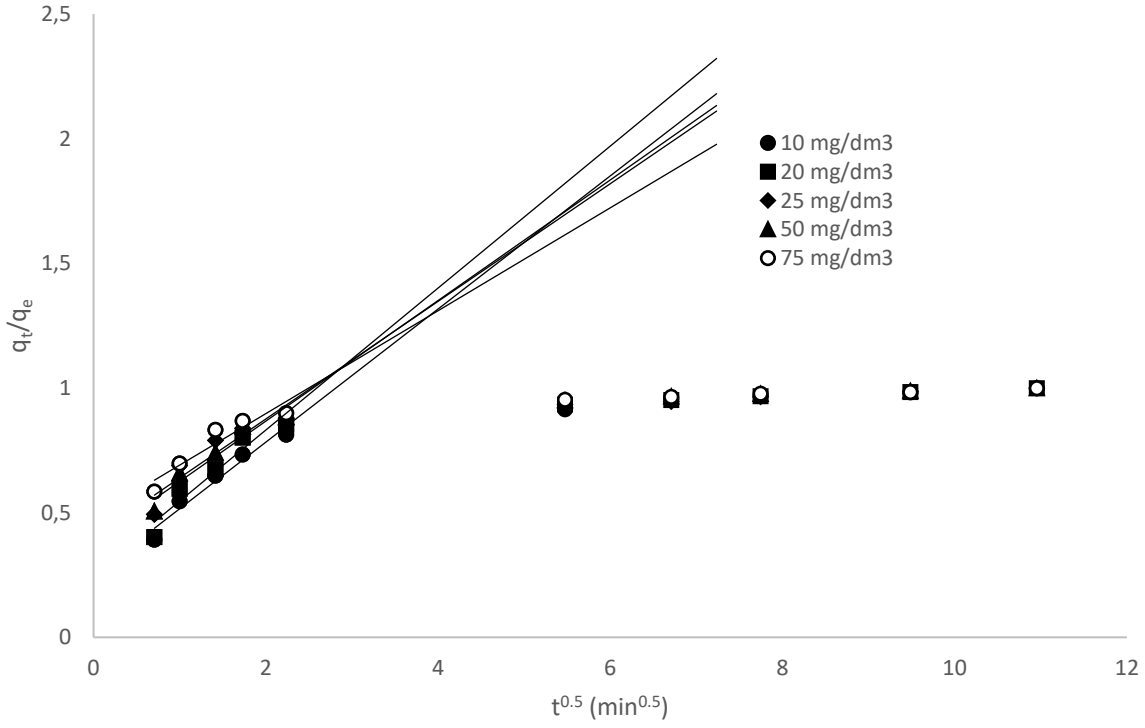

Fig 5.14a Fractional uptake of different initial concentrations of As(III) on MC binary metal oxide against the square root of time.

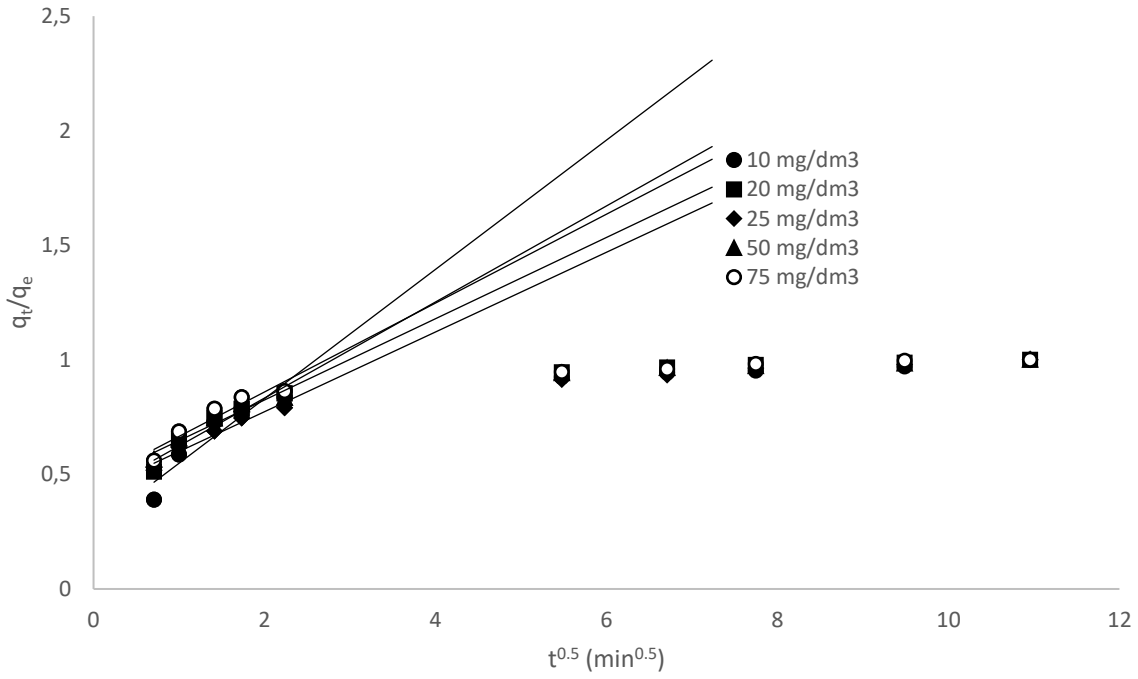

Fig 5.14b Fractional uptake of different initial concentrations of As(III) on MF binary metal oxide against the square root of time.

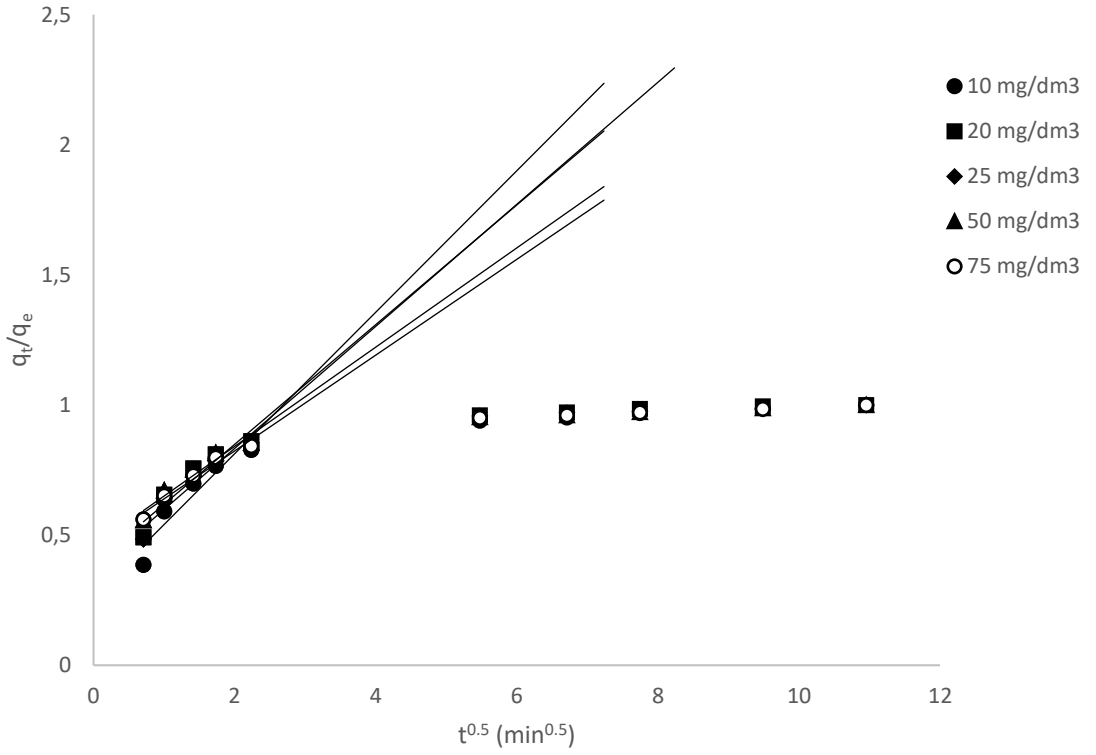

Fig 5.14c Fractional uptake of different initial concentrations of As(III) on MFC ternary metal oxide against the square root of time.

The Boyd plots presented in Figs 5.15a-c, for the MC, MF and MFC metal oxides show linear relationships which do not cut through the origin in the initial phase of the adsorption process at the different initial concentrations of As(III). This signifies that external mass transport controls the adsorption process during the initial phase. The y-intercepts for the MC, MF and MFC metal oxides as the initial bulk concentration increased from 10-75 mg/dm^3, were in the ranges of -0.0015-0.3802, -0.0066-0.3333 and 0.9881-0.3230. The y-intercept values for the binary MC and MF metal oxides shifted towards positive digits but the y-intercept values of the ternary MFC metal oxide shifted towards negative digits as the initial As(III) concentration increased. The increase in the positive nature of the y-intercept values for the binary MC and MF metal oxides was ascribed to an increase in external mass transfer processes, and the decrease in the positive nature of the y-intercept values for the ternary MFC metal oxide was attributed to a decrease in external mass transfer processes. The observed differences between the binary and the ternary metal oxides might be due to differences in adsorbent particle sizes and their surface conformations which in turn might affect the boundary effects as the initial concentration of the As(III) increased. The film diffusion coefficients, D_1 (cm^2/s), of the MC, MF and MFC metal oxides decreased as the initial As(III) concentration increased. The decrease in D_1 (cm^2/s) with increasing initial As(III) concentration was ascribed to the increase in boundary layer resistance caused by an increase in solution viscosity. The magnitudes of D_1 (cm^2/s) for the ternary MFC metal oxide were higher than for the binary MC and MF metal oxides. The larger values of D_1 (cm^2/s) for the ternary MFC metal oxide can be attributed to the larger MFC particle sizes which reduced the external surface area reducing the boundary layer effect. The pore diffusion coefficients, D_2 (cm^2/s), increased with an increase in the initial bulk concentration for the binary MC and MF metal oxides but decreased for the ternary MFC metal oxide. The increase of D_2 (cm^2/s) with an increase in initial As(III) concentration was attributed to an increase in the concentration driving force between the bulk solution and the external surface of the metal oxides as the initial As(III) concentration increased, thus enhancing the rapid diffusion of adsorbate particles into the pores on the adsorbent surface. The small binary MC and MF metal oxide adsorbent particles have small pore lengths, therefore experience less intraparticle diffusion resistance and this might account for the increase in their pore diffusion coefficients, D_2 (cm^2/s) with an increase in initial As(III) concentration. The decrease in the D_2 (cm^2/s) values for the ternary MFC metal oxide adsorbent might be due to an increase in intraparticle diffusion resistance due to the large ternary MFC metal oxide particles which have larger pore lengths. The ternary MFC metal oxide exhibited

larger D_2 (cm^2/s) values than for the binary MC and MF metal oxides. This suggests that the ternary MFC metal oxide surface was more porous or had pores of the right sizes to accommodate the entry of the As(III) species, enabling faster diffusion of the adsorbate particles into the pores. The diffusion coefficients of the metal oxides presented in Table 5.4a-c show that D_2 (cm^2/s) > D_1 (cm^2/s). This implies that the adsorbate particles encountered greater resistance to diffuse through the boundary layer than to diffuse into the pores, signifying that film diffusion controls the adsorption process at this stage.

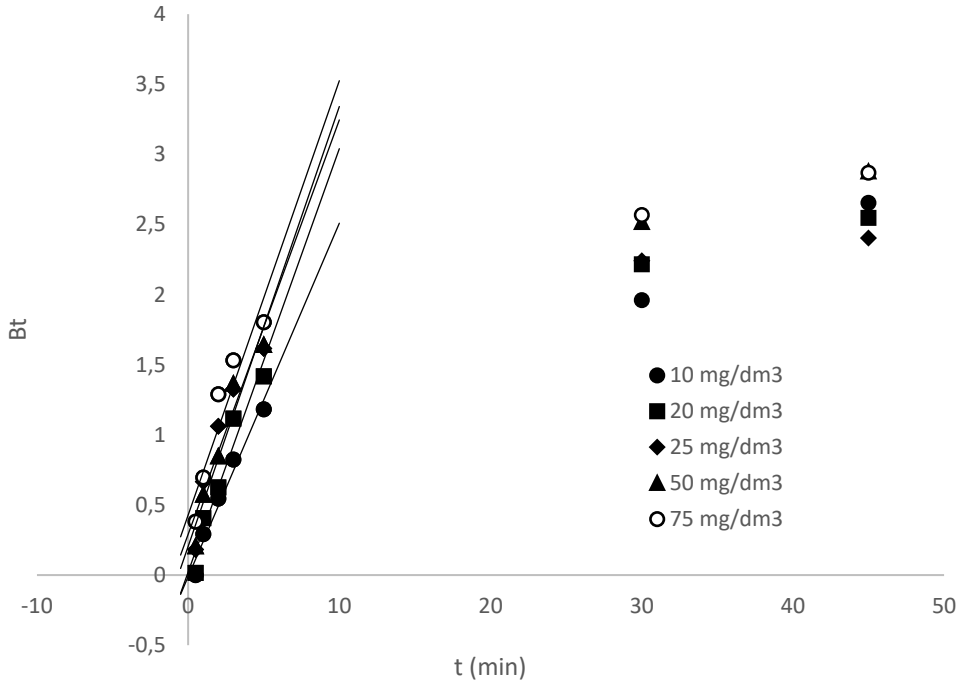

Fig 5.15a Boyd plots for adsorption of different initial concentrations of As(III) onto MC binary metal oxide.

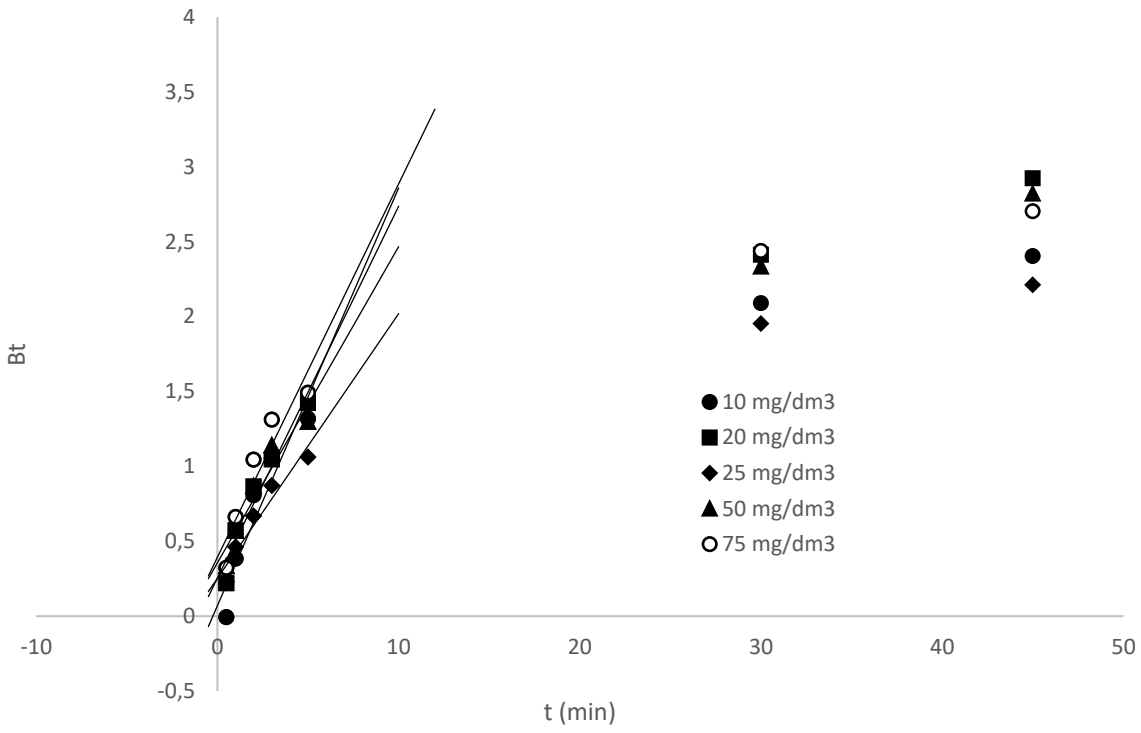

Fig 5.15b Boyd plots for adsorption of different initial concentrations of As(III) onto MF binary metal oxide.

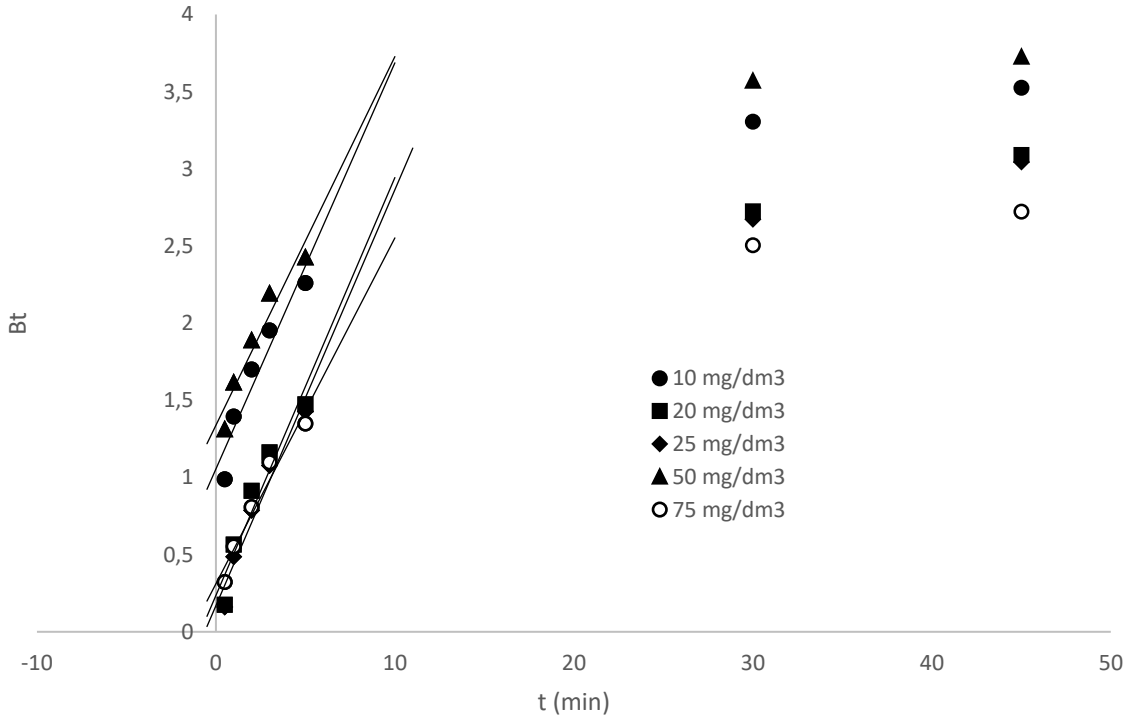

Fig 5.15c Boyd plots for adsorption of different initial concentrations of As(III) onto MFC ternary metal oxide.

5.2.3.2 *Effect of temperature on adsorption kinetics*

5.2.3.2.1 Kinetic models: Pseudo-first-order, pseudo-second-order and the Elovich rate equations

Chromium(VI): The kinetic parameters and error functions for pseudo-first-order, pseudo-second-order and Elovich rate equations for Cr(VI) adsorption on MC, MF and MFC nanostructured metal oxides are presented in Tables 5.5a-c. For the kinetic modelling of MC metal oxide adsorbent, the experimental adsorption capacities for the Cr(VI), q_e *(exp)* were 12.38, 10.99, 10.21, 9.92 and 9.59 mg/g at 299, 304, 309, 314 and 319 K, respectively. For the pseudo-first-order kinetic model, the adsorption capacities, q_e were 11.51, 10.29, 9.62, 9.32 and 8.98 mg/g, while the pseudo-first-order rate constants, k_1 were 0.4266, 0.6588, 0.9131, 1.0371 and 1.2039 (1/min) at 299, 304, 309, 314 and 319 K, respectively. The coefficient of determination, R^2 values were in the range 0.9498-0.9738 and the percent variable error, *% variance* values were in the range 0.2804-0.9089 as the initial temperature of the Cr(VI) increased from 299-319 K. For the pseudo-second-order kinetic model, the q_e values were 11.96, 10.71, 10.03, 9.72 and 9.37 mg/g; the pseudo-second-order rate constant, k_2 values were 0.0559, 0.1001, 0.1496, 0.1761 and 0.2125 g/mg.min; the initial adsorption rate constants, *h* were 7.99, 11.46, 15.05, 16.63 and 18.64 mg/g.min at 299, 304, 309, 314 and 319 K, respectively. The R^2 values were in the range 0.9874-0.9967, while the *% variances* were in the range 0.0447-0.2281 as the initial temperature of the Cr(VI) increased from 299-319 K. For the Elovich kinetic model, the initial adsorption rate constants, α were 51.42, 203.14, 414.79, 669.84 and 870.85 mg/g.min; the adsorption constant, β values were 0.52, 0.87, 1.09, 1.21 and 1.37 mg/g at 299, 304, 309, 314 and 319 K, respectively. The R^2 and *% variance* values were in the ranges 0.9438-0.9891 and 0.1917-0.6305, respectively with an increase in Cr(VI) initial temperature from 299-319 K.

Table 5.5a Kinetic modelling at different temperatures of 10 mg/dm^3 of Cr(VI) adsorption on MC binary metal oxide.

Kinetic model	Parameters	Temperature (K)				
		299	304	309	314	319
	q_e (mg/g) (*exp*)	12.38	10.99	10.21	9.92	9.59
pseudo-first-order	q_e (mg/g)	11.51	10.29	9.62	9.32	9.98
	k_1 (1/min)	0.4266	0.6588	0.9131	1.0371	1.2039
	R^2	0.9498	0.9666	0.9738	0.9698	0.9689
	% variance	0.9089	0.4479	0.2938	0.3099	0.2804
pseudo-second-order	q_e (mg/g)	11.96	10.71	10.03	9.72	9.37
	k_2 (g.mg.min)	0.0559	0.1004	0.1496	0.1761	0.2125
	h (mg/g.min)	7.99	11.46	15.05	16.63	18.64
	R^2	0.9874	0.9967	0.9947	0.9951	0.9946
	% variance	0.2281	0.0447	0.0591	0.0504	0.0501
Elovich equation	β (mg/g)	0.52	0.87	1.09	1.21	1.37
	α (mg/g.min)	51.42	203.14	414.79	669.84	870.85
	R^2	0.9891	0.9639	0.9438	0.9496	0.9511
	% variance	0.1971	0.4829	0.6305	0.5169	0.4553

Table 5.5b Kinetic modelling at different temperatures of 10 mg/dm^3 of Cr(VI) adsorption on MF binary metal oxide.

Kinetic model	Parameters	Temperature (K)				
		299	304	309	314	319
	q_e (mg/g) (*exp*)	15.94	13.66	13.23	12.81	12.24
pseudo-first-order	q_e (mg/g)	14.58	13.24	12.71	12.13	11.47
	k_1 (1/min)	0.4014	0.5292	0.5996	0.6524	0.0678
	R^2	0.9561	0.9736	0.9595	0.9605	0.9698
	% variance	1.3042	0.6081	0.8293	0.7339	0.5032
pseudo-second-order	q_e (mg/g)	15.61	13.71	13.18	12.62	11.94
	k_2 (g.mg.min)	0.0409	0.0629	0.0751	0.0842	0.0919
	h (mg/g.min)	9.40	11.83	13.04	13.42	13.11
	R^2	0.9866	0.9959	0.9955	0.9968	0.9978
	% variance	0.3974	0.0925	0.0923	0.0588	0.0364
Elovich equation	β (mg/g)	0.49	0.63	0.69	0.74	0.79
	α (mg/g.min)	53.14	129.64	197.72	237.59	250.89
	R^2	0.9865	0.9573	0.9683	0.9682	0.9605
	% variance	0.3996	0.9824	0.6496	0.5899	0.6573

Table 5.5c Kinetic modelling at different temperatures of 10 mg/dm^3 of Cr(VI) adsorption on MFC ternary metal oxide.

Kinetic model	Parameters	Temperature (K)				
		299	304	309	314	319
	q_e (mg/g) (*exp*)	16.95	15.51	14.63	13.74	13.05
pseudo-first-order	q_e (mg/g)	16.08	14.97	13.66	12.81	12.12
	k_1 (1/min)	0.4005	0.5336	0.7985	1.0525	1.7004
	R^2	0.9416	0.9498	0.9441	0.9477	0.9537
	% variance	2.0306	1.4296	1.2546	0.9926	0.7438
pseudo-second-order	q_e (mg/g)	16.65	15.47	14.22	13.35	12.65
	k_2 (g.mg.min)	0.0386	0.0582	0.0941	0.1322	0.2251
	h (mg/g.min)	10.71	13.93	19.01	23.55	36.01
	R^2	0.9814	0,9873	0.9908	0.9915	0.9922
	% variance	0.6455	0.3608	0.2064	0.1606	0.1248
Elovich equation	β (mg/g)	0.47	0.57	0.72	0.89	1.22
	α (mg/g.min)	71.22	180.42	270.66	291.45	802.34
	R^2	0.9900	0.9706	0.9753	0.9691	0.9811
	% variance	0.3467	0.8371	0.5529	0.5852	0.3036

For the kinetic modelling of MF metal oxide, the q_e *(exp)* values were 15.94, 13.66, 13.23, 12.81 and 12.22 mg/g at Cr(VI) initial temperatures of 299, 304, 309, 314 and 319 K, respectively. The pseudo-first-order kinetic model. q_e values were 14.58, 13.24, 12.71, 12.13 and 11.47 mg/g, while the pseudo-first-order rate constants, k_1 were 0.4014, 0.0.5292, 0.5996, 0.6524 and 0.6678 (1/min) at 299, 304, 309, 314 and 319 K, respectively. The R^2 values were in the range 0.9561-0.9736 and *% variances* were in the range 0.5032-1.3042 as the temperature of the Cr(VI) increased from 299-319 K. For the pseudo-second-order kinetic model, the q_e values were 15.61, 13.71, 13.18, 12.62 and 11.94 mg/g; the, k_2 values were 0.0409, 0.0629, 0.0751, 0.0842 and 0.0919 g/mg.min; the, *h* values were 9.40, 11.83, 13.04, 13.42 and 13.11 mg/g.min at Cr(VI) initial temperatures of 299, 304, 309, 314 and 319 K, respectively. The R^2 values were in the range 0.9866-0.9978, while the *% variances* were in the range 0.0364-0.3974 as the Cr(VI) initial temperature increased from 299-319 K. For the Elovich kinetic model, the initial adsorption rate constants, α were 53.14, 129.64, 197.72, 237.59 and 250.89 mg/g.min; the adsorption constant, β values were 0.49, 0.63, 0.69, 0.74 and 0.79 mg/g at each of Cr(VI) initial temperature of 299, 304, 309, 314 and 319 K, respectively. The R^2 and *% variance* values were in the ranges 0.9573-0.9865 and 0.3996-0.9824, respectively with an increase in Cr(VI) initial temperature from 299-319 K.

For the kinetic modelling of MFC metal oxide adsorbent, the experimental adsorption capacities, q_e *(exp)* were 16.95, 15.51, 14.63, 13.74 and 13.05 mg/g at Cr(VI) initial temperatures of 299, 304, 309, 314 and 319 K, respectively. For the pseudo-first-order kinetic model, the adsorption capacities, q_e were 16.08, 14.97, 13.66, 12.81 and 12.12 mg/g, while the pseudo-first-order rate constants, k_1 were 0.4005, 0.5336, 0.7985, 1.0525 and 1.7004 (1/min) at 299, 304, 309, 314 and 319 K, respectively. The coefficient of determination, R^2 values were in the range 0.9416-0.9537 and the percent variable error, *% variance* values were in the range 0.7438-2.0306 as the Cr(VI) initial temperature increased from 299-319 K. For the pseudo-second-order kinetic model, the q_e values were 16.65, 15.47, 14.22, 13.35 and 12.65 mg/g; the pseudo-second-order rate constant, k_2 values were 0.0386, 0.0582, 0.0941, 0.1322 and 0.2251 g/mg.min; the initial adsorption rate constants, *h* were 10.70, 13.93, 19.01, 23.55 and 36.01 mg/g.min at each of the Cr(VI) initial temperatures of 299, 304, 309, 314 and 319 K. The R^2 values were in the range 0.9814-0.9922, while the *% variances* were in the range 0.1606-0.6455 as the Cr(VI) initial temperature increased from 299-319 K. For the Elovich kinetic model, the initial adsorption rate constants, α were 71.22, 180.42, 257.66, 291.45 and 802.34 mg/g.min; the adsorption constant, β values were 0.47, 0.57, 0.72, 0.89 and 1.22 mg/g at each of Cr(VI)

initial temperatures of 299, 304, 309, 314 and 319 K, respectively. The R^2 and *% variance* values were in the ranges 0.9691-0.9900 and 0.3036-0.8371, respectively with an increase in Cr(VI) initial temperature from 299-319 K.

The experimental and the pseudo-first-order and the pseudo-second-order adsorption capacities, q_e (mg/g), for MC, MF and MFC metal oxide adsorbents decreased as the initial Cr(VI) temperature increased. The results highlighted that the adsorption of Cr(VI) is exothermic. The same conclusion was reported by Baral et al. (2006), on the adsorption of hexavalent chromate onto sawdust treated with formaldehyde. The decreases in the adsorption capacities were ascribed to an increase in the kinetic energy and mobility of the adsorbate particles resulting in desorption (Gheju et al., 2016). The magnitudes of the adsorption capacities for the mixed metal oxides were in the order MFC > MF > MC at the different initial temperatures for the Cr(VI). This showed that the MFC ternary metal oxide had the highest affinity and least desorption for the Cr(VI) oxyanions, with the MC binary metal oxide exhibiting the least affinity and highest desorption for the adsorbate particles as the initial temperature of the bulk solution increased from 299-319 K.

The pseudo-first-order rate constants, k_1 (1/min), for the MC, MF and MFC oxides increased with an increase in the initial temperature of the bulk solution at a fixed adsorbent mass. The larger the values of k_1, the shorter the time needed to reach adsorption equilibrium at higher initial Cr(VI) temperatures. At high initial adsorbate temperature, the time needed to attain equilibrium decreases and this might be due to a decrease in viscosity and an increase in kinetic energy of the adsorbate particles, causing a reduction in boundary layer effects (El Haddad et al., 2013). The magnitudes of the k_1 (1/min) values of the metal oxide adsorbents are in the order: MC > MF > MFC. For example, at an initial Cr(VI) temperature of 299 K, the k_1 (1/min) values for each of MC, MF and MFC metal oxides were 0.4266, 0.4014 and 0.4005, respectively. The observed differences in the rate constant values, k_1 (1/min), is attributed to the decrease in adsorbent particle sizes. The smaller the adsorbent particles, the larger the k_1 (1/min) values, since smaller particles have a larger exposed surface area (Vincent et al., 2014).

The pseudo-second-order rate constants, k_2 (g/mg.min), for the MC, MF and MFC metal oxide adsorbents increased as the initial pollutant temperature increased. The larger the k_2 value, the shorter the time needed to reach equilibrium. The observed variations in the magnitudes of the pseudo-second-order rate constants, k_2 (g/mg.min) for the metal oxides (MC > MF > MFC)

were attributed to variations in the size of adsorbent particles, that is, the smaller the adsorbent particle size, the larger the exposed number of adsorption active sites, resulting in shorter equilibrium attainment periods, hence larger k_2 values. The pseudo-second-order initial adsorption rate constants, h (mg/g.min) for the MC, MF and MFC metal oxides increased as the initial temperature of the bulk solution increased. The increase in the pseudo-second-order rate equation parameters, k_2 (g/mg.min) and h (mg/g.min), as the initial temperature of the bulk solution increased is attributed to an increase in kinetic energy of the adsorbate particles causing an increase in collision frequency between the adsorbent and absorbate. At an initial Cr(VI) temperature of 299 K, the magnitudes of the h (mg/g.min) values for the metal oxides were in the order: MFC > MF > MC, suggesting that the ternary MFC metal oxide surface showed greater affinity for the pollutant.

The modelling of the experimental kinetic data using the Elovich equation showed that the model parameters, that is, the initial adsorption rate constant, α (mg/g.min) and the adsorption constant, β (mg/g) increased as the initial temperature of Cr(VI) was increased. The noted increase of the Elovich kinetic parameter, α (mg/g.min) was attributed to an increase in collision frequency due to an increase in thermal energy of the adsorption system. The increase in β (mg/g) might be due to swelling of the adsorbent at high temperature, increasing the surface coverage.

The pseudo-second-order kinetic model was better suited than the pseudo-first-order and Elovich kinetic models in describing the adsorption experimental kinetic data as it showed higher R^2 (close to one) and lower *% variance* (close to zero) error values for the MC, MF and MFC metal oxide adsorbents, as the initial temperature of the Cr(VI) increased from 299-319 K. The pseudo-second-order modelled adsorption capacities q_e (mg/g) were also in close agreement with the experimental adsorption capacities, q_e (*exp*)(mg/g), than for the pseudo-first-order and Elovich kinetic models. This suggests that the adsorption kinetics followed a chemisorption mechanistic pathway at the different initial temperatures of the Cr(VI).

Arsenic(III): The kinetic parameters presented in Tables 5.6a-c show that the As(III) adsorption capacities, q_e (mg/g) obtained from the experiments and mathematical modelling using the pseudo-first-order and the pseudo-second-order rate equations increased as the initial temperature of the bulk solution increased from 299-319 K for the MC, MF and MFC metal oxide adsorbents. The experimental adsorption capacities, q_e (mg/g) increased in the ranges: MC, 11.01-14.71; MF, 8.94-13.41; and MFC, 15.89-30.87; the pseudo-first-order adsorption

capacities, q_e (mg/g) increased in the ranges: MC, 10.29-13.49; MF, 8.32-12.49; and MFC, 14.89-28.84; and the pseudo-second-order adsorption capacities, q_e (mg/g) increased in the ranges: MC, 10.72-14.15; MF, 8.68-13.01; and MFC, 15.55-29.81 as the initial temperature of the bulk solution increased from 299-319 K. This suggest that the adsorption process is endothermic. The increase in the adsorption capacities is attributed to an increase in kinetic energy of the adsorbate particles and swelling of the adsorbent, enhancing the attachment of the As(III) species onto the adsorbent surface. The adsorption capacities of the As(III) increased rapidly for the MC, MF and MFC metal oxide adsorbents in the initial 30 minutes of the adsorption process and thereafter became almost constant probably due to (1) saturation of adsorption active sites, (2) decrease in concentration gradient due to the initial rapid uptake of the As(III), and (3) repulsion and/or steric effects between adsorbed As(III) species and those in the bulk solution reducing access of adsorbate particles to the adsorption active sites (Nashine & Tembhurkar, 2016). The magnitudes of the As(III) adsorption capacities for the mixed metal oxides were in the order MFC > MF > MC at all the initial temperatures of the As(III). This suggests that the MFC ternary metal oxide had the highest affinity for the As(III) with the MF binary metal oxide exhibiting the least affinity for the adsorbate particles.

Table 5.6a Kinetic modelling at different temperatures of 10 mg/dm^3 of As(III) adsorption on MC binary metal oxide.

Kinetic model	Parameters	Temperature (K)				
		299	304	309	314	319
	q_e (mg/g) (*exp*)	11.01	11.65	12.58	13.67	14.71
pseudo-first-order	q_e (mg/g)	10.29	10.75	11.69	12.48	13.49
	k_1 (1/min)	0.7091	0.8521	1.2214	1.3007	1.5111
	R^2	0.9516	0.9186	0.9389	0.9246	0.9219
	% variance	0.6337	1.1206	0.9506	1.3352	1.5949
pseudo-second-order	q_e (mg/g)	10.72	11.22	12.23	13.08	14.15
	k_2 (g.mg.min)	0.1258	0.1262	0.1629	0.1674	0.1713
	h (mg/g.min)	14.56	15.89	24.37	28.64	34.29
	R^2	0.9937	0.9923	0.9909	0.9941	0.9918
	% variance	0.0824	0.2442	0.1424	0.2831	0.3726
Elovich equation	α (mg/g.min)	287.74	478.6705	690.16	742.34	873.76
	β (mg/g)	0.90	0.93	1.02	1.17	1.30
	R^2	0.9736	0.9772	0.9731	0.9799	0.9724
	% variance	0.3458	0.1767	0.2639	0.1797	0.1549

Table 5.6b Kinetic modelling at different temperatures of 10 mg/dm^3 of As(III) adsorption on MF binary metal oxide.

Kinetic model	Parameters	Temperature (K)				
		299	304	309	314	319
	q_e (mg/g) (*exp*)	8.94	9.89	11.35	12.54	13.41
pseudo-first-order	q_e (mg/g)	8.32	9.13	10.42	11.31	12.49
	k_1 (1/min)	0.8832	0.9421	1.2763	1.6931	1.7089
	R^2	0.9722	0.9561	0.9363	0.9413	0.9541
	% variance	0.2344	0.4378	0.7875	0.8239	0.7749
pseudo-second-order	q_e (mg/g)	8.68	9.54	10.91	11.81	13.01
	k_2 (g.mg.min)	0.1661	0.1796	0.1901	0.2394	0.2627
	h (mg/g.min)	12.51	16.35	22.63	33.39	44.46
	R^2	0.9971	0.9942	0.9981	0.9972	0.9937
	% variance	0.0247	0.0574	0.0466	0.0796	0.1065
Elovich equation	α (mg/g.min)	398.31	535.13	747.85	833.92	971.32
	β (mg/g)	1.23	1.41	1.60	1.63	1.71
	R^2	0.9515	0.9675	0.9747	0.9792	0.9741
	% variance	0.4084	0.3241	0.1893	0.4519	0.5686

Table 5.6c Kinetic modelling at different temperatures of 10 mg/dm^3 of As(III) adsorption on MFC ternary metal oxide.

Kinetic model	Parameters	Temperature (K)				
		299	304	309	314	319
	q_e (mg/g) (*exp*)	15.89	19.13	21.78	24.98	30.87
pseudo-first-order	q_e (mg/g)	14.89	18.01	20.41	23.17	28.47
	k_1 (1/min)	0.8212	0.0936	1.0271	1.1523	1.2693
	R^2	0.9615	0.9561	0.9498	0.9419	0.9283
	% variance	1.0487	1.4752	2.2209	3.2214	6.1648
pseudo-second-order	q_e (mg/g)	15.55	18.82	21.33	24.22	29.81
	k_2 (g.mg.min)	0.0854	0.1037	0.1109	0.1292	0.1334
	h (mg/g.min)	20.65	36.73	50.46	75.79	118.54
	R^2	0.9965	0.9967	0.9953	0.9913	0.9962
	% variance	0.0957	0.1118	0.2066	0.4816	1.1868
Elovich equation	α (mg/g.min)	521.47	612.41	808.17	920.53	1103.64
	β (mg/g)	1.68	1.71	1.77	1.87	1.94
	R^2	0.9617	0.9708	0.9734	0.9738	0.9779
	% variance	1.0429	0.9818	1.1762	0.8996	1.0385

The pseudo-first-order rate constants, k_1 (1/min), for the MC, MF and MFC oxides increased with an increase in the initial temperature of As(III). The increases in the k_1 (1/min) values for each metal oxide adsorbent were: MC, 0.7091-1.5111; MF, 0.8832-1.7089; and MFC, 0.8212-1.2693. The larger the values of k_1, the shorter the time needed to reach adsorption equilibrium at higher initial As(III) temperature. This is attributed to a decrease in boundary layer resistance due to a decrease in solution viscosity with an increase in the initial solution temperature. The magnitudes of the k_1 (1/min) values of the metal oxide adsorbents are in the order: MF > MC > MFC. For example, at an initial As(III) concentration of 75 mg/dm^3, the k_1 (1/min) values for each of MC, MF and MFC metal oxides were 1.7089, 1,5111 and 1.2693, respectively. The difference in the pseudo-first-order rate constants is attributed to the varying sizes of the adsorbent particles. The smaller the adsorbent particles, the larger the k_1 (1/min) values due to diminished pore length, shortening equilibration time for the adsorption process.

The pseudo-second-order rate constants, k_2 (g/mg.min), for the MC, MF and MFC metal oxide adsorbents exhibited an increase as the initial temperature of the As(III) increased. The k_2 (g/mg.min) values for the metal oxides increased as follows: MC, 0.1089-0.1713; MF 0.1661-0.2627; and MFC, 0.0854-0.1334, as the initial temperature of As(III) increased from 299-319 K. The larger the k_2 value, the shorter the time needed to reach equilibrium ($1/k_2$), at a high initial temperature of the adsorbate. The pseudo-second-order initial adsorption rate constants, h (mg/g.min) for the MC, MF and MFC metal oxides increased as the initial As(III) temperature concentration increased. The h (mg/g.min) values increased as follows: MC, 14.56-34.29; MF, 12.51-44.46; and MFC, 20.65-118.54. The increase in the pseudo-second-order initial rate constant as the initial temperature of the bulk solution is increased is attributed to an increase in collision frequency between the adsorbent and absorbate. The ternary MFC metal oxide adsorbent had higher h (mg/g.min) values at all initial concentrations of As(III) and the binary MF metal oxide adsorbent had the least. A higher initial adsorption rate constant suggests greater affinity by the adsorbent's surface for the pollutant.

The modelling of the experimental kinetic data using the Elovich equation showed that the model parameters, that is, the initial adsorption rate constant, α (mg/g.min) and the adsorption constant, β (mg/g) increased as the initial temperature of As(III) was increased. The magnitudes of the initial adsorption rate constants, α (mg/g.min) for the metal oxides increased in the following ranges: MC,287.74-873.76; MF, 398.31-971.32; and MFC, 521.47-1103.64. The increases in the adsorption constants, β (mg/g) for the metal oxides were: MC,0.90-1.30; MF, 1.23-1.71; and MFC, 1.68-1.94. The increase of the Elovich kinetic parameter, α (mg/g.min)

was attributed to an increase in kinetic energy of the adsorbate particles, thus increasing collision frequency. The increase in β (mg/g) might be due to swelling of the adsorbent at high temperature, enhancing attachment of the As(III) onto the adsorbent surface.

The rate equation best suited to describe the adsorption kinetics of As(III) at different initial temperatures onto the MC, MF and MFC metal oxides was determined using the kinetic isotherm plots on Figs 5.7a-c and error functions (coefficient of determination, R^2 and percentage variable error, *% variance*) presented on Tables 5.6a-c. For the pseudo first-order model: $0.9186 < R^2 < 0.9516$ and $0.6337 <$ *% variance* < 1.5949 for the MC oxide; $0.9363 < R^2 < 0.9722$ and $0.2344 <$ *% variance* < 0.8390 for the MF oxide; and $0.9283 < R^2 < 0.9615$ and $1.0487 <$ *% variance* < 6.1648 for the MFC oxide. For the pseudo second-order model: $0.9937 < R^2 < 0.9909$ and $0.0824 <$ *% variance* < 0.3726 for the MC oxide; $0.9937 < R^2 < 0.9981$ and $0.0247 <$ *% variance* < 0.1065 for the MF oxide; and $0.9913 < R^2 < 0.9967$ and $0.0957 <$ *% variance* < 1.1868 for the MFC oxide. For the Elovich model: $0.9724 < R^2 < 0.9799$ and $0.1549 <$ *% variance* < 0.3458 for the MC oxide; $0.9515 < R^2 < 0.9792$ and $0.1893 <$ *% variance* < 0.5686 for the MF oxide; and $0.9617 < R^2 < 0.9779$ and $0.8996 <$ *% variance* < 1.1762 for the MFC oxide. The error functions show that the pseudo-second-order model showed a better fit than either the pseudo-first-order or the Elovich models, to the experimental kinetic data for the adsorption of As(III) at different initial temperatures onto the MC, MF and MFC metal oxide adsorbents, with R^2 close to unity and *% variance* close to zero. The kinetic isotherm plots on Figs 5.7a-c also show good agreement between the experimental and the pseudo-second-order modelled adsorption capacities. The adsorption process seems to follow a chemisorption mechanism involving valence forces due to transfer or sharing of electrons.

5.2.3.2.2 Diffusion models: External mass transport, intraparticle diffusion and the Boyd diffusion models

Chromium(VI): The external mass transfer diffusion rate constant, k_s (1/min) was determined by plotting C_t/C_o at different initial temperatures of 10 mg/dm^3 Cr(VI) against time, and the results are presented in Figs 5.16a-c. The C_t/C_o versus t plots show that there is an increase in the rate of adsorption in the initial 5 minutes of the adsorption process as the initial temperature of Cr(VI) is increased. The rate of adsorption decreases as the adsorption process proceeds after the initial rapid stage. A similar observation was reported by McKay and Poots (1980) on the investigation of dye adsorption onto the wood adsorbent. The observed phenomenon was attributed to desorption of adsorbate due to the presence of large amounts of thermal energy in the adsorption system (Gheju et al., 2016).

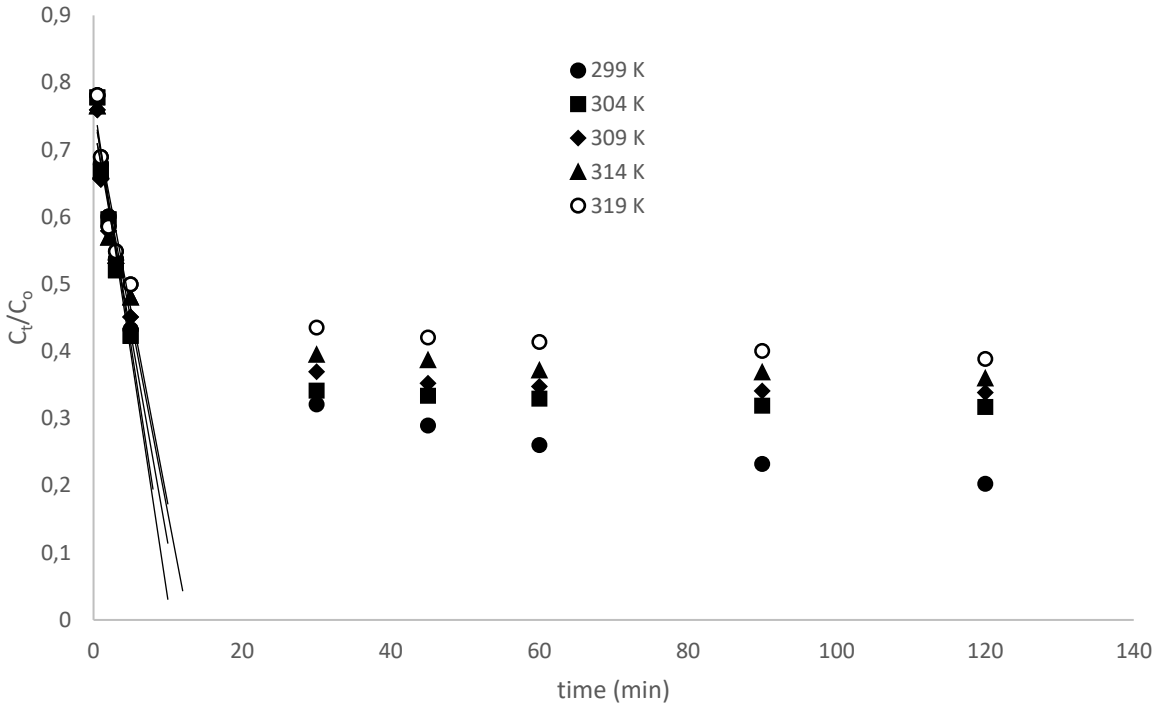

Fig 5.16a External mass transfer diffusion plot for Cr(VI) adsorption onto MF binary metal oxide at different temperatures.

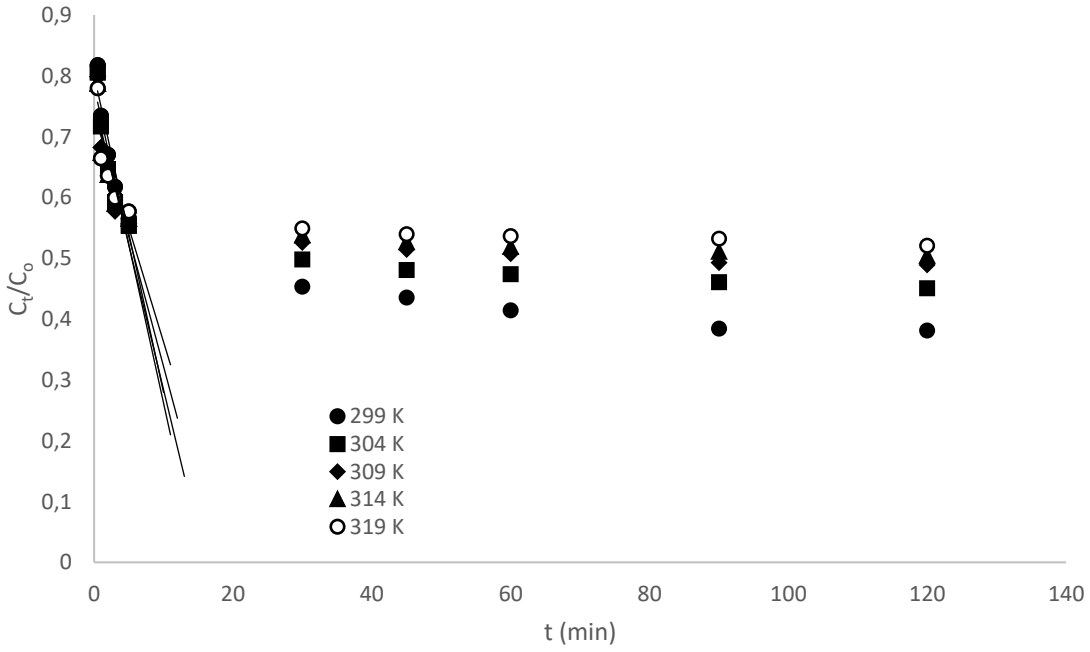

Fig 5.16b External mass transfer diffusion plot for Cr(VI) adsorption onto MC binary metal oxide at different temperatures.

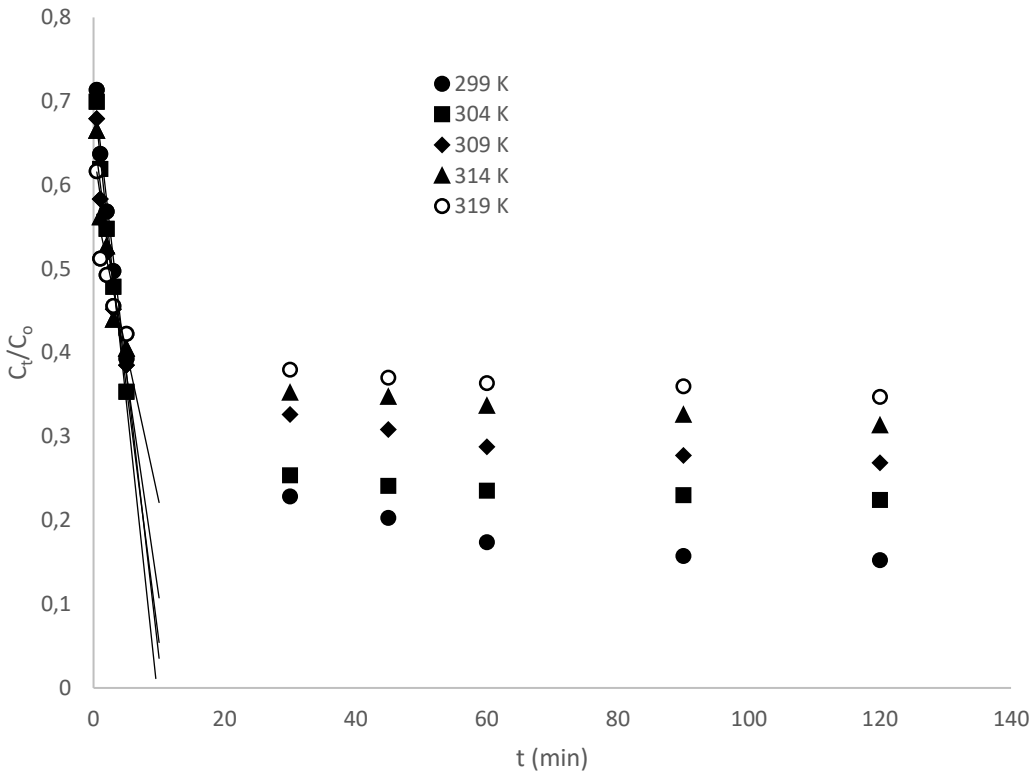

Fig 5.16c External mass transfer diffusion plot for Cr(VI) adsorption onto MFC ternary metal oxide at different temperatures.

The external mass transfer diffusion rate constants for the adsorption processes are presented in Tables 5.7a-c. The k_s (1/min) values for MC, MF and MFC oxides increased in the ranges 0.0522-0.0617, 0.0682-0.0735 and 0.0774-0.0813, respectively, as the initial temperature of the bulk solution increased from 299-319 K. The increase in the magnitudes of the external mass transfer diffusion rate constants, due to an increase in initial temperature of Cr(VI) pollutant is attributed to a decrease in boundary layer resistance. This decrease in boundary layer resistance is due to (1) a decrease in solution viscosity as the initial temperature increases, and (2) at a higher temperature, the adsorbent can swell, increasing the available surface area for adsorption, thus decreasing resistance to film diffusion. The MC metal oxide had the lowest external mass transfer diffusion rate constants, suggesting that external mass transfer was more controlling for this metal oxide than for the MF or MFC metal oxides.

Table 5.7a Diffusion coefficients for the adsorption of Cr(VI) onto MF binary metal oxide at different initial temperatures.

Diffusion parameters	Temperature (K)				
	299	304	309	314	319
External mass transfer					
k_s (1/min)	0.0682	0.0687	0.0676	0.0722	0.0735
R^2	0.9342	0.9649	0.9276	0.9349	0.9762
Intraparticle diffusion					
k_{id} (mg/g.min$^{0.5}$)	0.223	0.165	0.127	0.105	0.093
C (mg/g)	12.861	12.686	12.160	11.455	10.434
R^2	0.9892	0.9690	0.9551	0.9293	0.9906
Boyd diffusion model					
($D_1 \times 10^{-17}$) (cm^2/s)	2.546	2.675	2.841	2.993	3.616
R^2	0.9843	0.9831	0.9670	0.9429	0.9576
($D_2 \times 10^{-17}$) (cm^2/s)	7.634	9.991	10.617	10.828	12.292
R^2	0.9956	0.9734	0.9813	0.9939	0.9749

Table 5.7b Diffusion coefficients for the adsorption of Cr(VI) onto MC binary metal oxide at different initial temperatures.

Diffusion parameters	Temperature (K)				
	299	304	309	314	319
External mass transfer					
k_s (1/min)	0.0522	0.0521	0.0536	0.0551	0.0617
R^2	0.9278	0.9347	0.9459	0.9378	0.9561
Intraparticle diffusion					
k_{id} (mg/g.min$^{0.5}$)	0.283	0.167	0.137	0.119	0.094
C (mg/g)	9.438	9.198	8.778	8.655	8.532
R^2	0.9549	0.9788	0.9691	0.9736	0.9501
Boyd diffusion model					
($D_1 \times 10^{-17}$) (cm^2/s)	1.965	2.135	2.336	2.741	2.751
R^2	0.9697	0.9855	0.9679	0.9978	0.9901
($D_2 \times 10^{-17}$) (cm^2/s)	6.704	9.783	11.245	11.691	11.862
R^2	0.9783	0.9789	0.9943	0.9919	0.9892

Table 5.7c Diffusion coefficients for the adsorption of Cr(VI) onto MFC ternary metal oxide at different initial temperatures.

Diffusion parameters	Temperature (K)				
	299	304	309	314	319
External mass transfer					
k_s (1/min)	0.0774	0.0734	0.0796	0.0805	0.0813
R^2	0.9367	0.9712	0.9777	0.9689	0.9741
Intraparticle diffusion					
k_{id} (mg/g.min$^{0.5}$)	0.281	0.101	0.209	0.146	0.108
C (mg/g)	14.071	14.451	12.439	12.123	11.844
R^2	0.9026	0.9310	0.9344	0.9903	0.9623
Boyd diffusion model					
($D_1 \times 10^{-17}$) (cm^2/s)	4.171	5.681	7.494	6.143	7.005
R^2	0.9967	0.9871	0.9892	0.9936	0.9973
($D_2 \times 10^{-17}$) (cm^2/s)	1.508	2.086	2.224	2.310	2.408
R^2	0.9874	0.9976	0.9870	0.9913	0.9899

The plots of q_t against $t^{0.5}$ presented in Figs 5.17a-c show that no linear section of the graphs cuts through the origin. This implies that intraparticle diffusion is not the only rate-determining step in the adsorption of Cr(VI) onto the MC, MF and MFC metal oxides. The plots are divided into two linear segments signifying the presence of multiple mechanisms during the adsorption. The initial stage is fast and due to external surface adsorption controlled by film diffusion. The subsequent stage is due to slow adsorption of the Cr(VI) and is intraparticle diffusion-controlled. The results of the calculated intraparticle diffusion parameters are presented in Tables 5.7a-c. The results show that the magnitudes of the k_{id} (mg/g.min$^{0.5}$) and C (mg/g) values decrease with an increase in the initial temperature of the bulk solution. The decreasing values of k_{id} (mg/g.min$^{0.5}$) and C (mg/g) signify a reduction in boundary layer resistance, which corresponds with the observed increase in external mass transfer diffusion rate constants with an increase in initial temperature of the bulk solution. The decrease of the C (mg/g) values also implies the reduced influence of surface adsorption in the rate-controlling step. The magnitudes of the intraparticle diffusion parameters at different initial pollutant temperatures were large for the MFC metal oxide suggesting that intraparticle diffusion was more controlling during the adsorption process on the ternary MFC metal oxide.

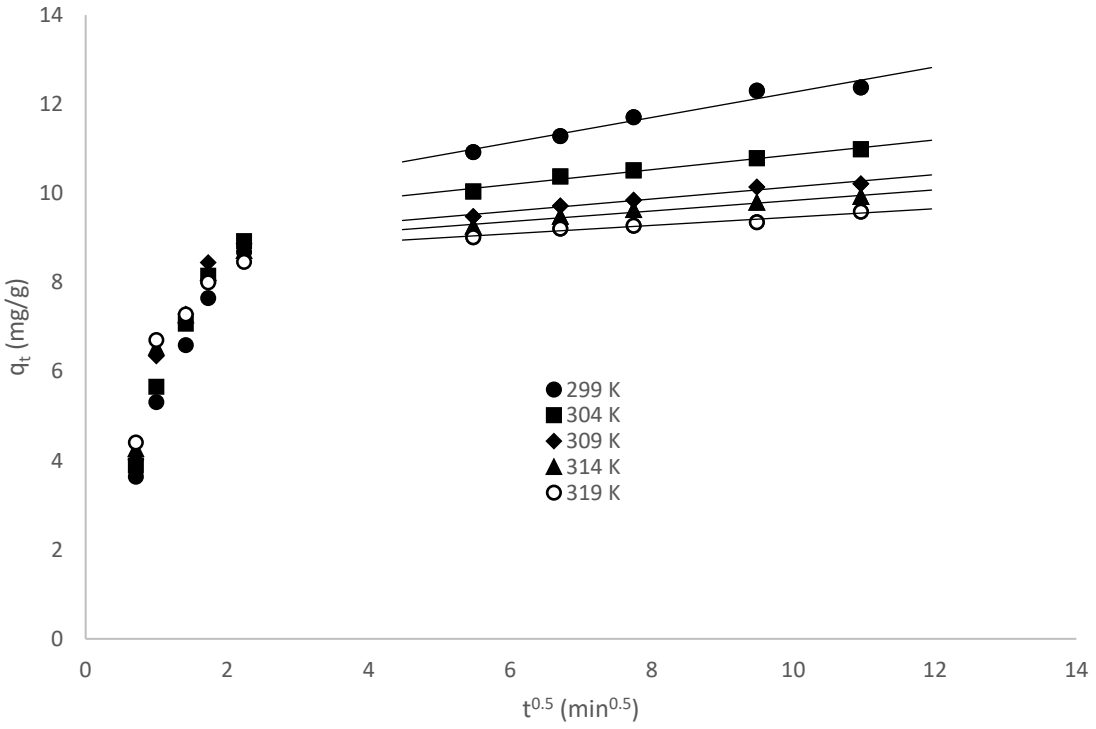

Fig. 5.17a Intraparticle diffusion treatment of Cr(VI) adsorption onto MC binary metal oxide at different initial temperatures.

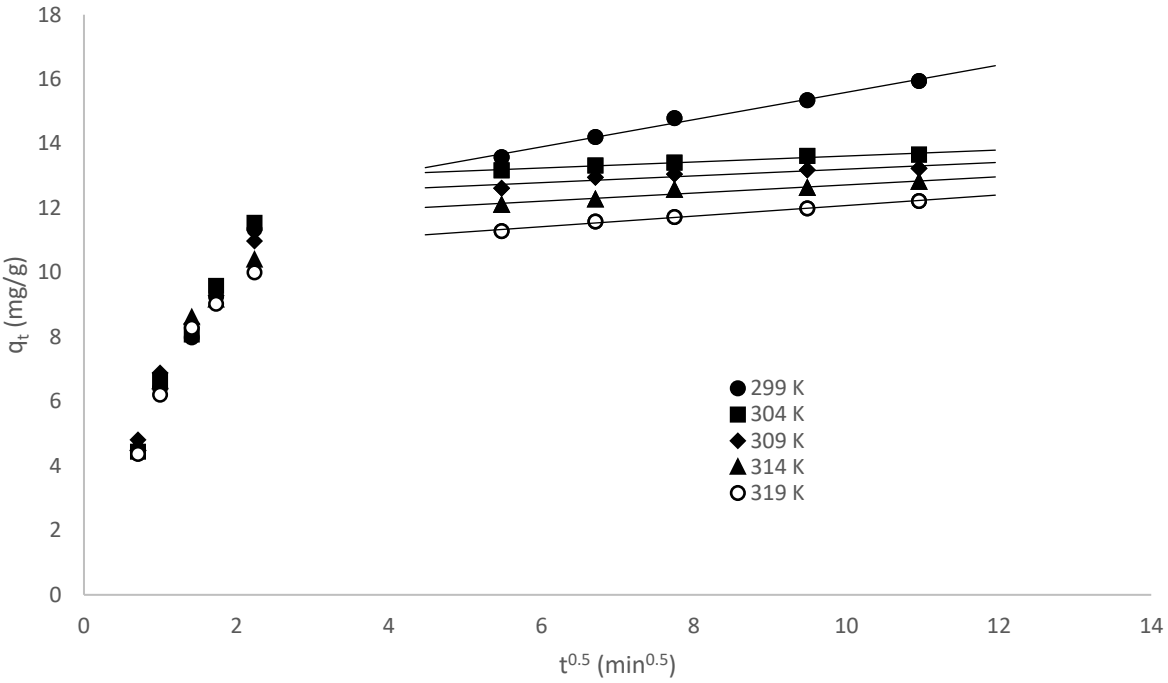

Fig. 5.17b Intraparticle diffusion treatment of Cr(VI) adsorption onto MF binary metal oxide at different initial temperatures.

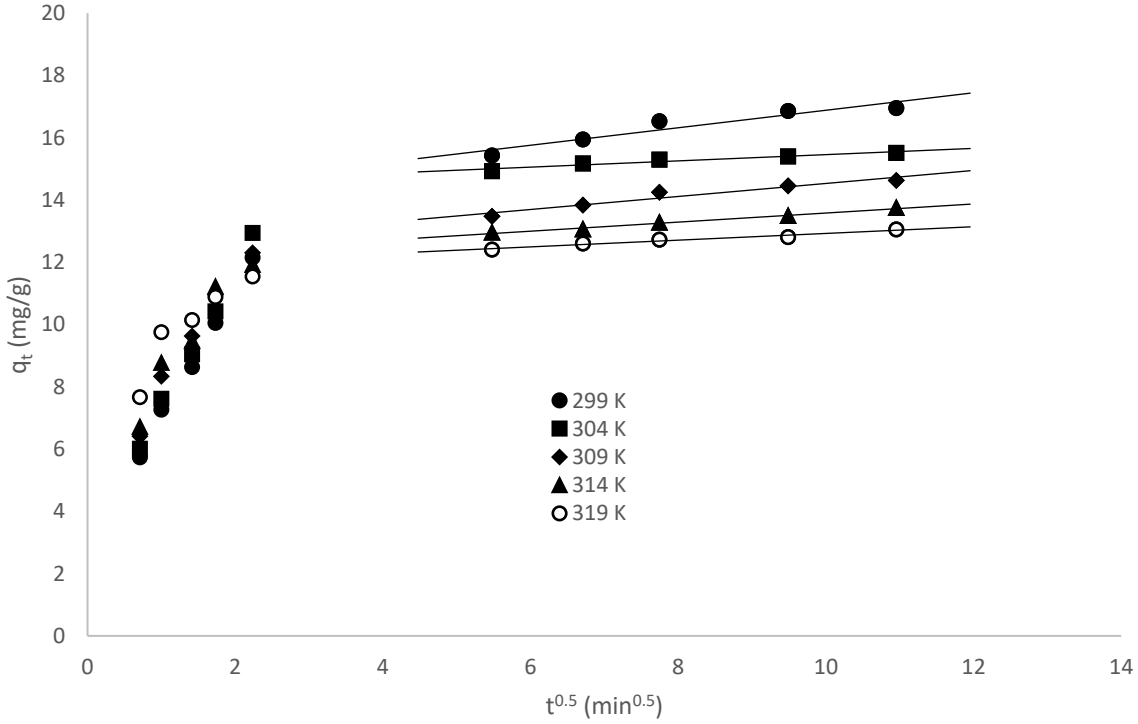

Fig. 5.17c Intraparticle diffusion treatment of Cr(VI) adsorption onto MFC ternary metal oxide at different initial temperatures.

The fractional uptake plots are presented in Figs 5.18a-c and the values of D_1 (cm^2/s) are outlined in Tables 5.7a-c.

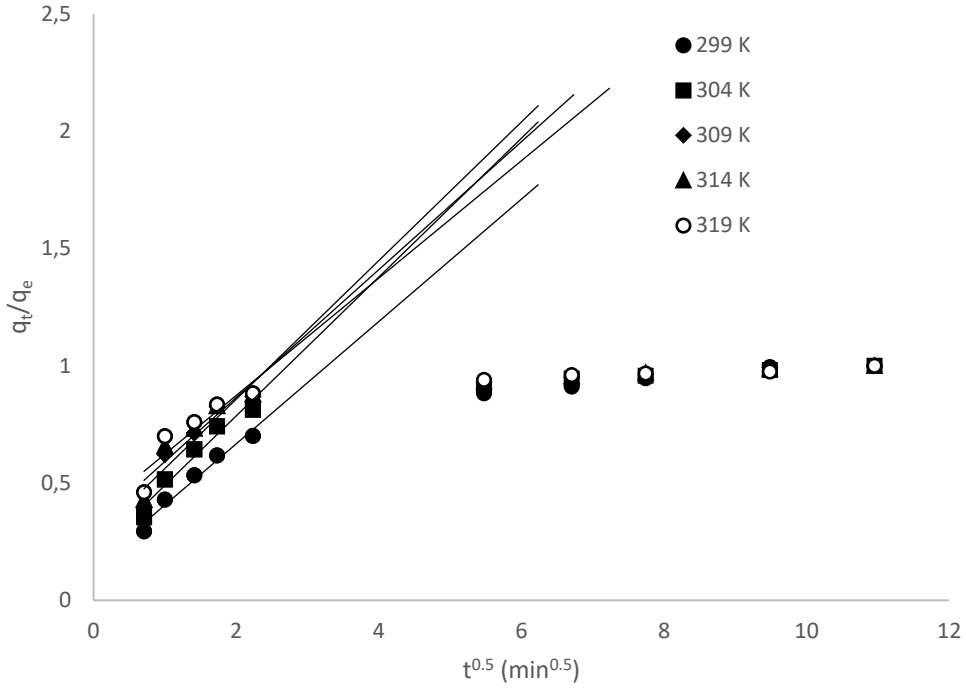

Fig 5.18a Fractional uptake of Cr(VI) at different temperatures on MC binary metal oxide against the square root of time.

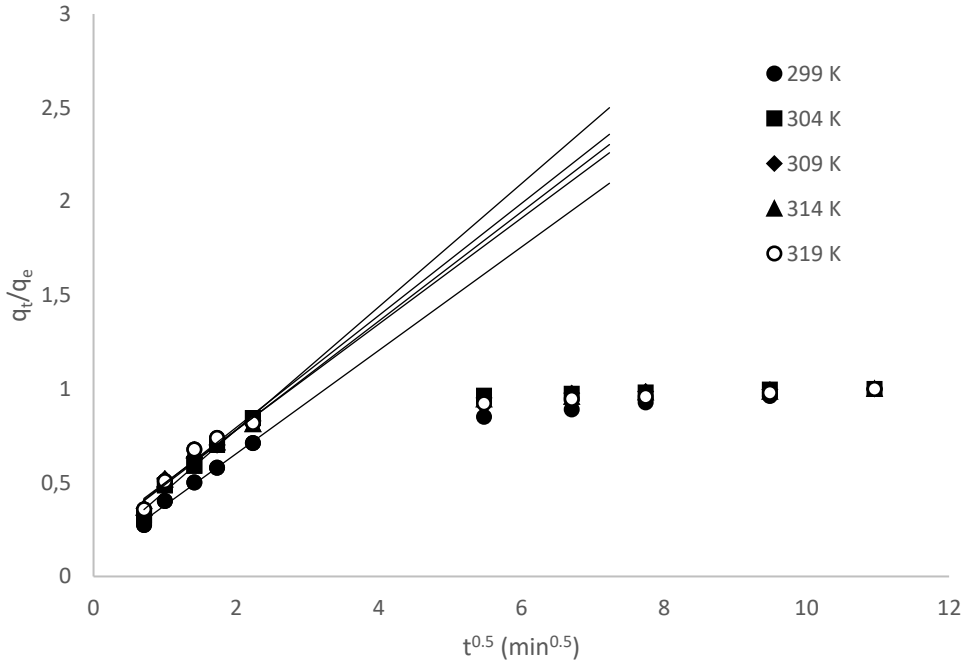

Fig 5.18b Fractional uptake of Cr(VI) at different temperatures on MF binary metal oxide against the square root of time.

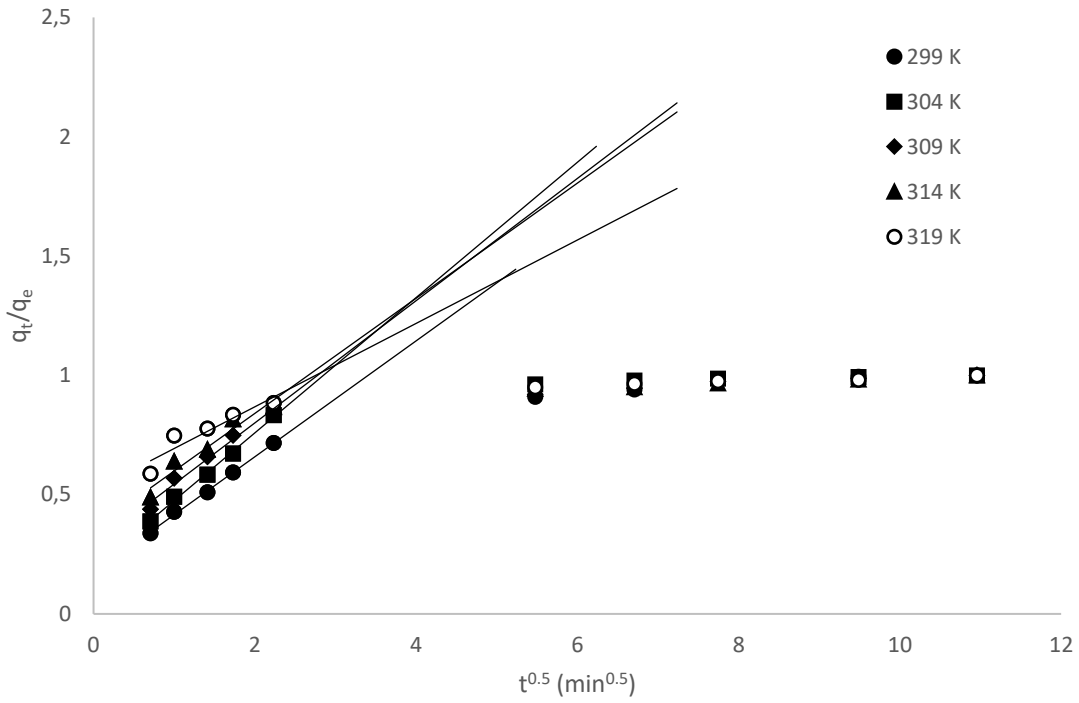

Fig 5.18c Fractional uptake of Cr(VI) at different temperatures on MFC ternary metal oxide against the square root of time.

The plots are divided into two linear segments, a fast initial stage which is followed by a slower uptake stage. The magnitudes of the pore diffusion coefficients, D_2 (cm^2/s), for the MC, MF and MFC metal oxides in Tables 5.7a-c, were determined from the Boyd plots of *Bt* versus *t*, presented in Figs 5.19a-c, and the Boyd expression (Eq 5.10) at the different initial temperatures of Cr(VI). The *Bt* versus *t* plots for the MC, MF and MFC metal oxides show straight lines which do not cut through the origin during the initial stage of the adsorption process, showing that the adsorption is controlled by external mass transfer processes and not intraparticle diffusion. The y-intercept values shifted towards positive digits as the initial pollutant temperatures increased from 299-319 K, signifying an increase in external mass transport [MC: -0.06-0.11; MF: -0.18-(-0.06); and MFC: -0.09-0.38]. This might be attributed to a decrease in boundary layer effects due to a decrease in solution viscosity. The ternary MFC metal oxide showed the largest shift in y-intercept values than the binary MC and MF metal oxides. The observed differences between the binary and the ternary metal oxides might be due to differences in adsorbent particle sizes and their surface conformations which in turn might affect the boundary effects as the initial temperature of the Cr(VI) increased. The ternary MFC metal oxide showed the largest shift of y-intercept values, implying an increase in the initial temperature of the Cr(VI) enhanced the external mass transfer processes on the ternary metal

oxide. The film diffusion coefficients, D_1 (cm^2/s), increased as the initial temperature of the bulk solution increased. The increase in D_1 (cm^2/s) with increasing initial solution temperature is due to a decrease in boundary layer resistance, probably due to a decrease in solution viscosity. The magnitudes of D_1 (cm^2/s) for the MFC metal oxide were higher than for the MC and MF metal oxides. The larger values of D_1 (cm^2/s) for the MFC metal oxide are due to the large sizes of the MFC metal oxide particles which results in a decrease in the external surface area reducing the boundary layer effect. The pore diffusion coefficients, D_2 (cm^2/s), increased with an increase in the initial bulk concentration. The increase of D_2 (cm^2/s) with an increase in initial Cr(VI) concentration was attributed to an increase in mobility of the adsorbate particles resulting in an increase in the diffusion of adsorbate particles into the pores on the adsorbent surface. The MFC metal oxide exhibited larger D_2 (cm^2/s) values than for the MC and MF metal oxides. This suggests that the MFC surface was more porous or had pores of the right sizes to accommodate entry of the Cr(VI) oxyanions, enabling faster diffusion of the adsorbate particles into the pores. The diffusion coefficients of the metal oxides presented in Table 5.7a-c show that D_2 (cm^2/s) > D_1 (cm^2/s). This implies that the adsorbate particles encountered greater resistance to diffuse through the boundary layer than to diffuse into the pores. Therefore, the adsorption process appears to be controlled by film diffusion.

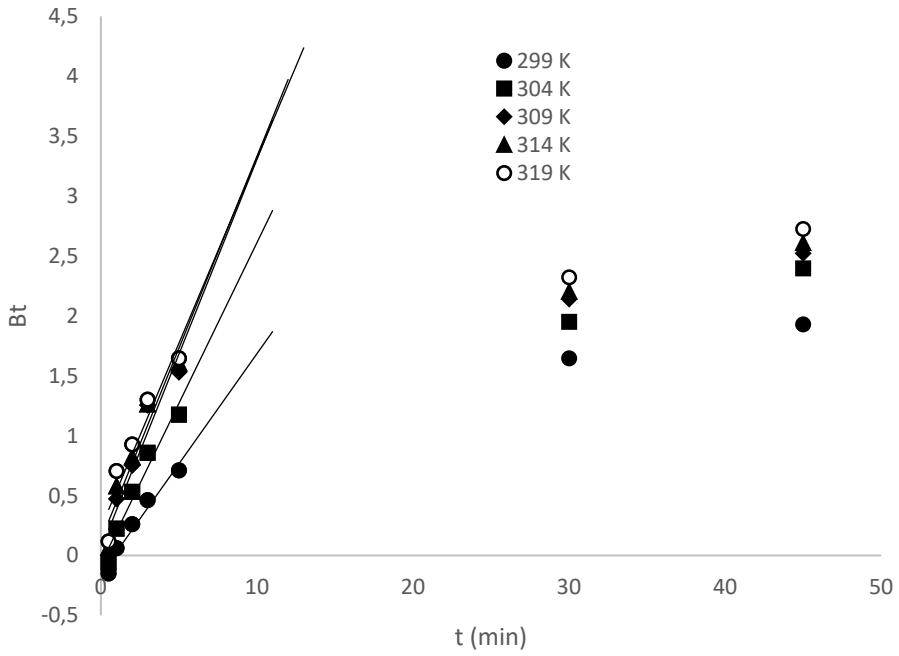

Fig 5.19a Boyd plots for adsorption of Cr(VI) on MC binary metal oxide at different temperatures.

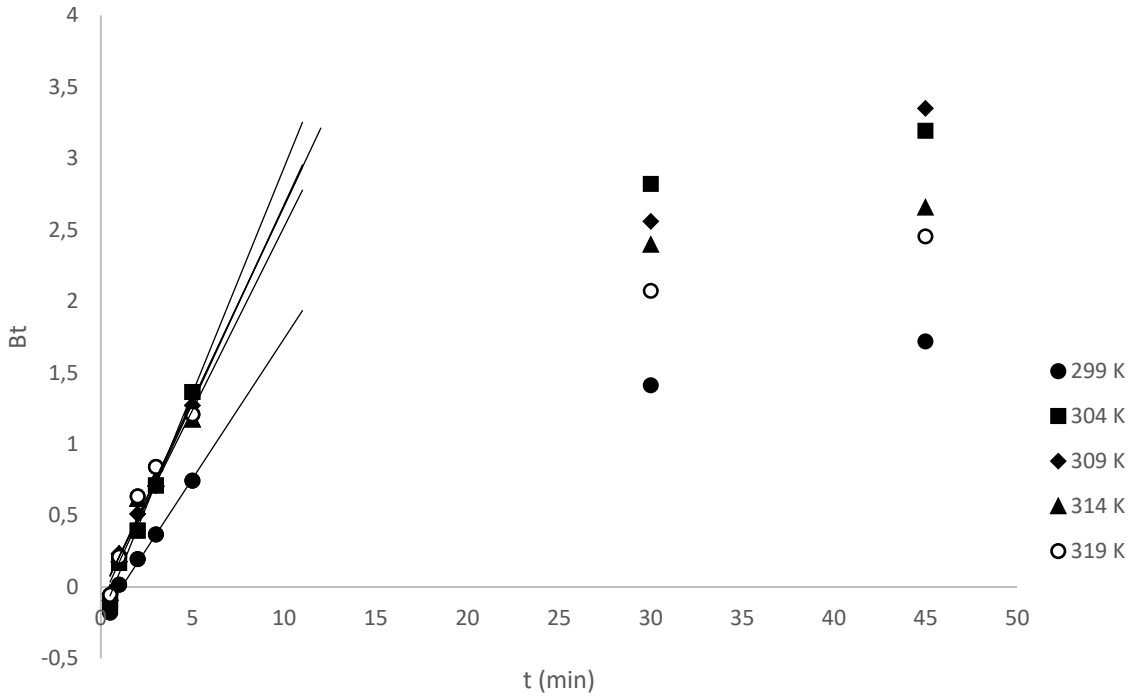

Fig 5.19b Boyd plots for adsorption of Cr(VI) on MF binary metal oxide at different temperatures.

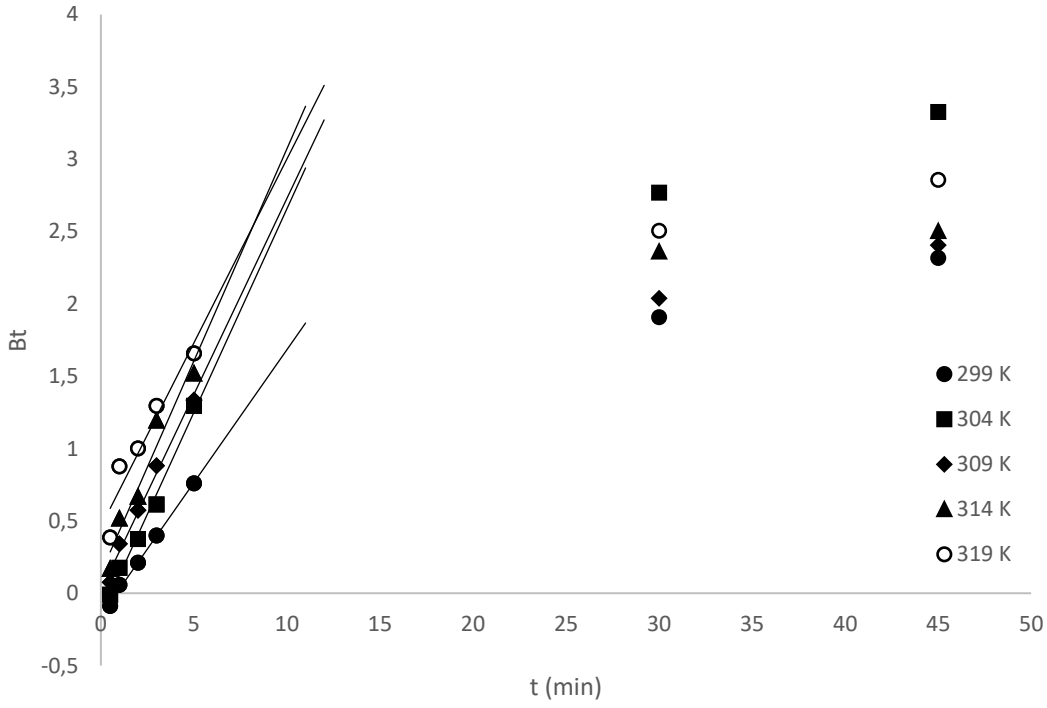

Fig 5.19c Boyd plots for adsorption of Cr(VI) on MFC ternary metal oxide at different temperatures.

Arsenic(III): The external mass transfer diffusion rate constants, k_s (1/min) were determined by plotting C_t/C_o at different initial temperatures of As(III) against time, and the results are presented in Figs 5.20a-c.

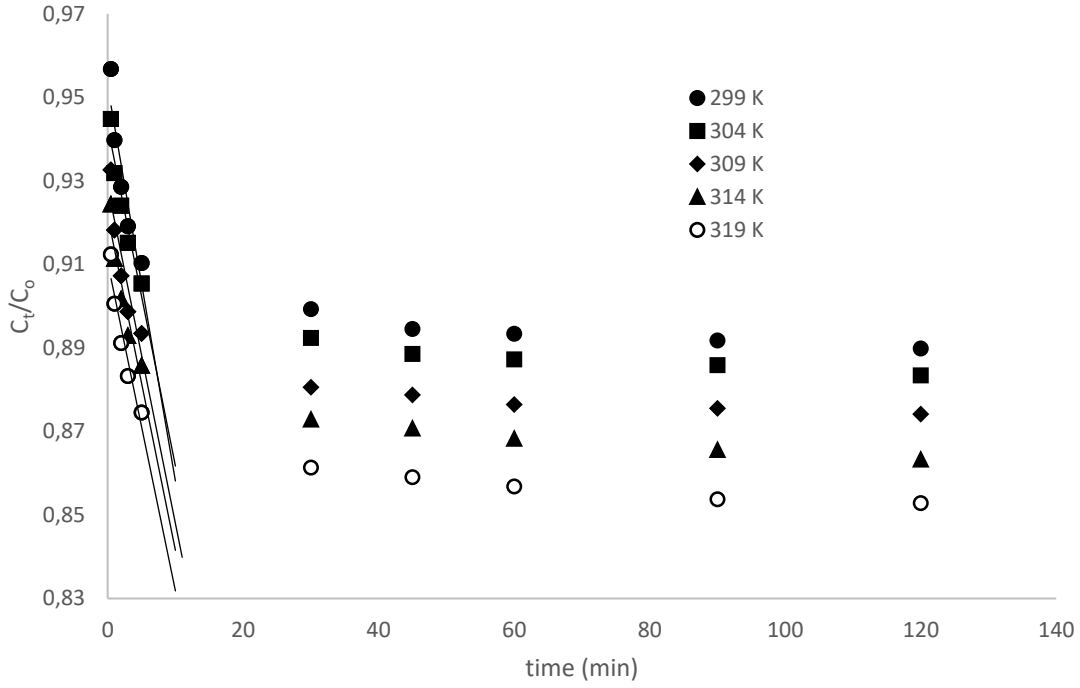

Fig 5.20a External mass transfer diffusion plot for adsorption of 10 mg/dm^3 As(III) at different initial temperatures onto MC binary metal oxide.

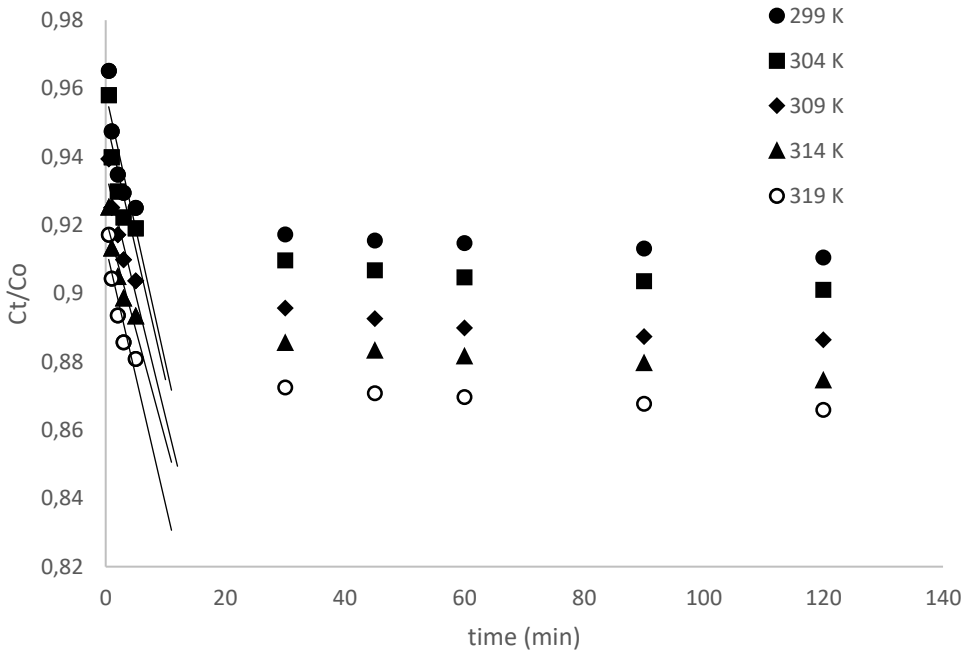

Fig 5.20b External mass transfer diffusion plot for adsorption of 10 mg/dm^3 As(III) at different initial temperatures onto MF binary metal oxide.

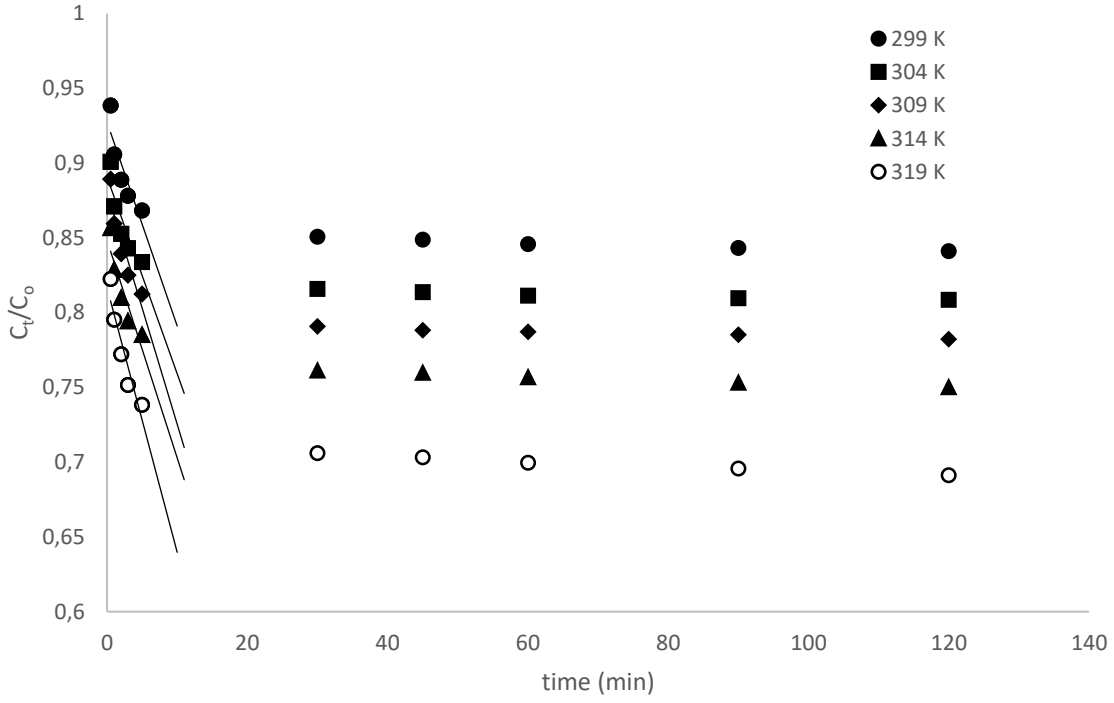

Fig 5.20c External mass transfer diffusion plot for adsorption of 10 mg/dm^3 As(III) at different initial temperatures onto MFC ternary metal oxide.

The external mass transfer diffusion rate constants, k_s (1/min) for the adsorption of 10 mg/dm^3 of As(III) at different initial temperatures onto MC, MF and MFC metal oxides are presented in Tables 5.8a-c. The k_s (1/min) values for the binary MC and MF metal oxides decreased in the ranges 0.0095-0.0079 and 0.0079-0.0065 respectively, as the initial temperature of the As(III) increased from 299-319 K. The k_s (1/min) decreased probably due to an increase in boundary layer resistance which can be due to the wide distribution of the small binary nanostructured metal oxides particle sizes resulting in agglomeration (Ociński et al., 2016). This reduces the available surface area for adsorption, increasing boundary layer effects as the initial temperature of the bulk solution increased. The k_s (1/min) values for the ternary MFC metal oxide increased from 0.0131-0.0171 with an increase in the initial temperature of the As(III) solution. This observation showed that there was a decrease in boundary effects around the ternary MFC metal oxide particles. This was attributed to a decrease in solution viscosity as the initial bulk solution temperature increased from 299-319 K. The noted differences in the k_s (1/min) values between the binary and the ternary metal oxides were ascribed to differences in particle sizes and surface conformation. The binary MF and MC metal oxides had lower k_s

(1/min) values than the ternary MFC metal oxide. This implies that the migration of adsorbate across the boundary layer to the adsorbent external surface was more controlling for the binary metal oxides than for the ternary MFC metal oxide.

To determine whether the adsorption of As(III) at different initial temperatures onto the MC, MF and MFC metal oxides is pore controlled, the Weber and Morris (1963) intraparticle diffusion model equation (Eq 5.7) was applied onto the kinetic experimental data. The intraparticle diffusion plots of q_t against $t^{0.5}$ are presented in Figs 5.21a-c and show that intraparticle diffusion is not the only rate-limiting step in the adsorption process. The plots are split into two linear sections which do not pass through the origin, showing that several mechanisms control the adsorption process. The initial rapid stage is attributed to external surface adsorption controlled by external mass transport since diffusion across the boundary layer to the adsorbent surface is only important at the beginning of the adsorption process (Cáceres-Jensen et al., 2013). The second stage signifies the slow adsorption of the adsorbate particles and is intraparticle diffusion-controlled. The switch in the adsorption mechanism can be ascribed to a decrease in the concentration driving force which increases the boundary effect as the adsorption process proceeds. The results of the calculated intraparticle diffusion parameters and the R^2 error functions are presented in Tables 5.8a-c. The results show that the magnitudes of the k_{id} (mg/g.min$^{0.5}$) and C (mg/g) increase as the initial concentration of the As(III) increases, suggesting an increase in boundary effects and influence of film diffusion to the adsorption process (Gheju et al., 2016). The magnitudes of the intraparticle diffusion rate constants at different initial temperatures of the As(III) were larger for the ternary MFC metal oxide than for the binary MC and MF metal oxides suggesting that intraparticle diffusion was more controlling on the ternary MFC metal oxide during the adsorption (Yoon et al., 2017). The smaller binary MC and MF metal oxide adsorbent particles experience less intraparticle diffusion resistance. The increase in the magnitude of ki_d (mg/g.min$^{0.5}$) with an increase in the initial temperature can also be attributed to the increase in the kinetic energy of the adsorbate, enhancing their entry into pores on the surface of the adsorbent (Ofomaja et al., 2010a). The precise non-conformity of the experimental adsorption kinetic data to the external mass transfer or the intraparticle diffusion models seems to suggest that the adsorption process is also controlled by a chemical reaction (Ociński et al., 2016).

Table 5.8a Diffusion coefficients for the adsorption of 10 mg/dm^3 of As(III) onto MC binary metal oxide at different initial temperatures.

Diffusion parameters	Initial As(III) temperature (K)				
	299	304	309	314	319
External mass transfer					
k_s (1/min)	0.0095	0.0081	0.0081	0.0080	0.0079
R^2	0.9721	0.9206	0.9409	0.9857	0.9129
Intraparticle diffusion					
k_{id} (mg/g.min$^{0.5}$)	0.1141	0.1470	0.1542	0.1609	0.1759
C (mg/g)	9.375	10.059	11.365	11.764	13.019
R^2	0.9987	0.9376	0.9460	0.9951	0.9716
Boyd diffusion model					
($D_1 \times 10^{-17}$) (cm^2/s)	2.239	1.436	1.271	1.037	0.085
R^2	0.9535	0.9777	0.9354	0.9627	0.9777
($D_2 \times 10^{-17}$) (cm^2/s)	9.192	8.736	7.981	7.904	7.849
R^2	0.9647	0.9820	0.9314	0.9594	0.9783

Table 5.8b Diffusion coefficients for the adsorption of 10 mg/dm^3 of As(III) onto MF binary metal oxide at different initial temperatures.

Diffusion parameters	Initial As(III) temperature (K)				
	299	304	309	314	319
External mass transfer					
k_s (1/min)	0.0079	0.0077	0.0075	0.0072	0.0065
R^2	0.9612	0.9607	0.9521	0.9512	0.9456
Intraparticle diffusion					
k_{id} (mg/g.min$^{0.5}$)	0.1147	0.1186	0.1461	0.1695	0.1864
C (mg/g)	7.646	8.302	9.588	10.403	12.110
R^2	0.9775	0.9567	0.9439	0.9603	0.9988
Boyd diffusion model					
($D_1 \times 10^{-17}$) (cm^2/s)	2.669	2.055	1.308	1.043	0.088
R^2	0.8773	0.8754	0.9394	0.9413	0.9391
($D_2 \times 10^{-17}$) (cm^2/s)	10.859	10.489	9.433	9.235	8.226
R^2	0.8900	0.8715	0.9493	0.9379	0.9418

Table 5.8c Diffusion coefficients for the adsorption of 10 mg/dm^3 of As(III) onto MFC ternary metal oxide at different initial temperatures.

Diffusion parameters	Initial As(III) temperature (K)				
	299	304	309	314	319
External mass transfer					
k_s (1/min)	0.0131	0.0136	0.0146	0.0156	0.0171
R^2	0.9812	0.9860	0.9439	0.9317	0.9783
Intraparticle diffusion					
k_{id} (mg/g.min$^{0.5}$)	0.1323	0.1474	0.1785	0.2091	0.2688
C (mg/g)	13.963	17.746	20.136	22.688	27.907
R^2	0.9888	0.9502	0.9780	0.9937	0.9968
Boyd diffusion model					
($D_1 \times 10^{-17}$) (cm^2/s)	5.226	3.359	3.540	2.369	2.242
R^2	0.8887	0.8943	0.9362	0.9284	0.9590
($D_2 \times 10^{-17}$) (cm^2/s)	22.225	22.126	21.601	19.607	18.392
R^2	0.9135	0.9155	0.9522	0.9264	0.9515

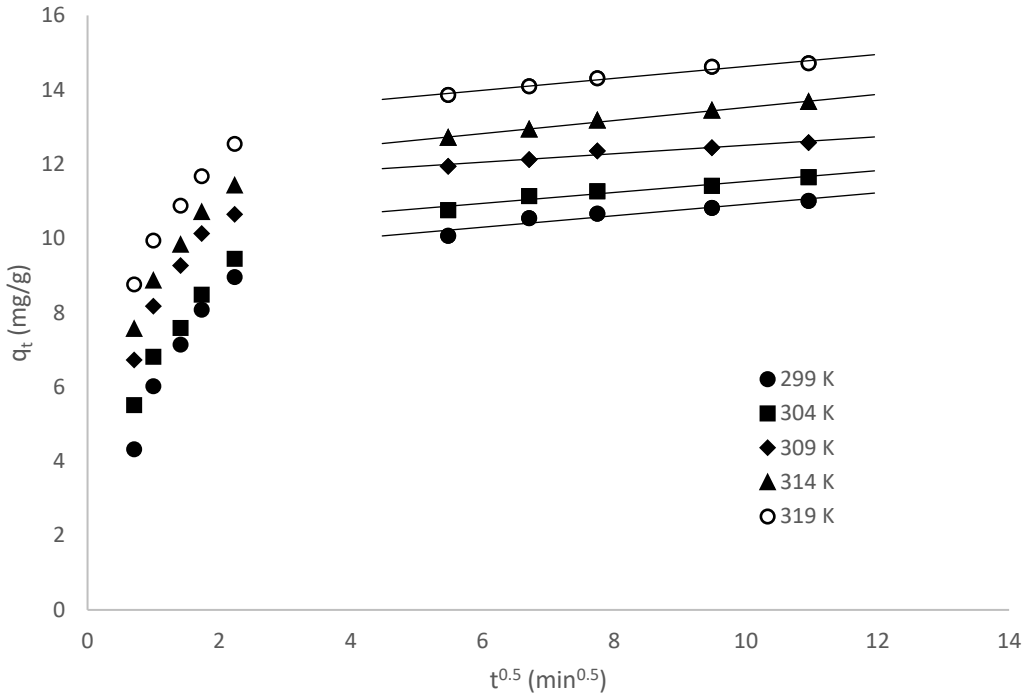

Fig. 5.21a Intraparticle diffusion treatment of 10 mg/dm^3 As(III) adsorption onto MC binary metal oxide at different initial temperatures.

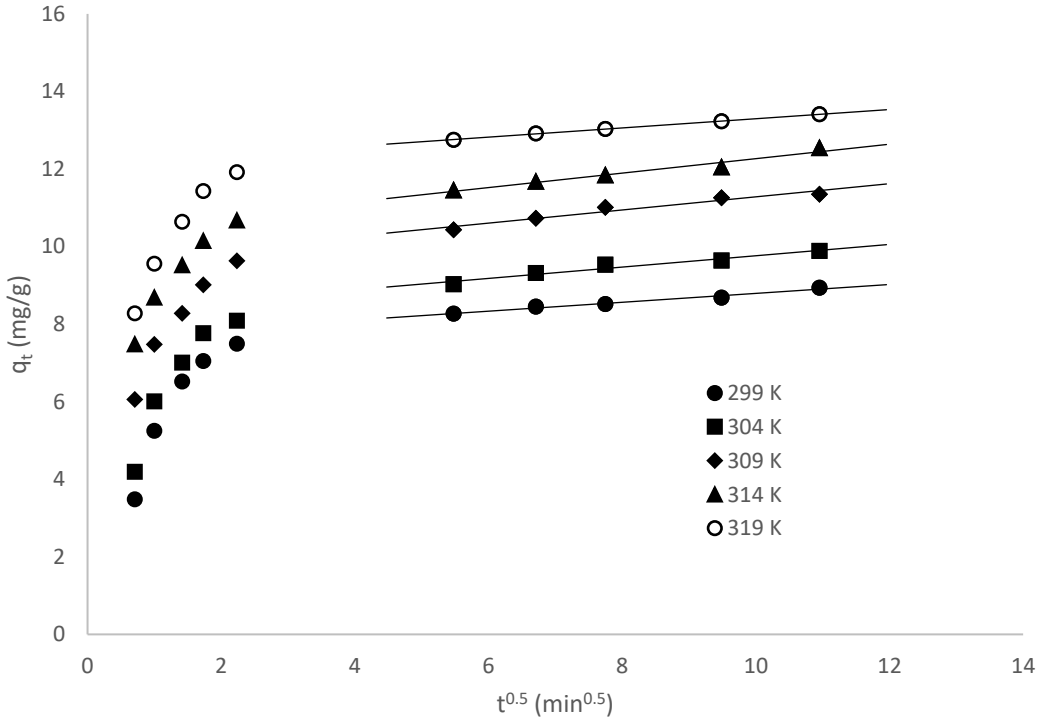

Fig. 5.21b Intraparticle diffusion treatment of 10 mg/dm^3 As(III) adsorption onto MF binary metal oxide at different initial temperatures.

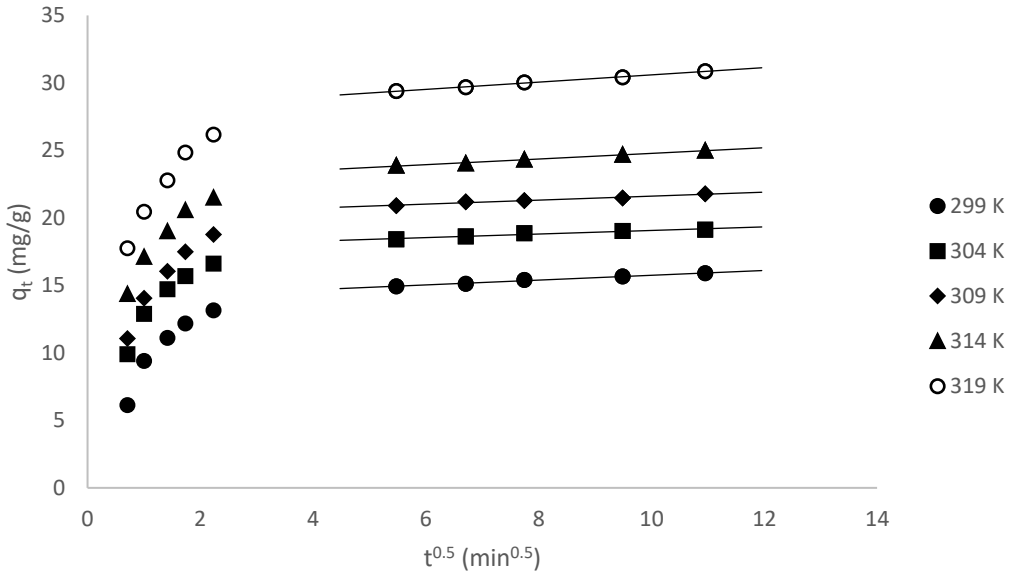

Fig. 5.21c Intraparticle diffusion treatment of 10 mg/dm^3 As(III) adsorption onto MFC ternary metal oxide at different initial temperatures.

The graphs of fractional uptake, q_t/q_e against the square root of time, $t^{0.5}$ ($min^{0.5}$) are presented in Figs 5.22a-c. The initial stage is fast and is followed by a much slower uptake stage.

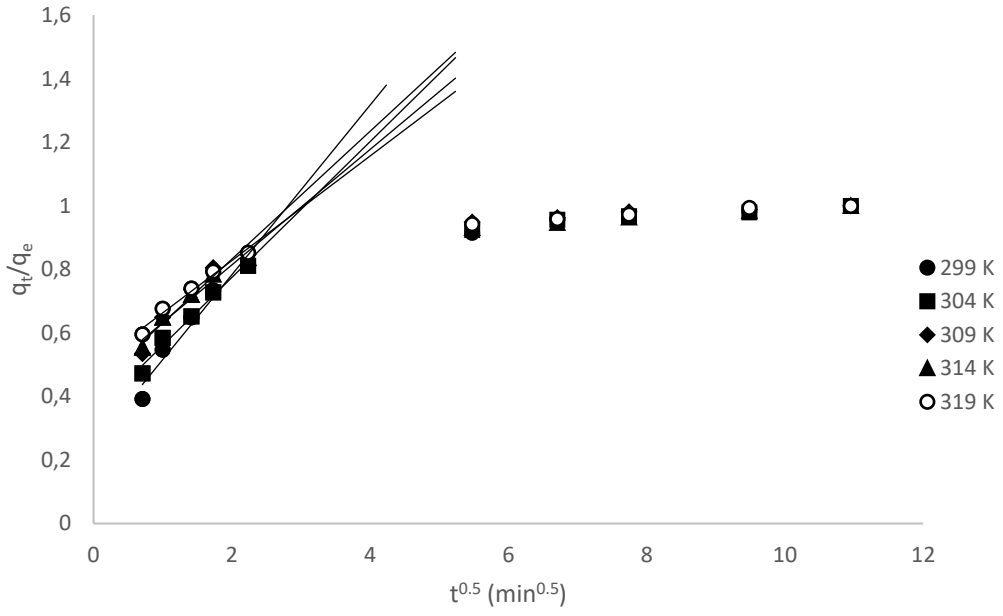

Fig 5.22a Fractional uptake of As(III) at different initial temperatures onto MC binary metal oxide against the square root of time.

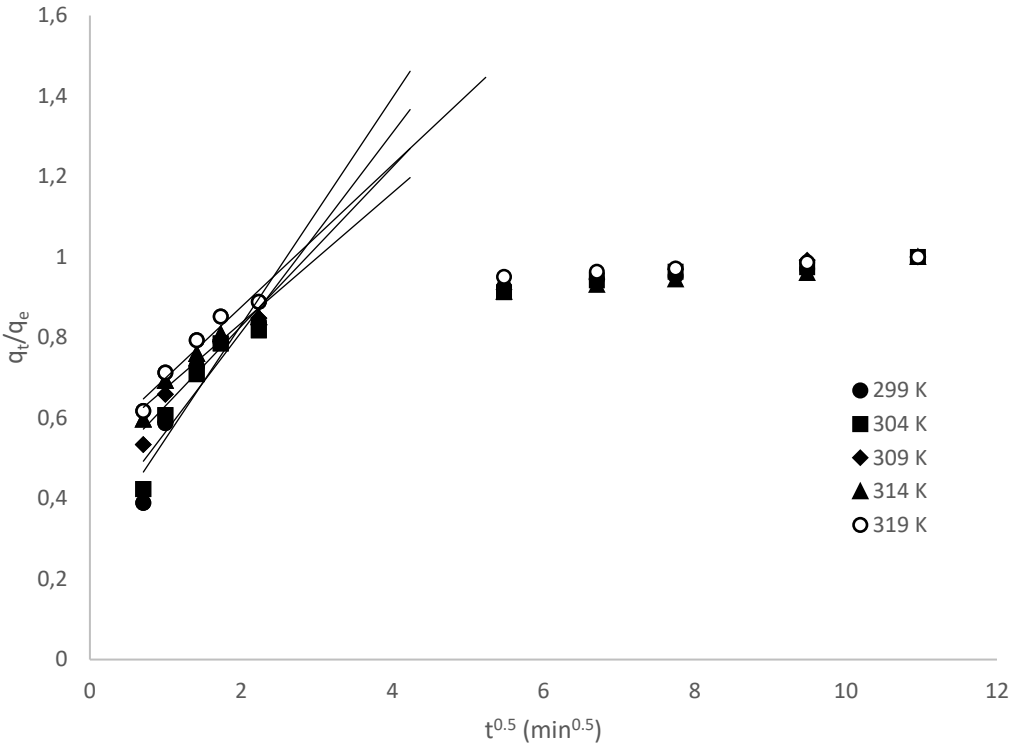

Fig 5.22b Fractional uptake of As(III) at different initial temperatures onto MF binary metal oxide against the square root of time.

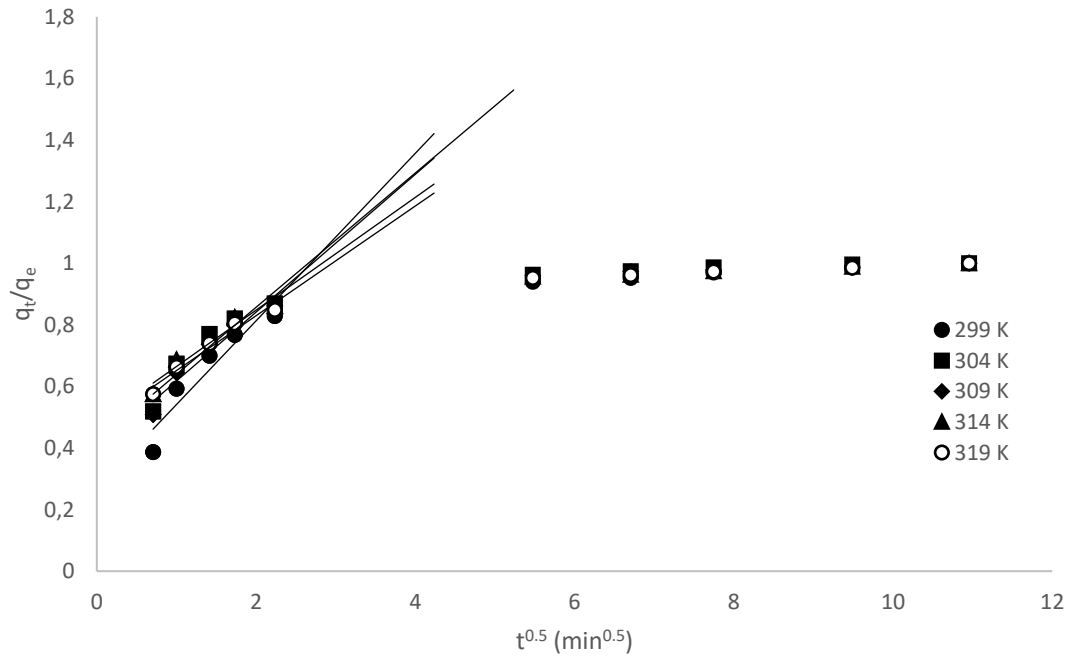

Fig 5.22c Fractional uptake of As(III) at different initial temperatures onto MFC ternary metal oxide against the square root of time.

The film diffusion coefficients, D_1 (cm^2/s) and the pore diffusion coefficient, D_2 (cm^2/s) for the MC, MF and MFC metal oxides at varying initial temperatures of As(III) are presented in Tables 5.8a-c. The Boyd plots presented in Figs 5.23a-c, for the MC, MF and MFC metal oxides show linear relationships which do not cut through the origin in the initial phase of the adsorption process at the different initial temperatures of As(III). This signifies that external mass transport controls the adsorption process during the initial phase. The film diffusion coefficients, D_1 (cm^2/s), for the MC, MF and MFC metal oxides decreased as the initial As(III) temperature increased. The decrease in D_1 (cm^2/s) with increasing initial As(III) temperature was ascribed to the increase in boundary layer resistance caused by the agglomeration of the adsorbent nanoparticles. The magnitudes of D_1 (cm^2/s) for the ternary MFC metal oxide were higher than for the binary MC and MF metal oxides. The larger values of D_1 (cm^2/s) for the ternary MFC metal oxide can be attributed to the larger MFC particle sizes which reduced the extent of agglomeration thereby reducing the boundary layer effect. The pore diffusion coefficients, D_2 (cm^2/s), decreased with an increase in the initial temperature of the bulk solution for the MC, MF and MFC metal oxides. The decrease of D_2 (cm^2/s) with an increase in initial As(III) temperature was attributed to an increase in surface reactions reducing the driving force for the adsorbate species to enter into the adsorbent pores. The increase in temperature appears to enhance agglomeration on the smaller binary MC and MF metal oxides, reducing access of the adsorbate particles to the pores on the binary MC and MF metal oxides, accounting for the observed smaller D_2 (cm^2/s) values. An increase in temperature might increase the bond lengths of the H_3AsO_3 adsorbate particles. This coupled with the agglomeration effect observed on the smaller binary MC and MF metal oxides might also enhance pore blockage reducing the ability of the adsorbate particles to enter small pores on the adsorbent surface causing a reduction in the magnitude of the D_2 (cm/s) values (Dai et al., 2016). The diffusion coefficients of the metal oxides presented in Tables 5.8a-c show that D_2 (cm^2/s) > D_1 (cm^2/s). This implies that the adsorbate particles encountered greater resistance to diffuse through the boundary layer than to diffuse into the pores, signifying that film diffusion controls the adsorption process at this stage.

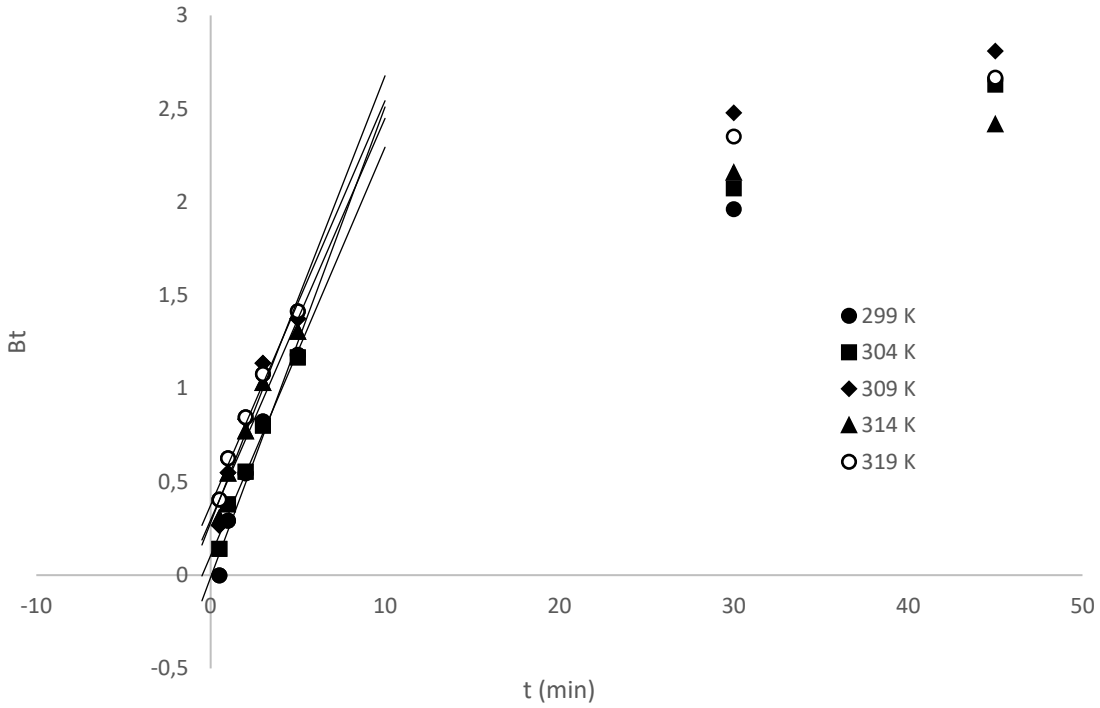

Fig 5.23a Boyd plots for adsorption of As(III) at different initial temperatures onto MC binary metal oxide.

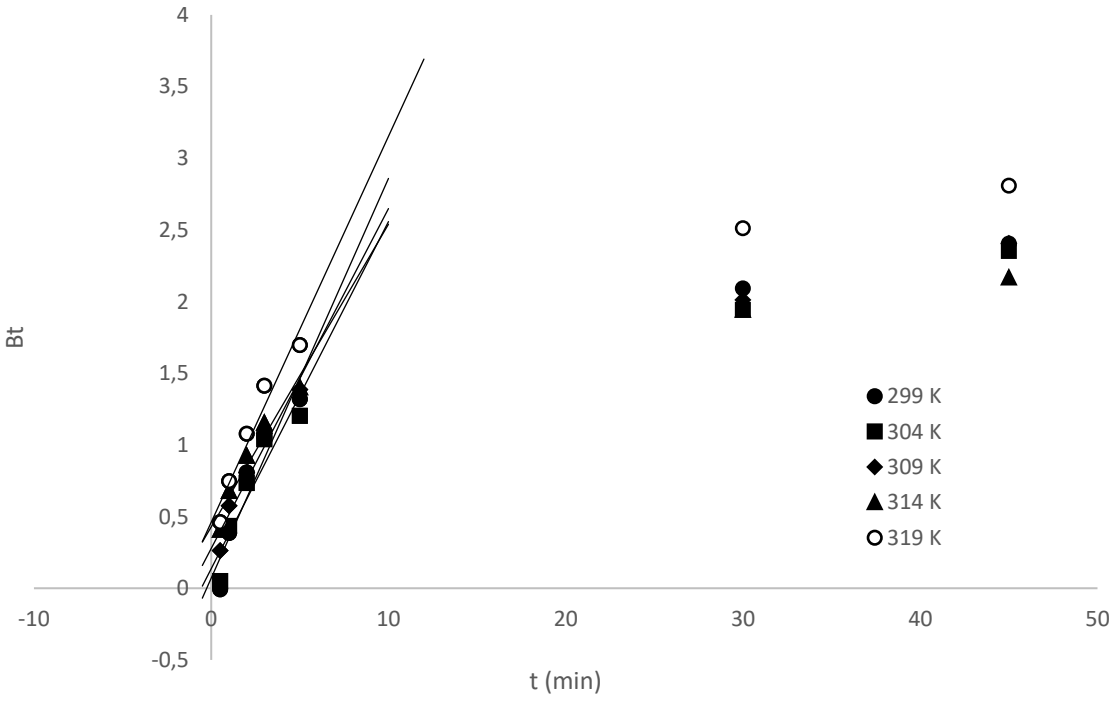

Fig 5.23b Boyd plots for adsorption of As(III) at different initial temperatures onto MF binary metal oxide.

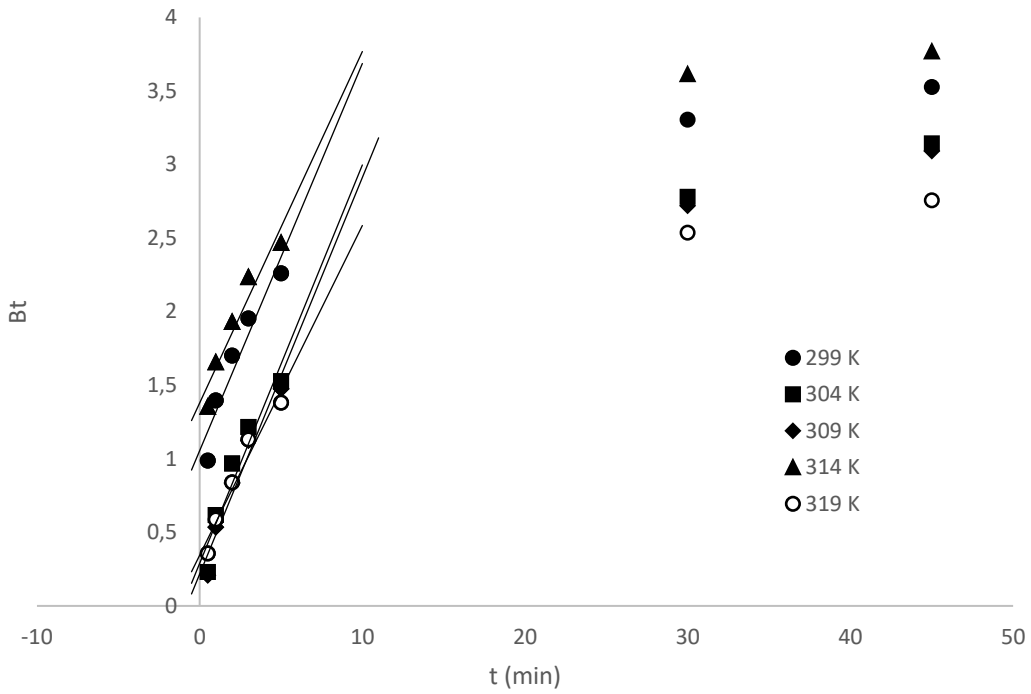

Fig 5.23c Boyd plots for adsorption of As(III) at different initial temperatures onto MFC ternary metal oxide.

5.2.3.2.3 Activation energies

Chromium(VI): The activation energies of the adsorption kinetic processes can be used to determine whether the diffusion pathway is film or pore-controlled (Zulfikar et al., 2013). The activation energy, E_a (kJ/mol), was calculated using the Arrhenius (1889) equation:

$$\ln k_2 = \ln k_o - \frac{E_a}{RT} \quad (5.12)$$

where, k_2 (g/mg.min) is the pseudo-second-order rate constant, k_o (g/mg.min) is the temperature-independent factor, E_a (kJ/mol) is the activation energy, R is the Arrhenius constant (8.314 J/mol.K) and T (K) is the solution temperature. The slope of the Arrhenius plot of $ln\ k_2$ against $1/T$ gives the activation energy, E_a (kJ/mol) and the plot is presented in Fig 5.24. The Cr(VI) adsorption activation energies, E_a (kJ/mol), on the MC, MF and MFC metal oxides, as the initial solution temperature was increased from 299-319 K, were found to be 18.007, 17,427 and 18,330. If the adsorption process is film diffusion-controlled, the E_a (kJ/mol) values are found to be between 17-21, and for pore diffusion-controlled adsorption, the E_a (kJ/mol) values are from 21-42 (Sparks, 1999; Namasivayam & Sangeetha, 2006). Thus,

the E_a values show that the adsorption of Cr(VI) onto the MC, MF and MFC metal oxides as the initial temperature is increased from 299-319 K is film diffusion controlled.

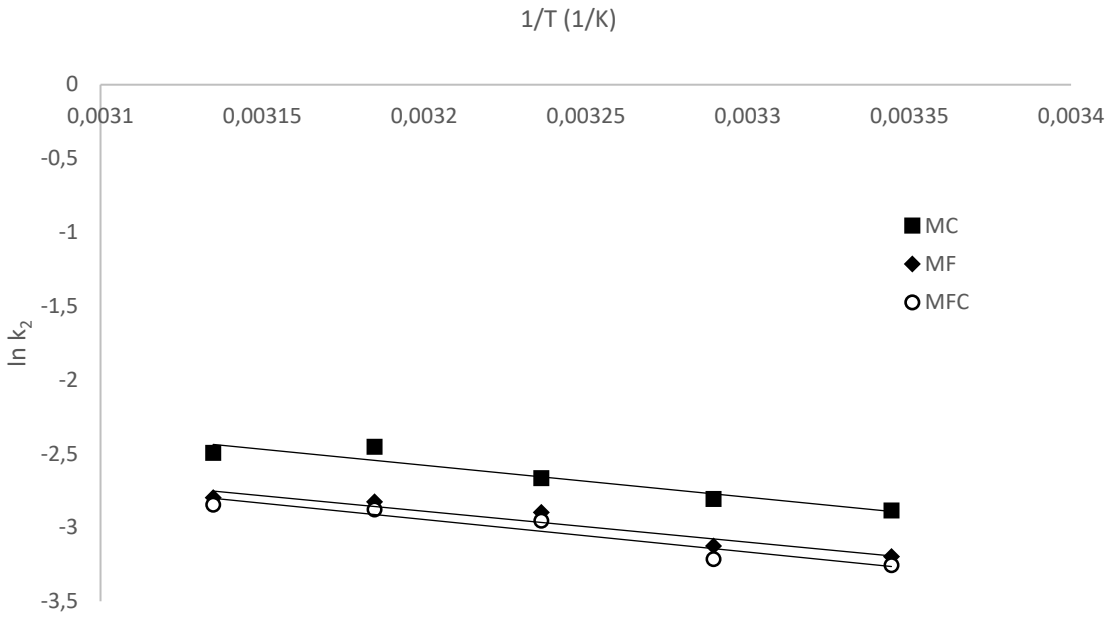

Fig 5.24 Arrhenius plots for the adsorption kinetics of Cr(VI) onto MC, MF and MFC metal oxide at different temperatures.

Arsenic(III): The Arrhenius plot of *ln* k_2 against *1/T* gives the activation energy, E_a (kJ/mol) and the plot is presented in Fig 5.25. The As(III) adsorption activation energies, E_a (kJ/mol), on the MC, MF and MFC metal oxides, as the initial temperature of the bulk solution was increased from 299-319 K, were found to be 14.318, 19.042 and 17.692. The E_a values show that the adsorption of As(III) onto the MC, MF and MFC metal oxides as the initial temperature is increased from 299-319 K is probably film diffusion controlled.

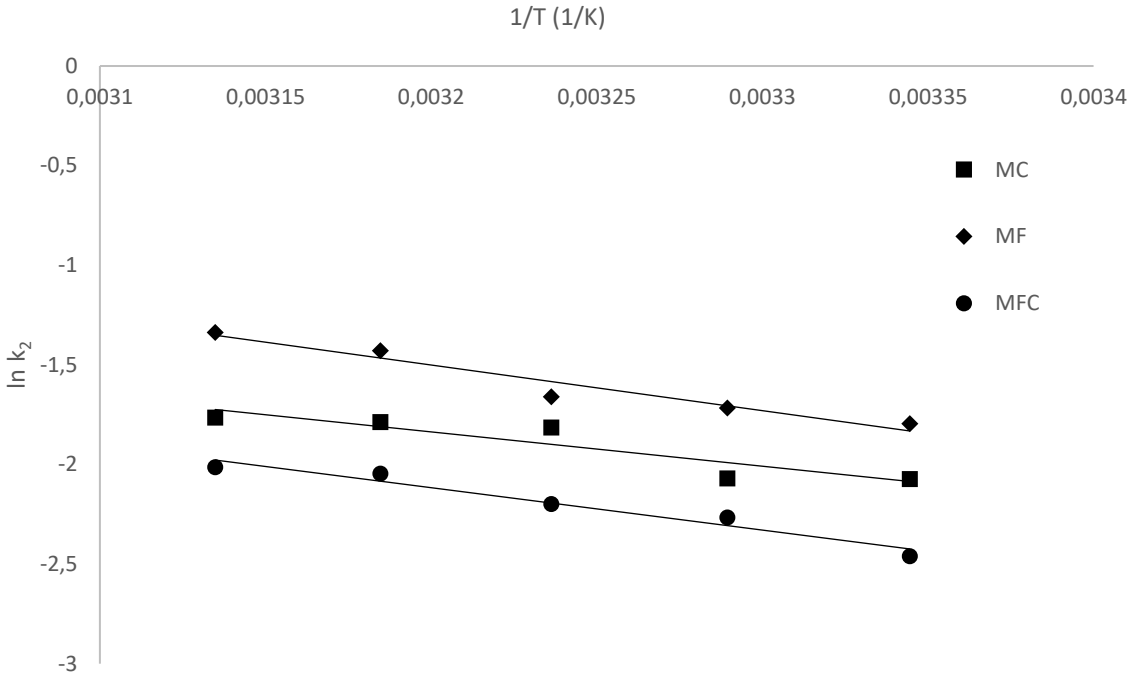

Fig 5.25 Arrhenius plots for the adsorption kinetics of As(III) onto MC, MF and MFC metal oxide at different temperatures.

5.3 CONCLUSION

The influence of solution pH and adsorbent dosage concentration on the uptake of Cr(VI) and As(III) from aqueous solution onto the MC, MF and MFC metal oxide composite is well presented in this chapter. An initial solution pH of 3 was found to be optimum for the non-specific uptake of Cr(VI) from the liquid phase onto the surface of the MC, MF and MFC metal oxides. For the specific adsorption of As(III), a solution pH of 8 was determined as the optimum for the MF metal oxide, whilst a pH of 9 was applied for the MC and MFC metal oxides. In both adsorption investigations, the optimum adsorbent dose was found to be 0.05 g for the MC, MF and MFC nanostructured metal oxide composites.

The non-linear kinetic models applied onto the adsorption of Cr(VI) and As(III) from solution showed that the pseudo-second-order rate equation was better suited in describing the time-dependence of the adsorption processes at different initial Cr(VI) and As(III) concentrations and temperatures onto the MC, MF and MFC metal oxides. The diffusion models showed that the adsorption processes are controlled by both film and pore diffusion at different stages of the adsorption. The precise non-conformity of the data to either film or pore diffusion seems

to suggest the participation of a chemical reaction in the adsorption processes. The suitability of the models to describe the experimental data was quantified by use of regression error functions (R^2 and *% variance*).

5.4 REFERENCES

1. AKRAM, M., BHATTI, H.N., IQBAL, M., NOREEN, S. and SADAF, S. (2017) Biocomposite efficiency for Cr (VI) adsorption: kinetic, equilibrium and thermodynamics studies, *Journal of Environmental Chemical Engineering*. 5, pp. 400-411.
2. ALGOTHMI, W.M., BANDARU, N.M., YU, Y., SHAPTER, J.G. and ELLIS, A.V. (2013) Alginate–graphene oxide hybrid gel beads: an efficient copper adsorbent material, *Journal of Colloid and Interface Science*. 397, pp. 32-38.
3. ARRHENIUS, S. A. (1889) Über die Dissociationswärme und den Einfluss der Temperatur auf den Dissociationsgrad der Elektrolyte, *Zeitschrift für Physikalische Chemie*. 4, pp. 96–116.
4. BARAL, S.S., DAS, S.N. and RATH, P. (2006) Hexavalent chromium removal from aqueous solution by adsorption on treated sawdust, *Biochemical Engineering Journal*. 31, pp. 216-222.
5. BARRERA-DIAZ, C.E., LUGO-LUGO, V. and BILYEU, B. (2012) A review of chemical, electrochemical and biological methods for aqueous Cr(VI) reduction, *Journal of Hazardous Materials*. 223-224, pp. 1-12.
6. BELACHEW, N. and HINSENE, H. (2020). Preparation of cationic surfactant-modified kaolin for enhanced adsorption of hexavalent chromium from aqueous solution, *Applied Water Science*. 10, pp. 38.
7. BLANCHARD, G., MAUNAYE, M. and MARTIN, G. (1984) Removal of heavy metals from waters by means of natural zeolites, *Water Research*. 18, pp. 1501-1507.
8. BOYD, G.E., ADAMSON, A.W. and MYERS Jr, L.S. (1947) The exchange adsorption of ions from aqueous solutions by organic zeolites. II. Kinetics1, *Journal of the American Chemical Society*. 69, pp. 2836-2848.
9. CÁCERES-JENSEN, L., RODRÍGUEZ-BECERRA, J., PARRA-RIVERO, J., ESCUDEY, M., BARRIENTOS, L. and CASTRO-CASTILLO, V. (2013) Sorption kinetics of diuron on volcanic ash derived soils, *Journal of Hazardous Materials*. 261, pp. 602-613.
10. CHANDRA, V., PARK, J., CHUN, Y., LEE, J.W., HWANG, I.C. and KIM, K.S. (2010) Water-dispersible magnetite-reduced graphene oxide composites for arsenic removal, *ACS Nano*. 4, pp. 3979-3986.

11. CHENG, W., ZHANG, W., HU, L., DING, W., WU, F. and LI, J. (2016) Etching synthesis of iron oxide nanoparticles for adsorption of arsenic from water, *RSC Advances*. 6, pp. 15900-15910.

12. CRANK, J. (1975) *The Mathematics of Diffusion*, 2nd edition, Claredon Press, Oxford.

13. CUMBAL, L. and SENGUPTA, A.K. (2005) Arsenic removal using polymer-supported hydrated iron (III) oxide nanoparticles: role of Donnan membrane effect, *Environmental Science & Technology*. 39, pp. 6508-6515.

14. DAI, M., XIA, L., SONG, S., PENG, C. and, LOPEZ-VALDIVIESO, A. (2016) Adsorption of As(V) inside the pores of porous hematite in water, *Journal of Hazardous Materials*. 307, pp. 312-317.

15. DURANOĞLU, D., TROCHIMCZUK, A.W. and BEKER, U. (2012) Kinetics and thermodynamics of hexavalent chromium adsorption onto activated carbon derived from acrylonitrile-divinylbenzene copolymer, *Chemical Engineering Journal*. 187, pp. 193-202.

16. EL HADDAD, M., SLIMANI, R., MAMOUNI, R., EL ANTRI, S. and LAZAR, S. (2013) Removal of two textile dyes from aqueous solutions onto calcined bones, *Journal of the Association of Arab Universities for Basic and Applied Sciences*. 14, pp. 51–59.

17. FRANCA, A.S., OLIVEIRA, L.S. and FERREIRA, M.E. (2009) Kinetics and equilibrium studies of methylene blue adsorption by spent coffee grounds, *Desalination*. 249, pp. 267-272.

18. GHEJU, M., BALCU, I. and MOSOARCA, G. (2016) Removal of Cr (VI) from aqueous solutions by adsorption on MnO_2, *Journal of Hazardous Materials*. 310, pp. 270-277.

19. GOLDBERG, S. and JOHNSTON, C.T. (2001) Mechanisms of arsenic adsorption on amorphous oxides evaluated using macroscopic measurements, vibrational spectroscopy, and surface complexation modelling, *Journal of Colloid and Interface Science*. 234, pp. 204–216.

20. GOSWAMI, A., RAUL, P.K. and PURKAIT, M.K. (2012) Arsenic adsorption using copper (II) oxide nanoparticles, *Chemical Engineering Research and Design*. 90, pp. 1387-1396.

21. GUO, J., YAN, C., LUO, Z., FANG, H., HU, S. and CAO, Y. (2019) Synthesis of a novel ternary HA/Fe-Mn oxides-loaded biochar composite and its application in cadmium (II) and arsenic (V) adsorption, *Journal of Environmental Sciences*. 85, pp. 168-176.

22. HO, Y.S., WASE, D.J. and FORSTER, C.F. (1996) Kinetic studies of competitive heavy metal adsorption by sphagnum moss peat. *Environmental Technology*. 17, pp. 71-77.

23. HOKKANEN, S., REPO, E., LOU, S. and SILLANPÄÄ, M. (2015) Removal of arsenic (V) by magnetic nanoparticle activated microfibrillated cellulose, *Chemical Engineering Journal*. 260, pp. 886-894.

24. HUANG, Z.N., WANG, X.L. and YANG, D.S., 2015. Adsorption of Cr (VI) in wastewater using magnetic multi-wall carbon nanotubes, *Water Science and Engineering*. 8, pp. 226-232.

25. INYANG, H.I., ONWAWOMA, A. and BAE, S. (2016) The Elovich equation as a predictor of lead and cadmium sorption rates on contaminant barrier minerals, *Soil and Tillage Research*, 155, pp. 124-132.

26. JARDINE, P.M., FENDORF, S.E., MAYES, M.A., LARSEN, I.L., BROOKS, S.C. and BAILEY, W.B. (1999) Fate and transport of hexavalent chromium in undisturbed heterogenous soil, *Environmental Science & Technology*. 33, pp. 2939-2944.

27. JIANG, W., PELAEZ, M., DIONYSIOU, D.D., ENTEZARI, M.H., TSOUTSOU, D. and O'SHEA, K. (2013) Chromium(VI) removal by maghemite nanoparticles, *Chemical Engineering Journal*. 222, pp. 527–533.

28. KNOCKE, W.R. and HEMPHILL, L.H. (1981) Mercury (II) sorption by waste rubber, *Water Research*. 15, pp. 275-282.

29. KUPETA, A.J.K., NAIDOO, E.B. and OFOMAJA, A.E. (2018) Kinetics and equilibrium study of 2-nitrophenol adsorption onto polyurethane cross-linked pine cone biomass, *Journal of Cleaner Production*. 179, pp. 191-209.

30. LAGERGREN, S. (1898) Zur theorie der sogenannten adsorption geloster stoffe, *Kungliga svenska vetenskapsakademiens, Handlingar*. 24, pp. 1-39.

31. LIMA, E.C., ADEBAYO, M.A. and MACHADO, F.M. (2015) Kinetic and equilibrium models of adsorption. In: *Carbon nanomaterials as adsorbents for environmental and biological applications*, pp. 33-69. Springer, Cham.

32. LIU, W., YANG, L., XU, S., CHEN, Y., LIU, B., LI, Z., JIANG, C. (2018) Efficient removal of hexavalent chromium from water by an adsorption–reduction mechanism with sandwiched nanocomposites, *RSC Advances*. 8, pp. 15087–15093.

33. LEMLEY, A.T., SCHWARTZ, J.J. and WAGENET, L.P. (2005) Iron and manganese in household drinking water, *Water Treatment*. 6, pp. 1-5.

34. McKAY, G. and POOTS, V.J. (1980) Kinetics and diffusion processes in colour removal from effluent using wood as an adsorbent, *Journal of Chemical Technology and Biotechnology*. 30, pp. 279-292.

35. NAMASIVAYAM, C. and SANGEETHA, D. (2006) Removal and recovery of vanadium (V) by adsorption onto $ZnCl_2$ activated carbon: Kinetics and isotherms, *Adsorption*. 12, pp. 103-117.

36. NASHINE, A.L. and TEMBHURKAR, A.R. (2016) Equilibrium, kinetic and thermodynamic studies for adsorption of As (III) on coconut (*Cocos nucifera L*.) fiber, *Journal of Environmental Chemical Engineering*. 4, pp. 3267-3273.

37. NOGUEIRA, A.E., GIROTO, A.S., NETO, A.B.S. and RIBEIRO, C. (2016) CuO synthesized by solvothermal method as a high capacity adsorbent for hexavalent chromium, *Colloids and Surfaces A: Physicochemical. Engineering. Aspects*. 498, pp. 161–167.

38. OCIŃSKI, D., JACUKOWICZ-SOBALA, I., MAZUR, P., RACZYK, J. and KOCIOŁEK-BALAWEJDER, E. (2016) Water treatment residuals containing iron and manganese oxides for arsenic removal from water–Characterization of physicochemical properties and adsorption studies, *Chemical Engineering Journal*. 294, pp. 210-221.

39. OFOMAJA, A.E. (2010a) Intraparticle diffusion process for lead(II) biosorption onto mansonia wood sawdust, *Bioresource Technology*. 101, pp. 5868–5876.
40. OFOMAJA, A.E. (2010b) Equilibrium studies of copper ion adsorption onto palm kernel fibre, *Journal of Environmental Management*. 91, pp. 1491-1499.
41. OFOMAJA, A.E. (2011) Kinetics and pseudo-isotherm studies of 4-nitrophenol adsorption onto mansonia wood sawdust, *Industrial Crops and Products*. 33, pp. 418-428.
42. OUMA, I.L., NAIDOO, E.B. and OFOMAJA, A.E. (2018) Thermodynamic, kinetic and spectroscopic investigation of arsenite adsorption mechanism on pine cone-magnetite composite, *Journal of Environmental Chemical Engineering*. 6, pp. 5409-5419.
43. PANDA, H., TIADI, N., MOHANTY, M. and MOHANTY, C.R. (2017) Studies on adsorption behavior of an industrial waste for removal of chromium from aqueous solution, *South African Journal of Chemical Engineering*. 23, pp. 132-138.
44. PEREIRA, R.C., ANIZELLI, P.R., DI MAURO, E., VALEZI, D.F., DA COSTA, A.C.S., ZAIA, C.T.B. and ZAIA, D.A. (2019) The effect of pH and ionic strength on the adsorption of glyphosate onto ferrihydrite, *Geochemical Transactions*. 20, p. 3.
45. PRAHARAJ, T., SWAIN, S.P., POWELL, M.A., HART, B.R. and TRIPATHY, S. (2002) Delineation of groundwater contamination around an ash pond: Geochemical and GIS approach, *Environment International*. 27, pp. 631-638.
46. RAJI, F. and PAKIZEH, M. (2014) Kinetic and thermodynamic studies of Hg (II) adsorption onto MCM-41 modified by $ZnCl_2$, *Applied Surface Science*. 301, pp. 568-575.
47. ROY, P., DEY, U., CHATTORAJ, S., MUKHOPADHYAY, D. and MONDAL, N.K. (2017) Modeling of the adsorptive removal of arsenic (III) using plant biomass: a bioremedial approach, *Applied Water Science*. 7, pp. 1307-1321.
48. SARKAR, A.K., PAL, A., GHORAI, S., MANDRE, N.R. and PAL, S. (2014) Efficient removal of malachite green dye using biodegradable graft copolymer derived from amylopectin and poly (acrylic acid), *Carbohydrate Polymers*, 111, pp. 108-115.

49. SHAN, C. and TONG, M. (2013) Efficient removal of trace arsenite through oxidation and adsorption by magnetic nanoparticles modified with Fe-Mn binary oxide, *Water Research*. 47, pp. 3411-3421.
50. SINGH, T.S. and PANT, K.K. (2006) Kinetics and mass transfer studies on the adsorption of arsenic onto activated alumina and iron oxide impregnated activated alumina, *Water Quality Research Journal*. 41(2), pp. 147-156.
51. SPARKS, D.L. (1999) Kinetics of sorption/release reactions at the soil mineral/water interface, *Soil Physical Chemistry*. 2, pp. 135-191.
52. SUTHERLAND, C. and VENKOBACHAR, C. (2010) A diffusion-chemisorption kinetic model for simulating biosorption using forest macro-fungus, fomes fasciatus, *International Research Journal of Plant Science*. 1, pp. 107-117.
53. TAN, K.L. and HAMEED, B.H. (2017) Insight into the adsorption kinetics models for the removal of contaminants from aqueous solutions, *Journal of the Taiwan Institute of Chemical Engineers*. 74, pp. 25-48.
54. TRAN, H.N., YOU, S.J. and CHAO, H.P. (2016) Thermodynamic parameters of cadmium adsorption onto orange peel calculated from various methods: a comparison study, *Journal of Environmental Chemical Engineering*. 4, pp. 2671-2682.
55. TRAN, H.N., YOU, S.J., HOSSEINI-BANDEGHARAEI, A. and CHAO, H.P. (2017) Mistakes and inconsistencies regarding adsorption of contaminants from aqueous solutions: A critical review, *Water Research*. 120, pp. 88-116.
56. VIEIRA, B.R., PINTOR, A.M., BOAVENTURA, R.A., BOTELHO, C.M. and SANTOS, S.C. (2017) Arsenic removal from water using iron-coated seaweeds, *Journal of Environmental Management*. 192, pp. 224-233.
57. VINCENT, T., TAULEMESSE, J.M., DAUVERGNE, A., CHANUT, T., TESTA, F. and GUIBAL, E. (2014) Thallium (I) sorption using Prussian blue immobilized in alginate capsules, *Carbohydrate Polymers*. 99, pp. 517-526.
58. WEBER, W.J. and MORRIS, J.C. (1963) Kinetics of adsorption on carbon from solution, *Journal of the Sanitary Engineering Division (ASCE)*, 89, pp. 31-59.
59. WEN, Z., ZHANG, Y., CHENG, G., WANG, Y. and CHEN, R. (2019) Simultaneous removal of As(V)/Cr(VI) and acid orange 7 (AO7) by nanosized ordered magnetic

mesoporous Fe-Ce bimetal oxides: Behavior and mechanism, *Chemosphere*. 218, pp. 1002-1013.

60. WU, B., PENG, D., HOU, S., TANG, B., WANG, C. and XU, H. (2018) Dynamic study of Cr (VI) removal performance and mechanism from water using multilayer material coated nanoscale zerovalent iron, *Environmental Pollution*. 240, pp. 717-724.
61. XIU, W., GUO, H., ZHOU, X., WANTY, R.B., KERSTEN, M (2018) Change of arsenite adsorption mechanism during aging of 2-line ferrihydrite in the absence of oxygen, *Applied Geochemistry*. 88, pp. 149-157.
62. YOON, Y., ZHENG, M., AHN, Y.T., PARK, W.K., YANG, W.S. and KANG, J.W. (2017) Synthesis of magnetite/non-oxidative graphene composites and their application for arsenic removal, *Separation and Purification Technology*. 178, pp. 40-48.
63. YOSHIOKA, K. (2002) KyPlot - a user-oriented tool for statistical data analysis and visualization, *Computational Statistics*. 17, pp. 425-437.
64. ZELDOWITSCH, J. (1934) Über den mechanismus der katalytischen oxydation von CO an MnO_2, *Acta Physicochim. URSS*. 1, pp. 364–449.
65. ZHANG, G., KHORSHED, A. and CHEN, J.P. (2013) Simultaneous removal of arsenate and arsenite by a nanostructured zirconium–manganese binary hydrous oxide: Behavior and mechanism, *Journal of Colloid and Interface Science*. 397, pp. 137-143.
66. ZHANG, Q., LI, Y., YANG, Q., CHEN, H., CHEN, X., JIAO, T., PENG, Q. (2018) Distinguished Cr(VI) capture with rapid and superior capability using polydopamine microsphere: Behaviour and mechanism, *Journal of Hazardous Materials*. 342, pp. 732–740.
67. ZHANG, G., LIU, H., LIU, R. and QU, J. (2009) Adsorption behavior and mechanism of arsenate at Fe–Mn binary oxide/water interface, *Journal of Hazardous Materials*. 168, pp. 820–825.
68. ZHANG, G., LIU, H., QU, J. and JEFFERSON, W. (2012) Arsenate uptake and arsenite simultaneous sorption and oxidation by Fe–Mn binary oxides: Influence of Mn/Fe ratio, pH, Ca^{2+}, and humic acid, *Journal of Colloid and Interface Science*. 366, pp. 141–146.
69. ZHANG, L., ZHU, T., LIU, X. and ZHANG, W. (2016) Simultaneous oxidation and adsorption of As (III) from water by cerium modified chitosan ultrafine nanobiosorbent, *Journal of Hazardous Materials*. 308, pp. 1-10.
70. ZHANG, W., LIU, C., ZHENG, T., MA, J., ZHANG, G., REN, G., WANG, L. and LIU, Y. (2018) Efficient oxidation and sorption of arsenite using a novel titanium (IV)-

manganese (IV) binary oxide sorbent, *Journal of Hazardous Materials*. 353, pp. 410-420.

71. ZULFIKAR, M.A., SETIYANTO, H. and DJAJANTI, S.D. (2013) Effect of temperature and kinetic modelling of lignosulfonate adsorption onto powdered eggshell in batch systems, *Songklanakarin Journal of Science & Technology*. 35, pp. 1-31.

CHAPTER 6

6 RESULTS AND DISCUSSION

6.1 INTRODUCTION

This chapter consists of two main sections. The first section is on the adsorption of Cr(VI) and As(III) onto the nanostructured binary MC, MF and ternary MFC metal oxide composites. This section is divided into sub-sections comprising of the equilibrium isotherms, thermodynamic parameters, proposed Cr(VI)/As(III) uptake mechanistic pathways, effect of co-existing ions, desorption and regeneration of the MC, MF and MFC nanostructured metal oxide composite adsorbents. The second part is on co-precipitation of the MFC ternary metal oxide system onto the biochar support to synthesize the MFCb nanocomposite. The spectroscopic characterization of the nanocomposite and its applications in the adsorption of Cr(VI) and As(III) is presented.

6.2 ADSORPTION ISOTHERM STUDIES

An adsorption isotherm is a curve showing the amount of adsorbate retained on the solid-phase per unit mass of adsorbent to that present in the liquid phase at equilibrium at constant temperature and solution pH. The isotherm describes the adsorbate-adsorbent interaction yielding information that is of paramount importance in the design and operation of an efficient adsorption system (Rangabhashiyam et al., 2014; Hu & Zhang, 2019). Several adsorption isotherm models have been postulated and are presented in section 2.8.2. These adsorption isotherms can be broadly classified into four main classes, that is, the S, L, H and C, according to the IUPAC isotherm classification system (Giles et al., 1974).

6.2.1 Isotherm modelling

The Cr(VI) and As(III) experimental adsorption data was fitted onto non-linear forms of the Langmuir (1918), Freundlich (1906) and the Dubinin-Radushkevich (1947) isotherm models using KyPlot version 5.0 software to determine the isotherm parameters. The Langmuir and Freundlich models describe the nature of adsorbent surface coverage by the adsorbate particles, while the Dubinin-Radushkevich model provides information about the dominant pollutant uptake mechanism onto the MC, MF and MFC metal oxides (Ouma et al., 2018).

The Langmuir adsorption isotherm model (Langmuir, 1918) assumes reversible monolayer adsorption and a finite number of energetically equivalent and structurally homogeneous adsorption active sites. The non-linear form of the Langmuir equation is represented as:

$$q_e = \frac{q_m K_L C_e}{1+K_L C_e} \tag{6.1}$$

where q_e (mg/g) and q_m (mg/g) are the adsorption capacity and the maximum saturation monolayer adsorption capacity at equilibrium, respectively, C_e (mg/dm^3) is the adsorbate concentration at equilibrium, and K_L (dm^3/mg) is the Langmuir constant depicting the affinity of the adsorbent for the adsorbate. A non-linear plot of q_e against C_e gives q_m (mg/g) and K_L (dm^3/mg). For isotherms which subscribe to the Langmuir model, the nature of the adsorption can be evaluated by calculating the dimensionless separation factor, R_L (Hall et al., 1966) represented as:

$$R_L = \frac{1}{1+K_L C_o} \tag{6.2}$$

where C_o (mol/dm^3) is the initial adsorbate concentration. The R_L values show if the adsorption is linear (R_L = 1), unfavourable (R_L > 1), favourable (0 < R_L < 1) or irreversible (R_L = 0). The Freundlich adsorption isotherm model (Freundlich, 1906) describes reversible multilayer adsorption on heterogeneous surfaces, with interaction between neighbouring adsorbed species, and its non-linear form is expressed as:

$$q_e = K_F C_e^{1/n} \tag{6.3}$$

where K_F (mg/g)/(mg/dm^3)^n is the Freundlich constant, and n (dimensionless) is the intensity parameter, which denotes the structural heterogeneity of the adsorption surface or the driving force for the adsorption. A non-linear plot of q_e against C_e gives K_F (mg/g)/(mg/dm^3)^n and n. The values of n show whether the adsorption is linear (n = 1), favourable (n < 1) or unfavourable (n > 1). When n = 1, the Freundlich equation reduces to Henry's law, a one-parameter isotherm equation. The Dubinin-Radushkevich (D-R) model (Dubinin & Radushkevich, 1947) is a temperature-dependent adsorption isotherm which considers the effect of pores on an adsorbent, and the non-linear form of the equation is:

$$q_e = q_{DR} e^{-K_{DR}\varepsilon^2} \quad (6.4)$$

where q_{DR} (mg/g) is the maximum adsorption capacity, K_{DR} (mol^2/J^2) is the D-R constant related to the adsorption energy, and ε (kJ/mol) is the Polanyi adsorption potential:

$$\varepsilon = RT \ln\left(1 + \frac{1}{C_e}\right) \quad (6.5)$$

where *R* is the universal gas constant (8.314 J/mol.K) and *T* is the temperature (K). A plot of q_e against ε^2 gives q_{DR} (mg/g) and K_{DR} (mol^2/J^2). The D-R constant, K_{DR} (mol^2/J^2) is used to calculate the mean free energy, *E* (kJ/mol) using the equation:

$$E = \frac{1}{\sqrt{2K_{DR}}} \quad (6.6)$$

The magnitude of the mean free energy, *E* (kJ/mol) gives an insight into the dominant adsorption mechanism. For physisorption, *E* < 8 kJ/mol, *E* is between 8-16 kJ/mol for chemisorption through ion exchange and E > 16 kJ/mol for particle diffusion-controlled adsorption (Argun et al., 2007; Lunge et al., 2014; Hu & Zhang, 2019).

Chromium(VI): The Langmuir, Freundlich and D-R isotherm model parameters together with the associated R^2 and *% variance* error functions are presented on Tables 6.1a-c. The Langmuir isotherm model showed the best fit to the experimental equilibrium data than the Freundlich and D-R isotherm models with R^2 > 0.9979 and *% variance* < 0.9559 for the adsorption of Cr(VI) onto MC, MF and MFC metal oxides. This suggests that the reversible uptake of Cr(VI) occurred on identical, energetically equivalent adsorption active sites with the adsorption process not proceeding beyond monolayer coverage. The separation factor, R_L values were between 0.0155-0.0263, showing that the adsorption of Cr(VI) was favourable on the MC, MF and MFC nanostructured metal oxides. The Langmuir isotherm parameters, that is, the maximum saturation monolayer adsorption capacity, q_m (mg/g) and the affinity constant, K_L (dm^3/mg) decreased with an increase in initial temperature of the bulk from 299-319 K, suggesting that the uptake of Cr(VI) was exothermic. The ternary MFC metal oxide had the largest q_m (mg/g) and K_L (dm^3/mg) values of 168.7061 and 0.6363 at 299 K, respectively

showing that the ternary MFC metal oxide surface had the greatest affinity for the Cr(VI) species than the binary MC (q_m=131.0787 mg/g; K_L=0.5064 dm^3/mg) and MF (q_m=142.1607 mg/g; K_L=0.5026 dm^3/mg) metal oxides during the adsorption process. The Langmuir maximum saturation monolayer adsorption capacity, q_m (mg/g) of the nanostructured MF, MC and MFC metal oxides compare favourably with other adsorbents reported in the literature. The comparison results are presented on Table 6.2.

The Freundlich and D-R isotherm models also showed reasonably good fits to the experimental equilibrium data with R^2 values from 0.9617-0.9791 and 0.9595-0.9891, respectively for the MC, MF and MFC metal oxides. The dimensionless Freundlich isotherm parameter, *n* for the MC, MF and MFC metal oxides had values from 0.5354-0.8605, showing that the Cr(VI) adsorption was favourable. The D-R isotherm showed that the dominant mechanism of Cr(VI) adsorption onto the MC, MF and MFC metal oxides was physical, since all the calculated mean free energy, *E* values were between 3.194-6.030 kJ/mol.

Table 6.1a Equilibrium parameters for adsorption of Cr(VI) onto binary MC metal oxide composite.

Isotherm model	Temperature (K)				
	299	304	309	314	319
Langmuir					
q_m (mg/g)	131.0787	120.3597	109.9617	105.4098	90.3749
K_L (dm^3/mg)	0.5064	0.4479	0.4245	0.3999	0.3702
R^2	0.9989	0.9992	0.9983	0.9979	0.9999
% variance	0.5294	0.2124	0.7716	0.9164	0.0812
R_L	0.0194	0.0218	0.0230	0.0244	0.0263
Freundlich					
K_F (mg/g)/(mg/dm^3)^n	1.1419	1.1819	1.1782	1.1677	1.1285
N	0.5749	0.6642	0.7442	0.7769	0.8605
R^2	0.9643	0.9618	0.9636	0.9624	0.9657
% variance	3.3507	3.2229	4.0264	5.2156	4.1840
Dubinin-Radushkevich (D-R)					
q_{DR} (mg/g)	126.7225	116.4777	105.3829	100.7861	88.1729
$K_{DR} \times 10^{-8}$ (mol^2/J^2)	2.366	3.109	4.522	4.901	2.562
E (kJ/mol)	4.597	4.010	3.325	3.194	4.418
R^2	0.9794	0.9891	0.9841	0.9853	0.9881
% variance	4.4293	2.8241	3.6921	2.8916	3.9953

Table 6.1b Equilibrium parameters for adsorption of Cr(VI) onto binary MF metal oxide composite.

Isotherm model	Temperature (K)				
	299	304	309	314	319
Langmuir					
q_m (mg/g)	142.1607	136.0316	118.1141	106.8832	105.6529
K_L (dm^3/mg)	0.5026	0.4909	0.4606	0.4302	0.4175
R^2	0.9998	0.9989	0.9999	0.9997	0.9984
% variance	0.6268	0.8737	0.1774	0.7092	0.9559
R_L	0.0195	0.0199	0.0212	0.0227	0.0234
Freundlich					
K_F (mg/g)/(mg/dm^3)^n	1.3283	1.2807	1.1834	1.1763	1.1688
N	0.6077	0.6281	0.6745	0.7515	0.7741
R^2	0.9682	0.9649	0.9617	0.9643	0.9699
% variance	3.4795	4.6498	3.2568	2.5442	2.1749
Dubinin-Radushkevich (D-R)					
q_{DR} (mg/g)	138.1583	131.2364	114.4799	103.7309	100.0788
$K_{DR} \times 10^{-8}$ (mol^2/J^2)	1.890	2.946	2.651	2.901	4.583
E (kJ/mol)	5.143	4.120	4.343	4.152	3.303
R^2	0.9529	0.9868	0.9794	0.9887	0.9876
% variance	7.7385	3.5037	5.7971	3.9128	2.1171

Table 6.1c Equilibrium parameters for adsorption of Cr(VI) onto ternary MFC metal oxide composite.

Isotherm model	Temperature (K)				
	299	304	309	314	319
Langmuir					
q_m (mg/g)	168.7061	157.2242	143.5321	127.6419	121.0739
K_L (dm^3/mg)	0.6363	0.5529	0.5297	0.4719	0.4489
R^2	0.9979	0.9992	0.9979	0.9993	0.9988
% variance	0.4269	0.4816	0.7886	0.7570	0.8304
R_L	0.0155	0.0178	0.0185	0.0208	0.0218
Freundlich					
K_F (mg/g)/(mg/dm^3)^n	1.4424	1.3904	1.3229	1.1609	1.1807
N	0.5354	0.5718	0.6103	0.6052	0.6582
R^2	0.9791	0.9674	0.9753	0.9786	0.9758
% variance	1.3205	1.7393	2.8952	3.1545	3.4146
Dubinin-Radushkevich (D-R)					
q_{DR} (mg/g)	168.8144	152.4139	137.6756	123.9527	116.8043
$K_{DR} \times 10^{-6}$ (mol^2/J^2)	1.375	2.002	2.649	2.218	2.695
E (kJ/mol)	6.030	4.998	4.345	4.748	4.307
R^2	0.9595	0.9856	0.9835	0.9837	0.9854
% variance	4.9957	1.7943	2.5791	3.9036	2.2139

Table 6.2 Comparison of Cr(VI) adsorption capacities onto various adsorbents.

Adsorbent	Langmuir capacity (mg/g)	References
CTAB-kaolin	22.72	Belachew et al., 2020
Pterospermum acerifolium	76.92	Rangabhashiyam et al., 2018
MnO_2-coated diatomite	48.20	Du et al., 2015
Magnetic Fe_3O_4	1.21	Parsons et al., 2014
$MnFe_2O_4$@SiO_2-CTAB	25.04	Li et al., 2017
Co-coated charcoal	45.45	Wang et al., 2012
Human hair	9.85	Mondal & Basu, 2019
Birnessite	47.20	Islam et al., 2019
Activated carbon-A*l*	33.74	Sun et al., 2014
Activated carbon-ZnCl_2	72.46	Ramirez et al., 2020
Graphene oxide-Fe_3O_4	124.50	Zhao et al., 2016
MC	131.08	This study
MF	142.16	This study
MFC	168.71	This study

Arsenic(III): The equilibrium isotherm model parameters together with the R^2 and *% variance* error functions for the adsorption of As(III) onto MC, MF and MFC metal oxides are presented on Tables 6.3 a-c. The Langmuir isotherm model showed the best fit to the experimental data than the Freundlich and D-R isotherm models with $R^2 > 0.9965$ and *% variance* < 0.6186. These results show that the adsorption was reversible and due to monolayer surface coverage on homogenous adsorption active sites. The R_L values were in the range of 0.0202-0.0649, suggesting favourable adsorption of As(III) on the MC, MF and MFC nanostructured metal oxides. The Langmuir isotherm parameters, that is, the maximum saturation monolayer adsorption capacity, q_m (mg/g) and the affinity constant, K_L (dm^3/mg) increased with an increase in initial temperature of the bulk from 299-319 K, suggesting that the uptake of As(III) was endothermic. The ternary MFC metal oxide had the largest q_m (mg/g) and K_L (dm^3/mg) values of 33.0707 and 0.1215 at 319 K, respectively showing that the ternary MFC metal oxide surface had the greatest affinity for the As(III) species than the binary MC (q_m=26.8454 mg/g; K_L=0.0653 dm^3/mg) and MF (q_m=23.4166 mg/g; K_L=0.0572 dm^3/mg) metal oxides during the adsorption process. The Langmuir maximum saturation monolayer adsorption capacity, q_m (mg/g) of the nanostructured MF, MC and MFC metal oxides compare favourably with other adsorbents reported in the literature. The comparison results are presented in Table 6.4.

The Freundlich and D-R isotherm models showed reasonably good fits to the experimental data with R^2 values from 0.9341-0.9578 and 0.9057-0.9895, respectively for the MC, MF and MFC metal oxides. The dimensionless Freundlich isotherm parameter, *n* for the MC, MF and MFC metal oxides had values from 0.5163-0.8987, showing that the As(III) adsorption was favourable. The values of the calculated mean free energy, *E* from the D-R isotherm showed chemisorption to be the dominant adsorption mechanism of As(III) onto the MC (8.334-9.597 kJ/mol), MF (6.433-8.533 kJ/mol) and MFC (11.468-15.089 kJ/mol) metal oxides. The magnitudes of the *E* values increased with an increase in initial solution temperature.

Table 6.3a Equilibrium parameters for adsorption of As(III) onto binary MC metal oxide composite.

Isotherm model	Temperature (K)				
	299	304	309	314	319
Langmuir					
q_m (mg/g)	22.0232	23.9324	24.5280	25.4533	26.8454
K_L (dm^3/mg)	0.0441	0.0449	0.0531	0.0625	0.0653
R^2	0.9956	0.9979	0.9992	0.9990	0.9984
% variance	0.3551	0.1942	0.0773	0.1077	0.2038
R_L	0.0536	0.0527	0.0450	0.0385	0.0369
Freundlich					
K_F (mg/g)/(mg/dm^3)^n	0.0808	0.0877	0.0911	0.0956	0.1011
N	0.7636	0.8113	0.8592	0.8775	0.8987
R^2	0.9341	0.9471	0.9437	0.9468	0.9482
% variance	7.2497	5.6942	8.0534	7.6702	6.9712
Dubinin-Radushkevich (D-R)					
q_{DR} (mg/g)	20.2722	22.1230	22.9252	24.0339	25.4237
$K_{DR} \times 10^{-9}$ (mol^2/J^2)	7.199	6.867	6.169	5.913	5.429
E (kJ/mol)	8.334	8.532	9.003	9.195	9.597
R^2	0.9140	0.9726	0.9790	0.9879	0.9895
% variance	9.7651	3.2186	2.9957	1.3059	1.2784

Table 6.3b Equilibrium parameters for adsorption of As(III) onto binary MF metal oxide composite.

Isotherm model	Temperature (K)				
	299	304	309	314	319
Langmuir					
q_m (mg/g)	18.3937	20.0499	21.1858	21.7577	23.4166
K_L (dm^3/mg)	0.0360	0.0375	0.0442	0.0542	0.0572
R^2	0.9968	0.9957	0.9970	0.9960	0.9979
% variance	0.1709	0.2745	0.2216	0.3206	0.1995
R_L	0.0649	0.0625	0.0535	0.0441	0.0419
Freundlich					
K_F (mg/g)/(mg/dm^3)^n	0.0661	0.0717	0.0774	0.0810	0.0870
N	0.5163	0.5635	0.5961	0.6131	0.6377
R^2	0.9427	0.9573	0.9459	0.9552	0.9477
% variance	6.5816	5.8932	7.9905	6.8379	6.7693
Dubinin-Radushkevich (D-R)					
q_{DR} (mg/g)	16.808	18.277	19.614	20.521	21.941
$K_{DR} \times 10^{-9}$ (mol^2/J^2)	12.082	12.043	9.382	7.300	6.867
E (kJ/mol)	6.433	6.443	7.300	8.276	8.533
R^2	0.9844	0.9894	0.9887	0.9856	0.9776
% variance	2.8736	2.6729	2.7341	3.4693	4.0672

Table 6.3c Equilibrium parameters for adsorption of As(III) onto ternary MFC metal oxide composite.

Isotherm model	Temperature (K)				
	299	304	309	314	319
Langmuir					
q_m (mg/g)	31.6677	32.2363	33.1329	34.0484	35.0701
K_L (dm^3/mg)	0.0797	0.1024	0.1107	0.1160	0.1215
R^2	0.9965	0.9968	0.9983	0.9993	0.9997
% variance	0.6186	0.5956	0.3379	0.1451	0.0796
R_L	0.0304	0.0238	0.0221	0.0211	0.0202
Freundlich					
K_F (mg/g)/(mg/dm^3)^n	0.1214	0.1249	0.1288	0.1325	0.1364
N	0.6837	0.6951	0.7163	0.7316	0.7695
R^2	0.9408	0.9578	0.9478	0.9569	0.9466
% variance	6.0339	5.7841	6.6957	5.9662	7.1278
Dubinin-Radushkevich (D-R)					
q_{DR} (mg/g)	30.0203	30.9258	31.8794	32.8543	33.9181
$K_{DR} \times 10^{-9}$ (mol^2/J^2)	3.802	2.881	2.513	2.366	2.196
E (kJ/mol)	11.468	13.174	14.104	14.537	15.089
R^2	0.9414	0.9309	0.9652	0.9560	0.9057
% variance	8.0956	9.6935	7.8201	7.1474	11.8516

Table 6.4 Comparison of As(III) adsorption capacities onto various adsorbents.

Adsorbent	Langmuir capacity (mg/g)	References
Pine cone-Fe_3O_4 composite	16.94	Ouma et al., 2018
Goethite	8.46	Zheng et al., 2020
Hydrilla verticilata	11.65	Nigam et al., 2013
Iron/olivine composite	2.83	Ghosal et al., 2018
Iron-coated brown seaweed	4.20	Vieira et al., 2017
Pine cone biochar	0.0057	Van Vinh et al., 2015
Azadirachta indica bark	0.17	Roy et al., 2017
Sugarcane bagasse	11.90	Tajernia et al., 2014
Saccharum officinarum	28.57	Gupta et al., 2015
Magnetite-pine cone	18.02	Pholosi et al., 2019
MF	23.42	This study
MC	26.85	This study
MFC	35.07	This study

6.2.2 Thermodynamic parameters of Cr(VI) and As(III) adsorption

The energy changes in the adsorption of Cr(VI) and As(III) onto the MC, MF and MFC metal oxides were investigated by determining the magnitudes of the changes in Gibbs free energy, $\Delta G°$ (kJ/mol), changes in entropy, $\Delta S°$ (J/mol.K), and changes in enthalpy, $\Delta H°$ (kJ/mol). These thermodynamic parameters are of paramount importance since they give an insight into the adsorption mechanism (Fu et al., 2015). The magnitudes of the adsorption thermodynamic parameters were determined using the Langmuir isotherm constant, K_L (dimensionless):

$$\Delta G° = -RT \ln(K_L) \tag{6.7}$$

From the third principle of thermodynamics (Lima et al., 2019a):

$$\Delta G° = \Delta H° - T\Delta S° \tag{6.8}$$

Combining Eq's 6.7 and 6.8 gives the Van't Hoff equation (1884):

$$\ln(K_L) = \frac{\Delta S^\circ}{R} - \frac{\Delta H^\circ}{RT} \quad (6.9)$$

The ΔG° values were calculated from Eq 6.7, while the values of ΔS° and ΔH° were computed from the intercept and slope of the linear plot of $\ln(K_L)$ against *1/T*, respectively.

Chromium(VI): The calculated thermodynamic parameters for the adsorption of Cr(VI) onto the MC, MF and MFC metal oxides are presented in Table 6.5. The ΔG° (kJ/mol) values for the MC [-25.302-(-26.164)], MF [-25.284-(-26.483)] and MFC [-25.870-(-26.676)] metal oxide adsorbents were negative, showing that the adsorption of Cr(VI) was spontaneous and thermodynamically feasible as the initial solution temperature increased from 299-319 K (Lima et al., 2019b). The ΔG° (kJ/mol) values became more negative as the initial temperature of the bulk increased, suggesting favourable uptake of Cr(VI) onto the MC, MF and MFC metal oxides at lower temperatures (Saha & Chowdhury, 2011). The negative ΔH° (kJ/mol) values of the MC (-11.755), MF (-7.971) and MFC (-13.603) metal oxides confirm that the adsorption process is exothermic. This also corresponds with the experimental adsorption kinetic and equilibrium data which showed that the adsorption capacities decreased as the initial solution temperature was increased from 299-319 K. The magnitudes of ΔH° (kJ/mol) during physisorption are between 2.1-20.9, while for chemisorption they are between 80-200 (Anastopoulos & Kyzas, 2016). The calculated ΔH° values are all less than -20.9 kJ/mol suggesting that the dominant adsorption mechanism of Cr(VI) onto the MC, MF and MFC metal oxides was physical. The positive ΔS° (J/mol.K) values for the MC (+45.152), MF (+58.001) and MFC (+40.859) metal oxides show the degree of affinity between the adsorbent and adsorbate and show the increase in randomness at the solid-liquid interface during the adsorption process as the initial solution temperature was increased from 299-319 K. The increase in randomness is attributed to (1) displacement of adsorbed solvent species by the adsorbate species (Saha & Chowdhury, 2011), (2) decrease in order due to structural changes on the adsorbate anions after adsorption (Ouma et al., 2018), and (3) desorption of the physisorbed adsorbate species at higher solution temperatures due to the presence of weak binding forces between the adsorbate particles and the adsorbent surface (Deng et al., 2019). This corresponds with the low adsorption capacities of the adsorbate observed as the initial temperature of the bulk was increased. The ternary MFC metal oxide showed the largest magnitude of the ΔG° (kJ/mol) and ΔH° (kJ/mol) values but the smallest magnitude of the ΔS° (J/mol.K) values than the binary MC and MF metal oxides. This suggests that the adsorption

of Cr(VI) is thermodynamically favoured on the ternary MFC than on the binary MC and MF metal oxides.

Table 6.5 Thermodynamic parameters for the adsorption of Cr(VI) onto the MC, MF and MFC metal oxide composite adsorbents.

	Thermodynamic parameter	Temperature (K)				
		299	304	309	314	319
MC	$\Delta G°$ (kJ/mol)	-25.302	-25.416	-25.696	-25.956	-26.164
	$\Delta H°$ (kJ/mol)	-11.755				
	$\Delta S°$ (J/mol.K)	+45.152				
MF	$\Delta G°$ (kJ/mol)	-25.284	-25.647	-25.906	-26.146	-26.483
	$\Delta H°$ (kJ/mol)	-7.971				
	$\Delta S°$ (J/mol.K)	+58.001				
MFC	$\Delta G°$ (kJ/mol)	-25.870	-25.948	-26.265	-26.388	-26.676
	$\Delta H°$ (kJ/mol)	-13.603				
	$\Delta S°$ (J/mol.K)	+40.859				

Arsenic(III): The calculated thermodynamic parameters for adsorption of As(III) are presented in Table 6.6. The obtained ranges of the $\Delta G°$ (kJ/mol) values for the nanostructured metal oxides as the initial temperature of the bulk was increased from 299-319 K were: MC [-19.641-(-22.183)], MF [-20.146-(-22.534)] and MFC [-21.617-(-24.181)]. The $\Delta G°$ values were all negative, implying that the adsorption of As(III) onto the MC, MF and MFC metal oxides was spontaneous and feasible, with the spontaneity and feasibility of the adsorption process increasing as the initial solution temperature increased from 299-319 K (Lima et al., 2019b). The positive change in enthalpy, $\Delta H°$ values of the MC (+17.680 kJ/mol), MF (+20.506 kJ/mol) and MFC (+15.463 kJ/mol) nanostructured metal oxides shows that the adsorption of the As(III) was endothermic. This corroborates the experimental adsorption data obtained from the kinetic and equilibrium investigations which showed that the adsorption capacities increased with an increase in the initial temperature of the bulk from 299-319 K. The positive change in entropy, $\Delta S°$ values for the MC (+126.190 kJ/mol), MF (+133.947 kJ/mol) and MFC

(+124.652 kJ/mol) metal oxides shows the degree of adsorbate-adsorbent affinity and the increase in randomness at the solid-liquid interface during the As(III) adsorption process as the initial solution temperature was increased from 299-319 K. The increase in randomness is due to the displacement of adsorbed solvent species by the adsorbate species (Saha & Chowdhury, 2011) and decrease in order due to structural changes on the adsorbed surface adsorbate particles (Ouma et al., 2018). The ternary MFC metal oxide exhibited the largest magnitude of the $\Delta G°$ values but the smallest $\Delta H°$ and $\Delta S°$ values in comparison to the binary MC and MF metal oxides. This implies that the adsorption of As(III) is more thermodynamically favoured on the ternary MFC than on the binary MC and MF metal oxides.

Table 6.6 Thermodynamic parameters for the adsorption of As(III) onto the MC, MF and MFC metal oxide composite adsorbents.

	Thermodynamic parameter	Temperature (K)				
		299	304	309	314	319
MC	$\Delta G°$ (kJ/mol)	-19.641	-20.073	-20.825	-21.695	-22.183
	$\Delta H°$ (kJ/mol)	+17.680				
	$\Delta S°$ (J/mol.K)	+126.190				
MF	$\Delta G°$ (kJ/mol)	-20.146	-20.528	-21.296	-22.067	-22.534
	$\Delta H°$ (kJ/mol)	+20.506				
	$\Delta S°$ (J/mol.K)	+133.947				
MFC	$\Delta G°$ (kJ/mol)	-21.617	-22.612	-23.184	-23.681	-24.181
	$\Delta H°$ (kJ/mol)	+15.463				
	$\Delta S°$ (J/mol.K)	+124.652				

6.2.3 Proposed Cr(VI) and As(III) uptake mechanisms

6.2.3.1 *Theory*

It is misleading to assign an adsorption mechanism based only on results from fitting experimental adsorption data onto kinetic models (Tran et al., 2017). Both macroscopic and

microscopic experimental techniques are crucial to gain insight into the adsorption mechanism. The elucidation of an adsorption mechanism is achieved by (1) use of analytical techniques such as FTIR, XPS, pH_{pzc}, NMR, SEM, DSC, TGA/DTA, XRD, N_2 adsorption-desorption isotherms, Boehm titration, et cetera, (2) adsorption thermodynamic data (E_a, $\Delta H°$ and $\Delta S°$), and (3) knowledge of the chemical nature of the adsorbent surface and adsorbate speciation (Lima et al., 2015; Lima et al., 2016; Tran et al., 2016).

6.2.3.2 *The change in surface charge (ΔpH_{pzc})*

Chromium(VI): The results of the pH_{pzc} of the MC, MF and MFC metal oxide surfaces before and after adsorption of Cr(VI) anions are plotted on Figs 6.1a-c. The plots show no change in magnitudes of the pH_{pzc} of the surfaces of MC, MF and MFC metal oxides before and after Cr(VI) adsorption. Zero or negligible shift in pH_{pzc} on the adsorbent surface after adsorption implies that the adsorption occurs by outer-sphere surface complexation due to electrostatic forces, while a significant shift in pH_{pzc} suggests that the adsorption takes place through inner-sphere surface complexation due to chemical bond formation (Goldberg & Johnston, 2001). The inner-sphere surface complexes have no water molecules between the adsorbent surface functions and adsorbate species, while outer-sphere surface complexes have one or more water molecules between the functional group on the surface of the adsorbent and the adsorbate. The formation of inner- and outer-sphere surface complexes between the MC, MF and MFC nanostructured metal oxides and Cr(VI) adsorbent at $pH < pH_{pzc}$ can be represented as Eq's 6.10 and 6.11, respectively:

$$-MOH_2^+ + HCrO_4^- \rightleftharpoons -MHCrO_4 + H_2O \quad (6.10)$$

$$-MOH_2^+ + HCrO_4^- \rightleftharpoons -MOH_2^+(HCrO_4^-) \quad (6.11)$$

where $-MOH_2^+$ represents the nanostructured metal oxide composites protonated surface adsorption active sites. The observed results suggest that outer-sphere surface complexation due to electrostatic forces (Eq 6.11) is the dominant Cr(VI) adsorption mechanism on the MC, MF and MFC nanostructured metal oxide composite adsorbents.

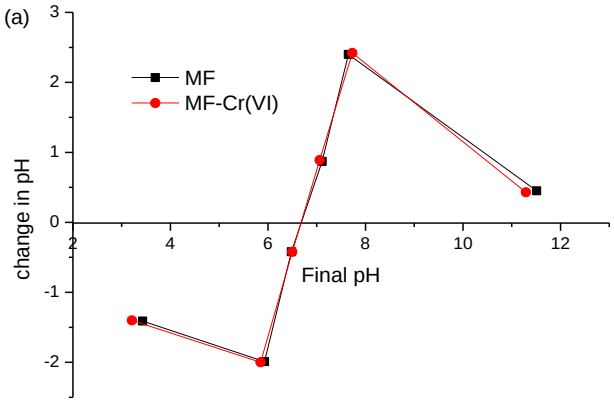

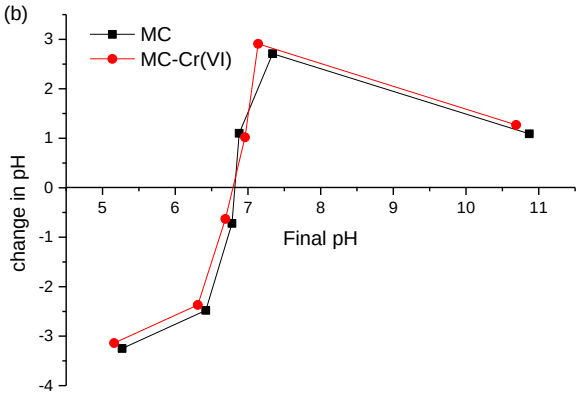

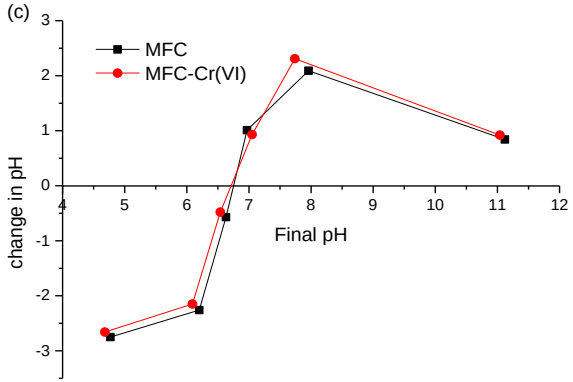

Fig 6.1 pH_{pzc} determination of (a) MF, (b) MC and (c) MFC metal oxides before and after Cr(VI) adsorption.

Arsenic(III): The pH_{pzc} of the MC, MF and MFC metal oxides before and after As(III) uptake are presented in Figs 6.2a-c. The plots show that the pH_{pzc} after As(III) uptake increased showing that the adsorbent surfaces became positively charged. The shifts in pH_{pzc} are characteristic of inner-sphere surface complex formation (Goldberg & Johnston, 2001). The increase in net positive charge on the surface of the MC, MF and MFC metal oxide adsorbents is attributed to specific adsorption of non-ionic H_3AsO_3 and eliminates electrostatic forces as controlling the As(III) adsorption process (Zhang et al., 2009). This signifies that the dominant As(III) adsorption mechanism is chemisorption due to inner-sphere surface complexation.

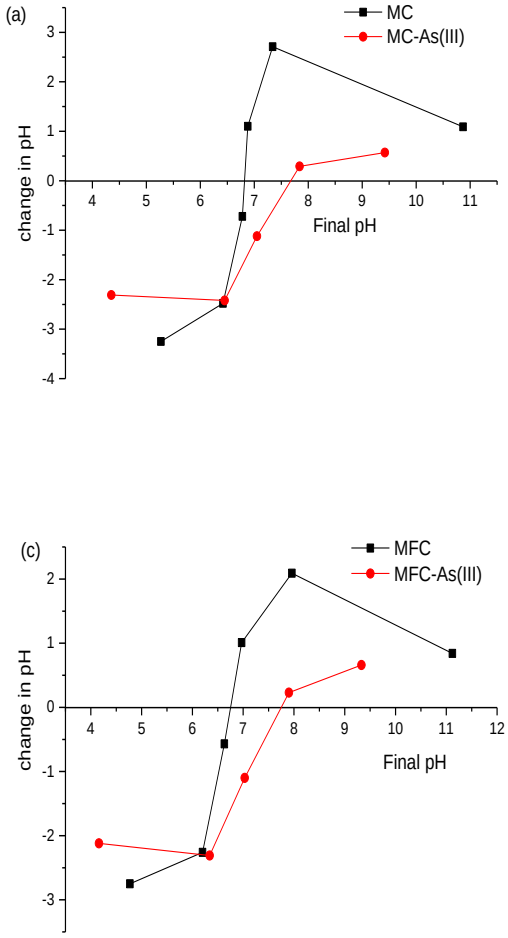

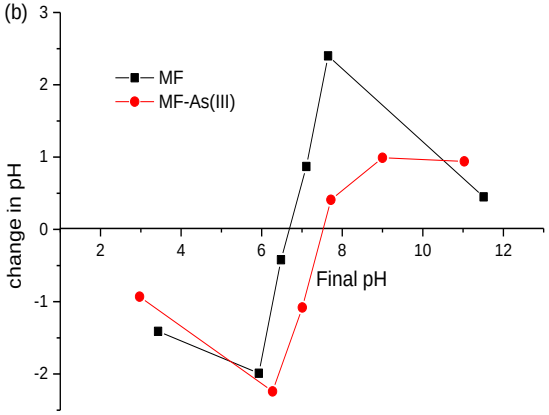

Fig 6.2 pH_{pzc} determination of (a) MC, (b) MF and (c) MFC nanostructured metal oxides before and after As(III) adsorption.

6.2.3.3 *Effect of ionic strength*

Chromium(VI): An increase in ionic strength can affect the electric potential and thickness of the electric double layer since ionic strength is a function of the background electrolyte concentration. This can interfere with the attachment of adsorbate ions onto the adsorbent surface (Lv et al., 2013). The contribution of ionic strength to Cr(VI) uptake onto the MC, MF and MFC metal oxides was determined at different concentrations of $NaNO_3$ electrolyte (0.00-0.2 mg/dm^3) at pH 3 and the results are plotted in Figs 6.3a-c. The results reveal a reduction in Cr(VI) adsorption capacity onto the nanostructured MC, MF and MFC metal oxide composites with increasing electrolyte concentration. An analogous result was reported by Ajouyed and co-researchers (2010) on the adsorption of Cr(VI) onto α-alumina oxide. The authors explained that a decrease in adsorption capacity due to an increase in electrolyte concentration signifies the formation of surface complexes during the adsorbent-adsorbate interactions. The ionic strength results suggest that monodentate outer-sphere surface complexation is the dominant Cr(VI) adsorption mechanism onto the MC, MF and MFC metal oxides, since inner-sphere surface complexes either exhibit small dependence on ionic strength or show an increase in adsorption capacity with an increase in ionic strength. Monodentate outer-sphere surface complexes are prone to changes in ionic strength (Johnston & Chrysochoou, 2014). The noted decrease in Cr(VI) anion adsorption capacity due to an increase in ionic strength on the nanostructured metal oxides is attributed to changes in the electric double layer (compression) or metal activity, increasing electrostatic repulsion between the adsorbent surface and the adsorbate (Ahmed et al., 2016; Gheju et al., 2016). The ionic strength results confirm the findings from the studies of changes of the pH_{pzc} of the MC, MF and MFC nanostructured metal oxide composites before and after Cr(VI) adsorption (section 6.2.3.2), that uptake of Cr(VI) onto the adsorbent was by electrostatic interactions through the formation of outer-sphere surface complexes.

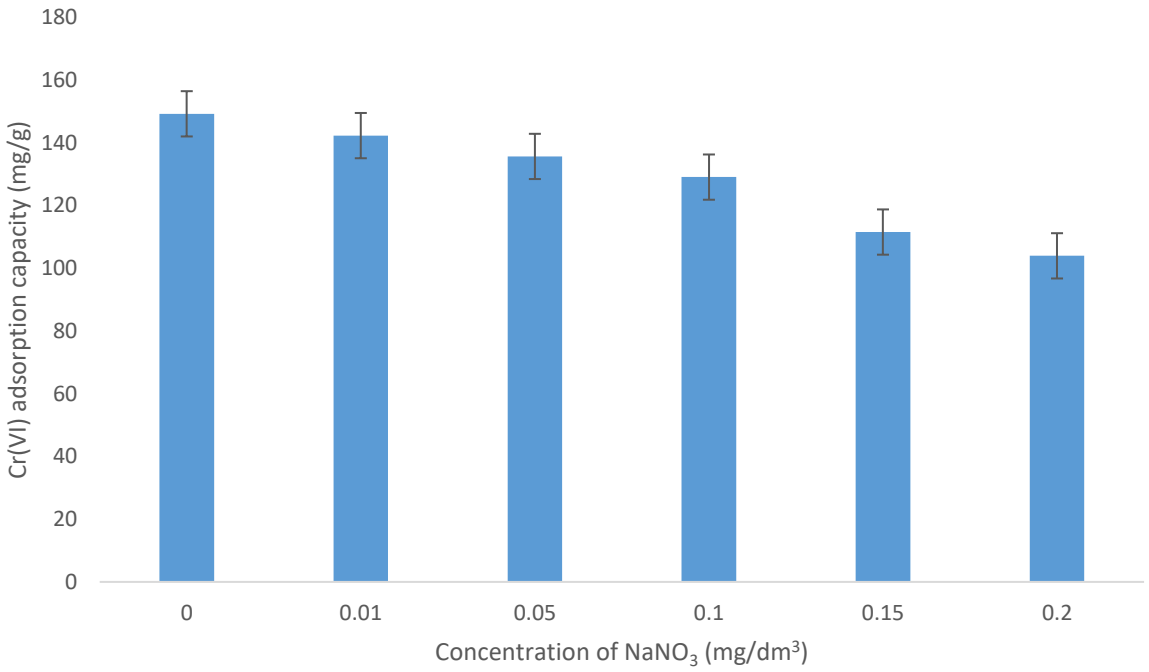

Fig 6.3a The effect of ionic strength on adsorption of Cr(VI) onto binary MC metal oxide composite.

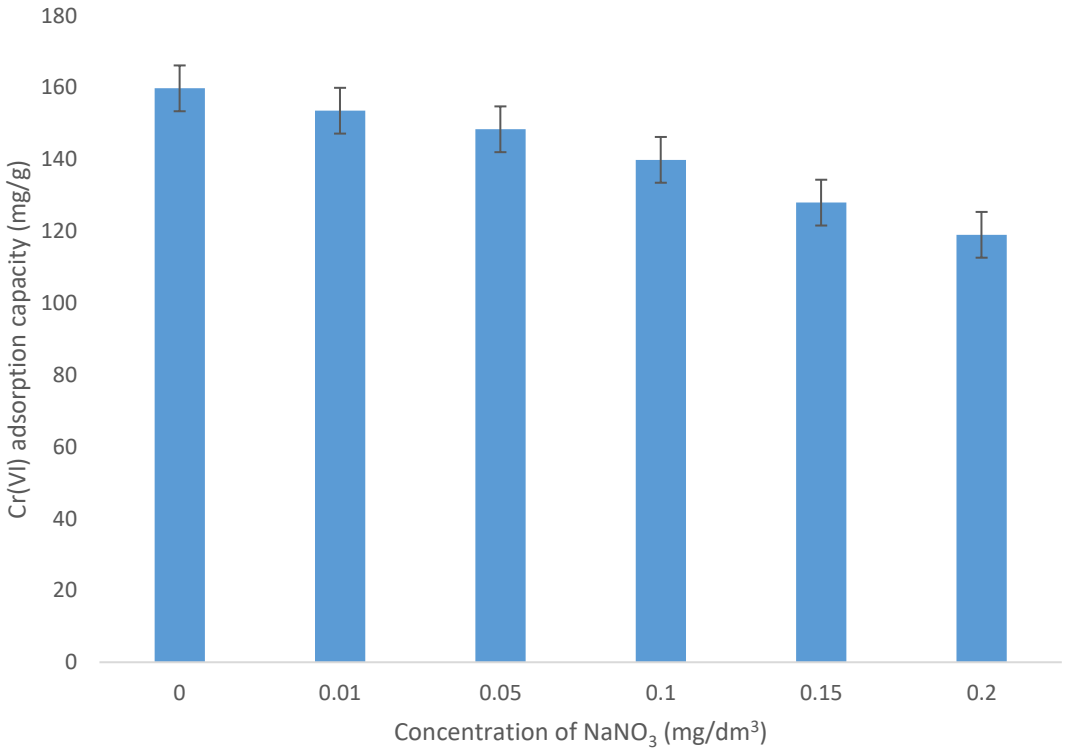

Fig 6.3b The effect of ionic strength on adsorption of Cr(VI) onto binary MF metal oxide composite.

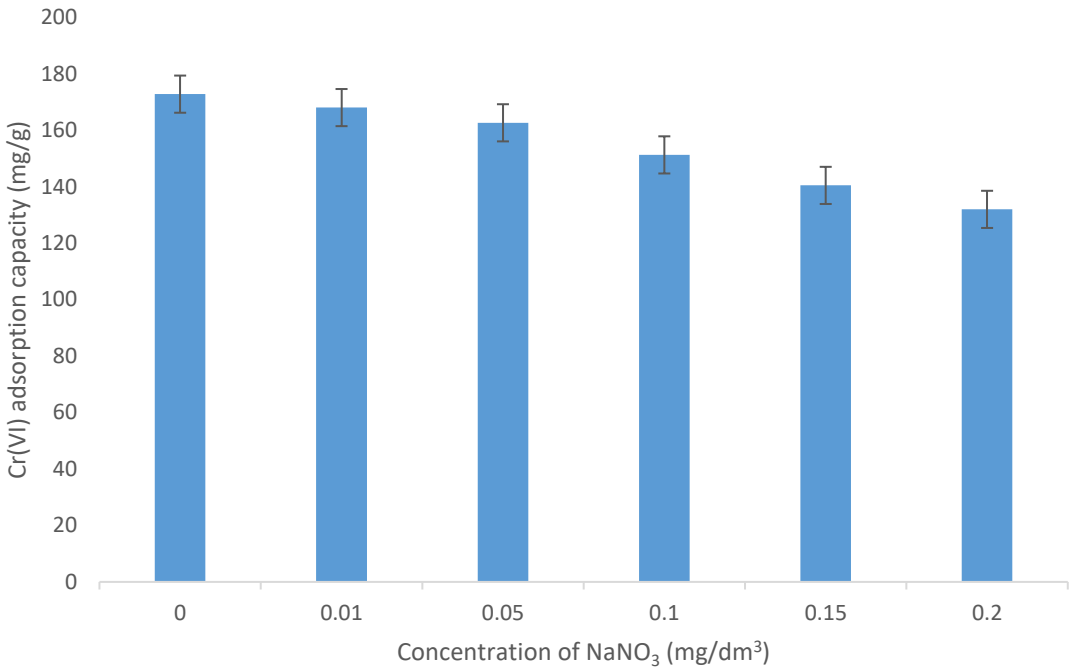

Fig 6.3c The effect of ionic strength on adsorption of Cr(VI) onto ternary MFC metal oxide composite.

Arsenic(III): The results of the effect of electrolyte strength on As(III) adsorption onto the MC, MF and MFC metal oxide composites at pH's 8 (MF) and 9 (MC and MFC) are plotted in Figs 6.4a-c. At pH 8, the adsorption capacities of As(III) onto the MF metal oxide increased from 27.31-28.56 mg/g. The As(III) adsorption capacities at pH 9 on the MC and MFC metal oxides increased from 28.03-29.97 mg/g and 34.05-35.14 mg/g, respectively. The results show a weak dependence of the As(III) adsorption onto the MC, MF and MFC metal oxide composites on electrolyte concentration which is attributed to the formation of inner-sphere surface complexes (Roy et al., 2017; Ouma et al., 2018). An increase in electrolyte strength reduces pk_a values of the surface hydroxyl groups making them labile and easily exchanged during the adsorption process (Roy et al., 2017; Pholosi et al., 2019). The increases of the As(III) adsorption capacities with an increase in electrolyte concentration followed the order MFC > MC > MF, implying enhanced inner-sphere surface complex formation by ligand exchange on the MFC metal oxide composite than either the MC or MF metal oxide composites during the adsorption process.

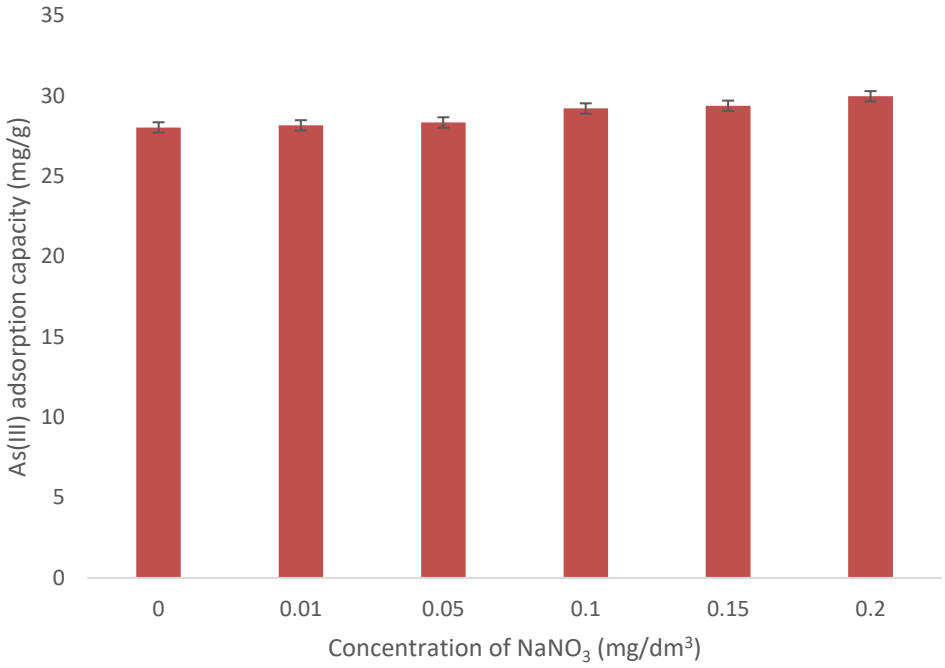

Fig 6.4a The effect of ionic strength on adsorption of As(III) onto binary MC metal oxide composite.

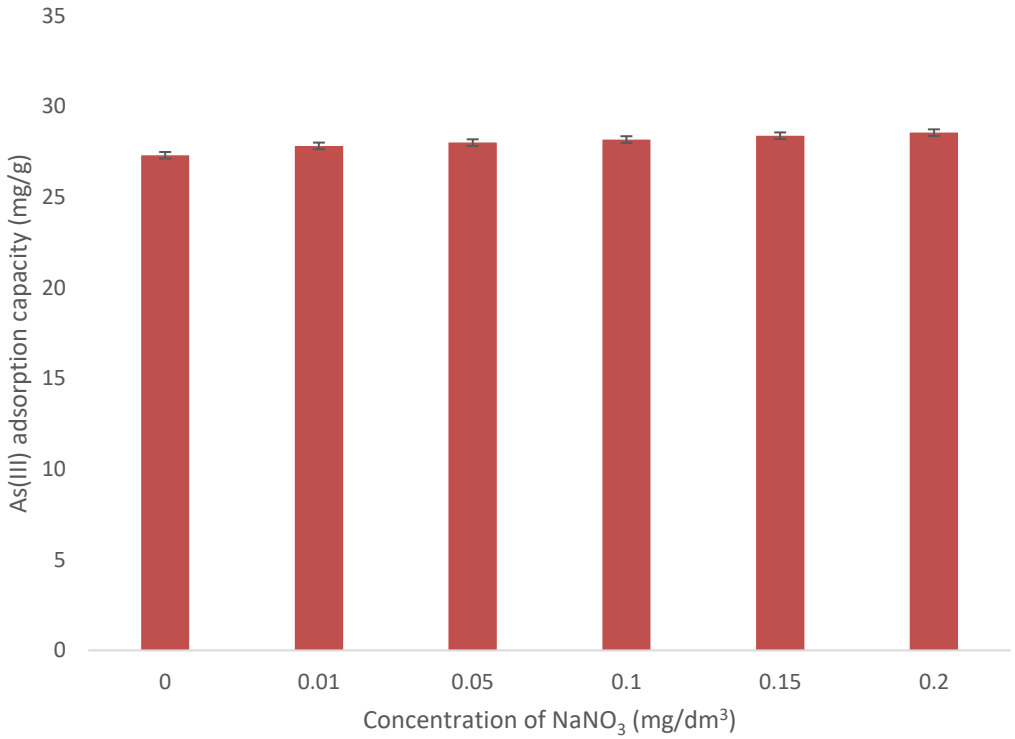

Fig 6.4b The effect of ionic strength on adsorption of As(III) onto binary MF metal oxide composite.

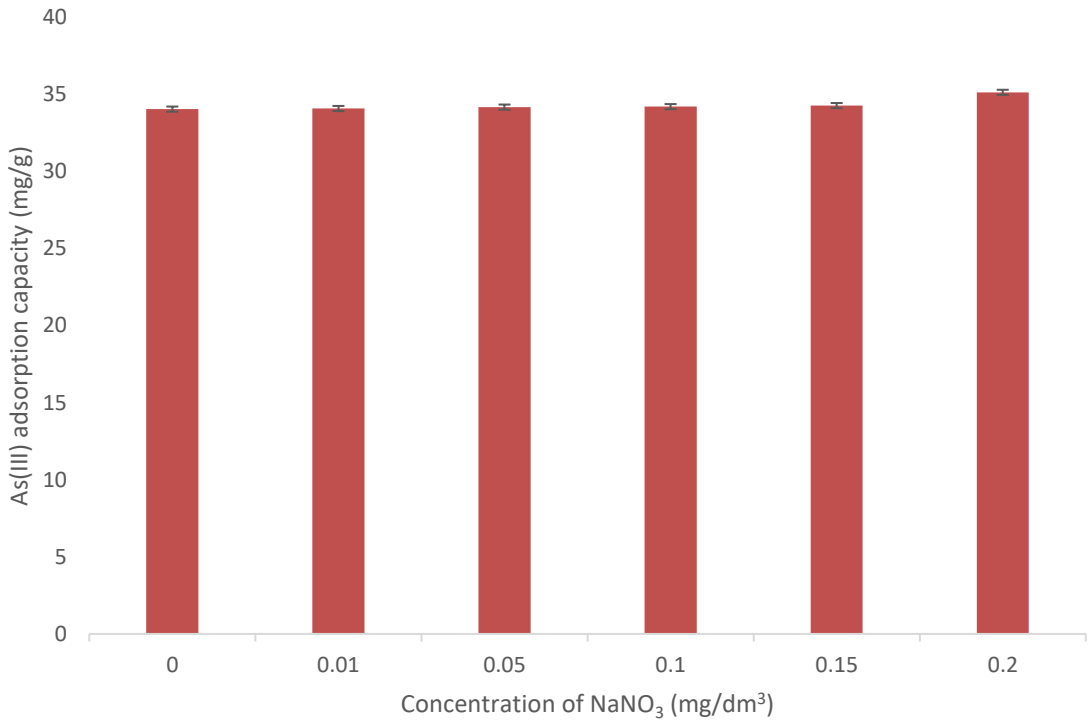

Fig 6.4c The effect of ionic strength on adsorption of As(III) onto ternary MFC metal oxide composite.

6.2.3.4 *FTIR spectral studies*

Chromium(VI): FTIR spectroscopy provides information about metal ion adsorbate binding sites on the adsorbent which is invaluable in the elucidation of the adsorption mechanism. The FTIR spectra of the nanostructured MC, MF and MFC metal oxides before and after adsorption of Cr(VI) anions at pH 3 are presented in Figs 6.5a-c. The spectra in Fig 6.5a showed the disappearance of the wide absorption at 3179 cm^{-1} after Cr(VI) adsorption onto the MC metal oxide. The wide peak is replaced with two new low-intensity absorptions at 3439 and 3331 cm^{-1} due to Cr-O or Cr=O stretching vibrations from complexation of Cr(VI) with the surface hydroxyl groups on the adsorbent (Du et al.,2015). The absorptions at 1660 and 1488 cm^{-1} due to –OH and adsorbed H_2O disappeared after Cr(VI) adsorption. This reveals that the surface hydroxyl groups on the nanocomposite interacted with the $HCrO_4^-$ oxyanion. The peak at 1090 cm^{-1} decreased in intensity and shifted to 1104 cm^{-1} after adsorption, while new peaks were observed at 983 and 857 cm^{-1}. The two new peaks were also observed by Ballav and co-workers (2014) on the investigation of Cr(VI) adsorption mechanism onto Fe_3O_4 glycine doped polypyrrole magnetic nanocomposite. These changes were attributed to stretching vibrations of Cr-O or Cr=O due to physical adsorption of $HCrO_4^-$ since the anion retained its hydration

shell and no direct chemical bond was formed with the adsorbent surface (Wang & Lo, 2009; Nogueira et al., 2016). The absorptions at 631, 591 and 448 cm^{-1} shifted to lower wavenumbers also due to Cr-O vibrations (Liu et al., 2012; Du et al., 2015; Mohan et al., 2015; Mishra, 2016). These results showed the presence of interaction between Cr(VI) and the oxygen-containing hydroxyl groups on the adsorbent surface.

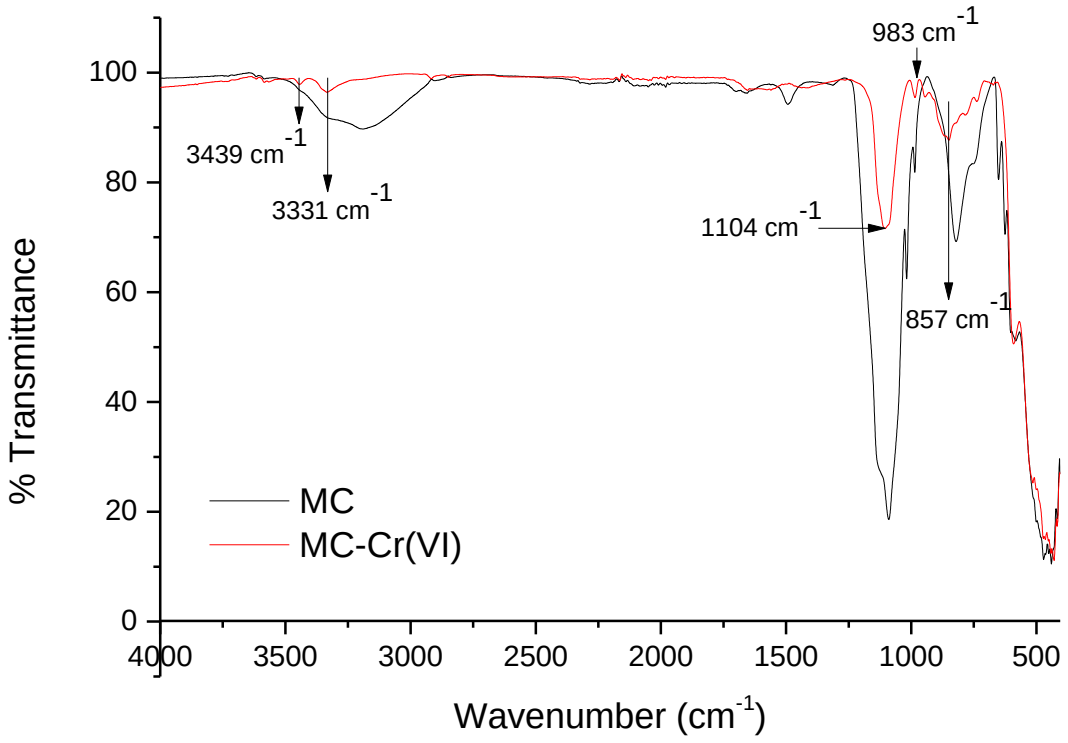

Fig 6.5a FTIR spectra of binary MC metal oxide composite before and after Cr(VI) adsorption.

The FTIR spectra in Fig 6.5b showed a reduction in the intensity of the wide O-H absorption band at 3342 cm^{-1} after Cr(VI) adsorption onto the MF metal oxide. This is attributed to the formation of surface complexes between the hydroxyl groups and Cr(VI). The physically adsorbed H_2O peak at 1619 cm^{-1} can also disappear due to vigorous stirring during the adsorption process. The Mn-OH absorption band reduced in intensity and shifted to 1079 cm^{-1} after Cr(VI) adsorption. Other peak shifts resulted in absorptions being noted at 895, 514 and 427 cm^{-1} after the adsorption process. The changes in the intensity of peaks and shifting of

peaks were ascribed to Cr-O stretching vibrations (Wang & Lo, 2009; Liu et al., 2012; Du et al., 2015). This reveals that Cr(VI) interacted with the adsorbent via surface hydroxyl groups.

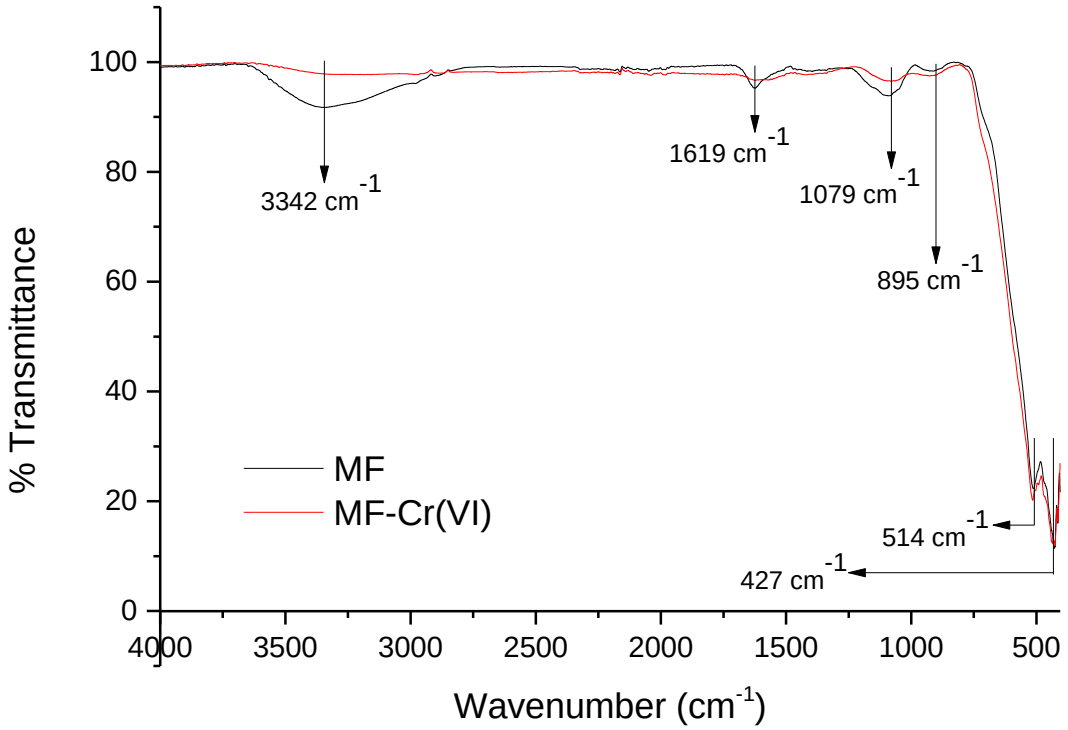

Fig 6.5b FTIR spectra of binary MF metal oxide composite before and after Cr(VI) adsorption.

Fig 6.5c showed a reduction in intensity and shift of the wide absorption to 3359 cm^{-1} after Cr(VI) adsorption onto the MFC metal oxide. This was ascribed to Cr-O or Cr=O stretching vibrations from complexation of Cr(VI) with the surface hydroxyl groups on the adsorbent (Du et al.,2015). The absorptions at 1665 and 733 cm^{-1} disappeared, while new peaks were observed at 1109, 1077, 938 and 862 cm^{-1} and the absorptions at 526 and 467 cm^{-1} shifted to lower wavenumbers after Cr(VI) adsorption. The changes were attributed to Cr-O or Cr=O stretching vibrations or bending modes of $HCrO_4^-$ (Wang & Lo, 2009; Liu et al., 2012; Ballav et al., 2014; Du et al., 2015; Mohan et al., 2015; Mishra, 2016). These results showed that the MFC metal oxide surface hydroxyl functions interacted with the Cr(VI) anions.

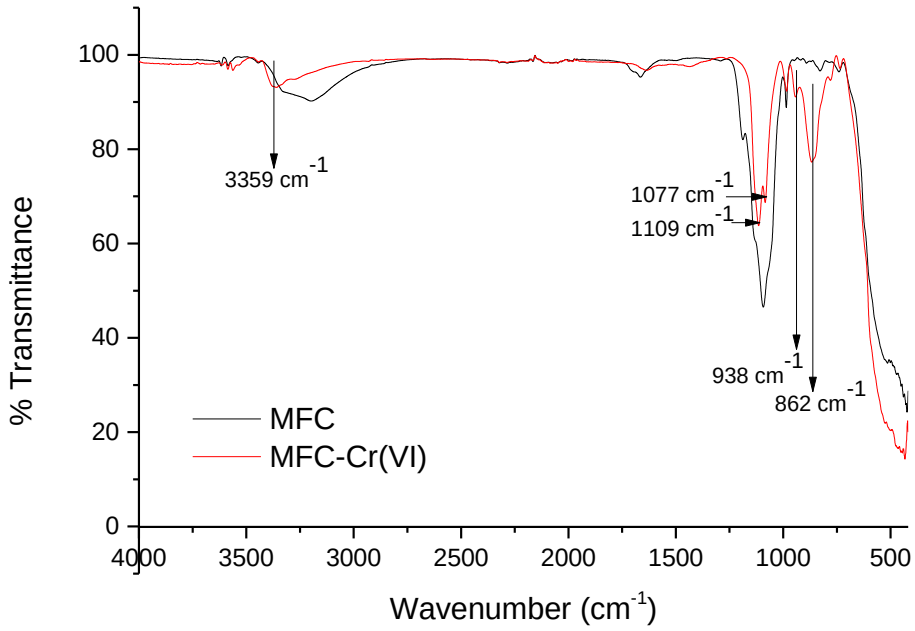

Fig 6.5c FTIR spectra of ternary MFC metal oxide composite before and after Cr(VI) adsorption.

The peaks on Figs 6.5a-c due to Cr-O vibrations show that the adsorbed Cr(III) or Cr(VI) interacted with oxygen-bearing functional groups on the surface of the adsorbent forming coordination and outer-sphere complexes, respectively (Liu et al., 2012). The infrared results suggest that the dominant uptake mechanism of Cr(VI) involved electrostatic interaction with the surface hydroxyl groups on the MC, MF and MFC nanocomposites forming outer-sphere complexes.

Arsenic(III): Figs 6.6a-c show the FTIR spectra of the nanostructured MC, MF and MFC metal oxides before and after As(III) adsorption. The FTIR spectrum for the MC metal oxide composite in Fig 6.6a shows a reduction in the intensity of the absorption bands at 3179, 1090 and 591 cm^{-1} after adsorption of As(III). The peaks at 1660 and 1488 cm^{-1} shifted to 1562 and 1397 cm^{-1}, respectively after the adsorption process. These infrared absorptions are either due to the vibration of metal-bonded or hydrogen-bonded surface hydroxyl groups. The observed spectral changes are attributed to the formation of Mn-O-As and Cu-O-As and confirm the formation of inner-sphere surface complexes during As(III) adsorption between the MC metal oxide composite surface hydroxyl groups and the hydroxyl groups on the arsenic species

(Ouma et al., 2018). The absorption peak at 825 cm^{-1} which can be due to S-O vibrations (Fernández-Carrasco et al., 2012) from SO_4^{2-} used during the MC metal oxide synthesis decreased in intensity after the adsorption of As(III). The observed peak is due to As-O vibrations characteristic of metal-O-As (Makreski et al., 2015). It could have been formed during SO_4^{2-}/As(III) ligand exchange between the adsorbent and the adsorbate (Wu et al., 2013). The results reveal that the As(III) interacted with both the Mn and Cu in the composite adsorbent by ligand exchange and the formation of inner-sphere surface complexes.

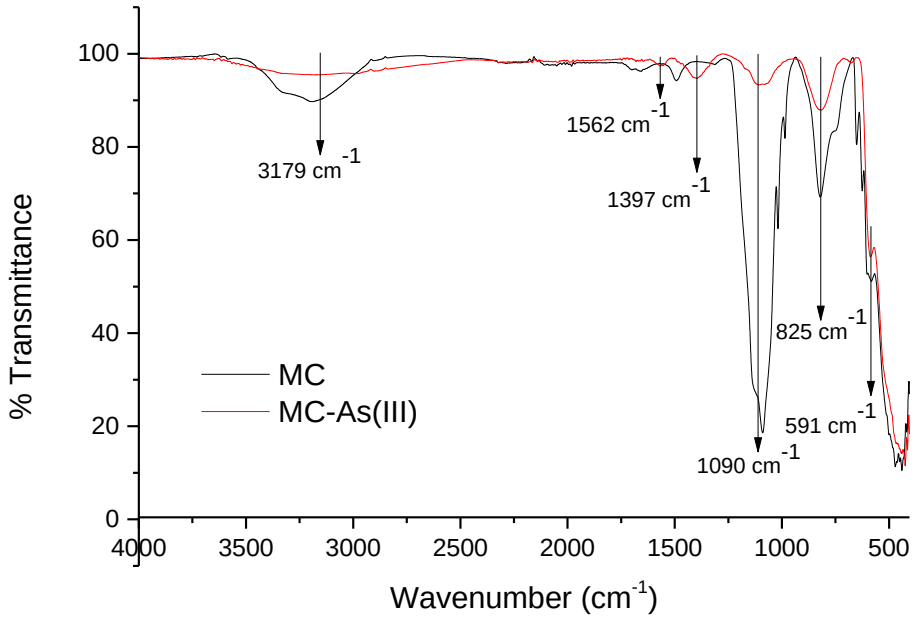

Fig 6.6a FTIR spectra of binary MC metal oxide composite before and after As(III) adsorption.

Fig 6.6b shows the FTIR spectra of MF metal oxide composite before and after As(III) adsorption. The absorption peaks at 3342 and 1619 cm^{-1} decreased in intensity, while the absorptions at 1099 and 916 cm^{-1} shifted to 1032 and 881 cm^{-1}, respectively after the adsorption. This is due to the formation of inner-sphere surface complexes between the hydroxyl groups on the adsorbent surface and the adsorbate resulting in As-O vibrations from Mn-O-As and Fe-O-As linkages (Makreski et al., 2015; Ouma et al., 2018). This is evidence that the As(III) interacted through valence forces and ligand exchange with the hydroxyl functions on Mn and Fe in the binary metal oxide during the adsorption process. The absorption peaks due to As-O vibrations in Fe-O-As have been attributed by some authors as being due to

As(V) formed from the oxidation of As(III). They reported that it is difficult for FTIR to detect As(III) adsorbed onto iron oxides (Goldberg & Johnston, 2001; Ren et al., 2011, Wu et al., 2013; Li et al., 2020).

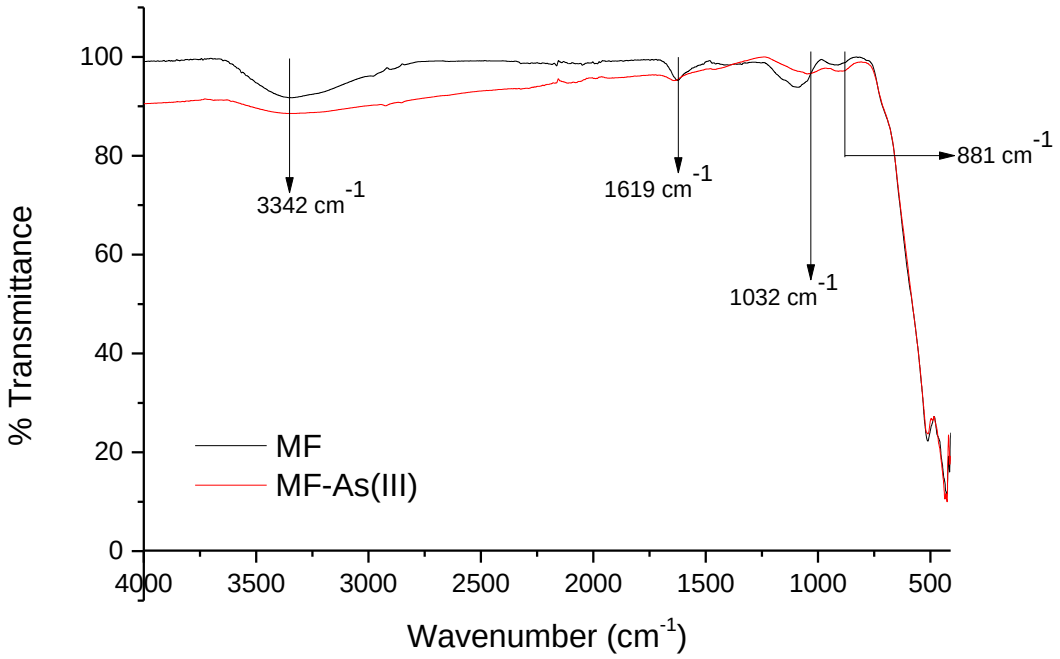

Fig 6.6b FTIR spectra of binary MF metal oxide composite before and after As(III) adsorption.

The FTIR spectra of the MFC metal oxide before and after As(III) adsorption is presented in Fig 6.6c. The spectrum shows decreases in the intensity of the absorption peaks at 3211 and 1665 cm^{-1} due to O-H vibrations after the adsorption due to formation of inner-sphere surface complexes between the adsorbate and surface hydroxyl groups on the adsorbent. The peak at 1086 cm^{-1} shifted to 1124 cm^{-1} after the adsorption due to the formation of Mn-O-As. The absorption at 811 cm^{-1} due to S-O vibrations in SO_4^{2-} (Fernández-Carrasco et al., 2012) increased in intensity and shifted to 838 cm^{-1} after the adsorption of As(III). This is attributed to As-O vibrations typical of Fe-O-As linkage (Makreski et al., 2015) formed through SO_4^{2-} /As(III) ligand exchange (Wu et al., 2013) during the formation of inner-sphere surface complexes. The absorption peak at 568 cm^{-1} due to Mn-O and Cu-O vibrations increased in intensity and shifted to 529 cm^{-1} after the adsorption. The FTIR results show that the As(III)

interacted with surface-oxygen containing functional groups on the metal oxide during the adsorption through ligand exchange and the formation of inner-sphere surface complexes (Ouma et al., 2018).

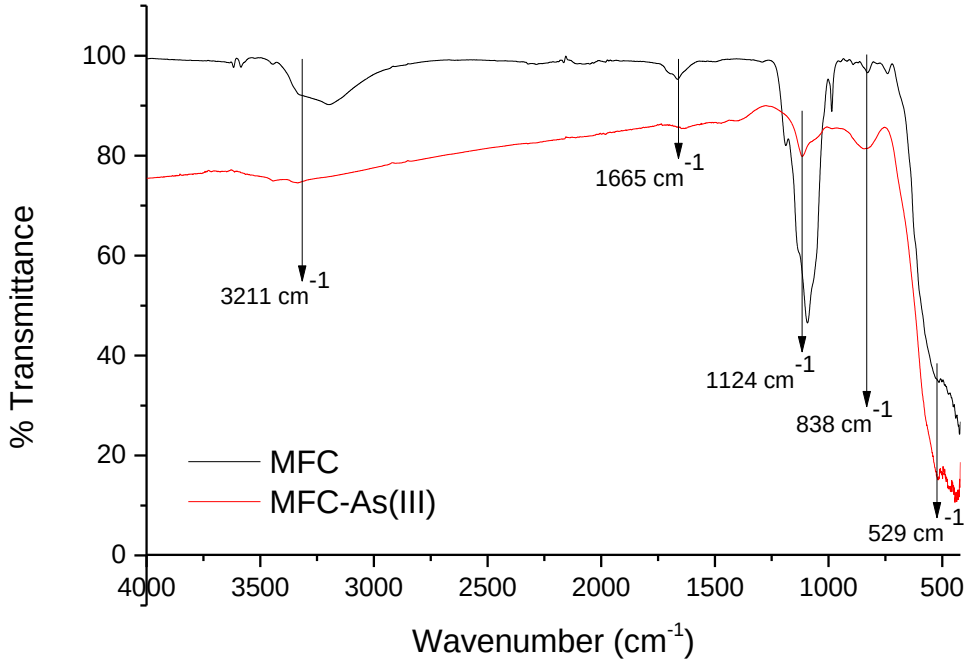

Fig 6.6c FTIR spectra of ternary MFC metal oxide composite before and after As(III) adsorption.

6.2.3.5 *XPS studies*

Chromium(VI): The X-ray photoelectron spectra of the MC, MF and MFC composites before and after the adsorption of Cr(VI) are presented in Figs 6.7a-f. The spectra show the emergence of two new peaks after the adsorption of Cr(VI) at 585.6 and 575.5 eV for the MC composite, 584.4 and 574.2 eV for the MF composite, 585.2 and 573.2 eV for the MFC composite, which corresponds to Cr $2p_{1/2}$ and Cr $2p_{3/2}$, respectively (Zhang et al., 2018). The multiplet Cr 2p photoelectron peaks revealed the presence of Cr(III) and Cr(VI) on the surface of the nanocomposites after the adsorption process (Cheng et al., 2016a; Qi et al., 2016). The results showed that toxic Cr(VI) was reduced to less harmful Cr(III) during the adsorption of the Cr(VI) onto the MC, MF and MFC nanocomposite surfaces. This suggests that the uptake of Cr(VI) from aqueous solution using the MC, MF and MFC nanometal oxide composites followed a reduction-adsorption coupled mechanistic pathway.

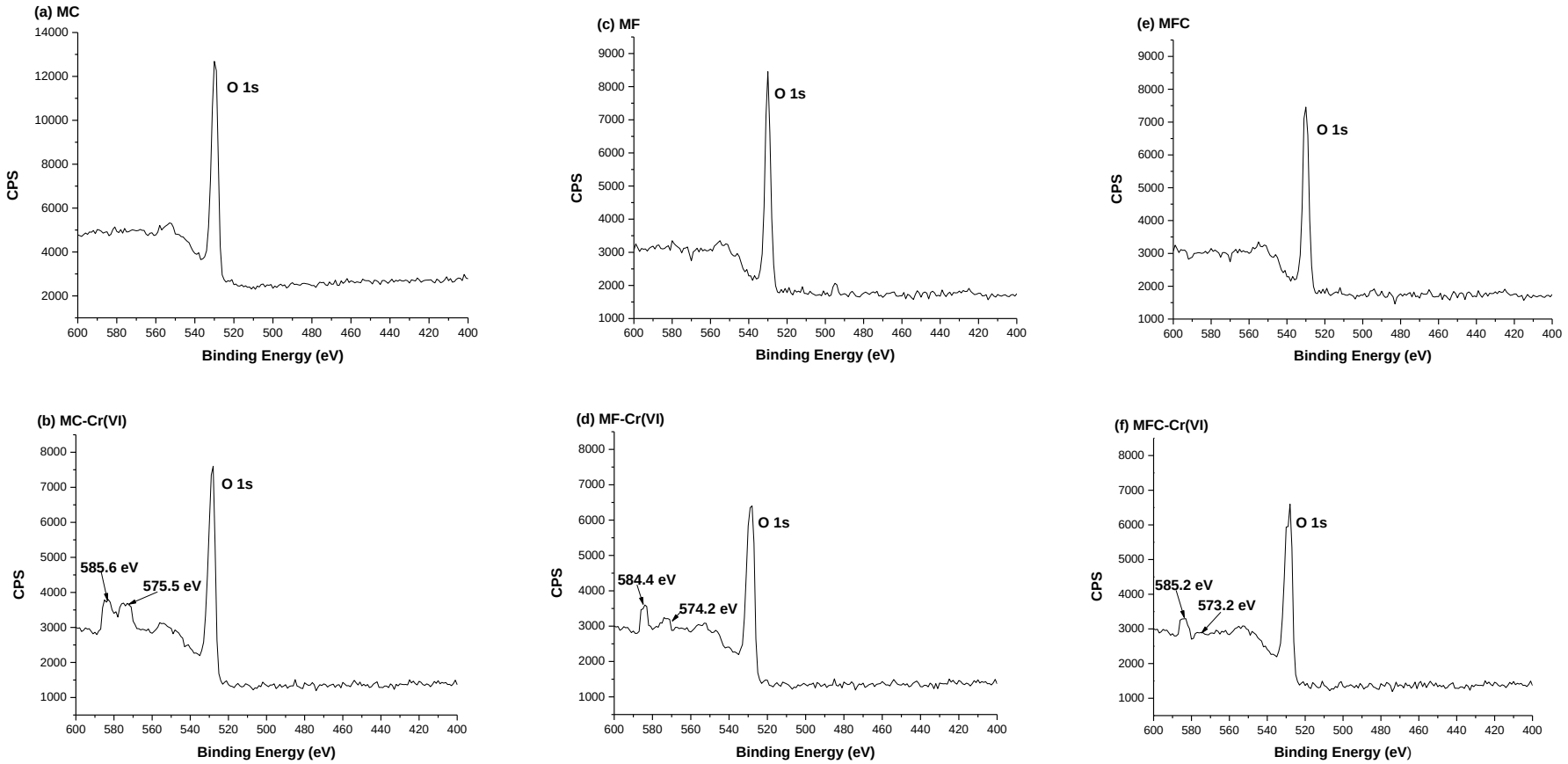

Fig 6.7 X-ray photoelectron spectra of the nanocomposite adsorbents before and after Cr(VI) adsorption.

Arsenic(III): The low-resolution survey scans of the MC, MF and MFC nanocomposites showed a new As 3d peak around electron binding energies of 44-46 eV after As(III) adsorption. This showed that the functional groups on the As(III) species interacted with the nanocomposite adsorbent surface functions during the adsorption process. Figs 6.8a-c (i and ii) show the high-resolution X-ray photoelectron spectra of O 1s before and after the adsorption of As(III) onto the MC, MF and MFC nanocomposites, respectively. The binding energies of the O 1s peaks increased by 0.1, 0.3 and 0.2 eV after As(III) adsorption onto the MC (530.0 to 530.1 eV), MF (529.7 to 530.0 eV) and MFC (530.1 to 530.3 eV) metal oxides, respectively. The O 1s electron binding energies increased due to a decrease in the electron charge density around the O shell caused by the specific interaction of the adsorbate species with –OH groups on the adsorbent surface (Lin et al., 2012). The multiplets of the O 1s photoelectron peaks in Figs 6.8a-c (i and ii) further revealed a decrease in surface oxygen amounts of –OH (MC from 47.23 to 43.74 %, MF from 34.27 to 31.71 % and MFC from 47.58 to 41.37 %) and H_2O (MC from 4.82 to 3.27, MF from 5.71 to 0.00 % and MFC from 5.46 to 4.81 %) groups and an increase in O^{2-} species after As(III) adsorption onto the nanocomposite adsorbents. The increase in percent amounts of O^{2-} species on the MC (47.95 to 52.99), MF (60.02 to 68.29) and MFC (46.96 to 53.11) surfaces after As(III) adsorption was ascribed to the formation of M-O-As (where M is either Mn, Fe or Cu). A similar finding was reported by Cui and co-workers (2012) during the adsorption of As(III) and As(V) onto amorphous ZrO_2. The noted decreases in percent amounts of surface oxygen groups were attributed to the specific interaction between the hydroxyl groups on the nanocomposite surface and the hydroxyl groups on the arsenic species forming inner-sphere surface complexes. This corroborates infrared analysis which showed decreases in –OH and H_2O groups and the emergence of As-O moieties on the adsorbent surface during the adsorption. The high-resolution X-ray photoelectron spectra of As 3d after adsorption of As(III) onto the MC, MF and MFC nanocomposites is presented in Figs 6.8a-c (iii), respectively. The Gauss-Lorentz fit of the As 3d photoelectron peaks showed the presence of duplets characteristic of As(III) and As(V). This implies that a part of the As(III) was oxidised to As(V) during the adsorption process on the surfaces of the nanocomposite metal oxides (Pholosi et al., 2018). The As(V) is also able to form inner-sphere surface complexes with the -OH groups on the adsorbent surface. The analysis of XPS confirmed the findings from ΔpH_{pzc}, ionic strength and FTIR studies which suggested that inner-sphere ligand exchange was the dominant As(III) uptake mechanism between the adsorbent surface –OH groups and the –OH functions on the arsenic species in solution.

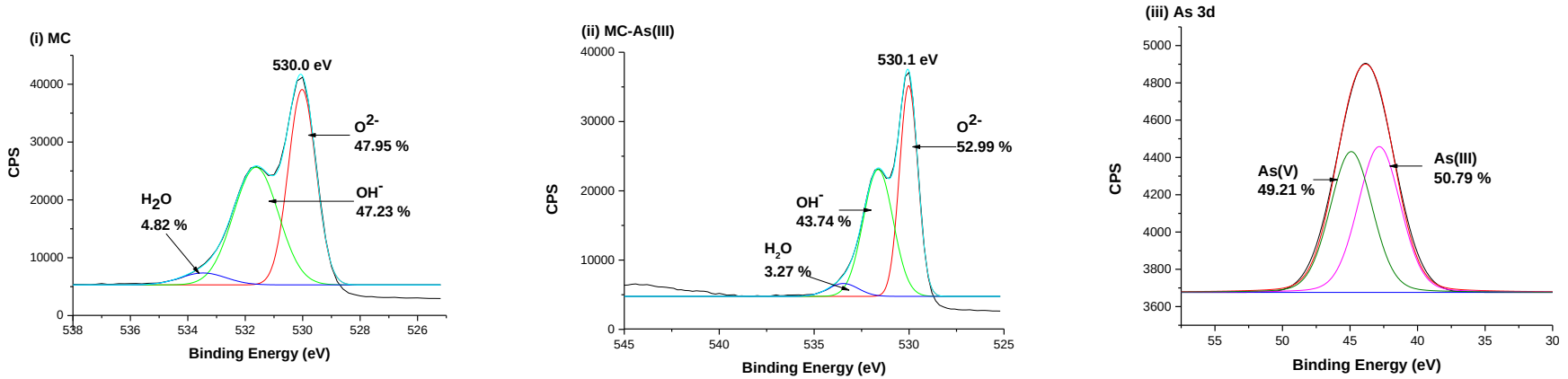

Fig 6.8a High-resolution XPS scan of O 1s for the MC nanocomposite (i) before and (ii) after adsorption of As(III) and (iii) As 3d after the adsorption process.

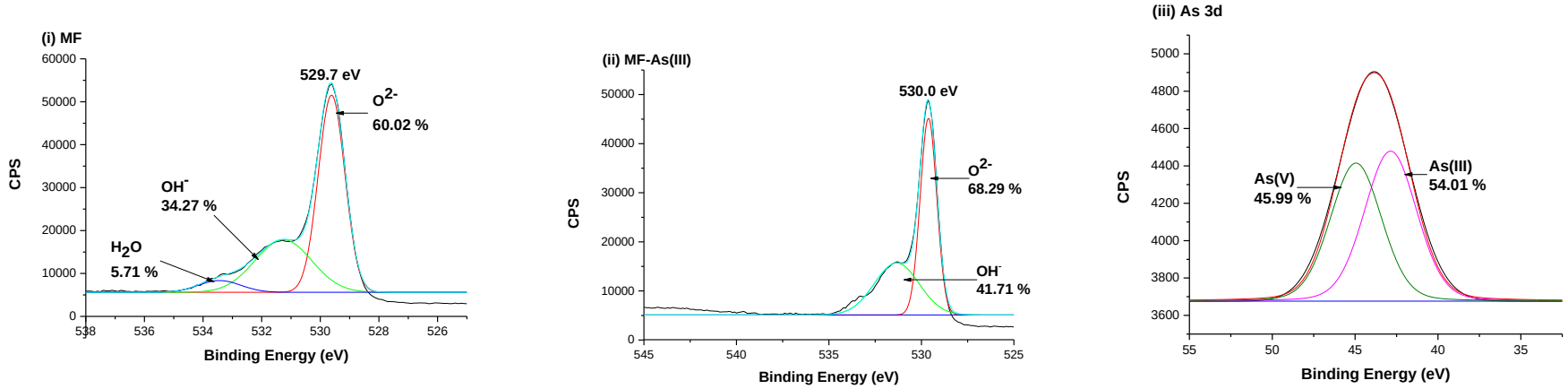

Fig 6.8b High-resolution XPS scan of O 1s for the MF nanocomposite (i) before and (ii) after adsorption of As(III) and (iii) As 3d after the adsorption process.

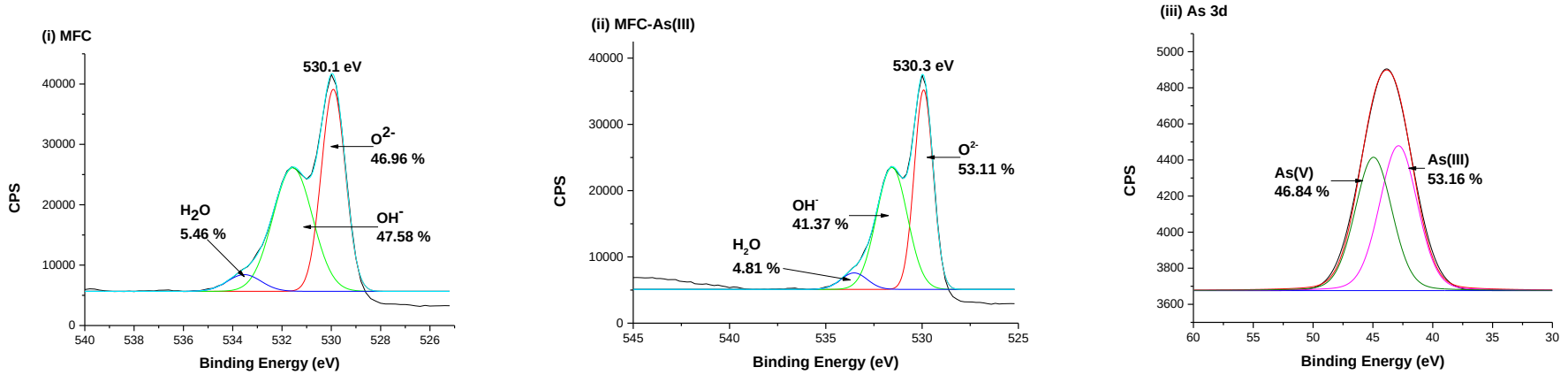

Fig 6.8c High-resolution XPS scan of O 1s for the MFC nanocomposite (i) before and (ii) after adsorption of As(III) and (iii) As 3d after the adsorption process.

6.2.3.6 *As(III)/NO_3^- exchange coefficients*

The As(III)/NO_3^- exchange coefficient ($R_{As(III)/NO_3^-}$) is the ratio of the concentration of adsorbed As(III) to the concentration of released NO_3^- ions. It shows whether ligand or ion exchange took place during the adsorption of As(III) via the formation of inner-sphere surface complexes (Wu et al., 2013). Table 6.7 shows the variation of the As(III)/NO_3^- exchange coefficients of the metal oxide composite adsorbents with an increase in the initial concentration of As(III). The results show that a general increase in the initial concentration of As(III) increased the magnitude of the As(III)/NO_3^- exchange coefficients on the MC, MF and MFC metal oxides. The As(III)/NO_3^- exchange coefficients increased from 0.058-0.554, 0.082-0.678 and 0.115-0.743 for the MC, MF and MFC metal oxide composites, respectively, with an increase in the initial concentration of As(III) from 0-50 mg/dm^3 showing that the exchange of NO_3^- with arsenic ions occurred during the As(III) adsorption process. This suggests that ligand or ion exchange was part of the As(III) adsorption process. Ouma and co-workers (2018) reported a similar result during the adsorption of As(III) onto Fenton-treated pine cone-magnetite composite adsorbent. In their investigation, the As(III)/NO_3^- exchange coefficients increased from 0.05-0.51. The higher As(III)/NO_3^- exchange coefficients observed for the MFC metal oxide showed that ligand or ion exchange was more pronounced on the MFC metal oxide composite than either the MC or MF metal oxide composites during the adsorption of As(III).

Table 6.7 The variation of As(III)/NO_3^- exchange coefficients.

	[As(III)] (mg/dm^3)	$R_{As(III)/NO_3^-}$
MC	0	0.
	5	0.082
	10	0.116
	25	0.256
	50	0.678
MF	0	0
	5	0.058
	10	0.144
	25	0.311
	50	0.554
MFC	0	0
	5	0.115
	10	0.295
	25	0.416
	50	0.743

6.2.3.7 *Summary of Cr(VI) and As(III) adsorption reaction pathways*

Chromium(VI): The modelling of experimental adsorption data onto the D-R isotherm model suggested that physical adsorption was the dominant Cr(VI) uptake mechanism onto the MC, MF and MFC metal oxide composites since the calculated mean free energy, *E* values were between 3.194-6.030 kJ/mol with an increase in initial temperature of solution from 299-319 K. An analysis of thermodynamic parameters revealed that the adsorption was exothermic with magnitudes of $\Delta H°$ < -20.9 kJ/mol suggesting that the dominant adsorption mechanism of Cr(VI) onto the MC, MF and MFC metal oxides was physical. The adsorption of Cr(VI) onto the MC, MF and MFC metal oxide composites was dependent on pH as it influenced adsorbent surface charge, adsorbate speciation and the adsorbate availability for adsorption. The mechanistic pathway for Cr(VI) removal from aqueous solution at pH 3 using the nanostructured MC, MF and MFC metal oxide composites involved the protonation of the adsorption binding sites:

$$-M-OH+H^{+}\rightarrow -M-OH_{2}^{+} \quad (6.12)$$

where $-M-OH$ is the adsorbent surface binding site. The protonated adsorbent surface interacted with the Cr(VI) oxyanions forming non-specific outer-sphere surface complexes through electrostatic interactions (Johnston & Chrysochoou, 2014):

$$-M-OH_{2}^{+}+HCrO_{4}^{-}\rightarrow -M-OH_{2}^{+}\ldots HCrO_{4}^{-} \quad (6.13)$$

Some of the Cr(VI) was reduced at the low acidic solution pH to Cr(III) as in Eq 6.14:

$$HCrO_{4}^{-}+7H^{+}+3e^{-}\rightarrow Cr^{3+}+4H_{2}O \quad (6.14)$$

and/or Eq 6.15:

$$3Fe^{2+}+HCrO_{4}^{-}+7H^{+}\rightarrow 3Fe^{3+}+Cr^{3+}+4H_{2}O \quad (6.15)$$

Due to microprecipitation, the formed Cr(III) forms coordinate bonds with hydroxyl groups on the metal oxide composites adsorption binding sites:

$$-M-(OH)_{x}+Cr^{3+}\rightarrow -M-(OH)_{3}Cr^{3+} \quad (6.16)$$

Arsenic(III): D-R isotherm modelling showed that ligand exchange was the dominant As(III) adsorption mechanism onto the MC, MF and MFC metal oxide composites since the calculated mean free energy, *E* values were between 6.433-15.089 kJ/mol with an increase in initial solution temperature from 299-319 K. The computation of adsorption parameters revealed that the adsorption was endothermic suggesting that the dominant adsorption mechanism of As(III) onto the MC, MF and MFC metal oxides was chemical. The adsorption of As(III) onto the MC, MF and MFC metal oxide composites was dependent on pH as it influenced adsorbent surface charge, adsorbate speciation and the availability of the adsorbate for adsorption. The adsorption mechanism for removal of As(III) at pH 8 (MF) and pH 9 (MC and MFC) involved the specific formation of inner-sphere surface complexes by ligand exchange between the hydroxyl groups on the adsorbent surface and the hydroxyl groups on the arsenic species (Wu et al., 2013; Cheng et al., 2016b). At solution pH > pH_{pzc} the adsorbent surface is negatively charged:

$$-M-OH+OH^{-}\rightarrow M-O^{-}+H_2O \quad (6.17)$$

where $-M-OH$ is the adsorbent surface binding site. The deprotonated adsorbent surface interacts with the dominant H_3AsO_3 species

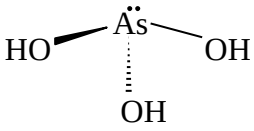

through ligand exchange forming inner-sphere surface complexes:

$$-M-O^{-}+H_3AsO_3\rightarrow -MHAsO_3+H_2O \quad (6.18)$$

or

$$-M-O^{-}+H_2AsO_3^{-}\rightarrow -MAsO_3+H_2O \quad (6.19)$$

A part of the As(III) was oxidised to As(V) in the presence of manganese oxides:

$$MnO_2+H_3AsO_3+2H^{+}\rightarrow Mn^{2+}+H_3AsO_4+H_2O \quad (6.20)$$

The dominant As(V) species at pH's 8 and 9 is $HAsO_4^{2-}$,

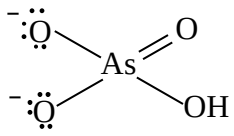

H_3AsO_4
pk_{a1} = 2.2
pk_{a2} = 6.98
pk_{a3} = 11.6

Some of the As(V) species present in solution at pH 8 and 9 might also have been formed through the following reaction (Vieira et al., 2017):

$$H_3AsO_3+H_2O\rightarrow HAsO_4^{2-}+4H^{+}+2e^{-} \quad (6.21)$$

and it interacts with the negatively charged adsorbent surface forming an inner sphere surface complex by ligand exchange:

$$-M-O^{-}+HAsO_4^{2-}\rightarrow -MAsO_4+OH^{-} \quad (6.22)$$

The As(V) can interact with the metal oxide nanocomposite adsorbents by electrostatic or Lewis acid-base interactions unlike As(III) which can only have Lewis acid-base interactions (Cumbal & Sengupta, 2005). The electrostatic interactions between the adsorbent surfaces and As(V) were ruled out since the adsorption processes occurred at solution pH's > pH_{pzc}.(Chandra et al., 2010, Cheng et al., 2016b; Roy et al., 2017).

6.2.4 Effect of co-existing anions

Chromium(III): The presence of co-existing anions affects the ionic strength of the solution and enhances competition with the adsorbate anions for the adsorption active sites, with the latter having a more pronounced effect on the adsorption of adsorbate anions (Lv et al., 2013). The effect of naturally co-existing anions ($PO_4^{3-}, CO_3^{2-}, SO_4^{2-}$ and Cl^{-}) in solution on the adsorption of $HCrO_4^{-}$ anions onto the nanostructured MC, MF and MFC metal oxide composites at pH 3 is presented on Figs 6.9a-c. The plots show that the co-existing anions ($PO_4^{3-}, CO_3^{2-}, SO_4^{2-}$ and Cl^{-}) compete with the $HCrO_4^{-}$ anion for the adsorption active sites on the MC, MF and MFC metal oxides. Several factors such as molecular dimensions, ionic radii, charge density, extend of hydration, et cetera, determine the magnitude of competition for adsorption active sites between adsorbate and co-existing anions (Duranoğlu et al., 2012). The inhibitive effect of the co-existing anions on adsorption of $HCrO_4^{-}$ follows the order: $PO_4^{3-} > CO_3^{2-} > SO_4^{2-} > Cl^{-}$. The co-existing anions in the investigation have charge densities greater than that of $HCrO_4^{-}$, hence can reduce the Cr(VI) adsorption capacities onto the MC, MF and MFC metal oxides. The PO_4^{3-} ions with the highest charge density, similar ionic radii and molecular dimensions to the $HCrO_4^{-}$ adsorbate ions confers the greatest competitive force for the adsorption active sites, while the Cl^{-} ions with the least charge density amongst the co-existing anions exhibit the least competitive effect to the adsorbate anions on the adsorption active sites (Qi et al., 2016; Lin et al., 2018). The CO_3^{2-} ions can form inner-sphere surface (oxy) hydroxyl carbonate complexes with the metals on the adsorption active sites thus reducing the $HCrO_4^{-}$ adsorption capacity (Lv et al., 2013).

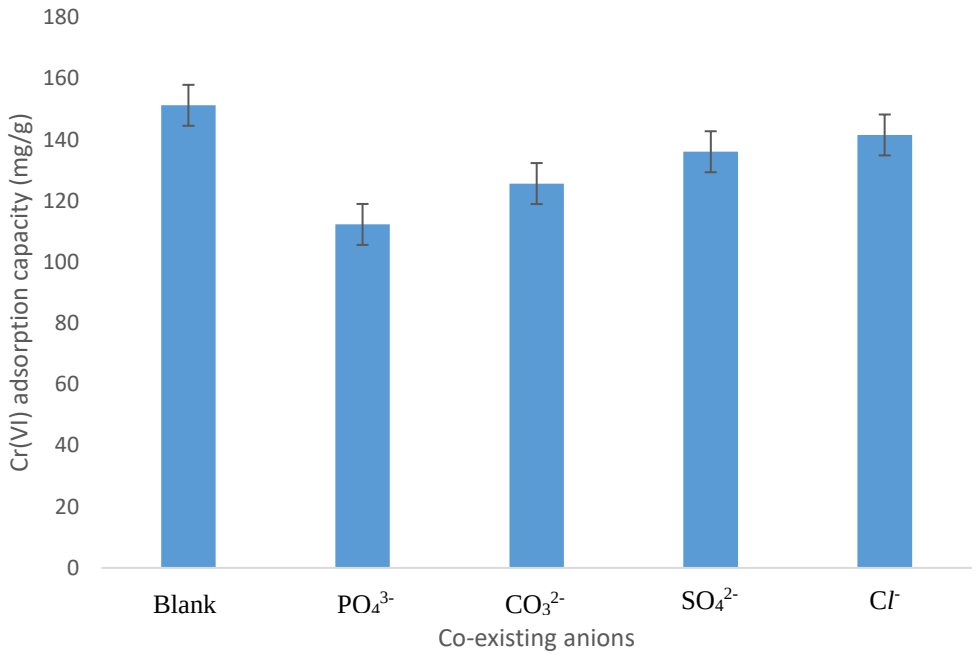

Fig 6.9a The effect of co-existing anions on adsorption of Cr(VI) onto binary MC metal oxide composite.

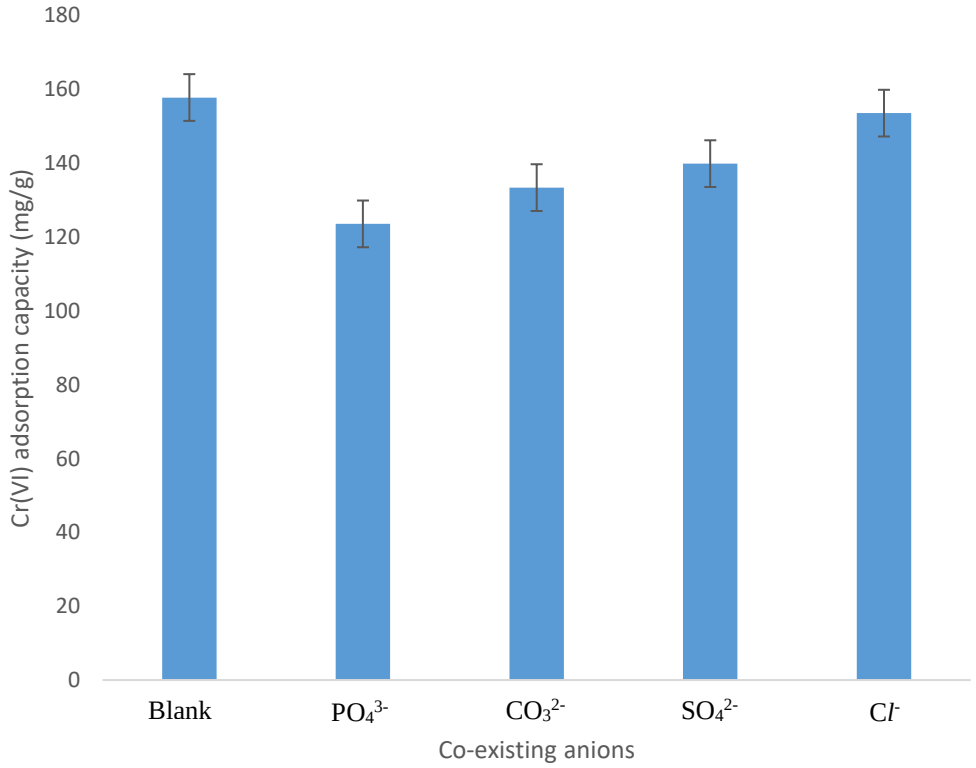

Fig 6.9b The effect of co-existing anions on adsorption of Cr(VI) onto binary MF metal oxide composite.

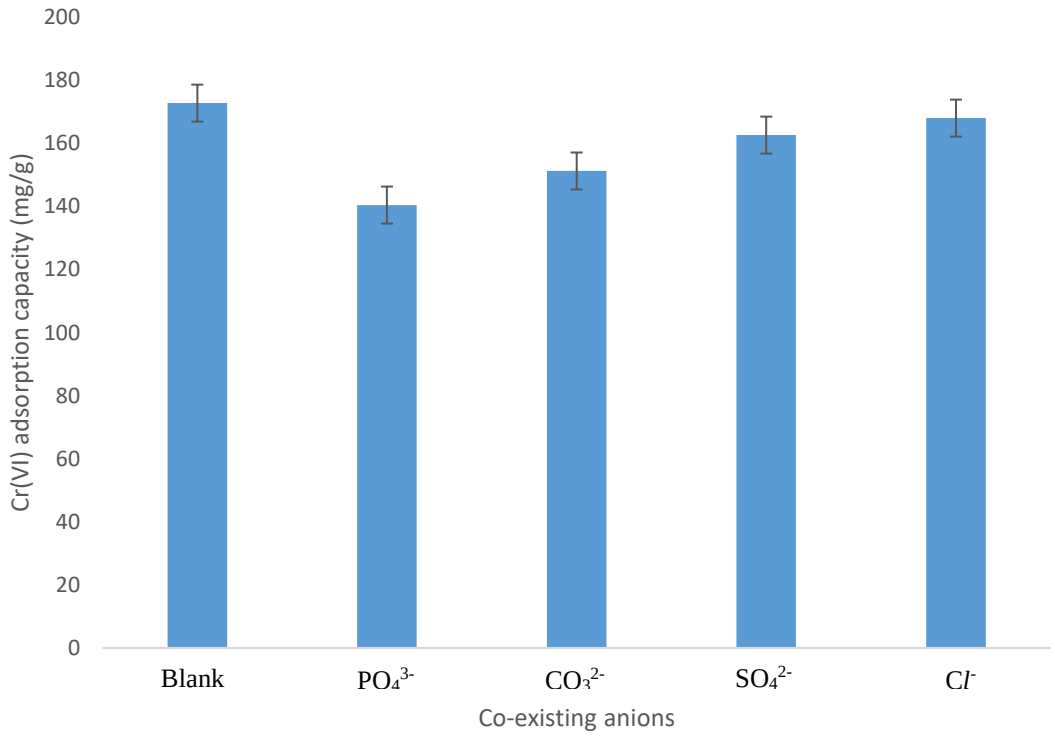

Fig 6.9c The effect of co-existing anions on adsorption of Cr(VI) onto ternary MFC metal oxide composite.

Arsenic(III): The effects of co-existing anions ($PO_4^{3-}, CO_3^{2-}, SO_4^{2-}$ and Cl^-) found in natural water bodies on As(III) adsorption onto the MC, MF and MFC metal oxide nanocomposites at pH 8 for the MF metal oxide and pH 9 for the MC and MFC metal oxide composites are presented in Figs 6.10a-c. The plots reveal that the As(III) adsorption capacities onto the metal oxide nanocomposites were dependent on pH and increased in the presence of Cl^-, CO_3^{2-} and SO_4^{2-} anions but decreased in the presence of PO_4^{3-}. The observed increases in the As(III) adsorption capacities followed the order $Cl^- > SO_4^{2-} > CO_3^{2-}$. A similar observation was reported by Pholosi and co-workers (2018) on the adsorption of As(III) onto magnetite-pine cone composite. The authors attributed the increase in As(III) adsorption capacities to weaker binding affinities between the nanocomposite metal oxide adsorbents and the Cl^-, CO_3^{2-} and SO_4^{2-} anions (Yu et al., 2013). The inhibitory effect of PO_4^{3-} anions on the adsorption of As(III) onto the metal oxide nanocomposites was ascribed to the ability of PO_4^{3-} to form stronger chemical interactions with the adsorbent than As(III). This is due to similar chemical properties between phosphate and arsenic species since P and As are in the same group on the periodic table (Li et al., 2017; Pholosi et al., 2018). The phosphate ions form hydroxyl groups in aqueous

media which compete with the hydroxyl groups of As(III) for the surface hydroxyl groups on the adsorbent (Pholosi et al., 2019). For example, at pH 7, the phosphate ion exists as:

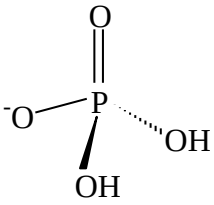

The PO_4^{3-} is thus able to reduce the As(III) adsorption capacity through charge diffusion and competitive adsorption (Goldberg, 2002). The phosphate ion can also form stable complexes with transition metals [such as $Fe(H_2PO_4)_3$] than either the Cl^-, SO_4^{2-}, or CO_3^{2-} anions (Wu et al., 2013). An analogous finding was reported by Sahu and co-researchers (2017) on the adsorption of As(III) using cigarette soot activated carbon modified with Fe_3O_4. The largest decrease in the reduction of As(III) adsorption due to presence of PO_4^{3-} was observed on the ternary MFC metal oxide nanocomposite (30.11 %) than on the MC (21.33 %) and MF (23.02 %) binary metal oxides. This suggests that ligand exchange was more pronounced on the ternary than on the binary metal oxide nanocomposites.

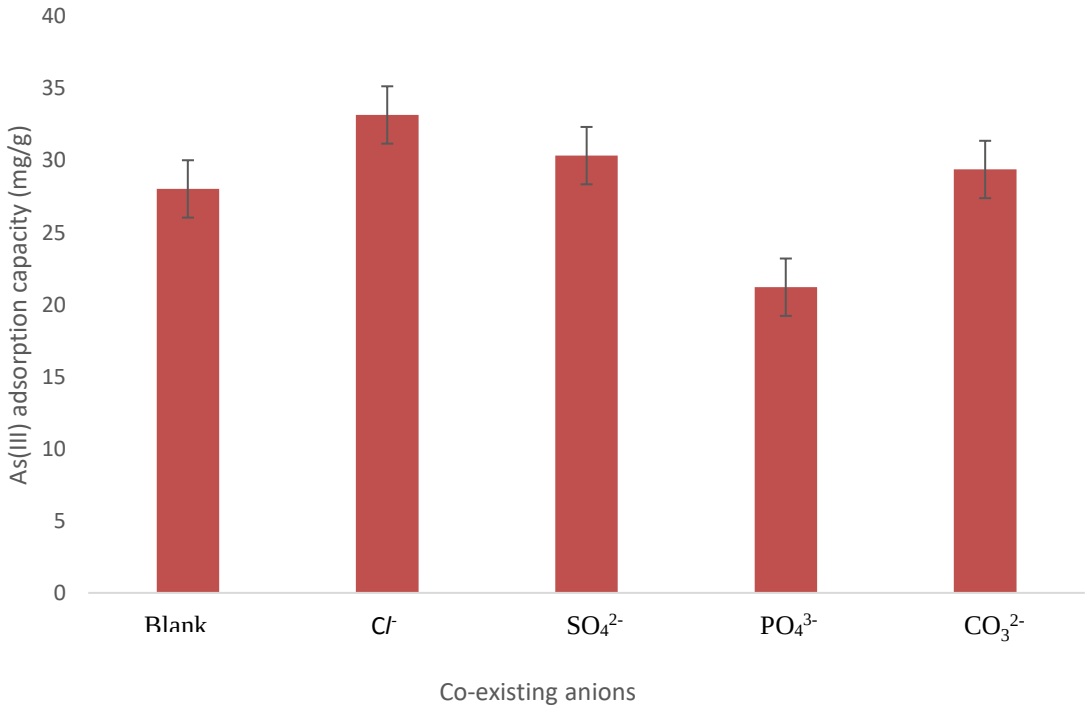

Fig 6.10a The effect of co-existing anions on adsorption of As(III) onto binary MC metal oxide nanocomposite.

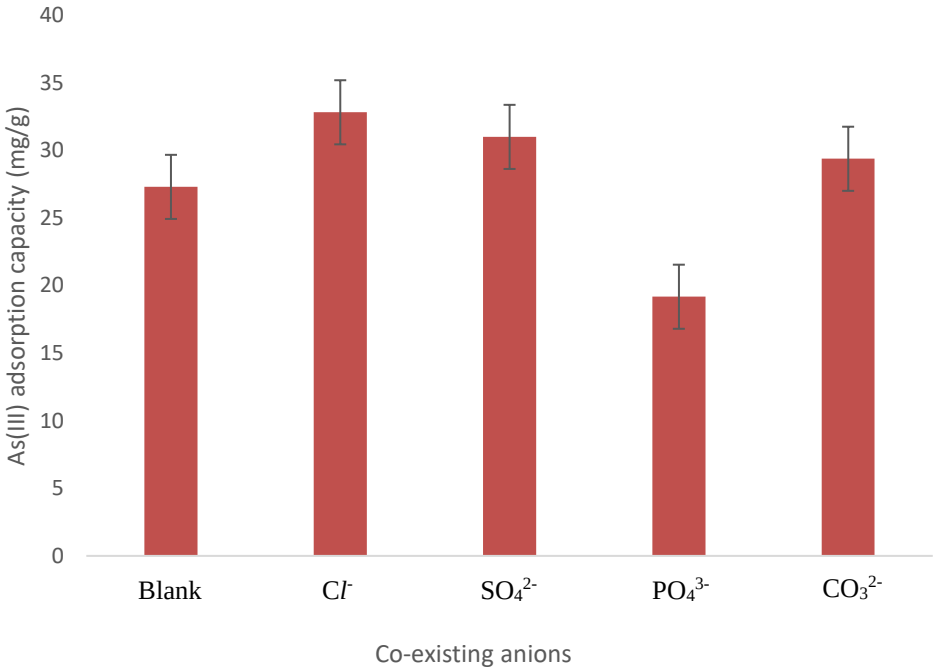

Fig 6.10b The effect of co-existing anions on adsorption of As(III) onto binary MF metal oxide nanocomposite.

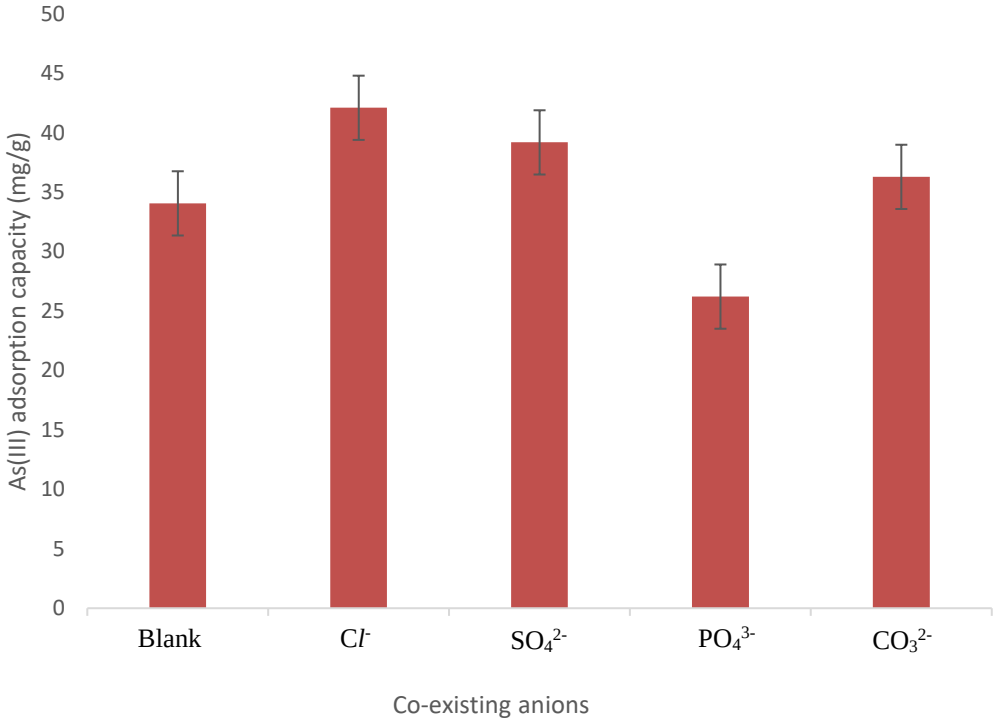

Fig 6.10c The effect of co-existing anions on adsorption of As(III) onto ternary MFC metal oxide nanocomposite.

6.2.5 Desorption studies

The type of eluent (NaOH or CH_3COOH or H_2O) which effectively desorbs the adsorbate can give an insight into the adsorption mechanism. If the desorbing agent is water, the adsorbate-adsorbent interaction could be physical with weak electrostatic forces. If the desorption is achieved with a strong acid or base such as HC*l* or NaOH, the dominant adsorption mechanism might be ion exchange. If the metal ion adsorption occurs by chemisorption, the eluent is acetic acid, CH_3COOH (Pholosi et al., 2013).

Chromium(VI): The desorption experimental results are presented in Fig 6.11 and showed that the desorption profiles of the nanostructured MC, MF and MFC metal oxides followed a similar pattern. The desorbing ability of the eluents followed the order NaOH > H_2O > CH_3COOH. The Cr(VI) desorption percentages with 0.1 mol/dm^3 NaOH eluent were 81.67 for MC, 86.39 for MF and 89.07 for MFC, and with H_2O as eluent, the Cr(VI) desorption percentages were 49.68 for MC, 61.29 for MF and 57.61 for MFC. The desorption percentages with 0.1 mol/dm^3 CH_3COOH eluent were 19.03 for MC, 31.37 for MF and 27.95 for MFC. The results suggest that the dominant adsorption mechanism for Cr(VI) onto the nanostructured MC, MF and MFC metal oxides involved ionic interactions and ion-exchange. The same conclusion was derived by Aigbe et al. (2018) and Lin et al. (2018), who utilised basic NaOH as a desorbing agent for Cr(VI) from polypyrrole magnetic nanocomposite and modified rice straw, respectively and in both investigations, the optimum adsorption occurred in acidic media (pH 2).

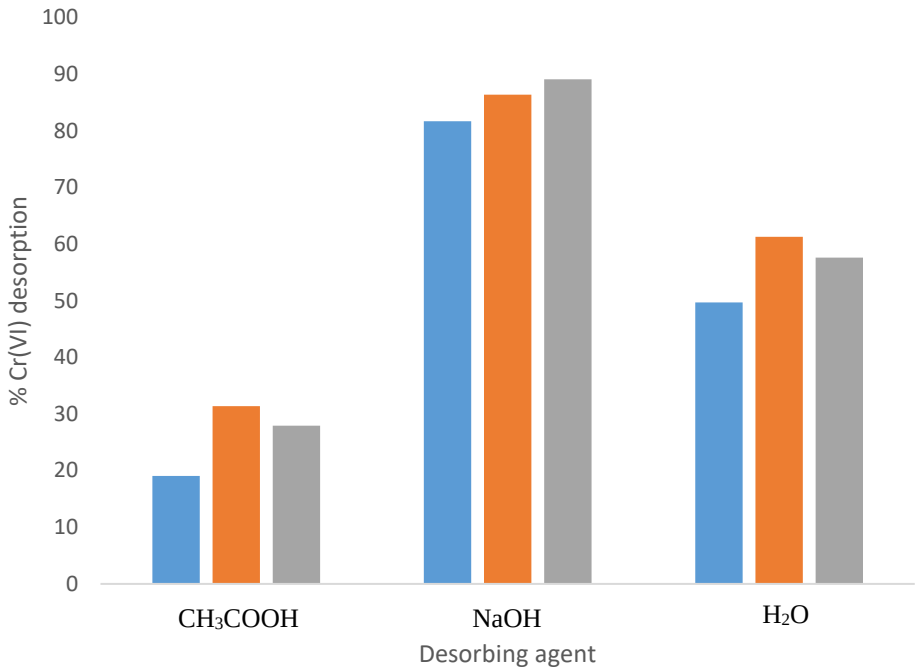

Fig 6.11 % amounts of desorbed Cr(VI) from the nanostructured metal oxide composites using different eluents.

Arsenic(III): The results showing the % desorption of As(III) from the metal oxide nanocomposite surfaces are presented in Fig 6.12. The results revealed that 0.1 mol/dm^3 NaOH showed the highest desorption percentages of the As(III) from the MC (90.23 %), MF (91.58 %) and MFC (93.47 %) metal oxide adsorbent surfaces. The As(III) desorption percentages were the least for H_2O, that is, 6.89, 4.35 and 8.11 for the MC, MF and MFC metal oxides, respectively. The results showed that H_2O was a weak As(III) eluent from the adsorbent surfaces implying that the contribution of physical adsorption to the adsorbate binding mechanism was not significant. The desorption profiles showed a similar trend and the desorbing ability of the eluents was in the order NaOH > HC*l* > CH_3COOH > H_2O. The observed results suggest that the dominant binding mechanism of the As(III) onto the metal oxide nanocomposites was through inner-sphere exchange reactions. Several researchers have reported on the ability of NaOH and HC*l* to effectively desorb As(III) from an adsorbent surface (Zhou et al., 2014; Yoon et al., 2017; Pholosi et al., 2018).

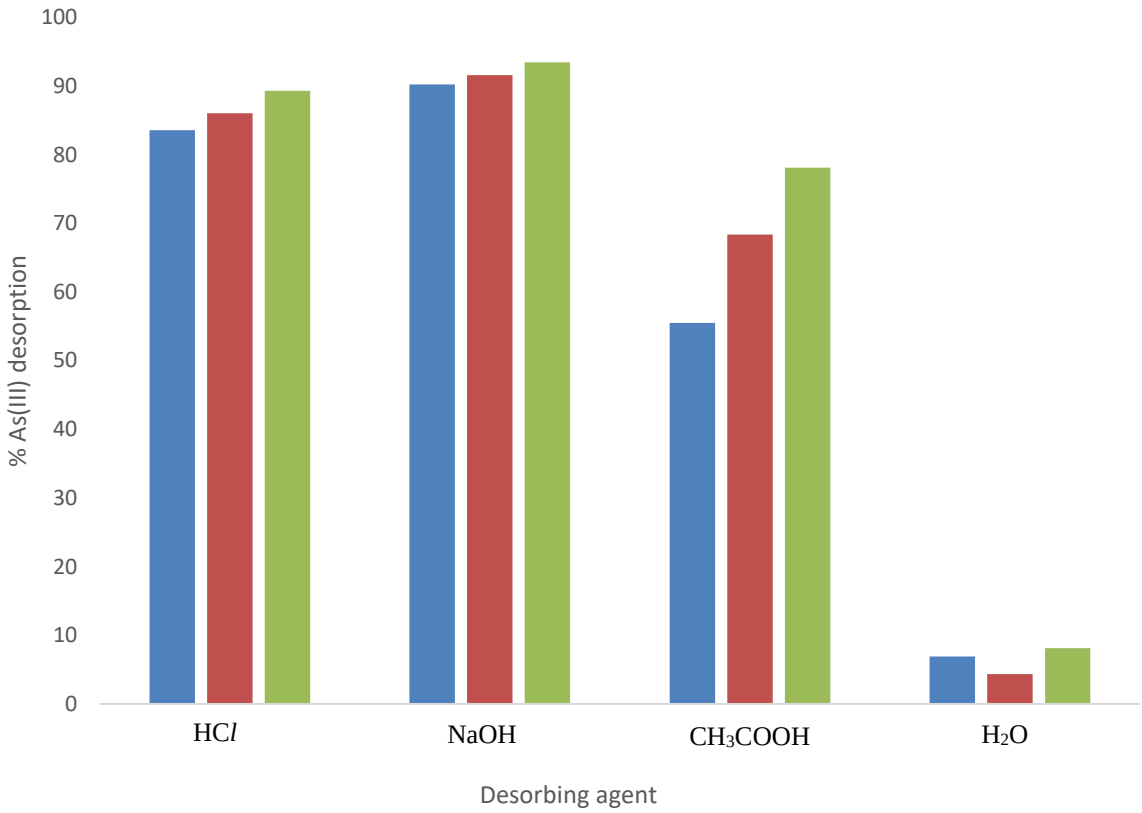

Fig 6.12 % amounts of desorbed As(III) from the metal oxide nanocomposites using different eluents.

6.2.6 Regeneration and reuse

The regeneration of exhausted adsorbents greatly determines the cost-effectiveness of the metal ion wastewater remediation technology and facilitates the recovery/recycling of metals from the effluent (Dubey & Sharma, 2017).

Chromium(VI): The regeneration and reuse of the nanostructured MC, MF and MFC metal oxide composites was determined by performing five successive Cr(VI) adsorption/desorption cycles using 0.1 mol/dm^3 NaOH as the eluent and the results are presented in Fig 6.13. For the MC metal oxide the Cr(VI) adsorption capacities decreased from 47.89-43.91 mg/g (8.31 % decrease), for the MF metal oxide the capacities decreased from 51.99-45.76 mg/g (11.98 % decrease) and for MFC metal oxide decreased from 63.78-59.81 mg/g (3.97 % decrease) during the five adsorption/desorption cycles. The ternary MFC metal oxide composite had the lowest decrease in Cr(VI) adsorption capacity of 3.97 % showing that the ternary metal oxide system is more applicable and stable over successive adsorption/desorption cycles than the binary metal oxides. The nanostructured metal oxides exhibited the same pattern after each cycle, that

is, only small differences in Cr(VI) adsorption capacities were noted after each adsorption/desorption cycle. The observed small difference in adsorption capacity after each cycle was attributed to the coordination species formed from Cr(III) and the surface hydroxyl groups on the metal oxide composites (Lin et al.,2018):

$$-M-(OH)_x + Cr^{3+} \rightleftharpoons -M-(OH)_3Cr^{3+} \quad (6.23)$$

The formed coordination species, $-M-(OH)_3Cr^{3+}$ is not easily eluted with the strong base due to the formation of a strong dative covalent bond affecting the regeneration of some adsorption active sites. The MFC metal oxide showed higher adsorption capacities at each adsorption-desorption cycle than either the MC or MF metal oxides. This implies that its adsorption sites are reproducible making it a suitable adsorbent for Cr(VI) decontamination from aqueous solutions.

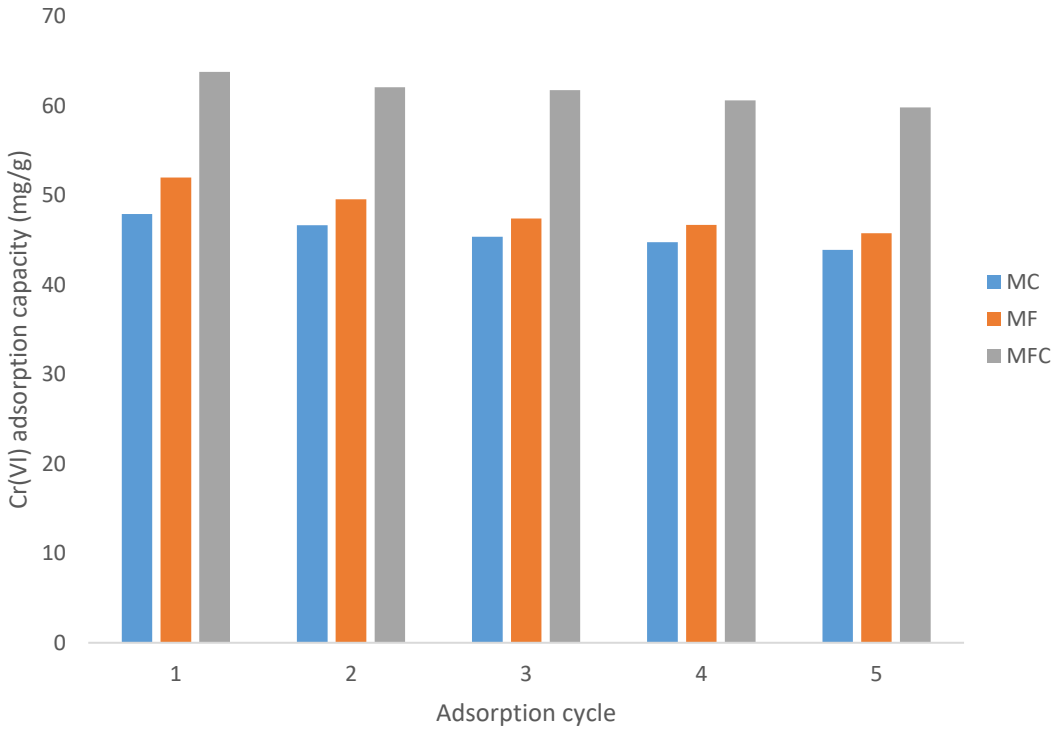

Fig 6.13 The effect of cycle times on Cr(VI) adsorption onto the nanostructured MC, MF and MFC metal oxides.

Arsenic(III): The results of the effect of adsorption/desorption cycles on As(III) adsorption

onto the MC, MF and MFC metal oxide nanocomposites are presented on Fig 6.14. After each adsorption/desorption cycle, a small decrease in As(III) adsorption capacity was observed on each of the nanostructured MC, MF and MFC metal oxides. For the MC metal oxide the As(III) adsorption capacities decreased from 25.89-19.91 mg/g (23.09 % decrease), for the MF metal oxide the capacities decreased from 23.99-18.76 mg/g (21.80 % decrease) and for MFC metal oxide decreased from 33.78-30.81 mg/g (8.79 % decrease) during the five adsorption/desorption cycles. The ternary MFC metal oxide composite had the lowest decrease in As(III) adsorption capacity of 8.79 % showing that the ternary metal oxide system is more applicable and stable over successive adsorption/desorption cycles than the binary metal oxides.

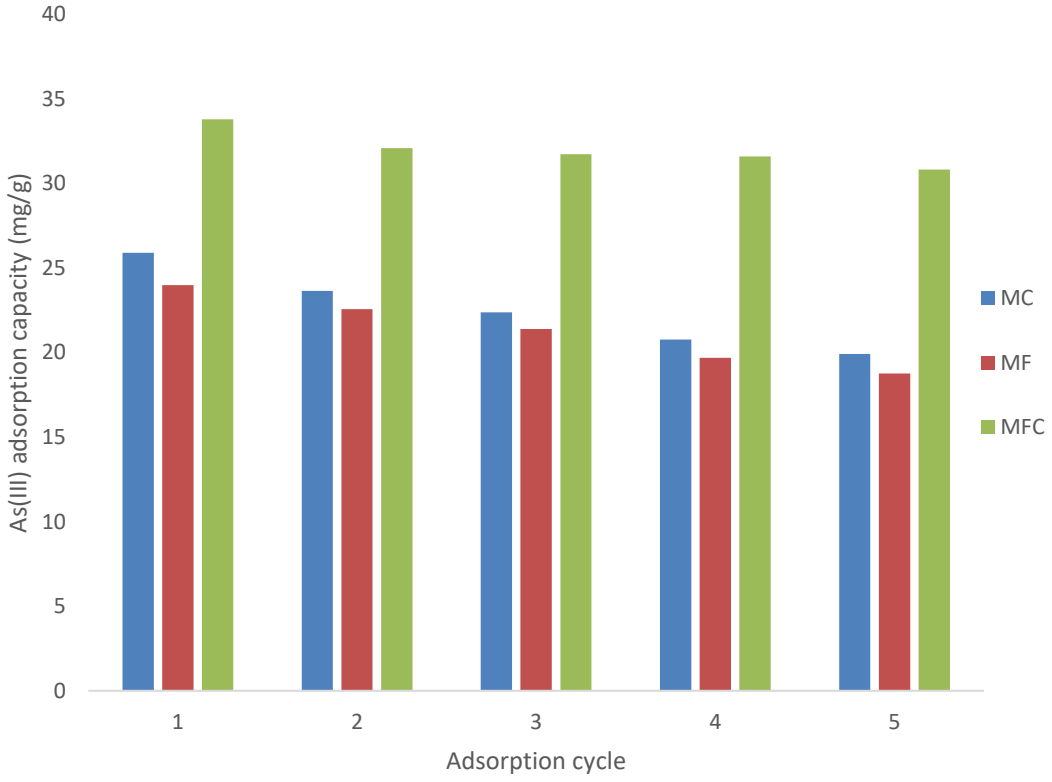

Fig 6.14 The effect of adsorption cycles on As(III) adsorption onto the MC, MF and MFC metal oxide nanocomposites.

6.3 MFC-BIOCHAR COMPOSITE

6.3.1 Characterization of MFCb composite

6.3.1.1 *Fourier-transform infrared (FTIR) spectroscopy*

The FTIR spectrum of the MFCb composite is shown in Fig 6.15. The absorption bands at 3585, 3565, 3382 and 3260 cm^{-1} are characteristic of O-H vibrations from hydroxyl groups on the surface of the composite (Wang et al., 2013). The peak at 1646 cm^{-1} was assigned to C=O stretching vibrations due to ester or carbonyl linkages on the biochar support (Gan et al., 2015). The peaks at 1481 and 1191 cm^{-1} were ascribed to Mn-OH structural vibrations (Du et al., 2015). The absorption peaks at 1361 and 1081 cm^{-1} were attributed to O=C-O and C-O-C stretching vibrations from the biochar surface functional groups (Dong et al., 2017). The peaks at 992, 941 and 861 cm^{-1} were due to Mn-O vibrations (Wei et al., 2019). The absorption peaks at 776 and 725 cm^{-1} were assigned to overlap of Fe-O and Mn-O vibrations (Chen et al., 2011; Wei et al., 2019). The weak absorption band at 630 cm^{-1} was attributed to vibrations of aromatic structures on the biochar support (Gan et al., 2015). The absorption at 592 cm^{-1} was assigned to overlap of Mn-O and Cu-O stretching vibrations (Morales et al., 2009; Nogueira et al., 2016).

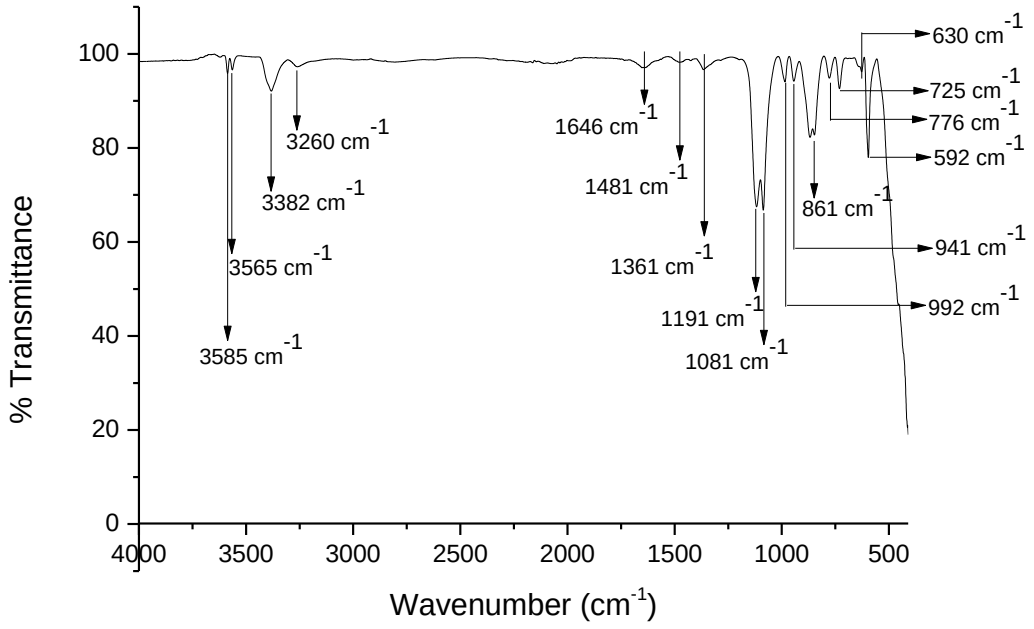

Fig 6.15 FTIR spectrum of MFCb composite.

6.3.1.2 *Scanning electron microscopy (SEM)*

The scanning electron micrograph on Fig 6.16a shows the surface morphology of MFCb composite. The micrograph shows fluffy and porous nanograins. The oxide surface appears rough and amorphous indicating the availability of a large surface area (Roy et al., 2017). The elemental surface distribution of the composite obtained from energy-dispersive X-ray spectroscopy (EDS) is presented on Fig 6.16b. It shows the elemental weight percent composition of the MFCb composite to be: manganese 26.86, iron 29.81, copper 5.94, oxygen 21.06, carbon 11.10 and phosphorus 4.46. The EDS analysis data can only be used qualitatively since it is representative of a small portion of the nanomaterial. The obtained data suggest that the elements were distributed throughout the composite.

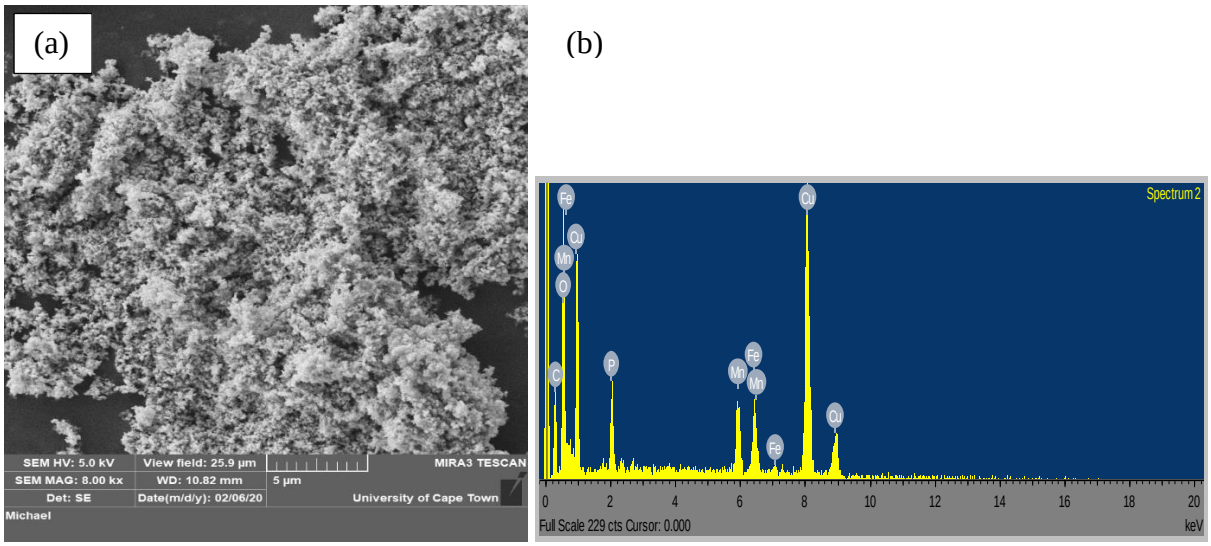

Fig 6.16 Surface analysis of MFCb composite (a) scanning electron micrograph and (b) EDS elemental analysis.

6.3.1.3 *Transmission electron microscopy (TEM)*

The transmission electron micrograph of the MFCb composite is presented on Fig 6.17a. It shows less aggregation than the TEM image of the MFC metal oxide (section 4.3.3.3). On some parts of the image, the particles are well distributed suggesting the even distribution of the MFC metal oxide system onto the biochar support. Image J software was used to determine the particle size distribution and the result is shown on Fig 6.17b. The particle sizes range from 0.3 to 0.8 nm with an average particle size of 0.56 ± 0.05 nm.

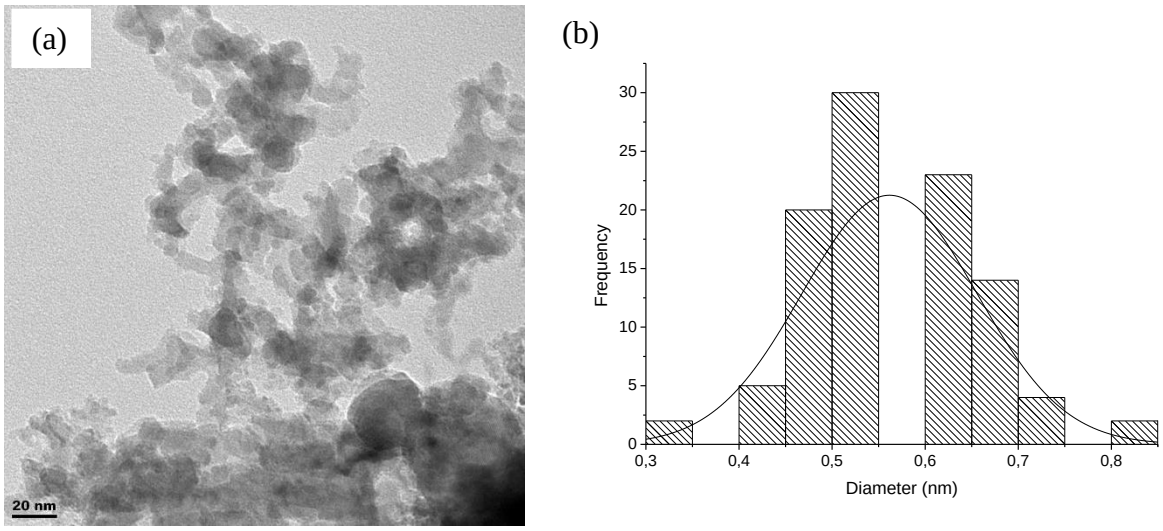

Fig 6.17 (a) Transmission electron micrograph and (b) particle size distribution of MFCb composite.

6.3.1.4 *Textural properties*

The textural properties of the raw biochar, MFC and MFCb are presented in Table 6.8. The average surface area was calculated using the BET method while the average pore volume and average pore size were computed using the BJH adsorption method. The results show that the raw biochar had a BET surface area of 0.1989 m^2/g, a pore volume of 0.0046 cm^3/g and average pore size of 0.1620 nm. The MFC and MFCb composites had BET surface areas of 77.2427 and 84.8730 m^2/g, pore volumes of 0.2409 and 0.2319 cm^3/g and pore sizes of 14.7560 and 12.9656 nm, respectively. The poor adsorptive capabilities of the raw biochar towards Cr(VI) and As(III) were attributed to its small average surface area, pore volume and pore size (Dong et al., 2017). This made the biochar a good candidate as a support for the MFC metal oxide system as its presence was anticipated not to interfere with the adsorption of Cr(VI) and As(III) in the MFCb composite. The average surface area of the MFCb composite was larger than for the MFC metal oxide and this might have been due to the distribution/impregnation of the MFC metal oxide system onto the biochar surface reducing aggregation of the nanoparticles and increasing the number of available adsorption binding sites.

Table 6.8 Textural properties for raw biochar, MFC and MFCb adsorbents.

Sample	BET surface area (m^2/g)	Pore volume (cm^3/g)	Pore size (nm)
Raw biochar	0.1989	0.0046	0.1620
MFC	77.2427	0.2409	14.7560
MFCb	84.8730	0.2319	12.9656

The N_2 adsorption/desorption isotherm for the MFCb composite is shown in Fig 6.18a. It shows a type II isotherm according to the IUPAC classification with an H3 type hysteresis loop at P/P_0 = 0.10 to 0.98 due to formation of slit-shaped pores. The reversible type II isotherm is characteristic of macroporous adsorbents (Sing et al., 1985; Luo et al., 2003; Lou et al., 2017). The pore size distribution for MFCb composite is presented on Fig 6.18b. The result shows the presence of pores in the mesoporous and macroporous regions in the range 2-130 nm (Sing et al., 1985, Rouquerol et al., 1994).

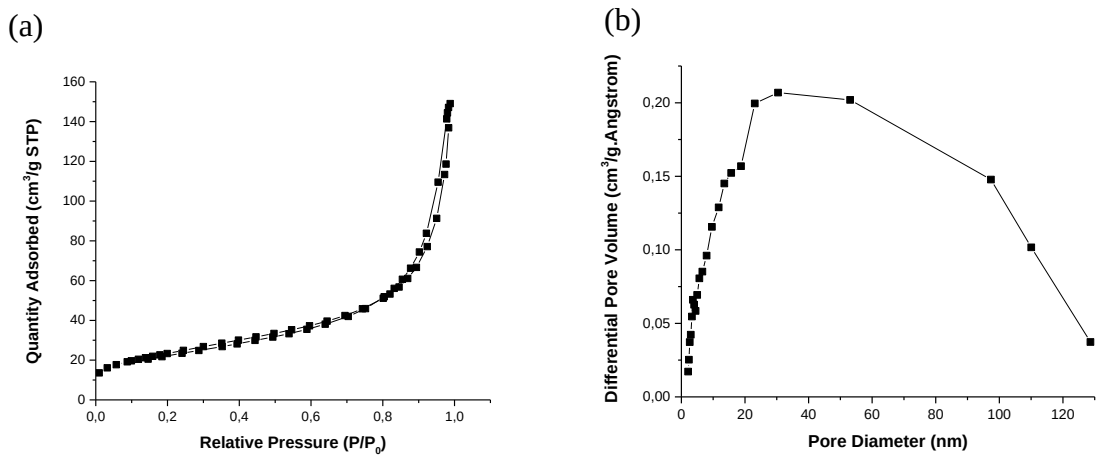

Fig 6.18 (a) N_2 adsorption/desorption isotherm and (b) pore size distribution of MFCb composite.

6.3.1.5 *Surface charge*

The MFCb pH_{pzc} was found to be 6.84. The difference between the pH_{pzc} values for MFC (6.75) and MFCb was 0.09. This information is invaluable as it reveals that the magnitudes of the surface charges on the MFC and MFCb as a function of pH are more or less the same giving an insight into the adsorption mechanisms taking place on the surfaces of the composites.

6.3.2 Adsorption of Cr(VI) and As(III)

6.3.2.1 *pH studies*

Chromium(VI): The adsorption capacity of Cr(VI) onto the MFC and MFCb composites as a function of solution pH is presented in Fig 6.19. The pH investigation using MFCb was conducted from solution pH 3-7 since leaching of adsorbent metal components at pH 2 was determined to be above the acceptable maximum contaminant levels prescribed by WHO. The plots in Fig 6.19 showed a similar pattern on the variation of adsorption capacity as a function of pH. At pH 3, the observed maximum Cr(VI) adsorption capacities were 168.13 and 183.51 mg/g on the MFC and MFCb composites, respectively. This translated into an adsorption capacity increase of 9.15 % and showed that the biochar particles were not significantly involved in the Cr(VI) sequestration mechanism. A similar result was reported by Dong and co-workers (2017) on the adsorption of Cr(VI) onto raw biochar and Fe-biochar composite. The authors noted that the contribution of the biochar to the adsorption capacity of Cr(VI) onto the Fe-biochar was small and that the biochar merely acted as support in the Fe-biochar composite. Since the variation of Cr(VI) adsorption capacity followed the same pattern on the MFC and MFCb composites, the result in Fig 6.19 suggests that the adsorption of Cr(VI) onto the MFCb composite occurred through the formation of outer-sphere surface complexation by electrostatic interactions between $HCrO_4^-$ and the functions on the surface of the ternary metal oxide system with the biochar acting as a support. At low pH, the composite surface is protonated and interacted through electrostatic attraction with the dominant $HCrO_4^-$ species increasing the Cr(VI) adsorption capacity. As the solution pH increased, the composite surface became deprotonated and negatively charged. This increased the electrostatic repulsion between the negative composite surface and $HCrO_4^-$ or CrO_4^{2-}. The slight increase observed on the Cr(VI) adsorption capacity onto the MFCb composite was attributed to (1) the even distribution of the MFC metal oxide nanocomposite onto the biochar resulting in an increase in exposed and available adsorption binding sites and (2) the Cr(III) might have interacted with functions on the biochar forming precipitates on the composite surface (Dong et al., 2017).

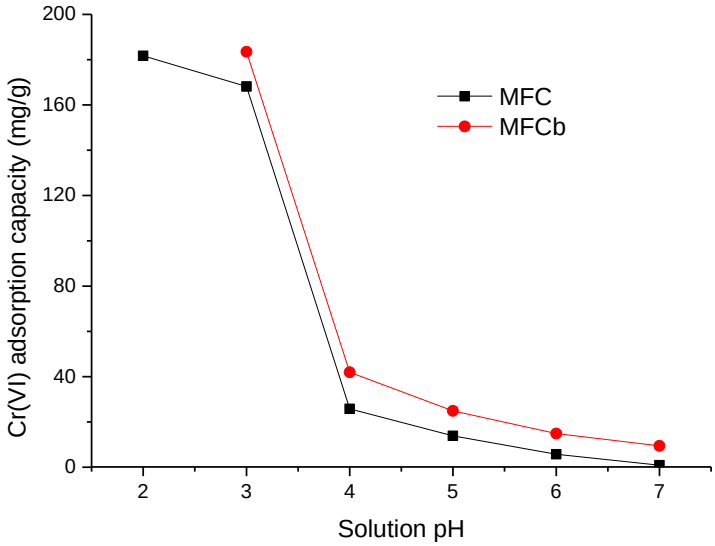

Fig 6.19 The adsorption capacity of Cr(VI) onto MFC and MFCb composites as a function of solution pH.

To show that the adsorption of Cr(VI) occurred on the MFC metal oxide system with the biochar acting as a support, the results of the pH_{pzc} studies on the MFC and MFCb composites before and after adsorption of Cr(VI) anions are plotted on Figs 6.20a and b. The plots showed a similar pattern and no changes in the magnitudes of the pH_{pzc} of the MFC and MFCb composites before and after the adsorption of Cr(VI). The similarity of the pH_{pzc} plots suggests that the dominant adsorption mechanism is the same in both the MFC and MFCb composites. On the MFCb composite, the Cr(VI) was removed from solution by the formation of outer-sphere surface complexes through electrostatic interactions between the functional groups on the MFC nanoparticles and the adsorbate (just as with the MFC oxide) with the biochar playing the role of adsorbent support.

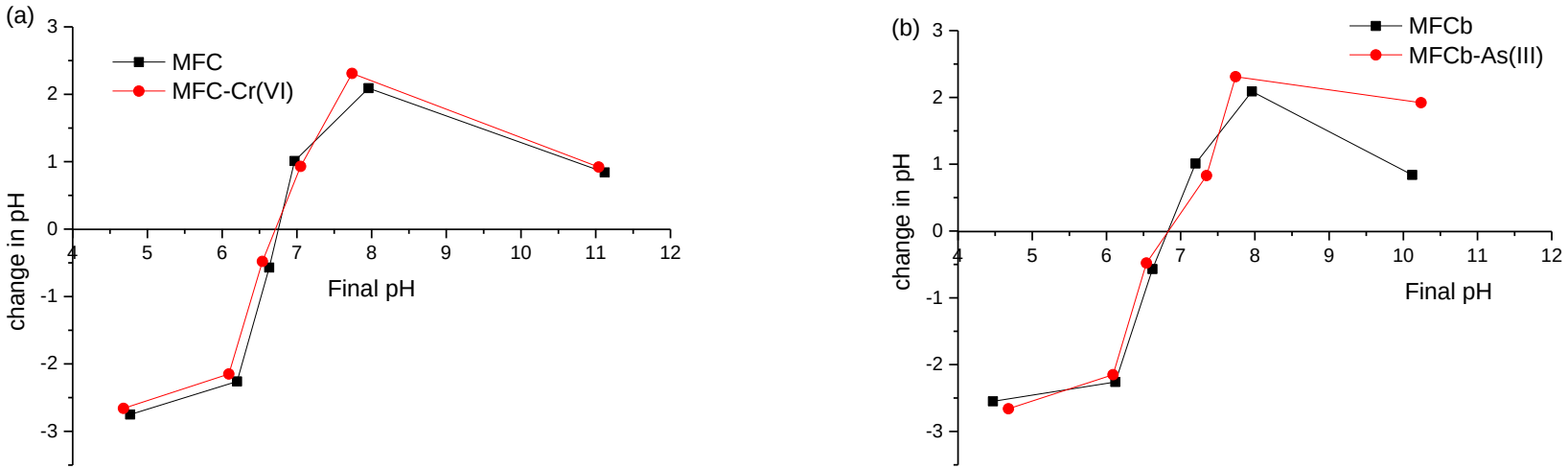

Fig 6.20 pH_{pzc} determination of (a) MFC and (b) MFCb composites before and after Cr(VI) adsorption.

Arsenic(III): To determine the effect of the biochar support on the adsorption process of As(III) onto the MFCb composite, the As(III) adsorption capacities of the MFC and MFCb composites were determined from pH 2-12. The results showing the variation of the As(III) adsorption capacities as a function of pH onto the MFC and MFCb composites are presented in Fig 6.21. The plots in Fig 6.20 reveal that the As(III) adsorption capacities onto the MFCb were slightly higher than on the MFC but followed the same pattern. This signified that the influence of the biochar on the As(III) adsorption mechanistic pathway was not very significant and that the adsorption predominantly took place on the MFC metal oxide system, with the biochar only acting as a support for the trimetal oxide system. The observed small increase in As(III) adsorption capacity was attributed to the even distribution of the MFC metal oxide system onto the biochar support. This increased the magnitude of exposed and available adsorption binding sites. At low solution pH, the As(III) adsorption capacities onto the MFCb composite were lower due to reduced affinity between the protonated adsorbent surface and the neutral H_3AsO_3. As the solution pH was increased the adsorption capacities increased until pH 9 due to inner-sphere surface exchange reactions between the functions on the composite surface and the adsorbate. At the optimum pH (9), the As(III) adsorption capacities were 42.34 and 47.11 mg/g on the MFC and MFCb composites, respectively. The presence of biochar resulted in an 11.27 % increase in the adsorption capacity at the optimal pH. The decrease in adsorption on the MFCb composite at high pH was due to (1) an increase in electrostatic repulsion between the dominant $H_2AsO_3^-$ and $HAsO_3^{2-}$ anionic forms of As(III) and the negatively charged adsorbent surface (since the solution pH > pH_{pzc}), and (2) the increase in competition for active sites between the OH^- ions and the arsenite anions. As the maximum adsorption of As(III) is at solution pH > pH_{pzc} of the MFCb (pH_{pzc}=6.84), inner-sphere surface complexation by ligand exchange and not electrostatic forces controls the uptake of the adsorbate from solution (Chandra et al., 2010; Cheng et al., 2016b)

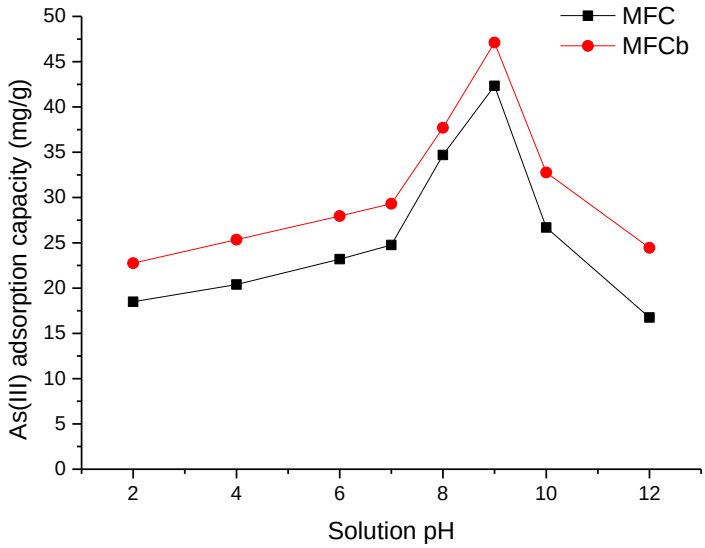

Fig 6.21 The adsorption capacity of As(III) onto MFC and MFCb composites as a function of solution pH.

Further evidence that the adsorption of As(III) predominantly took place on the MFC metal oxide system was provided by experimental studies on the changes in pH_{pzc} before and after As(III) adsorption. The plots of pH_{pzc} of the MFC and MFCb composites before and after the adsorption of As(III) are presented on Figs 6.22a and b. The plots reveal a similar trend that the pH_{pzc} after As(III) uptake increased signifying formation of inner-sphere surface complexes on the composite surface (Goldberg & Johnston, 2001). This suggests that the same uptake mechanism of As(III) was dominant on both the MFC and MFCb composites implying that the adsorption process onto the MFCb composite occurred mainly on the MFC metal oxide system with the biochar acting as a support for the metal oxide system adsorbent.

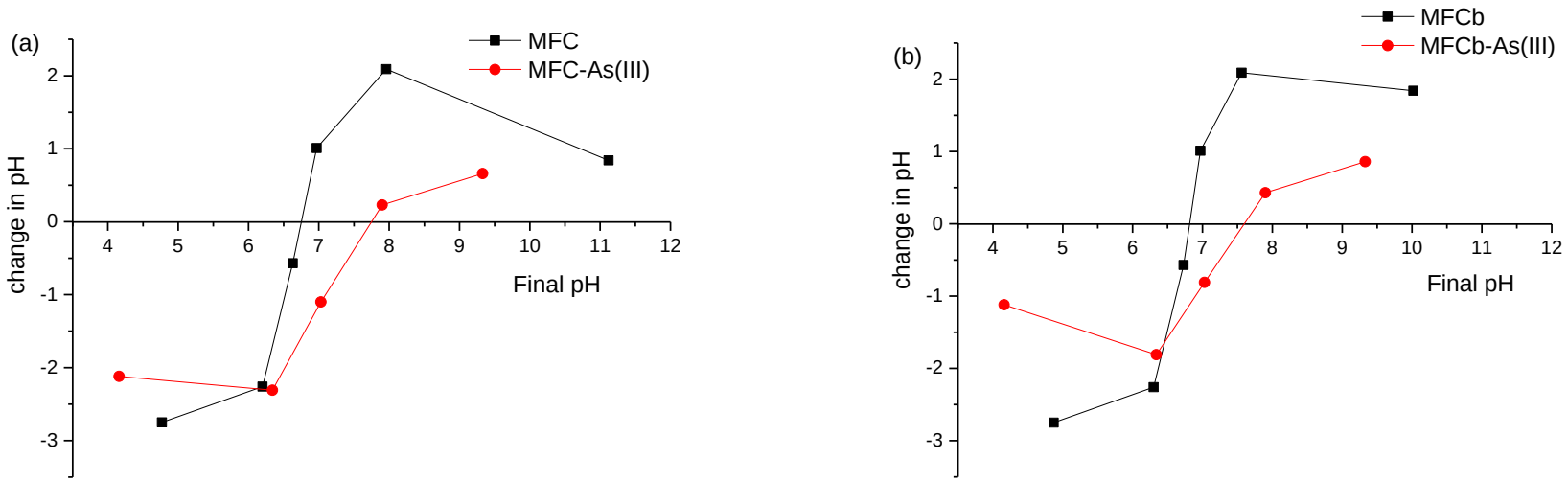

Fig 6.22 pH_{pzc} determination of (a) MFC and (b) MFCb composites before and after As(III) adsorption.

6.3.2.2 *Cr(VI) and As(III) adsorption mechanism*

Chromium(VI): The changes in FTIR spectra and the magnitude of surface charge on the MFCb composite surface before and after Cr(VI) adsorption were used to elucidate the adsorption mechanism of Cr(VI) onto the MFCb composite. The results showed that the adsorption predominantly took place on the MFC metal oxide system surface with the biochar acting as a support for the adsorbent. The FTIR spectra of MFCb composite before and after Cr(VI) adsorption is presented in Fig 6.23. The peaks at 3446 and 3332 cm^{-1} after Cr(VI) adsorption were ascribed to Cr-O or Cr=O stretching vibrations from complexation of Cr(VI) with the surface hydroxyl groups on the adsorbent (Du et al.,2015). The absorptions at 1646, 1481 and 1361 cm^{-1} disappeared after Cr(VI) adsorption suggesting an interaction between the adsorbent surface-oxygen groups ($-COO^-$) and the adsorbate during the adsorption process. The absorption peaks at 1096, 843 and 592 cm^{-1} after Cr(VI) adsorption were attributed to Cr-O or Cr=O vibrations due to the interactions between hydroxyl groups on the MFC metal oxide system and the carboxyl groups on the biochar support.

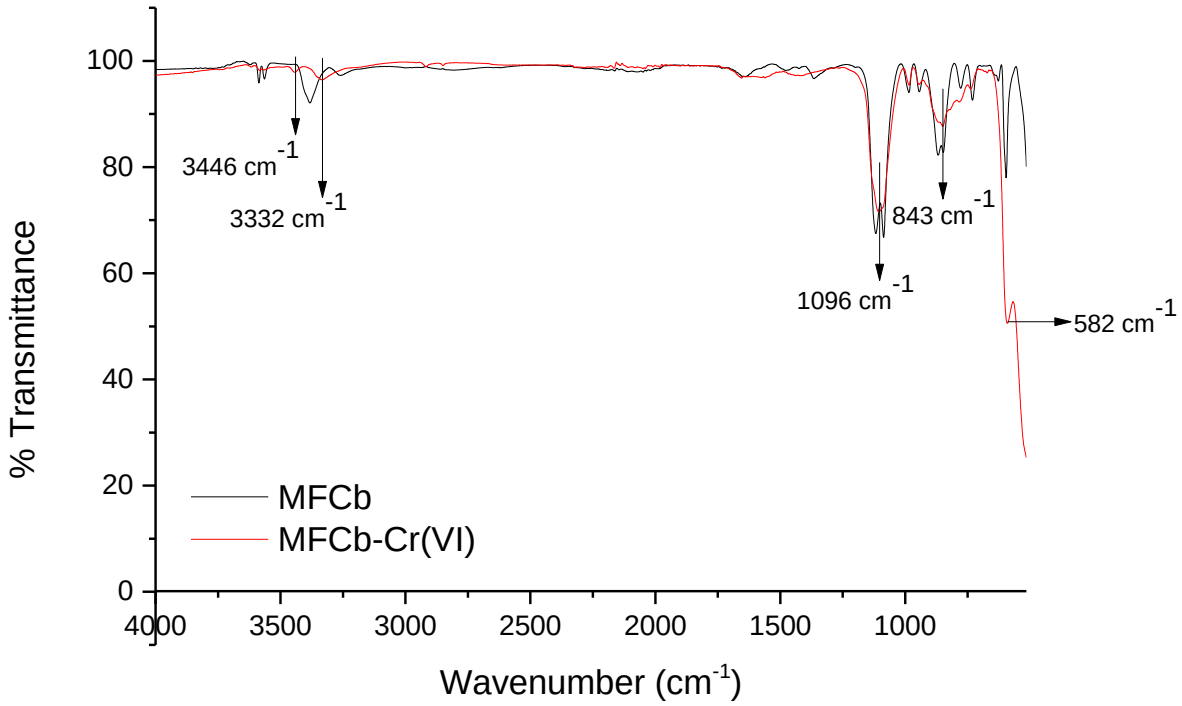

Fig 6.23 FTIR spectrum of MFCb composite before and after Cr(VI) adsorption.

The studies on changes of the pH_{pzc} of the MFCb composite before and after Cr(VI) adsorption (section 6.3.2.1) provided further evidence that the adsorption was by outer-sphere surface complexation. The mechanistic pathway of Cr(VI) adsorption onto the MFCb composite at pH 3 was postulated to have at least four stages: (1) protonation of the MFCb composite surface, (2) the interaction of surface functional groups on the adsorbent and Cr(VI) anions through outer-sphere complexation, (3) the reduction of Cr(VI) to Cr(III), and (4) dative-covalent bonding of the Cr(III) to hydroxyl or carboxyl groups on the MFC metal oxide system and biochar support, respectively.

$$-M-OH+H^{+}\rightarrow -M-OH_{2}^{+} \tag{6.24}$$

where $-M-OH$ is the MFC metal oxide system surface. The protonated surface interacted with the Cr(VI) oxyanions forming monodentate outer-sphere surface complexes through electrostatic forces (Johnston & Chrysochoou, 2014):

$$-M-OH_{2}^{+}+HCrO_{4}^{-}\rightarrow -M-OH_{2}^{+}\ldots HCrO_{4}^{-} \tag{6.25}$$

Some of the Cr(VI) was reduced at the low acidic solution pH to Cr(III):

$$HCrO_{4}^{-}+7H^{+}+3e^{-}\rightleftharpoons Cr^{3+}+4H_{2}O \tag{6.26}$$

During the reduction of Cr(VI), the carbon from the biochar can act as a source of electrons and become oxidised to a carboxyl group (Liu et al., 2012).

$$HCrO_{4}^{-}+C+3H^{+}\rightarrow Cr^{3+}+COO^{-}+2H_{2}O \tag{6.27}$$

The formed Cr(III) can form coordinate bonds with the hydroxyl groups on the metal oxide system and the carboxyl groups on the biochar support:

$$-M-(OH)_{x}+Cr^{3+}\rightarrow -M-(OH)_{3}Cr^{3+}\downarrow \tag{6.28}$$

$$-b-(COO^{-})_{x}+Cr^{3+}\rightarrow -b-(COO^{-})_{3}Cr^{3+}\downarrow \tag{6.29}$$

where $-b-(COO^{-})_{x}$ denotes the carboxyl groups on the biochar surface. The adsorption binding sites with adsorbed Cr(III) might be difficult to regenerate in subsequent adsorption processes since the formed coordinate bonds can be difficult to reverse (Lin et al., 2018).

Arsenic(III): Infrared and surface charge studies on the MFCb composite before and after the adsorption of As(III) revealed that the adsorption predominantly took place on the MFC metal oxide system surface with the biochar acting as a support for the adsorbent. The FTIR spectra of MFCb composite before and after As(III) adsorption is presented in Fig 6.24. The peaks at 3585, 3565, 3382 and 3260 cm^{-1} were replaced by a broad weak absorption at 3267 cm^{-1} after As(III) adsorption. This was attributed to As-O vibrations due to the interaction between the surface hydroxyl groups on the MFC metal oxide system surface and the hydroxyl groups on the As(III) species through inner-sphere ligand exchange reactions. The absorption bands due to O=C-O vibrations from ester or carbonyl groups on the biochar surface at 1646, 1361 and 1081 cm^{-1} decreased in intensity after the adsorption. This revealed that the As(III) species interacted with the surface-bearing oxygen functions on the biochar support. The peak at 1481 cm^{-1} due to vibrations of O-H in Mn-OH shifted to 1479 cm^{-1} after the adsorption of As(III). The absorption peaks at 992, 941, 861, 776 and 725 cm^{-1} disappeared after the adsorption of As(III) and a new peak characteristic of As-O vibrations was observed at 823 cm^{-1} (Ouma et al., 2018). This provided evidence that the metal hydroxyl groups on the MFC metal oxide system interacted with the As(III) species forming As-O-Mn and As-O-Fe linkages through inner-sphere surface complexation and ligand exchange. The absorption peak due to As-O vibration in Fe-O-As has been attributed to As(V) formed from the oxidation of As(III) since it is difficult for FTIR to detect As(III) adsorbed onto iron oxides (Goldberg & Johnston, 2001; Ren et al., 2011, Wu et al., 2013; Li et al., 2020). This revealed that a part of the As(III) was oxidised to As(V) during the adsorption process. The absorption peak at 577 cm^{-1} after adsorption was attributed to As-O vibration in Cu-O-As. The infrared spectral changes after adsorption of As(III) showed that adsorbate uptake was through inner-sphere ligand exchange reactions between oxygen-bearing surface functions on the composite and the hydroxyl groups on the As(III) species.

The increase in the pH_{pzc} on the MFCb composite surface after As(III) adsorption (section 6.3.2.1) provided further evidence for the formation of inner-sphere surface complexes during

the adsorption. The mechanistic pathway of As(III) adsorption onto the MFCb composite at pH 9 (pH > pH_{pzc}) first involved the deprotonation of the MFCb composite surface:

$$-M-OH+OH^{-}\rightarrow M-O^{-}+H_2O \tag{6.30}$$

where $-M-OH$ is the MFC metal oxide system surface binding site. The deprotonated adsorbent surface interacts with the dominant H_3AsO_3 species through ligand exchange forming inner-sphere surface complexes:

$$-M-O^{-}+H_3AsO_3\rightarrow -MHAsO_3+H_2O \tag{6.31}$$

and/or

$$-M-O^{-}+H_2AsO_3^{-}\rightarrow -MAsO_3+H_2O \tag{6.32}$$

and on the biochar surface:

$$-b-COO^{-}+H_3AsO_3\rightarrow -b-COHAsO_3+H_2O \tag{6.33}$$

and/or

$$-b-COO^{-}+H_2AsO_3^{-}\rightarrow -b-COAsO_3+H_2O \tag{6.34}$$

where $-b-COO^{-}$ denotes the oxygen-containing surface functions on the biochar. A part of the As(III) was oxidised to As(V) in the presence of manganese oxides:

$$MnO_2+H_3AsO_3+2H^{+}\rightarrow Mn^{2+}+H_3AsO_4+H_2O \tag{6.35}$$

The dominant As(V) species at pH 9 is $HAsO_4^{2-}$. A part of the As(V) species present in solution at pH 9 might also have been formed through the following reaction (Vieira et al., 2017):

$$H_3AsO_3+H_2O\rightarrow HAsO_4^{2-}+4H^{+}+2e^{-} \tag{6.36}$$

and it interacts with the negatively charged MFC metal oxide surface forming an inner sphere surface complex by ligand exchange:

$$-M-O^{-}+HAsO_4^{2-}\rightarrow -MAsO_4+OH^{-} \quad (6.37)$$

The dominant form of the formed As(V) was anticipated to interact with the COO- groups on the biochar surface through inner-sphere ligand exchange:

$$-b-COO^{-}+HAsO_4^{2-}\rightarrow -b-COAsO_4+OH^{-} \quad (6.38)$$

The electrostatic interactions between the adsorbent surfaces and As(V) were ruled out since the adsorption processes occurred at solution pH's > pH_{pzc}.(Chandra et al., 2010, Cheng et al., 2016; Roy et al., 2017).

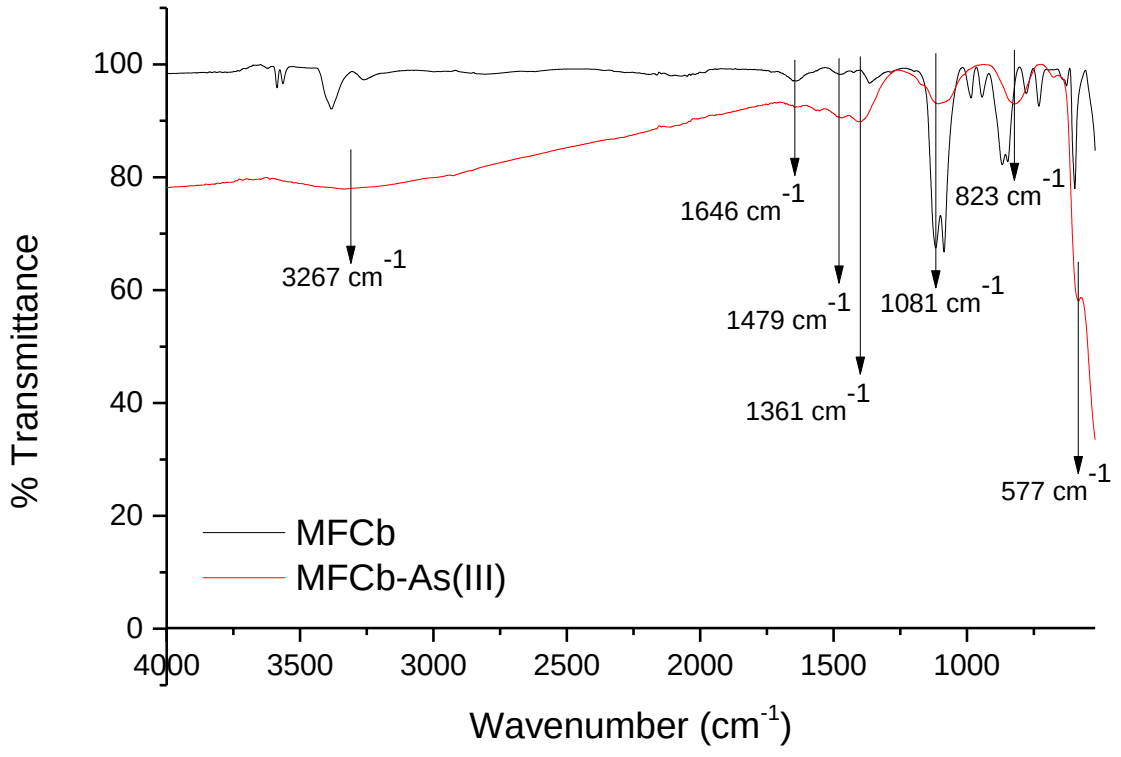

Fig 6.24 FTIR spectra of MFCb composite before and after As(III) adsorption.

6.3.2.3 *Regeneration and reuse*

The ability to desorb the adsorbate from the adsorption binding site on the MFCb composite determines the applicability of the composite in Cr(VI) and As(III) decontamination from aqueous solution.

Chromium(VI): The results for the regeneration and reuse of the MFCb composite for five successive adsorption/desorption cycles are presented in Fig 6.25. The plot revealed that the adsorption capacities decreased gradually from 67.89 to 65.65, 64.37, 62.77 and 61.91 mg/g from the first to the fifth adsorption cycle. This translated into a decrease of 8.81 % in adsorption capacity between the first and the fifth adsorption cycle. The decreases in adsorption capacities at each adsorption cycle were attributed to the formation of $-M-(OH)_3Cr^{3+}$ and $-b-(COO^-)_3Cr^{3+}$ precipitates through coordination bonding between the surface hydroxyl groups on the MFC metal oxide system, carboxyl groups on the biochar support and Cr(III) from the reduction of a part of the Cr(VI) (Lin et al.,2018). The formed coordination species, $-M-(OH)_3Cr^{3+}$ and $-b-(COO^-)_3Cr^{3+}$ are not easily desorbed using a strong base due to the formation of a strong dative covalent bond affecting the regeneration of some adsorption active sites. This rendered the attached adsorption binding sites unavailable for bonding in successive adsorption cycles. The results showed that the MFCb composite was stable and still applicable to the adsorption of Cr(VI) after five adsorption/desorption cycles.

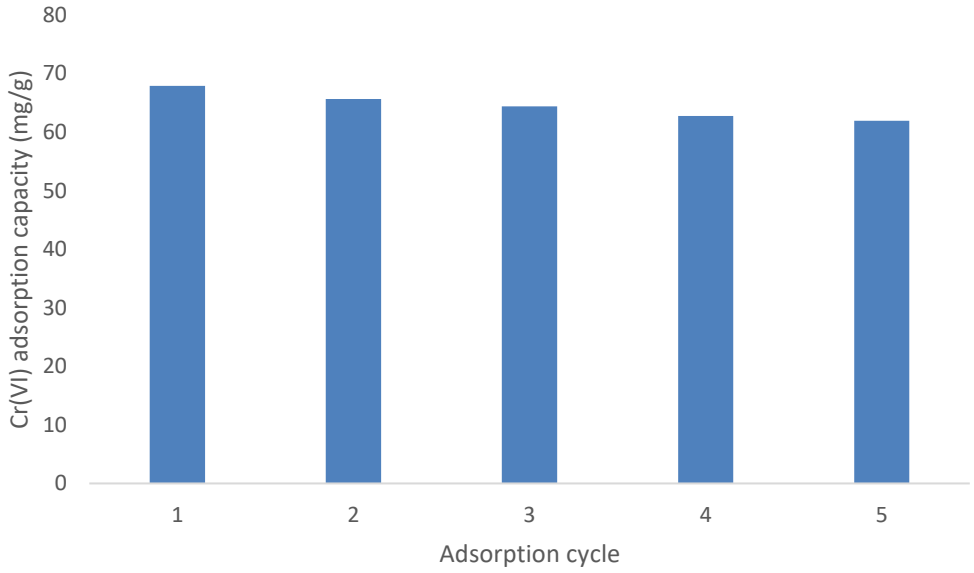

Fig 6.25 The effect of adsorption cycles on Cr(VI) adsorption onto the MFCb composite.

Arsenic(III): Fig 6.26 shows the results for five As(III) adsorption/desorption cycles of the MFCb composite adsorbent. The plot revealed that the adsorption capacities decreased gradually from 38.91 to 37.56, 35.73, 34.79 and 33.69 mg/g from the first to the fifth adsorption cycle. This was a decrease of 13.89 % in adsorption capacity between the first and the fifth adsorption cycle. The results showed that the MFCb composite was stable after five adsorption/desorption cycles.

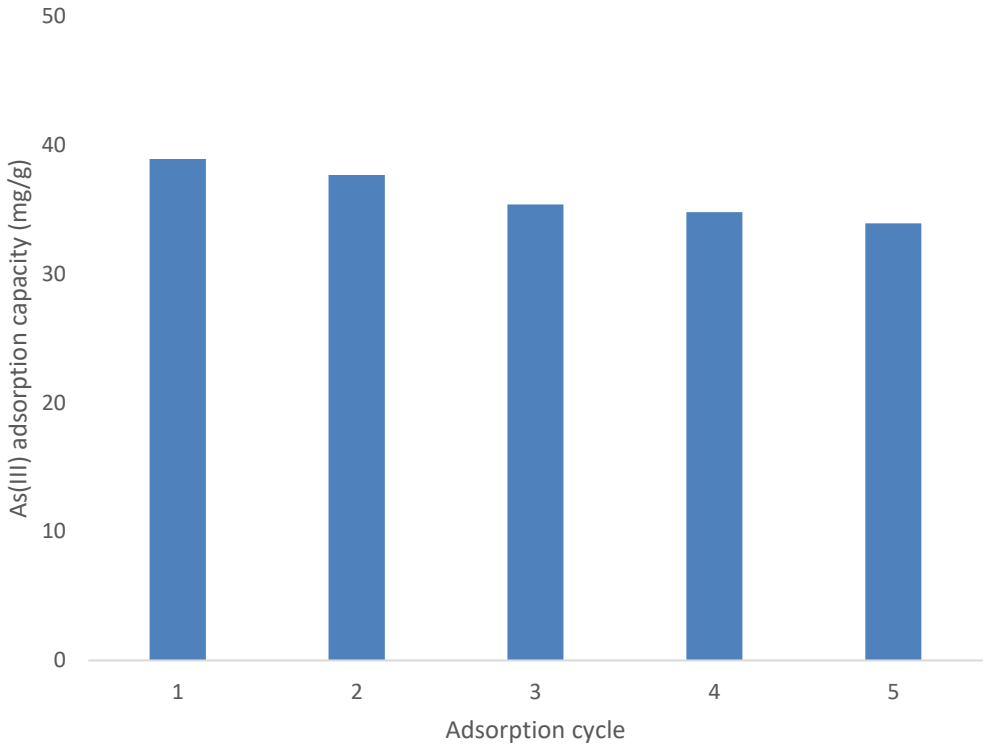

Fig 6.26 The effect of adsorption cycles on As(III) adsorption onto the MFCb composite.

6.4 CONCLUSION

The Langmuir and Freundlich models described the nature of adsorbent surface coverage, while the Dubinin-Radushkevich model provided information about the dominant As(III) and Cr(VI) uptake mechanism onto the MC, MF and MFC metal oxides. The calculated thermodynamic parameters showed the feasibility, spontaneity and type of the adsorption processes. The adsorption of Cr(VI) onto the nanocomposites was predominantly due to reduction of Cr(VI) to Cr(III) and outer-sphere surface complexation through electrostatic forces, while the adsorption of As(III) was proposed to mainly proceed by the oxidation of As(III) to As(V) and inner-sphere ligand exchange reactions. The MFC metal oxide system

was successfully precipitated on biochar support to form the MFCb nanocomposite to facilitate ease of adsorbent separation from the treated wastewater.

6.5 REFERENCES

1. AHMED, M.J.K. and AHMARUZZAMAN, M. (2016) A review on potential usage of industrial waste materials for binding heavy metal ions from aqueous solutions, *Jo urnal of Water Process Engineering*. 10, pp. 39-47.

2. AIGBE, U.O., DAS, R., HO, W.H., SRINIVASU, V. and MAITY, A. (2018) A novel method for removal of Cr (VI) using polypyrrole magnetic nanocomposite in the presence of unsteady magnetic fields, *Separation and Purification Technology*. 194, pp. 377-387.

3. ANASTOPOULOS, I. and KYZAS, G.Z. (2016) Are the thermodynamic parameters correctly estimated in liquid-phase adsorption phenomena?, *Journal of Molecular Liquids*. 218, pp. 174-185.

4. ARGUN, M.E., DURSUN, S., OZDEMIR, C. and KARATAS, M. (2007) Heavy metal adsorption by modified oak sawdust: Thermodynamics and kinetics, *Journal of Hazardous Materials*. 141, pp. 77-85.

5. BALLAV, N., CHOI, H.J., MISHRA, S.B. and MAITY, A. (2014) Synthesis, characterization of Fe_3O_4@glycine doped polypyrrole magnetic nanocomposites and their potential performance to remove toxic Cr(VI), *Journal of Industrial and Engineering Chemistry*. 20, pp. 4085–4093

6. BELACHEW, N. and HINSENE, H. (2020) Preparation of cationic surfactant-modified kaolin for enhanced adsorption of hexavalent chromium from aqueous solution, *Applied Water Science*. 10, pp. 38.

7. CHANDRA, V., PARK, J., CHUN, Y., LEE, J.W., HWANG, I.C. and KIM, K.S. (2010) Water-dispersible magnetite-reduced graphene oxide composites for arsenic removal, *ACS Nano*. 4, pp. 3979-3986.
8. CHEN, H., CHU, P.K., HE, J., HU, T. and YANG, M. (2011) Porous magnetic manganese oxide nanostructures: Synthesis and their applications in water treatment, *Journal of Colloid and Interface Science*. 359, pp. 68-74.

9. CHENG, W., DING, C., WANG, X., WU, Z., SUN, Y., YU, S., HAYAT, T. and WANG, X. (2016a) Competitive sorption of As (V) and Cr (VI) on carbonaceous nanofibers, *Chemical Engineering Journal*. 293, pp. 311-318.

10. CHENG, W., ZHANG, W., HU, L., DING, W., WU, F. and LI, J. (2016b) Etching synthesis of iron oxide nanoparticles for adsorption of arsenic from water, *RSC Advances*. 6, pp. 15900-15910.

11. CUI, H., LI, Q., GAO, S. and SHANG, J.K. (2012) Strong adsorption of arsenic species by amorphous zirconium oxide nanoparticles, *Journal of Industrial and Engineering Chemistry*. 18, pp. 1418-1427.

12. CUMBAL, L. and SENGUPTA, A.K. (2005) Arsenic removal using polymer-supported hydrated iron (III) oxide nanoparticles: role of Donnan membrane effect, *Environmental Science & Technology*. 39, pp. 6508-6515.

13. DENG, F., LUO, X.B., DING, L. and LUO, S.L. (2019) Application of Nanomaterials and Nanotechnology in the Reutilization of Metal Ion From Wastewater. In *Nanomaterials for the Removal of Pollutants and Resource Reutilization*. Elsevier.

14. DONG, H., DENG, J., XIE, Y., ZHANG, C., JIANG, Z., CHENG, Y., HOU, K. and ZENG, G. (2017) Stabilization of nanoscale zero-valent iron (nZVI) with modified biochar for Cr(VI) removal from aqueous solution, *Journal of Hazardous Materials*. 332, pp. 79-86.

15. DU, Y., WANG, L., WANG, J., ZHENG, G., WU, J. and DAI, H. (2015) Flower-, wire-, and sheet-like MnO_2-deposited diatomites: Highly efficient absorbents for the removal of Cr (VI), *Journal of Environmental Sciences*. 29, pp. 71-81.

16. DUBEY, S and SHARMA, Y.C. (2017) *Calotropis procera* mediated one pot green synthesis of Cupric oxide nanoparticles (CuO-NPs) for adsorptive removal of Cr(VI) from aqueous solutions, *Applied Organometallic Chemistry*. 31, pp. 1-15.

17. DUBININ, M.M. and RADUSHKEVICH, L.V. (1947) Equation of the characteristic curve of activated charcoal, *Proceedings of the Academy of Sciences (USSR)*. 55, pp. 331-333.

18. DURANOĞLU, D., TROCHIMCZUK, A.W. and BEKER, U. (2012) Kinetics and thermodynamics of hexavalent chromium adsorption onto activated carbon derived from acrylonitrile-divinylbenzene copolymer, *Chemical Engineering Journal*. 187, pp. 193-202.

19. FERNÁNDEZ-CARRASCO, L., TORRENS-MARTÍN, D., MORALES, L.M. and MARTÍNEZ-RAMÍREZ, S. (2012) Infrared spectroscopy in the analysis of building and construction materials, *Infrared Spectroscopy—Materials Science, Engineering and Technology. INTECH*. pp. 369-82.

20. FREUNDLICH, H. (1906) Über die adsorption in lösungen, *Zeitschrift für Physikalische Chemie*. 57, pp. 385-470.

21. FU, J., CHEN, Z., WANGA, M., LIU, S., ZHANG, J., ZHANG, J., HAN, R., XU, Q. (2015) Adsorption of methylene blue by a high-efficiency adsorbent (polydopamine microspheres): Kinetics, isotherm, thermodynamics and mechanism analysis, *Chemical Engineering Journal*. 259, pp. 53–61.

22. GAN, C., LIU, Y., TAN, X., WANG, S., ZENG, G., ZHENG, B., LI, T., JIANG, Z. and LIU, W. (2015) Effect of porous zinc–biochar nanocomposites on Cr (VI) adsorption from aqueous solution, *RSC Advances*. 5, pp. 35107-35115.

23. GHEJU, M., BALCU, I. and MOSOARCA, G. (2016) Removal of Cr (VI) from aqueous solutions by adsorption on MnO_2, *Journal of Hazardous Materials*. 310, pp. 270-277.

24. GHOSAL, P.S., KATTIL, K.V., YADAV, M.K. and GUPTA, A.K. (2018) Adsorptive removal of arsenic by novel iron/olivine composite: Insights into preparation and adsorption process by response surface methodology and artificial neural network, *Journal of Environmental Management*. 209, pp. 176-187.

25. GILES, C.H., SMITH, D. and HUITSON, A. (1974) A general treatment and classification of the solute adsorption isotherm. I. Theoretical, *Journal of Colloid and Interface Science*. 47, pp. 755-765.

26. GOLDBERG, S. (2002) Competitive adsorption of arsenate and arsenite on oxides and clay minerals, *Soil Science Society of America Journal*. 66, pp. 413-421.

27. GOLDBERG, S. and JOHNSTON, C.T. (2001) Mechanisms of arsenic adsorption on amorphous oxides evaluated using macroscopic measurements, vibrational spectroscopy, and surface complexation modelling, *Journal of Colloid and Interface Science*. 234, pp. 204–216.

28. GUPTA, A., VIDYARTHI, S.R. and SANKARARAMAKRISHNAN, N. (2015) Concurrent removal of As (III) and As (V) using green low cost functionalized biosorbent–Saccharum officinarum bagasse, *Journal of Environmental Chemical Engineering*. 3, pp. 113-121.

29. HALL, K.R., EAGLETON, L.C., ACRIVOS, A. and VERMEULEN, T. (1966) Pore- and solid-diffusion kinetics in fixed-bed adsorption under constant-pattern conditions, *Industrial & Engineering Chemistry Fundamentals*. 5, pp. 212-223.

30. HU, Q. and ZHANG, Z. (2019) Application of Dubinin–Radushkevich isotherm model at the solid/solution interface: A theoretical analysis, *Journal of Molecular Liquids*. 277, pp. 646-648.

31. ISLAM, M.A., ANGOVE, M.J., MORTON, D.W., PRAMANIK, B.K. and AWUAL, M.R. (2019) A mechanistic approach of chromium (VI) adsorption onto manganese oxides and boehmite, *Journal of Environmental Chemical Engineering*. pp. 103515.

32. JOHNSTON, C.P. and CHRYSOCHOOU, M. (2014) Mechanisms of chromate adsorption on hematite, *Geochimica et Cosmochimica Acta*. 138, pp. 146-157.

33. LANGMUIR, I. (1918) The adsorption of gases on plane surfaces of glass, mica and platinum, *Journal of American Chemical Society.* 40, pp. 1361-1403.

34. LI, J., GYOTEN, H., SONODA, A., FENG, Q. and XUE, M. (2017) Removal of trace arsenic to below drinking water standards using a Mn–Fe binary oxide, *RSC Advances*. 7, pp. 1490-1497.

35. LI, N., FU, F., LU, J., DING, Z., TANG, B. and PANG, J. (2017) Facile preparation of magnetic mesoporous $MnFe_2O_4$@ SiO_2−CTAB composites for Cr (VI) adsorption and reduction, *Environmental Pollution*. 220, pp. 1376-1385.

36. LI, Y., ZHU, X., QI, X., SHU, B., ZHANG, X., LI, K., WEI, Y. and WANG, H. (2020) Removal and immobilization of arsenic from copper smelting wastewater using copper

slag by in situ encapsulation with silica gel, *Chemical Engineering Journal*. 394, pp. 124833.

37. LIMA, É.C., ADEBAYO, M.A. and MACHADO, F.M. (2015) Kinetic and equilibrium models of adsorption. In *Carbon nanomaterials as adsorbents for environmental and biological applications*, pp. 33-69). Springer, Cham.
38. LIMA, E.C., CESTARI, A.R. and ADEBAYO, M.A. (2016) Comments on the paper: a critical review of the applicability of Avrami fractional kinetic equation in adsorption-based water treatment studies, *Desalination and Water Treatment*. 57, pp. 19566-19571.
39. LIMA, E.C., HOSSEINI-BANDEGHARAEI, A., MORENO-PIRAJÁN, J.C. and ANASTOPOULOS, I. (2019a) A critical review of the estimation of the thermodynamic parameters on adsorption equilibria. Wrong use of equilibrium constant in the Van't Hoff equation for calculation of thermodynamic parameters of adsorption, *Journal of Molecular Liquids*. 273, pp. 425-434.
40. LIMA, E.C., HOSSEINI-BANDEGHARAEI, A. and ANASTOPOULOS, I. (2019b) Response to "Some remarks on a critical review of the estimation of the thermodynamic parameters on adsorption equilibria. Wrong use of equilibrium constant in the Van't Hoff equation for calculation of thermodynamic parameters of adsorption - Journal of Molecular Liquids 273 (2019) 425–434.", *Journal of Molecular Liquids*. 280, pp. 298–300.
41. LIN, S., LU, D. and LIU, Z. (2012) Removal of arsenic contaminants with magnetic γ-Fe_2O_3 nanoparticles, *Chemical Engineering Journal*. 211, pp. 46-52.
42. LIN, C., LUO, W., LUO, T., ZHOU, Q., LI, H. and JING, L. (2018) A study on adsorption of Cr (VI) by modified rice straw: Characteristics, performances and mechanism, *Journal of Cleaner Production*. 196, pp. 626-634.
43. LIU, W., ZHANG, J., ZHANG, C. and REN, L. (2012) Preparation and evaluation of activated carbon-based iron-containing adsorbents for enhanced Cr (VI) removal: mechanism study, *Chemical Engineering Journal*. 189, pp. 295-302.
44. LOU, Z., CAO, Z., XU, J., ZHOU, X., ZHU, J., LIU, X., BAIG, S.A., ZHOU, J. and XU, X. (2017) Enhanced removal of As(III)/(V) from water by simultaneously

supported and stabilized Fe-Mn binary oxide nanohybrids, *Chemical Engineering Journal*. 322, pp. 710–721.

45. LUNGE, S., SINGH, S. and SINHA, A. (2014) Magnetic iron oxide (Fe_3O_4) nanoparticles from tea waste for arsenic removal, *Journal of Magnetism and Magnetic Materials*. 356, pp. 21-31.

46. LUO, H., WANG, C. and YAN, Y. (2003) Synthesis of mesostructured titania with controlled crystalline framework, *Chemistry of Materials*. 15, pp. 3841-3846.

47. LV, X., HU, Y., TANG, J., SHENG, T., JIANG, G. and XU, X. (2013) Effects of co-existing ions and natural organic matter on removal of chromium (VI) from aqueous solution by nanoscale zero valent iron (nZVI)-Fe_3O_4 nanocomposites, *Chemical Engineering Journal*. 218, pp. 55-64.
48. MAKRESKI, P., STEFOV, S., PEJOV, L. and JOVANOVSKI, G. (2015) Theoretical and experimental study of the vibrational spectra of (para) symplesite and hörnesite, *Spectrochimica Acta Part A: Molecular and Biomolecular Spectroscopy*. 144, pp. 155-162.
49. MISHRA, M.K. (2016) Fourier transform infrared spectrophotometry studies of chromium trioxide-phthalic acid complexes, *Chemical Science Transactions*. 5, pp. 770-774.

51. MOHAN, S., SINGH, Y., VERMA, D.K. and HASAN, S.H. (2015) Synthesis of CuO nanoparticles through green route using Citrus limon juice and its application as nanosorbent for Cr(VI) remediation: Process optimization with RSM and ANN-GA based model, *Process Safety and Environmental Protection*. 96, pp. 156–166.
52. MONDAL, N.K. and BASU, S. (2019) Potentiality of waste human hair towards removal of chromium(VI) from solution: kinetic and equilibrium studies, *Applied Water Science*. 9, https://doi.org/10.1007/s1320 1-019-0929-5.
53. MORALES, M.R., BARBERO, B.P., LOPEZ, T., MORENO, A. and CADÚS, L.E. (2009) Evaluation and characterization of Mn–Cu mixed oxide catalysts supported on TiO_2 and ZrO_2 for ethanol total oxidation, *Fuel*. 88, pp. 2122-2129.
54. NIGAM, S., GOPAL, K. and VANKAR, P.S. (2013) Biosorption of arsenic in drinking water by submerged plant: *Hydrilla verticilata*, *Environmental Science and Pollution Research*. 20, pp. 4000-4008.

55. NOGUEIRA, A.E., GIROTO, A.S., NETO, A.B.S. and RIBEIRO, C. (2016) CuO synthesized by solvothermal method as a high capacity adsorbent for hexavalent chromium, *Colloids and Surfaces A: Physicochemical. Engineering. Aspects*. 498, pp. 161–167.

50. OUMA, I.L., NAIDOO, E.B. and OFOMAJA, A.E. (2018) Thermodynamic, kinetic and spectroscopic investigation of arsenite adsorption mechanism on pine cone-magnetite composite, *Journal of Environmental Chemical Engineering*. 6, pp. 5409-5419.

51. PARSONS, J.G., HERNANDEZ, J., GONZALEZ, C.M. and GARDEA-TORRESDEY, J.L. (2014) Sorption of Cr (III) and Cr (VI) to high and low pressure synthetic nano-magnetite (Fe_3O_4) particles, *Chemical Engineering Journal*. 254, pp. 171-180.

52. PHOLOSI, A., NAIDOO, B.E. and OFOMAJA, A.E. (2018) Clean application of magnetic biomaterial for the removal of As (III) from water, *Environmental Science and Pollution Research*. 25, pp. 30348-30365.

53. PHOLOSI, A., NAIDOO, E.B. and OFOMAJA, A.E. (2019) Enhanced Arsenic (III) adsorption from aqueous solution by magnetic pine cone biomass, *Materials Chemistry and Physics*. 222, pp. 20-30.

54. PHOLOSI, A., OFOMAJA, A.E. and NAIDOO, E.B. (2013) Effect of chemical extractants on the biosorptive properties of pine cone powder: Influence on lead (II) removal mechanism, *Journal of Saudi Chemical Society*. 17, pp. 77-86.

55. QI, W., ZHAO, Y., ZHENG, X., JI, M. and ZHANG, Z. (2016) Adsorption behavior and mechanism of Cr (VI) using Sakura waste from aqueous solution, *Applied Surface Science*. 360, pp. 470-476.

56. RAMIREZ, A., OCAMPO, R., GIRALDO, S., PADILLA, E., FLÓREZ, E. and ACELAS, N. (2020) Removal of Cr(VI) from an aqueous solution using an activated carbon obtained from teakwood sawdust: Kinetics, equilibrium, and density functional theory calculations, *Journal of Environmental Chemical Engineering*. 8, pp. 103702.

57. RANGABHASHIYAM, S., ANU, N., NANDAGOPAL, M.G. and SELVARAJU, N. (2014) Relevance of isotherm models in biosorption of pollutants by agricultural byproducts, *Journal of Environmental Chemical Engineering*. 2, pp. 398-414.

58. REN, Z., ZHANG, G. and CHEN, J.P. (2011) Adsorptive removal of arsenic from water by an iron–zirconium binary oxide adsorbent, *Journal of Colloid and Interface Science*. 358, pp. 230-237.

59. ROUQUEROL, J., AVNIR, D., FAIRBRIDGE, C.W., EVERETT, D.H., HAYNES, J.H., PERNICONE, N., RAMSAY, J.D.F., SING, K.S.W. and UNGER, K.K. (1994) Recommendations for the characterization of porous solids, *Pure & Applied Chemistry*. 66, pp. 1739-1758.

60. ROY, P., DEY, U., CHATTORAJ, S., MUKHOPADHYAY, D. and MONDAL, N.K. (2017) Modeling of the adsorptive removal of arsenic (III) using plant biomass: a bioremedial approach, *Applied Water Science*. 7, pp. 1307-1321.

61. SAHA, P. and CHOWDHURY, S. (2011) Insight into adsorption thermodynamics, *Thermodynamics*. pp. 349-364.

62. SAHU, U.K., SAHU, S., MAHAPATRA, S.S. and PATEL, R.K. (2017) Cigarette soot activated carbon modified with Fe_3O_4 nanoparticles as an effective adsorbent for As (III) and As (V): material preparation, characterization and adsorption mechanism study, *Journal of Molecular Liquids*. 243, pp. 395-405.

63. SING, K.S.W., EVERETT, D.H., HAUL, R.A.W., MOSCOU, L., PIEROTTI, R.A., ROUQUEROL, J., SIEMIENIEWSKA, T. (1985) Reporting physisorption data for gas/solid systems with special reference to the determination of surface area and porosity, *Pure & Applied Chemistry*. 57, pp. 603-619.

64. TAJERNIA, H., EBADI, T., NASERNEJAD, B. and GHAFORI, M. (2014) Arsenic removal from water by sugarcane bagasse: an application of response surface methodology (RSM), *Water, Air, & Soil Pollution*. 225, p. 2028.

65. TRAN, H.N., YOU, S.J. and CHAO, H.P. (2016) Thermodynamic parameters of cadmium adsorption onto orange peel calculated from various methods: a comparison study, *Journal of Environmental Chemical Engineering*. 4, pp. 2671-2682.

66. TRAN, H.N., YOU, S.J., HOSSEINI-BANDEGHARAEI, A. and CHAO, H.P. (2017) Mistakes and inconsistencies regarding adsorption of contaminants from aqueous solutions: a critical review, *Water Research*. 120, pp. 88-116.

67. VAN'T HOFF, J.H. (1884) *Études de dynamique chimique*, Frederik Muller & Co, Amsterdam.

68. VAN VINH, N., ZAFAR, M., BEHERA, S.K. and PARK, H.S. (2015) Arsenic (III) removal from aqueous solution by raw and zinc-loaded pine cone biochar: equilibrium, kinetics, and thermodynamics studies, *International Journal of Environmental Science and Technology*. 12, pp. 1283-1294.

69. VIEIRA, B. R. C., PINTOR, A. M. A., BAVENTURA, R. A. R., BOTELHO, C. M. S. and SANTOS, S. C. R. (2017) Arsenic removal from water using iron-coated seaweeds, *Journal of Environmental Management*. 192**,** pp. 224-233.

70. WANG, P. and LO, I.M. (2009) Synthesis of mesoporous magnetic γ-Fe_2O_3 and its application to Cr (VI) removal from contaminated water, *Water Research*. 43, pp. 3727-3734.

71. WANG, Y., WANG, X.J., LIU, M., WANG, X., WU, Z., YANG, L.Z., XIA, S.Q. and ZHAO, J.F. (2012) Cr (VI) removal from water using cobalt-coated bamboo charcoal prepared with microwave heating, *Industrial Crops and Products*. 39, pp. 81-88.

72. WANG, Z., ZHENG, H., LUO, Y., DENG, X., HERBERT, S. and XING, B. (2013) Characterization and influence of biochars on nitrous oxide emission from agricultural soil, *Environmental Pollution*. 174, pp. 289-296.

73. WEI, Z., WANG, Z., YAN, J., LIU, Y., WU, Y., FANG, Y., YU, L., CHENG, G., PAN, Z. and HU, G. (2019) Adsorption and oxidation of arsenic by two kinds of *β*-MnO_2. *Journal of Hazardous Materials*. 373, pp. 232-242.

74. WU, K., LIU, R., LI, T., LIU, H., PENG, J. and QU, J. (2013) Removal of arsenic(III) from aqueous solution using a low-cost by-product in Fe-removal plants—Fe-based backwashing sludge, *Chemical Engineering Journal*. 226, pp. 393-401.

75. YOON, Y., ZHENG, M., AHN, Y.T., PARK, W.K., YANG, W.S. and KANG, J.W. (2017) Synthesis of magnetite/non-oxidative graphene composites and their application for arsenic removal, *Separation and Purification Technology*. 178, pp. 40-48.

76. YU, X., TONG, S., GE, M., ZUO, J., CAO, C. and SONG, W. (2013) One-step synthesis of magnetic composites of cellulose@ iron oxide nanoparticles for arsenic removal, *Journal of Materials Chemistry A*. 1, pp. 959-965.

77. ZHANG, S.H., WU, M.F., TANG, T.T., XING, Q.J., PENG, C.Q., LI, F., LIU, H., LUO, X.B., ZOU, J.P., MIN, X.B. and LUO, J.M. (2018) Mechanism investigation of anoxic Cr (VI) removal by nano zero-valent iron based on XPS analysis in time scale, *Chemical Engineering Journal*. 335, pp. 945-953.

78. ZHAO, D., GAO, X., WU, C., XIE, R., FENG, S. and CHEN, C. (2016) Facile preparation of amino functionalized graphene oxide decorated with Fe_3O_4 nanoparticles for the adsorption of Cr(VI), *Applied Surface Science*. 384, pp .1-9.

79. ZHENG, Q., HOU, J., HARTLEY, W., REN, L., WANG, M., TU, S. and TAN, W. (2020) As (III) adsorption on Fe-Mn binary oxides: Are Fe and Mn oxides synergistic or antagonistic for arsenic removal?, *Chemical Engineering Journal*. 389, pp. 124470.

80. ZHOU, S., WANG, D., SUN, H., CHEN, J., WU, S. and NA, P. (2014) Synthesis, characterization, and adsorptive properties of magnetic cellulose nanocomposites for arsenic removal, *Water, Air, & Soil Pollution*. (225, pp. 1945.

CHAPTER 7

7 CONCLUSION AND RECOMMENDATIONS

The chapter entails the conclusion of the findings of the investigation and the recommendations for future research work.

7.1 CONCLUSION

A novel nanostructured ternary MFC metal oxide composite was synthesized from manganese, iron and copper salts via facile co-precipitation. The optimization of the adsorbent synthesis working parameters was determined using central composite design of the response surface methodology. The spectroscopic microstructural analysis of the ternary MFC metal oxide nanocomposite revealed the presence of porous mixed metal oxides with surface hydroxyl groups.

The MFC nanocomposite was successfully applied for Cr(VI) and As(III) adsorption from contaminated water. The adsorption of Cr(VI) onto the MFC nanocomposite was dependent on pH with maximum capacity at pH 3. The adsorption kinetic data was best fitted to the pseudo-second-order model (R^2 = 0.9814-0.9977) and was controlled by film and pore diffusion processes at different stages of the adsorption. The Langmuir (R^2 = 0.9979-0.9993) and Freundlich (R^2 = 0.9617-0.9791) adsorption isotherms described adsorbate surface coverage, and the D-R (R^2 = 0.9595-0.9891) isotherm showed that the adsorption was physical with mean energy values between 4.307-6.030 kJ/mol. The ternary MFC metal oxide showed superior adsorption capabilities over the binary MC and MF metal oxides. At equilibrium, the Langmuir adsorption capacities (q_m) at pH 3 were 168.71, 142.16 and 131.08 mg/g for the ternary MFC, binary MF and MC metal oxide nanocomposites, respectively. The computed thermodynamic parameters showed that the adsorption of Cr(VI) onto the MFC nanocomposite was spontaneous, feasible ($\Delta G°$ = -25.870-(-26.676) kJ/mol), exothermic ($\Delta H°$ = -13.603 kJ/mol) and increased randomness ($\Delta S°$ = +40.859 J/mol/K) at the solid-liquid interface. The uptake of Cr(VI) involved the formation of outer-sphere surface complexes through electrostatic interactions. A part of the Cr(VI) was reduced to Cr(III) and microprecipitated on the MFC nanocomposite surface. The analysis of FTIR and XPS spectra revealed that the dominant $HCrO_4^-$ anion of Cr(VI) at pH 3 interacted with the nanocomposite surface hydroxyl groups

during the adsorption process. The adsorption was sensitive to changes in ionic strength and the presence of naturally occurring anions in the environment (Cl^-, SO_4^{2-}, PO_4^{3-} and CO_3^{2-}). The nanocomposite metal oxide adsorbents underwent five successive adsorption/desorption cycles with 0.1 mol/dm^3 NaOH as eluent. The adsorption capacities decreased from 63.78-59.81 mg/g (3.97 % decrease) for the ternary MFC nanometal oxide. For the binary MC nanometal oxide, the Cr(VI) adsorption capacities decreased from 47.89-43.91 mg/g (8.31 % decrease) and the capacities decreased from 51.99-45.76 mg/g (11.98 % decrease) for the binary MF nanometal oxide. The ternary MFC metal oxide nanocomposite exhibited enhanced stability after five successive adsorption/desorption cycles than the binary MC and MF metal oxide nanocomposites.

The adsorption of As(III) onto the MFC metal oxide nanocomposite was pH-dependent with maximum adsorption capacity at pH 9. The pseudo-second-order (R^2 = 0.9913-0.9967) kinetic equation was better able to describe the adsorption kinetic data than the pseudo-first-order (R^2 = 0.9283-0.9615) and Elovich (R^2 = 0.9617-0.9879) kinetic rate equations. The precise non-conformity of the kinetic diffusion data to either film or pore diffusion showed that a chemical reaction was part of the dominant pathway in the As(III) adsorption mechanism. The experimental adsorption equilibrium data was best fitted to the Langmuir (R^2 = 0.9913-0.9967) isotherm. The D-R isotherm showed that the adsorption was chemical with mean energy values between 6.433-8.533 kJ/mol. The Langmuir adsorption capacities (q_m) at pH 9 were 31.67, 22.02 and 18.39 mg/g for the ternary MFC, binary MF and MC metal oxide nanocomposites, respectively, showing the superior As(III) adsorption capability of the ternary metal oxide system. The calculated thermodynamic parameters showed that the adsorption of As(III) onto the ternary MFC metal oxide nanocomposite was spontaneous, feasible ($\Delta G°$ = -21.617-(-24.181) kJ/mol), endothermic ($\Delta H°$ = +15.463 kJ/mol) and increased randomness ($\Delta S°$ = +124.652 J/mol/K) at the solid-liquid interface. A part of the As(III) was oxidised to As(V) on the nanocomposite surface. The uptake of As(III) and As(V) occurred through specific inner-sphere ligand exchange reactions. The analysis of XPS and FTIR spectroscopic data before and after the adsorption of As(III) showed that the hydroxyl groups on the dominant species of As(III) and As(V) at pH 9 interacted with the nanocomposite surface hydroxyl groups during the adsorption process. The adsorption was insensitive to changes in ionic strength but the presence of Cl^-, SO_4^{2-}, PO_4^{3-} and CO_3^{2-} anions. After five successive adsorption/desorption cycles with 0.1 mol/dm^3 NaOH eluent, the adsorption capacities decreased from 33.78-30.81

mg/g (8.79 % decrease) for the ternary MFC nanometal oxide, from 25.89-19.91 mg/g (23.09 % decrease) for the binary MC nanometal oxide and from 23.99-18.76 mg/g (21.80 % decrease) for the binary MF nanometal oxide. This showed enhanced stability of the ternary MFC metal oxide nanocomposite over the binary MC and MF metal oxide nanocomposites after five successive adsorption/desorption cycles.

The MFC trimetal oxide system was co-precipitated onto biochar support synthesized from pine cone powder which is an agro-waste product in the paper and pulp industry. The raw biochar showed low selectivity and affinity for Cr(VI) and As(III) species in solution. This made it a good candidate to act as support for the MFC trimetal oxide system as it did not interfere with the sequestration pathways of Cr(VI) and As(III). The biochar support reduced aggregation or agglomeration of the MFC nanoparticles and facilitated ease of adsorbent removal from the treated effluent. The fabricated MFC-biochar (MFCb) composite showed stability after five adsorption/desorption cycles.

7.2 RECOMMENDATIONS FOR FUTURE WORK

This investigation showed the enhanced selectivity, superior adsorption capabilities and sequestration pathways of Cr(VI) and As(III) from simulated single-solute systems onto the ternary MFC metal oxide nanocomposite. The following recommendations were proposed for future research work:

- Application of the novel ternary MFC metal oxide nanocomposite in the sequestration of Cr(VI) and As(III) from simulated binary-solute systems.
- Application of the ternary MFC nanometal oxide for the adsorption of organics and dyes.
- To study the application of the ternary MFC metal oxide nanocomposite in continuous or flow-through systems using real industrial/municipal wastewater samples.
- Upscaling of the adsorption system to treat large volumes of effluent.